

Proceedings of the
European Navigation Conference 2018
(ENC 2018)
Abstracts and Technical Papers

May 2018

edited by J. Johansson and G. Elgered



CHALMERS

RI
SE

LANTMÄTERIET



IEEE
Advancing Technology
for Humanity



**Proceedings of the European Navigation Conference 2018
ENC 2018**

Abstracts and Technical Papers

edited by

Jan Johansson and Gunnar Elgered

Chalmers University of Technology
Gothenburg, Sweden

The authors are responsible for the content of their papers.
The use of the contents has to follow the laws of copyright and ownership.

ISBN 978-91-88041-14-2

Preface — Welcome to Sweden

On behalf of the Swedish Board of Radio Navigation, RISE Research Institutes of Sweden, Lantmäteriet (The National Mapping, Cadastral and Land Registration Authority) and Chalmers University of Technology, it is my pleasure to welcome all of you to the European Navigation Conference—ENC 2018. This annual conference is organised under the umbrella of the European Group of Institutes of Navigation (EUGIN). ENC 2018 is the twenty-sixth conference in the series, and the first one in Sweden. The European Navigation Conference is the premier conference in Europe in the fields of positioning, navigation and timing. It will showcase state-of-the art and innovations in the field of terrestrial and satellite-based navigation and its applications. The conference comprises technical sessions, a poster session, invited keynotes, and a best paper award. Following ENC 2016 and 2017 our Scientific Committee has continued the cooperation with the Aerospace and Electronic Systems Society of IEEE. Papers in the scientific track have been reviewed by peers and will be published in the IEEE Xplore database. The abstract review procedure holds for the technical track contributions with publication in the conference digital programme. Even though the scientific and technical agenda dominates the conference, hopefully, you will have some time also to discover the city of Gothenburg and the surroundings at the West Coast of Sweden. A success of the ENC depends on the dedication of the Organising Committee, authors, exhibitors, sponsor and participants. I wish to express my thanks to all of you and hope that you will have fruitful and memorable days in Gothenburg, Sweden.

Jan Johansson

ENC 2018 General Chair



Participants in front of the conference venue during the lunch break on Tuesday May 15

ENC 2018 organising committees

Local Organising Committee (LOC)

Jan Johansson, Chalmers and RISE — General Conference Chair

Gunnar Elgered, Chalmers — Technical Programme Chair

Mikael Hägg, RISE

Peter Wiklund, The National Mapping, Cadastral and Land Registration Authority

Mikael Lilje, The National Mapping, Cadastral and Land Registration Authority

Per Olof Hedekvist, RISE — Exhibition Manager

Anna Axelsson, RISE

Lars Ulander, IEEE-AESS

Special thanks to *Ewa Bråthe* and *Petra Wernisch* at MEETX for the help with registration and hotel reservations, and to *Pernilla Bylund* at Chalmerskonferens for the help with exhibition and local arrangements at the venue.

Technical Programme Committee and Reviewers

Sten Bergstrand, RISE
Edward Breeuwer, ESA
Anders Carlström, RUAG
Erik Dierikx, VSL
Gunnar Elgered, Chalmers
Ragne Emardson, RISE
Cristofer Englund, RISE
Ignacio Fernández Hernández,
European Commission
Börje Forsell, NTNU
Salvatore Gaglione,
Parthenope University of Naples
Alain Geiger, ETH Zurich
Pierre-Yves Gilleron, EPFL
Jon Glenn Gjevestad, NTNU
Rüdiger Haas, Chalmers
Jörg Hahn, ESA
Harald Hauglin, JV
Per-Olof Hedekvist, RISE
Gunnar Hedling, Lantmäteriet
Manuel Hernández-Pajares,
Universitat Politcnica de Catalunya
Thomas Hobiger, Chalmers
Martin Håkansson, Lantmäteriet
Kenneth Jaldehag, RISE
Per Jarlemark, RISE
Anna B.O. Jensen, KTH
Jan Johansson, Chalmers
Martin Johansson, ESA
Bo Jonsson, BNB Consulting

Martti Kirkko-Jaakkola, FGI
Norvald Kjerstad, NTNU
Heidi Kuusniemi, NLS
Gérard Lachapelle, University of Calgary
Martin Lidberg, Lantmäteriet
Elena Simona Lohan, TUT
Scott MacKinnon, Chalmers
Tor Melgaard, Fugro
Bertrand Merminod, EPFL
Tong Ning, Lantmäteriet
Stefan Nord, RISE
Thomas Porathe, NTNU
Roberto Prieto Cerdeira, ESA
Carsten Rieck, RISE
Chris Rizos, UNSW
Laura Ruotsalainen, FGI
Patrik Sandin, RUAG
Steffen Schön, University of Hannover
Isaac Skog, Linköping Universitet
Simo Särkkä, Aalto / IndoorAtlas
Stefan Söderholm, FGI
Sarang Thombre, FGI
Javier Ventura Traveset, ESA
Sandra Verhagen, TU Delft
Martin Vermeer, Aalto
Johan Vium Andersson, WSP
René Warnant, University of Liege
Tom Willems, Septentrio
Henk Wymeersch, Chalmers
Ola Øvstedal, NMBU

Program and Table of Content

Opening Session (plenary, PL1)

Date & Time: Tuesday, May 15, 2018 (9:00–10:30)

Chair: *J. Johansson*, Chalmers University of Technology

Jan Petter Hansen, Head of Department Space, Earth and Environment,
Chalmers University of Technology

Pia Sandvik, CEO, RISE Research Institutes of Sweden

Mikael Lilje, Head of Department, Lantmäteriet, Sweden

Hamid Zarghampour, Chief Strategist, Swedish Transport Administration

Paul Flament, Head of Department, European Commission

Bertrand Merminod, President of EUGIN, École Polytechnique Fédérale de Lausanne

Jan Johansson, ENC 2018 General Chair, Chalmers University of Technology

GNSS Panel (plenary, PL2)

Date & Time: Tuesday, May 15, 2018 (11:00–12:30)

Chair: *C. Rizos*, University of New South Wales

Representatives for Galileo, Glonass, Beidou, GPS, QZSS and IRNSS-GAGAN

Galileo Innovations (plenary, PL3)

Date & Time: Tuesday, May 15, 2018 (13:30–15:00)

Chair: *G. Lachapelle*, University of Calgary

Galileo evolution

Eric Guyader, European Commission

Market and R&D opportunities with Galileo

Justyna Redelkiewicz, European GNSS Agency

European Navigation Plan

Joaquim Fortuny-Guasch, European Commission

Galileo 2nd generation — R&D phase

Martin Johansson, European Space Agency

GNSS Signals & Signal Processing (A1)

Date & Time: Tuesday, May 15, 2018 (15:30–17:00)

Chair: *S. Verhagen*, Delft University

15:30 Galileo Service Operations Monitoring	1
Technical paper	
<i>H. Denks, A. Salonico</i>	
Spaceopal gmbH, Germany; Spaceopal gmbH, Italy	
15:48 GNSS Core Technologies Enabling Application Dependability: the FANTASTIC Project	3
Technical paper	
<i>M. Pini¹, B. Bougard², W. De Wilde², G. Seco Granados³, D. Egea-Roca³, D. Calle⁴, A. Popugaev⁵</i>	
¹ Istituto Superiore Mario Boella, Italy; ² Septentrio S.A, Belgium;	
³ Universitat Autònoma de Barcelona, Spain; ⁴ GMV, Spain;	
⁵ Fraunhofer Institute for Integrated Circuits, Germany	
16:06 Minimum Detectable Velocity Based on GNSS Doppler Phase Observables	5
IEEE Scientific paper	
<i>R. Hohensinn, A. Geiger, M. Meindl</i>	
ETH Zürich, Switzerland	
16:24 A Comparison Between Resistant GNSS Positioning Techniques in Harsh Environment	6
IEEE Scientific paper	
<i>A. Angrisano¹, S. Gaglione², A. Maratea²</i>	
¹ Università telematica Giustino Fortunato, Italy;	
² Università degli Studi di Napoli Parthenope, Italy	
16:42 Galileo E1/E5 Measurement Monitoring — Theory, Testing and Analysis	7
IEEE Scientific paper	
<i>A. Pirsiavash, A. Broumandan, G. Lachapelle, K. O’Keefe</i>	
University of Calgary, Canada	

Navigation Augmentation & Communication (A2)

Date & Time: Tuesday, May 15, 2018 (15:30–17:00)

Chair: *H. Rohling*, Technical University Hamburg-Harburg

15:30 The IGSO SBAS: Signal Availability in the Polar Regions8

Technical paper

T. Sakai, M. Kitamura, T. Aso

National Institute of Maritime, Port and Aviation Technology, Japan

15:48 EDAS (EGNOS Data Access Service): Differential GPS Corrections Performance Test with State-of-the-Art Precision Agriculture System10

Technical paper

J. Vázquez¹, E. Lacarra¹, M. Sánchez¹, J. Rioja², J. Bruzua²

¹ESSP-SAS, Spain;

²Topcon Agriculture, Spain

16:06 A Global Navigation Augmentation System Based on LEO Communication Constellation21

IEEE Scientific paper

Y. Meng¹, L. Bian¹, L. Han², W. Lei¹, T. Yan¹, M. He³, X. Li⁴

¹China Academy of Space Technology, China;

²Academy of Space Electronic Information Technology, China;

³China Great Wall Industry Corporation, China;

⁴Wuhan University, China

16:24 Satellite Based Navigation in Iceland22

Technical paper

S. Thorsteinsson¹, T. Palsson², G. Sigurdsson³

¹University of Iceland, Iceland;

²Reykjavik University, Iceland;

³Icelandic Road and Coastal Administration, Iceland

16:42 Up-to-Date SBAS DFMC Service Volume Prototype (DSVP) to Support DFMC Performance Characterization Activities27

IEEE Scientific paper

D. Salos¹, J. Vuillaume¹, A. Kanj², F. Dufour², N. Suard², C. Boulanger²

¹Egis, France;

²CNES, France

Multi-Sensor Systems (plenary, PL4)

Date & Time: Wednesday, May 16, 2018 (9:00–10:30)

Chair: *B. Merminod*, École Polytechnique Fédérale de Lausanne

09:00 **Keynote 1:**

**Will Tomorrow’s GNSS Capability Be Good Enough for New
Market Demands?** **28**

Abstract

Chris Rizos

University of New South Wales

09:45 **Keynote 2:**

Cognizant Autonomous Vehicles: Opportunities and Challenges . . . **29**

Abstract

Zak Kassas

University of California, Riverside

Autonomous Vehicles (B1)

Date & Time: Wednesday, May 16, 2018 (11:00–12:30)

Chair: *S. Nord*, RISE Research Institutes of Sweden AB

- 11:00 **Robust Radio Localization with FLIP** **30**
IEEE Scientific paper
R. Müllner, T. Burgess
indoo.rs GmbH, Austria
- 11:18 **TAPAS - Testbed in Aarhus for Precision Positioning
and Autonomous Systems** **31**
Technical paper
*C. Jepsen¹, M. Grøntved¹, B. Rosenkranz¹, P. Nielsen¹, P. Thomsen²,
L. Stenseng², T. Durgonics²*
¹Danish Agency for Data Supply and Efficiency, Denmark;
²Danish Technical University, Denmark
- 11:36 **GNSS for Taximeter Verification and Calibration of Road
Segments** **33**
Technical paper
H. Hauglin¹, R. Hughes¹, A. Gård², J. Holmen¹, H. Skjolden¹, H. Karlsson¹
¹Norwegian Metrology Service, Norway;
²Norwegian University of Science and Technology, Norway
- 11:54 **VDM-Based UAV Attitude Determination in Absence
of IMU Data** **35**
IEEE Scientific paper
M. Khaghani, J. Skaloud
École Polytechnique Fédérale de Lausanne, Switzerland
- 12:12 **Automated Exploration with Multi-Sensor
Equipped UAV/UGV** **36**
Technical paper
S. Batzdorfer, M. Becker, M. Bobbe, U. Bestmann
Technische Universität Braunschweig, Institute of Flight Guidance, Germany

Aerospace & Atmosphere (B2)

Date & Time: Wednesday, May 16, 2018 (11:00–12:30)

Chair: *R. Haas*, Chalmers University of Technology

11:00 **Effects of a X9.3-Class Solar Flare on EGNOS Performance** **45**

Technical paper

P. Pintor, C. Paparini, J. Rupiewicz, R. Chaggara

ESSP-SAS, Spain; ESSP-SAS, France

11:18 **GRAS-2 Next Generation of Radio Occultation Instrument** **47**

Technical paper

T. Liljegren, A. Carlström, J. Christensen

RUAG Space AB, Sweden

11:36 **Software Defined Radio for Ground and Airborne GNSS Reflectometry** **49**

Technical paper

T. Hobiger¹, J. Strandberg¹, R. Gähwiler², R. Haas¹

¹Chalmers University of Technology, Sweden;

²Tallinn University of Technology, Estonia

11:54 **Ionosphere Prediction Service for GNSS Applications** **51**

Technical paper

R. Ronchini¹, F. Rodriguez¹, S. Di Rollo¹, E. Guyader²

¹Telespazio, Italy;

²European Commission, Belgium

12:12 **Metre-Wave Synthetic Aperture Radar the Practical Application for Precise Point Positioning** **59**

Technical paper

J. Arvidsson¹, P. Dammert¹, A. Åhlander¹, T. Hobiger²

¹Saab AB, Sweden;

²Chalmers University of Technology, Sweden

GNSS Interference, Monitoring & Mitigation (C1)

Date & Time: Wednesday, May 16, 2018 (13:30–15:00)

Chair: *B. Forsell*, Norwegian University of Science and Technology

13:30 Sub-Band Robust GNSS Signal Processing for Jamming Mitigation	61
IEEE Scientific paper	
<i>D. Borio</i>	
European Commission, Joint Research Centre, Italy	
13:48 Classification of Spoofing Attack Types	62
IEEE Scientific paper	
<i>J. van der Merwe, X. Zubizarreta, I. Lukcin, A. Rügamer, W. Felber</i>	
Fraunhofer Institute for Integrated Circuits, Germany	
14:06 Collaborative Integrity Monitoring Solution Based on Majority Voting for Critical Applications	63
Technical paper	
<i>P. Brocard, L. Montloin</i>	
Airbus Defence and Space, France	
14:24 Design and Development of a Software for Performance Comparison of GNSS Signal Interference Detection and Analysis Algorithms	74
Technical paper	
<i>M. Shahzaib¹, F. Khan², J. Tian¹</i>	
¹ Beihang University, China;	
² SUPARCO, Pakistan	
14:42 Standardization of GNSS Threat Reporting and Receiver Testing Through International Knowledge Exchange, Experimentation and Exploitation [STRIKE3]: Validation of Reporting and Testing Standards	77
Technical paper	
<i>M. Pattinson¹, M. Dumville¹, D. Fryganiotis¹, Z. Bhuiyan², S. Thombre², G. Ferrara², M. Alexandersson³, E. Axel³, P. Eliardsson³, M. Pölöskey⁴, V. Manikundalam⁵, S. Lee⁶, J. Reyes Gonzalez⁷</i>	
¹ Nottingham Scientific Ltd, United Kingdom;	
² Finnish Geospatial Research Institute, National Land Survey of Finland, Finland;	
³ Swedish Defence Research Agency, Sweden;	
⁴ AGIT mbH, Germany;	
⁵ GNSS labs, India;	
⁶ ETRI, Korea;	
⁷ European GNSS Agency, Czech Rep.;	

GNSS Orbits & Reference Frame (C2)

Date & Time: Wednesday, May 16, 2018 (13:30–15:00)

Chair: *P. Wiklund*, Lantmäteriet, Sweden

- 13:30 **Multi-GNSS Measurement Campaign in Southeast Asia Using the MGSE-System** **79**
IEEE Scientific paper
A. Rügamer¹, D. Seybold²
¹Fraunhofer Institute for Integrated Circuits, Germany;
²TeleOrbit GmbH, Germany
- 13:48 **Lunar Module Navigation Using Visual Based Absolute Navigation and Direct Sparse Odometry** **80**
Technical paper
P. Hsu, C. Chu, K. Chiang, S. Jan, S. Jheng, Y. Hsieh, Y. Tsai, Y. Tien
National Cheng Kung University, Taiwan
- 14:06 **Improvement of GPS and BeiDou Extended Orbit Predictions with CNNs** **82**
IEEE Scientific paper
J. Pihlajasalo, H. Leppäkoski, S. Ali-Löytty, R. Piché
Tampere University of Technology, Finland
- 14:24 **VLBI with GNSS Signals on Intercontinental Baselines** **83**
Technical paper
R. Haas¹, T. Hobiger¹, G. Klopotek¹, J. Yang¹, L. Combrinck², A. de Witt², M. Nickola², E. Skurikhina³, A. Mikhailov³
¹Chalmers University of Technology, Sweden;
²Hartebeesthoek Radio Astronomy Observatory, South Africa;
³Institute of Applied Astronomy of the Russian Academy of Sciences, Russia
- 14:42 **EUREF and the Infrastructure for High Performance GNSS Applications in Europe** **85**
Technical paper or abstract
M. Lidberg¹, C. Bruyninx², A. Kenyeres³, M. Poutanen³, W. Söhne²
¹Lantmäteriet, Sweden;
²Royal Observatory of Belgium, Belgium;
³BFKH FTFF Satellite Observatory, Hungary;
⁴Finnish Geospatial Research Institute, Finland;
⁵Bundesamt für Kartographie und Geodäsie, Germany

Multi-Sensor Systems (plenary, PL5)

Date & Time: Wednesday, May 16, 2018 (15:30–17:30)

Chair: *Zak Kassas*, University of California, Riverside

15:30 AstaZero Active Safety and Automated Driving	
Proving Ground	87
Abstract	
<i>M. Ringvik</i>	
AstaZero AB, Sweden	
15:50 H2020 PRoPART project presentation — Precise and Robust	
Positioning for Automated Road Transports	88
Abstract	
<i>S. Nord</i>	
RISE Research Institutes of Sweden	
16:10 GNSS for automation of heavy vehicles — challenges	
and opportunities	89
Abstract	
<i>J. Hammenstedt</i>	
AB Volvo — Vehicle Automation, Sweden	
16:30 Efficient distribution of GNSS correction data via cellular	
networks, ongoing work in 3GPP	90
Abstract	
<i>F. Gunnarsson</i>	
Ericsson Research	
16:50 High accuracy GNSS for autonomous platforms	91
Abstract	
<i>J. Tidd</i>	
Waysure Sweden AB	
17:10 Location system performance requirements in the T-pod,	
a level 4 self-driving vehicle	92
Abstract	
<i>T. Ohlson</i>	
Einride	

Maritime Navigation (plenary, PL6)

Date & Time: Thursday, May 17, 2018 (9:00–10:15)

Chair: *Mikael Hägg*, RISE Research Institutes of Sweden

09:00 Keynote 3:

The Resilience of Maritime Navigation and Positioning **93**

Abstract

P. Williams, C. Hargreaves, A. Grant, M. Bransby, N. Ward

General Lighthouse Authorities, United Kingdom

09:30 Keynote 4:

European Emergency Warning Service

Frédéric Doms

European Commission

10:00 Keynote 5:

Sea Traffic Management enhancing safety of navigation **94**

Abstract

M. Hägg¹, U. Siwe², F. Karlsson², A. Andersson²

¹Research Institute of Sweden, RISE;

²Swedish Maritime Administration

GNSS Signals, Multipath & Reflections (D1)

Date & Time: Thursday, May 17, 2018 (10:45–12:15)

Chair: *T. Hobiger*, Chalmers University of Technology

10:45 Study on Code Multipath Mitigation Technology for BDS-3 B2a Signal	96
IEEE Scientific paper	
<i>Y. Wang, W. Liu, J. Li, F. Wang</i>	
National University of Defense Technology, China	
11:03 Characterization of Range and Time Performance of Indoor GNSS Signals	97
IEEE Scientific paper	
<i>T. Marathe, A. Broumandan, A. Pirsiavash, G. Lachapelle</i>	
University of Calgary, Canada	
11:21 Isolation of the Effect of Snow and Ice to a GNSS Antenna in the Measurement Domain	98
Abstract	
<i>Y. Han, T. Fang, D. Kim</i>	
Korea Research Institute of Ships and Ocean Engineering, Korea	
11:39 Inverse Modeling of Reflected GNSS Signals for Measurement of the Environment	99
Technical paper	
<i>J. Strandberg, T. Hobiger, R. Haas</i>	
Chalmers University of Technology, Sweden	
11:57 Analysis of Receiver Performance Using GNSS Signal Generation Simulator in Multipath, High Maneuverability Environment	101
Technical paper	
<i>G. Jo, J. Lee, J. Noh, S. Lee, J. Kim</i>	
Chungnam National University, Korea	

Maritime Navigation (D2)

Date & Time: Thursday, May 17, 2018 (10:45–12:15)

Chair: *S. Gaskin*, Royal Institute of Navigation, UK

- 10:45 **SBAS Maritime Service: EGNOS Preliminary Performance**
Based on IMO Res. A.1046 (27) **109**
Technical paper
P. Pintor¹, C. De La Casa¹, M. Lopez², R. Roldan¹
¹ESSP-SAS, Spain;
²European GNSS Agency, Czech Republic
- 11:03 **Testing Multi-Network TDOA Algorithm with Kinematic Data** .. **111**
Technical paper
C. Gioia, D. Tarchi
European Commission, Joint Research Centre, Italy
- 11:21 **Distribution of Nautical Information, Positions Etc. Digitally**
Directly in to the Navigation System of a Sea Traffic
Management Equipped Ship or Rescue Unit **117**
Technical paper
F. Kokacka
Swedish Maritime Administration, Sweden
- 11:39 **Workload and Navigational Control: the Control Levels of**
COCOM As Framework for Ship Bridge HMI Design **119**
IEEE Scientific paper
T. Porathe
Norwegian University of Science and Technology, Norway
- 11:57 **Maritime Integrity Concept** **120**
Technical paper
C. Hargreaves, P. Williams
General Lighthouse Authorities, United Kingdom

Multi-Sensor Systems (E1)

Date & Time: Thursday, May 17, 2018 (13:00–14:30)

Chair: *M. Johansson*, European Space Agency

- 13:00 **Performance Evaluation of a Tightly Coupled GNSS/IMU
Integration Algorithm with Multi-Constellation/Multi-
Frequency GNSS** **128**
Technical paper or abstract
B. Reuper, M. Becker, S. Leinen
Technische Universität Darmstadt, Germany
- 13:18 **Simulation and Verification for New Generation BDS
Satellite Signals** **137**
Technical paper
Y. Wang, T. Yan
China Academy of Space Technology, China
- 13:36 **Precise Positioning with Android** **143**
Technical paper
M. Håkansson
Lantmäteriet / KTH Royal Institute of Technology, Sweden
- 13:54 **Modulation and Signal-Processing Tradeoffs for Reverse-GPS
Wildlife Localization Systems** **145**
IEEE Scientific paper
A. Leshchenko, S. Toledo
Tel-Aviv University, Israel
- 14:12 **SWEPOS — A National Infrastructure for 3-Dimensional
Positioning in Sweden** **146**
Abstract
P. Wiklund
Lantmäteriet, Sweden

Time & Frequency (E2)

Date & Time: Thursday, May 17, 2018 (13:00–14:30)

Chair: *P. O. Hedekvist*, RISE Research Institutes of Sweden

- 13:00 **Results of DEMETRA Time Integrity Service Tested on Galileo** **147**
Abstract
G. Signorile¹, I. Sesia¹, P. Tavella¹, P. Defraigne², F. Fiasca³, L. Galleani⁴
¹INRiM, Italy;
²Royal Observatory of Belgium, Belgium;
³Aizoon, Italy;
⁴Politecnico di Torino, Italy
- 13:18 **GNSS Time Interoperability Based on Broadcast Corrections** ... **148**
Technical paper
P. Bogdanov, A. Druzhin, T. Primakina
Russian Institute of Radionavigation and Time, Russia
- 13:36 **Study on Method of Laser Time and Frequency Transfer Between Satellite and Ground Station** **150**
IEEE Scientific paper
G. Wang, Y. Meng, L. Bian, Y. Yao, T. Yan, W. Lei
China Academy of Space Technology, China
- 13:54 **UTC(K) Time Distribution Using Network RTK** **151**
Technical paper
C. Rieck¹, P. Jarlemark¹, K. Jaldehag¹, G. Hedling², A. Frisk²
¹RISE Research Institutes of Sweden AB, Sweden;
²Lantmäteriet, Sweden
- 14:12 **A Robust Timing Service for Future EGNSS** **153**
Technical paper or abstract
H. Zelle¹, H. Veerman¹, K. Aarmo², J. Boyero², M. Kirkko-Jaakkola³, S. Honkala³, S. Söderholm³, S. Thombre⁴
¹Netherlands Aerospace Center, Netherlands;
²European Commission, Belgium;
³National Land Survey of Finland, Finland;
⁴Finnish Geospatial Research Institute, Finland;

Poster Session

Date & Time: Tuesday May 15 – Thursday, May 17, 2018

- GNSS Spoofing of Unmanned Aerial Vehicle with GNSS/INS
Integrated Navigation System 155**
Technical paper
L. Sun, W. Huang, Y. Zhou
National University of Defense Technology, China
- Autonomous and Autonomy of GNSS Constellations on the Age
of Intelligent 156**
Abstract
W. Huang, Y. Zhou, L. Sun
National University of Defense Technology, China
- GNSS ISL Based Navigation of Satellites in Geotransfer Orbits 157**
Abstract
Y. Zhou, W. Huang, L. Sun
National University of Defense Technology, China
- Development of a Real Time Kinematic Algorithm for Low-Cost
GNSS Receiver Use in Suburban Areas 158**
Abstract
S. Lin¹, F. Yu²
¹National Taiwan Ocean University, Taiwan;
²Minghsin University of Science and Technology, Taiwan
- A NLOS Reduction Architecture Embedded Navigation Algorithm
Based on LiDAR SLAM-Aided Ins/GNSS Integration System 159**
Technical paper
G. Tsai¹, K. Chiang¹, N. El-Sheimy²
¹National Cheng Kung University, Taiwan;
²University of Calgary, Taiwan
- Novel GPS Interference PDOA-Localization Method 161**
Technical paper
M. Nyström¹, R. Blay², D. Akos²
¹Luleå University of Technology, Sweden;
²University of Colorado Boulder, United States
- BDS Adjusted Box-Wing Physical Solar Radiation Pressure Model
Considering the Yaw Attitude 163**
Technical paper
X. Wang, K. Xi, Q. Zhao
Shanghai Astronomical Observatory, Chinese Academy of Sciences, China

Visual-Inertial Slam by Fusing Stereo and Inertial Measurement Units Based on Orb-Slam	167
Technical paper	
<i>Y. Sun, S. Jan</i>	
National Cheng Kung University, Taiwan	
Vision Based Navigation for Asteroid Explorer	169
Technical paper	
<i>Y. Hsieh, S. Jan, K. Chiang</i>	
National Cheng Kung University, Taiwan	
Estimation and Analysis of GPS Satellite DCB Using Regional GPS Network	171
Technical paper	
<i>D. Han, D. Kim, C. Kee</i>	
Seoul National University, Korea	
Motion Conflict Detection in the Smart Tachograph	176
IEEE Scientific paper	
<i>D. Borio, E. Cano, G. Baldini</i>	
European Commission, Joint Research Centre, Italy	
The Performance Analysis of Applying Differential Distance Correction in BLE-Based Indoor Positioning System	177
Technical paper	
<i>Y. Kuo, J. Liao, K. Chiang</i>	
National Cheng Kung University, Taiwan	
Analysis on the Performance Degradations of Maritime DGPS Reference Station by Radio Environment	179
Abstract	
<i>S. Park, S. Park, Y. Han</i>	
Korea Research Institute of Ships and Ocean Engineering, Korea	
Building High-Resolution Contact Networks Using WiFi Localization ..	180
Technical paper	
<i>C. Gioia, G. Strona, P. Beck, D. Tarchi</i>	
European Commission, Joint Research Centre, Italy	
Theoretical Performance Analysis and Comparison of VDFLL and Traditional FLL Tracking Loops	183
IEEE Scientific paper	
<i>N. Alam¹, J. Tian¹, F. Khan²</i>	
¹ Beihang University, China;	
² SUPARCO, Pakistan	

Inequality Test and Robust Estimation for Reliable Navigation	
Solution	184
Technical paper	
<i>C. Gioia</i>	
European Commission, Joint Research Centre, Italy	
A Direct Positioning Method for a Stand-Alone Global Navigation	
Satellite System (GNSS) Receiver	192
Technical paper	
<i>M. Khalaf-Allah</i>	
Chemnitz University of Technology, Germany	
Galileo Second Generation Improvements for the Everyday User	196
Abstract	
<i>P. Sandin</i>	
RUAG Space AB, Sweden	
Collaborative Error Estimation and Integrity Monitoring	
Algorithms for Critical Applications	198
Technical paper	
<i>L. Montloin, P. Brocard</i>	
Airbus Defence and Space, France	
High Precision Separation Method of Baseband Waveform for	
GNSS Signals	210
Technical paper	
<i>T. Yan, Y. Wang, X. Liu</i>	
China Academy of Space Technology, China	
GNSS Signals Simulation to Assess the Immunity of Navigation	
Equipment with Spatial Interference Cancellation	215
Technical paper	
<i>A. Kaverin, V. Logutov, S. Chernov</i>	
FSUE VNIIFTRI, Russia	
GNSS Performance Monitoring Platform	217
Technical paper	
<i>P. Casenove, J. Marchal, N. Suard</i>	
CNES, France	
GNSS-Based Earth's Center of Mass Motion Observation	219
Technical paper	
<i>N. Delong, A. Couhert, F. Mercier</i>	
CNES, France	

Small UAV's Attitude Estimation with Tightly Coupled Low-Cost GNSS/INS Integration Using Multiple GNSS Receivers	221
Technical paper	
<i>M. Farkas¹, S. Rozsa², B. Vanek¹</i>	
¹ Hungarian Academy of Sciences Institute for Computer Science and Control, Hungary;	
² Budapest University of Technology, Hungary	
Enhancing Robot Navigation Using Sensor Fusion and Fuzzy Kalman Filter for Obstacle Avoidance	224
Technical paper	
<i>A. Bassiri¹, M. Oskoei², A. Basiri³</i>	
¹ Qazvin Islamic Azad University, Iran;	
² Allameh Tabataba'i University, Iran;	
³ University College London, United Kingdom	
Design Analysis of a Hyperbolic Landing Navigation System for Aircraft	232
IEEE Scientific paper	
<i>T. Le, P. Makula, J. Bajer, M. Richterova</i>	
University of Defence, Czech Rep.	
Adaptive Carrier Tracking for Vehicular Communication Under High Dynamic Environment	233
Technical paper	
<i>J. Yin, R. Tiwari, M. Johnston</i>	
Newcastle University, United Kingdom	
Performance Analysis of BDS B1I Using the Augmentation Service Information of BDS	239
Technical paper	
<i>J. Noh¹, J. Lee¹, G. Jo¹, S. Lee¹, J. Lee²</i>	
¹ Chungnam National University, Korea;	
² Navcours, Korea	
R-Mode — Safe Navigation in the Baltic Sea	245
Technical paper	
<i>S. Gewies¹, C. Rieck², J. Bäckstedt³, P. Gustafson⁴</i>	
¹ German Aerospace Center, Germany;	
² RISE Research Institutes of Sweden AB, Sweden;	
³ Swedish Maritime Administration, Sweden;	
⁴ Gutec AB, Sweden	

GPS Multipath Mitigation Technique with Low Hardware Complexity	247
--	------------

Technical paper

J. Lee¹, J. Noh¹, G. Jo¹, S. Lee¹, C. Park²

¹Chungnam National University, Korea;

²Chungbuk National University, Korea

Using Smartphones for Positioning in a Multipath Environment	251
---	------------

Technical paper

S. Thorsteinsson¹, G. Sigurdsson²

¹University of Iceland, Iceland;

²Icelandic Road and Coastal Administration, Iceland

A Proposed Fault Detection and Exclusion Method Applied to Multi-GNSS Single-Frequency	253
---	------------

IEEE Scientific paper

A. Innac¹, S. Gaglione¹, S. Troisi¹, A. Angrisano²

¹Universit degli Studi di Napoli Parthenope, Italy;

²Universit telematica Giustino Fortunato, Italy

Closing Session (plenary, PL7)

Date & Time: Thursday, May 17, 2018 (14:30–15:00)

Chair: J. Johansson, Chalmers University of Technology

14:30 Introducing the European Navigation Conference 2019

Krzysztof Czaplewski

President of Polish Navigation Forum

14:45 Closing remarks ENC2018

Bertrand Merminod

President of EUGIN

Galileo service operations monitoring

Holmer Denks *, Antonio Salonic *

* Spaceopal GmbH Munich, Germany

holmer.denks@spaceopal.com

This abstract describes how Spaceopal GmbH, the Galileo Service Operator (GSOp), is routinely monitoring the service operations performance by means of Key Performance Indicators (KPI) and provides few examples of KPI trends to exemplarily show the applied mechanisms which will be updated for selected performance parameters in the presentation.

The first services offered by Galileo are available to the users since the European Commission Initial Services declaration occurred on 15th December 2016. The Galileo Service performance and Minimum Performance Levels (MPLs) targeted for the specific service are defined in the relevant Service Definition Document available in the Galileo Service Center web site (<https://www.gsc-europa.eu/>).

After a successful handover of the Galileo system and operations from the European Space Agency, Galileo Initial Services are managed by the European GNSS Agency (GSA).

Starting from 1st July 2017, Spaceopal GmbH, a joint venture founded by DLR Gesellschaft für Raumfahrtanwendungen (GfR) mbH and Telespazio S.p.A. (a Leonardo and Thales Company), is operating the Galileo satellite fleet under the Galileo Service Operator (GSOp) contract with the GSA ensuring seamless provision of the Galileo services to the worldwide community.

Quality monitoring of the GSOp service operations is performed by means of Key Performance Indicators (KPIs) and metrics which are routinely measured and reported every month to the European GNSS Agency.

These KPIs and metrics are grouped into two main categories:

- Transversal (Operations, Maintenance, User and Interfaces)
- Galileo Service related (Open Service, Public Regulated Service , Commercial Service)

All these KPIs are measured on a monthly basis based on various input data types.

The first half year under GSOP contract allowed collecting first experience with the KPI definitions, implementations and associated targets. A good KPI and its target value is designed such, that the fulfillment is possible when the operations are well executed. It shall be not imply wrong incentives nor shall it be trivial to be reached (in the latter case, the KPI will not provide any benefit to the program).

The following figure provides an example for a KPI measured within the given thresholds. However, the amplitude of the measurement is significant; a violation is deemed likely in case the lower level Subcontractor is not carefully controlling the associated maintenance activities. For this KPI no positive nor negative trend is observed but a relatively constant performance which is well in line with the Customer's expectations.

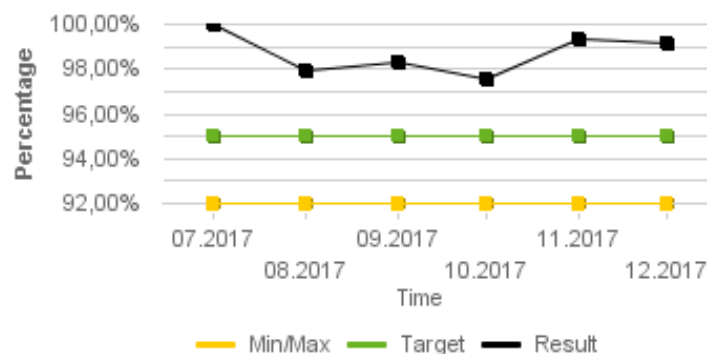


Fig. 1: Availability of GMS Navigation including planned outages

The Open Service and the Public Regulated Service KPIs are focused on navigation performance parameters in the ranging, timing and position domains. In particular they measure:

- Ranging availability and accuracy for both single frequency and dual frequency users
- UTC dissemination and Galileo System Time To GPS time Offset (GGTO) availability and accuracy
- Position accuracy and availability for both single frequency and dual frequency users

As shown in Fig. 2 these navigation KPIs are measured by KPI tools employed by Spaceopal starting from:

- the observation and navigation data collected by the Galileo Sensor Stations (GSS)
- the reference products generated by the Galileo Mission Segment located in Fucino (Abruzzo, Italy), the Time Service Provider and the Geodetic Reference Service Provider

In Fig. 3 the GGTO dissemination availability KPI is reported as an example: the availability was lower than 100% in September and October but always above the monthly target of 90%. The users were informed about the GGTO unavailability events with the relevant NAGU (Notice Advisory to Galileo Users).

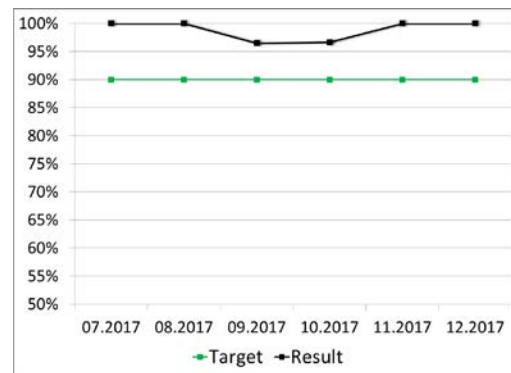


Fig. 3: Availability of GGTO Dissemination

Fig. 2: Computation of Navigation KPI Overview

The trend of the KPIs during the first analysis period shows a regular service provision which enabled Spaceopal to achieve the Galileo service operations performance levels.

Acknowledgments

We would like to thank the entire Spaceopal Industrial team and the European GNSS Agency (GSA) for their support and contribution to this abstract.

GNSS core technologies enabling application dependability: the FANTASTIC project

M. Pini, B. Bougard*, W. De Wilde*, G. Seco Granados#, D. Egea-Roca#, D. Calle\$, A. Popugaev+

Istituto Superiore Mario Boella, Torino, Italy, pini@ismb.it

*Septentrio, Leuven, Belgium

#Universitat Autònoma de Barcelona, Barcelona, Spain

\$GMV, Madrid, Spain

+Fraunhofer IIS, Erlangen, Germany

Summary

Professional applications based on Global Navigation Satellite Systems (GNSS) are getting a significant boost in terms of adoption and absolute performance, mainly driven by the growing number of satellites and signals. Furthermore, the wide use of correction services, like EGNOS, Precise Point Positioning (PPP), regional and nation-wide Real Time Kinematics (RTK) networks, offers sub-decimeter accuracy, with a continuously improved availability and reliability with respect to standalone GNSS.

Nevertheless, the number of applications posing stringent requirements, beyond the pure positioning accuracy, is high. Examples include the control of driverless machineries in precision farming (where the use of digital maps is not always possible), autonomous vehicles, and GNSS-based systems resilient to interference, to mention a few. Indeed, not only the position accuracy matters, but also the dependability is becoming of utmost importance. The term dependability indicates that users can have confidence in the GNSS technology, integrated into a mission-critical system. Dependability implies three dimensions: the availability of the Position Navigation and Time (PNT) data, its reliability and the associated security.

This paper will present the objectives, the main technological developments and the early results of the FANTASTIC project¹. FANTASTIC is the acronym of **F**ield **A**ware **N**avigation and **T**iming **A**uthentication **S**ensor for **T**iming **I**nfrastructure and **C**entimeter level positioning. It is funded by the European GNSS Agency (GSA), under the European Union's Fundamental Elements research and development program. The paper will firstly provide examples of unsolved problems, emerging in new GNSS-based applications in different market sectors. The improvements introduced by FANTASTIC, leveraging on specific features of the Galileo signals (i.e.: the E1 Open Service Navigation Message Authentication (OS-NMA) and the E6 Commercial Service (CS)) will then be investigated in the paper. It will also detail the high-level characteristics of the "field aware" antenna and the multi-frequency receiver under development, presenting early results of simulations and lab tests. Ways forward will be also commented, starting from the on-field demonstrations planned for the end of 2018.

Motivation of the work and early results

FANTASTIC addresses three specific applications: the paper will comment their needs, highlighting the performance enhancements expected at the end of the project.

1. Trusted GNSS receiver for timing applications. Under proper working conditions and configurations, a GNSS receiver can achieve the same performance of atomic clocks, but at a lower cost. For this reason, GNSS is the timing source for the synchronization of networks used in mobile communications, energy distribution and finance, and has been recently defined as "the backbone of the connected world"². However, natural radio propagation impairments or, far more, Radio Frequency (RF) interference can disrupt the signal integrity, undermining the receivers' performance and limiting the system reliability at the user's level. Leveraging on this vulnerability, RF attacks of intentional nature, known in the specialized literature as jamming or spoofing, are a reality, and the panorama is expected to worsen³.

¹ <http://gnss-fantastic.eu/>

² Jones, S., "GPS pioneer warns on network's security," Financial Times, February 13, 2014.

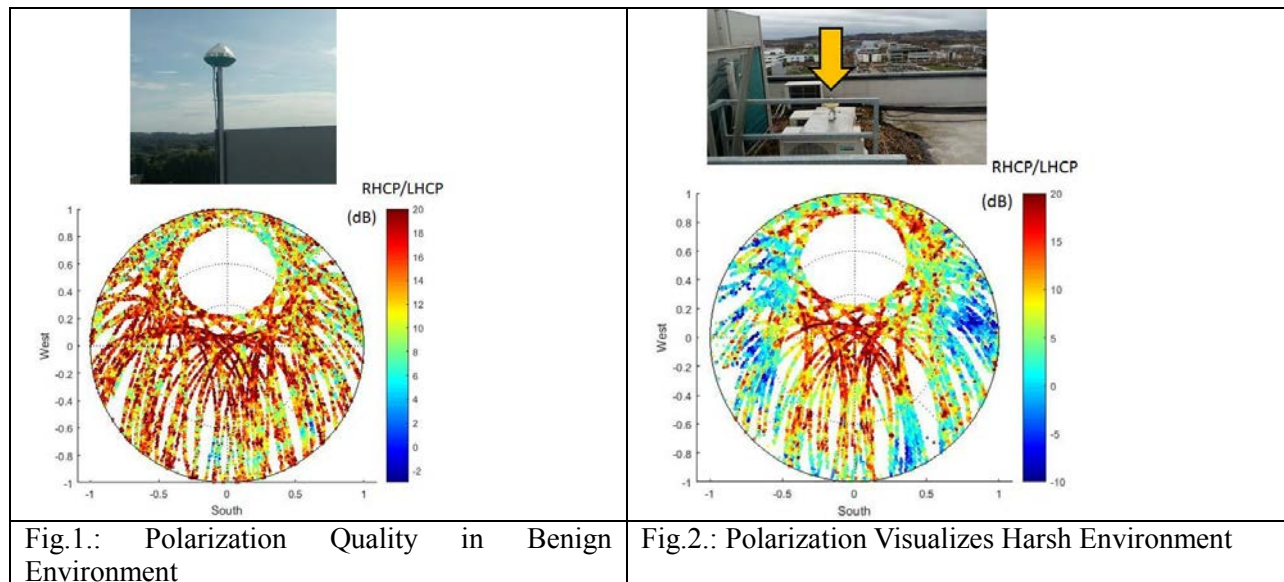
³ D. Margaria and M. Pini, "The Spoofing Menace," Chapter 3 in GNSS Interference Threats and Countermeasures, edited by F. Dovis, Artech House, ISBN: 978-1-60807-810-3, January 2015

2. Commercial Service based precise positioning. PPP is the preferred positioning technique in many systems deployed at locations, in which the setting up of RTK reference stations is impossible or undesirable. The operative scenarios cannot be always considered open sky. Indeed, in marine constructions, cranes, masts and other obstacles cause obstructions and multipath reflections. PPP corrections are broadcasted over the L-band channel of the satellite networks like Inmarsat, but the geostationary nature of these satellites results in the unavailability of service at high latitudes (i.e.: off-shore applications in Canadian Arctic) and in the high sensitivity to shadowing of the signal by surrounding objects at moderate latitudes.

3. Machine control for construction and precision farming. Phase based positioning is the technology currently used for controlling machines in large constructions (e.g.: digging works) and in precision farming (e.g.: plant crops alternatingly, automatic tractors guide). RTK positioning is the most common positioning technique to achieve the accuracy requirements for these applications. It relies on GNSS carrier phase measurements, which should have errors of less than 10% of a 20-cm wavelength and avoid cycle slips. However, some new emerging applications pose requirements not yet achieved by current state-of-the-art RTK GNSS receivers (e.g. reliable positioning under tree canopy and in urban canyons).

Motivated by the open problems summarized above, FANTASTIC develops innovative core technologies. To tackle the effects of intentional interference, the team works towards a secure commercial product, implementing time authentication based on the Galileo E1 OS-NMA and spoofing monitoring algorithms that processes both the RHCP and LHCP signal components. As far as the precise positioning is concerned, the innovations introduced by FANTASTIC are based on the tracking, demodulation and processing of the new Galileo E6 CS signals. Indeed, the high accuracy service offered by Galileo on the E6 band is expected to overcome limitations at high latitudes and solve signal shadowing conditions, being based on orbiting satellites, evenly scattered in the sky. Finally, the improvement of the RTK processing will be demonstrated in harsh environments, where the received signal is likely to be corrupted by obstacles and foliage. To enhance robustness, the work focuses on a dual polarized multi-band antenna, a new strategy to combine inertial measurement unit (IMU) and GNSS measurements and on interference mitigation algorithms. As an example, the figures below show the results of an early test carried out to analyze the performance of the new dual polarized antenna. They show the ratio of the desired RHCP signal component to the spurious LHCP component in a polar azimuth-elevation plot. This was done in a benign environment (left) and harsh environment (right). The figures are based on continuous tracking of both polarizations from two frequencies of all GPS, GLONASS, GALILEO and BeiDou satellites in view. The antenna has excellent cross-polar ratio in open sky environments and clearly detects signals which have been corrupted by diffraction and reflections.

Figures



Minimum Detectable Velocity Based on GNSS Doppler Phase Observables

Roland Hohensinn, Alain Geiger and Michael Meindl
Institute for Geodesy and Photogrammetry
ETH Zurich, Switzerland
Email: rolandh@ethz.ch

Abstract—A focus of the Institute for Geodesy and Photogrammetry (IGP) lies on the GNSS data processing for the monitoring of slope movements in high Alpine regions in the Swiss Alps. Thawing of permafrost areas (e.g. rock glaciers) can cause threats for humans and infrastructure. In order to bridge the gap from monitoring in post-processing to early warning in real-time, the IGP is developing and testing algorithms for the instant detection of hazardous slope movements by means of estimates of the instantaneous station velocity based on GNSS Doppler phase observations. This paper focuses on the derivation of a *Minimum Detectable Velocity (MDV)* for this method. Experimental tests reveal that depending on the sampling interval velocities down to the mm/s-level can be detected. Simulations of the MDV based on static GNSS measurements reveal that it can even be possible to detect movements at the sub-mm/s level. Advantages of this method are the 'standalone' solution and the real-time provision of movement information. It thus will strongly contribute to a landslide early warning system.

Full paper in IEEE Xplore

A comparison between resistant GNSS positioning techniques in harsh environment

Antonio Angrisano
Giustino Fortunato University
Benevento, Italy

Salvatore Gaglione, Antonio Maratea
Parthenope University
Napoli, Italy

Abstract—Environments as urban areas are critical for GNSS, because several obstacles block, attenuate and distort the signals; consequently, frequent blunders are present among the measurements and their effect on the position could be harmful. Two approaches are usually adopted to tackle the blunder issue, RAIM and robust estimation, and both are effective in case of high redundancy and single blunders. An alternative method, based on bootstrapping, i.e. random sampling with replacement, the available measurements, has recently emerged. The performance of the considered methods could be augmented by exploiting suitable measurement error models, which are used to differently weighting the measurements in RAIM and robust estimators, and to defining not uniform sampling probabilities in bootstrap; several models, based on the most common measurement quality indicators, carrier-to-noise ratio and satellite elevation, are herein analyzed. In this work, the three techniques, coupled with several error models, are compared in terms of mean, RMS and maximum position errors, processing data from urban scenario. The results demonstrate the best performance of bootstrap method, which works effectively in case of multiple blunders and/or the lack of redundancy, when RAIM and robust techniques are often unsuccessful. Moreover, the results highlight the importance of a careful choice of a measurement error model.

Keywords—*bootstrap; GNSS; blunder; RAIM; robust estimators*

Full paper in IEEE Xplore

Galileo E1/E5 Measurement Monitoring - Theory, Testing and Analysis

Ali Pirsiavash, Ali Broumandan, Gérard Lachapelle and Kyle O'Keefe

PLAN Group, Department of Geomatics Engineering
Schulich School of Engineering, University of Calgary
Calgary, Canada

Abstract—This research investigates various measurement monitoring techniques to mitigate the effect of GNSS code multipath. After a comprehensive review of different monitoring approaches, the paper focuses on methods that detect and exclude faulty measurements from the position solution. Detection metrics are investigated for single and dual-frequency cases and a new Geometry-Free (GF) detection metric is presented for reliable multipath mitigation. Given the capability of the proposed metric to be combined with a preceding Code-Minus-Carrier (CMC)-based error correction, a detection procedure is performed based on a combination of time-averaging of monitoring metrics and *M of N* detection strategy. The analytical results are tested by using Galileo E1/E5 data collected in a real multipath environment.

Keywords— *Global Navigation Satellite System (GNSS); Galileo satellite system; measurement monitoring; multipath detection and mitigation*

Full paper in IEEE Xplore

The IGSO SBAS: Signal Availability in the Polar Regions

Takeyasu Sakai, Mitsunori Kitamura, and Takahiro Aso

Electronic Navigation Research Institute, National Institute of Maritime, Port and Aviation Technology
Chofu-Shi, Tokyo, Japan, sakai@mpat.go.jp

Summary

The authors propose usage of inclined geosynchronous satellites (IGSO) for implementation of SBAS, in addition to the current geostationary satellites, to improve availability of the SBAS service in the polar regions. It is shown that Japanese QZSS (quasi-zenith satellite system) could be used for this implementation.

Motivation

The SBAS, satellite-based augmentation system, is the international standard navigation service for aviation and maritime users. The DFMC (Dual-Frequency Multi-Constellation) SBAS which is the second generation SBAS transmitted on the L5 frequency is free from ionospheric effects thanks to dual-frequency operation. This means the DFMC SBAS fundamentally provides its service worldwide.

The remaining problem is, however, the availability of SBAS signal; In the polar regions it sometimes becomes difficult to receive the SBAS signal continuously due to low elevation angle of geostationary satellites. As a candidate solution for such problems, it can be considered to use another orbit for SBAS satellite, for example, inclined geosynchronous orbit (IGSO). The IGSO satellites can transmit signals from higher elevation even in the polar regions.

Japanese QZSS (quasi-zenith satellite system) has IGSO satellites and transmits the L5 augmentation signal called L5S. The authors have conducted the real-time SBAS trial with the live QZSS L5S signal to confirm the concept of DFMC SBAS service by IGSO satellites.

Results

Fig. 1 shows the configuration for this experiment. The prototype DFMC SBAS¹² developed by the Electronic Navigation Research Institute of the National Institute of Maritime, Port and Aviation Technology which is capable of processing GPS, GLONASS, and Galileo has been used for the experiments. The prototype receives GNSS measurements from the GEONET observation network and generates the L5 SBAS message stream in real time. The message is immediately sent to the QZSS MCS and transmitted by the QZSS L5S signal.

Fig. 2 shows the horizontal user error observed at the center of the service area for 6 hours, 01:00 to 07:00 UTC of 13 Nov. 2017. The 95 percent horizontal accuracy is improved from 2.80m to 0.82m. Fig. 3 shows horizontal and vertical protection levels and it is confirmed that the DFMC SBAS can provide approach service with 100% availability.

¹ T. Sakai, "The Status of Dual-Frequency Multi-Constellation SBAS Trial by Japan", International Symposium on GNSS, Hong Kong, Dec. 2017.

² M. Kitamura, T. Aso, T. Sakai, and K. Hoshinoo, "Development of DFMC SBAS Prototype System using L1 and L5 band Signals of GPS, Galileo, and QZSS", ION International Technical Meeting, Reston, VA, Jan. 2018.

Figures

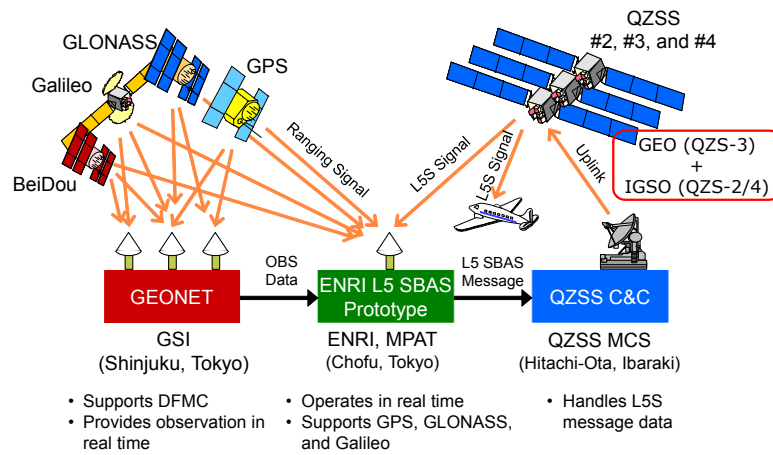


Fig. 1: Configuration of the experiments.

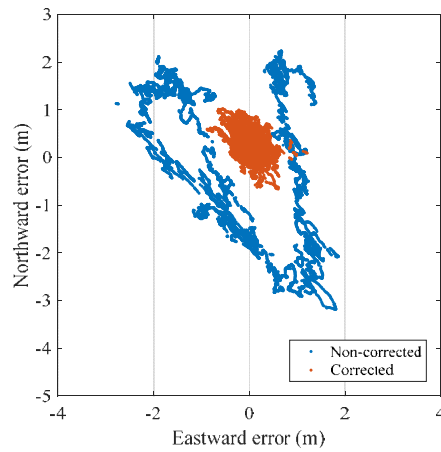


Fig. 2: Horizontal user error example for 6 hours.

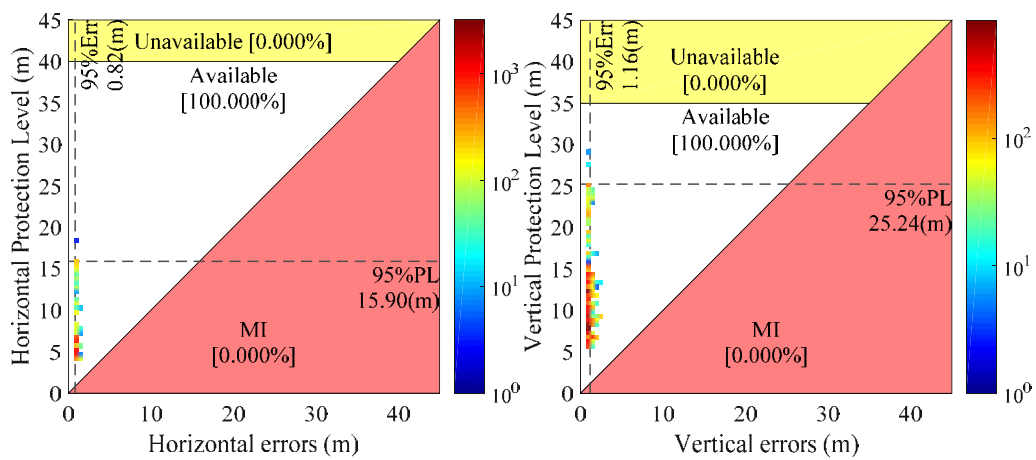


Fig. 3: Horizontal and vertical protection levels.

EDAS (EGNOS Data Access Service): Differential GPS corrections performance test with state-of-the-art precision agriculture system

J. Vázquez, E. Lacarra, M.A. Sánchez,
ESSP, SAS,
Torrejón de Ardoz, Spain

J. Rioja, J. Bruzual,
Topcon Agriculture,
Tres Cantos, Spain

Abstract— EDAS (EGNOS Data Access Service) is the EGNOS internet broadcast service, which provides free of charge access to the data generated and collected by the EGNOS infrastructure. EDAS gathers all the raw data coming from the GPS, GLONASS and EGNOS GEO satellites collected by all the receivers located at the EGNOS reference stations, which are mainly distributed over Europe and North Africa. Once the data are received and processed, EDAS disseminates them over the Internet in real time and also through an FTP archive. The EDAS services portfolio is the result of various protocols and formats supported, along with several types of information made available to users by each service. This paper investigates the potential use of EDAS Differential GNSS corrections to support precision agriculture applications, by analysing the achieved performance during a dedicated in-field test campaign that has been conducted by ESSP and Topcon Agriculture.

EDAS service provision is performed by ESSP, as EGNOS Service Provider, under contract with the European GNSS Agency (GSA), the EGNOS program manager. The European Commission (EC) is the owner of EGNOS system (including EDAS) and has delegated the exploitation of EGNOS to the GSA. ESSP also manages the EGNOS Helpdesk, which provides technical support to users by answering to any potential question or by providing clarifications about EGNOS services, thus including EDAS.

In 2016, ESSP presented [21] the EDAS DGPS corrections performance achieved by applying EDAS DGPS corrections to the GNSS measurements from public reference GNSS stations (EUREF) at selected European locations in real-time during a 5-week period [21]. That study showed that horizontal accuracies below 1 meter (95th percentile) can be achieved using EDAS DGPS corrections up to a distance of 250 km from the designated EGNOS station and that, within that range, pass-to-pass accuracies (15 minutes, 95%) were expected to remain below 20 cm. However, those pass-to-pass results were considered preliminary since they were based on post-processed static data (according to ISO 12188-1) and needed to be confirmed by in-field tests, i.e.

considering the environmental and dynamic conditions of farming operations. This year, ESSP complements the study presented in 2016 by conducting in-field tests aiming at measuring the pass-to-pass accuracy that can be supported by EDAS DGPS corrections in a dynamic and real-life environment.

In order to assess and validate the in-field tests, Topcon Agriculture joined ESSP for the activity. Topcon receivers, vehicles and guidance systems were used in order to confirm the suitability of the EDAS DGPS corrections for precision agriculture.

Firstly, this paper introduces the EDAS system and its architecture, presenting the main types of data disseminated through its services and the online information available to the users. As part of this introduction, special attention is put on the description of the EDAS Ntrip service. This service has been the main enabler for the performance tests presented in the scope of this paper, since it provides differential corrections to the GPS and GLONASS satellites in RTCM format, taking the EGNOS stations as reference stations.

Then, the paper describes the test scenarios and setups at the selected farm in Europe. Two different Topcon guidance systems on board tractors were running simultaneously to assess the EDAS DGPS positioning performance with respect to a reference, which was provided by an RTK-based Topcon solution. In each test, multiple runs with the rover tractor were performed over the reference patterns previously defined in the Topcon guidance systems. This paper presents a detailed analysis of the data recorded during the tests, especially in terms of the key performance indicators of the EDAS DGPS solution with respect to the RTK one.

The in-field tests results show that the DGNSS corrections broadcast by EDAS could be a suitable solution for cereal farms (in particular for spraying/spreading of any crop type and tilling and harvesting of cereal), when located within a reasonable distance (below 250 km approximately) to the target

EGNOS reference station. It is to be noted that cereal farms represent around 80% of the farms in Southern Europe.

Keywords— EGNOS; EDAS; GSA; ESSP; Topcon; GNSS; DGNSS; precision agriculture; in-field test; pass-to-pass.

I. INTRODUCTION TO EDAS

A. EDAS Overview

EGNOS, the European Satellite Based Augmentation System (SBAS), currently provides corrections and integrity information to GPS signals over a broad area over Europe and is fully interoperable with other existing SBAS systems (e.g. WAAS, the North American SBAS).

ESSP (European Satellite Services Provider) is the EGNOS system operator and EGNOS Service provider, under contract with the European GNSS Agency (GSA), for the following three services:

- EGNOS Open Service (OS), freely available to any user [2].
- EGNOS Safety of Life (SoL) Service, that provides the most stringent level of signal-in-space performance for safety critical applications [3].
- EGNOS Data Access Service (EDAS), which is the EGNOS terrestrial data service offering free of charge access to GNSS data to authorised users [1].

As it can be observed in Fig 1, EDAS gathers all the raw data coming from the GPS, GLONASS and EGNOS GEO satellites collected by all the receivers located at the EGNOS stations. The EGNOS operational system comprises 38 ground stations (Ranging and Integrity Monitoring Station - RIMS) and 4 uplink stations (Navigation Land Earth Stations - NLES), mainly distributed over Europe and North Africa. EDAS disseminates this GNSS data in real time and through an FTP archive to EDAS users and/or Service Providers.

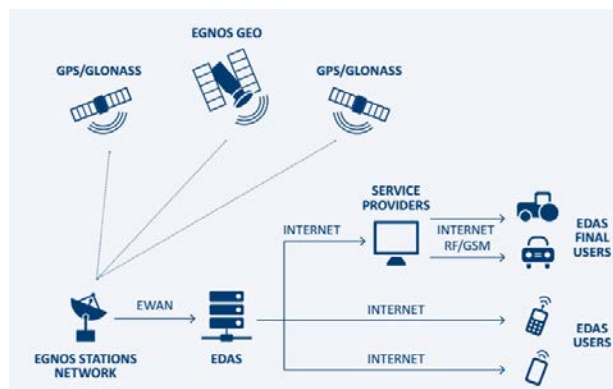


Fig 1: EDAS High-Level Architecture [1]

EDAS provides an opportunity to deliver EGNOS correction data to users who cannot always view the EGNOS satellites (such as in urban canyons), or GNSS data to support a variety of other services, applications and research projects.

Nowadays, EDAS offers the following services (please refer to the EDAS Service Definition Document [1] - for a detailed description, http://egnos-user-support.essp-sas.eu/new_egnos_ops/content/egnos-sdds):

- Main Data Streams [4]: GNSS data is provided through the Internet in real time in ASN.1 format [8] (Service Level 0) and RTCM 3.1 [9] format (Service Level 2).
- Data Filtering [4]: GNSS data can be received from pre-defined (according to RIMS location) subsets of RIMS stations when connecting to EDAS Service Level 0 and Service Level 2. Users can choose among 6 pre-defined groups of RIMS.
- SISNet Service [6]: EGNOS messages are provided in real time using the ESA's SISNet protocol [10].
- FTP Service [5]: Historical GNSS data are available through an FTP site including:
 - EDAS SL0, SL2 raw data.
 - GPS/GLONASS navigation and observations (RINEX [12] format)
 - EGNOS messages (EMS [13] + RINEX-B formats)
 - Ionosphere information in IONEX [14] format.
- Ntrip service [7]: GNSS measurements and corrections are delivered in real time using Ntrip protocol, in RTCM 2.1 [15], 2.3 [16] and 3.1 [9] formats. In particular, EDAS Ntrip service provides differential GNSS corrections (RTCM 2.1, 2.3) and phase measurements as well as additional messages for RTK (Real-time kinematic) positioning (RTCM 3.1).

The following table summarizes the types of data that can be retrieved via the different EDAS services.

TABLE 1: EDAS SERVICES

Mode	EDAS Service	Type of Data				Protocol	Formats
		Observation & navigation	EGNOS messages	RTK messages	DGNSS corrections		
Real Time	SL/DF 0	X	X			EDAS	ASN.1
	SL/DF 2	X	X			EDAS	RTCM 3.1
	SISNeT		X			SISNeT	RTCA DO-229D
	Ntrip	X		X	X	Ntrip v2.0	RTCM 2.1, 2.3, 3.1
Archive	FTP	X	X			FTP	RINEX 2.11, RINEX B 2.10, EMS, IONEX, SL0 and SL2 raw binary data

EGNOS data coming from the EDAS Services can be used for the development of applications based on GNSS data streams, or for the provision of added-value services based on EDAS.

B. EDAS registration

In order to request an EDAS account, users should follow the steps detailed below:

1. Register in the EGNOS User Support Website: <http://egnos-user-support.essp-sas.eu>
2. Fill and submit the EDAS registration form (only accessible upon registration in the web)

C. EDAS online information

The following means of information are made available by ESSP regarding EDAS through the EGNOS User Support Website (<http://egnos-user-support.essp-sas.eu>):

- EDAS Service Definition Document [1]: The EDAS SDD provides information on the EDAS services and their conditions of use. The EDAS SDD describes the EDAS system architecture and the current EDAS services (data type, formats, protocols and committed performance).
- EGNOS User Support Website: Up-to-date information about the EDAS services, the real-time status of the services, the access to the EGNOS helpdesk and the process to register to EDAS can be found in the EGNOS User Support Website [22].

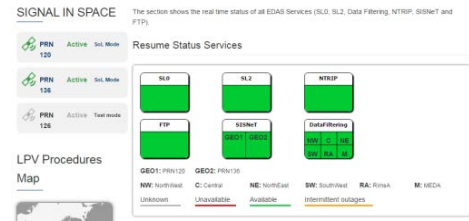


Fig 2: Real-time EDAS services status

- EGNOS Monthly performance report: Monthly reports contain the EDAS performance in terms of availability and latency for all services.

D. EDAS Services Performances

The EDAS SDD [1] defines the committed performance levels for EDAS (levels that should always be met in a nominal situation) in terms of availability and latency:

- **Availability:** percentage of time in which EDAS is providing its services according to specifications. The availability is measured at the EDAS system output (excluding user access network performance).
- **Latency:** time elapsed since the transmission of the last bit of the navigation message from the space segment until the data leaves the EDAS system (formatted according to the corresponding service specification). EDAS latency is a one-way parameter defined for real-time services.

Based on the above definitions, the table below provides EDAS services' minimum availability and maximum latency:

TABLE 2: EDAS SERVICES MIN AVAILABILITY AND MAX LATENCY

Performance	SL0	SL2	SISNet	FTP	Ntrip	Data Filtering	
						SL0	SL2
Availability	98.5%	98.5%	98%	98%	98%	98%	98%
Latency (sec)	1.30	1.45	1.15	N/A	1.75	1.60	1.75

Nominally, EDAS availability is above 99.5% for all EDAS Services and the latency is below 1 second for all services. As an example, see below the EDAS performances observed in December 2017.

TABLE 3: EDAS PERFORMANCES ON DECEMBER 2017

EDAS Service	Availability	Latency (ms)
Service Level 0	-	99.99%
Service Level 2	-	99.99%
Ntrip Service	-	99.74%
SISNeT Service	GEO Operational 1	99.69%
	GEO Operational 2	99.72%
Data Filtering Service	RIMS A	99.96%
	Central	99.95%
	MEDA	99.95%
	North-East	99.95%
	North-West	99.96%
	South-West	99.95%
FTP Service	-	99.96%

II. EDAS FOR DGNSS POSITIONING

Differential GNSS (DGNSS) corrections are sent through the EDAS Ntrip Service via Internet in order to support differential operation, obtaining accuracies of sub-meter level for navigation applications.

EDAS disseminates this information in real time through the Ntrip (version 2.0) protocol [11], which uses RTSP (Real Time Streaming Protocol) for stream control in addition to TCP (Transmission Control Protocol) and RTP (Real Time Transport Protocol) for data transport on top of the connectionless UDP (User Datagram Protocol).

The EGNOS Stations (RIMS and NLES) are considered as static reference receivers, which are placed at fixed and known surveyed locations. Then, since the satellite positions and the reference antenna location are known, the ranges can be determined precisely. By comparing these ranges to those obtained from the satellite observation measurements, the pseudorange errors can be accurately estimated (i.e. ionospheric delays, tropospheric delays, ephemeris errors and satellite clock errors), and corrections determined. These DGNSS corrections can then be broadcast to nearby users, who apply them to improve their position solutions.

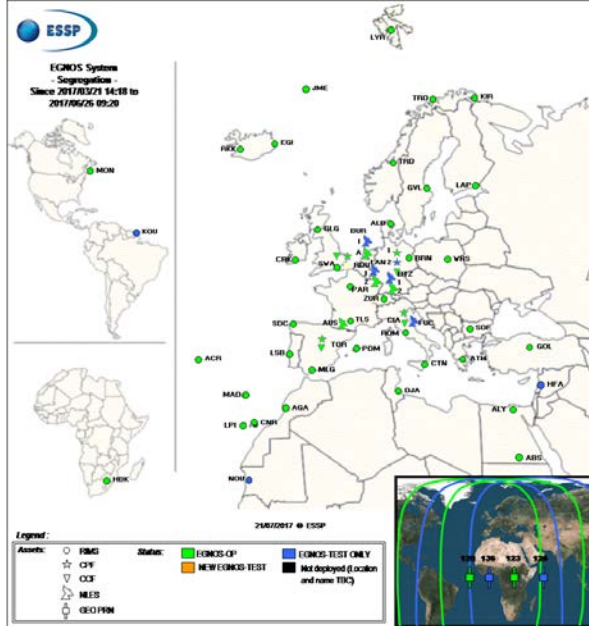


Fig 3: EGNOS RIMS stations

The DGNSS corrections are sent through the EDAS Ntrip Service in RTCM 2.1 and RTCM 2.3 formats, using the messages shown in following table:

TABLE 4: EDAS DGNSS MESSAGE TYPES

EDAS DGNSS Messages	Message Types	
	RTCM 2.1	RTCM 2.3
Differential GPS Corrections	1	1
GPS Reference Station Parameters	3	3
Reference Station Datum	N/A	4
Extended Reference Station Parameters	N/A	22
Antenna Type Definition Record	N/A	23
Antenna Reference Point (ARP)	N/A	24
Differential GLONASS Corrections	N/A	31
GLONASS Reference Station Parameters	N/A	32

For detailed information about the connection and usage of the EDAS Ntrip service, the EDAS Ntrip User Information Package [7] is available for registered users. EDAS Ntrip supports internet access including wireless internet access through mobile IP networks, and allows simultaneous PC, laptop, PDA, or receiver connections to a broadcasting host. Using this service, GNSS receivers can improve the accuracy of satellite-based positioning systems up to sub-meter level applying DGNSS techniques.

As already mentioned, EDAS DGNSS corrections are provided for the EGNOS stations and the user performance is driven by the physical distance to the closest site. Also, Internet coverage is required to access the EDAS Ntrip service.

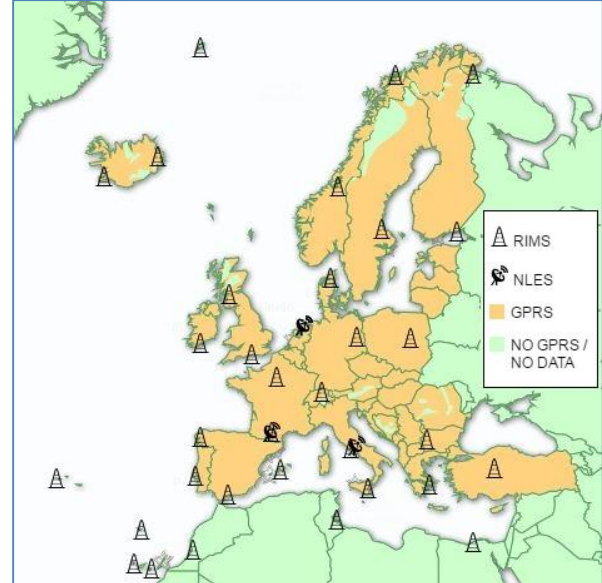


Fig 4: Estimated GPRS coverage (Europe) and EGNOS stations

The GPRS coverage information available from the European states is shown in orange taking into account the coverage maps of several telecommunications providers (it should be noted that the GPRS coverage information is qualitative, and has been obtained from the public information provided by the main telecomm

providers in Europe). Those land masses not analysed or in which no GPRS Coverage is identified, are plotted as light green in Fig 4.

A. Previous work and motivation

In the related article from 2016 [21], the EDAS DGPS corrections performance was analysed by applying EDAS DGPS corrections to the GNSS measurements from multiple public reference stations (static data) at selected European locations in real-time during a 5-week period. That study showed that horizontal accuracies below 1 meter (95th percentile) can be achieved using EDAS DGPS corrections up to a distance of 250 km from the designated EGNOS reference station and that, within that range, pass-to-pass accuracies (15 minutes, 95%) were expected to remain in the order of 20 cm (see Fig 5 and Fig 6). For that assessment, the pass-to-pass accuracy was computed based on static receivers following the process described in ISO 12188-1 [20].

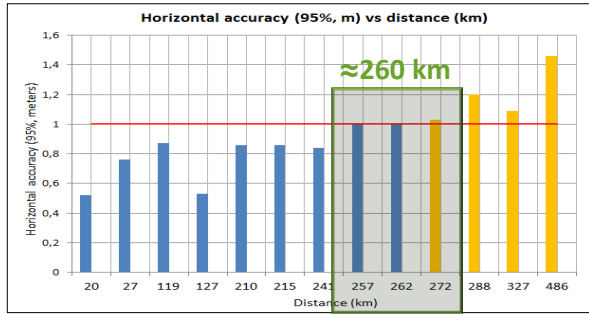


Fig 5: EDAS based DGPS solutions horizontal accuracy vs baseline (02/07/2016-06/08/2016) [21]

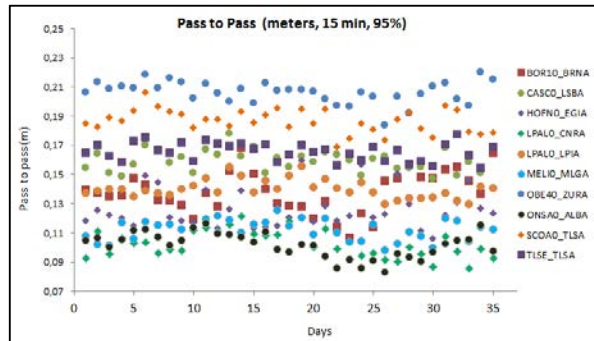


Fig 6: EDAS based DGPS: daily pass to pass accuracy[21]

In the agriculture domain, the pass-to-pass accuracy is the key performance indicator to assess the precision of guidance systems, characterizing the short-term dynamic performance determined from off-track errors along the straight segment passes (error with respect to the desired path in the direction perpendicular to the tractor trajectory). In addition to a sufficient absolute horizontal accuracy (at least 1 meter -95th percentile- is required for cereal and dry soil cultivation), the repeatability of the position solutions is critical (underperformance above the allowed margins can have serious economic impacts). In

order to cover a given field, farmers typically (other types of patterns –identical curve, centre pivot- are used for specific cases) define a pattern which is composed by a set of parallel lines separated by the implement distance. In this manner, if the guidance system allows precisely following the reference pattern, the efficiency and productivity of operations is maximized ensuring that the same soil is not covered twice and avoiding that a certain part of the field is not treated.

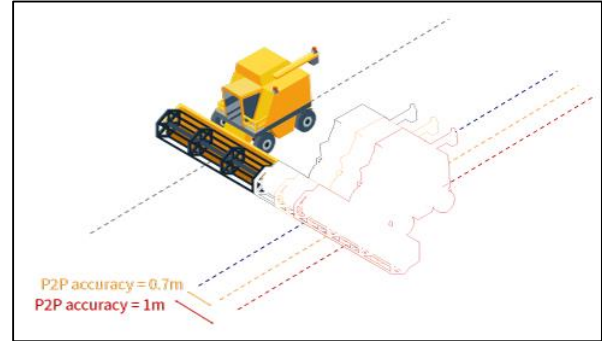


Fig 7: Pass-to-pass concept [23]

Looking at the results obtained in [21], from the point of view of precision agriculture applications, it was concluded that “If these results obtained from static data were confirmed by in-field tests, EDAS DGPS corrections could be used in a wide range of agriculture applications, such as seeding, planting, spreading and spraying for cereals and dry soil cultivation.”

Hence, the objective of the study presented in the current paper was to confirm if the pass-to-pass performance results obtained in 2016 (based on static data and post-processed according to [20]) would also be observed in a real-life scenario, considering the environmental and dynamic conditions of farming operations.

In order to achieve that goal, Topcon Agriculture, joined ESSP for the activity. Topcon receivers, vehicles and guidance systems have been used for the test campaign that is presented in the following sections.

III. EDAS DGPS FOR PRECISION AGRICULTURE: TEST CAMPAIGN

A. Test set-up

The test campaign that is presented in this section was performed at a farm in Marchena (Seville, Spain) on June 13th, 2017.

For the test, a tractor was equipped with two different Topcon guidance systems running simultaneously in order to be able to assess the EDAS DGPS positioning performance with respect to the reference, which was provided by a top-performing RTK-based Topcon solution (HiperV RTK base).

Hence, two independent positioning outputs were continuously available (placed along the same longitudinal axis on the roof of the tractor):

- RTK position: provided by the AGI-4 receiver fed by *Topcon's HiperV* RTK base.
- DGPS position: provided by the AGI-4 receiver fed by the EDAS Ntrip service.

With regards to the EDAS Ntrip input, it should be noted that, due to the geographical location of the farm that was selected for the tests, the DGPS corrections used for the test came from the EGNOS RIMS station in Malaga, 110 km away from the test location.



Fig 8: Topcon AGI-4 receivers used for the test (left: receiver fed by EDAS DGPS, right: receiver fed by Topcon's HiperV RTK base).

On board the tractor, 2 *Topcon X35* consoles were installed, each one connected to one of the receivers shown in Fig 8. Additionally, a *Topcon AES-25 electric steering system* was installed on the tractor so that the selected navigation input (either the RTK or the EDAS DGPS input) could be used to automatically guide the tractor along the defined reference pattern.

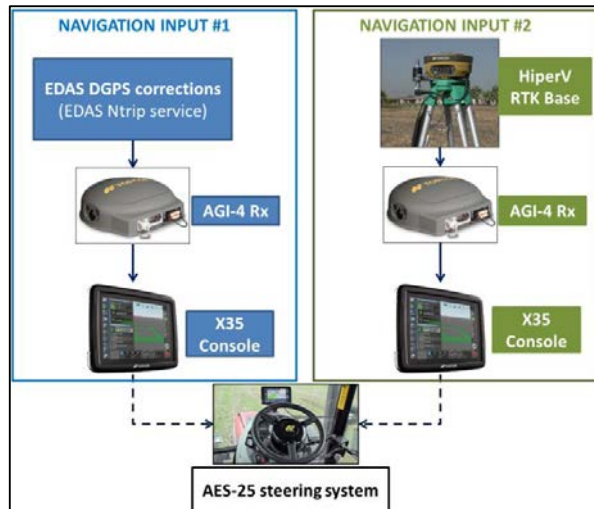


Fig 9: Navigation inputs used for the tests.

During the whole test duration, the logging function of the *X35 Consoles* was active so that, on top of the measurements taken in-field, an exhaustive data analysis could be performed after the tests.

Another relevant parameter in terms of configuration is the target separation between the parallel lines that compose the pattern defined for the trials (Fig 10). Although no implement was attached to the tractor for the tests, a theoretical implement with a width of 3 meters was configured in the *X35 consoles*. This means that, in the best case and as the different lines are covered with the tractor, the actual lateral separation between consecutive lines should match that implement width.

B. Tests Execution

Once the set-up was ready and the required calibration of the steering system was complete, the first action was the pattern definition in the two *X35 Consoles*. Considering the shape of the farm (rectangular), it was decided to work with parallel AB lines.

In order to define the reference pattern, the tractor was placed on one side of the farm (Point A in Fig 10). After marking that point in both *X35 consoles* simultaneously, the tractor followed (manually guided) a straight line parallel to the edge of the farm. At a distance of approximately 200 metres from Point A, the second reference point was defined (Point B in Fig 10). The imaginary straight line from Point A to Point B became our line #0. Then, the parallel lines automatically defined by the *X35 Console* with a lateral separation equal to the configured implement width (3 metres in our case) completed the definition of the pattern to be used for the tests. Due to the dimensions of the field and the configured implement width, 8 A-B lines (#0 to #7) composed our working pattern (see Fig 10).

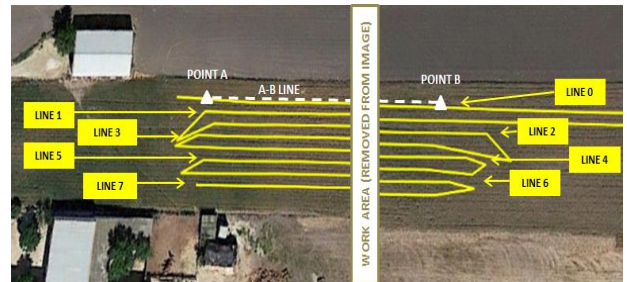


Fig 10: Farm field and pattern lines.

Based on the above pattern, three different complete runs covering the defined A-B lines were performed. Two key aspects characterise those runs:

- Navigation system connected to the steering system: depending on the run, the AGI-4 fed by *Topcon's HiperV* RTK Base or the one fed by EDAS was connected to the automatic steering system.
- Main procedure for pass-to-pass performance assessment: on top of the information provided by the *X35 Consoles*, which provide an estimated deviation with respect to the reference pattern in real-time (see deviation indication inside red circle in Fig 11), two different approaches have been used to measure the pass-to-pass accuracy:
 - Post-processing: the data logged by the *X35 Consoles* was post-processed to compute the cross track error of the EDAS DGPS solution with respect to the RTK one (reference) along the pattern.
 - In field measurements: when the *AGI-4* receiver fed by the EDAS DGPS corrections was connected to the steering system, the lateral separation between consecutive lines was manually measured in field.

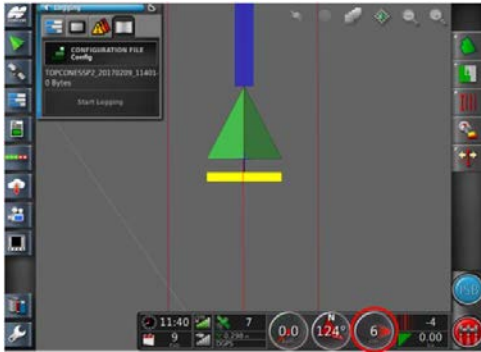


Fig 11: Topcon X35 Console interface.

The following table summarises the key features characterising the three test runs that were performed:

TABLE 5: TEST RUNS - DEFINITION

Test Run #	Navigation input- auto-steering	Performance assessment	Duration
Run #1	RTK (Topcon's HiperV base)	Post-processing	20 min
Run #2	RTK (Topcon's HiperV base)	Post-processing	18 min
Run #3	DGPS (EDAS Ntrip – Malaga)	In-field measurement	40 min

The following paragraphs provide a detailed review of the tests results for the runs introduced by Table 5.

C. Test Results: Run #1

As described in Table 5, for this run, the RTK system (Topcon's HiperV base station) was feeding the tractor's automatic steering system. The onboard *X35 consoles* allowed monitoring the estimated deviations reported by EDAS DGPS positioning solution and the RTK one along the different A-B lines in real-time. At this point, it is important to recall that identical Topcon AGI-4 receivers (see Fig 8) were in charge of the computation of both navigation solutions.

Regarding the trajectory followed by the tractor in order to cover the defined pattern during this run, the following A-B lines were covered consecutively: line #0, #1, #2, #3, #4, #5, #6.

The main inputs used for the pass-to-pass performance assessment corresponding to this run were the log files generated by the onboard *X35 Consoles* which included, with 1 Hz logging frequency: *time, latitude, position, speed, heading, number of satellites used in the position computation, correction source, HRMS and engage status*.

Among the above parameters, and apart from the time stamp of each recorded data set, the following parameters were the key ones for the performance assessment of the results:

- *Position* reported by each *X35 Console* (comparison of the computed position provided by the RTK fed receiver and the EDAS DGPS fed receiver). The position output provided by the RTK fed receiver has been taken as the reference/truth, considering that the typical error of the RTK solution is negligible for the current study (RTK errors at centimetre level versus decimetre level errors to be studied).
- *Engage status and heading*: these two parameters were key since they allowed identifying the straight trajectory segments matching each A-B line (i.e. excluding turns or transitions between lines).
 - The engage status indicates that the auto steering function is activated (situation along the different lines but not during turns which are manually performed).
 - The heading was also used in order to exclude the manoeuvres performed by steering system when entering a given A-B line and retain only the straight part of the trajectory guided by the steering system.

Once the data set corresponding to each straight line within the test run was identified for the two console outputs, the positions reported by both *X35 Consoles* (each fed by one *AGI-4* receiver) were post-processed to compute the instantaneous cross track error of the EDAS DGPS solution with respect to the RTK one (i.e.

difference between sensor outputs in transversal direction to the corresponding A-B line). After that, the instantaneous pass-to-pass error along the corresponding A-B line for any given couple of consecutive lines is obtained by subtracting the instantaneous cross track errors of the current line and the previous one. Fig 12 illustrates this process.

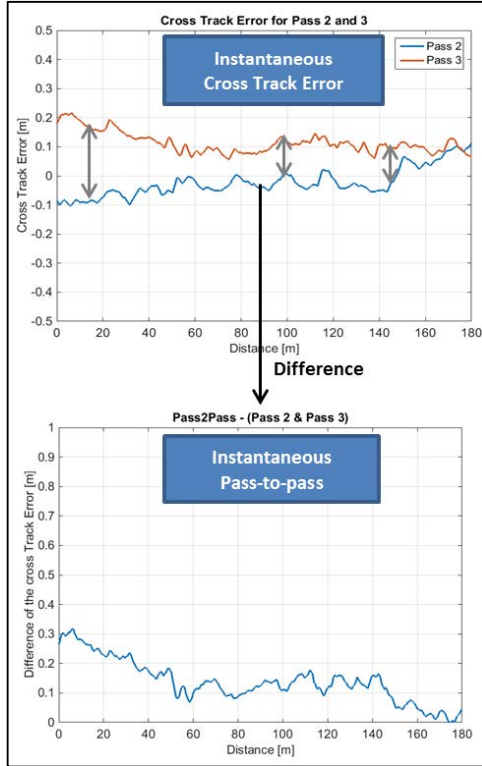


Fig 12: Instantaneous pass-to-pass performance computation (post-processing).

Following the procedure described above, Fig 13 depicts the instantaneous pass-to-pass error obtained during run#1 for the different couples of A-B lines.

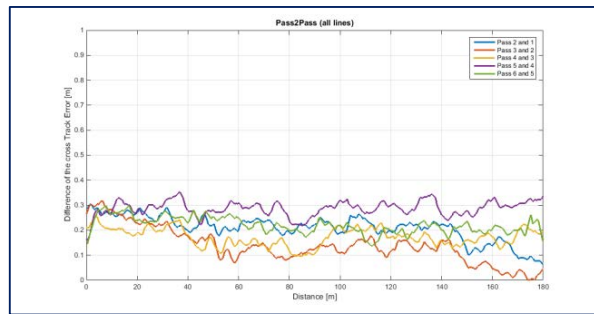


Fig 13: Instantaneous pass-to-pass accuracy – Run#1.

As shown in Fig 13, the instantaneous pass-to-pass accuracy for the first test run, considering all the A-B lines and taking the RTK position as the reference, was typically in the 15-25 cm range.

Table 6 shows the average of the instantaneous pass-to-pass accuracy for each couple of consecutive passes and also the average of the complete run.

TABLE 6: AVERAGE EDAS DGPS PASS-TO-PASS ACCURACY– RUN#1

Passes	1 & 2	2&3	3&4	4&5	5&6	Full Run
Pass-to-pass accuracy (average)	20 cm	14 cm	16 cm	28 cm	22 cm	21 cm

D. Test Results: Run #2

For the second test run (Run#2), as for run#1 (see Table 5), the RTK system (*Topcon's HiperV* RTK base station) was feeding the tractor's steering system.

The main difference with respect to run#1 was linked to the way to connect the different A-B lines in order to cover the reference pattern. In this case, wider turns without reversing were used, resulting in the following A-B lines sequence: line #0, #2, #4, #6, #7, #5, #3, #1 (refer to Fig 10).

Fig 14 depicts the instantaneous pass-to-pass accuracy achieved during run#2. The results are quite similar to those from run#1 (pass-to-pass accuracy in the 15-25 cm range) although the repeatability seems to be slightly better in this case.

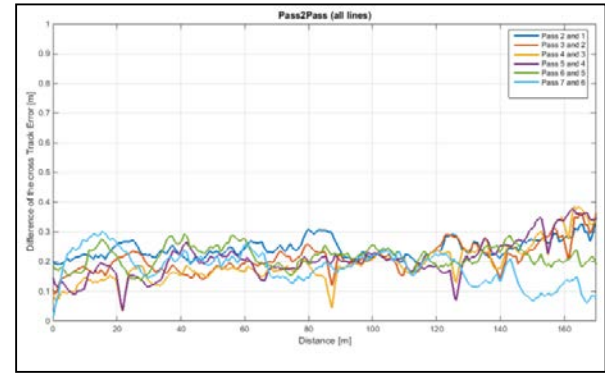


Fig 14: Instantaneous pass-to-pass accuracy – Run#2.

The average instantaneous pass-to-pass accuracy for each couple of lines and the overall average of the run (see Table 6) confirm that the observed pass-to-pass accuracy remains in the order of 20 cm, showing quite consistent values along the complete run.

TABLE 7: AVERAGE EDAS DGPS PASS-TO-PASS ACCURACY– RUN#2

Passes	1 & 2	2&3	3&4	4&5	5&6	6&7	Full Run
Pass-to-pass accuracy (average)	23 cm	20 cm	18 cm	19 cm	22 cm	19 cm	22 cm

E. Test Results: Run #3

For run#3 (see Table 5), the *AGI-4* receiver fed by the EDAS DGPS corrections provided by the EDAS Ntrip service for Malaga RIMS station was connected to the Topcon *AES-25 electric steering system*. Hence, during run#3, the auto-guidance function was based on EDAS

input. In this case, the main procedure used for the pass-to-pass accuracy performance assessment was based on in-field measurements of the achieved lateral separation between consecutive lines. It should be noted that this is the procedure that farmers typically follow to check the pass to pass performance.

At this point, it is important to recall that the configured implement width was 3 meters. Hence, for each couple of consecutive lines, the actual lateral separation was determined in-field (the error with respect to the 3 meters target being the measured pass-to-pass accuracy).

The process for the in-field measurement of the pass-to-pass accuracy for a given couple of A-B lines is depicted in Fig 15, and consists on the following steps:

- 1) The tractor, having the steering system engaged to the EDAS DGPS navigation input, is stopped at a designated area (*Measurement Area* in Fig 15) within a given A-B line. Using a physical point of the tractor's external body work, a first mark is done on the ground (*Orange X* in Fig 15).
- 2) With the steering function engaged to the EDAS navigation system output, the designed A-B line length is covered by the tractor (*Line 0* in Fig 15).
- 3) At the end of the line, the tractor is manually turned to the next line (*Line 1* in Fig 15) and the steering system is engaged again to the EDAS navigation system input.
- 4) Once the tractor has covered the full line in the opposite direction as the previous one, the tractor is stopped at the *Measurement area*. Then, using the same physical reference of the tractor's external body work as in step 1, a second mark is done (*Blue X* in Fig 15); this second mark needs to be aligned with the first mark (*Orange X* in Fig 15) perpendicularly to the subject A-B lines.
- 5) The distance in the transversal direction to concerned A-B lines is measured (target distance is 3 metres in this case –implement width-). The deviation of this measurement from the 3 metres target is the pass-to-pass accuracy for the concerned lines – *Line 0* and *Line 1* in Fig 15).
- 6) Then, the process is restarted (Step 1) for the next couple of A-B lines.

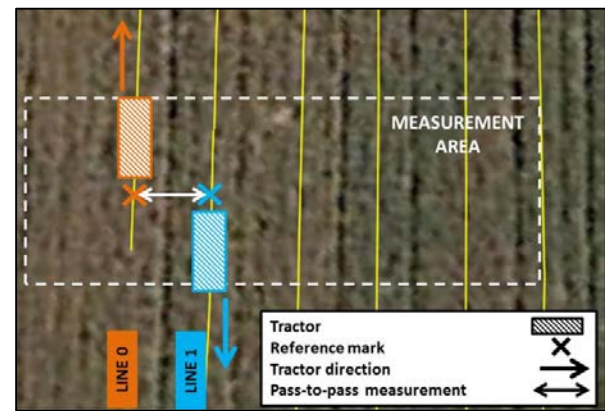


Fig 15: In-field pass-to-pass measurement (procedure).

Table 8 summarises the pass-to-pass measurements that were obtained for the available couples of A-B lines (see Fig 10) using the procedure described above.

TABLE 8: EDAS DGPS PASS-TO-PASS ACCURACY–
RUN#3

Passes (In-field)	0 & 1	2&3	4&5	6&7
Pass-to-pass accuracy	3-4 cm	10-12 cm	1-3 cm	7-8 cm

As one can easily see, the achieved results obtained through this process exceeded the expectations, being 12 cm the maximum measured pass-to-pass accuracy.



Fig 16: EDAS DGPS Pass-to-pass (lines 0 & 1).

IV. CONCLUSIONS AND FUTURE WORK

The current paper is focused on the EDAS Ntrip Service, which can be used for DGNSS positioning since it provides DGNSS corrections for the EGNOS stations, located mainly over Europe and North of Africa, in real-time over the internet.

In the related article from 2016 [21], the EDAS DGPS corrections performance was analysed by applying EDAS DGPS corrections to the GNSS measurements from multiple public reference stations (static data) at selected European locations in real-time during a 5-week period. That study showed that horizontal accuracies below 1 meter (95th percentile) can be achieved using EDAS DGPS corrections up to a distance of 250 km from the designated EGNOS station and that, within that range, pass-to-pass accuracies (15 minutes, 95%) were expected to remain in the order of 20 cm. However, those pass-to-pass results were considered preliminary since they were based on post-processed static data (according to ISO 12188-1).

As a natural continuation of the work presented in 2016, the present article reports on the results of 1 day in-field test session, conducted by Topcon Agriculture and ESSP, which aimed at analysing the pass-to-pass accuracy performance that could be achieved with EDAS DGPS corrections considering the environmental and dynamic conditions of farming operations. Topcon Agriculture supported ESSP by providing the required receivers, vehicles and guidance systems that have enabled the test executions.

For the test executions and considering the designated farm for the tests, the EDAS DGPS corrections provided for the Malaga RIMS station have been used. That translates into an EDAS based DGPS solution analysed with an estimated baseline distance of 110 km. For the whole test duration, a *Topcon* RTK solution has always been running in parallel to the EDAS DGPS solution to provide the required reference for the post-processing of the recorded data.

As part of the tests, three different runs over the defined reference pattern were done. For two of them, the pass-to-pass accuracy performance was obtained by post-processing the data logged during the tests. Average pass-to-pass accuracies of 21 and 22 cm were supported by the EDAS based DGPS position solution during those runs. Finally, during the third run, after connecting the receiver using EDAS DGPS corrections to the tractor's steering system, in-field measurements of the supported pass-to-pass accuracy were taken. During this run, the measured pass-to-pass accuracy supported by EDAS DGPS corrections remained below 12 cm for the analysed couples of lines.

In summary, the observed EDAS DGPS pass-to-pass accuracy performance during the test execution shows that EDAS DGPS corrections can support pass-to-pass

accuracies in the order of 20 cm in a consistent manner and with a high degree of repeatability. Such performance level is considered to be appropriate for most cereal farm operations. In particular, the observed performance is sufficient to support the following precision agriculture applications:

- Spraying/Spreading of any crop type.
- Tilling of cereal.
- Harvesting of cereal.

Additionally, although more in-field tests are required to conclude on this point, EDAS DGPS could also be a suitable solution for seeding of cereal.

Hence, the test campaign that is reported in this article, jointly performed by Topcon Agriculture and ESSP, indicates that EDAS DGPS corrections could support a wide range of precision agriculture applications and become an attractive alternative for cereal farms, when located in the vicinity of an EGNOS RIMS station.

In order to improve the current understanding of the actual performance delivered by EDAS DGPS corrections from the point of view of precision agriculture applications, Topcon Agriculture and ESSP will engage in further testing activities. As part of those tests, it is foreseen to verify the observed EDAS DGPS pass-to-pass accuracy performance in different geographical locations (different baselines for the EDAS based DGPS solution) and performing actual agriculture operations (with a real implement attached to the tractor).

ACKNOWLEDGMENTS

The authors would like to acknowledge the efforts done by the European Commission (EC) and the European GNSS Agency (GSA) to continuously support the EGNOS programme.

Finally, the authors would like to express their gratitude to their colleagues Francisco Cantos (Sogeti High Tech), Héctor Pámpanas (Sogeti High Tech), Julián Sedano and Patricia Rivas (Topcon Agriculture) for the invaluable support in the elaboration of this paper. Also, the collaboration of José Miguel Sánchez López, who provided the tractor and the access to the farm used for the tests, was key to enable the tests execution.

REFERENCES

- [1] EGNOS Data Access Service (EDAS) Definition Document, EGN-SDD EDAS, v2.1, 19/12/2014
- [2] EGNOS Open Service - Service Definition Document v2.2, 12/02/2015
- [3] EGNOS Safety of Live Service Definition Document v3.1, 26/09/2016
- [4] EDAS Client SW User Manual, ESSP-DRD-6977
- [5] EDAS FTP Service – User Information Package
- [6] EDAS SISNet Service – User Information Package
- [7] EDAS Ntrip Service– User Information Package
- [8] Introduction to ASN.1 – <http://www.itu.int/ITU-T/asn1/introduction/index.htm>
- [9] RTCM 10403.1 recommended standards for differential GNSS Services Version 3.1.
- [10] SISNet User Interface Document, E-RD-SYS-31-010, Version 3, Revision 1, 15/05/2006. <http://www.egnos-pro.esa.int/Publications/SISNET>
- [11] Networked Transport of RTCM via Internet Protocol (Ntrip), version 2.0
- [12] RINEX: The Receiver Independent Exchange Format Version 2.11
- [13] EGNOS Message Server (EMS) User Interface Document E-RD-SYS-E31-011-ESA 2.0 26/11/04
- [14] IONEX: The IONosphere Map EXchange Format Version 1 25/02/98
- [15] RTCM 10402.1 Recommended Standards for Differential Navstar GPS Service, Version 2.1
- [16] RTCM 10402.3 Recommended standards for differential GNSS Service Version 2.3.
- [17] MOPS for GPS/WAAS Airborne Equipment, RTCA DO-229, Revision D, Issued 13 December 2006.
- [18] GSM specification. www.3gpp.org/specifications
- [19] “EDAS (EGNOS Data Access Service): alternative source of differential GPS corrections for maritime users”, ION GNSS 2015, E. Lacarra et al., ESSP SAS and Alberding GmbH.
- [20] ISO 12188-1, Tractors and machinery for agriculture and forestry- Test procedures for positioning and guidance systems in agriculture- Part1: Dynamic testing of satellite-based positioning devices.
- [21] EDAS (EGNOS Data Access Service): Differential GNSS corrections for land applications, ION GNSS 2016, J. Vázquez et al., ESSP SAS.
- [22] EGNOS User Support Website (https://egnos-user-support.essp-sas.eu/new_egnos_ops/index.php)
- [23] Pass to pass concept explanation (https://egnos-user-support.essp-sas.eu/new_egnos_ops/pass_to_pass)

A Global Navigation Augmentation System Based on LEO Communication Constellation

Yansong Meng, Lang Bian, Lin Han, Wenying Lei,
Tao Yan
China Academy of Space Technology (Xi'an)
Xi'an, China
mengys_504@163.com

Mu He
China Great Wall Industry Corporation
Beijing, China
hemu577@163.com

Xingxing Li
Wuhan University
Wuhan, China
364547447@qq.com

Abstract—In the background of booming development of low earth orbit (LEO) communication systems, a global navigation augmentation system based on LEO communication constellation is proposed in this paper. The LEO satellites can serve both as space-based monitoring stations and as navigation information broadcasting sources. The system can be developed together with the LEO communication system, and do not need to build a new system. The Hongyan LEO communication system under construction by China Aerospace and Technology Corporation (CASC) is adopted for the analysis in the paper. When served as space-based monitoring stations, the LEO satellites can jointly determine the precise orbits and clock errors of GNSS satellites and LEO satellites with the data from the mounted high precision GNSS monitoring receiver and the ground based monitoring stations. When served as navigation information broadcasting sources, the Assistant GNSS (AGNSS) architecture is used to broadcast assistant navigation information, and the general-purpose GNSS receiver can realize fast signal acquisition in the extremely complicate environment and achieve better anti-jamming capability for the navigation availability augmentation. For the navigation precision augmentation, besides the precise orbit, precise clock error, and integrity augmentation information, an additional navigation augmentation signal is broadcasted to realize global precise point positioning (GPPP) with sub-meter positioning precision level in dynamic mode and sub-decimeter precision level in static mode. The convergence time of precise point positioning is shorten from 30 minutes using a GNSS system alone to less than 5 minutes using a GNSS system together with the LEO global navigation augmentation system.

Keywords—Navigation Enhancement; Low orbit constellation; Hongyan System

Full paper in IEEE Xplore

Satellite based Navigation in Iceland

Saemundur E Thorsteinsson
Dep. of Electrical and Computer
Engineering
University of Iceland
saemi@hi.is

Thorgeir Pálsson
School of Science and
Engineering
Reykjavik University
tpalsson@ru.is

Greipur G. Sigurdsson
Maritime Division
The Icelandic Road and
Coastal Administration
ggs@vegagerdin.is

Arnor B. Kristinsson
Dep. of Research and
Development
Isavia ohf.
arnork@isavia.is

Abstract— An overview of Satellite based Navigation in Iceland is given, beginning with a short history of radio navigation. GNSS usage by the maritime sector is treated including a survey of EGNOS usage by the Icelandic fleet. Future maritime needs are reviewed. A similar treatment is given for the aviation sector in Iceland, outlining the challenges at hand in utilizing SBAS. Due to the country's northerly latitude there are challenges that require specialized solutions that are addressed in the paper.

Keywords—GNSS, SBAS, EGNOS, WAAS, High Latitude, Approach profiles

I. INTRODUCTION

Since the discovery of Iceland, navigation has been vital for the well-being of the population. Vikings from Scandinavia discovered the country but how they navigated to the shores of Iceland is still to some extent a mystery. It is e.g. postulated that they really made use of the so-called „sunstone“ (solsten) that allegedly enabled them to see or detect the sun's location despite cloudy skies. They also made observations of cloud formations and other natural phenomena to determine their whereabouts. It is beyond doubt that the Vikings possessed superb navigation skills that later led to their discovery of Greenland and the American mainland.

Iceland has always depended on communications to the European mainland and later to America. The nation's fortunes and communications to and from the country, primarily in the form of sea transport, have been highly correlated throughout the centuries. Navigation is one of the primary enablers of transport and therefore of high importance to Iceland. Fishing became the nation's main industry in the 20th century and is still one of the main pillars of the economy. Accurate positioning is essential to efficient fishing operations and safety at sea. Icelanders have operated air services on North Atlantic routes since 1945, using Iceland as a hub with destinations in Europe and North America. In recent years, Iceland has become a popular destination for tourism, which is an industry that depends heavily on satellite navigation, perhaps sometime without realizing or recognizing its importance to that growing segment of the economy.

The advent of GPS in the early nineties marked a milestone in navigation and positioning all over the world. In Iceland, the number of accidents at sea and in the air has dropped markedly due to more readily available positioning. All ships and aircraft now carry GNSS receivers and we await even more progress and cost savings from the utilization of GNSS. Autonomous

ships are likely to appear on the oceans within a few years and aviation will seek new modes of operation and cost benefits from GNSS. In countries located at high latitudes like Iceland, there are specific issues that must be addressed before all those potential benefits can be fully enjoyed. Those issues will be described and addressed in this paper..

II. A BRIEF HISTORY OF RADIO NAVIGATION IN ICELAND

In the early 20th century, fishing in Icelandic waters became a large-scale industry. With the advent of radio navigation, the fishing fleet began to utilize the new technology for increased efficiency of operation and to reduce cost. With Loran-A, which became available to civil users after WWII, fishing vessels were able to locate and record good and generous fishing spots and return to them later with a relatively high degree of accuracy. Furthermore, they could avoid areas where the fishing trawls were endangered. Fishermen with gillnet or longline could now check their nets or hooks with increased certainty. Radio navigation became an essential aid for fishing and with the availability of Loran-C in the nineteen-sixties the coverage area was greatly extended and the accuracy of positioning increased. In the 1990s, Loran-C operation in the North Atlantic was reduced and the Icelandic Loran-C station at Sandur was shut down at the end of 1994. The replacement was in the form of basic civil GPS service with Selective Availability (SA) with a positioning error of approximately 100 m. This error magnitude was unacceptable for the fishing fleet which had become used to the high precision of Loran-C due to its outstanding repeatability. The Icelandic Differential GPS system was therefore initiated in 1994 [1]. Corrections were transmitted from seven radio beacons on the Icelandic coastline and the fleet enjoyed positioning with errors under 5 m. SA was turned off in 2000 and uncorrected GPS had improved to the point of being good enough for the fishing fleet. The DGPS system was turned off in 2016 nearly without protest, partly because 10 m GPS error is sufficient for the fishing fleet and partly because the fleet is now using EGNOS, a GPS overlay system designed primarily for aviation. There are two EGNOS RIMS (Ranging and Integrity Monitoring Stations) in Iceland but the availability of EGNOS signals is limited. The signals are transmitted from geostationary satellites that are viewed at a low angle in northerly latitudes yielding difficulty of reception in narrow fjords where increased accuracy is needed for maneuvering.



Figure 1. Road distance from Reykjavik to Akureyri is 387 km and 652 km to Egilsstaðir

Icelandic society depends heavily on air transport as air services are the only practical means of travelling to the rest of the world. Notably the connections across the North Atlantic to Europe and North America as well as domestic services which connect distant regions with the capital area constitute this network. In 2017 more than 80 international destinations could be reached directly from Keflavik Airport with high frequency. Domestic aviation is also vital for the population outside the capital area. Driving from Reykjavik to Akureyri, the largest city outside the capital area, takes nearly 5 hours in optimal conditions, Figure 1. Approach and landing is complicated due to terrain close to important airports such as Akureyri and Isafjörður where GPS based approach profiles have been designed. Future landing systems will be increasingly GNSS based requiring high integrity GNSS overlay/augmentation systems especially in order to provide accurate vertical guidance. The fact that Iceland is on the boundary of EGNOS and WAAS services presents a particular problem that is being addressed by Isavia, the Air Navigation Service Provider in Iceland.”

III. SATELLITE BASED MARITIME NAVIGATION

Satellite navigation systems are available in virtually all Icelandic ships and boats. The Icelandic fishing fleet is generally well equipped with navigation, communication and fish finding gear. A typical new trawler is shown in Figure 2..

A. Current situation

Current performance of GPS is satisfactory for most maritime operations like fishing and general navigation between ports. Furthermore, it is also used for fisheries control and automatic safety monitoring of all Icelandic vessels that are required by law to report position, heading and speed with regular intervals to the Maritime Watch Centre. This reporting is based on the Automatic Identification System (AIS) for sea area A1 according to IMO classification, but fishing vessels out of AIS range report over a satellite link. This safety monitoring has been operated since 1967, and was set up due to high accident rates and many lives lost at sea. The service was manual until the early nineties when it became automatic using position reporting over VHF that was later replaced by AIS.

Recent measurements of L1, C/A code GPS performance in Reykjavik indicate a very small horizontal error. The measurements were done with a stationary U-blox NEO-8T receiver located on a building with free sight to all directions. The scatter diagram is shown in Figure 3. All measurement points are within a radius of 4 m and only a few outside 3.5 m.

Despite this accuracy, EGNOS is deployed in many Icelandic vessels. The main reason is not that the navigators demand EGNOS but rather that it is already a feature of the GPS receivers purchased. More advanced systems for SOLAS vessels emit a warning sound when EGNOS is not functioning. This is a nuisance to the vessel crew and therefore EGNOS is manually disabled in many vessels. The alarms are frequent due to the low availability of EGNOS west of Iceland and in fjords where visibility to the EGNOS satellites is hindered. It is likely that a majority of the larger Icelandic vessels do have EGNOS enabled GPS receivers. Many of them however do not deploy the EGNOS service or they are not aware that it is available in their receivers. This confirms the hypothesis that the accuracy offered by uncorrected GPS suffices for their operations. Of course there are applications at sea where more accuracy is needed, e.g. by many projects taken on by the Icelandic Coast Guard and Coastal Administration, e.g. in placing buoys. In such cases, the expert users are well aware of EGNOS and its advantages and limitations.

B. Future needs

The introduction of unmanned navigation of vessels is probably going to cause a paradigm shift in the field of maritime navigation in a near future [2]. Being very dependent upon shipping for freight and fishing, Iceland needs to follow the development closely and be prepared to install the necessary infrastructure. Furthermore, Iceland needs to have a voice in international bodies that both decide upon and build infrastructure to support autonomous navigation. Among the key areas to be developed to enable the introduction of autonomous vessels are accurate navigation systems that are resilient against jamming and spoofing, accurate maps of harbors, tidal areas, rivers and monitoring of sandbars and other underwater obstructions [3]. Furthermore, shore support facilities need to be installed, equipped with high data rate communication systems between vessel and shores.



Figure 2. A typical new Icelandic trawler, Björgúlfur EA312. (Photo by Haukur Sigtryggur Valdimarsson)

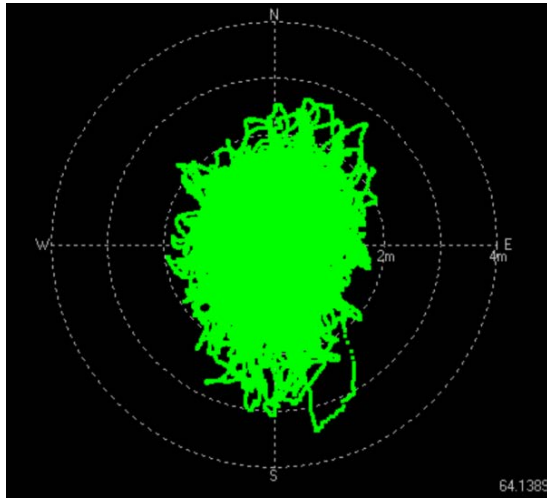


Figure 3. Scatter diagram from GPS measurements in Reykjavik during 24 hours in early May 2018

IV. SATELLITE BASED NAVIGATION FOR AVIATION

Like the rest of the world, Iceland enjoys a good situation in terms of GNSS availability and accuracy for en-route flying based primarily on the use of the basic civil services provided by GPS. Virtually all Icelandic aircraft are equipped with GNSS navigation equipment and this is in practice their main navigational aid although the traditional systems of VOR/DME and even Non-Directional Beacons (NDB) are still the backbone of the route network where ILS is only available on a limited basis except for Keflavik Airport. Using GNSS for precision approaches of aircraft is a challenging task that would be highly rewarding in Iceland. This is a mountainous country, especially along the Western, Northern and Eastern coastlines where small towns and villages are located in fjords and inlets. These communities depend on good and reliable air travel, notably Isafjörður in the Westfjords and Akureyri in the North in addition to ambulance services that provide priority air transport of patients to the National University Hospital in Reykjavik. Rescue services by helicopter, provided by the Icelandic Coast Guard also require precision navigation into locations everywhere in the country and also at sea.

A. Current situation

A Google Earth view of Isafjörður is shown in Figure 4, where the approach by air has been drawn in red color. The town is surrounded by high mountains and the airport is located on a spit of land beneath one of the mountains in the small fjord of Skutulsfjörður where the town of Isafjörður is situated. Landing is only possible by descending into the larger Isafjörður bay towards the North-West until flight under Visual Flight Rules (VFR) is reached and the approach can be continued visually to the single runway shown in the picture which depicts the more difficult landing path in northerly winds. Reception of Geostationary Satellite signals, such as those transmitting EGNOS signals is not possible at Isafjörður due to mountain blocking. The EGNOS transmitting satellites Inmarsat 3-F2 at 15.5°W is at 15.3° look angle from Isafjörður and the SES-f at 5.0°E is at 12.4° look angle. Hence, EGNOS

reception is not possible flying low during approach into the airport.

The situation at Akureyri is not as dramatic as in Isafjörður. The runway lies North-South and landings are possible from both directions. However, mountainous terrain affecting the approach profile is located in all directions except due North. The approach to Akureyri is considered complicated with the main approach requiring a knee-bend change of course to align with the final approach at a critical point. An Instrument Landing System (ILS) is in place for a straight-in approach towards North, however requiring a steep approach path of 5.5 degrees instead of the standard 3.0 degrees. No ILS is yet available for approach from the other direction although this is now being planned. This has had the consequence that foreign pilots, not familiar with the surrounding area, have decided to abandon landing at Akureyri Airport and have turned instead to the international airport in Keflavik.

Iceland is close to the boundary between the EGNOS and the WAAS service areas. The WAAS service area extends to the region south-west of Greenland. Iceland on the other hand is at the western edge of the EGNOS area. The two EGNOS RIMS ground stations in Iceland are located one in the Eastern part at Egilsstaðir Airport and the other at Reykjavik Airport in the South-West. Accuracy and Integrity of EGNOS data in Iceland is therefore up to standards. However, as can be seen in Figure 5 [4], availability is limited. The availability referred to in this case is in accordance to APV-1 performance criteria. This means that the signal may be used for approach operations with vertical guidance where the required horizontal accuracy is 16 m and the vertical accuracy is 20 m. ICAO requires at least 99% availability for APV-1, which generally means EGNOS may not be unavailable for more than 14 minutes per 24 hour window. The colored areas vary with time and depend upon ionospheric conditions. From the map it is obvious that APV-1 availability requirements are met only in the easternmost part of Iceland. This is however not guaranteed at all times because the red area “breaths” a few degrees East and West, depending on the ionospheric conditions.



Figure 4. Google Earth view on Isafjörður. An approach path is drawn in red

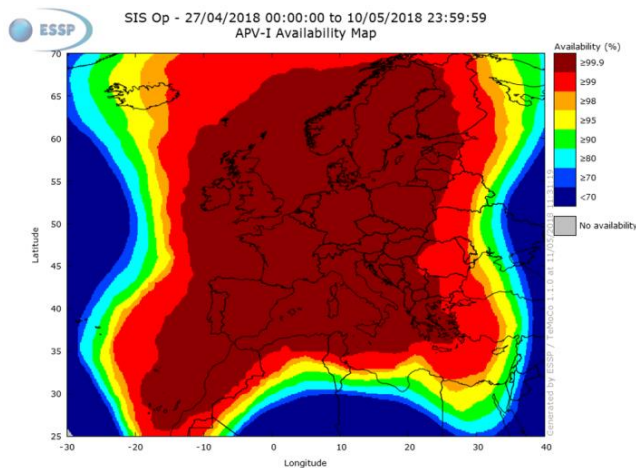


Figure 5. Availability of EGNOS averaged over 14 days

B. Future needs

The airports at Akureyri at 18.1°W and Husavik at 17.4°W do not reach the 99% availability area in all cases as is shown in Figure 5. However a collaboration between Isavia and the European Satellite Service Provider (ESSP) in 2016, based on Iceland-specific data collection demonstrated that Husavik Airport is on the boundary of the 99% availability area. Therefore has the Icelandic Transport Authority (Samgöngustofa) permitted Isavia, to design EGNOS supported approach paths for airports east of 19°W [5]. This is mainly for research and demonstration purposes. If it can be demonstrated that Husavik Airport can make use of EGNOS APV-1, this will apply for all airports east of Husavik. Additionally, Akureyri Airport is of interest due to the high traffic volume through Iceland's second largest domestic airport. EGNOS based approach e.g. in Akureyri would greatly enhance air operations to and from Akureyri and make Akureyri a viable destination for international flights, in particular, as it would lower the minimum ceilings of missed approaches as well as increasing pilot confidence. For this to happen, EGNOS signals need to be available at Akureyri in a form receivable by standard airborne EGNOS-enabled navigation systems. This can be achieved in two ways:

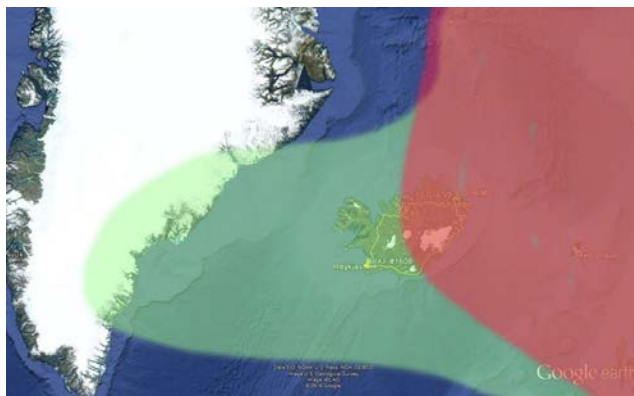


Figure 6. An EGNOS availability "dream" scenario for Iceland

- i. A technical solution could be to install a pseudolite at the Akureyri Airport site, i.e. a transmitter that transmits EGNOS corrections on the L1 frequency using the same signal structure as a GPS satellite. This possibility has not been investigated but it would require permits and certifications from relative authorities, both domestic and international.
- ii. Another possibility is for Icelandic authorities to seek negotiations with the European Union and ESA to enhance EGNOS coverage over Iceland. There are ideas to install high elliptical orbit (HEO) satellites that would provide good coverage over Scandinavia and the North Atlantic [5]. This would have the advantage that the look angle in high latitudes would no more be small and enable EGNOS approaches into many airports, even similar to the one at Isafjörður.

It would be very advantageous for Iceland to enlarge and extend the EGNOS service area to the West of Iceland. This would require at least one EGNOS RIMS station on the Greenland East coast that would support the Icelandic RIMS and increase their availability and integrity. A coverage map with this scenario is shown in Figure6.

CONCLUSIONS

Satellite based navigation plays an important role for the main pillars of the Icelandic economy especially transport, tourism and the fisheries. It is also essential for the safety and well-being of the general population inasmuch as it enables ambulance and search and rescue services to be delivered with the highest level of navigation performance. This field enjoys a rapid pace of development that enables new possibilities and services previously unthinkable. If the Icelandic society wants to enjoy those benefits, Icelandic authorities must take on a more proactive role and increase their co-operation with the neighbouring states. Investments in knowledge and co-operation in this field are likely to provide very good returns, as has been experienced by many neighbouring nations.

ACKNOWLEDGMENT

Parts of this work have been supported by the Icelandic Road and Coastal Administration's Research and Development fund.

REFERENCES

- [1] S. Thorsteinsson, T. Gunnarsson, G. Gudmundsson, G. Tryggvason, P. Enge, D. Young, L. Scheynblat, B. Westfall, C. Daniel and J. T. Helgason, "Iceland's Network of Differential GPS Radiobeacons," *Navigation, Journal of the Institute of Navigation*, vol. 42, no. 4, pp. 557-580, 1995-96.

- [2] MUNIN Consortium, “MUNIN-final-brochure,” EU Seventh Framework Programme, <http://www.unmanned-ship.org/>, 2016.
- [3] European Global Navigation Satellite Systems Agency, “MARITIME, 1ST GALILEO ASSEMBLY - USER CONSULTATION PLATFORM – TRANSPORT-,” 28 November 2017. [Online]. Available: <https://www.gsa.europa.eu/sites/default/files/gsa-mkd-mar-mom-236052-ucp2017-transport-maritime.pdf>. [Accessed 12 April 2018].
- [4] European Global Navigation Satellite Systems Agency, “EGNOS user Support,” European Global Navigation Satellite Systems Agency, 11 May 2018. [Online]. Available: https://egnos-user-support.essp-sas.eu/new_egnos_ops/availability_evolution. [Accessed 11 May 2018].
- [5] A. B. Kristinsson, “Introduction and overview to satellite based air navigation in Iceland,” in *Reykjavik Flight Safety Symposium*, Reykjavik, 2018.

Up-to-date SBAS DFMC Service Volume Prototype (DSVP) to support DFMC performance characterization activities

D. Salos, J. Vuillaume
Egis Avia
France

A. Kanj, F. Dufour, N. Suard, C. Boulanger
CNES (French Space Agency)
France

Abstract—GNSS is one of the navigation means approved by the International Civil Aviation Organization (ICAO) for use in civil aviation navigation. The modernization of current GNSS constellations, like GPS, and the deployment of new ones, like Galileo or BDS, broadcasting dual-frequency signals in the Aeronautical Radio Navigation Service (ARNS) bands will lead in the near future to a Dual-Frequency Multi-Constellation (DFMC) GNSS environment for civil aviation. This new GNSS environment with additional and enhanced signals will support navigation services with improved positioning performances and robustness.

GNSS augmentation systems like ABAS, SBAS and GBAS also need to evolve to support the new DFMC environment. Standardization of these new DFMC GNSS elements is a key step before their approval for operational use in civil aviation. The SBAS DFMC Service Volume Prototype (DSVP) is a software tool developed specifically to support the upcoming standardization activities of SBAS DFMC use for civil aviation. This paper presents the up-to-date SBAS DSVP tool along with its evolutions to comply with the latest SBAS DFMC standard. The paper also provides some examples of achievable SBAS DFMC system and user performances to test various system configurations and/or different interpretations or utilizations of the SBAS DFMC standard.

Keywords—SBAS; DFMC; standardization; performance analysis

Full paper in IEEE Xplore

Will Tomorrow's GNSS Capability Be Good Enough for New Market Demands?

Chris Rizos (University of New South Wales, Sydney, Australia)

Abstract:

GPS has been a reliable, highly versatile, generally available and very accurate positioning technology for over three decades. Within a few years a number of other Global Navigation Satellite Systems (GNSS) and regional systems will have been fully deployed. This world of multi-constellation GNSS will deliver more satellites, more frequencies and more trackable signals, bringing benefits to a wide range of users. In addition new augmentation concepts, such as Precise Point Positioning and Space-Based Augmentation Systems, will expand the toolbox of precise GNSS positioning techniques. New hardware and software designs promise smaller, cheaper and more capable receivers, that can address even more user markets. The biggest mass market for enhanced multi-GNSS positioning will be the Transport Sector, in particular that associated with highly automated driving. Governments invest in new ground and space GNSS infrastructure, industry invests in the development of new systems, scientists continue to squeeze higher and higher performance from GNSS, and users embrace more and more applications. However, this future is more confusing and more challenging because of a massive increase in GNSS capability, in the variety of GNSS-based systems, the GNSS configurations, the GNSS augmentations and the GNSS user requirements. The coming years for government decision-makers, systems developers, researchers and engineers, will be exciting, and not a little daunting. This presentation is intended to challenge the notion that GNSS's future is rosy, predictable and free of hard choices.

Cognizant Autonomous Vehicles: Opportunities and Challenges

Zak M. Kassas (University of California, Riverside)

Abstract:

The predicted economical and societal impacts of future autonomous vehicles are astounding. For example, unmanned aerial vehicles (UAVs) over 10-years could generate 100K high-paying technical jobs and contribute \$82B to the U.S. economy; while self-driving cars could save annually 30K lives and \$190B in healthcare costs associated with accidents in the U.S., conserve 7B liters of fuel, and save hundreds of billions of dollars in lost productivity. However, despite these optimistic predictions, these systems are not yet ready for prime time and could introduce unintentional problems beyond our foreseen imagination. This talk will discuss some of the technical and ethical challenges associated with developing cognizant autonomous vehicles, particularly GNSS jamming and spoofing, AI limitations and its recent missteps, and autonomy failure.

The talk will also present some recent research results aimed at providing resilient and accurate autonomous navigation in GNSS-denied environments by exploiting ambient signals of opportunity. Experimental results will be presented demonstrating sub-meter level accurate ground vehicle and UAV navigation with signals of opportunity, in the absence of GNSS signals. Moreover, research results will be presented highlighting the importance of adapting the autonomous vehicle's decision making strategy to environmental uncertainty.

Robust radio localization with FLIP

Reinhard Müllner, Thomas Burgess

Research Department

indoo.rs GmbH

Geyschlägergasse 14

1150 Vienna, Austria

<{reinhard, thomas}@indoo.rs>

Abstract—Radio fingerprinting based localization relies on comparing observations to a database of reference radio fingerprint point data. For complex buildings these databases can be very large. As mobile devices have limitations in storage capacity, working memory, processing speed, and power usage, making an on-terminal system that works well even in large installations is challenging. Moreover, the reported Received Signal Strength Indication (RSSI) scale often differ between devices, so that naive approaches for fingerprint similarity easily can fail to produce reliable results.

In this paper, FLeXible Indoor Position (FLIP) is presented to address these issues. It provides efficient device independent positioning even in complex buildings, while also taking inhomogeneous transmitter power levels and radio map irregularities into consideration. Despite plain accuracy not being the main goal of FLIP, when it was evaluated on the raw `UJIIndoorLoc` WiFi database it yielded a median positioning error of 4.7 m (and above 93 % floor level/building identification success rate), which is competitive to other significantly more computation intense approaches. In commercial applications with dedicated `iBeacon` infrastructures, FLIP routinely reaches median errors below 2 m.

Index Terms—Indoor positioning, Fingerprint based positioning, Floor estimation, RSSI, Bluetooth, Wireless Local Area Networking (WiFi), Mobile Computing

Full paper in IEEE Xplore



TAPAS

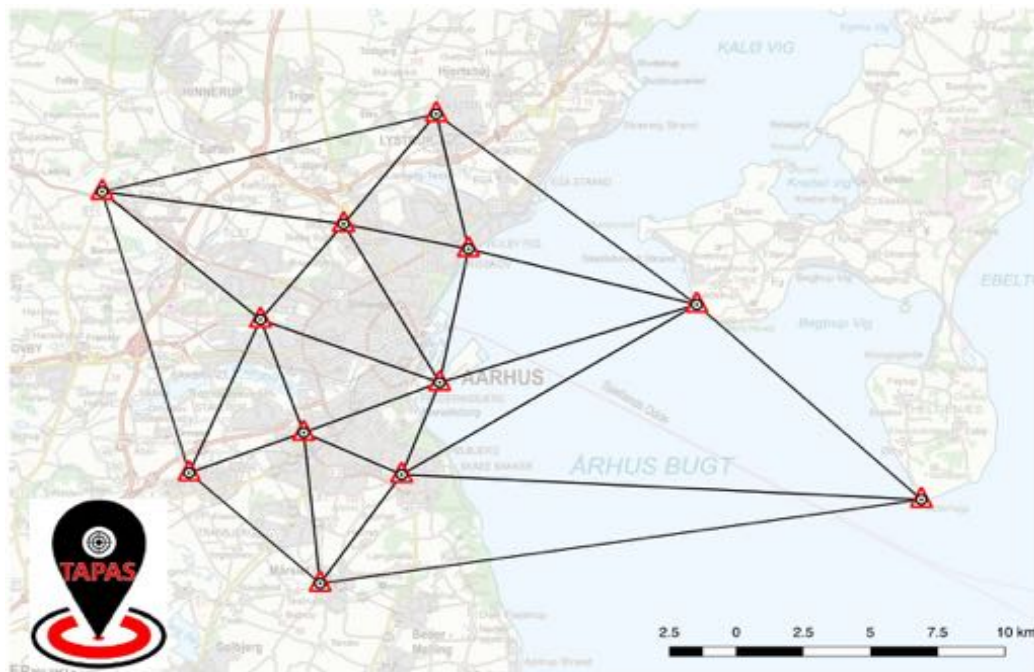
- Testbed in Aarhus for Precision Positioning and Autonomous Systems

The demands for basic infrastructures in modern societies are increasing in line with the desire for increased growth and efficiency. Testbed in Aarhus for Precision Positioning and Autonomous Systems (TAPAS) is a science and research project aimed to verify to which extent an improved infrastructure can contribute to exploit the full advantage of the technical achievements of the new Global Navigation Satellite Systems (GNSS). Geodetic reference systems are the fundamental infrastructure that provides the basis for precision positioning and navigation using GNSS. Available systems of today are primarily based on GPS measurements, with supplement of local Real Time Kinematic (RTK) systems.

Additional global GNSS systems are these years being implemented such as BeiDou (China) and not least Galileo (European). These systems are now forming the basis for new terrestrial networks and the basis for both faster and better position determination. TAPAS will establish a sound ground based network test bed, to support and test new advanced technological developments with a need for fast, efficient and flexible precision positioning. It will be designed as a geodetic innovation platform, in form of physical and virtual networks. The ambition is to exploit the full potential of Galileo and evaluate this system's quality in relation to GPS. Further, and in particular, it is the goal to achieve unprecedented precision positioning in real-time.

Autonomous systems within transport, agriculture or environmental monitoring, e.g. automated vehicles and machines, drones, marine units, constitute to a very large growth area within a wide range of business opportunities. Since these systems are inseparably linked to geodetic reference systems, RTK and associated communications networks (Wi-Fi, 5G etc.) it is expected that TAPAS can provide necessary technical insight in order to obtain an infrastructure where autonomous systems can be operating.

Initially, TAPAS will focus on the area around Aarhus city and harbor as a test bed for in situ trials. The location in this densely populated area also provides opportunities for observing disturbing elements of a city, such as urban-canyons/canopies.



The TAPAS network is currently being implemented in an Alpha version and at the end of 2018 the Network is available for continued research projects, open for third parties to test own ideas and innovative prototypes on the platform to gain knowledge. 11 Class B stations and one Class A GNSS station forms the network. The stations are being designed in a flexible way to use latest state of the art technologies, as well as to ensure future technical iterations and updates. Stations will be interconnected in a network to a RTK GNSS server, which calculates and stream relevant corrections and integrity information to the users.

TAPAS is being developed, to accommodate both new geodetic and autonomous reference systems, as well as current and future communication networks. I.e. this innovation research platform attempts to integrate these systems, test concrete initiatives and utilize satellite-based Earth observation data.

The network is funded by Danish Agency for Data Supply and Efficiency and developed in close corporation with the GNSS Experts from DTU Space.



Agency for Data Supply and Efficiency



Contacts:

Agency for Data Supply and Efficiency

- Casper Jepsen
caj@sdfе.dk
+45 72545281
- Martin Skjold Grøntved
maskg@sdfе.dk
+45 26857326
- Brigitte Christine Rosenkranz
bicro@sdfе.dk
+45 72545203
- Per Kolbeck Nielsen
pekon@sdfе.dk
+45 72545711

Danish Technical University

- Per Lundahl Thomsen
plt@space.dtu.dk
+45 45259727
- Lars Stenseng
stenseng@space.dtu.dk
+45 45259792
- Tibor Durgonics
tibdu@space.dtu.dk
+45 45259658

GNSS for taximeter verification and calibration of road segments

Harald Hauglin^{1,2}, Robert Hughes¹, Alexander Gård³, Jan-Erik Holmen¹, Håkon Skjolden¹, Helge Karlsson¹

¹Justervesenet - Norwegian Metrology Service, Kjeller, Norway

²Department of Technology Systems, University of Oslo, Norway

³Department of Informatics, Norwegian University of Science and Technology, Trondheim, Norway

Email: hha@justervesenet.no

Summary

There is a need for efficient and flexible methods for taximeter verification and for calibration of reference road segments. National tolerance requirements for taximeters are 3%, while reference road segments need to be determined with an uncertainty better than 1 m over 1000 m (0.1%). We demonstrate agreement at better than 0.05 % between distances estimated from time series of uncorrected L1 GPS+GLONASS PVT samples and reference calibrations traceable to the SI meter. We find that estimates based on velocity samples have better reproducibility due to low biases and near white noise properties of velocity estimation,

Methods and equipment

Distance can be calculated from time series of PVT data (1) from position estimates \mathbf{p} as $l_{\text{pos}} = \sum_{i=1}^{N-1} |\mathbf{p}_{i+1} - \mathbf{p}_i|$ and (2) from velocity estimates \mathbf{v} as $l_{\text{velocity}} = \Delta t \sum_{i=1}^N |\mathbf{v}_i|$, where Δt is the sample period. Ideally, velocities correspond directly to changes in position. In practice, they may be estimated in different parts of the receiver tracking/correlation/estimation loop and have different sensitivities to receiver noise, to clock and ephemeris errors and e.g. ionospheric delay. The detailed interdependence of position and velocity samples are likely implementation specific and not explicitly known to the end user.

Tests were carried out using a vehicle-mounted single frequency (L1) GPS and GLONASS receiver (Septentrio AsteRx1 + PolaNTGG antenna). Binary data was streamed from the receiver to a tablet/PC and processed in real time as well as stored for off-line analysis. GNSS correction services were not used. Measurement runs were started with the test vehicle at rest and aligned with reference marking, proceeded by normal acceleration to a speed 15 – 20 m/s followed by a normal deceleration and stop near the endpoint. The distance between the actual stop and the endpoint reference marking was measured with a calibrated tape measure and used as a correction to the GNSS-based distance estimate. Auxilliary ‘zero test’ of 60 second GNSS measurements with the vehicle at rest were performed immediately before and after each run. Zero tests provide an estimate of a systematic bias in the GNSS velocity estimates. Time series of velocity samples were corrected off-line with a bias estimate based on the average of the corresponding zero tests.

Results

GNSS estimates are summarized in fig.1 for road segment lengths calculated from (1) and (2). Velocity-based estimates have been corrected by velocity biases determined by ‘zero-tests’ summarized in fig. 2. We find that both estimates l_{pos} and l_{velocity} provide agreement with a conventional traceable calibration at a level better than 0.05 %. However, velocity based estimates show much better repeatability than those based on position changes. Inspection of zero-tests shows that direct velocity estimates (fig. 3, left) are much less correlated than the velocities determined from the rate of change in the position (fig. 3, left). In practice, velocity noise is therefore more effectively averaged out over the typical duration of a measurement run, than noise in position estimates. For the test runs presented in fig. 1, velocity bias corrections calculated off-line contribute less than 10 cm (0.01 %) to the overall result, and, if left out, could be included simply as an additional component in the uncertainty estimate.

Figures

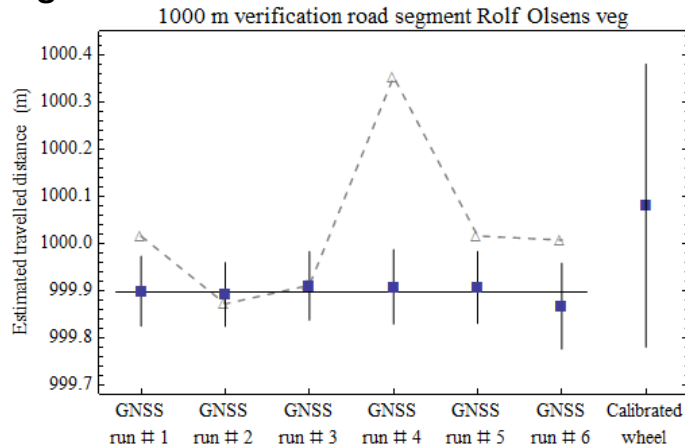


Fig. 1: Comparison between GNSS estimates of road segment length and a reference calibration traceable to the SI meter. GNSS estimates are based on time series of 10 Hz velocity (blue) and position samples (gray) from a vehicle mounted L1 GPS+GLONASS receiver/antenna. The rightmost value is from a calibrated wheel/odometer. Error bars represent the expanded uncertainty (95% confidence interval).

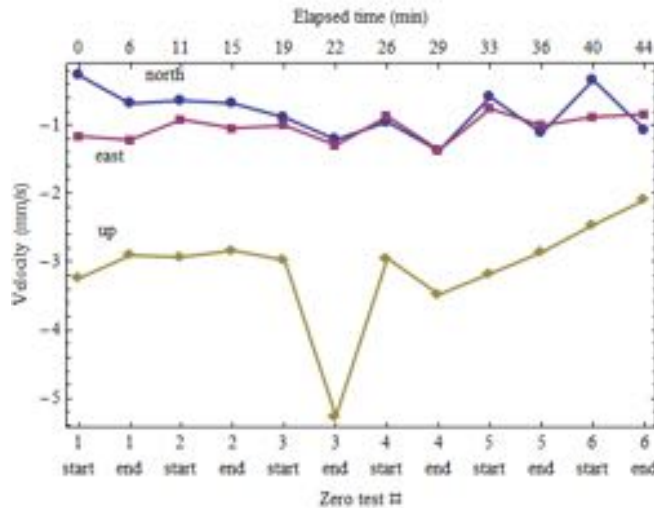


Fig. 2: GNSS velocity bias estimates from 'zero tests' based on the average 600 samples (10 Hz) recorded at rest immediately before the start and after the end of each measurement run.

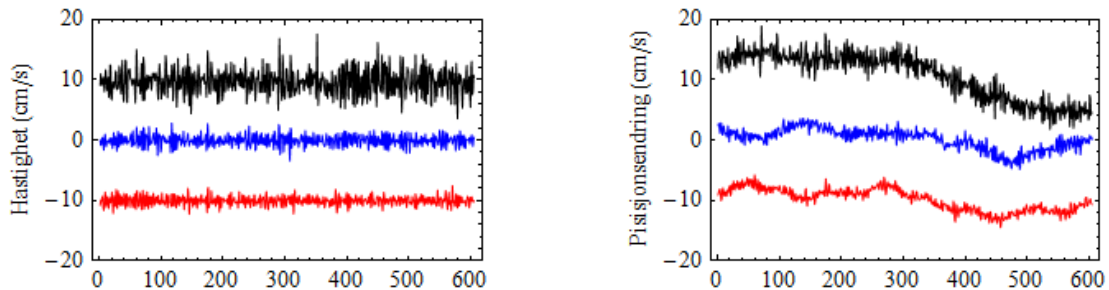


Fig. 3: 60 s duration time series of 10 Hz GNSS velocity samples (left) and first differences of position estimates divided by the sample period (right) for east (red), north (blue) and up (black). Data is recorded with the test vehicle at rest. Values are offset by 10 cm/s for clarity.

VDM-based UAV Attitude Determination in Absence of IMU Data

Mehran Khaghani

Geodetic Engineering Laboratory (TOPO)
Swiss Federal Institute of Technology (EPFL)
Lausanne, Switzerland
Email: mehran.khaghani@epfl.ch

Jan Skaloud

Geodetic Engineering Laboratory (TOPO)
Swiss Federal Institute of Technology (EPFL)
Lausanne, Switzerland
Email: jan.skaloud@epfl.ch

Abstract—The capability of a previously proposed VDM (vehicle dynamic model) based navigation method for UAVs is assessed in attitude determination without IMU data. This method utilizes the VDM as main process model within the navigation filter and treats data from IMU (if available) and other sensors as observations. Experimental results from a test flight and a Monte Carlo simulation are presented to compare the performance of the VDM-based navigation against the conventional INS-based navigation. While the attitude estimation performance of VDM/GNSS integration is comparable to that of INS/GNSS in simulations, experimental results reveal the need for improved VDM parameter calibration.

Index Terms—UAV, Navigation, Attitude Determination, Vehicle Dynamic Model, IMU failure, Kalman Filter

Full paper in IEEE Xplore

Automated Exploration with Multi-Sensor Equipped UAV/UGV

S. Batzdorfer, M. Becker, M. Bobbe, U. Bestmann

Institute of Flight Guidance, Technische Universitaet Braunschweig
Braunschweig, Germany
s.batzdorfer@tu-braunschweig.de, m.becker@tu-braunschweig.de,
m.bobbe@tu-braunschweig.de, u.bestmann@tu-braunschweig.de

Abstract— For exploring disaster scenarios unmanned systems like aerial or ground based vehicle (UAV/UGV) have become more relevant in recent time as a supporting system for action forces to increase the situational awareness. To take advantage of using such systems the relationship between quality of support and additional workload for the operator has to be well-balanced. Therefore a system consisting of multiple UAV and UGV has been built-up within the joint research project ANKommEn – german acronym for Automated Navigation and Communication for Exploration. The vehicles are equipped with different environmental sensors like optical or thermal camera or a LiDAR and are controlled by a central ground station. This ground station serves as an user interface to define missions and tasks and also to visualize online the exploration task results. Depending on the exploration task results, in form of pictures, 2D stitched orthophoto or LiDAR point clouds are transmitted via datalinks and displayed or will be processed in short-term after a mission, e.g. 3D photogrammetry. For georeferencing of the exploration results reliable positioning and attitude information is required, which is also indispensable to monitor and control the UAV/UGV during mission execution. This is gathered using an integrated GNSS/IMU positioning system. In order to increase availability of positioning information in GNSS challenging scenarios, a GNSS-Multiconstellation based approach is used, amongst others. The present paper focuses on the system design including sensor setups on the UAVs and UGVs and the ground station, the underlying positioning techniques as well as 2D and 3D exploration based on a RGB camera mounted on board the UAV and its evaluation based on real world field tests and also the benefit of such systems in a destructive flood scenario will be presented.

Keywords—positioning for automated UAV/UGV; Multi-constellation-GNSS; Photogrammetry; SLAM

I. INTRODUCTION

Within a disaster scenario like fire scenarios, flood areas or search-and-rescue tasks the action forces are faced with complex situation and a good situational awareness is indispensable to cope with the tasks. In most cases a priori known map data information is outdated and an efficient situational proceeding like e.g. path planning or creation of a search pattern (SAR), cannot be performed. Up to the present, this information often can only be provided by manned exploration using ground or airborne systems with the

limitation of contemporary availability. The motivation of the joint research project *ANKommEn* (german acronym for *Automated Navigation and Communication for Exploration*) is to create an automated unmanned system which closes this gap by providing up-to-date information of the scenario and also increases the safety of human resources by using unmanned vehicles, aerial (UAV) as well as ground based (UGV).

The project *ANKommEn* is a german joint research project. Project partners are the Institute of Flight Guidance (IFF), the Institute of Mobile Machines and Commercial Vehicles (IMN) – both Technische Universitaet Braunschweig – and the AirRobot® GmbH & Co. KG, a german manufacturer of multirotor UAVs. Additionally, the professional fire brigade of Braunschweig and the NLWKN (Lower Saxony Water Management, Coastal Defense and Nature Conservation Agency) participate as associated project partners. These institutions as potential users take a great interest in getting up-to-date information of the operational scenario and supported the definition of several requirements for the developed system, like the ability to focus on a self-defined area for more detailed information.

To provide up-to-date information of the desired destination area, all vehicles are equipped with identical positioning and communication hardware complemented by diverse sensors (RGB camera, IR camera, LiDAR) for visual exploration. The visual sensor information is transmitted to a central ground station for visualization and/or analyses. In order to increase the advantage using the built-up system, the unmanned systems should have a high grade of automation to reduce the workload of the operator. To meet this requirement only basic inputs have to be done by the operator. For example, just by marking a destination area and choosing a predefined task, the mission will be planned automatically and after the corresponding waypoint-list has been transmitted to the vehicles, the mission will start.

Especially automated procedures of an UAV require valid position information related to accuracy, availability and continuity. In exploration areas where the UAV operates in low altitude or using an UGV, the reception of the GNSS signal can be degraded by the topology (building etc.). To increase the availability of position information the usage of

more than one GNSS system provides advantages. For vehicle control and georeferencing the environmental sensor data and exploration results high frequent absolute position and attitude and heading information is required. This data is gathered by fusing GNSS data and IMU measurements.

II. OVERALL SYSTEM DESIGN

The overall system consists of three UAV, two UGV (Fig. 1) and a central ground and control station (Fig. 6). The latter serves as a central human machine interface to monitor and manage cooperative operation of the UAVs/UGVs by an operator (Fig. 7). Based on a priori known map data, exploration areas and tasks are defined and assigned to the UAVs/UGVs and will be updated with actual information of the visual sensors while performing a mission.



Fig. 1. UAVs and UGVs of ANKommEn

This is done by an online 2D georeferenced photo stitching based on pictures transmitted via data link to the ground station. Path planning is then automatically conducted and transmitted via data links to the unmanned machines. The user interface developed by the IMN is capable to integrate multiple real-time sensor streams of all UAVs/UGVs to get a comprehensive overview of the scenario. Furthermore the control station can be used to adjust communication parameters like bandwidth, protocol and rate of each sensor data stream to avoid a loss of communication especially in rough terrains and to meet demands of the current mission. A scheme of the interaction and information exchange between the different vehicles and sensors is shown in Fig. 2. For further information of the data exchange and communication see [1].

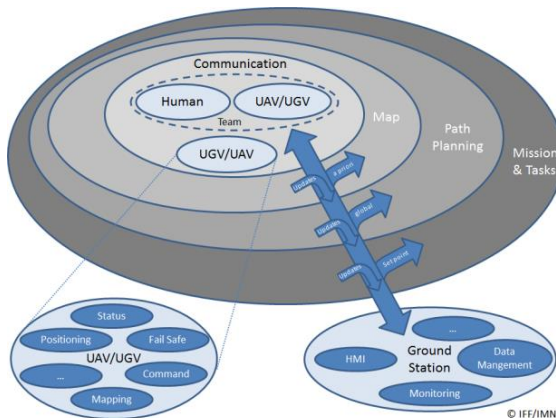


Fig. 2. Diagram of interaction and information exchange

For this purpose all UAVs/UGVs are equipped with a “navigation and communication unit” (NAV/COM-unit) and an “environmental sensor payload unit” (ENV-unit), including a RGB camera, thermal camera or a LiDAR respectively.

A. UAV/UGV and Sensor Hardware

The UAVs are modified hexacopter type AR200, manufactured by AirRobot® GmbH & Co. KG, with a payload of 2.7 kg (NAV/COM-unit, mounted in the upper compartment, and ENV-unit mounted under the UAV) and a corresponding flight time of up to 30 minutes depending on actual meteorological conditions (Fig. 3 (left)).



Fig. 3. UAV Type AR200 (modified) (left) and UGV Type Summit XL (Robotnik) (right)

The payload-sensors are carried and stabilized by a 2-axis-gimbal, manufactured by AirRobot and equipped with sensors and processing units by TU Braunschweig (Fig. 3, left). For ground based exploration two Robotnik Summit XL have been chosen. (Fig. 3, right) They have a 4-wheel-drive and are carrying a pan tilt zoom (PTZ) camera at the top of front chassis. Additionally the UGVs are equipped with a LiDAR and a thermal camera or stereo RGB camera respectively.

The navigation and communication unit mounted as a stack includes a network processor board type Ventana GW5520 for communication and data exchange between the UAV/UGV and the central ground and control station. For position calculation and GNSS-NTP-based time server, an embedded Cortex A9 processing board type Phytex phyBOARD®-Mira i.MX6 has been chosen. The data for the position calculation is provided by a custom-designed break-out-board by the Institute of Flight Guidance, which combines an Analog Devices inertial measurement unit (IMU) type ADIS16488 and a multi-constellation capable GNSS receiver type u-blox LEA-M8T (Fig. 4).

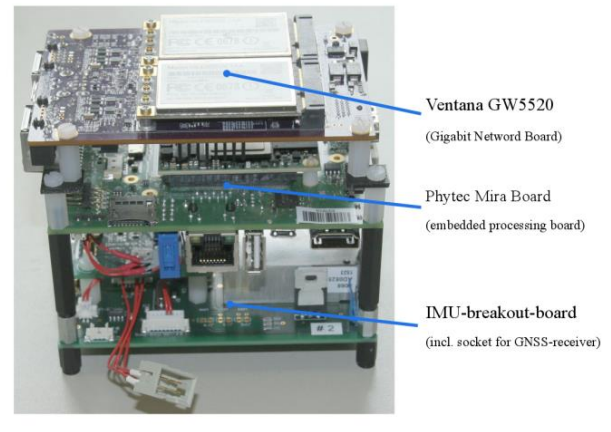


Fig. 4. Navigation and communication unit

The environmental sensor payload unit is based on three different types of sensors which are interchangeable between the different UAV, using the proprietary payload interface of the AR200:

1. RGB camera (Allied Vision Manta G-917)
2. LiDAR (Velodyne VLP-16)
3. IR camera (FLIR A65sc)



Fig. 5. RGB camera, LiDAR and IR camera

Concerning the UGVs, each one has a fixed environmental sensor setup. Both are equipped with a PTZ camera and a top mounted LiDAR. Additionally, one UGV carries a RGB-stereo-camera and the second one an IR camera (Fig. 5, right). Data traced by these sensors cannot be sent directly to the ground station because of the huge data amount and the limited bandwidth of the communication link. Therefore another processor-board, an Intel NUC-board, is mounted on the gimbal and connected to the visual sensor via gigabit Ethernet. The NUC-board itself is connected to the communication board within the modified AR200. Data from the sensors are preprocessed and/or compressed on the Intel NUC and after that transmitted to the ground station.

B. Ground Station

The ground station shown in Fig. 6 is the central device for command, control and visualization of the total system. It provides several options to display the data from the different sensors and vehicles (UAV/UGV) and a combination of them. Furthermore, the automated path planning for different missions and calculation of the 3D reconstruction (photogrammetry) and online 2D stitched orthophoto is realized within it. The user can switch between various options/windows for sensor data visualization, defining missions and setting waypoints for path planning which are transmitted to desired vehicle and/or set parameters for the 3D reconstruction, as well as monitoring the UAVs and UGVs.



Fig. 6. Ground station and integrated PCBox

Fig. 7 shows an example of the display while an UGV is performing a mapping mission using the top mounted LiDAR. The layout can be customized by the user.

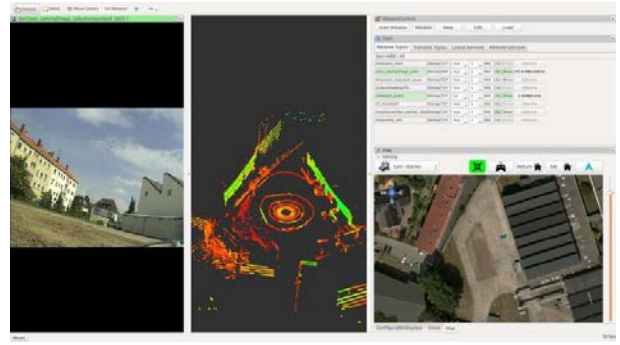


Fig. 7. HMI with combined visualization of different sensors

The screenshot (Fig. 7) shows from left to right, the actual view by the PTZ camera onboard the UGV, the point cloud gathered by the LiDAR and mission parameters (top-right) as well as a map in form of an aerial view (bottom-right)

C. Software-Frameworks

The basic software for determining the vehicle's state in manner of 3D position, velocity, attitude and heading is established within the modular build-up navigation software framework of the Institute of Flight Guidance, with the option to process data of different sensors in real-time as well as postprocessing for data evaluation and development purpose. Several algorithms for sensor data fusion are implemented. The algorithm which has been chosen for IMU/GNSS fusion is based on an Extended Kalman Filter and also provides an IMU data based state vector, stabilized by GNSS information, for the visual sensors. This state vector is published by using a ROS framework (Robot Operating System). ROS, basically designed for applications for robots, is a framework for inter process communication and is based on a TCP or UDP publisher/subscriber concept. The visual sensors and embedded PCs subscribe to different ROS messages, e.g. the state-vector-message or information of other sensors.

III. POSITIONING OF UAV AND UGV

Automated operation of UGV and UAVs requires valid position as well as attitude and heading information. In the case of using only one GNSS system, e.g. GPS, the signal quality and availability can be degraded by environment (buildings) and can result in a less precise or even a lack of position information.

A. GNSS-Multi-Constellation

In order to overcome the risk of poor availability of GNSS based position information – for example when operating the UAV/UGV in GNSS challenging areas – one way is parallel usage of different GNSS systems to raise the number of received satellite signals. Today there are four satellite positioning systems available, the common GPS (actually 31 satellites [11]) and GLONASS (actually 24 satellites [5]) and the evolving Galileo (actually 12 satellites [4]) and BeiDou (actually 14 satellites [6]). In respect of the fact that one is able to receive signals only of a subset of all available satellites, the usage of different constellations can increase the availability significantly. In the worst case, a multi-

constellation based position is still equal to the single-constellation solution of positioning.

When using a multi-constellation approach for positioning, one has to take care of several aspects which differ between those GNSS systems [10], [7], [3], [2]. All satellite based navigation systems use different geodetic reference frames and time basis. That means one has to transform measurements gathered from another GNSS system into the reference frame of the desired system.

- *GPS*: World Geodetic System 1984 (WGS84) [10]
- *GLONASS*: Parametry Zemli 1990 (Parameter of the Earth 1990 PZ-90) [7]
- *Galileo*: Galileo Reference Frame (GTRF) [3]
- *BeiDou*: China Geodetic Coordinate System 2000 (CGCS2000) [2]

All these reference frames are in compliance with the International Terrestrial Reference Frame (ITRF) and can be transferred into each other.

Due to the fact, that the different GNSS systems have a different time base, a different approach is needed in order to get reliable position solutions. This inter-system offset has to be taken into account for combined position solution. A way to handle this problem is to extend the estimated state vector by adding a clock error for each GNSS system, which leads to

$$\vec{x} = \begin{pmatrix} x \\ y \\ z \\ c \cdot \Delta t_{GPS} \\ c \cdot \Delta t_{GLO} \\ c \cdot \Delta t_{GAL} \\ c \cdot \Delta t_{BDS} \end{pmatrix} \quad (1)$$

where \vec{x} = state vector

x, y, z = position

$\Delta t_{GPS}, \Delta t_{GLO}, \Delta t_{GAL}, \Delta t_{BDS}$ = constellation specific clock error

c = speed of light

By including the different clock errors in the state vector the number of unknown variables increases, so for solving this equation more GNSS measurements are required. In the case displayed in (1) seven variables have to be determined. If no measurements of a specific GNSS system are available, the estimation can be simplified by excluding the corresponding clock error from estimation.

The geometric distribution of the satellites is improved by using more than one GNSS constellation, indicated by a lower value of Dilution of Precision (DOP). On the one hand this indicates a better mapping of per-range accuracy to position accuracy which provides not necessarily a higher accuracy compared to a single constellation solution but on the other hand it will improve the overall availability.

The navigation software framework of the IFF is designed for real-time computation and also for postprocessing. In postprocessing the recorded sensor data is streamed to the software framework with the option that one can change several parameters and settings for calculation in order to analyze and evaluate the implemented techniques and

algorithms. One option is to exclude satellites at low elevation from position calculation by changing the cut-off-elevation for these satellites. This parameter will be changed for simulating environmental conditions that block receiving GNSS signals, like buildings within urban scenarios, to compare the availability of received GNSS signals for single- and multi-constellation based position calculation. Recorded data of a real world test serve as the database for the postprocessing with different cut-off-elevation parameters. At the beginning of the field test, there was a short time initialization period in order to boot the OS and to start basic processes for positioning. After that a predefined mission was flown and the GNSS measurements have been recorded for described postprocessing.

The postprocessing has been performed with different parameters regarding the cut-off-elevation for the satellites. Starting point for the comparison is cut-off elevation of 5° . This is a common value for GNSS-Position calculation and excludes low satellites, the signals of which on the one hand have to path a long distance through the troposphere and on the other hand are more vulnerable to multipath effects.

The result is shown in Fig. 8 and illustrates that the number of received GNSS satellites is higher than the number that is used for position calculation. This is caused by the predefined cut-off-elevation and further quality checks like signal-to-noise-ratio aiming to eliminate the influence of model-based output of the GNSS receiver.

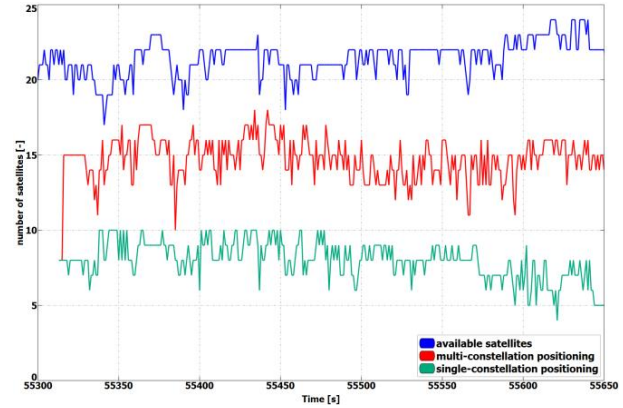


Fig. 8. Number of available satellites vs. used for position solution with cut-off-elevation of 5°

At the beginning of the initialization period the number of received satellites is 21 and after approximately 15 seconds when all ephemeris have been received, 7 satellites are used for a GPS based single-constellation positioning. A multi-constellation based positioning is also available and the number of satellites used for positioning increases to 15. During the flight of the UAV, the number of available satellites varies, which is caused by maneuvers of the UAV to fulfil the predefined mission as well as compensating wind gusts. Overall the number of satellites used for multi-constellation based positioning is nearly twice the number of satellite of a single-constellation based positioning.

To simulate a degraded GNSS reception during the flight, the cut-off elevation is increased to 20° . This is comparable to e.g. a flight in an urban scenario or other areas with obstacles like

trees, and it reduces the number of satellites used for a single-constellation position solution to 6 or less and to 10 or less respectively for a multi-constellation solution (Fig. 9). Compared to the deviation with a cut-off-elevation of 5° (Fig. 8), the number varies not so much, which means that the effect of degraded GNSS reception by self-shadowing of the UAV during maneuvers for satellites with a low elevation is minimized.

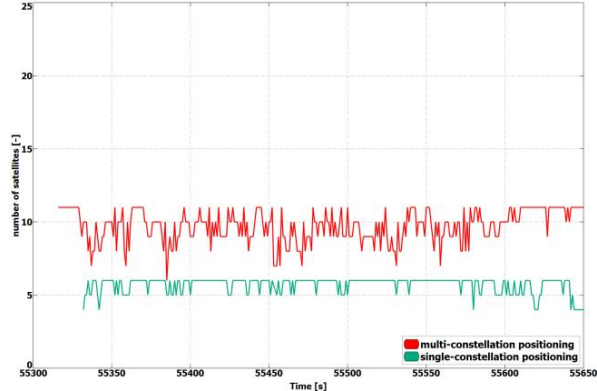


Fig. 9. Number of satellites used for position solution with cut-off elevation of 20°

The last case of the comparison is that only satellites with an elevation higher than 35° are used for position calculation. This case is especially reasonable for an UAV operating in similar scenarios as described in the previous paragraph but working at a lower altitude so the GNSS signals might be blocked by the environment. On the other hand this can be a case for an UGV operating near buildings or other obstacles. The graphs in Fig. 10 indicates that in this case the reception of GNSS signals is extremely reduced and a valid GPS based positioning starts approximate 50 seconds later than a valid positioning using a multi-constellation approach. While using only a GPS based single-constellation the number of satellites is reduced to the minimum of required satellites for position calculation of four in contrast to 5-7 available satellites for a multi-constellation based solution.

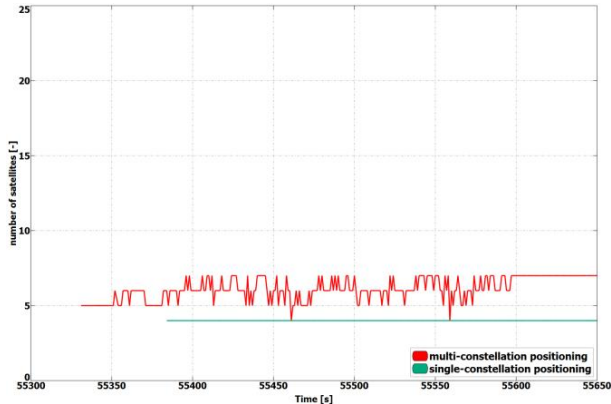


Fig. 10. Number of satellites used for position solution with of cut-off elevation of 35°

Especially this case shows the benefit of a higher availability of GNSS satellites by using more than one GNSS system for positioning.

B. GNSS/IMU-Fusion

Using the described GNSS multi-constellation approach availability of position information could be increased. For attitude and heading determination, an Inertial Measurement Unit is nevertheless indispensable. Additionally, the frequency of the pure GNSS based positioning information usually is between 1Hz to 5Hz within the described hardware setup. For a meaningful georeferencing of the above described and used environmental sensors much higher frequent position and attitude information is required.

So the GNSS based positioning is used for aiding the IMU measurements within an Extended Kalman Filter using the navigation software framework of the IFF. The mentioned ADIS IMU provides high frequent, three dimensional measurements of accelerations and angular rates. Using common strapdown algorithm processing, high frequent position, velocity, attitude and heading information is provided in real time. Due to the short time stability of pure inertial navigation, the GNSS positioning results are used for aiding purpose within the Kalman Filter's update step. To overcome the absence of GNSS aiding information even when using multi-constellation, mainly two options are possible. Firstly, a short coasting period is possible after the data fusion has reached steady state. Secondly, it is possible due to the high modularly design of the IFF's navigation software framework to use position and/or attitude increments from environmental sensor data processing for aiding the IMU.

The determined vehicle's state vector is then distributed with high frequency within the system for georeferencing measurements of the used environmental sensors especially the RGB camera and the LiDAR for photogrammetry and SLAM applications.

IV. PHOTOGRAMMETRY AND SLAM

When thinking of major fire scenarios, up-to-date information is required, whereas a priori information like maps could be out-of-date. Therefore techniques have been developed to gather a 2D overview based on several single RGB pictures taken and processed on-board an UAV and transmitted to the ground station via data links. Additional processing of a 3D reconstruction of the scenario is an integrated feature within the ground station. Both approaches were implemented with the goal to get an automated rapid aerial mapping solution.

In the case of the 2D overview, SLAM algorithms, often used in robotic research, are adapted for this specific use-case. These algorithms provide good results for a rapid aerial mapping solution to get an overview of the scenario, because the map is updated incrementally with every new image, but they are less precise, which can be compensated by using the photogrammetric 3D-reconstruction. The live mapping (SLAM) approach is based on the ORB-SLAM algorithm and the photogrammetry based approach uses the commercially available photogrammetry software Agisoft Photoscan.

The systems, on the UAV for 2D and for 3D on the ground station, use the ROS-Framework for processing the visual sensor data and the described techniques for positioning,

georeferencing and attitude determination. For data exchange between these Frameworks several software interfaces have been implemented. Fig. 11 displays a flowchart of the implemented workflow.

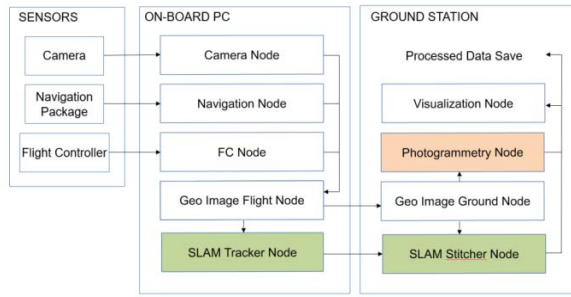


Fig. 11. ROS node layout with SLAM (green) and photogrammetry workflow (red)

The sensor/input data is received by corresponding nodes on the aerial vehicle. After adding the camera pose information to the image in the Geo Image Flight Node, the image is sent to the Geo Image Ground Node on the Ground Station. The SLAM process is separated into two parts. The SLAM Tracker Node calculates the transformation between images and the SLAM Sticher Node applies the transformations. The transformed images are displayed by the Visualization Node. The Photogrammetry Node receives the georeferenced images, stores the data and initiates the photogrammetric processing ones the survey is finished. The results can also be displayed by the Visualization Node and exported in a desired format.

A. Visual SLAM

During the past few years computer vision, especially SLAM (Simultaneous localization and mapping) based algorithms have developed rapidly. In 2007 Klein and Murray presented a method to estimate a pose by using monocular image processing, known as Parallel Tracking and Mapping (PTAM). On the one hand, they integrated a bundle adjustment (BA) and on the other hand separated the tracking and the mapping procedure into different threads which led to a real-time capable framework [8]. Mur-Artal and Montiel used these basic principles of PTAM and integrated a robust loop closing and another method of relocalization, which is known as ORB SLAM 2 (*Oriented FAST and Rotated BRIEF*). The structure of the ORB SLAM is shown in Fig. 12.

Fig. 12 shows the approach of separating the Tracking, Local Mapping and the Loop Closing into different threads (gray boxes) and the main map and place recognition in the middle.

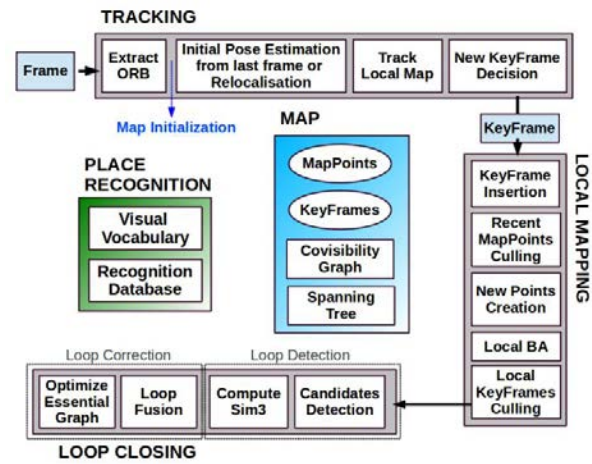


Fig. 12. ORB SLAM system overview [9]

The tracking thread predicts the current pose from the last known position and movement by using a constant velocity model and performs a guided search of map points. If these points are found near the estimated position, the velocity model is valid and the tracking procedure continues. Otherwise the tracking is lost and a relocalization in the global map starts by using a subset of features, which are increased after detection of corresponding features in other keyframes to optimize the camera pose and finally, the tracking procedure continues. The last step of this procedure is to decide whether the current frame contains enough information to be inserted as a new keyframe for further calculations. To mark a frame as a new keyframe, the frame must fulfill all of the following conditions:

- 1) More than minimum number of frames has passed
- 2) Local mapping is on idle or condition 1 fulfilled
- 3) A minimum number of 50 points is observed
- 4) A maximum of 90% of the features is already observed by the other frames.

When a new keyframe is passed to the local mapping procedure and is inserted as node into a covisibility graph structure, new correspondences are searched in the connected keyframes to triangulate new points. Based on the information accumulated during the tracking, a point culling is done in order to keep only high quality points in the map as well as a culling of redundant keyframes.

After finishing the keyframe culling in the local mapping process, a loop closing is performed. This is one of the main improvements compared to PTAM. If a loop is detected the drift accumulated in the loop is computed, and both sides of the loop are aligned and visible points are fused. In a final step a pose graph optimization is done to achieve global consistency.

This information of the 3D camera pose is used to generate a 2D orthophoto in real-time while the vehicle is flying. To create a 2D orthophoto, a common reference frame is approximated, which is orthogonal to all camera measurements. The projection is performed by using a projection model based on a pinhole camera.

$$\underline{x} = \underline{\underline{R}}^1 (\underline{\underline{K}} \underline{s} \underline{u}) \quad (3)$$

where \underline{x} = world point
 $\underline{\underline{R}}^1$ = exterior orientation (3x3)
 $\underline{\underline{K}}$ = interior calibration (3x3)
 \underline{u} = point in homographic coordinates (image plain)
 \underline{t} = exterior position of the camera
 s = scale factor of projection direction vector

For a compensation of geometric distortion caused by the lens, image point can be distorted by using

$$x_{cor} = x + [2p_1xy + p_2(r^2 + 2x^2)] \quad (4)$$

$$y_{cor} = y + [p_1(r^2 + 2y^2) + 2p_1xy] \quad (5)$$

After the compensation and distortion the whole images can be stitched to the current global map.

B. Photogrammetry

This approach uses off-the-shelf photogrammetric processing software Agisoft Photoscan. The processing is triggered automatically when the survey is completed and all images are transferred to the Ground Station via data link. For georeferencing of the images, the camera location and the inner camera geometry were written to the EXIF file of each image by the Geo Image Ground Node (Fig. 11). To ensure an acceptable compromise between orthophoto quality and the required processing time, an analysis regarding the impact of the most relevant processing parameters has been performed, cf. section V.

Generally, the process of the Photogrammetry consists of 4 steps:

1. Camera alignment (optimize the homographic equation)
2. Mesh creation by generated tie points
3. Orthophoto creation (dense cloud or Digital Elevation Model)
4. Export

V. PERFORMED PROFILE ANALYSES AND EVALUATION

To evaluate the correct workflow of both approaches of 2D-live-stitching and the 3D-photogrammetry, a real world flight test above an agricultural crop land has been performed and the results of both approaches are shown in Fig. 13 and Fig. 14. Generally, agricultural crop land and its mean textured surface pose a challenge for mapping processes because of the limited number of trackable features.

For analyses and evaluation four predefined profiles were used to cover the requirement of well-balanced compromise between processing duration and quality of the generated orthophoto. The profiles are given in Table 1.

Table 1. Photogrammetry parameter profile definition

profile	alignment accuracy	mesh face count
Agi lowest	lowest	lowest
Agi low	low	low
Agi medium	medium	medium
Agi high	high	high

To estimate the accuracy of the created maps by the different profiles, five Ground Reference Points (GRPs) were distributed over the mission area. The location of the GRPs was determined using a RTK-GNSS system leading to a horizontal RMSE below 2 cm. To enable robust processing for this scenario the overlap and the sidelap was chosen to be 70%. A ground sampling distance (GSD) of 2 cm was needed to identify the GRPs. This resulted in a mission consisted of 6 times 100 m lines with a distance of 25 m in an altitude of 60 m over ground. During the flight time of 4.5 minutes 271 images were taken.

To compare the presented profiles, they were triggered one after another with the same set of images. The created results are shown in Fig. 13. All profiles resulted in consistent solutions and were successfully georeferenced. The map based on the lowest profile could not recreate the complete area (Fig. 13, right). The remaining profiles led to similar results without notable differences to visual inspection. The processing time varied between 1.2 and 3.6 minutes. A comparison of this and other criteria is given in Fig. 15.

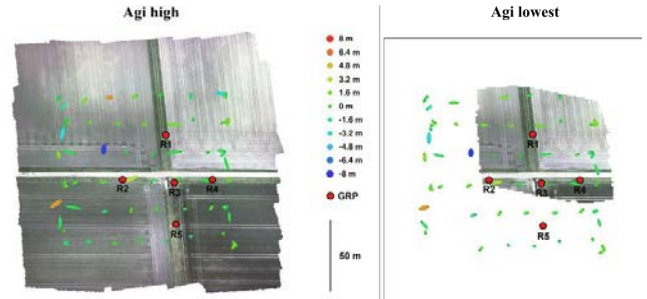


Fig. 13. Orthophotos created with the profiles high and lowest (including Ground Reference Points)

The created final image of the SLAM pipeline is shown in Fig. 14. The image was updated with every new image and was therefore finished before the copter landed. The mean location error measured using the reference points was about 8 m which is significantly larger than the errors observed in the photogrammetry results. In Fig. 13 the results are contrasted to the results of the photogrammetry-approach.

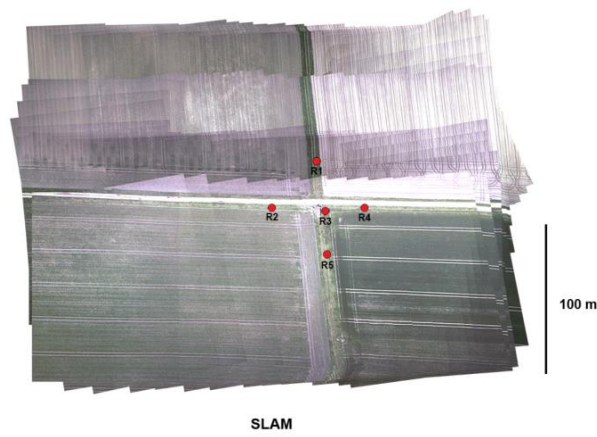


Fig. 14. Orthophotos created with 2D live stitching approach of a crop land. While the mean error in the low profile is half as high as in the lowest profile, the calculated errors using the medium and high profiles are not enhancing significantly. The number of tie points created by the lowest profile is an order a magnitude lower compared to the other three profiles.

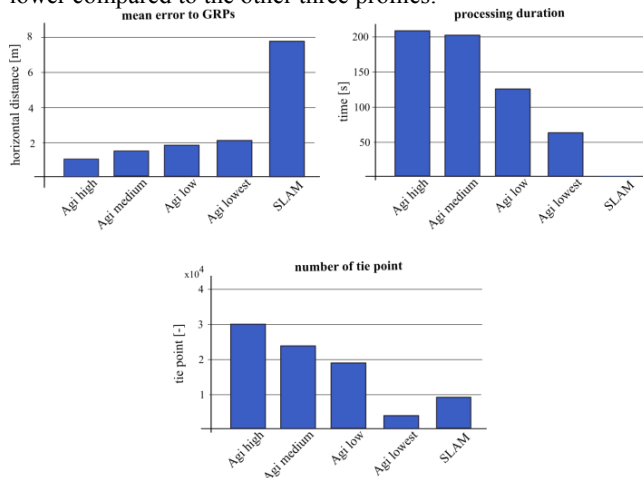


Fig. 15. Evaluation and Comparison of defined AgiSoft profiles and Visual SLAM

In cooperation with the associated partner NLWKN as a potential user of such a system, flight tests have been performed on the island Langeoog in the German Ocean (North Sea). The NLWKN was interested in getting actual information of their efforts to protect the coastline of the island by erosion by water. For this reason sand was selective washed up to the coastline by dredgers at the beginning of 2017/10. In the period of time of the 10/26 and the 10/31 due to severe weather with a storm flood, a huge erosion of the washed up sand occurred and the result is shown in Fig. 16. The level of erosion was determined by comparison of the orthophoto of the same area. The dislocation averaged out to 9.9 m with some peaks up to 17.6 m.



Fig. 16. Evaluation of erosion

The 3D-photogrammetry provides a more detailed image (Fig. 16) compared to the image of the 2D-live-stitching approach (Fig. 17), but both approaches are capable to provide the desired information of the area.

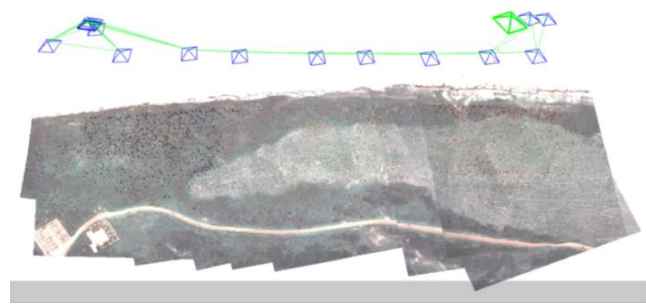


Fig. 17. Result of the SLAM approach with camera poses and tracked features

Both implemented approaches were successfully integrated to get the desired full automated rapid aerial mapping solution. This also includes the basic tasks of the automated mission planning, camera control, image transport to ground station, automated processing and the visualization of the results.

VI. CONCLUSION

In this paper, the benefits of a multi-constellation GNSS based positioning have been demonstrated with a focus on UAVs and UGVs operating in catastrophic scenarios, especially in situations where a GNSS signal reception might be blocked by obstacles or the environment. This position information is also used for georeferencing of images and therefore for a visual reconstruction of the exploration area. The introduced overall system has demonstrated the capability of an automated orthophoto generation. Both implemented mapping methods, a 2D live stitching and a 3D photogrammetry, provided results which fulfill the requirements to get an instantaneous 2D overview and a contemporary 3D reconstruction of the area.

ACKNOWLEDGMENT

The presented work was done within the joint research project “*ANKommEn*” funded by the German Federal Ministry of Economic Affairs and Energy administered by the Space Administration of the DLR (funding code: 50NA1518).



Federal Ministry
for Economic Affairs
and Energy

REFERENCES

- [1] Harms, H., Schattenberg, J., Schmiemann, J., Frerichs, L., 2016, “A Communication Layer for UAV/UGV Swarm Applications, in *5th International Conference on Machine Control & Guidance (MCG)*, Vichy, France, October 5-6th, 2016
- [2] BDS, 2016. BeiDou Navigation Satellite System , Signal in Space, Interface Control Document, Open Service Signal (Version 2.1), November 2016
- [3] GSA, 2016. European GNSS (Galileo) Open Service: Signal-in-Space Interface Control Document, OS SIS ICD V1.3, December 2016
- [4] GSA, 2017. European GNSS Service Center. *Constellation Information*. 08.07.2017.
URL: <http://www.gsc-europa.eu/system-status/Constellation-Information>
- [5] IAC, 2017. Information-Analytical Centre, Federal Space Agency. *GLONASS constellation status*. 08.07.2017.
URL: <https://www.glonass-iac.ru/en/GLONASS/>
- [6] IGS, 2017. International GNSS service. *MGEX - BeiDou Satellites*. 08.07.2017.
URL: http://mgex.igs.org/IGS_MGEX_Status_BDS.html
- [7] ISTC, 2008. Russian Institute of Space Device Engineering, „Global Navigation Satellite System GLONASS: Interface Control Document. Edition 5.1,“ 2008
- [8] Klein, G., Murray, D., 2007, “Parallel tracking and mapping for small AR workspaces,” in *IEEE and ACM International Symposium on Mixed and Augmented Reality (ISMAR)*, Nara, Japan, November 2007, pp. 225–234.
- [9] Mur-Artal, R., Montiel, J. M. M., Tardós, J. D., 2015, "ORB-SLAM: A Versatile and Accurate Monocular SLAM System," in *IEEE Transactions on Robotics*, vol. 31, no. 5, October 2015, pp. 1147-1163
- [10] NAVCEN, 2016. Global Positioning Systems Directorate Systems Engineering & Integration, Interface Specification, IRN-IS-200H-003, 28 July 2016
- [11] NAVCEN, 2017. U.S. Department of Homeland Security. *GPS constellation status*. 08.07.2017.
URL: <http://www.navcen.uscg.gov/?Do=constellationStatus>

Effects of a X9.3-class solar flare on EGNOS performance

Pedro Pintor, Claudia Paparini⁺, Joanna Rupiewicz, Ridha Chaggara⁺
ESSP SAS, Madrid, Spain, pedro.pintor@essp-sas.eu

⁺ESSP SAS, Toulouse, France

The European Geostationary Navigation Overlay Service (EGNOS) improves the open public service offered by the GPS. As the European Satellite-Based Augmentation System (SBAS), EGNOS provides both corrections and integrity information about the GPS system, delivering opportunities for accurate positioning for improving existing applications or developing a wide range of new ones.

Space weather can affect Global Navigation Satellite System (GNSS) and SBAS. Ionosphere variability and gradients and in general disturbances related to space weather events are one of the biggest concerns of users enabled with single frequency satellite navigations equipment.

This paper addresses the space weather incident that occurred in September 2017 and investigates the EGNOS response at both system and signal in space levels. Actually and as reported by NOAA space weather center, on 6th September 2017 at 12:02 UT, sunspot AR2673 unleashed a major X9.3-class solar flare being the strongest solar flare in more than a decade. X-rays (Fig.1) and UV radiation from the blast ionized the top of Earth's atmosphere.

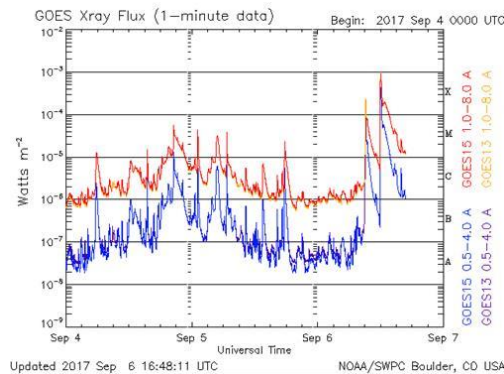


Figure 1: GEOs X-ray flux from 4th to the 6th September 2017.

This event caused a strong shortwave radio blackout over Europe, Africa and the Atlantic Ocean and it produced a Coronal Mass Ejection (CME) impacting the Earth's magnetic field and consequently generating a G4 (Severe) geomagnetic storm (Fig. 2) in the following days 7th (late hours) and 8th September 2017.

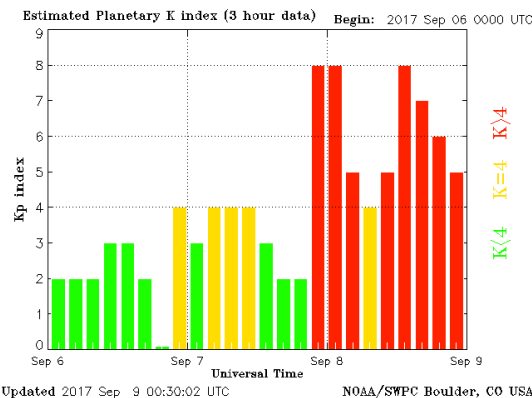


Figure 2: NOAA planetary Kp index from the 6th to 8th September 2017.

In relation with the described space weather event (on the 6th September 2017), EGNOS system and performance have been impacted in terms of IGP (Ionosphere Grid Point) and GPS monitoring degradation. In particular EGNOS system handled the space weather event and it reacted (maintaining the integrity) by setting some IGP (mainly located in the southern part of ECAC area) to higher Grid Ionospheric Vertical Error index (GIVEi) values and others to Not Monitored (Fig.3).

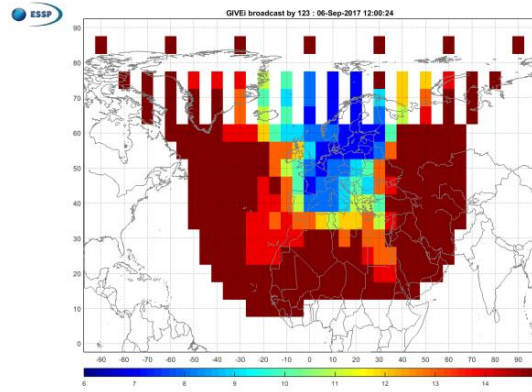


Figure 3: EGNOS GIVEi broadcast at 12:00:24 on the 6th September 2017.

In terms of SV monitoring, the number of monitored SV decreased quickly (from 17 to 4 monitored satellites) in around two minutes. As for the IGP situation, SV monitoring was then gradually recovered within few minutes.

In terms of overall performance, APV-1 and LPV200 were degraded for approximately 40 minutes. Indeed, in terms of APV-1 and LPV-200 coverage, a nominal situation was recovered at around 12:40. As already stressed, the space weather event on the 6th September 2017 produced a CME that impacted Earth on late 7th and 8th September 2017 with Kp index of 8. This kind of geomagnetic storm is not uncommon in terms of performance impact for EGNOS system and typically causes a signal phase scintillation leading to L2 signal loss of lock over Northern stations. (Fig.4)

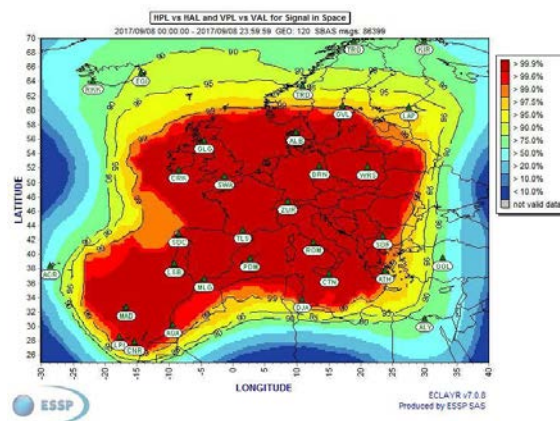


Figure 4: EGNOS APV-I availability on the 8th September 2017.

GRAS-2 Next Generation of Radio Occultation Instrument

Thomas Liljegren, Anders Carlström, Jacob Christensen
RUAG Space AB, Gothenburg, Sweden, thomas.liljegren@ruag.com, anders.carlstrom@ruag.com,
jacob.christensen@ruag.com,

Abstract

In a world today when the effects of extreme weather are reported on the news and many people are troubled for the long-term climate change there is a need for precise weather and climate monitoring of the earth.

GNSS Radio Occultation is now an established data type and an important part of the global observation system. In numerical weather predictions and climate research it has a significant impact. The radio occultation measurements contributes to our knowledge of the actual atmospheric temperature, as well as water vapour, air pressure and electron density. Radio occultation is a technique to measure atmospheric bending angle as function of impact parameter through carrier phase and amplitude tracking of GNSS signals passing through the atmosphere using a tracking receiver onboard a satellite in low earth orbit. It gives global coverage also over the big oceans compared to the traditional weather balloons. Characteristic for the measurements are the good vertical resolution and measurements that can be used without bias correction. The radio occultation measurement is an anchor measurement for weather forecast and climate analyses.

The Radio Occultation (RO) instrument for MetOp Second Generation (MetOp-SG) is under development at RUAG Space. It will succeed the GRAS instrument presently operating on the MetOp series of satellites and it is often referred to as GRAS-2.

GRAS-2 will support European GALILEO and American GPS signals in the L1 and L5 frequency bands and the hardware supports also other constellations transmitting in those bands (e.g. Chinese Beidou and Russian GLONASS). The signal acquisition and tracking is designed for continuous open loop recording to achieve measurements to very low altitudes including super-refractive situations where the signal is not available for a substantial period within the total occultation time span.

GRAS-2, the new generation, is improved in a number of ways:

- Full open loop from -300 km SLTA
- Multiple GNSS capability at L1/L5
- DME/TACAN mitigation device in the L5 receive chain
- Ionospheric capability up to 500 km

The previous generation of GRAS instruments are operating on the MetOp satellites, launched 2006 and 2012, providing operational meteorological observations from polar orbit. MetOp Second Generation two series polar satellites, three satellites in each series, will continue the operational weather and climate observations from MetOp in the next 25 years.



Figure 1: Qualification model of the Radio Occultation instrument for MetOp-SG.

Software defined radio for ground and airborne GNSS reflectometry

Thomas Hobiger^{1*}, Joakim Strandberg¹, Reto Gähwiler^{2,1}, Rüdiger Haas¹

(1) Department of Space, Earth and Environment, Chalmers University of Technology, Gothenburg, Sweden

(2) Thomas Johann Seebeck Department of Electronics, Tallinn University of Technology, Tallinn, Estonia

* Contact: thomas.hobiger@chalmers.se

Abstract—Software defined radio (SDR) appears as a suitable solution for dedicated GNSS reflectometry (GNSS-R) applications. Not only does the flexibility of SDR allow for easy and rapid prototyping, but also do recent technological developments of SDR front-ends support real-time operation of GNSS-R. Our presentation includes a discussion about the technical aspects of SDR for GNSS-R and we show results from a ground-based GNSS-R SDR receiver which was operated continuously over a more than a month at the Onsala Space Observatory. A summary of our current activities in relation to airborne GNSS-R solutions and initial results in the form of Delay-Doppler Maps (DDMs) will conclude the presentation.

Keywords—GNSS-R, software defined radio, signal processing, sea level, delay doppler maps

1. SDR for GNSS-R

Software-defined radio (SDR) is a very powerful and flexible concept for prototyping and quick realization of projects without the need of application-specific integrated circuit (ASIC) boards. Thus, SDR is a very appealing solution which helps to implement a novel GNSS-R concept with much lower prototyping and development cost. As signal processing can be carried out on the CPU, a GNSS-R solution can be built with off-the-shelf components and adapted in a very flexible way before or during any development phase. As discussed in the following, SDR has been also chosen for the development of a ground-based GNSS-R instrument which allows for correlation between the direct and reflected signals transmitted from the GLONASS constellation. SDR is also currently considered for the development of a light-weight GNSS-R Delay-Doppler Map (DDM) receiver which is expected to be operated from airborne platforms and balloons.

2. Realizing the “GLONASS-R” concept by means of SDR

The correlation of direct and reflected signals is not possible without certain hardware changes. However, in the case of Russian Global Navigation Satellite System (GLONASS) which makes use of the frequency division multiple access (FDMA) encoding scheme cm-level precision from ground-based GNSS-

R installations can be obtained [1]. However, the need for complex and expensive RF front-ends, down-conversion stages and A/D converters made the so-called GLONASS-R system rather unattractive for being duplicated at other sites. This problem was overcome by replacing those inflexible components with off-the-shelf software-defined radio equipment. This did not only lead to a drastic price reduction but also increases the flexibility of the GLONASS-R concept. Results from such a prototype system are documented in [2].

3. Preparations for a lightweight airborne receiver

Although the USRP N210 front-ends used for the ground-based solution discussed in Section 2 were sufficient to demonstrate the feasibility of the GLONASS-R concept and operate the system in real-time, their size and weight does not make them the optimal choice for a SDR based GNSS-R solution that can be mounted on an airborne platform with payload weight restrictions. Thus, another front-end solution was sought for and found in crowdfunding project LimeSDR shown in Figure 1.



Figure 1: The LimeSDR front-end, which has been chosen for this project, is based on field programmable RF transceiver technology, combined with FPGA and microcontroller chipsets.

This front-end offers a continuous frequency range between 100 kHz and 3.8 GHz, two RX channels with bandwidths of up to 61 MHz and an easy interface via the USB3.0. Moreover, the weight of about 60 g makes it an ideal candidate for the SDR front-end sought for our airborne GNSS-R system.

4. Results from initial tests

First tests in the GPS L1 band (see Figure 2) revealed that the obtained I/Q samples from the LimeSDR have enough dynamic resolution to deal with unwanted interference and the datalink via USB3.0 has been proven to sustain data rates corresponding to sampling rates of up to 10 Msps.

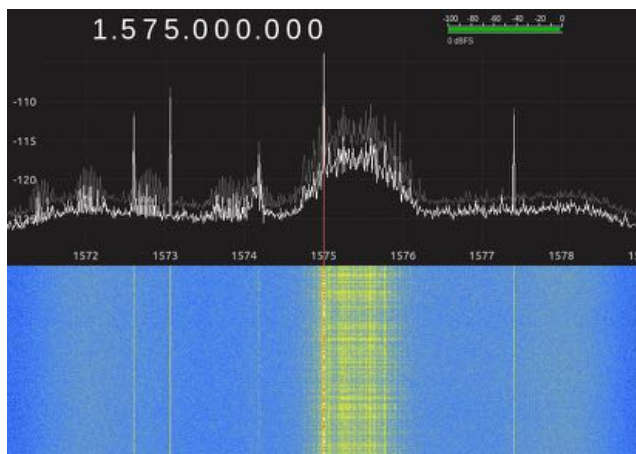


Figure 2: Screenshot of the GQRX SDR spectrum analyzer which was interfacing to the LimeSDR board. The GPS signal power at the L1 frequency is clearly received, while the board was tuned to a center frequency to 1575 with a sampling rate of 10 Msps.

5. Outlook

The software receiver for real-time computation of DDMs (Fig. 3) is currently under development and will be tested with the SDR front-end once all its functionalities have been validated. Initial tests will be performed at a location which oversees open water from a high vertical distance. Follow-on tests will then be carried out from an aerial platform.

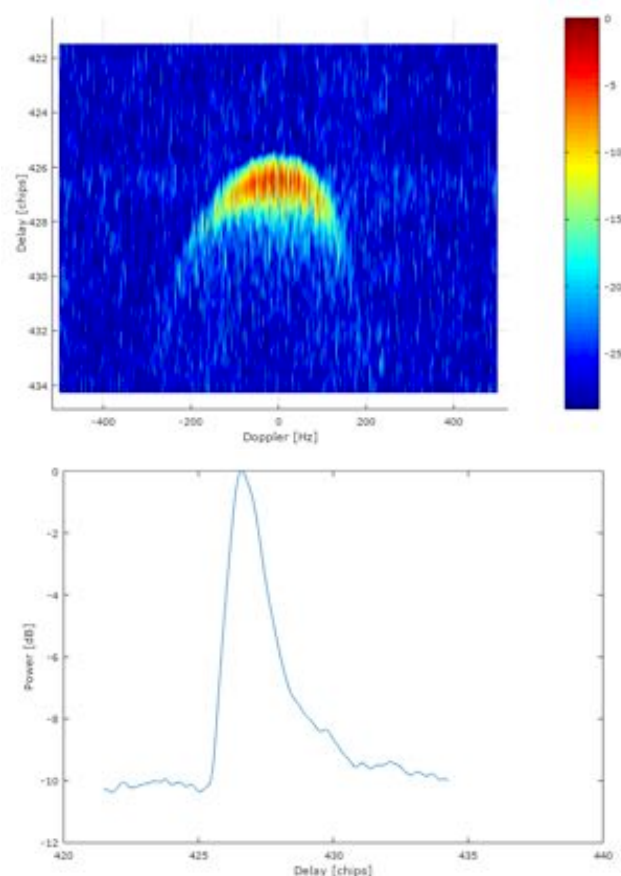


Figure 3: Example output of the software receiver. Results are based on recorded raw sampling data from an airborne GNSS-R experiment kindly provided from ICE-CSIC/IEEC, Spain. The upper plot depicts a DDM of a GPS satellite and the corresponding waveform is shown in the lower plot. The slope of the trailing relates to sea-surface roughness and can be used for wind-speed retrieval.

Acknowledgment

This research has been conducted with support from "Stiftelsen Lars Hiortas Minne" (FO2014-0663) and "Adlerbertska forskningsstiftelsen". Test data set for the validation of the DDM processing chain were kindly provided from the Institute of Space Sciences, CSIC of the Spanish National Research Council. The authors also thank teams from the workshop and the electronics laboratory at the Onsala Space Observatory for preparation of the infrastructure at the test site.

References

- [1] T. Hobiger, R. Haas, and J. Löfgren, "GLONASS-R: GNSS reflectometry with a Frequency Division Multiple Access-based satellite navigation system", *Radio Science*, vol. 49, iss. 4, pp. 271-282, 2014.
- [2] T. Hobiger, R. Haas, and J. Löfgren, "Software defined radio direct correlation GNSS reflectometry by means of GLONASS", *IEEE-JSTARS*, vol. 9, iss. 10, pp. 4834-4842, 2016.

Ionosphere Prediction Service for GNSS Applications

Roberto Ronchini, Filippo Rodriguez, Stefano Di Rollo
Science and Navigation Programs
Telespazio
Rome, Italy

Eric Guyader
The European Commission
Brussels, Belgium

Abstract — Space weather events related to solar activity can affect both ground and space-based infrastructures, potentially resulting in failures or service disruptions across the globe and causing damage to equipment, systems and infrastructures. Global Navigation Satellite Systems (GNSS) represent one of such infrastructures that can suffer from electromagnetic phenomena in the ionosphere, in particular due to the interaction of the RF signals with the ionosphere.

The effects on a GNSS receiver can include the (slow or sudden) decrease of accuracy in the position and timing computations, potential loss of integrity, complete loss of one or more satellite signals etc. With society and economies increasingly relying on the services provided by GNSS, a more accurate analysis of the impact due to those phenomena is warranted and prevention methods must be developed.

This understanding can be achieved by means of the deployment of dedicated monitoring networks and the development of ionospheric models, which can help limiting their disruptive effects thanks to early warning alerts.

The Ionosphere Prediction Service (IPS) is a project funded by European Commission to develop a prototype of a monitoring and prediction service of potential ionosphere-related disturbances affecting the GNSS user communities. Its objective is to inform and alert the GNSS users in due time of an upcoming ionospheric event potentially harmful for GNSS and for the related operations in the given application field.

This paper initially provides a general introduction to the IPS and its nowcast and forecast services, showing its capabilities in meeting final user requirements and giving a detailed description of the scientific and engineering reports that is capable to deliver to the users in near real-time mode.

Special attention is paid to civil aviation applications, where ionospheric events may potentially result in hazardous misleading information especially in the case for approach and landing operations.

Then, special emphasis is given to the IPS component devoted to the analysis of GNSS systems performance.

If the scientific products that report on the solar and ionosphere activity normally are aimed to scientist and space-weather specialists, this solution, instead, has been designed to inform non-scientific users about the current and future performances that a GNSS equipment would realistically experience, taking into account the effect of the ionosphere as well as all the other main sources of errors, like satellite clocks and orbits.

This with the aim to help GNSS final users to cope with the effects of the ionosphere and mitigate the related effects for the specific GNSS-based application/service.

Keywords: *Space-Weather, Ionosphere, Scintillation, Forecast, Performance Monitoring, Aviation.*

I. INTRODUCTION

The aim of the IPS project is to design and develop a service prototype to translate the observations of the sun and of the ionosphere into the prediction of the performance of the GNSS systems at user level.

The project team consists of the following entities: Telespazio (coordinator), Nottingham Scientific Ltd, Telespazio Vega DE, The University of Nottingham, The University of Rome – Tor Vergata and the “Istituto Nazionale di Geofisica e Vulcanologia” (INGV).

The IPS development is founded on two pillars: the design and development of the prototype service and the research activity that will run along the whole project.

- The design and development of the service is organized in four phases: the user requirements collection, the architecture specification, the implementation and prototype validation.
- The research activity is the scientific backbone of IPS to provide models and algorithms for the calculation of the forecasting products.

A special attention in the IPS design is paid to the requirements of the aviation community [1]. Aviation requires the monitoring of the GNSS systems to assess the effects of the principal error sources, like the ionosphere disturbances, on the GNSS services.

To collect such requirements the IPS project conducted a survey among several European ANSPs.

Requirements from aviation users may originate from technical and operational needs, drafted by each country and specific to the involved user type (ATM/ATC operators, aircrew and pilots, airlines, ground handlers, etc.), and derive from the guidelines approved and published by ICAO.

This means that ICAO technical documentation can be considered as a reference for the definition of GNSS performance indicators to be adopted in the aviation domain.

Aviation operations include navigation, surveillance and timing, and are relying more and more on GNSS services.

- For navigation, en-route segments, approaches and landing operations GNSS is already largely used.

- For the surveillance domain GNSS-based services already enhance radar systems and an increasing part of the surveillance domain will rely on GNSS services in the coming years.
- Another important application is the use of GNSS as a time reference: GNSS is already used for some radar and multi-lateration systems synchronization and an increasing number of networks will rely on GNSS time.

When a severe space weather event occurs, several effects can result and have a relevant impact on aviation applications:

- Degradation of radio/satellite communication: During solar events, some disturbance may affect HF and satellite communication, which can have side effects on high-distance Controller-Pilot data link communications, ADS-C, Aeronautical Operational Control, etc. However, line of sight VHF communication and low-distance links may not be impacted.
- On-board system failure due to radiation: during a radiation storm, when striking a sensitive node, radiation may induce shortcuts, change of state or burnout in on-board electronic devices. This phenomenon is called “Single Event Upset (SEU)”. Its impact may vary a lot from unnoticeable to a complete failure of the system. This kind of failure may become more frequent in the future because modern electronic equipment is more vulnerable to radiation due to the smaller size of electronic devices.
- Radiation doses: During radiation storms, unusually high levels of ionizing radiation may lead to an excessive radiation dose for air-travellers and crew. The dose received by passengers and crew is higher at higher altitudes and latitudes.
- GNSS based aviation operation: High energy particles and radiation ejected by the sun may cause strong disturbances in the ionosphere. The GNSS radio signals are strongly affected under severe disturbance. As a result, unexpected position and timing errors can occur at the level of the user receiver. In extreme cases, the GNSS receiver can lose reception of the satellites altogether and the position can no longer be computed. As a side effect, GNSS based surveillance applications can be unavailable. SBAS or GBAS augmented services, used for approach and landing, are more demanding in terms of accuracy and integrity than the en route/TMA GNSS based navigation. As a consequence, the safety monitors of those systems are also more sensitive to space weather events, and the unavailability of these services would be more frequent.
- Other effects, not under control of the aviation community, might have side effects impacting aviation:
 - Power grid and ground public communication failure: Geomagnetic storms create induced

electrical currents in the power or communication grid which may lead to electrical and ground public communication failure (telephone, internet ...).

- Satellite failure: High energy particles ejected by the sun may hit satellites and cause failure of on-board equipment.

II. THE IPS PROTOTYPE SERVICE CONCEPT

The mission of the IPS Service is to provide each of its user communities of now-cast and forecast indicators relevant to the GNSS applications that can be affected by unexpected ionosphere behaviour [2].

This section gives a description of the IPS service concept in terms of functions and architecture designed to support the IPS mission; finally, the IPS prototype architecture is introduced to test the validity of its service concept.

A. IPS concept

Based on the analysis of the collected user requirements, the service concept has been designed to rely on the following main four functions:

1. Observations data of the sun activity and of the ionosphere state to derive a prediction of the GNSS performance at user level in a given geographical area. This observation function requires the connection to external sensors providing the observation data. The solar activity that is monitored consists of:
 - a. Flare forecasting and research on magnetic reconnection (as trigger of flares and Coronal Mass Ejections).
 - b. Detection of solar active regions and evaluation of the flare probability using the main outcomes of magnetic reconnection models;
 - c. Measurements of Solar Energetic Particle, GCR and related research activities.
2. The morphology and the dynamics of the ionospheric plasma are also studied to develop Total Electron Content and scintillation mapping and modelling tools on different temporal and spatial scales. Data from available GNSS networks (global and regional) are used to derive TEC and scintillation related products.
3. Statistical approaches and PVT algorithms fed with ionospheric models, augmentation models and observation data to develop nowcast, short-term and long-term forecast of GNSS systems performance, on global, regional and local scale.
4. Algorithm output provided in form of grid values are ingested and managed to generate and send alerts to users when it is expected that a given physical parameter will soon get outside the range indicated by the user. The alerts are delivered via email or SMS, and displayed on the web-portal.

5. Other relevant IPS functions are:

- a. Statistical analysis. This function allows the user to continuously calculate statistical parameters on the basic IPS products (like moments, PDF, CDF, etc.) to be displayed on the web-portal personal page through one of the several widgets available or in form of a table.
- b. Alerting service. This function allows to monitor the behaviour of specific physical parameters against a user-defined threshold or intervals; when the parameter gets outside the interval of validity, e.g. in the event of a forecast of an upcoming ionospheric threat that would need to be notified to the aviation community, a message or notification is send to any registered user.
- c. Forecast Retro-Validation. This is a periodic report with the output of the comparison between the past forecast analysis and the corresponding actual value computed at the same time and for the same physical quantity. This function allows to assess how good the forecast algorithms actually perform in predicting the future behaviour of the monitored quantities.

B. IPS architecture

As shown in Figure II-1, the IPS logical architecture is based on the following three layers:

- **Sensors:** this layer collects all the elements used to gather raw data for the generation of space weather and ionosphere products. Sensors are normally external to the IPS processing facilities and remotely located with respect to the RPFs. There are many types of sensors in IPS: GNSS receivers belonging to regional or global networks, on-board satellite sensors (like coronagraph), terrestrial magnetograph, etc.
- **Remote Processing Facilities (RPFs):** these elements continuously generate space weather and ionospheric products starting by collected raw data or intermediate products generated by other RPFs. They interacts both with the remote sensors for the collection of the needed input data and the central storage to save the generated products, to retrieve and process data from other RPFs or to trigger one or more functionalities implemented in the central unit. RPFs are also in charge to evaluate the current and future impact of ionosphere behaviour on the full PVT solution experienced by an ABAS or SBAS GNSS avionics.
- **Central Storage and Processing Facility (CSPF):** this central facility implements all the functionalities related to the collection and distribution of the products and the interaction with service users including also the transmission of notification and warnings.

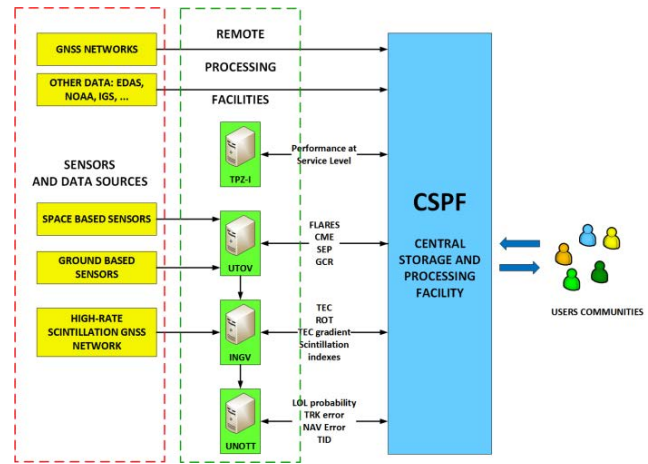


Figure II-1. IPS logical architecture

III. INPUT DATA SOURCES

The sensors that are directly maintained by the IPS consortium belong to several GNSS networks. These networks are currently run by INGV and the University of Nottingham in cooperation with several hosting institutions:

- The **ISMIR ionospheric network** of Figure III-1 controls 12 GNSS stations (10 active and 2 with historical data) equipped with dual frequency receivers (NovAtel GSV4004) or with special scintillation high rate receivers (50 Hz Septentrio PolaRxS). This network covers the northern Europe (Great Britain and Scandinavian peninsula), the central Italy with one station in Rome and some islands in the Mediterranean sea



Figure III-1. RING Geodetic Network (INGV)

- The **RING geodetic network** of Figure III-2 is made of about 180 GPS standard dual frequency receivers distributed over Italy. The L1 and L2 signals from GPS

satellites are acquired by the RING receivers at 30s sampling rate and transmitted to two main servers located at INGV premises in Rome and Grottaminarda (Southern Italy). Receiver observations in RINEX format are available with a latency of about 15 minutes and managed by a virtual machine hosted at INGV in Rome.

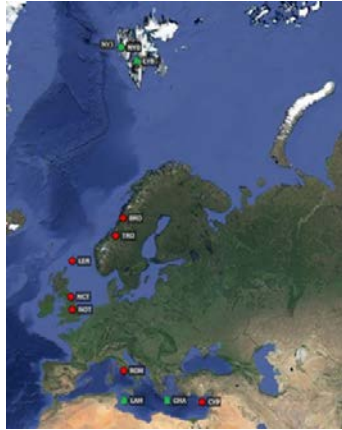


Figure III-2. ISMR Network (UNOTT and INGV)

The IPS makes also use of data acquired by public GNSS data providers like IGS, EUREF and EDAS.

IPS space weather monitoring and forecasting processes depend also on terrestrial and satellite sensors like magnetographs or coronagraphs. Sensors are not directly managed by the IPS researchers, but their readings can be retrieved and processed for real-time flare detection, flare and CME forecasting and SPE detection:

- NSO/GONG (Global Oscillation Network Group) H Alpha Network is a worldwide terrestrial network composed by 6 sites each equipped with a Fourier tachometer, an instrument based on a Michelson interferometer;
- MOTH (Magneto-Optical filters at Two Heights) 20 cm telescope equipped with 2k x 2k CMOS cameras providing magnetogram (potential field extrapolation), intensity and velocity maps using a MOF. This telescope is located at Maui Island (Hawaii);
- Helioseismic and Magnetic Imager (HMI) is an instrument designed to study oscillations and the magnetic field at the solar surface, or photosphere. HMI is one of three instruments on the Solar Dynamics Observatory (SDO) spacecraft launched on February 11, 2010;
- Atmospheric Imaging Assembly (AIA) is an instrument designed to provide an unprecedented view of the solar corona, taking images that span at least 1.3 solar diameters in multiple wavelengths nearly simultaneously, at a resolution of about 1 arcsec and at a cadence of 10 seconds

or better. Together with HMI, AIA is aboard the SDO spacecraft;

- Large Angle and Spectrometric Coronagraph (LASCO) is one of a number of instruments aboard the Solar and Heliospheric Observatory satellite (SOHO).

IV. THE IPS WEB-PORTAL

One of the most innovative components of IPS is its web-portal that represents also the principal interface between the users and the service itself.

The IPS web-portal has been designed to give an immediate view of the ionosphere and Solar activity status to every user, allowing a high level of interaction and customization.

However, the most valuable IPS service options are available only to the registered users. The registration to IPS is free and can be requested by filling the registration form available on the project website.

Some of the options reserved to the IPS users are:

- Access to the “specialized” report pages customized for each one of the user communities monitored by IPS: Solar Physics and Ionosphere Research, Aviation ABAS and SBAS LP/LPV, High Accuracy, Mass Market, and Critical Infrastructures. The service administrator makes available to each user the report pages that seem to be more appropriate to its profile. Each of these pages has been customized by the service administrator to show a selected subset of all IPS available products that are relevant to that user community.
- The user can freely customize its own personal page adding one of the available web components (e.g. image viewers, plots, maps, gauges, tables, etc.) to monitor specific performance figures of its own interest. As an example, the user can add a viewer to monitor the trend of a performance figure of one of the IPS GNSS stations close to a desired location or monitor the behavior of ionospheric TEC focusing on a specific location or an area of its interest. Currently, IPS is able to generate and make available to the users more than 160 different performance products related to the ionosphere status and its effects on GNSS.
- Moreover, it is even possible to setup a watchdog alarm for one of the monitored nowcast or forecast physical quantities to warn the user when such quantity gets outside a specified interval; the IPS is capable to timely send alarm notifications to the user by e-mail.
- The user can even calculate statistics or mathematical functions on each available product or restrict a worldwide analysis to a limited region of its interest by specifying region or location coordinates.

Some of such innovative functions have been already introduced in paragraph II.A, point 5. As from summer 2018, the IPS Prototype web portal will be available at the internet address www.ips.telespazio.com.

V. PERFORMANCE ANALYSIS PRODUCTS

A specific component of the IPS Prototype is devoted to implement batch, nowcast and forecast performance analysis for GNSS Aviation Services. Two main solutions are available in IPS, this paragraph gives a short description and several examples of some of the available output reports for each of them.

A. GNSS Performance Nowcast Analysis for a network of Reference Stations

First solution allows the evaluation of short-term and long-term past performances of ABAS and SBAS systems in terms of integrity, accuracy, availability and continuity for En-Route and Approach/Landing operations, depending on the required application, compliant with accepted and referred aviation standards ([2], [4], [5], [6] and [7]).

The aim of this solution is to report on the recent and current impact of Solar and ionospheric activity on aviation operation, by monitoring a network of ground GNSS stations located, when possible, in strategic locations like airports.

In IPS a network of not less than 30 European stations is real-time monitored generating performance reports with an average latency of 10 minutes depending on the input data availability, computational complexity and the interval of analysis. Input data is retrieved from specific GNSS data providers like IGS, EUREF, etc.

More in detail, this service implements the following functions for each station of the monitoring network:

- Position and integrity analysis:
 - Un-augmented GPS L1 PVT (without integrity);
 - Un-augmented GPS L1 ABAS PVT solution, integrating RAIM-FDE capabilities compliant with [2];
 - GPS L1 SBAS augmented PVT, emulating the processing of a SBAS-capable airborne receiver compliant with [4] for both LP and LPV navigation modes.
- Performance analysis reports:
 - Position error and integrity analysis provided as plot and report-table; an example is given in Figure V-1 for the Kiruna IGS station where the integrity HPL parameter is the output of the RAIM-FDE algorithm;
 - Statistical analysis (95% – 99% position error accuracy, PDF/CDF plots, Normality tests, etc.);
 - Analysis of satellite geometry (Dilution of Precision parameters timeseries);
 - Availability and continuity diagram for different aircraft operations; the example of Figure V-2 is

the output of the ABAS analysis for Non-Precision approach operations, from En-Route to NPA, at IGS Kiruna station;

- Constellation status analysis (URE/URA analysis satellite health status, condition usage in the position calculation, signal power level);
- Horizontal and Vertical integrity diagrams (Stanford Diagrams) for both ABAS and SBAS solutions;
- RAIM-FDE performance diagrams;

B. GNSS Performance Forecast and Nowcast over Areas or Volumes

This solution uses standard GNSS data and forecast models to produce GNSS systems nowcast and forecast performance maps at specific locations, regions or volumes at worldwide level. This analysis is carried out through a volume simulator.

The main difference with the solution addressed in the paragraph V.A is that in this case the analysis can be run not only at specific locations (i.e. at given user coordinates) but even on trajectories, areas or airspace volumes. This is done by implementing a real PVT calculation for each node of a dense grid of virtual GNSS stations whose ideal pseudoranges are generated by using GNSS navigation data (ephemeris), precise products (i.e. orbits and clocks), accurate UERE budget models and the IPS ionosphere forecast products.

The effective coverage of this service depends on the type of analysis, the requested computation burden and actual model and data availability. More in detail, this service implements the following functions:

- Evaluation of current EGNOS performances in terms of service availability and continuity over the coverage area for several operations, from En-Route to LP/LPV Precision Approaches; the exemplary plots of Figure V-3 and Figure V-4 show the result of hourly EGNOS (PRN 120) availability and continuity analysis for different LP and LPV aircraft procedures.
- Forecast analysis of the expected receiver position error and protection levels (e.g. HPL/VPL) for both ABAS and SBAS avionic solutions; these reports are maps over the entire service coverage area (currently European and worldwide). Figure V-5 is the plot of the total position error forecast expected for the ABAS receiver; the forecast report is provided to the users one hour in advance and a new map is generated every 15 minutes. The user can access to several other forecast reports, like xDOP maps, average HPL/VPL maps, aircraft operation availability maps and RAIM-FDE availability maps. Figure V-6 is an example of average HPL forecast map for RAIM-FDE. Figure V-7 map is an example of a RAIM-FDE availability map, where the green color indicates the regions where the RAIM-FDE integrity is available.

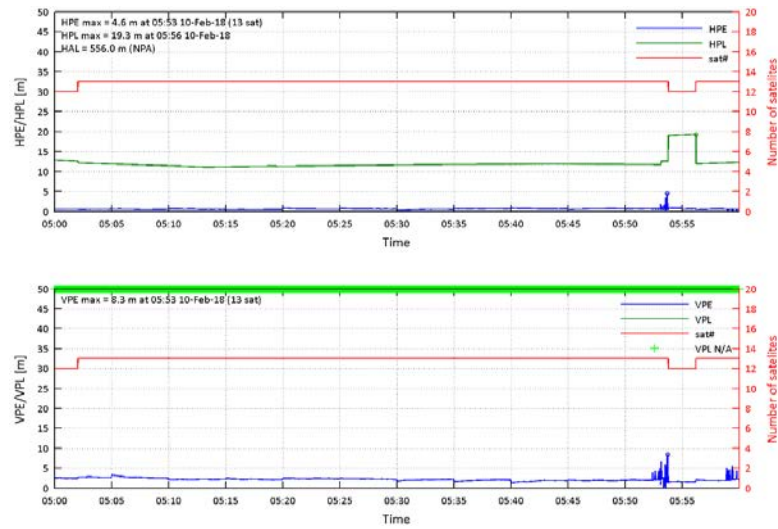


Figure V-1. Position Error and Integrity Analysis

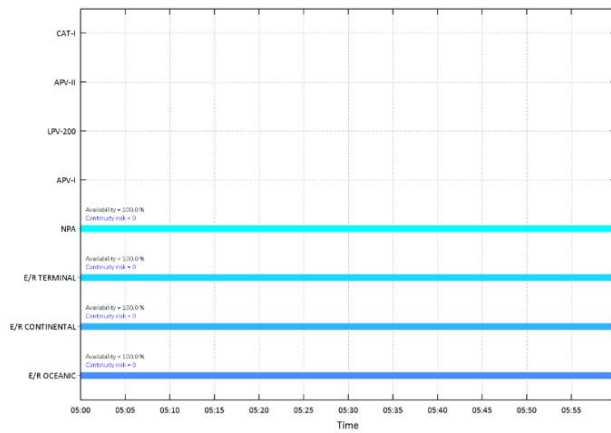


Figure V-2. NPA Procedure Availability Timeseries

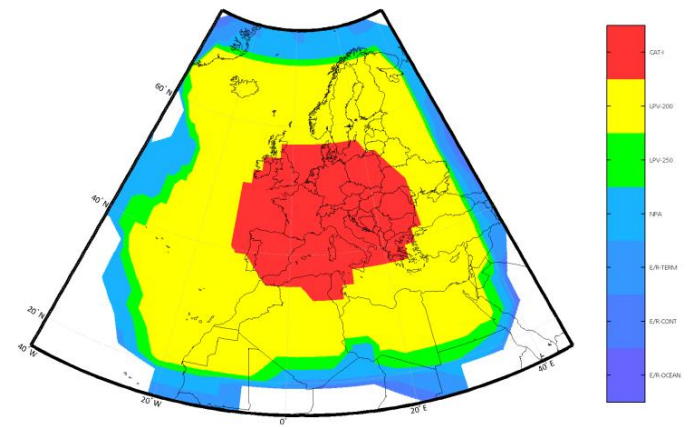


Figure V-3. Aircraft Operations Availability Map for SBAS LP/LPV

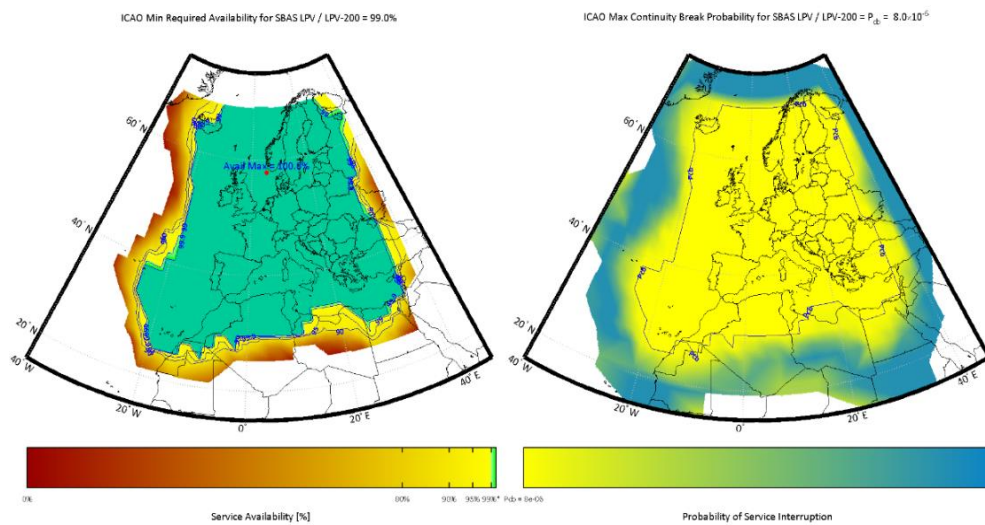


Figure V-4. SBAS Availability and Continuity maps (EGNOS PRN120)

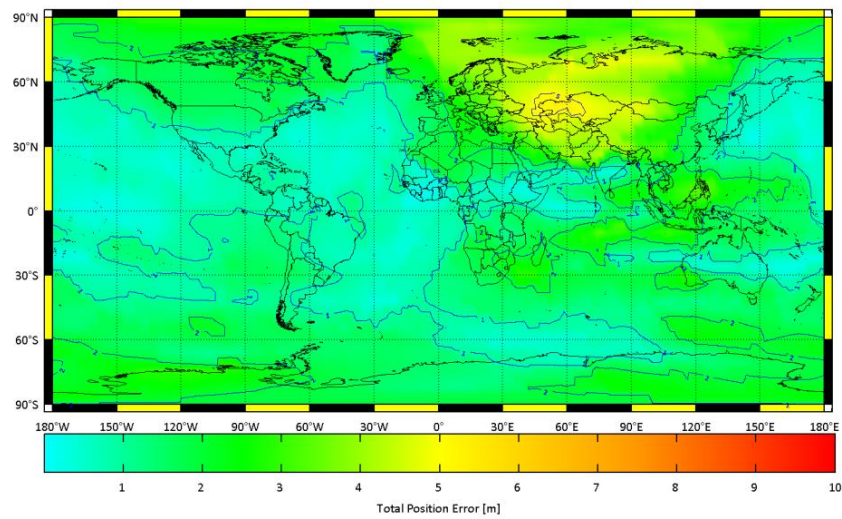


Figure V-5. Position error forecast map for ABAS avionic solution

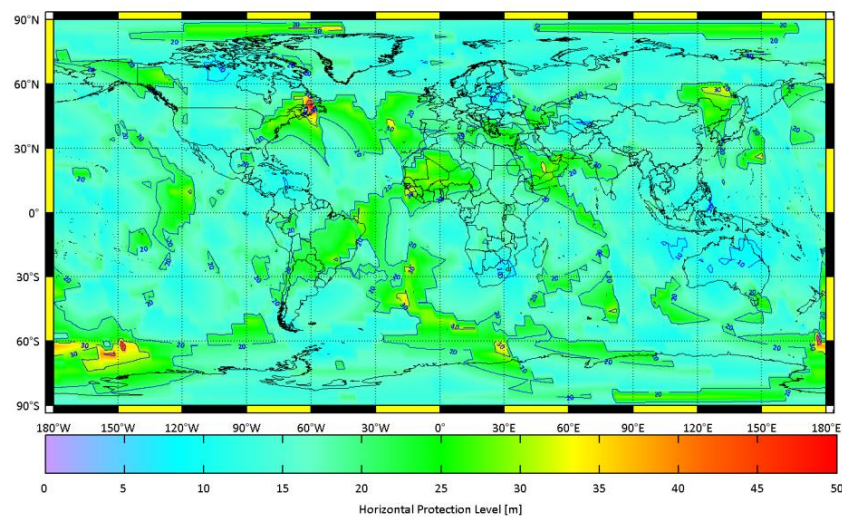


Figure V-6. Average RAIM-FDE Horizontal Protection Level map

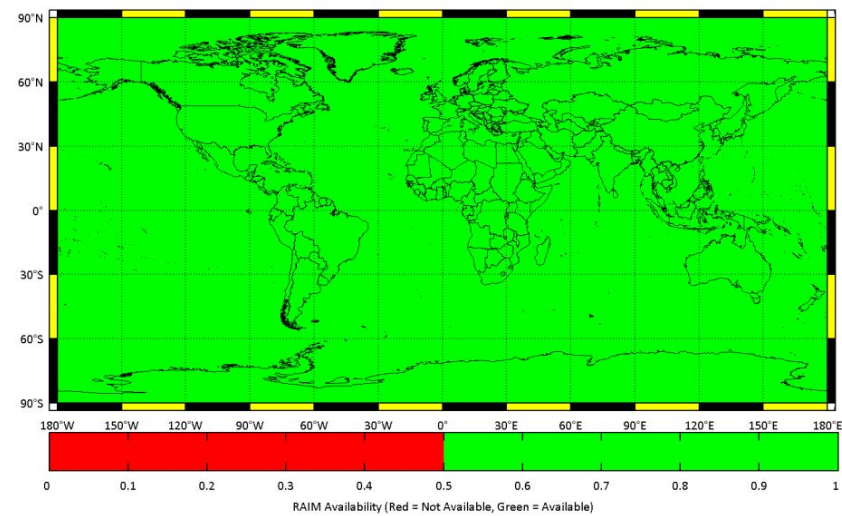


Figure V-7. RAIM-FDE availability forecast map

VI. CONCLUSIONS AND WAY FORWARD

The target of IPS project is to develop a service prototype to translate the observations of the sun and of the ionosphere into the prediction of the performance of the GNSS services.

Several aspects make this service innovative in comparison to other existing similar solutions:

- a wide number of forecast products and reports is available to the users (from solar physics and ionosphere to the effect on GNSS);
- specialized report pages have been arranged to monitor performance indicators relevant to each one of the several user communities defined for IPS: Solar Physics and Ionosphere Research, Aviation ABAS and SBAS LP/LPV, High Accuracy, Mass Market, and Critical Infrastructures;
- IPS web-portal highly-customizable interface: the user can configure its personal page to add monitors to follow the behavior of the performance figures of its interest: IPS makes available more than 160 performance products related to the ionosphere status and its effects on GNSS;
- possibility to setup a watchdog alarm for a monitored nowcast quantity and receive an e-mail notification when it gets outside a validity interval specified by the user;
- possibility to calculate statistics or mathematical functions on each available product or restrict a worldwide analysis to a limited region of interest.

The IPS project has almost completed the development and integration phase; initial operations of the prototype are starting at the time of document's writing (early 2018).

The IPS initial operation phase is foreseen to take place during the last six months of the project, after the completion of the integration phase. The system will be on-line during the whole duration of this phase and periodical reports on the operations status will be submitted. This phase has the objective to validate the IPS service, especially its forecasting capabilities through the "retro-validation" function:

- This function is introduced to verify and validate the reliability of IPS forecast analysis through the comparison, for the same physical quantity and at the same time, of its current and forecasted values (when available).

- This analysis will be restricted to a limited set of physical forecast figures properly selected for their relevance and in respect of technical feasibility constraints.

Corrective maintenance of the IPS prototype will be also carried out to fix non-conformances and any HW/SW installation issue could rise during this period.

During the same phase, user feedback on the service concept (suggestions for new features, interface improvements, but also to report anomalies, etc.) will be collected, notably through dedicated workshops. After this important phase of direct feedback from the users the IPS prototype will gain sufficient inputs to evolve in a more mature service.

IPS is a service devoted to the whole GNSS community and for this reason it is planned in the future to be provided by the EU GNSS Service Centre located in Madrid, Spain.

The role of the GSC is to inform users about the status of the service pushing notification to the GNSS users/communities about performance, and IPS will have to meet in its evolution the GSC specific needs and adapt accordingly.

REFERENCES

- [1] E. Guyader, F. Rodriguez, R. Ronchini, S. Di Rollo, Ionosphere Prediction Service, NAVITECH 2016, ESA ESTEC, 14-16 December 2016
- [2] E. Guyader, F. Rodriguez, R. Ronchini, S. Di Rollo, Ionosphere Prediction Service for GNSS users, ICAO Working Paper, Navigation Systems Panel (NSP) Joint Working Groups Meeting, Montreal, June 2017.
- [3] RTCA, Minimum Operational Performance Standards for Global Positioning System / Aircraft-Based Augmentation System Airborne Equipment, RTCA DO-316, April 2009
- [4] RTCA, Minimum Operational Performance Standards for Global Positioning System / Wide Area Augmentation System Airborne Equipment, RTCA DO-229D, December 2006
- [5] "Aeronautical Telecommunications Annex 10 To The Convention On International Civil Aviation Volume I (Radio Navigation Aids)", Sixth Edition, July 2006, Amendment 89, November 2014
- [6] "Global Positioning System Standard Positioning Service Performance Standard", DoD and GPS NavStar, 4th edition September 2008
- [7] ICAO GMDG, Flimsy 21, Appendix D, GNSS Monitoring Provisions (Attachment D - Draft Proposed Changes To GNSS Manual Doc 9849, updated section 7.8), Navigation Systems Panel (NSP) Flimsy, GNSS SARPs Subgroup, Montreal, 1-11 December 2015

Metre-Wave Synthetic Aperture Radar the Practical Application for Precise Point Positioning

Jonathan Arvidsson, Patrik Dammert
and Anders Åhlander
Airbourne Surveillance Systems
Saab AB
Göteborg, Sweden
Email: jonathan.arvidsson@saabgroup.com
Telephone: +46 10 216 06 07

Thomas Hobiger
Department of Space, Earth and Environment
Chalmers University of Technology
Göteborg, Sweden
Email: thomas.hobiger@chalmers.se
Telephone: +46 31 772 55 49

Abstract—The Global Navigation Satellite System location accuracy enhancing technique Precise Point Positioning is evaluated for SAR imaging navigation requirements. Requirements where high precision during a minute is more important than high accuracy. The achieved precision of ≈ 2 cm results in minimal image degradation compared with the Real Time Kinematic reference technique. Precise Point Positioning can therefore be used for Synthetic Aperture Radar imaging with near Real Time Kinematics performance without the use of a local reference base station.

I. INTRODUCTION

Precise Point Positioning (PPP) is a stand-alone GNSS performance improving method which uses additional satellite corrective data in its processing. PPP is capable of achieving cm location accuracy, however it suffers to some extent from long convergence times compared to other GNSS performance improving methods such as Real Time Kinematics (RTK). During this convergence time the resulting location will have coarse accuracy due to a bias, but can still have fine precision. This fine precision is key for a Synthetic Aperture Radar (SAR).

SAR is a technique where a large synthetic aperture is generated by the movement of a small aperture, where multiple recordings from different positions are combined. In order for the recordings to be correctly combined, the relative position of each recording is required, as this correspond to the shape of the synthetic aperture. If the change of the location bias of the PPP method is negligible during a SAR recording, then the shape of the synthetic aperture is unaffected by it.

CARABAS is an airborne SAR developed by Saab AB for ground imaging, it operates on VHF and UHF frequencies 30-350 MHz. The addition of PPP to its navigation system will allow it to create SAR images in areas without the GNSS reference base stations required for RTK.

II. PRECISE POINT POSITIONING

Satellite clock and orbit drift account for a large part of the single point position GPS error budget [1]. The satellites

orbits are constantly tracked and their clocks are monitored by the GPS control segment which sends correction data to the satellites so that they might update the Navigation Message they broadcast to the GPS receivers, this keeps the resulting pseudo-range error to a few metres. The process is however done quicker and more frequent by other organisations such as the International GNSS Service (IGS) [2], [3]. The essence of PPP is to use these corrections together with a Kalman filter for more precise positioning. The method however often require a long convergence time, from initiation or if interrupted, during which a bias exist, before it can reach its maximum accuracy [4].

III. SYNTHETIC APERTURE RADAR

SAR is an imaging technique capable of higher spatial resolution than what is conventionally possible for a radar of a given aperture size. This is because it allows for multiple recordings from different positions to be combined thus creating a large synthetic aperture. Typically a SAR image is recorded by having a radar move in a straight line while looking down to the side as this allows for high depth of field. Deviations between the actual position and this straight line introduces phase errors which deteriorate the image. If the deviations are known these phase errors can be compensated for [5].

The requirements on the accuracy of the measurement of this deviation depends on the geometries involved and the frequency of the deviation over the aperture. The resulting phase error from an uncompensated constant or low frequency location deviation will not degrade the image but instead translate or rotate it, a high frequency deviation will however defocus the image [5], [6]. These requirements corresponds well with the typical behaviour of PPP.

IV. METHOD

Evaluation of the PPP method for SAR purposes was done on GPS data previously recorded with a 10 Hz Javad Duo-

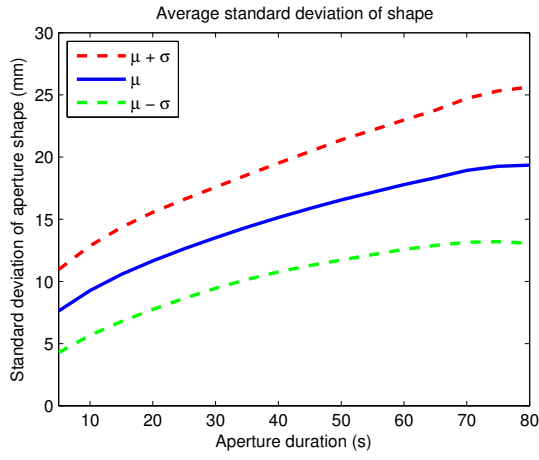


Fig. 1. Standard deviation of the difference between reference position solution and rigidly rotated PPP solution, μ averaged for aperture duration. $\mu \pm \sigma$ is the 1-sigma confidence.

G2D receiver during SAR test flights with the CARABAS in 2016. The PPP flight paths were computed using RTKLIB [7] and the IGS Ultra Rapid Products (IGU). The reference flight paths were calculated with RTK in Waypoint GrafNav. Each PPP flight path shape was analysed in comparison with the reference flight path, after a rigid rotation to align the PPP flight path with the reference flight path, to remove constant biases and rotations. Both the PPP and RTK flight path solutions were respectively used as basis for the deviation compensation in the SAR processing. The resulting images were compared using the SAR image quality metrics: peak intensity I , resolution ρ , integrated sidelobe ratio (ISLR) and peak sidelobe ratio (PSLR). The mainlobe area is defined by twice the theoretical resolution [6]:

$$\rho_r = K_r \frac{c}{2B} \quad (1)$$

$$\rho_\alpha = K_\alpha \frac{\lambda}{2\theta} \quad (2)$$

where ρ_r and ρ_α are the resolution in the direction perpendicular and parallel to the flight direction, c the speed of light, B the bandwidth, λ the wavelength of the centre frequency, θ the integration angle and K_r & K_α the mainlobe widening, here taken to be 1.25.

V. RESULT

For apertures of short duration, 10 s the standard deviation of the difference in shape between the PPP and reference path was 10 mm on average. For longer apertures, 60 s the standard deviation increased to 20 mm as a result of slow changes to the bias, see Fig 1. For longer apertures, 60 s the average drift of the bias was 5 cm or 0.8 mm/s.

The resulting image quality metrics show some difference between the PPP and reference paths, see Table I and Fig. 2. The peak intensity I in a single pixel is increased, the resolution is coarser, and the ISLR and PSLR are higher.

TABLE I
PPP FLIGHT PATH EFFECTS ON SAR IMAGE QUALITY

Path	Peak I dB	ρ^2 dBm ²	ISLR dB	PSLR dB
REF	112.18	-4.53	-5.47	-15.87
PPP	112.23	-4.51	-5.24	-15.55

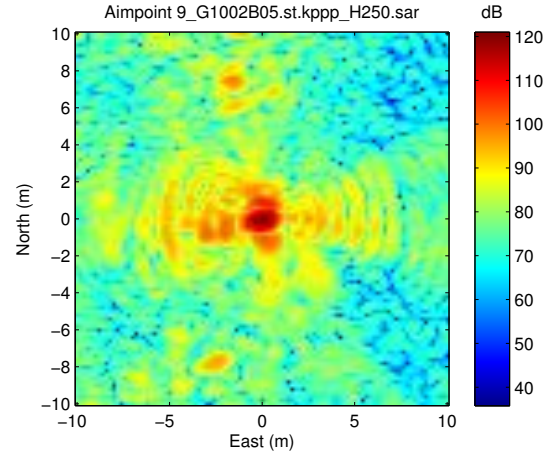


Fig. 2. SAR image of reflector and a few trees. Made from PPP recorded aperture. The colour axis is in uncalibrated intensity $I = |A|^2$.

VI. CONCLUSION

During the registration of a synthetic aperture image, a bias in the flight path solution reached with PPP can be omitted. PPP will then perform equally well as RTK. For longer apertures, 60 s the bias might drift, this can then reduce the quality of the recorded aperture. The average image quality in the results show that PPP is differs slightly but sufficiently close for most applications. Aperture recording for metre-wave synthetic aperture radar is an application where the precision of precise point positioning can be fully utilised.

ACKNOWLEDGMENT

IGS for correction product and Tomoji Takasu for RTKLIB.

REFERENCES

- [1] E. D. Kaplan. *Understanding GPS : Principles and Applications*. Norwood, MA: Artech House, 1996.
- [2] J. Dow, R. Neilan and C. Rizos. *The International GNSS Service in a changing landscape of Global Navigation Satellite Systems*, Journal of Geodesy, 2009, 191-198.
- [3] Y. Gao, K. Chen. *Performance analysis of precise point positioning using real-time orbit and clock products*. Journal of Global Positioning Systems: Scientific Research Publishing, 2004, 95-100
- [4] S. Bisnath, Y. Gao. *Current State of Precise Point Positioning and Future Prospects and Limitations*. Observing our Changing Earth. Berlin, Heidelberg: Springer, 2009, 615-623.
- [5] H. Hellsten, *Meter-Wave Synthetic Aperture Radar: For Concealed Object Detection*, 1st ed. Norwood, MA: Artech House, 2017.
- [6] W. G. Carrara, R. S. Goodman and R. M. Majewski, *Spotlight Synthetic Aperture Radar: Signal Processing Algorithms*, Norwood, MA: Artech House, 1995.
- [7] T. Takasu, and Y. Akio. *Development of the low-cost RTK-GPS receiver with an open source program package RTKLIB*, International symposium on GPS/GNSS. International Convention Center Jeju Korea, 2009.

Sub-band Robust GNSS Signal Processing for Jamming Mitigation

Daniele Borio

European Commission, Joint Research Centre (JRC), Ispra (VA), Italy

Emails: daniele.borio@ieee.org

Abstract—Jammers, illegal devices, which broadcast powerful signals in the Global Navigation Satellite System (GNSS) frequency bands, can significantly degrade the performance of GNSS receivers. A possible approach to mitigate the impact of jamming is the implementation of Pulse Blanking (PB) that is an effective mitigation technique for pulsed interference. Clean samples are however required for receiver processing. In order to achieve this condition, filtering can be used: the jamming signal usually sweeps large frequency bands. When filtering is applied, the jamming signal periodically enters and exits the filter bandwidth resulting in pulsed interference. For wide-band GNSS signals, a Filter Bank (FB) can be adopted: the input signal is split into several sub-bands and PB is applied independently on each sub-band. The jamming signal impacts only one sub-band at the time resulting in a sequence of pulses in the different sub-band channels. In this paper, sub-band signal processing is combined with robust Zero-Memory Non-Linearities (ZMNLs) and a general scheme for interference mitigation is proposed. In particular, PB is replaced by ZMNLs that introduce robustness to the processing of GNSS signals. Sub-band decomposition is performed using a uniform Discrete Fourier Transform (DFT) FB, which is efficiently implemented using polyphase decomposition. Different FB configurations and different ZMNLs are considered. Hardware simulations and real GNSS data are used to demonstrate the effectiveness of the mitigation schemes proposed.

Index Terms—GNSS signals, Filter Bank, Interference Mitigation, Jamming, Robustness

Full paper in IEEE Xplore

Classification of Spoofing Attack Types

J. Rossouw van der Merwe, Xabier Zubizarreta, Ivana Lukčin, Alexander Rügamer and Wolfgang Felber

Fraunhofer IIS

Nuremberg, Germany

johannes.roussouw.vandermerwe@iis.fraunhofer.de

Abstract— All spoofer attacks have different requirements, impacts, success rates and objectives; therefore, to assess the threat and to develop appropriate counter measures, a clear classification is needed. Being aware of the different existing types of threats, allows an improved design of preventative measures to counter these attacks. This paper classifies spoofer attacks with a layered model. This allows assessing the risks and strategies of operational spoofers with the goal of prevention. The layered model consists of the deployment architectures, the take-over strategy, the control strategy and the application. The paper expands the strategies to manipulate a position of receiver, highlights operational difficulties and suitable counter measures. This emphasises that even if a signal is successfully spoofed, controlling a target receiver is not trivial. Additionally, the most probable spoofing attacks are presented and the applicable anti-spoofing methods are outlined.

Index Terms—Spoofing, global navigation satellite system (GNSS), receiver design, receiver hardening, preventative engineering.

Full paper in IEEE Xplore

Collaborative Integrity Monitoring Solution based on Majority Voting for Critical Applications

Philippe Brocard, Airbus Defence and Space
Leslie Montlouis, Airbus Defence and Space

ABSTRACT

Critical navigation applications are extensively based on GNSS for positioning, guidance or timing. Most of the critical applications are intended to fulfil integrity requirements. This paper proposes a new GNSS integrity monitoring algorithm based on a GNSS collaborative approach in which GNSS receivers of a network share data to improve their integrity and availability performances. The proposed algorithm aims at enhancing the integrity and availability of the GNSS collaborators with respect to the infrastructure-free non-collaborative algorithms (ABAS), while presenting low infrastructure costs and requiring low amount of exchanged data between the receivers of the network.

The principle of the proposed approach that relies on a majority voting fault detection is firstly presented. An integrity algorithm aiming at estimating the Protection Levels (PLs) in the context of this approach is presented and the availability performances of this algorithm are assessed. The sensitivity of these performances with respect to the number of GNSS receivers in the network is discussed. Finally, the limitations of this algorithm are outlined and an optimized algorithm is proposed to overcome these drawbacks. The performance gain of the optimized algorithm with respect to the basic algorithm is analyzed.

The results show that the proposed GNSS integrity collaborative approach provides high availability performance with respect to classical ABAS algorithms. The system architecture (optimal number of GNSS receivers) can be adjusted knowing the integrity requirements of the targeted application. Finally, the optimized algorithm leads to significantly enhance the integrity and availability performance with respect to basic algorithms, at the expense of an increase of the computation complexity.

INTRODUCTION

Several fields of application require vehicles to be equipped with devices that provide, real time, precise and trustable positioning. There is a growing interest of using GNSS receivers for such purpose because this technology does not rely on any ground infrastructures and is available everywhere on the globe. Historically, civil aviation has been the first safety critical application to use GNSS receivers for guidance, but maritime, rail and road (with autonomous car) applications are showing a growing interest in this technology. Other applications such as UAV positioning and guidance are currently using GNSS. These applications are associated with Required Navigation Performances (RNP) that must be fulfilled by the positioning system. These applications have in common the fact that standalone GNSS cannot fulfill such requirements, in particular the integrity ones. Integrity relates to the level of trust that can be placed in the information provided by the positioning system. It includes the ability of the system to provide timely and valid warnings to users when the position error exceeds a tolerable alert limit for the intended operation. GNSS augmentation systems have been developed to tackle this issue.

Existing augmentation systems are classified into Ground Based Augmentation System (GBAS), Satellite Based Augmentation System (SBAS) and Aircraft Based Augmentation System (ABAS). ABAS augmentation is a flexible and infrastructure free approach, but it has limited availability performances because the fault detection process has to be performed autonomously. On the other hand, GBAS and SBAS present improved availability performances because the fault detection process is performed by a dedicated ground segment and because they include correction to nominal errors. However, GBAS and SBAS present two main drawbacks. Firstly, they are less flexible than ABAS as they require infrastructures. Secondly, they have been designed for civil aviation applications. This may lead to a lack of compatibility regarding other applications because these

systems are not designed to mitigate and protect users from GNSS threats specific to non-aviation applications, and because performance requirement levels targeted by GBAS and SBAS systems may not be compatible with non-aviation applications (too conservative for roads or UAVs, not enough for rails).

The challenge is thus to propose an innovative integrity monitoring system that combines:

- Low infrastructure cost,
- Improved availability performance compared to existing infrastructure-free approaches (ABAS),
- Flexibility/adaptability of the system design regarding the integrity requirement level demanded by the targeted application.

The proposed solution presented in this paper is a GNSS integrity collaborative approach. In this approach, the GNSS receivers that are part of a network of collaborative users share fault detection test results in order to derive decisions and detect feared events. Thus it improves the integrity and availability of the position solution of each user. In addition, the system architecture can be adapted to the integrity requirement demanded by the targeted application. Any collaborative system presented in this paper is assumed to consist of:

- the user segment which consists of the collaborative GNSS receivers, and a guaranteed data link to exchange data with the processing facility,
- the central processing facility which collects the data transmitted by the GNSS receivers, processes them and broadcasts data to the receivers with a guaranteed data link.

Several techniques based on the GNSS collaborative approach have been proposed in the literature. Most of these techniques aim at improving the accuracy of the user solutions by improving GNSS signal acquisition or tracking performance, or by mitigating GNSS errors, or by fusing GNSS data from several users so as to gain accuracy performance. As examples, some papers propose to fuse GNSS data from a user network at antenna and signal processing level in order to recover attenuated GNSS signals [1] [2] and mitigate interference [1]. [3] and [4] fuse GNSS ranging measurements from a GNSS receiver network, as well as relative distances or angles or arrival between each network receiver to improve the position accuracy performance. Other publications propose to use the double difference technique between GNSS satellites and network receivers on the GNSS code and carrier measurements through an Extended Kalman Filter (EKF) to improve receiver position accuracy [5]. Few publications deal with the integrity enhancement through collaborative approaches. [6] and [7] propose a GNSS integrity collaborative approach in which the central facility collects and combines GNSS code range residual vectors from all collaborative receivers order to

monitor common-mode faults (faults correlated among multiple receivers located in proximity) [6] and specific faults (faults uncorrelated across receivers) [7]. [5] extends the concept of Carrier phase Receiver Autonomous Integrity Monitoring (CRAIM) to collaborative networks. Both approaches require the users to broadcast the GNSS measurements to the facility and the facility to detect the GNSS faults. Hence, it requires a relatively important amount of data exchanged with the server and relatively complex computations in the facility that performs the fault detection algorithm.

In the new approach proposed in this paper, the fault detection algorithm is performed at user level. Thus it has the advantage of requiring the users to transmit estimated health status values or arrays, which demands very low data rates and complexity. The proposed solution is adapted to system architectures that require a low data rate and a low computation complexity at the processing facility level.

The outline of the paper is as follows:

- Section I describes the principle of majority voting multiple user fault detection approach. The majority voting approach is the integrity collaborative approach that consists in sharing the fault detection test results from all collaborators in the central facility. This is the approach analysed in this paper.
- Section II describes the principle of the “equal split algorithm” that is a GNSS integrity monitoring algorithm based on the majority voting approach. This section also assesses the performance of this proposed algorithm.
- Section III analyses the limits of the “equal split approach”, and proposes an “optimized split algorithm”, that is an advanced GNSS integrity monitoring algorithm based on the majority voting detection approach. This section also assesses the performance of the “optimized split algorithm”, and compares these performances to those of the “equal split algorithm”.
- Section IV presents the conclusions of this paper and proposes future works related to this analysis.

I. Majority voting based fault detection approach

I.1. Integrity background

A positioning failure (*HMI*) is said to occur if the positioning error exceed the *AL* without an alarm being raised within *TTA*. For critical applications, the probability of positioning failures shall be lower than the operational integrity risk requirement ($P_{INT,req}$):

$$P_{HMI} = P_{HMI,H_0} + P_{HMI,local} + P_{HMI,Sis} \leq P_{INT,req} \quad (1)$$

where:

- P_{HMI,H_0} is the probability of positioning failure under nominal conditions (H_0). It can be reduced by using differential corrections. The present paper does not focus on this aspect.
- $P_{HMI,local}$ is the probability of positioning failure assuming an anomaly intrinsic to the user (multipath, user clock offset, user receiver bias jump).
- $P_{HMI,SiS}$ is the probability of positioning failure assuming a SiS anomaly (e.g. SV clock offset, faulty ephemeris, unscheduled SV maneuver, SV IFB jump). Such anomaly would affect every user in the area of visibility of the satellite, with an impact that depends of the geometry. It is thus likely to be detected by several of them if they are equipped with a Fault Detection (FD) mechanism.

For any fault mode (indexed by i) affecting SiS, the integrity risk can be conservatively bounded by assuming a probability of integrity impact of one ($P_{MI|MD,i} = 1$):

$$P_{HMI,SiS} \leq \sum_i P_{OCC,i} P_{MD,i} \quad (2)$$

where:

- $P_{OCC,i}$ is the probability of occurrence of the feared event i ,
- $P_{MD,i}$ is the probability of miss detection of feared event i associated to a FD algorithm such as RAIM.

Failures that affect the GNSS SiS do impact all the receivers that process the faulty satellite(s). An important assumption made in the rest of this paper is that the GNSS receivers of the network are in the same area (the spatial disparity of the GNSS network is around 50km maximum), and the GNSS receivers process data from the same satellites at a given time epoch. Hence, the impact of the GNSS SiS failure on one or several satellites is the same on each receiver of the network.

It is intuitive that a communication link between the receivers would enhance the FD(E) process, as the receivers that have detected a potentially faulty satellite would be able to warn the other receivers that did not detect it (due to a missed detection event), thus reducing $P_{MD,i}$.

1.2. Principle

Majority voting is the most basic approach to integrate information from different sources. Each receiver is assumed equipped with its own FD(E) algorithm (RAIM, ARAIM, AAIM). Let us assume that each receiver is able to transmit to the server either:

- a binary value (denoted s) where a 1 is transmitted if the FD algorithm has not detected any failure and 0 if it has.
- a binary array where the status of each SV is characterized by a value of 1 if it has not been classified as faulty by the FDE and 0 if it has.

The central facility compares the status values/vectors and decides by majority voting whether a SiS event has occurred or not, as represented in Figure 1.

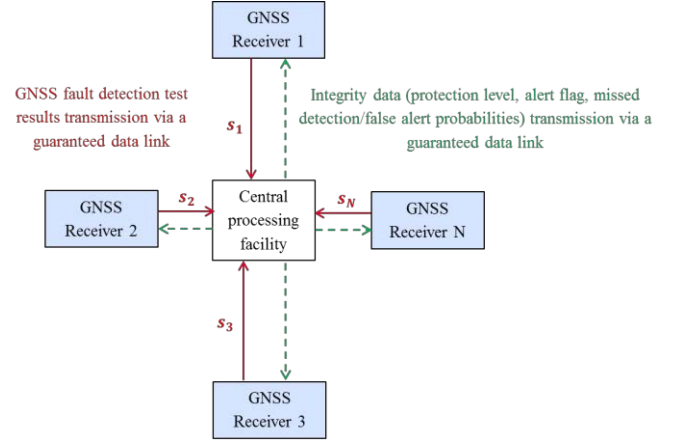


Figure 1 Principle of majority voting based fault detection approach

Several data link can be envisaged for this architecture. If the receivers of the network are in proximity, the Dedicated Short-Range Communications (DSRC) is a candidate. It is a wireless communication channel designed specifically to support vehicle to vehicle (V2V) and vehicle to infrastructure (V2I) communications. Further details about the frequency band and bandwidth allocated to DSRC are available here [8].

Remark that the central processing facility can be an external infrastructure or one of the GNSS receivers of the network. In this case, the proposed cooperative integrity approach only uses Vehicle to Vehicle (V2V) communications, and no Vehicle to Infrastructure (V2I) communications.

Let us assume that N_{SV} satellites are seen by a set of N_{usr} users. Let us denote $P_{MD,macro}$ the probability of miss detection of a fault in SiS by the collaborative system. Let us assume that the SiS is declared faulty by the processing facility if the number of flag raised is higher than or equal to Th . The probability of missed detection and probability of false alarm by the central facility are given by, respectively:

$$P_{MD,macro} = P(\sum_{k=1}^{N_{usr}} s_k < Th | SiS \text{ fault}) \quad (3)$$

$$P_{FA,macro} = P(\sum_{k=1}^{N_{usr}} s_k \geq Th | no \text{ SiS fault}) \quad (4)$$

Intuitively, the higher the number of users to share their integrity flags, the better the detection ability, the lower the probability of false detections and the lower the protection levels related to SiS faults PL_{SiS} .

Two approaches have been developed to derive the protection levels related to SiS faults for each receiver of the collaborative network. The first approach, namely the equal split approach, it presented in the next section.

II. Equal split approach

II.1. Principle

In the equal split approach, it is assumed that the missed detection events by each receiver are independent event, with the same probability of occurrence $P_{MD,usr}$. The number of missed detection by the central facility follows a Binomial law, and the probability of missed detection by the central facility is given by:

$$P_{MD,macro} = CDF_{B(N_{usr}, 1-P_{MD,usr})}(Th - 1) \quad (5)$$

where:

- $CDF_{B(n,p)}(.)$ is the cumulative density function of the Binomial distribution with parameters (n, p) .

Similarly, it is assumed that the false detection events by each receiver are independent event, with the same probability of occurrence $P_{FA,usr}$. $P_{FA,macro}$ can be expressed by:

$$P_{FA,macro} = 1 - CDF_{B(N_{usr}, P_{FA,usr})}(Th - 1) \quad (6)$$

Figure 2 illustrates the evolution of $P_{MD,macro}$ and $P_{FA,macro}$ for given values of $P_{MD,usr}$ and $P_{FA,usr}$ ($P_{MD,usr} = 10^{-3}/\text{sample}$, $P_{FA,usr} = 10^{-5}/\text{sample}$). At constant Th , increasing the number of users highly improve the detection ability at the cost of a slight increase of $P_{FA,macro}$.

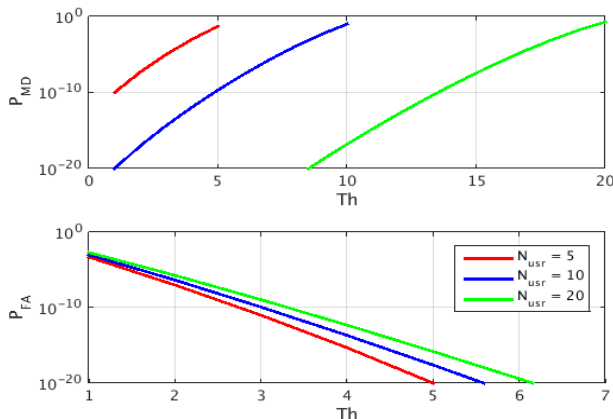


Figure 2 $P_{FA,macro}$ and $P_{MD,macro}$ for different values of N_{usr} and Th ($P_{MD,usr} = 10^{-3}/\text{sample}$, $P_{FA,usr} = 10^{-5}/\text{sample}$)

To express the gain from the user point of view, the problematic must be reformulated because the actual objective of the collaborative approach is to improve the availability while ensuring a sufficient level of integrity and continuity. Let us assume that the receivers are operating with the same integrity and continuity requirements. The collaborative system shall verify:

$$\begin{cases} P_{FA,macro} \leq P_{FA,req} \\ P_{MD,macro} \leq P_{MD,req} \end{cases} \quad (7)$$

where:

- $P_{FA,req}$ and $P_{MD,req}$ are the allocation of the integrity and continuity budget requirement to the SiS feared events.

Apart from majority voting status decision, the objective of the central facility is to minimize the size of the protection levels (associated to feared event that affects all users) which expression is:

$$PL_{SiS} = \max_i [PL_i(Th, P_{FA,usr}, P_{MD,usr}, maxSlope, N_{SV})] \quad (8)$$

where:

- i refers to any SiS fault mode that affects all the users,
- $maxSlope$ depends on the geometry of the GNSS satellites processed by the users, and on the expected measurement error models related to these satellites.

Optimizing the protection level associated to the SiS fault is achieved by finding the threshold Th and the user level probabilities $P_{FA,usr}$ and $P_{MD,usr}$ that minimize the protection level associated to the SiS fault, while constraining the probability of missed detection and the probability of false alarm by the central facility to be equal to their maximal acceptable values (i.e. to $P_{MD,req}$ and $P_{FA,req}$). This is done by solving the following the minimization problem with two constraints:

$$\begin{aligned} & \min_{Th, P_{FA,usr}, P_{MD,usr}} PL_{SiS}(Th, P_{FA,usr}, P_{MD,usr}, maxSlope, N_{SV}, N_{usr}) \\ & \text{subject to: } \begin{cases} P_{MD,req} = CDF_{B(N_{usr}, 1-P_{MD,usr})}(Th - 1) \\ P_{FA,req} = 1 - CDF_{B(N_{usr}, P_{FA,usr})}(Th - 1) \end{cases} \end{aligned} \quad (9)$$

This optimization process shall be conducted in the processing facility. It either requires the user to transmit their $maxSlope$, or it shall be predicted by the facility using the GNSS satellite elevation angle estimates at each receiver position. These elevation angles can be estimated using the coarse positions of the receivers and the GNSS satellite position estimates from the navigation messages.

Moreover, to use the protection levels and alarm taking advantage of the collaborative system, the alarms shall be raised with a sufficiently short delay ($\leq TTA$), which may not be met in case of network issues. A degraded mode using FDE with probabilities derived for a non-collaborative user shall run in parallel as backup at least during such outage.

II.2. SiS faulty protection level reduction assessment

This paragraph aims at assessing the reduction of the protection level associated to a SiS fault achieved using the equal split approach presented in the previous paragraph.

For this analysis, it is assumed that protection levels of each receiver of the collaborative network are computed using a standard RAIM FD algorithm. The expression of the protection level associated to the faulty SiS mode in the collaborative network of N_{usr} receivers is given by [9]:

$$PL_{SiS}(N_{usr}) = \maxSlope \sqrt{\lambda(Th, P_{FA,usr}, P_{MD,usr}, N_{SV}, N_{usr})} \quad (10)$$

where:

- λ is a non-centrality parameter computed by solving the following equation:

$$P_{MD,usr} = CDF_{\chi^2_{\lambda, N_{SV}-4}}(Th_{FA}) \quad (11)$$

where:

- $CDF_{\chi^2_{\lambda, n}}(.)$ is the cumulative density function of the chi-squared distribution with non-centrality parameter λ and n degrees of freedom
- $Th_{FA} = CDF_{\chi^2_{N_{SV}-4}}^{-1}(1 - P_{FA,usr})$
- $CDF_{\chi^2_n}^{-1}$ is the inverse cumulative density function of the centered chi-squared distribution with n degrees of freedom
- $P_{FA,usr}, P_{MD,usr}$ are the probabilities of missed detection and false alert allocated to each user using Equation 9. They depend on N_{usr} and Th .

Let us assess the protection level reduction obtained by the collaborative approach as a function of the number of receivers in the network N_{usr} . For this purpose, an estimation of the PL size reduction ratio $\left(1 - \frac{PL_{SiS}(N_{usr})}{PL_{SiS}(N_{usr}=1)}\right)$ as a function of N_{usr} is plotted in Figure 3. In this plot, it is assumed that $P_{MD,req} = 10^{-3}/\text{sample}$, $P_{FA,req} = 10^{-5}/\text{sample}$ and $N_{SV} = 8$.

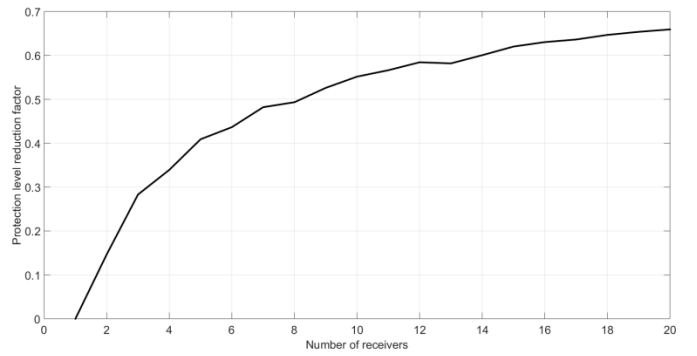


Figure 3 Faulty SiS PL size reduction factor as a function of the number of GNSS receivers in the network

It can be inferred from **Erreur ! Source du renvoi introuvable.** that increasing N_{usr} from 1 to 20 reduces the size of the protection level related to a SiS feared event by 70%.

Let us now assess the protected level reduction as a function of the number a satellites in view N_{SV} . For this purpose, a network of 20 GNSS receivers has been simulated in Toulouse, France. A GPS constellation has been simulated over Toulouse over 48 hours with a frequency rate of 1Hz. An estimation of the PL size reduction ratio as a function of the simulation time is plotted in Figure 4. The number of visible GPS satellites (elevation mask of 5° is considered) over the 48hr simulation is also plotted in this figure. It is also assumed here that $P_{MD,req} = 10^{-3}/\text{sample}$, $P_{FA,req} = 10^{-5}/\text{sample}$ and $N_{usr} = 20$.

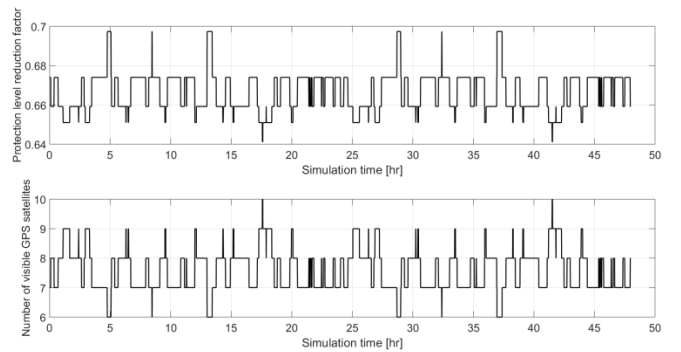


Figure 4 Faulty SiS PL size reduction factor as a function of the number of visible satellites

It is concluded from **Erreur ! Source du renvoi introuvable.** that the protection level reduction due to the collaborative approach is inversely proportional to the number of satellites in view N_{SV} . The reduction is between 65% and 70% for a 20 receiver network in Toulouse, France, with a single GPS constellation. Hence, the collaborative approach has slightly more benefits in single constellation than in multi constellation configuration.

II.3. Availability gain assessment

This paragraph aims at assessing the benefits of reduction of the protection level associated to a SiS fault using the equal split approach on the availability of the system. It shall be kept in mind that a GNSS receiver of the network is said to be available in terms of integrity if the following condition is met:

$$PL < AL, \text{ with } PL = \max[PL_{H_0}, PL_{Local}, PL_{SiS}] \quad (12)$$

where:

- AL is the alert limit assigned to the GNSS receivers,
- PL_{H_0} is the protection level associated to the fault-free conditions,
- PL_{Local} is the protection level associated to local feared events, such as non-light-of-sight (NLOS) multipath or interference.

Remark that, from Equation 12, the PL_{SiS} reduction due to the collaborative approach outlined in the previous paragraph does not match the PL effective reduction. Indeed, the PL effective reduction is limited due to the fact that the PL size is lower bounded by $\max(PL_{H_0}, PL_{Local})$.

Let's assess the availability gain given by the equal split collaborative approach through a simple example. A network of GNSS receivers equipped with standard RAIM algorithms has been simulated in Toulouse, France (elevation mask of 5° is considered). A GPS constellation has been simulated over Toulouse over 24 hours with a frequency rate of 0.1Hz.

It is assumed that no local threats affect the GNSS measurements used by the GNSS receivers. The protection levels associated to the local threats are thus not estimated in this analysis. The fault-free protection levels PL_{H_0} are estimated assuming that the GPS L1 nominal code measurement error model follows a zero-mean Gaussian distribution with a standard distribution of:

$$\sigma = \sqrt{\sigma_{eph+satClock}^2 + \sigma_{iono}^2 + \sigma_{tropo}^2 + \sigma_{noise+multi}^2} \quad (13)$$

where:

- $\sigma_{eph+satClock}$ is the standard deviation of GPS code ranging errors due to satellite clock and ephemeris inaccuracies and is set to 2.0m, that is the minimal URA value broadcast in GPS navigation message [10].
- σ_{iono} is standard deviation of the L1 residual ionosphere code ranging error [m]. Since it is

assumed that Klobuchar ionosphere error model is used to mitigate the ionosphere error on the GPS code ranging measurements, σ_{iono} corresponds to the code ranging error after Klobuchar correction developed in [11].

- σ_{tropo} is standard deviation of the residual troposphere code ranging error [m] developed in [11].
- $\sigma_{noise+multi}$ is standard deviation of the receiver noise and multipath code ranging error and is set to 1.0m in this simulation.

Finally, the SiS faulty protection levels PL_{SiS} are computed using Equations 9 and 10. It is assumed in this computation that $P_{MD,req} = 10^{-3}/\text{sample}$, $P_{FA,req} = 10^{-5}/\text{sample}$.

An estimation of the fault-free horizontal protection levels PL_{H_0} and SiS faulty horizontal protection levels PL_{SiS} as a function of the simulation time is plotted in Figure 5 for different numbers of receivers N_{usr} ($N_{usr} = 1, N_{usr} = 10, N_{usr} = 20$).

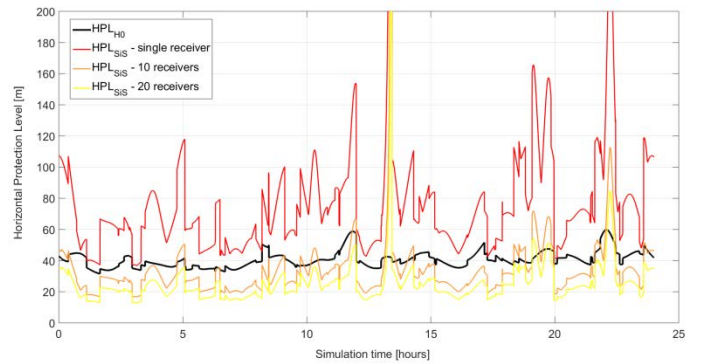


Figure 5 Fault-free and faulty SiS HPL in Toulouse, France

From Figure 5, the final PL is dominated by the faulty SiS PL when the GNSS receiver network is composed of 1 user. Thanks to the SiS faulty PL reduction from the collaborative approach, the final PL is mainly dominated by the fault-free PL for $N_{usr} = 20$. Hence, the optimal network size N_{usr} can be chosen as the minimal number of receivers:

- that leads the global PL to be dominated by the fault-free PL.
- or that leads the faulty SiS PL to be below the alert limit.

As a consequence, the minimal number of receiver must be chosen depending on the integrity requirements related to the targeted operation.

Figure 6 depicts the evolution of the GNSS receiver mean availability (in the horizontal dimension) over the 24hr

simulation as a function of the network size N_{usr} for a given horizontal alert limit $HAL = 45m$.

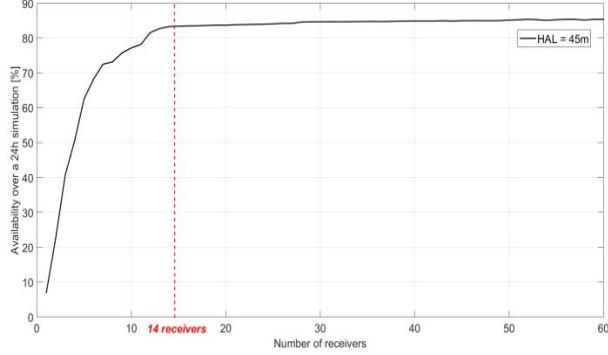


Figure 6 Mean availability of GNSS receivers in the collaborative network in Toulouse, France

From Figure 6, above $N_{usr} = 14$, the availability is roughly constant as a function of the network size. Indeed, the global PL is dominated by the fault-free PL from $N_{usr} = 14$. This means that there is no benefit in increasing the network size above 14 receivers in this example.

III. Optimized split approach

III.1. Equal split approach limitations

As discussed previously, two approaches have been developed to derive the protection levels related to SiS faults for each receiver of the collaborative network. The equal split approach, presented in Section II, assumes that all GNSS receivers of the network have the same missed detection probability $P_{MD,usr}$ and the false alert probability $P_{FA,usr}$ associated to the SiS fault events. In addition, it is assumed that the GNSS receivers are concentrated in the same area (the distance between receivers is assumed to be below 50km) and process the data from the same satellites, so the relative geometry between the receivers of the network and the GNSS constellation is the same for each receiver. Hence, the SiS faulty protection levels PL_{SiS} are the same for each GNSS receiver in the equal split approach.

As an example, Figure 7 represents the PL_{SiS} size computed at the first epoch of the simulation scenario fully described in Section II.3. In this figure, it is assumed that the network size is $N_{usr} = 3$.

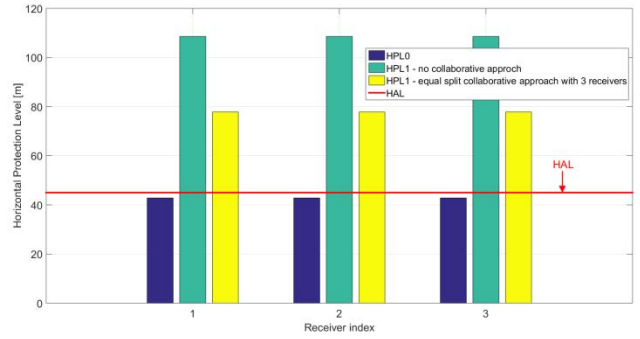


Figure 7 Fault-free and faulty SiS HPL in Toulouse, France, for the 1st epoch of the 24hr simulation, and for $N_{usr} = 3$

From Figure 7, no GNSS receiver is available using the equal split approach at this specific epoch. It is proposed to develop an optimized split approach aiming at improving the GNSS network availability. The proposed approach, namely the optimized split approach, aims at reducing the PL_{SiS} size of one or more GNSS receivers of the network, at the expense of an increase the PL_{SiS} of other GNSS receivers of the network.

III.2. Principle

In the optimized split approach, it is assumed that the false alert and missed detection events by each receiver are independent events. Each GNSS receiver of the network is categorized in one of the following categories:

- group A consists of N_A receivers that have the same SiS protection levels, namely $PL_{SiS,A}$. This protection level is such as $PL_{SiS,A} = AL$. The N_A receivers have the same missed detection and false alert probabilities, denoted as $P_{FA,usr,A}$ and $P_{MD,usr,A}$.
- group B consists of $N_{usr} - N_A$ receivers that have the same SiS protection levels, namely $PL_{SiS,B}$. This protection level is such as $PL_{SiS,B} > AL$. These receivers have the same missed detection and false alert probabilities, denoted as $P_{FA,usr,B}$ and $P_{MD,usr,B}$.

In this approach, the number of missed detection and false alert by the central facility follows a Poisson Binomial law. The probabilities of missed detection and false alert by the central facility are given by, respectively:

$$P_{MD,macro} = CDF_{PB(p_{MD})}(Th - 1) \quad (14)$$

$$P_{FA,macro} = 1 - CDF_{PB(p_{FA})}(Th - 1) \quad (15)$$

where:

- $CDF_{PB(p_1, p_2, \dots, p_N)}(.)$ is the cumulative density function of the Poisson Binomial distribution with parameters $[p_1, p_2, \dots, p_N]^T$.

$$\begin{aligned}
 \bullet \quad \mathbf{p}_{MD} &= \begin{bmatrix} 1 - P_{MD,usr,A} \\ \vdots \\ 1 - P_{MD,usr,A} \\ 1 - P_{MD,usr,B} \\ \vdots \\ 1 - P_{MD,usr,B} \end{bmatrix} \begin{matrix} N_A \\ N_{usr} - N_A \end{matrix} \\
 \bullet \quad \mathbf{p}_{FA} &= \begin{bmatrix} P_{FA,usr,A} \\ \vdots \\ P_{FA,usr,A} \\ P_{FA,usr,B} \\ \vdots \\ P_{FA,usr,B} \end{bmatrix} \begin{matrix} N_A \\ N_{usr} - N_A \end{matrix}
 \end{aligned}$$

The probabilities $P_{FA,usr,A}$, $P_{MD,usr,A}$, $P_{FA,usr,B}$ and $P_{MD,usr,B}$ and the number of receivers N_A shall be chosen so as to verify:

$$\begin{cases} P_{FA,macro} \leq P_{FA,req} \\ P_{MD,macro} \leq P_{MD,req} \end{cases} \quad (16)$$

The algorithm used to determine the PL_{SiS} for each receiver in the optimized split approach is represented in Figure 8.

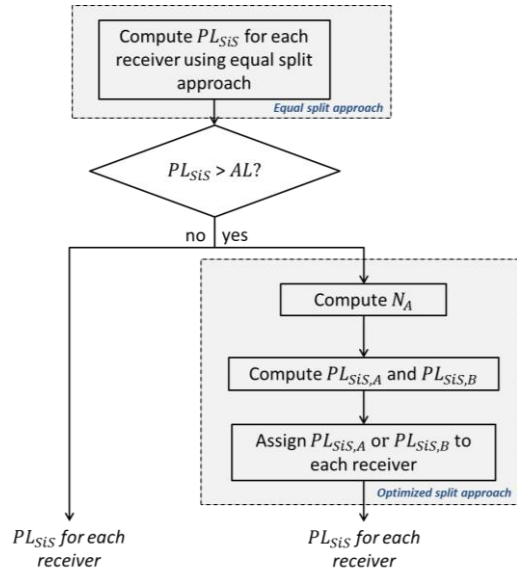


Figure 8 SiS protection level computation algorithm for optimized split approach

As shown in Figure 8, the optimized split approach is not applied when the equal split strategy provides GNSS receivers with SiS protection levels lower than the AL. Indeed, the network availability cannot be improved in this situation. When the SiS protection levels from the equal split strategy are higher than the AL, the optimized approach is adopted and is made of 3 consecutive steps.

The first step consists in estimating N_A , that is the maximal number of GNSS receivers that will have a SiS protection level equal to the AL. This is achieved by solving the following optimization problem with 3 constraints:

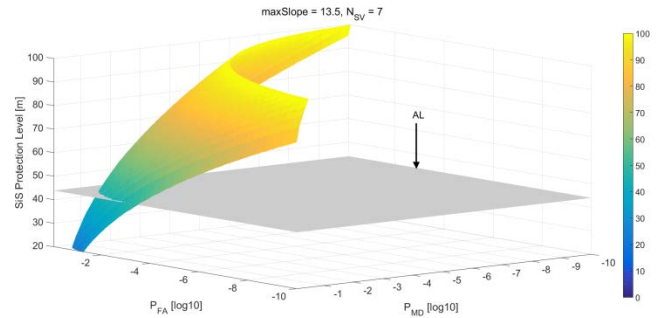
$$\begin{aligned}
 & \max_{N_A \in \llbracket 0, N_{usr} - 1 \rrbracket} N_A \\
 & \text{subject to: } \begin{cases} P_{MD,req} \geq CDF_{PB}(\mathbf{p}_{MD})(Th - 1) \\ P_{FA,req} \geq 1 - CDF_{PB}(\mathbf{p}_{FA})(Th - 1) \\ (P_{FA,usr,A}, P_{MD,usr,A}) \in \mathcal{C}_{AL} \end{cases} \quad (17)
 \end{aligned}$$

where:

- \mathcal{C}_{AL} represents the pairs of false alert/missed detection probabilities that lead to a SiS protection level PL_{SiS} equal to AL.
- $CDF_{PB}(\mathbf{p}_{MD})(Th - 1)$ and $CDF_{PB}(\mathbf{p}_{FA})(Th - 1)$ depends on N_A , as developed in Equations 14 and 15.

In order to estimate all possible pairs \mathcal{C}_{AL} , the surface representing the SiS protection level PL_{SiS} as a function of the false alert probability and missed detection probability is estimated. The pairs \mathcal{C}_{AL} are extracted by estimating the intersection between this surface and the plan at $PL_{SiS} = AL$.

As an example, Figure 9a depicts the SiS horizontal protection level HPL_{SiS} as a function of $P_{FA,usr}$ and $P_{MD,usr}$ for the 1st epoch of the 24hr simulation presented in the previous section ($maxSlope = 13.5$, $N_{SV} = 7$). The protection levels have been estimated using Equation 10. The horizontal plan corresponds to $HPL_{SiS} = HAL$, and HAL is set to 45m in this example. The black curve of Figure 9b represents the pairs \mathcal{C}_{AL} for this epoch.



(9a)

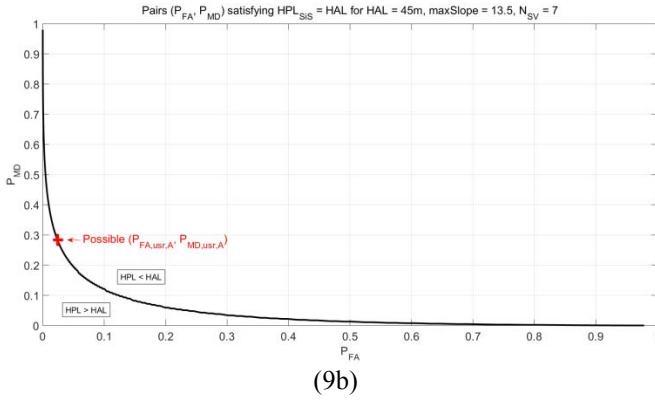


Figure 9 Estimation of the pairs \mathcal{C}_{AL} leading to $HPL_{SiS} = HAL$ for $maxSlope = 13.5, N_{SV} = 7, HAL = 45m$

The second step consists in estimating:

- $P_{FA,usr,A}$ and $P_{MD,usr,A}$, that are the false alert/missed detection probabilities allocated to the GNSS receivers having a SiS protection level $PL_{SiS,A}$ equal to AL .
- $P_{FA,usr,B}$ and $P_{MD,usr,B}$, that are the false alert/missed detection probabilities allocated to the GNSS receivers having a SiS protection level $PL_{SiS,B}$ higher than AL .

Optimizing the protection level associated to the SiS fault is achieved by finding the user level probabilities $P_{FA,usr,B}$ and $P_{MD,usr,B}$ that minimize the SiS protection level for receivers of group B $PL_{SiS,B}$, while constraining the probability of missed detection and the probability of false alarm by the central facility to be lower or equal to their maximal acceptable values (i.e. to $P_{MD,req}$ and $P_{FA,req}$), and the SiS protection level $PL_{SiS,A}$ to be equal to the AL . This is done by solving the following minimization problem with three constraints:

$$\begin{aligned} \min_{Th, P_{FA,usr,B}, P_{MD,usr,B}} & PL_{SiS,B}(Th, P_{FA,usr,B}, P_{MD,usr,B}, maxSlope, N_{SV}, N_{usr}, N_A) \\ \text{subject to: } & \begin{cases} P_{MD,req} \geq CDF_{PB}(P_{MD})(Th - 1) \\ P_{FA,req} \geq 1 - CDF_{PB}(P_{FA})(Th - 1) \\ (P_{FA,usr,A}, P_{MD,usr,A}) \in \mathcal{C}_{AL} \end{cases} \end{aligned} \quad (18)$$

In order to properly solve Equation 18, a deterministic approach would consist in finding the pair $(P_{FA,usr,B}, P_{MD,usr,B})$ that minimizes the $PL_{SiS,B}$ for each pair $(P_{FA,usr,A}, P_{MD,usr,A}) \in \mathcal{C}_{AL}$, then collecting the minimal $PL_{SiS,B}$ for each pair $(P_{FA,usr,A}, P_{MD,usr,A}) \in \mathcal{C}_{AL}$, and then selecting the pair $(P_{FA,usr,A}, P_{MD,usr,A})$ that minimizes the collected $PL_{SiS,B}$. The main drawback of this approach is the computation time. In addition, simulations show that the minimal $PL_{SiS,B}$ is roughly constant over all pairs $(P_{FA,usr,A}, P_{MD,usr,A}) \in \mathcal{C}_{AL}$. For this reason, a statistical approach is rather adopted. It consists in selecting randomly a pair

$(P_{FA,usr,A}, P_{MD,usr,A}) \in \mathcal{C}_{AL}$, then finding the pair $(P_{FA,usr,B}, P_{MD,usr,B})$ that minimizes the $PL_{SiS,B}$ with the constraints written in Equation 18, and then stopping the algorithm. This enables limiting the computation time.

The following information are available at the second step output:

- The SiS protection level of the GNSS receivers having a PL_{SiS} above AL ($PL_{SiS,B}$),
- The number of the GNSS receivers having a PL_{SiS} equal to AL (N_A), and hence the number of the GNSS receivers having a PL_{SiS} higher than AL ($N_{usr} - N_A$).

The third step consists in choosing:

- The N_A receivers having a SiS protection level equal to AL ($PL_{SiS,A}$),
- The $N_{usr} - N_A$ receivers having a SiS protection level above AL ($PL_{SiS,B}$).

In this paper, it is assumed that all GNSS receivers of the network have the same availability requirements. Hence, it is proposed to choose the N_A receivers characterized by a minimal SiS protection level using a discrete uniform distribution. Note that, if the GNSS receivers of the network have different availability requirements, it can be suggested to choose a more adapted statistical distribution to select GNSS receivers characterized by the minimal SiS protection level.

As an illustration of the results of the optimized split approach, Figure 10 depicts the SiS horizontal protection level HPL_{SiS} for a network of size $N_{usr} = 3$, and for the 1st epoch of the 24hr simulation presented in the previous section ($maxSlope = 13.5, N_{SV} = 7, HAL = 45m$). As observed in this figure, $N_A = 2$ for the analyzed time epoch.

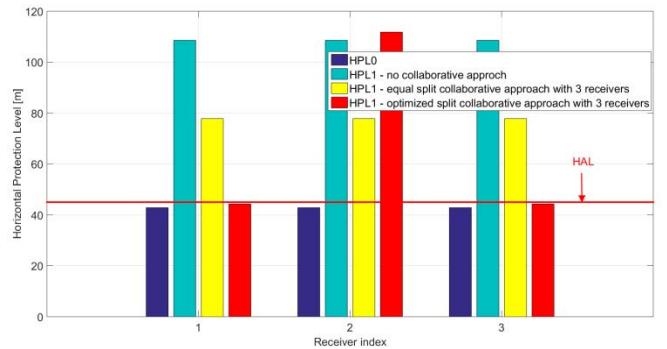


Figure 10 Comparison of HPL_{SiS} between equal and optimized split approaches, for $maxSlope = 13.1, N_{SV} = 8, HAL = 45m$

It can be observed in Figure 10 that the network availability was 0% with the equal split approach for the analyzed time epoch, while 66% of the GNSS receivers

are available with the optimized split approach at the same time epoch. Hence, the optimized split approach is expected to improve the availability performance of the GNSS receiver network.

III.3. Availability gain assessment

This paragraph aims at assessing the benefits of the optimized split approach on the availability of the system. The simulation scenario detailed in Section II.3 is re-used in this paragraph.

Figure 11 depicts the mean availability (in the horizontal dimension) of each GNSS receiver of the network ($N_{usr} = 3$) over the 24hr simulation. The horizontal alert limit is set to $HAL = 45m$.

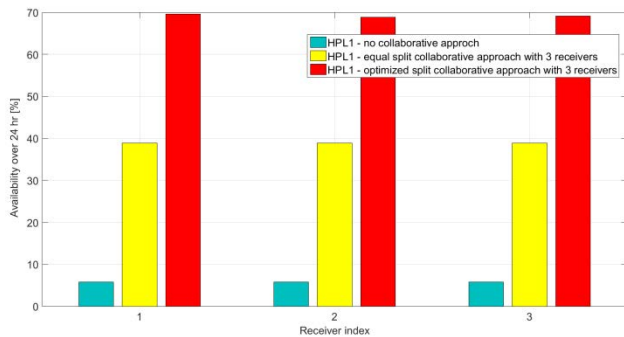


Figure 11 Mean availability of the GNSS receivers using the equal and optimized split approaches in Toulouse, France, for $HAL = 45m$

From Figure 11, the mean availability is roughly constant over the GNSS receivers for the optimized approach. This is because the GNSS receiver(s) having the lowest SiS protection levels are uniformly chosen at each time epoch of the simulation. In addition, it can be inferred that the optimized approach leads to improve the mean availability of each receiver compared to the equal split approach. As an illustration, in the proposed example, the mean availability of each receiver is roughly 40% with the equal split approach and is increased to roughly 70% with the optimized split approach.

IV. CONCLUSIONS

This paper proposes a new GNSS integrity monitoring algorithm based on a GNSS collaborative approach in which GNSS receivers of a network share data to improve their integrity and availability performances. More specifically, the proposed approach, namely the majority voting fault detection approach, presents low infrastructure costs and requires low amount of exchanged data between the receivers of the network. It enables improving the detection performance of SiS failures.

Two integrity algorithms aiming at estimating the Protection Levels (PLs) under the majority voting fault detection approach are proposed. Both algorithms enable reducing the protection level sizes related to SiS failures. The PL reduction factor is proportional to the number of receivers in the network, and reaches 70% when 8 satellites are in view and 20 receivers are present in the network. The optimal network size is achieved when the the global PL is no more dominated by the SiS PL, but by the local PL or by the fault-free PL, or when the SiS PL is below the alert limit related to the targeted operation. Hence, the GNSS receiver network size must be adapted to integrity requirements demanded by the targeted operation. As an illustration, a simple analysis has been conducted in Toulouse, France, in order to quantify the optimal network size for a given set of integrity requirements.

The first integrity algorithm aiming at estimating the PLs, namely the equal split approach, enables low computation complexity in the facility center, but shows sub-optimal performance in terms receiver network availability. In order to overcome this issue, an optimized PLs computation algorithm is proposed. The main drawback of this optimized approach is an increase of the computation complexity in the central facility. Methods are suggested to lower this computation complexity. A simple analysis has been conducted in Toulouse, France, in order to quantify the availability gain due to the optimized approach with respect to the equal split approach. A given set of integrity requirements has been selected for this analysis. Results show that the optimized approach enables improving the availability of each receiver from 40% to 70% compared to the equal split approach.

REFERENCES

- [1]: "Collaborative signal processing", A. Soloviev, J. Dickman, GPS world, 2014
- [2]: "Peer-to-Peer Cooperative Positioning: Part I, GNSS-aided acquisition", R. Garello, L. Lo Presti, G. E. Corazza, J. Samson, Inside GNSS, March/April 2012
- [3]: "Peer-to-Peer Cooperative Positioning Part II: Hybrid Devices with GNSS & Terrestrial Ranging Capability", R. Garello, J. Samson, M. A. Spirito, H. Wymeersch, Inside GNSS, July/August 2012
- [4]: "Angle-of-Arrival Assisted GNSS Collaborative Positioning", B. Huang, Z. Yao, X. Cui, M. Lu, Sensors MDPI, 2016
- [5]: "A closed loop EKF and multi-failure diagnosis approach for cooperative GNSS positioning", Liu,

Haiying, Meng, Xiaolin, Chen, Zhiming, Stephenson, Scott, Peltola, Pekka, GPS Solutions, 2016

[6]:“Collaboration-Enhanced Receiver Integrity Monitoring (CERIM)”, J. Rife, IEEE, 2011

[7]:“Collaboration-Enhanced Receiver Integrity Monitoring with Common Residual Estimation”, J. Rife, PLAN, 2012

[8]: “Collaborative Positioning – Concepts and Approaches for more Robust Positioning”, A. Kealy, G. Retscher, C. Toth, D. Brzezinska, FIG Congress 2014 Engaging the Challenges, 2014

[9]: “Receiver Autonomous Integrity Monitoring of GNSS Signals for Electronic Toll Collection”, D. Salos, A. Martineau, C. Macabiau, B. Bonhoure, D. Kubrak, IEEE Transactions on Intelligent Transportation Systems, 2014

[10]: “Navstar GPS Space Segment/Navigation User Interfaces interface specification, IS-GPS-200-D”, Navstar Global Positioning System, 2004

[11]: “Minimum Operational Performance Standards for Global Positioning System / Aircraft Based Augmentation System Airborne Equipment, DO-316”, RTCA, SC-159, April 2009

Design and Development of a Software for performance comparison of GNSS signal interference detection and analysis algorithms

Muhammad Shahzaib

International School
Beihang University
Beijing, China
muhammadshahzaib786@gmail.com

Faisal A. Khan

GNSS Division
SUPARCO
Karachi, Pakistan

Jin Tian

International School
Beihang University
Beijing, China

Abstract—This paper presents the design of a research platform that enables signal simulation in interference/jamming environment and performance evaluation of interference/jamming detection and mitigation algorithms. Although a wide variety of these tools are available, the platform proposed in this paper will be of modular nature in which the user will be able to insert their newly designed as well as under investigation algorithms before the implementation/evaluation of the same in hardware.

Keywords— GNSS, Interference, Jamming, Software, Interference mitigation

I. INTRODUCTION

GNSS, rapidly becoming an indispensable technology is now highly relied upon by life, safety and reliability critical applications. However, in a typical operational scenario, GNSS user equipment is exposed to RF radiations, both intentional and otherwise that may limit GNSS technology usage or render it unusable altogether. This may include not only in-band unwanted signals but also out-of-band signals with harmonics falling in GNSS bands [1], [2], [3]. In order to overcome this issue, a prudent approach necessitates employment of interference detection and mitigation algorithms that can alleviate this situation. To cater for a wide variety of expected interferers/jamming signals, researches have been made to develop different types of interference mitigation algorithms which can be broadly classified as antenna based or receiver based algorithms [4]. Subspace decomposition method [5] and Joint Polarized and Spatial Domain method [6] are two examples of interference mitigation algorithms. Design, development and performance evaluation of such algorithms calls for a platform to be utilized that can enable evaluation of such algorithms. This paper presents the platform, to achieve this purpose.

This will be a situation aware platform taking signal propagation channel's impairments into account and will allow the user to insert their channel models to suit their operational requirements. Although the platform will be well

suited to all GNSS/RNSS constellations, this paper evaluates the scenario for one existing (GPS) signals. The paper considers the impact of Narrowband interference. Furthermore, the platform will allow consideration/incorporation of atmospheric effects as per user requirement. The results show acquisition of GPS L1 signal in presence of continuous narrowband interference with and without implantation of Interference mitigation algorithm.

II. METHODOLOGY

The design of the software platform is given below,

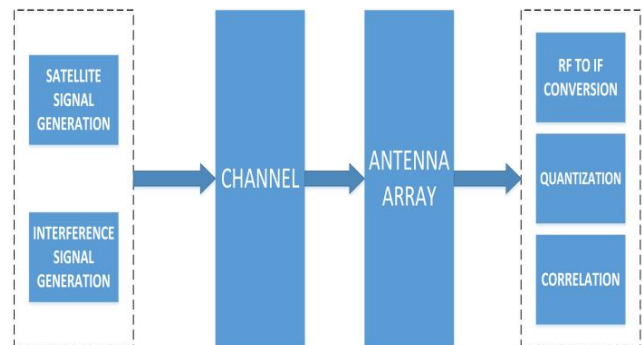


Figure 1. Flowchart of Software Platform

The software first simulates a Satellite Signal. The generated Signal can be represented as,

$$s(t) = (\sqrt{2 * p}) * C / A * \cos(2\pi ft)$$

Here,

P = Signal Power = 20 Watts

f = GPS L1 Frequency = 1.57542 GHz
 C/A = Coarse Acquisition Code for any given Satellite

The signal is then passed through a modeled channel to incorporate Free Space Losses, atmospheric losses, propagation delay, phase delay and Doppler shift. Free Space losses can be expressed as [7],

$$FSL = 20 * \log_{10} \left(\frac{4\pi R}{\lambda} \right)$$

Here,
 R = Distance between Satellite and Receiver
 λ = Wavelength of the Signal

However, for simplicity purposes, atmospheric losses are considered to be 2dB while propagation delay, phase delay and Doppler shift are neglected for the scenario presented in this paper.

Similarly, an interference signal is also generated to visualize the effects of interference on the Satellite signal and validate the implementation of Interference mitigation algorithm. The type of interference (Narrowband or wideband) can also be selected depending on the test scenario. Typical mathematical representation for a narrowband interference signal can be given as,

$$j(t) = (\sqrt{2 * P_j}) * Rand * \cos(2\pi ft)$$

Here,

P = Signal Power = 10 Watts
 f = GPS L1 Frequency = 1.57542 GHz
 $Rand$ = Stream of Random Number. The frequency of Random number is same as GPS C/A code frequency

Interference signal is also subjected to the Channel effects. Antenna block then collects both signals. Antenna can be selected as a Single Antenna or an Antenna Array. This gives the liberty to simulate effects of variety of spatial Interference mitigation algorithms.

Receiver block is responsible for down-conversion, quantization and performing signal acquisition.

III. SIMULATION

A test scenario is generated with these parameters; 1) Signal type: Single Satellite GPS L1 signal, 2) Interference Type: continuous narrowband interference, 3) Interference mitigation algorithm: Canceller. Simulation setup consists of two antenna, a weight assigning block and Software Receiver.

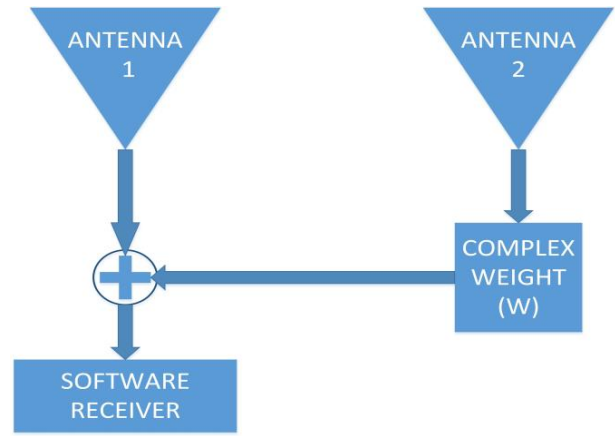


Figure 2. Simulation Setup Design

It is assumed that one antenna has visibility to both Satellite signal and Interference Signal whereas the other antenna has the visibility to Interference Signal and no or very poor visibility to Satellite signal. Practical example of such system can be UAVs with one antenna at top and other antenna at bottom of UAV.

IV. RESULTS

Fig.3 & 4 shows frequency spectrum of the generated and received satellite signals. Generated frequency spectrum verifies that the generated signal has same frequency as GPS L1 signal. Received Signal frequency spectrum shows that satellite signal is received successfully at the antenna.

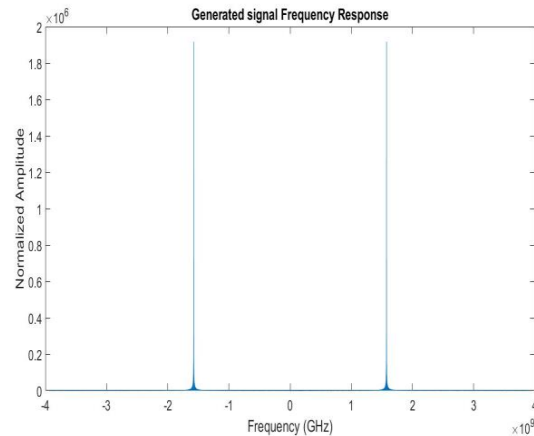


Figure 3. Frequency Spectrum of Jamming Signal at 1st Antenna

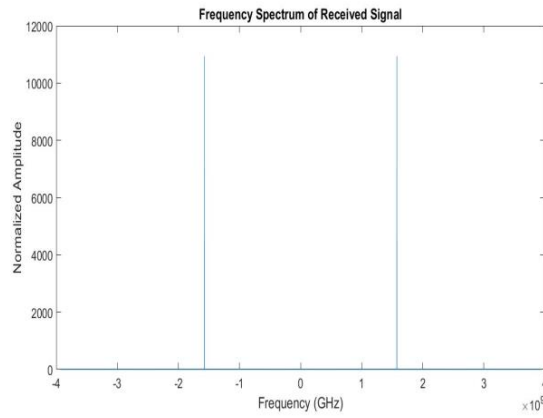


Figure 4. Frequency Spectrum of Received Signal

Figure 5&6 shows the frequency spectrum of the narrowband Interference signal received at both antenna.

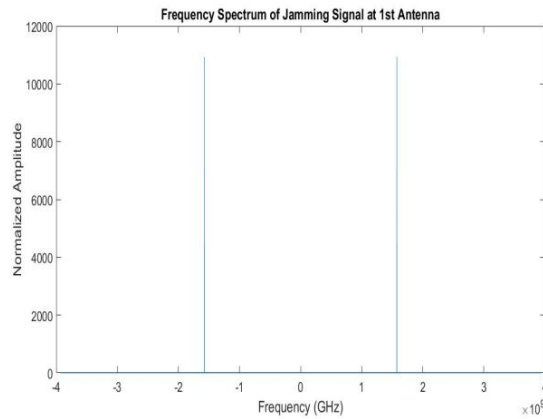
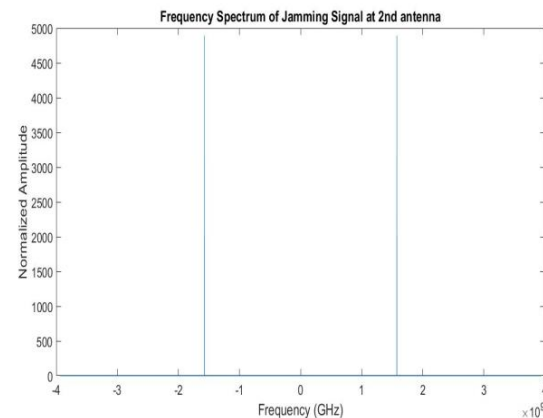
Figure 5. Frequency Spectrum of Jamming Signal at 1st AntennaFigure 6. Frequency Spectrum of Jamming Signal at 1st Antenna

Fig.7 shows acquisition result when no interference mitigation algorithm is in use and it can be seen that no signal acquisition

is achieved. Fig.8 shows acquisition result when Canceller algorithm is used and signal is successfully acquired by the Receiver.

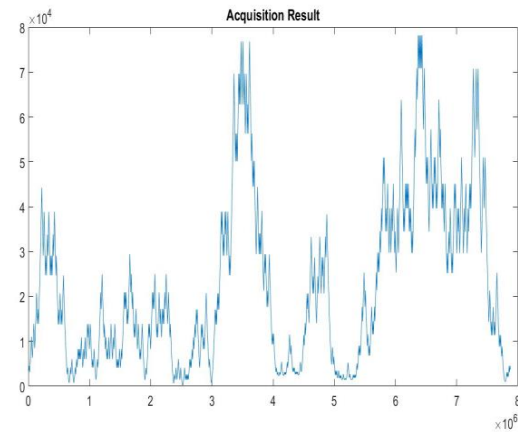


Figure 7. Correlation Result in presence of Jamming without Canceller

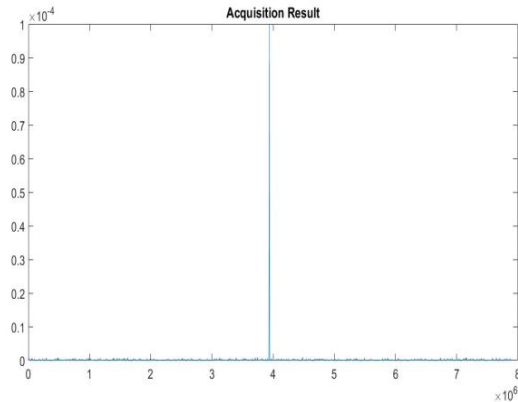


Figure 8. Correlation Result in presence of Jamming with Canceller

REFERENCES

- [1] A. Dempster, "How vulnerable is GPS?" Transportation, 2001.
- [2] Ryan H. Mitch, Ryan C. Dougherty, Mark L. Psiaki, Steven P. Powell, Brady W. O'Hanlon, Jahshan A. Bhatti, and Todd E. Humphreys "Signal Characteristics of Civil GPS Jammers", Proceedings of ION GNSS, Portland, Oregon, 2011
- [3] Logan Scott, "Spoofs, Proofs & Jamming", InsideGNSS, p. 42-53, September/October 2012.
- [4] Steve Rounds, "Part II : Antenna Enhancements, Jamming Protection of GPS Receivers", GPS World, 6, p. 38-45, 2004.
- [5] Hou You-guo, Guo Wei, Jin Xiao-zhang, "An anti-jamming GPS receiver based on subspace decomposition method", International Conference on Communication Software and Networks, 2009.
- [6] Wei Zeng, Ling Wang, Yinghui Wang, Zhaolin Zhang, Meng Zhang, "Joint Polarized and Spatial Domain Anti-jamming Method for GNSS", ICSPCC 2013
- [7] Proakis, J. *Digital Communications*. New York: McGraw-Hill, 2001

Standardization of GNSS Threat reporting and Receiver testing through International Knowledge Exchange, Experimentation and Exploitation [STRIKE3]: Validation of Reporting and Testing Standards

Michael Pattinson¹, M Dumville¹, D Fryganiotis¹, M. Z. H. Bhuiyan², S. Thombre², G. Ferrara², M Alexandersson³, E Axell³, P Eliardsson³, M Pölöskey⁴, V Manikundalam⁵, S Lee⁶, J Reyes Gonzalez⁷

michael.pattinson@nsl.eu.com, ¹Nottingham Scientific Ltd, UK,

²Finnish Geospatial Research Institute, National Land Survey of Finland, Finland

³Swedish Defence Research Agency (FOI), Sweden

⁴Automotive & Rail Innovation Center (ARIC) of AGIT mbH, Germany

⁵GNSS Labs, India, ⁶ETRI, Republic of Korea, ⁷European GNSS Agency (GSA)

Summary

STRIKE3 is a European initiative to support the increasing use of GNSS within safety, security, governmental and regulated applications. To do this STRIKE3 persistently monitors the international GNSS threat scene to capture the scale and dynamics of the problem and works with international GNSS partners to develop, negotiate, promote and implement standards for threat reporting and receiver testing. This is being achieved through the deployment and operation of an international GNSS interference monitoring network.

This paper shows initial results from the central STRIKE3 monitoring database, where interference events from a global network report of monitoring equipment are reported in using a common format and methodology. The importance of this aspect is to validate the proposed reporting standards to demonstrate that the reports from different types of equipment can be compatible. In addition, the paper presents preliminary results of testing receivers against events detected in the field by the monitoring network, in order to test receiver resilience to real-world threats.

Motivation

GNSS is being used for an ever expanding range of safety, security, business and policy critical applications. GNSS functionality is being embedded into many parts of critical infrastructures and European economies are now dependent on uninterrupted access to GNSS positioning, navigation and timing services. At the same time, GNSS vulnerabilities are being exposed and threats to denial of GNSS service are increasing. Reports of events of loss of GNSS services are commonplace. To ensure GNSS is protected, there is now a need to respond at an international level to ensure that there is (i) a common standard for GNSS threat monitoring and reporting, and (ii) a global standard for assessing the performance of GNSS receivers and applications under threat. This will ensure the dominance of GNSS as the backbone to our positioning, navigation and timing needs.

Results

Over the course of the past two years, STRIKE3 has built up a network of over 20 interference monitoring sites in 14 different countries around the World. This provides a valuable resource for determining the level of interference and types of signal that affect real-world installations at a variety of locations (see Fig.1). Although such a network in itself provides useful information over a wide area, the depth of understanding will be greatly enhanced if information from different networks and different types of equipment can be combined. The proposed STRIKE3 threat reporting standards enable different types of equipment to report events in a standardized form to a common database. The results in this paper demonstrate the validity of the standards by showing the combined results in the common database (see Fig.2). In addition, this widescale monitoring has been used to identify the most common types of intentional threat that are detected in the real-world (see Fig.3), and these can be used to test receiver resilience. In this paper, we will be describing the test set up for mass-market and professional grade receivers (see Fig.4) followed by the presentation of the test results.

Figures

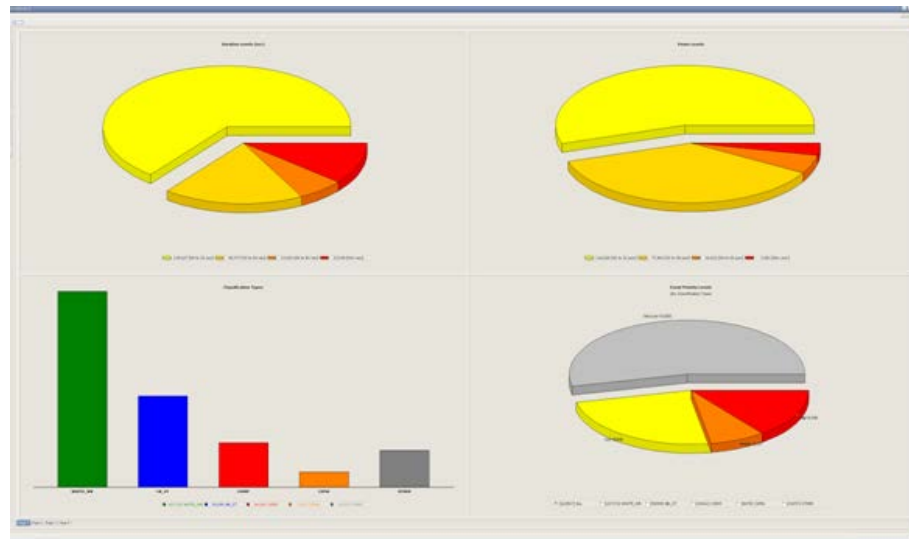


Fig. 1: Overview of All Detected Interference Events in 2017

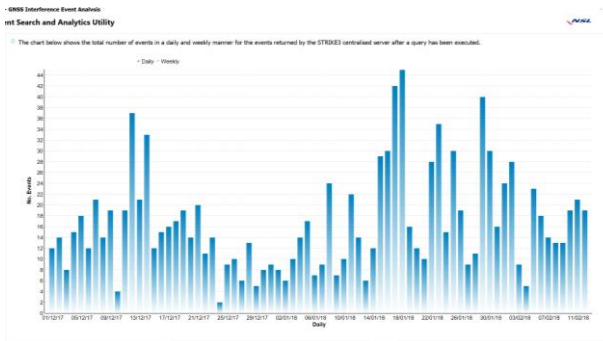


Fig. 2: Summary of First 2 months of Standardised Events from Centralised STRIKE3 Database

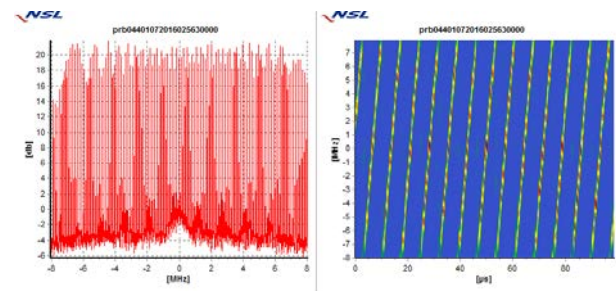


Fig. 3: Example of Common Detected Signal Type

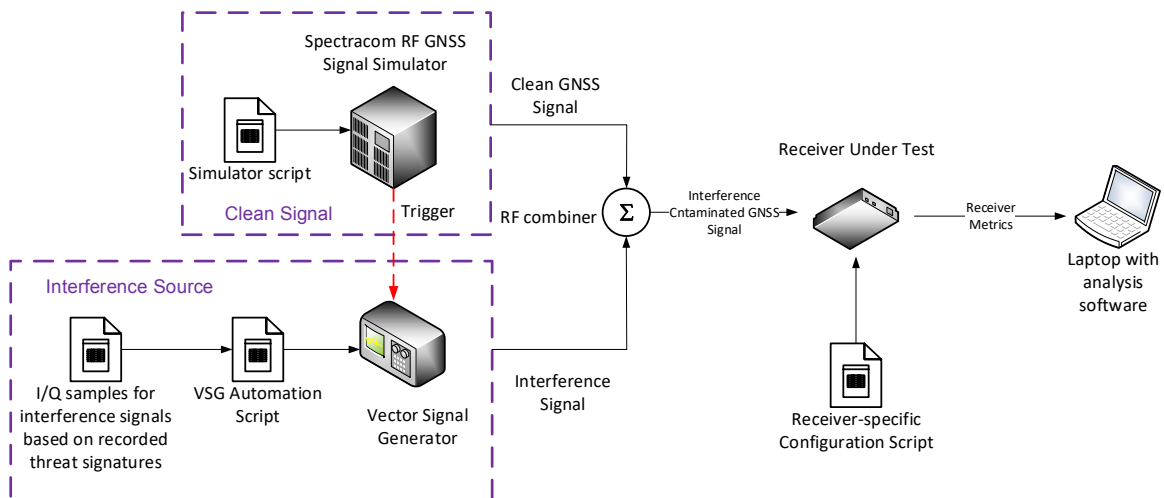


Fig. 4: Test set-up for Validation of Mass-Market and Professional Grade Receivers under Threat Conditions

Multi-GNSS Measurement Campaign in Southeast Asia using the MGSE-System

Alexander Rügamer
Fraunhofer IIS
Nuremberg, Germany

Daniel Seybold
TeleOrbit GmbH
Nuremberg, Germany

Abstract—The Multi-GNSS Simulation & Test Environment (MGSE) provides unique capabilities in synthetically generating, recording and replaying nearly all satnav signals. In a measurement campaign carried out in Hanoi, Vietnam, in October 2017, MGSE was used to record different sets of wideband L1, E6, L5 and S-band signals. After the campaign, the recorded intermediate sample raw data files were replayed using the MGSE and evaluated using a commercial GNSS receiver. The datasets contain multi-GNSS signals of more than 50 different satnav signals but also interferences. Moreover, the IRNSS signals on L5 and S-band are evaluated in their reception quality using a software GNSS receiver. Lastly, the observed interference signals were analyzed.

Index Terms—Satellite navigation systems, Global Positioning System, Record & Replay, Multi-GNSS, Interference

Full paper in IEEE Xplore

Lunar Module Navigation using Visual Based Absolute Navigation and Direct Sparse Odometry

Pei-Ching Hsu*, Chien-Hsun Chu*, Kai-Wei Chiang*, Shau-Shiun Jan⁺, Siang-Lin Jheng⁺,
Yu-Tse Hsieh⁺, Yi-Cheng Tsai*, Yi-Ting Tien*

*Department of Geomatics, National Cheng Kung University, Tainan, Taiwan, peggy831103@gmail.com

⁺Department of Aeronautics and Astronautics, National Cheng Kung University, Tainan, Taiwan

Summary

The development of lunar exploration has flourished in recent years. Since there is no satellite positioning system available in moon, image positioning is the alternative way to help the lunar module find the destination. In this study, a visual based integrated navigation system, which contains visual based absolute navigation algorithm derived from photogrammetry and visual based relative navigation algorithm Direct Sparse Odometry (DSO), is implemented to produce the navigation trajectory that can be applied to guide the lunar module in the exploration mission. The applied lunar images are produced from lunar digital elevation model (DEM), which is made by PANGU (Planet and Asteroid Natural Scene Generation Utility) software. Then, space resection method with photogrammetric approach is applied to calculate the exterior orientation parameters including positions and orientations of the camera. The taken images are matched with the image database to find the feature points for calculating the absolute position of the lunar module. In addition, DSO is used as the visual odometry (VO) algorithm to generate relative position and attitude while moving. Owing to DSO results are not absolute position and the error would accumulate over time, the visual based absolute navigation algorithm can help provide the initial value and update position and attitude information. Through the integrate navigation system from those two methods, there would only need to use the images taken by the lunar module to complete the positioning process. In the experiment result, the final horizontal position error after 80 kilometers flight distance is 44.43 meters, which is good enough for lunar module landing in target destination.

Motivation

With the development of space technology, more and more lunar researches are performed by different countries. For the pin-point landing mission formulated by NASA, a good positioning and navigation system with error less than 100 meters is needed in order to make the lunar module land safely at the exact destination on lunar surface¹. Since the lunar environment doesn't have satellite positioning system, visual based navigation technology which has high autonomy and accuracy for positioning is needed.

Two image positioning methods are achieved in this research. One is visual based absolute navigation algorithm, which uses photogrammetry space resection method to recalculate the position and attitude of the camera photography center from the known control points. This research use speeded up robust features (SURF) to extract the feature point between the images. After matching the reference image from the image database with the taken image from the lunar module, control point coordinates can be obtained, and finally the absolute position of the lunar module would be solved. Another method is visual odometry for relative position calculation. DSO is the visual odometry algorithm that is more robust and faster computing than ever before². This method tracks points in images, and uses the minimization of photometric errors to estimate camera displacement and attitude changes. This research completes a set of integrated system of two visual based navigation method in order to reach the accuracy requirements for lunar exploration landing mission.

¹ Bilodeau, V. Simard, et al. "Optical Navigation System for Pin-Point Lunar Landing", IFAC Proceedings Volumes 47.3, 10535-10542, 2014.

² Engel, Jakob, Vladlen Koltun, and Daniel Cremers. "Direct sparse odometry", IEEE Transactions on Pattern Analysis and Machine Intelligence, 2017.

Results

The experiment simulates flight process which starts at 10 kilometers and ends at 2 kilometers above sea level of lunar, and the total length of flight is 80 kilometers. The PANGU software is used to produce simulated images of lunar surface for image database and test images. The lunar DEM with resolution of 10 meters is provided by NASA for producing the lunar surface images, and the photography center is based on the calculated trajectory coordinates and camera parameters.

Currently, the visual based absolute navigation algorithm mode can only be used up to 4.9 kilometers above sea level of lunar, due to the images made by lunar DEM don't have enough resolution for SURF algorithm. Thus, the final trajectory is calculated by the DSO algorithm, which is corrected the cumulative error by visual based absolute navigation mode. The result trajectory of the algorithm and simulated track as shown in Figure 1. In the figure, red line is simulated track, blue line is result trajectory of the algorithm, and blue crosses are absolute position calculated by visual based absolute navigation algorithm. The final error in 2 kilometers height above the lunar surface is 44.43 meters in horizontal direction, 291.69 meters in vertical direction, and 295.06 meters in three-dimension distance error. The result reaches the accuracy requirements of lunar exploration landing that needs the error less than 100 meters in horizontal direction.

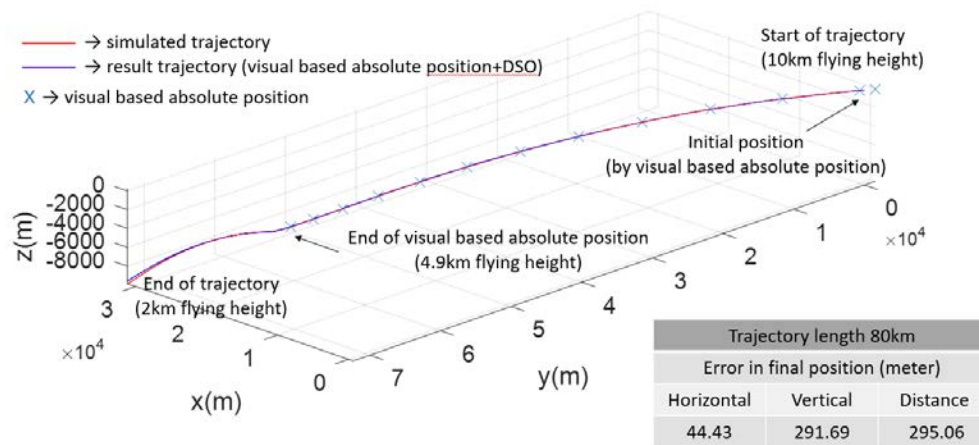


Fig. 1: Lunar module trajectory calculation results

In this research, only camera is used as navigation sensor. The visual based absolute navigation algorithm is mainly based on feature points and visual odometry is based on tracking continuous images, so the result would be different since the images are extremely vulnerable to environmental light and shadow change. In the future, the lunar visual based navigation system can integrate with inertial measurement unit (IMU). IMU is an autonomous sensor that detects the acceleration and angular velocity of the carrier, which is less sensitive to the external environment. Integrating IMU and visual based positioning methods into the same navigation system can provide automated position solvers and reduce the error during lunar exploration landing mission.

Improvement of GPS and BeiDou extended orbit predictions with CNNs

Jaakko Pihlajasalo, Helena Leppäkoski, Simo Ali-Löytty, Robert Piché
Tampere University of Technology, Tampere, Finland
Email: {jaakko.pihlajasalo, helena.leppakoski, simo.ali-loytty, robert.piche}@tut.fi

Abstract—This paper presents a method for improving the accuracy of extended GNSS satellite orbit predictions with convolutional neural networks (CNN). Satellite orbit predictions are used in self-assisted GNSS to reduce the Time to First Fix of a satellite positioning device. We describe the models we use to predict the satellite orbit and present the improvement method that uses CNN. The CNN estimates future prediction errors of our model and these estimates are used to correct our orbit predictions. We also describe how the neural network can be implemented into our prediction algorithm. In tests with GPS and BeiDou data, the method significantly improves orbit prediction accuracy. For example, the 68% error quantile of 7 day orbit prediction errors of GPS satellites was reduced by 45% on average.

Full paper in IEEE Xplore

VLBI with GNSS signals on intercontinental baselines

Rüdiger Haas^{1*}, Thomas Hobiger¹, Grzegorz Kłopotek¹, Junu Yang¹, Ludwig Combrinck², Alet de Witt², Marisa Nickola², Elena Skurikhina³, Andrey Mikhailov³

(1) Department of Space, Earth and Environment, Chalmers University of Technology, Gothenburg, Sweden

(2) Hartebeesthoek Radio Astronomy Observatory, Krugersdorp, South Africa

(3) Institute of Applied Astronomy of the Russian Academy of Sciences, St. Petersburg, Russia

* Contact: rudiger.haas@chalmers.se

Abstract—The International Terrestrial Reference Frame (ITRF) is constructed based on analysis results of several space geodetic techniques, among them geodetic Very Long Baseline Interferometry (VLBI) and Global Navigation Satellite Systems (GNSS). The meaningful combination of the different techniques requires possibilities to link the various instruments and their reference points. So-called co-location stations that are equipped with instrumentation for several techniques play an important role for the ITRF combination since so-called local-tie vectors on the ground enable the connection between the various instruments. Since several years, ideas have been discussed to include additional possibilities to link the different techniques, with the main goal to improve the ITRF. One of these ideas is to use GNSS signals for VLBI observations and by this improve the link between VLBI and GNSS. In our presentations we describe so-called GNSS-VLBI experiments performed in 2017 with VLBI stations at intercontinental distances. The observations, data correlation and data analysis is described and initial results are presented.

Keywords—VLBI, GNSS, ITRF, co-location

1. The idea of co-location in space

During the last years, society has realised the necessity of an accurate global terrestrial reference frame [1], such as the International Terrestrial Reference Frame (ITRF) [2]. However, it has been questioned whether the current global terrestrial reference frame is accurate enough to study global change processes such as sea level rise [3]. This refers in particular to the quality of the so-called local ties at co-location stations that are often criticized to be insufficient [4], [5]. Thus, since several years the idea of Very Long Baseline Interferometry (VLBI) observations using signals of Global Navigation Satellite System (GNSS) satellites is discussed as a potential approach to improve the accuracy of the International Terrestrial Reference Frame (ITRF), see e.g. [6]. The expectation is that such observations could improve the link between the two space geodetic techniques GNSS and VLBI. The techniques are traditionally linked at co-location ground stations where so-called local-tie vectors are measured. However, adding further possibilities to link the techniques, could improve the accuracy of the ITRF.

2. GNSS-VLBI experiments in 2017

During 2017 we performed a series of GNSS-VLBI experiments involving the VLBI stations Onsala (Sweden),

Hartebeesthoek (South Africa), and Zelenchukskaya (Russia). Previously such kind of observations were primarily done in regional networks in Europe and Australia. The series of sessions in 2017 was the first one with intercontinental baselines. The observations are part of a pilot project of the European Space Agency (ESA) within their Alcantara programme and aim at achieving synergies between VLBI and GNSS. Figure 1 depicts spectra observed locally at Onsala during one of the sessions.

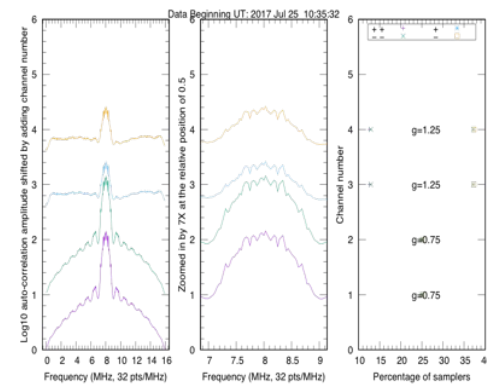


Figure 1: Example of the spectrum of a GPS satellite observed at Onsala.

3. Data correlation and analysis

Data were successfully collected for several sessions, correlated and post-processed, and analyzed with a geodetic VLBI data analysis software. The software correlator DiFX [7] was used for correlation, the post-correlation processing with Fourfit [8], and the geodetic analysis was done with the C5++ software [9]. Figure 2 depicts a so-called fringe plot, i.e. the interferometric observation of a GNSS signal on a baseline between two VLBI stations.

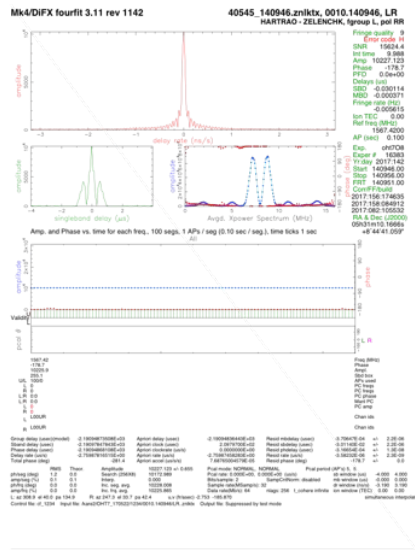


Figure 2: Example of a fringe plot from the observation of a Galileo satellite on the baseline HarTRAO-Zelenchukskaya.

4. Preliminary results

The resulting data bases with observed interferometric delays were analysed with C5++ [9] and a set of geodetic parameters were estimated. Figure 3 depicts as an example the resulting residuals for one of the sessions. The RMS of the residuals is below 10 centimetres.

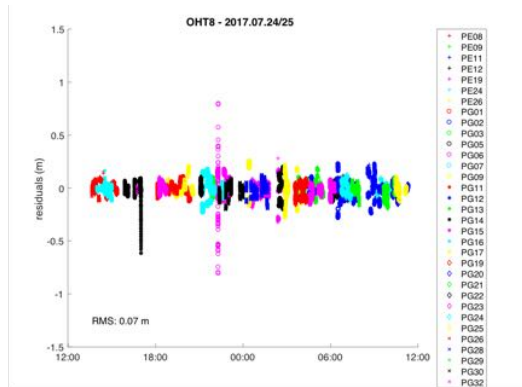


Figure 3: Post-fit residuals after a geodetic analysis of the OHT8 session.

5. Outlook

The GNSS-VLBI experiments performed during 2017 show that the concept is feasible. We successfully performed the complete chain, from experiment planning, over observing, data correlation, and finally geodetic data analysis. The postfit residuals from the geodetic analysis are below a decimeter. These results are encouraging for further experiments with larger networks including more stations.

References

- [1] United Nations General Assembly (2015) UN General Assembly resolution: A global geodetic reference frame for sustainable development. http://www.un.org/ga/search/view_doc.asp?symbol=A/69/L.53
- [2] Altamimi Z, Rebischung P, Métivier L, Xavier C (2016) ITRF2014: A new release of the International Terrestrial Reference Frame modeling nonlinear station motions. *J. Geophys. Res. Solid Earth*, 121, 6109–6131, doi:10.1002/2016JB013098
- [3] Blewitt G, Altamimi Z, Davis J, Gross R, Kuo C Y, Lemoine F G, Moore A W, Neilan R E, Plag H-P, Rothacher M, Shum C K, Sideris M, Schöne T, Tregoning P, Zerbini S (2010) Geodetic Observations and Global Reference Frame Contributions to Understanding Sea-Level Rise and Variability. In: J. A. Church, P. L. Woodworth, T. Aarup, W. S. Wilson (eds.), *Understanding Sea-Level Rise and Variability*, 1st edition, Blackwell Publishing Ltd., 256–284, doi:10.1002/9781444323276.ch9
- [4] Altamimi Z, Collilieux X, Métivier L (2011) ITRF2008: an improved solution of the international terrestrial reference frame. *J Geod*, 85(8), 457–473
- [5] Seitz M, Angermann D, Bloßfeld M, Drewes H, Gerstl M (2012) The 2008 DGF realization of the ITRS: DTRF2008. *J Geod*, 86(12), 1097–1123.
- [6] Plank L, Böhm J, Schuh H (2014) Precise station positions from VLBI observations to satellites: a simulation study. *J Geod* 88(7):659–673, doi:10.1007/s00190-014-0712-1
- [7] Deller, A.T. & Briskin, W.F. & Phillips, C.J. & Morgan, J & Alef, W & Cappallo, R & Middelberg, E & Romney, J & Rottmann, Helge & Tingay, Steven & Wayth, R. (2011). *DIFX-2: A More Flexible, Efficient, Robust, and Powerful Software Correlator*. Publications of The Astronomical Society of The Pacific - PUBL ASTRON SOC PAC. 123. 275-287. 10.1086/658907.
- [8] Fourfit, <https://www.haystack.mit.edu/tech/vlbi/hops.html>
- [9] Hobiger, Thomas & Gotoh, Tadaihiro & Otsubo, Toshimichi & Kubooka, Toshihiro & Sekido, Mamoru & Takiguchi, Hiroshi & Takeuchi, Hiroshi. (2010). *c5++ - Multi-technique Analysis Software for Next Generation Geodetic Instruments*. 212-216.

EUREF and the infrastructure for high performance GNSS applications in Europe

Martin Lidberg^{1*}, Carine Bruyninx², Ambrus Kenyeres³, Markku Poutanen⁴, Wolfgang Söhne⁵

(1) Lantmäteriet, Sweden

(2) Royal Observatory, Belgium

(3) BFKH FTFF Satellite Observatory, Hungary

(4) Finnish Geospatial Research Institute, Finland

(5) Bundesamt für Kartographie und Geodäsie, Germany

*Contact: martin.lidberg@lm.se

Abstract

Precise applications of GNSS rely on well-defined geodetic reference frames, satellite orbit and clock information, and the infrastructure of continuously operating GNSS reference stations (CORS). For almost three decades, EUREF has served Europe with geodetic reference frames, and since more than two decades, the EUREF Permanent Network, EPN, forms a robust infrastructure including CORS and mature products and services.

EUREF, as the IAG (International Association of Geodesy) Regional Reference Frame Sub-Commission for Europe, is responsible for the maintenance and the development of the European Terrestrial Reference System 89 (ETRS89). This is the standard precise GNSS reference system throughout Europe, supported by EuroGeographics and endorsed by the INSPIRE Directive 2007/2/EC. It forms the backbone for geolocation data on the European territory, both for national as well cross border applications (<http://www.euref.eu>).

The EUREF Permanent Network (EPN) is a science-driven network of permanent GNSS tracking stations (<http://epncb.oma.be/>). Through its daily and weekly computed network solutions it is used by EUREF to realize and provide access to the ETRS89. The EPN includes:

- a network of about 300 continuously operating GNSS (Global Navigation Satellite Systems, such as GPS, GLONASS, Galileo, Beidou, ...) reference stations,
- data centres providing access to the station data,
- analysis centres that routinely analyze the GNSS data,
- product centres and coordinators that generate the EPN products,
- and a Central Bureau that is responsible for the daily monitoring and management of the EPN.



The EUREF Permanent Network, EPN.

The EPN provides access to the ETRS89 by making publicly available the GNSS tracking data as well as precise positions, velocities and tropospheric parameters of all EPN stations. Based on these products, the EPN contributes also to monitoring of crustal deformations in Europe, and supports long-term climate monitoring, numerical weather prediction and the monitoring of sea-level variations.

The EPN tracking stations are also integrated in the successive realizations of the International Terrestrial Reference System, which is the basis for the European Terrestrial Reference System. Since the EPN is the European densification of the network of the International GNSS service, IGS (<http://igscb.jpl.nasa.gov/>), a complete harmonization of standards between the global and European network is put forward.

All contributions to the EPN are provided on a voluntary “best effort” basis, with more than 100 European agencies/universities involved. The EPN operates under well-defined standards and guidelines which guarantee the long-term quality of the EPN products.

In the presentation, we will stress the importance of the basic infrastructure for GNSS and describe the operational procedures, products and services of EUREF and EPN.

AstaZero – Active Safety and Automated Driving Proving Ground

Monica Ringvik (AstaZero AB)

Abstract:

AstaZero is a leading testbed for the automated transportation system of the future. Located in Sweden with its heritage within vehicle active safety and with an ownership consisting of an institute, RISE and a university, Chalmers, AstaZero is uniquely positioned to take an active role in the transformation of society. The testbed provides unique capabilities needed in research, development and validation of self-driving and connected vehicles as well as the surrounding infrastructure. Positioning is of central importance for the testbed when controlling and supervising the increasing number of objects in test scenarios with growing complexity due to higher demands from active safety systems and automated vehicles.

H2020 PRoPART project presentation – Precise and Robust Positioning for Automated Road Transports

Stefan Nord (RISE Research Institutes of Sweden)

Abstract:

Autonomous vehicles and advanced driver assistance systems contribute towards “Vision Zero”, i.e. a future where no humans are killed or impaired by accidents. Predictions indicate that these technologies will also contribute to reduced traffic density through increased road efficiency and will create new business models for mobility. It has already been proven to reduce both the number and extent of injuries and insurance costs. Precise and robust positioning is a required key technology in both advanced driver assistance systems and connected autonomous vehicle applications. The main idea behind the PRoPART project is to develop and enhance an RTK (Real Time Kinematic) software solution by both exploiting the distinguished features of Galileo signals as well as combining it with other positioning and sensor technologies.

GNSS for automation of heavy vehicles – challenges and opportunities

Jimmy Hammenstedt (AB Volvo – Vehicle Automation)

Abstract:

To solve the sub-decimeter positioning needs for the autonomous vehicles, different solutions are currently being evaluated, many of these involves the refinement of the accuracy of GNSS. Techniques like N-RTK and PPP are standing out as promising candidates for reliable, robust and accurate positioning. GNSS, however, comes with its own set of challenges that will have to be mitigated for its use in the autonomous vehicle. Combinations of sensors or adaptation of current infrastructure could be possible solutions.

Efficient distribution of GNSS correction data via cellular networks, ongoing work in 3GPP

Fredrik Gunnarsson (Ericsson Research)

Abstract:

GNSS has enabled a vast number of applications by providing reasonably accurate positioning. Moreover, more strict accuracy requirements have also been catered for by correction data systems, based on observations at terrestrial stations with accurately known positions and antenna configurations. With fairly advanced GNSS devices, and frequent correction data updates, it is possible to reach accuracies well within one centimeter, meeting requirements from various professional services such as land survey, construction support, automated farming, etc. The interest in such corrections is increasing, not the least due to autonomous vehicles, but also due to the advanced receivers becoming affordable. Therefore, it is important to enable an efficient provisioning of the correction data in an interoperable manner. In 3GPP Rel. 15 to be finalized 2018, there is ongoing work to design such correction data distribution means.

High accuracy GNSS for autonomous platforms

James Tidd (Waysure)

Abstract:

Autonomous robots are becoming a part of everyday life, with vacuum cleaners and lawn mowers taking care of repetitive tasks without the need for human intervention...most of the time. In industry, autonomous robots have been around for a long time. For example, complete mines can operate with only remote observation from a control centre required. This technology is making its way into more complex environments; the most talked about being Advanced Driver Assistance Systems. One of the key requirements for these applications to perform safely and efficiently is accurate positioning. Global Navigation Satellite Systems (GNSS) offer an inexpensive and highly accurate method for estimating position. In combination with other sensors and accurate detailed map data, GNSS enables autonomous platforms to perceive the world around them. With reliable perception, the platform can more safely and efficiently execute its mission.

Location system performance requirements in the T-pod, a level 4 self-driving vehicle

Thomas Ohlson (Einride)

Abstract:

Einride is installing a sustainable transport system for the future. A key technology component of the system is the T-pod. A battery electric autonomous transport vehicle.

The T-pod and its level four self driving capabilities put specific requirements on the localization subsystems. There need to be a guaranteed uptime, a minimum level of availability and a sufficiently high localization precision. The talk will discuss these requirements based on the vehicle performance requirements they stem from. Possible solutions for fulfilling these will also be covered.

The Resilience of Maritime Navigation and Positioning

Dr. Paul Williams, Mr. Chris Hargreaves, Dr. Alan Grant, Mr. Martin Bransby and Dr. Nick Ward

Research and Radionavigation Directorate, The General Lighthouse Authorities of the United Kingdom and Ireland

Today's mariner is about to witness two major maritime technological advances; autonomous or remotely piloted vessels, and e-Navigation. Both concepts are intended to increase safety, productivity, efficiency and convenience for the mariner and the entire supply chain.

The IMO's e-Navigation concept has been slow in coming, but is progressing, with projects, testbeds and demonstrations taking place in Europe and in Asia. Autonomous ship technology is also progressing with major household names, such as Google and Rolls-Royce involved. These developments are taking place in a modern world that, in recent times, has seen the rise of security risks, both physical and cyber related.

At the same time maritime navigation across the globe has adopted Global Navigation Satellite Systems (GNSS) as the primary source of electronic position fixing. The world has abundant electronic navigation systems, from the Global Positioning System (GPS), to GLONASS and others. GNSS continue to improve and grow in number, but these upgrades will provide marginal increases in robustness and reliability for those equipped to access the systems. Moreover, satellites alone are unable to provide IMO's "...robust, reliable and dependable" signals, first called for, for safety of navigation and other safety of life applications. The resilience of Position, Navigation and Timing information provided by GNSS afloat can no longer be taken for granted.

All GNSS transmit very faint signals in the same general frequency band. These can easily be disrupted by natural phenomena, malicious actors and even system failures. Successful implementation of autonomous/remotely operated vessels and/or eNavigation will require that this fundamental shortfall be addressed. GNSS must be paired with another source, or sources, such that the combined systems are virtually impossible to disrupt.

This paper outlines some of the work performed by the GLAs, and others, on the subject of Resilient PNT.



Sea Traffic Management enhancing safety of navigation:

Increase safety of navigation by using a standardizes way of exchanging route information between ships and between ship and shore.

Mikael Hägg (Research Institute of Sweden, RISE), Ulf Siwe (Swedish Maritime Administration), Fredrik Karlsson (Swedish Maritime Administration), Andreas Andersson (Swedish Maritime Administration)

In safe navigation two means of positioning should be used continuously. The frequency is set by the operating conditions like area of navigation, ship's size and speed, and environmental conditions. With the introduction of GNSS and electronic charts, positions are now automatically plotted directly on the chart with a high frequency. Hence, navigation has moved from monitoring the ship's position to monitoring the ship's route. This means that route information is one of the most essential types of navigation information.

In the EU projects MONALISA, MONALISA 2.0 and Sea Traffic Management Validation Project, the Sea Traffic Management (STM) concept has been defined, demonstrated and validated. One of the corner stones in the STM concept is the exchange of route information, between ship-to-ship, and ship-to-shore. It is important that exchange formats are open and aligned with international standards. In the STM concept, route information is exchanged according to two modes of operations:

- Ship-to-ship using a new AIS ASM route message, and
- Ship-to-shore using RTZ format specified in IEC 61174 (ECDIS - Operational and performance requirement, methods of testing and required test results).

Ship-to-ship route exchange

Ships participating in the STM test beds can exchange routes, both sending and receiving route segments ship-to-ship. The route segment is send by using AIS ASM and displayed at adjacent ship's navigation display, if equipped with STM compatible equipment. This information is used to increase situational awareness in traffic situation and the information should be used in the ship's strategic navigation e.g. to avoid traffic congestions.

Ship-to-shore route exchange

The STM concept provides improved situational awareness through enhanced navigation information by route exchange ship-to-shore and which opens up new possibilities for assistance of ships en-route. Examples of enhanced operational services are:

- Navigational warnings along the route;
- Enhanced monitoring and shore-based navigation assistance;
- Pilot routes; and
- Dynamic ice routes.

A large part of the basic bathymetric data in the Baltic Sea comes from measurements performed in the MONALISA and FAMOS projects. New data helps to improve not only the hydrographic charts but also the operational services like the monitoring and navigation assistance. The improved bathymetric accuracy in the measurements could allow ships to take more cargo and still meet the safety margins. New services and solutions could be built on the hydrographic data e.g back-up and cross reference navigation based on sonar and the depth database; and Under Keel Clearance routing taking into account temporal sea levels and squat effects.



Acknowledgements

The MONALISA, MONALISA 2.0, FAMOS, and the STM Validation Project are co-funded by the EU in the TEN-T/CEF program. Further, RISE has received co-funding from by Swedish public funding for research, development, innovation and demonstration activities in the maritime transport sector and by the Region Västra Götaland.

Key words: Sea Traffic Management, STM, marine navigation

Study on Code Multipath Mitigation Technology for BDS-3 B2a Signal

Yaoding Wang, Wenxiang Liu, Jingyuan Li, Feixue Wang

College of Electronic Science, National University of Defense Technology
Changsha, Hunan, China

Email: wangfeixue365@sina.com

Abstract—The construction and development of BDS is divided into three phases: BDS-1, BDS-2, and BDS-3 in sequence. In December 2017, China Satellite Navigation Office published the open service signal B2a transmitted from the BDS space segment to the BDS user segment. The B2a signal is transmitted by the Medium Earth Orbit (MEO) satellites and the Inclined Geosynchronous Satellite Orbit (IGSO) satellites of BDS-3, and provides open services. When the signal is transmitted to the ground, it can be reflected or scattered into the receiver through the ground object. This phenomenon is called multipath. The multipath signal will be attached to the direct signal, and that causes the autocorrelation function to be distorted which causes the error of measuring at the end. This paper introduces the characteristics of B2a signal briefly at first, and then analyzes the Narrow Correlator Spacing Technique, the Early/Late Slope Technique (ELS), the Double-Delta Correlator Technique, and the Code Correlation Reference Waveform Technique (CCRW) for B2a signal. The simulation results show that the W4 waveform of CCRW is the best for the multipath mitigation for B2a signal, and the multipath error envelope is reduced by 67.31% compared with the Narrow Correlator Technique with the infinite bandwidth.

Keywords—BDS-3; B2a Signal; Multipath Mitigation; Multipath Error Envelope; CCRW

Full paper in IEEE Xplore

Characterization of Range and Time Performance of Indoor GNSS Signals

Thyagaraja Marathe, Ali Broumandan, Ali Pirsiavash, Gérard Lachapelle

PLAN Group

Department of Geomatics Engineering

Schulich School of Engineering

University of Calgary, Canada

Abstract—Small cells are now widely used to provide indoor wireless services and are gaining further importance as technology enablers for emerging applications. These techniques rely on accurate synchronization of signals broadcast from neighboring base stations. Therefore, the latter must have access to reliable and accurate time reference. GNSS signals can be used to provide a reliable global time reference in open sky conditions. However, owing to low levels of signals indoors, the detection and processing of these signals and obtaining an accurate time indoors are still a challenge. It is assumed that accurate position estimates are known for indoor static applications which are obtained either using GNSS or other indoor positioning technologies. Under this assumption, fine timing solution can be provided with reliable single satellite information. As such this paper characterizes GPS based measurement and timing accuracies for indoor signals.

This study specifically focuses on assessing range and timing accuracies for static indoor locations. Actual GPS data was collected at two indoor sites having different indoor characteristics for duration of more than ten minutes at each site. Assuming a known user position, measurement accuracies are analyzed over time while simultaneously observing received signal power. Ranging (timing) accuracy in the order of 10 m (30 ns) was achievable for the indoor scenarios considered. Finally, to assess the capability of indoor measurements to sustain good time synchronization accuracy over a longer duration, two-minute data segments were collected at intervals of 30 minutes for three hours. The time variations of the pseudorange (time) and position errors are studied.

Keywords—GNSS; Weak signal; Range; Time; synchronization

Full paper in IEEE Xplore

Isolation of the Effect of Snow and Ice to a GNSS Antenna in the Measurement Domain

Younghoon Han, Tae Hyun Fang, Don Kim⁺

Marine Safety and Environmental Research Department, Korea Research Institute of Ship & Ocean Engineering, Daejeon, South Korea, yghan@kriso.re.kr

Korea Research Institute of Ships and Ocean Engineering (KRISO) has been working on underwater positioning and navigation based on acoustic sensor technology for Remotely-Operated Vehicle (ROV) or Autonomous Unmanned vehicle (AUV). Recently, the use of AUV in the polar region is being studied due to the increased interest of global climate change and natural resources. AUV technology enables us to explore some places with limited accessibility because of an extreme condition. The most of AUVs in the polar region have a mission for exploring the underwater of ice. Position information is important for setting waypoints of AUV.

Long baseline (LBL) acoustic positioning system is one of AUV's underwater positioning techniques. It can estimate AUV's positions by measuring the distance of multiple transponders of baseline stations. Precise positions of baseline transponders can improve the accuracy of underwater AUVs. Generally, GNSS is used to establish the precise position of each baseline transponder.

However, precise positioning using GNSS in the polar region faces to some challenges such as strong ionosphere activity, low visibility of GNSS satellite, snow and ice loading effects and strong wind. Extremely low temperature is also one of the serious challenges. As a GNSS antenna should be installed outside to receive satellite signal, the antenna can be covered with snow and ice.

This phenomenon can affect GNSS performance to some degree. One previous study modelled the refraction effect of snow and ice to the GNSS antenna as a signal time delay. Another research analyzed the effect of snow and ice loading to geoscience monitoring system and modelled the effect of rime ice on a GNSS antenna.

Isolation of the effect of snow and ice covered on a GNSS antenna in the measurement domain could provide us with some useful analysis tools. Therefore, in this paper we analyzed the effect of snow and ice to a GNSS antenna in the raw measurements of a GNSS receiver. We tried to isolate the effect of snow and ice from other error sources in the GNSS measurements, including hardware delay, receiver clock error, multipath, thermal noise and so on. We used two GNSS antennas - one with ice and another without ice - and two receivers, respectively. Conventional single difference technique between two receivers was carried out. To eliminate receiver clock errors, a common cesium clock was used. Hardware delay from the antenna to each receiver was calibrated using zero baseline test of each antenna. Icing the GNSS antenna was carried out in a cold room of the ice basin facility at KRISO under -25 Celsius degrees.

In this paper, we present the following test results as: First, signal power distortion due to the ice on the GNSS antenna. We compare signal-to-noise ratio (SNR) values between the ice-covered antenna and clean antenna. Second, the effect of ice in the measurement domain. These results are processed according to previously described isolation method and compare between an ice-covered condition and a normal condition. Finally, precise Real-Time Kinematic (RTK) positioning is performed.

Inverse modeling of reflected GNSS signals for measurement of the environment

Joakim Strandberg, Thomas Hobiger, Rüdiger Haas

Department of Space, Earth and Environment, Chalmers University of Technology, Gothenburg, Sweden,
joakim.strandberg@chalmers.se

Summary

We have developed and tested a new method for measuring the surroundings of a GNSS receiver using inverse modeling of reflected GNSS signals. The method can inherently use measurements from all GNSS satellites, regardless of the system and frequency, and it is shown that the addition of several systems is beneficial for the accuracy of the retrievals.

Motivation

In traditional GNSS applications, multipath is to be avoided at all costs, or at least, its effect should be mitigated as much as possible. However, to paraphrase an old adage 'one man's noise is another man's signal'. This is certainly true for multipath signals in GNSS which have spawned the field of ground based GNSS reflectometry (GNSS-R). The field thrives on the existing GNSS infrastructure; around the world there is a multitude of permanent GNSS stations operating continuously, collecting the signal-to-noise ratio (SNR) data that can be used for GNSS-R. Various applications have been conceived for ground based GNSS-R, such as measuring soil moisture, snow depth, sea level, and vegetation, depending on the antenna location. Thus with the widespread networks of permanent GNSS stations, GNSS-R can provide climatologists and hydrologists with measurements from all around the globe.

Traditionally, ground based GNSS-R utilizes spectral methods to derive information from the oscillating behavior of the SNR due to multipath interference. However, in using only the frequency of the oscillations these methods discard other information contained in the shape of the time series of SNR. Therefore we use a more detailed physical model to inverse model the SNR series and retrieve more of the information. In addition to the oscillation frequency, which depends on the height between the reflecting surface and the antenna, the model contains factors accounting for the varying signal strength, the phase of the oscillations, and the damping that the oscillations exhibit with increasing satellite elevations due to scattering on rough surfaces. Our implementation also use B-splines to represent fluctuating reflector heights, such as in the case of sea level measurements, creating a smooth representation of the reflector height, shown in Fig. 1. With the use of a continuous height function we can combine SNR from different GNSS in one single, coherent inversion process.

Results

By testing the inverse modeling approach on data from the GTGU GNSS-R installation at Onsala Space Observatory, we have shown that the method increases the precision of sea level retrievals compared to earlier methods, and conversely of snow height measurements, and that it also can be used to measure new properties that have not been detected by GNSS-R previously. We also show that the inherent capability of the inverse modeling approach of combining data from multiple GNSS at the observation level is beneficial to the stability and accuracy of the retrieved solutions (Fig. 2). The method can also simultaneously monitor properties such as snow height and vegetation without any modifications, as shown in Fig. 3.

References

Strandberg, J., T. Hobiger, and R. Haas (2016), *Improving GNSS-R sea level determination through inverse modeling of SNR data*, *Radio Science*, 51, 1286–1296

Strandberg, J., T. Hobiger, and R. Haas (2017), *Coastal sea ice detection using ground-based GNSS-R*, *IEEE: Geoscience and Remote Sensing Letters*, 14(9), 1552–1556

Figures

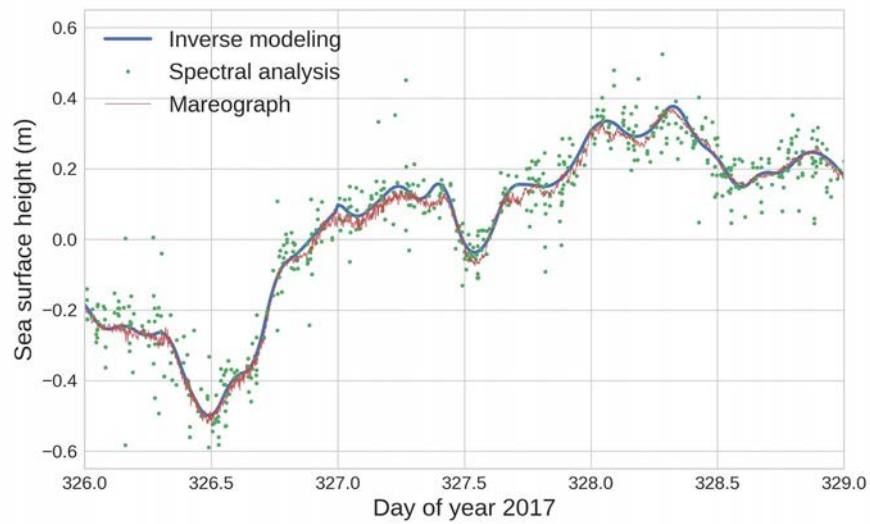


Fig. 1: Time series of sea surface height measurements from the tide gauge at Onsala Space Observatory as well as sea surface height derived from GNSS reflectometry using spectral analysis and inverse modeling.

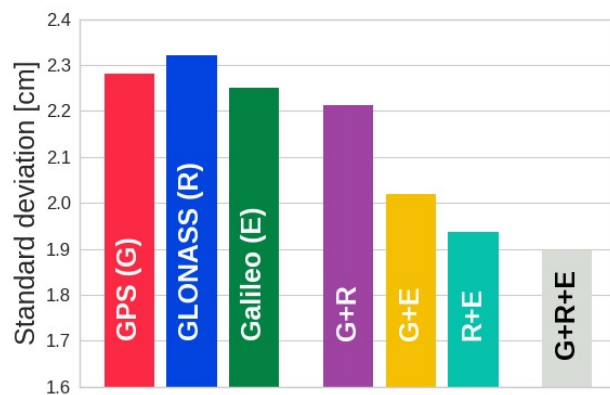


Fig. 2: Comparison of standard deviation between the tide gauge and GNSS reflectometry using different combinations of satellite systems. Adding more data improves the GNSS-R retrieval.

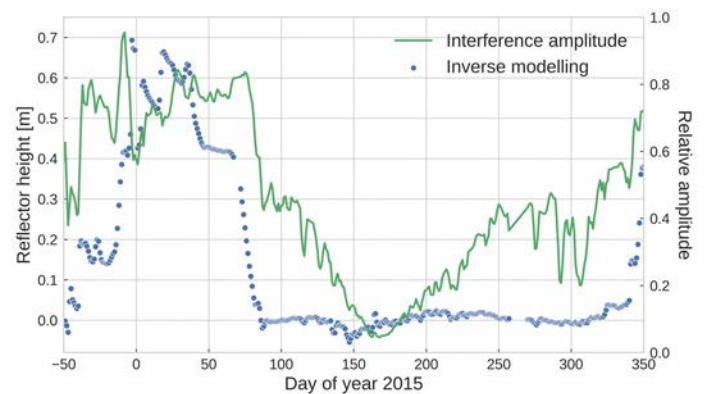


Fig. 3: Snow level derived from GNSS-R and amplitude of the SNR oscillations. During bare ground season, the latter correlates negatively with the growth cycle of the vegetation in the vicinity of the antenna.

Analysis of receiver performance using GNSS signal generation simulator in multipath, high maneuverability environment

Gwang Hee Jo, Jin Hyuk Lee, Jae Hee Noh,
Sang Jeong Lee⁺

Department of Electronic engineering
Chungnam National University
Daejeon, Republic of Korea

j_ghee@cnu.ac.kr, jh_lee@cnu.ac.kr, jhnoh3555@cnu.ac.kr,
eesjl@cnu.ac.kr

Jun O Kim

Department of Electronic engineering
Chungnam National University
Daejeon, Republic of Korea

Navigation Division
Agency for Defense Development,
Daejeon, Republic of Korea
hl5pue@hanmail.net

Abstract— In this paper, we investigate how the signal acquisition performance degrades due to multipath and how tracking error differs in tracking loop. Using a PC, Intermediate Frequency (IF) data, which is a satellite signal that does not contain noise, is generated and input to a Software Defined Receiver (SDR) based on MATLAB. Then, the signal output from the NI Vector Signal Generator (VSG) is received by NI Universal Software Radio Peripheral (NI USRP) and input to the same MATLAB-based SDR. The experimental case for analyzing signal acquisition and tracking performance is defined as the case where there is only one satellite signal and the case where there are four satellites capable of navigation. The data in both cases generates a signal that contains the effects of the multipath and only the direct signal. Multipath reflections are assumed to exist only in the reflection from the asphalt and the concrete, and the attenuation factor according to the surface type is applied. And in the high maneuverability environment, the Doppler frequency is included in consideration of the relative speed when there are four satellite signals, and the generated data is compared with the data of the stationary environment previously used.

Keywords—GPS; multipath; high maneuverability; tracking error; acquisition

I. INTRODUCTION

Multipath is a phenomenon that occurs when signals transmitted from satellites propagate through various paths with reflections and diffractions caused by ground or buildings. Since the path to reflection is longer than the direct path, multipath arrival is delayed relative to direct path. When multipath is involved, distortion occurs in the correlation function and affects code and carrier phase measurements. Since errors are generated in the pseudo range, the receiver position also includes errors. At this time the receiver will not cause a pseudorange error if the multipath delay is about 300 m [1]. However, if the multipath reflections occur near the receiver and the delay is small, it can distort the correlation function between the composite (direct plus multipath) signal

and the reference generated by the receiver [2]. Because it uses an incorrect correlation function to perform signal tracking, it affects pseudorange measurements and includes errors in the navigation results. This can be a significant source of error in applications that require precise location estimates or in limited conditions.

In a high maneuverability environment such as a missile, the Doppler frequency changes more than when it is stationary due to the relative speed of the receiver. In order to apply to high maneuverability environment, It is necessary to increase the bandwidth of the signal tracking part of the receiver [3]. However, we do not change the bandwidth because we will compare signal acquisition and tracking performance when the receiver structure or specification is the same.

In this paper, we investigate how the signal acquisition performance degrades due to multipath and how tracking error differs in tracking loop. Using a PC, Intermediate Frequency (IF) data, which is a satellite signal that does not contain noise, is generated and input to a Software Defined Receiver (SDR) based on MATLAB. Then, the signal output from the NI Vector Signal Generator (VSG) is received by NI Universal Software Radio Peripheral (NI USRP) and input to the same MATLAB-based SDR. The experimental case for analyzing signal acquisition and tracking performance is defined as the case where there is only one satellite signal and the case where there are four satellites capable of navigation. The data in both cases generates a signal that contains the effects of the multipath and only the direct signal. Multipath reflections are assumed to exist only in the reflection from the asphalt and the concrete, and the attenuation factor according to the surface type is applied. The multipaths of the satellite signals were set to move different paths, and the propagation delay reflected the path errors of direct signal and multipath signals. The correlation results were used to verify that the multipath effects were reflected. And we analyze the signals before and after multipath is reflected as histogram in time domain. In the high maneuverability environment, the Doppler frequency is

included in consideration of the relative speed when there are four satellite signals, and the generated data is compared with the data of the stationary environment previously used.

II. BACKGROUND

A. Multipath

Multipath is the reflected or diffracted signal of the desired signal. And it is delayed and attenuated than the direct signal and arrives at the receiver. The effects of these signals distort the composite phase, pseudorange, and carrier phase measurements of the received signal. As a result, errors in position, speed, and time are included. Errors caused by the multipath signal depend on the relative delay and power of these signals. The multipath model can be expressed in terms of delayed phase and attenuated amplitude rather than direct signal [1].

The multipath signal is represented as:

$$\sum_{i=0}^L a_i s(t - \tau_i) \quad (1)$$

Where, $s(t)$ is a direct signal, L is the number of reflected paths, and τ_i is the i th propagation delay.

The signal transmitted from the satellite is represented as:

$$s(t) = c(t)m(t)\sqrt{2P} \cos(2\pi f_{L1} + \phi) \quad (2)$$

Where $c(t)$ is the C / A code, $m(t)$ is the navigation data, P is the signal power, ϕ is the initial phase, and f_{L1} is L1 carrier 1575.42 MHz. The result of the distorted correlation function affected by multipath is shown in Fig. 1.

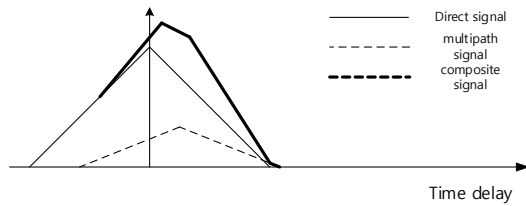


Fig. 1 correlation after constructive interference with reflected ray

B. High maneuverability

In the high - maneuverability environment, rapid dynamic characteristics can affect GPS satellite signal acquisition and tracking performance, which can deteriorate navigation performance. Therefore, unlike general terrestrial receivers, it has an RF receiver that can acquire and track wide bandwidth signals. The speed of a moving satellite in orbit must balance the gravity's pull and the inertia of the satellite's motion in which the satellite is constantly trying to move. This speed is approximately 27,359 km / h. The frequency shift due to the

relative motion of the satellite and the receiver can be represented as

$$\Delta f = \frac{\Delta v}{c} f_0 \quad (3)$$

Where, Δf is $f - f_0$, $\Delta v = v_r - v_s$ is the velocity of the receiver relative to the source.

III. SIMULATION SETUP

In this study, a binary file is generated from a C language based signal generator on a PC. This binary file contains the power, Doppler frequency, and time delay of the signal arriving at the receiver. Each satellite signal is generated independently, and the effect of multipath reflects the time delay along the path. And adds all of the satellite signals to generate data arriving at the receiver. The propagation attenuation is based on the attenuation factor according to the surface type. The reflected path is assumed to be reflected one by one on the ground and the building, and each attenuation factor is -18.3 (asphalt), -7.87 (concrete). The multipath signal generation structure is shown in Fig. 2. Table 1 shows the distance of multipath by PRN number used at this time.

Using the NI embedded controller, the NI AWG (Arbitrary Waveform Generator), a sub-module of the NI VSG, outputs the IF data generated by the PC to the IF signal. And then up-converted to the L1 band by mixing with the RF carrier. The RF signal is received by NI USRP and transmitted to the PC via Ethernet and stored as a binary file. Then thermal noise is included in the ideal data where only satellite signals exist. Input this data into the MATLAB-based SDR and compare it with the results of ideal data before thermal noise is included.

The high maneuverability environment should include the influence of the relative speed of the satellite and the receiver. The satellite moves about to Mach 20, but ballistic missiles can move at similar speeds. We assume relative velocity -Mach 5, Doppler frequency -8000 Hz, moving to Mach 15 in the same direction as the satellite.

Multipath assumes that the receiver is stationary. In the ideal case, we generate data with only one satellite signal and four satellite signals to compare signal acquisition and tracking performance. Then compare the performance when the four satellite signals are transmitted through the NI VSG and when the thermal noise is included with the ideal case. Ideal cases with four satellite signals have already been provided. Therefore, in the high maneuverability environment, only relative velocity is shown for -Mach 5 and compared with the ideal case. In the multipath environment, we analyze the histogram in the time domain.

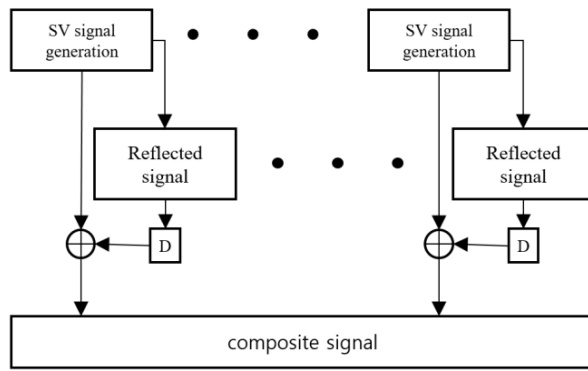


Fig. 2 multipath signal generation

TABLE 1 MULTIPATH DISTANCE

SV num	1st multipath [m] (asphalt)	2nd multipath [m] (concrete)
1	20	40
3	30	50
4	20	30
17	10	20

IV. RESULTS

A. Multipath

It is assumed that the receiver has received the direct signal and two multipaths of the PRN4 satellite signal. Verify that the effects of multipath are well covered first. Correlation function to confirm the full search results. Next, tracking performance and histogram are shown. In Fig. 3, the correlation value of the composite signal (direct plus multipath) is larger and distorted due to time-delayed signals.

In the ideal case, we compare the correlation and tracking performance with and without multipath effects when there is only one satellite. The signal acquisition results using the FFT method are shown in Fig. 4 and 5. When multipath was included, the peak was increased by about 2 dB and the peak position was delayed by 0.1 chip. As seen in Fig. 5, we can see that the effect of multipath is well included.

Comparing the direct signal with the composite signal in Fig. 6 and 7, the carrier tracking error is larger when multipath is included. In Fig. 8 and 9, the code tracking error generates a larger number of errors when there is a multipath rather than a direct signal.

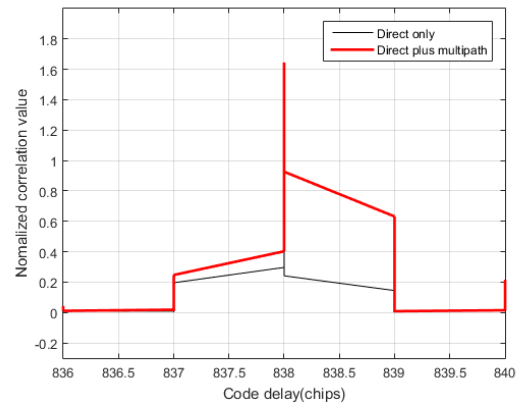


Fig. 3 autocorrelation function

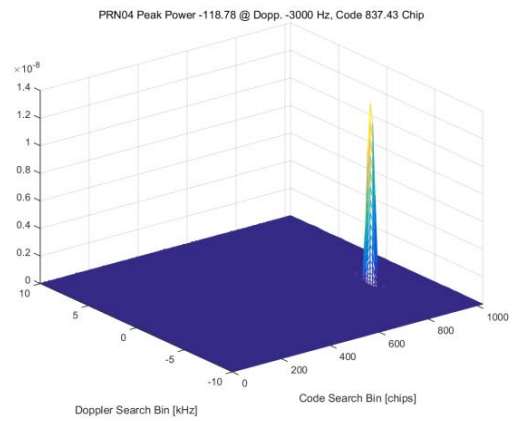


Fig. 4 acquisition (direct, 1SV)

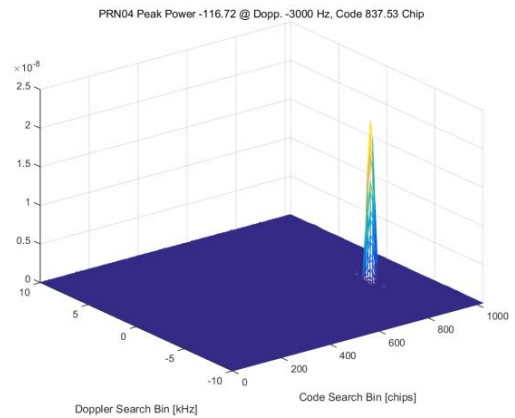


Fig. 5 acquisition (multipath, 1SV)

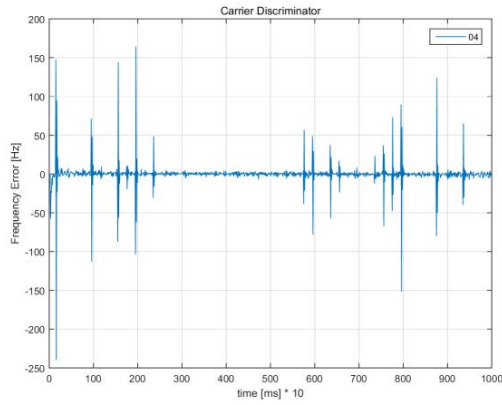


Fig. 6 carrier tracking error (direct, 1SV)

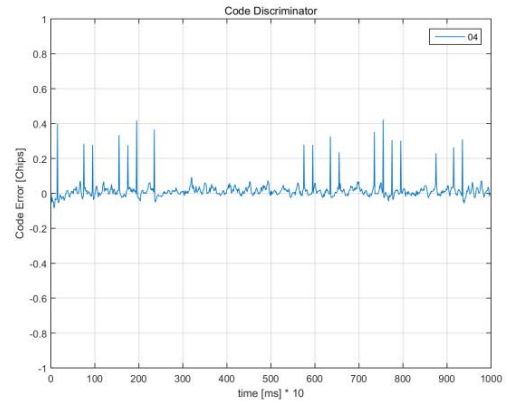


Fig. 9 code tracking error (multipath, 1SV)

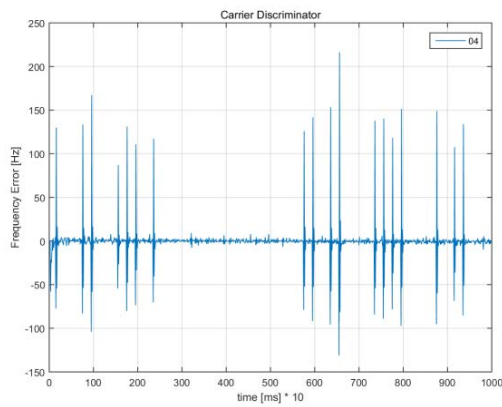


Fig. 7 carrier tracking error (multipath, 1SV)

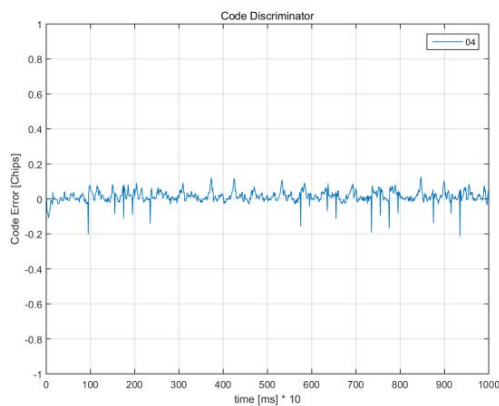


Fig. 8 code tracking error (direct, 1SV)

In Fig. 10. There is a correlation result of four satellite signals for which the multipath is not reflected. It shows the same code delay and peak power similar to when there is only one satellite signal. Other satellite signals have little effect on signal acquisition. In Fig. 11, the results of four satellites reflecting multipath are similar to those obtained when only one satellite signal is present. Peak increased by about 2 dB and was delayed by 0.1 chip.

Signals from Four satellites were transmitted by the NI VSG and received by the USRP. This result is shown in Fig. 12, and Fig. 10 shows a difference of about 18 dB in peak. This was done by using a DC block to remove the DC component of the transmitted signal from the equipment and adjusting the transmit power. And the Doppler frequency is 1250 Hz lower. The reason for the frequency offset is due to the frequency mismatch between transmitter and receiver oscillators. The difference in code delay is not considered because it is caused by the time delay that occurs during transmission and reception of the signal. In Fig. 13, the peak power of the signal including the multipath was lower than that before the thermal noise was included. The time delayed signal and noise cancel each other, the peak power is lowered and the correlation value of the other cells is relatively increased.

The carrier / code tracking error increased with the inclusion of thermal noise rather than the ideal data only. And comparing the direct signal with multipath, the frequency of large errors is high when multipath is included.

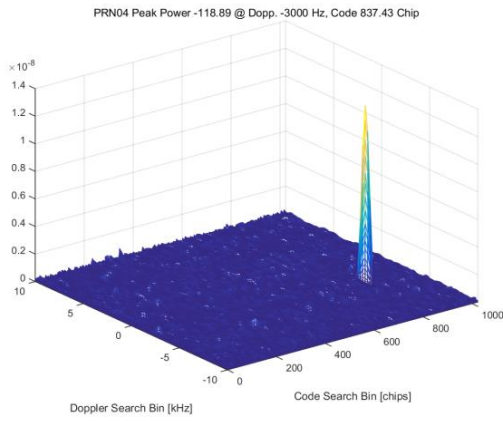


Fig. 10 acquisition (direct, 4SV)

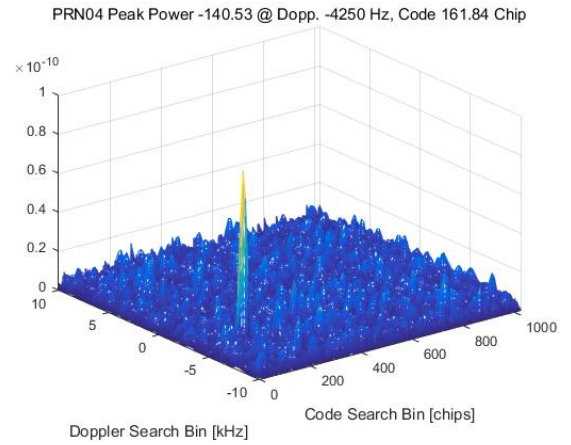


Fig. 13 acquisition including thermal noise (multipath, 4SV)

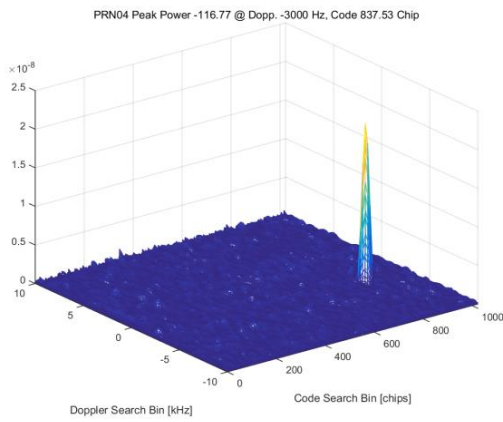


Fig. 11 acquisition (multipath, 4SV)

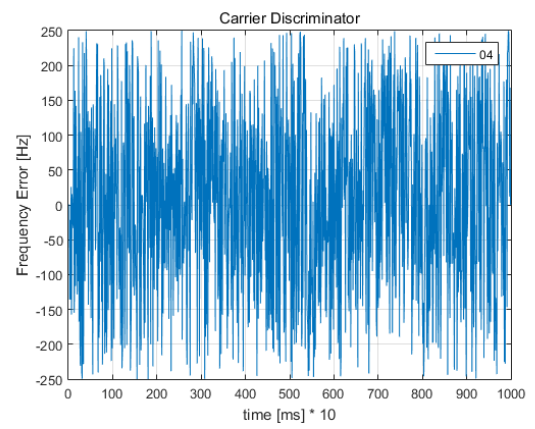


Fig. 14 carrier tracking error including thermal noise (direct, 4SV)

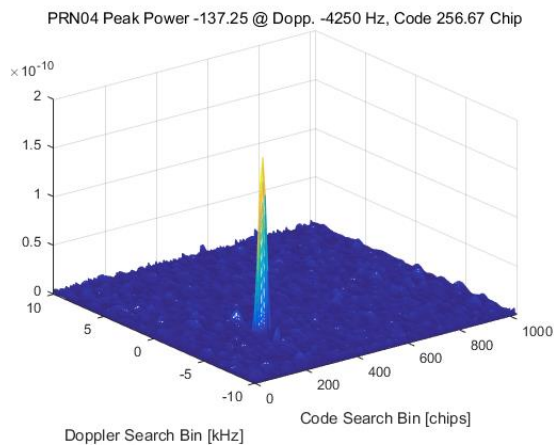


Fig. 12 acquisition including thermal noise (direct, 4SV)

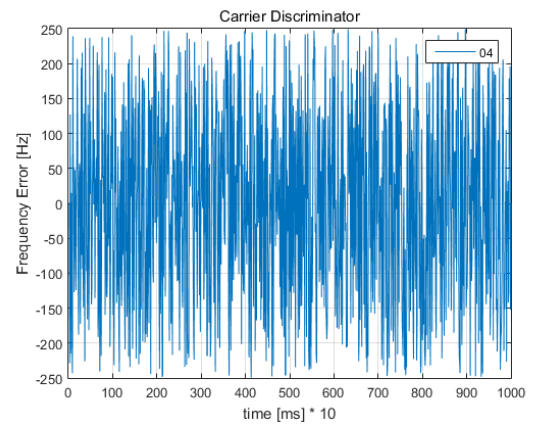


Fig. 15 carrier tracking error including thermal noise (multipath, 1SV)

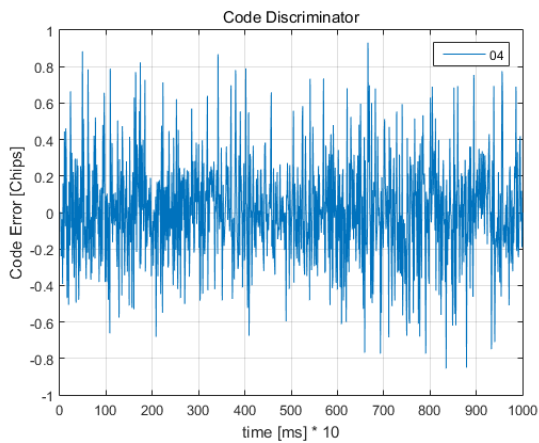


Fig. 16 code tracking error including thermal noise (direct, 4SV)

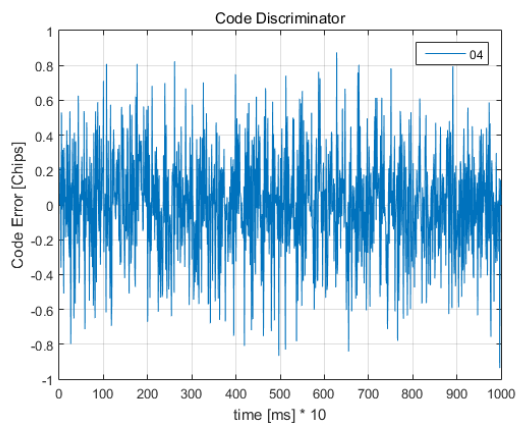


Fig. 17 code tracking error including thermal noise (multipath, 4SV)

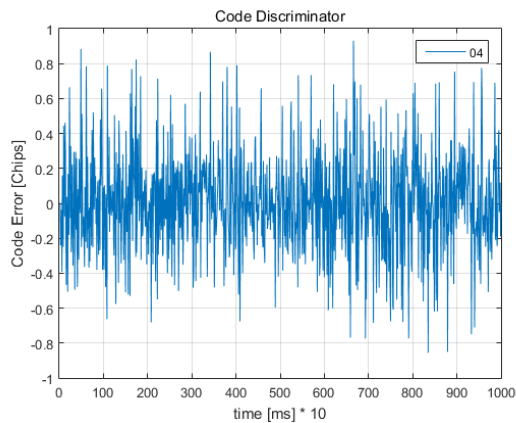


Fig 18 code tracking error including thermal noise (direct, 4SV)

Finally, the target to compare the direct signal with the multipath is the histogram. The histogram is a collection of data for 1 ms in the time domain. In Fig. 19 and 20, the left side of the histogram resembles the mirror image of the right side. The distribution of data is almost symmetric. Fig. 22 shows that the maximum value increases due to the multipath effect and the similar patterns are repeated on both sides. In Fig. 21, Four satellite signals with direct signal only show a pattern similar to a normal distribution, as opposed to only one satellite signal. The signal containing the influence of the multipath is a pattern in which the histogram of only one satellite is repeated. In other words, it looks similar to one that contains a satellite multipath. It is possible to acquire and track signals by showing a pattern of shapes similar to those of a satellite with only one direct signal.

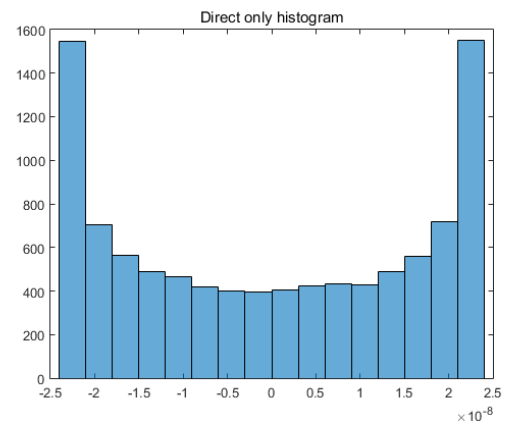


Fig. 19 histogram (direct, 1SV)

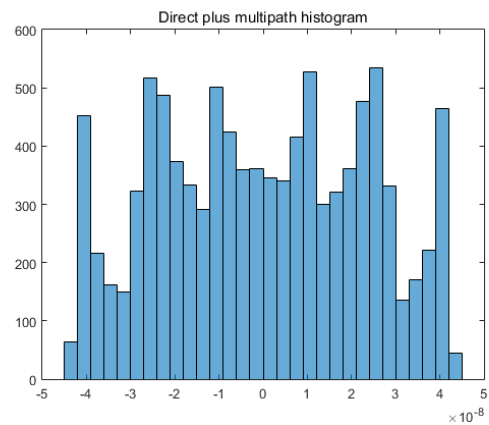


Fig. 20 histogram (multipath, 1SV)

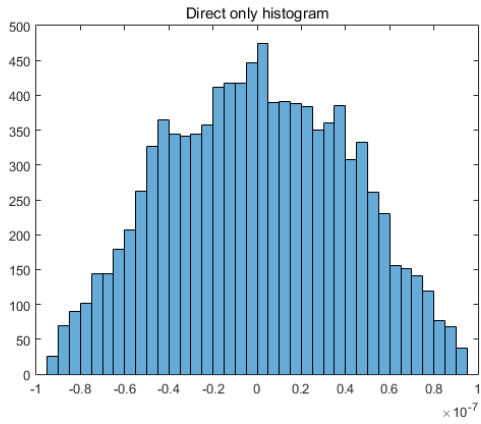


Fig. 21 histogram (direct, 4SV)

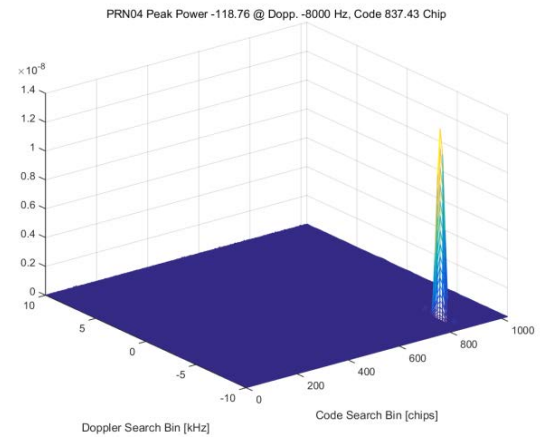
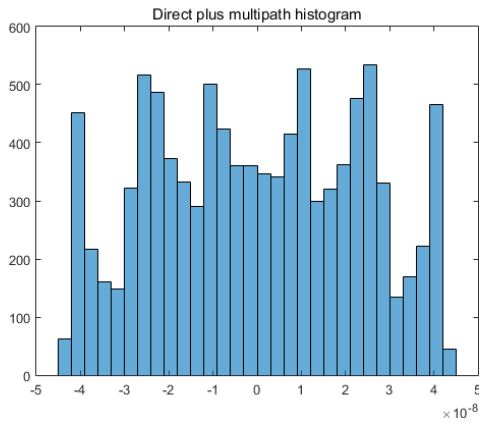
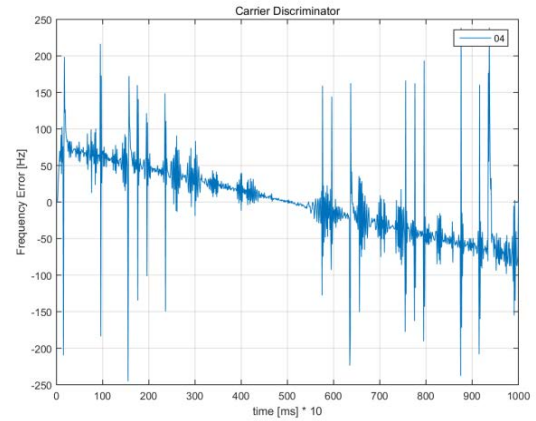
Fig. 23 acquisition
(high maneuverability, 4SV)

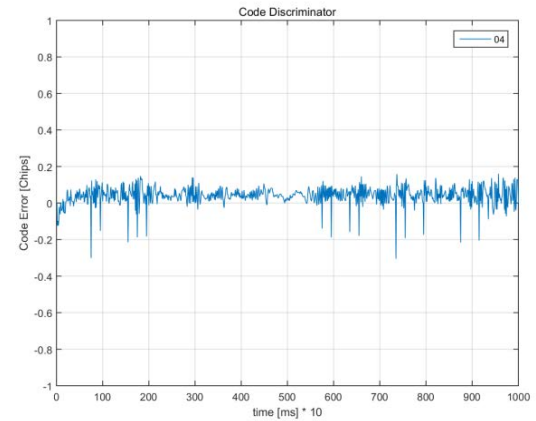
Fig. 22 histogram (multipath, 4SV)

Fig. 24 carrier tracking error
(high maneuverability, 4SV)

B. High maneuverability

In the high maneuverability environment, signal acquisition and tracking performance are confirmed when only the relative motion between the satellite and the receiver is considered. The Doppler frequency is -8000 Hz because it is said to travel at Mach 15 speed in the same direction as the satellite. The satellite signal contains four signals as in the case of multipath. In Fig. 23, the signal acquisition results, which are ideal and contain only direct signals, are similar to the peak magnitudes of a typical situation.

Carrier tracking errors, as seen in Fig. 24, are less frequent than in direct signal tracking in a typical environment. However, the frequency error tends to decrease linearly. In Fig. 25, the code tracking error is similar to that of multipath.

Fig. 25 code tracking error
(high maneuverability, 4SV)

V. CONCLUSIONS

When GPS receivers were navigating, we observed the effects of multipath and high maneuverability, which could cause errors. If multipath is included even though many satellite signals are received, there is no problem in signal acquisition because it has a symmetrical histogram similar to that of a single satellite signal. However, if the time delayed signal is included, the position of the peak is later than the ideal case. Also, the influence of the multipath signal is included, and the peak size increases and the correlation value is distorted. As a result, the code tracking error increases the frequency of large errors.

High maneuverability has no problem with signal acquisition, but carrier tracking error tends to decrease continuously, and code tracking error is similar to the general case.

REFERENCES

- [1] P. Misra, and P. Enge, "GLOBAL POSITIONING SYSTEM Signals, Measurements, and Performance", Ganga-Jamuna Press, pp. 175-177, 420-421, 2006
- [2] P. J. G. Teunissen, and O. Montenbruck, "Springer Handbook of Global Navigation Satellite System," Springer, pp. 444-445, 2017.
- [3] D.H. Shin, D.B. Park, S.B. Kwon and S.B. Son, "Lab and field test plan for anti-jamming performance evaluation of velocity-aiding technique", *Proc. KSASFallAM. Mlg.*, pp. 570-573, 2008.

SBAS Maritime Service: EGNOS preliminary performance based on IMO Res. A.1046 (27)

Pedro Pintor, Carlos de la Casa, Manuel Lopez⁺, Roberto Roldan
ESSP SAS, Madrid, Spain, pedro.pintor@essp-sas.eu
⁺GSA, Prague, Czech Republic

Summary

The European Geostationary Navigation Overlay Service (EGNOS) augments the open public service offered by GPS and makes GPS suitable for safety critical applications thanks to enhanced accuracy and integrity. As a Satellite-Based Augmentation System (SBAS), EGNOS offers three services (Open Service, Safety-of-life Service and EDAS). The EGNOS Safety-of-life (SoL) Service is intended for transport applications in different domains and currently is in use by Aviation.

This paper addresses two technical activities being executed by GSA and ESSP SAS to pave the way for the EGNOS maritime service based on IMO Res. A.1046 (27): **identify a list of performance parameters to completely characterize the SBAS maritime performance and assess the level of EGNOS performance attained for maritime.**

Motivation

Since 2014, the development of a new EGNOS service for maritime based on IMO Res. A.1046 (27) is under study with the contribution of the European Commission (EC), the European GNSS Agency (GSA), the EGNOS service provider (ESSP SAS) and the European Space Agency (ESA). This service can complement Differential GNSS (DGNSS) in poorly covered environments or where there is no infrastructure for the provision of enhanced accuracy and integrity. EGNOS functionality is supported by most of the maritime GNSS receivers used in both merchant and leisure market segments.

Results

The first activity is the identification and definition of a set of service performance parameters for a complete characterization of EGNOS maritime service. The service performance parameters list is derived from IMO Res. A.1046 (27) parameters and includes Signal Availability, Horizontal Accuracy 95%, Position update rate, Service Coverage for “Ocean Waters” and two additional parameters such as Service Continuity and Time To Alarm for “Harbour entrances, Harbour approaches and Coastal waters”. Additionally to IMO’s, ESSP SAS, GSA and EMRF¹ consider that a new parameter, Service Availability, is needed to characterize EGNOS maritime service, what is due to EGNOS particularities as radionavigation aid. This parameter indicates the percentage of time a position solution, calculated using EGNOS, is available in a specific location. The rationale behind the need of this parameter is explained in this paper following the recommendations in IALA Guidelines 1112 on performance assessment and monitoring of DGNSS services.

The second task is a preliminary performance assessment of the EGNOS service based on IMO Res. A.1046 (27) for a 21 months period from May 2016 to December 2017. The performance parameters listed and detailed in the first task are calculated using real GPS and EGNOS data to know what level of performance was attained by EGNOS. The assessment was done using both EGNOS Ranging and Integrity Monitoring Stations (RIMS) and fault-free techniques fed with actual data. The performance is shown for each parameter in the list and for “Ocean Waters” and “Harbour entrances, Harbour approaches and Coastal waters” operations (Fig.1, Fig.2 and Fig.3). The work also includes Service Coverage maps (Fig. 4) understood as a preliminary (but not final) and potential service area representing where EGNOS maritime service based on IMO Res. A.1046 (27) is adequate.

¹ European Maritime RadioNavigation Forum, <http://emrf.eu>

Figures

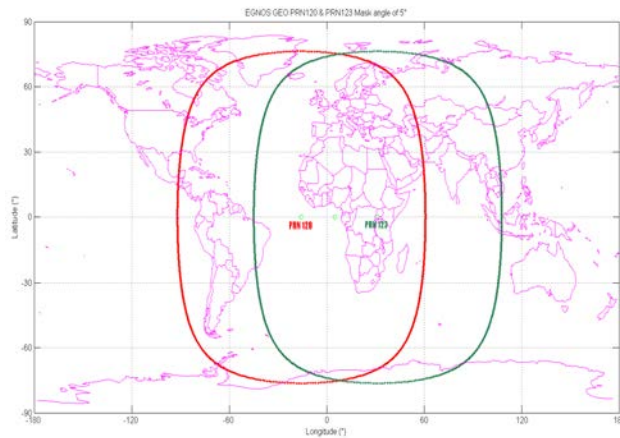


Fig. 1: Operational EGNOS GEOs footprint (PRN 120 & PRN 123).

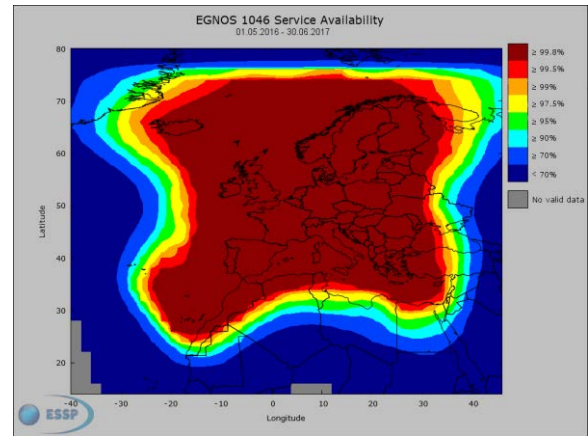


Fig. 2: EGNOS 1046 preliminary Service Availability from May 2016 to June 2017.

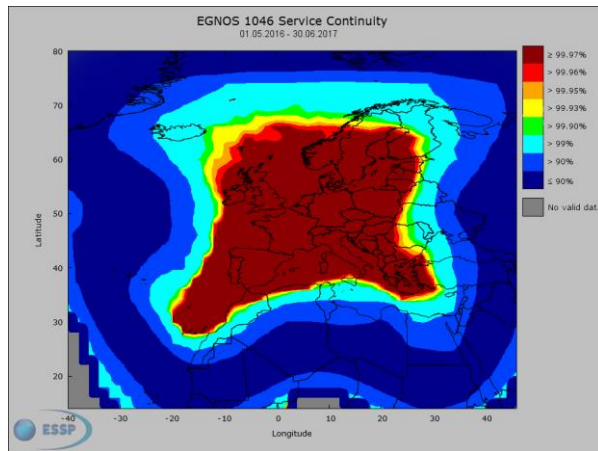


Fig. 3: EGNOS 1046 preliminary Service Continuity from May 2016 to June 2017.

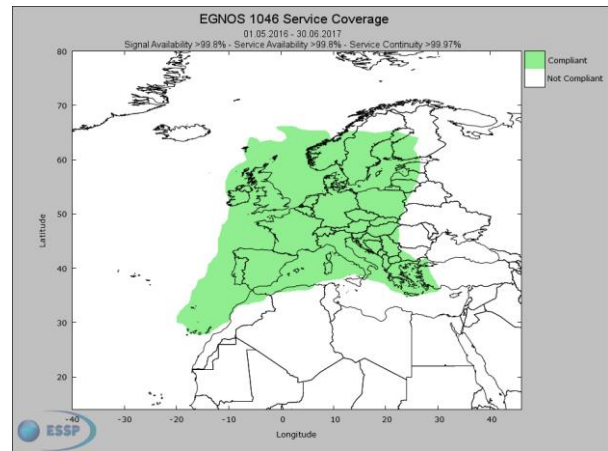


Fig. 4: EGNOS 1046 preliminary Service Coverage for "harbour entrances, harbour approaches and coastal waters" from May 2016 to June 2017.

Testing Multi-network TDOA algorithm with kinematic data

Ciro Gioia, Dario Tarchi

¹European Commission, Joint Research Centre (JRC),
Directorate for Space, Security and Migration,

Demography, Migration & Governance Unit, Via E. Fermi 2749, I-21027 Ispra (VA), Italy
Email: ciro.gioia@ec.europa.eu

Abstract—In the recent years there has been a growing number of applications relying on position of vessel on the sea. Such applications, usually exploit Automatic Identification System (AIS) information, however the information provided by the AIS receivers on board of the vessels need to be verified. In order to check the position information reported in the AIS messages, several techniques have been developed; in this work an extension of the traditional Time Difference Of Arrival (TDOA) localization techniques is proposed. The technique merges TDOA measurement from asynchronous receivers. The technique has been tested using simulated data in kinematic conditions. From the tests, the robustness of the proposed algorithm, with respect to the traditional algorithm, clearly emerges.

Keywords—TDOA, Asynchronous nodes, Multi-network, AIS

I. INTRODUCTION

Navigational systems and equipment are identified in the Chapter V of [1]. In 2000, the introduction of an additional requirement has been proposed by International Maritime Organization (IMO), the ships have to be equipped with a device able to provide information about the ship to other ships and to coastal authorities automatically. Specifically, all ships of 300 gross tonnage and upwards operating on international route, cargo ships of 500 gross tonnage and upwards not engaged on international voyages and all passenger ships irrespective of size have to be equipped with Automatic Identification Systems (AISs). Ships shall maintain AIS in operation at all times except where international agreements. AIS provides ship's identity, type, position, course, speed and other safety-related information; moreover the system can receive information from other ships, this information can be used to monitor and track ships. Originally, the AIS was designed for collision avoidance, the recent increase of terrestrial networks and satellite constellations of receivers is providing global tracking data that enable a wide spectrum of applications beyond collision avoidance. The collaborative nature and the openness of the transmission protocol make AIS attractive for different applications, for example: AIS data can be used to identify threats to a sovereign border before they reach dry land, or to monitoring port traffic increasing the efficiency of the transfer of vessels between harbors and the sea. Moreover, AIS improves Ship to ship communication reducing the need for sending a transmission to all ships within range.

The growth of the applications relying on AIS bring to the light the need of verification of the trustworthiness of AIS data. This is becoming a key problem to exploit the full potential

of AIS technology not only for safety but also for security applications. The cooperative nature of AIS and the lack of intrinsic security make it vulnerable to false or missing declarations requiring the implementation of measures increasing the trustworthiness of AIS messages. AIS relies on different sub-system whose are exposed to different types of attacks. Specifically, AIS relies on Global Navigation Satellite System (GNSS)-based positioning, which can be disrupted by natural, e.g. ionospheric disturbances, and artificial interferences such as spoofing and jamming. One of the solutions proposed, for instance, is the use of physical systems, such as array of receiving antennas to prevent the spoofing of the connected Global Positioning System (GPS) system.

Then there is the ship to ship communication and the communication with the base station which are vulnerable points, AIS messages are sent in an unencrypted and unsigned form, making them trivial to intercept and modify. A solution to this has been proposed in [2]. Moreover, no authentication is present into the AIS protocol, hence anyone can impersonate any other vessel, and all receiving vessels will treat the message as fact. Marine Traffic is an AIS provider which by themselves offer an app for smartphones that allows to transmit simulated AIS signals. However, the signal is sent directly to their server and not transmitted on the standard AIS frequencies, a malicious user can modify the app to broadcast such information creating an AIS spoofer. In [3], the authors propose a secure ship-to-ship information sharing scheme to provide reliable communication between ships and between ships and Vessel Traffic Service (VTS).

The analyzed approaches provide answer to the problem of protecting AIS transponder from intentional tampering, these aim to the increase of the protection against attempts to alter the hardware and or software part of the device on board of the vessel. All the proposed approaches are based on the introduction of new systems on-board of the vessel and on the modification of the AIS protocol and scheme. In this paper a technique to perform a check on the authenticity of the vessel position, reported in the AIS messages is presented: position estimated using the AIS signal and the position reported in the AIS message can be compared.

The AIS Radioloc method exploits the data of the existing terrestrial AIS network, the traditional method proposed has some limitations due to: the poor timing synchronization among the nodes, the limited coverage of the network and the displacement of the stations. The main limitations to the proposed approach are:

- The typical node in the network is a high performance and costly AIS base-station which needs to be optimized in terms of timing and synchronization capabilities, i.e. standard AIS base-station may not be able to record the Time Of Arrival (TOA) of the AIS message with sufficient accuracy to enable AIS Radioloc.
- The terrestrial network coverage is limited to the line-of-sight.
- The deployment of the existing national networks is not designed nor optimized for applying radiolocation techniques; on the contrary the design tends to minimize the overlapping among coverage of different nodes.

To fill this gap, an improvement of the traditional approach based on Time Difference Of Arrival (TDOA), namely ‘Multi-Network’ (MN) TDOA, is proposed [4]. This approach allows accounting for heterogeneous networks of receivers that can be carried by: vessels, aircrafts, buoys and balloons. Despite it has been conceived, and hereby presented, to be applied AIS signals, the developed technique can be easily extended to all kind of Radio Frequency (RF) signals that can be transmitted by the maritime target, such as: VHF communications; FM radio; mobile phones; etc. Therefore, without loss of generality, in the following the authors refer to ‘AIS radiolocation’, meaning a technique which can be applied to many different RF signals.

The basic idea behind the improvement of the traditional radiolocation approach is to be able to account for a network of low-cost AIS receivers that can be carried by drones, balloons, fluctuating buoys or by any other kind of deployable platform. In fact, radiolocation relies on radio receivers, referred to as ‘nodes’, which are passive sensors that can be relatively cheap. Besides, a platform carrying this kind of sensor would be quite simple, requiring a GNSS receiver, a transmitting device and a relatively low power bank. Therefore, a ship or an aircraft deploying many nodes over a wide area could create a large network capable to provide wide scale surveillance. Once the area to be surveyed changes, the deployed nodes could be recollected from the same ship/aircraft or, eventually, they could be disposable.

So far, the major limitation to the employment of this approach has been related to the synchronization problems between the various nodes. In fact, a small offset between some of the nodes can lead to relevant errors in the results of the TDOA algorithm. In this paper, the traditional radiolocation algorithm has been extended including measurements from non-homogeneous devices such as the prototype developed in [5]. In [4], the developed ‘Multi-Network’ (MN) TDOA algorithm has been described and tested on simulated data, assuming a static reference target. The tests developed in this work are kinematic test, including trajectories with different speeds headings and static points. The total duration of the test is some 4.5 hours, corresponding to 16503 epochs with an assumed data rate of 1Hz. From the tests, the robustness of the proposed algorithm, with respect to the traditional algorithm, clearly emerges. In particular, thanks to the introduced enhancement of the actually employed radiolocation technique (which resolve synchronization issues between different receivers), it is possible to enlarge an existing network of ground-based coastal

receivers (or shipborne receivers) with additional deployable low-cost receivers, extending considerably the system coverage.

The remaining part of the paper is structured as follows: in Section II, the TDOA algorithms are briefly presented; the experimental set-up is described in Section III, the results are commented in Section IV. Finally, Section V concludes the paper.

II. TDOA ALGORITHMS

In this section, the formulation of the traditional and Multi-Networks TDOA (MN) algorithms are presented.

The proposed algorithm has been developed to compute transmitter position using MN TDOA; the proposed approach is an extension of the traditional TDOA technique. Both approaches rely on TOA measurements defined as in [6] [7] [8]. TOA observables cannot be directly used for radiolocation, because the offset between the transmitter and the receiver clock is generally unknown. In fact, neglecting this offset can lead to large ranging uncertainties. Moreover, the transmitter timing error is device-dependent because of differences in the electronics of dissimilar transmission equipment [5]. In order to overcome such a limitation, the difference between two TOAs (that is between the delay recorded at two different nodes) is computed, generating the TDOAs measurements:

$$TDOA_{i,j} = TOA_i - TOA_j, \quad (1)$$

where TOA_i and TOA_j are the TOAs estimated respectively by the i^{th} and j^{th} receivers. TDOA measurements can be exploited for target localization, using the approach shown in [9]. The main limitation of this approach is the fact that the difference among the timing receiver errors is unknown. In fact, such a difference can lead to the divergence of the localization algorithm.

When using nodes (receivers) with similar characteristics, belonging to the same network, the offset among receivers can be calibrated or estimated with *a priori* information. On the contrary, if nodes with different characteristics are used, then the inter-network time bias cannot be calibrated or known *a priori*. In order to fill this gap, a different measurements model has to be adopted. In particular the TDOAs from dissimilar nodes can be modeled as shown in [10]. The main differences between the traditional and the MN algorithms are summarized in Table I.

TABLE I. MAIN DIFFERENCES BETWEEN THE TRADITIONAL AND MN ALGORITHMS

traditional	Parameter	MN
$TDOA_{i,j} = \frac{d_i}{c} - \frac{d_j}{c} + \epsilon_{TDOA}$	Measurement Model	$TDOA_{i,j} = \frac{d_i}{c} - \frac{d_j}{c} + c \cdot ISN + \epsilon_{TDOA}$
$H_{TDOA} = [a, b]$	Design Matrix	$H_{TDOA} = [a, b, f]$
$\Delta x = [\Delta E, \Delta N]$	State Vector	$\Delta x = [\Delta E, \Delta N, \Delta ISN]$

Where:

- d is the geometric distance between the transmitter and the receiver;
- $a = \frac{E_0 - E_T^1}{d_0^1} + \frac{E_0 - E_T^2}{d_0^2}$, $b = \frac{N_0 - N_T^1}{d_0^1} + \frac{N_0 - N_T^2}{d_0^2}$;

- f is zero when node with similar characteristics are considered and one when measurements from heterogeneous nodes are used;
- $\Delta E, \Delta N$ are the errors used to update the *a-priori* target position;
- ΔISN is the estimate of the inter-network bias.

A complete mathematical description of the proposed approach is available in [4].

III. EXPERIMENTAL SET UP

In this section, the simulated tests used to validate the MN TDOA algorithm are described.

A kinematic test has been simulated, including trajectories with different speeds headings and static points. The total duration of the test is some 4.5 hours, corresponding to 16503 epochs with an assumed data rate of $1Hz$. The schematic representation of the test is shown in Fig. 1 and then plotted on map in Fig. 2, together with the position of the receivers. In the first section, the vessel moves with a constant speed of about $25km/h$ (approximately 13.5 knots) and a heading of $45deg$ (NE direction); then a stop of $30min$ is simulated. After the stop, the vessel moves again along a circular path with a constant tangential velocity of $15.7km/h$ (8.5 knots). The radius of the path is $5km$ and the total length of the circular path is $15.7km$ (8.5 nm). After the circular path, the vessels stops for $10min$, then it moves with velocity of $36km/h$ (19.5 knots) and heading $286deg$ (SSE direction) for $16min$ and $40sec$, covering a distance of $10km$ (5.4 nm). The total length of the path is more than $75km$ (about 40.5 nm). In Table II, the parameters describing the simulated path are summarized.

Two types of receivers have been simulated: low-cost and professional. The two receivers categories are characterized by different performance: in both cases the measurement errors are modelled as Gaussian process, but with different characteristics. The parameters used for the errors distribution are reported in Table III.

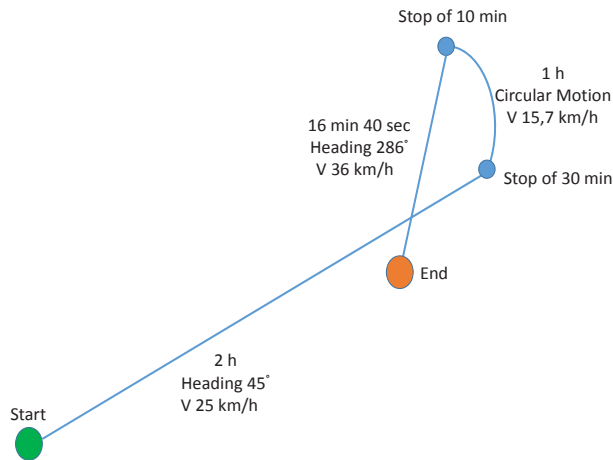


Fig. 1. Schematic representation of the simulated test for the proposed radiolocation algorithm.

TABLE II. PARAMETERS OF THE SIMULATED PATH DECOMPOSED BY DIFFERENT KINEMATICS AND TRAJECTORIES.

Phase	Type of motion	Heading	Average Speed	Duration	Distance
1	Linear	$45deg$	$25km/h$	2 hours	$50km$
2	Static	N.A.	$0km/h$	30 min	$0km$
3	Circular	N.A.	$15.7km/h$	1 hour	$15.7km$
4	Static	N.A.	$0km/h$	10 min	$0km$
5	Linear	$286deg$	$36km/h$	16 min 40 sec	$10km$



Fig. 2. Position of: the three coastal base stations (*Base #*); the additional receivers (*Add Rx #*). The simulated trajectory of the target vessel leaving the Tunisian coast and heading toward Pantelleria island is represented by a cyan line.

The test has been performed considering a variable number

TABLE III. TOA ERROR PARAMETERS FOR THE TWO TYPES OF SIMULATED RECEIVERS.

Receiver Type	σ [msec]	Mean [msec]
Professional	0.0017	$3.336 \cdot 10^{-5}$
Low-cost	0.0034	$3.336 \cdot 10^{-4}$

of additional receivers: from one to 50. The position of the ground based base stations and of the additional receivers, together with the simulated trajectory of the transmitting target, are shown in Fig. 2. The base stations are considered as professional receivers, whereas all the remaining receivers are considered low-cost devices. The additional receivers have been placed randomly, but respecting the environmental limitations: no additional receivers are placed on land.

IV. RESULTS

In this section, the results obtained using the proposed MN TDOA algorithm are presented. The performance of the traditional TDOA and of the MN algorithms are compared in terms of geometry and horizontal position error.

The geometry conditions are shown in Fig. 3, where the mean Horizontal DOP (HDOP) is shown as a function of the number of additional receivers. The Dilution Of Precision (DOP) is defined as:

$$DOP_{matrix} = (H^T H)^{-1} \quad (2)$$

and each component has the related DOP, East DOP (EDOP), North DOP (NDOP) and Time DOP (TDOP) in the case of the multi-network approach, EDOP and NDOP can be combined to obtain the HDOP.

The geometry conditions are strongly improved passing from one to five additional receivers: the HDOP is reduced by

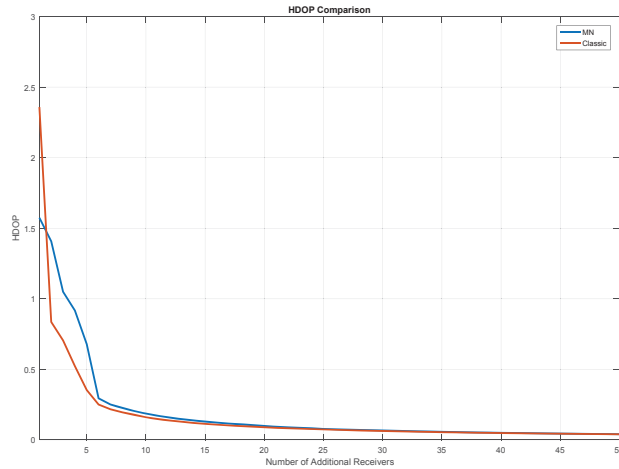


Fig. 3. Comparison of the HDOP between the traditional TDOA and the MN TDOA algorithms as a function of the number of additional low-cost receivers.

almost a factor six passing from 2.4 to 0.4 for the traditional algorithm; for the MN case the HDOP passes from 1.6 to 0.4 and it is reduced by a factor four. However, it can be noted that both algorithms converge to the same HDOP value.

The mean DOP obtained using the MN approach and its breakdown by components (EDOP, NDOP and TDOP) are shown as a function of the number of additional receivers in Fig. 4. The three DOPs have a similar behaviour in all the cases an asymptotic behaviour can be noted: considering more than 20 additional receivers no benefits can be appreciated. In the first part of the graph, from 1 to 5 additional receivers, the TDOP is lower than EDOP and NDOP; while in the second part, the TDOP is higher than the other components.

In order to analyse the effects of the introduction of additional

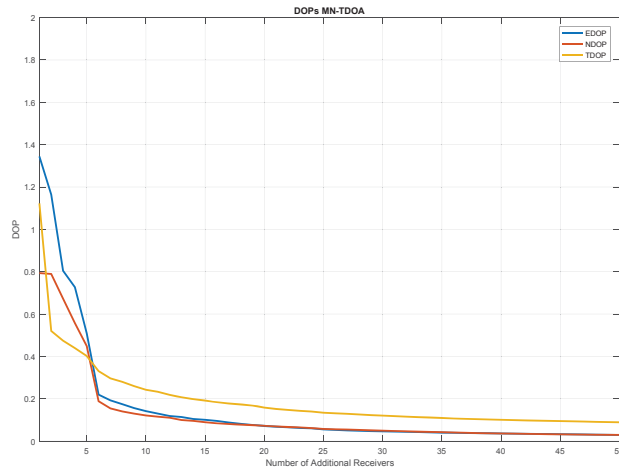


Fig. 4. DOP as a function of the number of additional receivers for the MN TDOA algorithm. East, North and Time components of the DOP are represented respectively in blue, red and yellow.

receivers in the position domain, the estimated trajectories using the MN and traditional algorithms are shown in Fig.

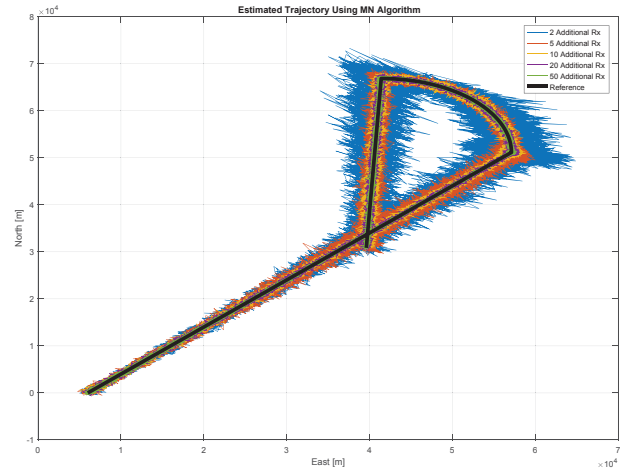


Fig. 5. Trajectory of the simulated target estimated with the MN TDOA algorithm. The actual trajectory is represented by the bold black line, whereas the different colors represent estimation of the trajectory carried out with a different number of additional low-cost receivers (from 2 to 50).

5 and Fig. 6 respectively. In order to have a reduced number of lines, only five configurations are considered in both figures. Specifically, the configurations considering 2, 5, 10, 20 and 50 additional receiver are shown. The benefits of the inclusions of additional receivers for the MN case are evident from Fig. 5, from which it can be noted that the estimation noise is clearly reduced by enhancing the number of additional receivers. The main improvements are obtained passing from 2 to 5 additional receivers. However all the trajectories properly represent the reference trajectory (black line) and no relevant bias can be noted. In Fig. 6, the trajectories obtained using the traditional algorithm are shown. Also in this case, the benefit of the introduction of additional receivers are clear, but, contrarily from the previous case, a bias can be clearly noted between the estimated trajectories and the reference one. The bias is due to the unknown offset between the not synchronized nodes of the network, which is not kept into account by the traditional algorithm.

In order to directly compare the trajectory obtained using the two algorithms, the estimated solutions are shown in Fig. 7. In each box a different configuration is considered: in the upper left box 2 additional receivers are considered, in the upper right box 5 additional receivers are considered, in the bottom left box 10 additional receivers are considered and finally in the bottom right box 20 additional receivers are considered. From the figure, the benefits of the MN algorithm are evident. The estimates using the MN algorithm (blue lines) are centered on the reference trajectory (black lines); whereas a bias can be noted when the traditional algorithm is adopted.

To further investigate the benefits of the introduction of additional receivers, the CDFs of the horizontal position errors are shown in Fig. 8. Moreover, Fig. 8 allows a comparison between the performance of the two algorithms. For both algorithms, the benefits due to inclusion of additional receivers observed in the previous figures are confirmed. From the comparison of the two algorithms, it clearly emerges that the MN algorithm (continuous lines) outperform the traditional algorithm (dashed lines). No bias can be appreciated for the

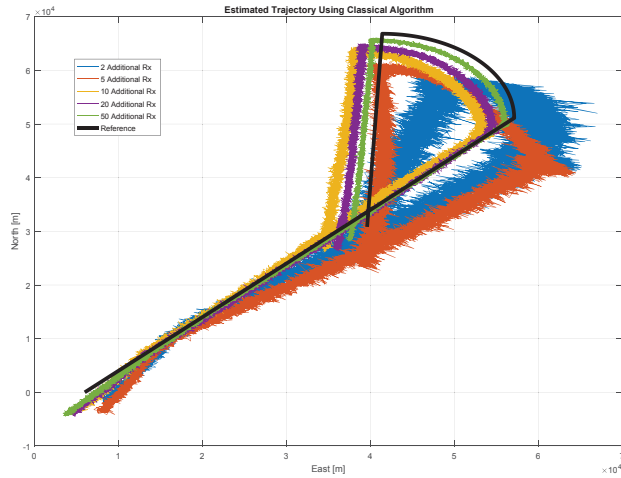


Fig. 6. Trajectory of the simulated target estimated with the traditional TDOA algorithm. The actual trajectory is represented by the bold black line, whereas the different colours represent estimation of the trajectory carried out with a different number of additional low-cost receivers (from 2 to 50).

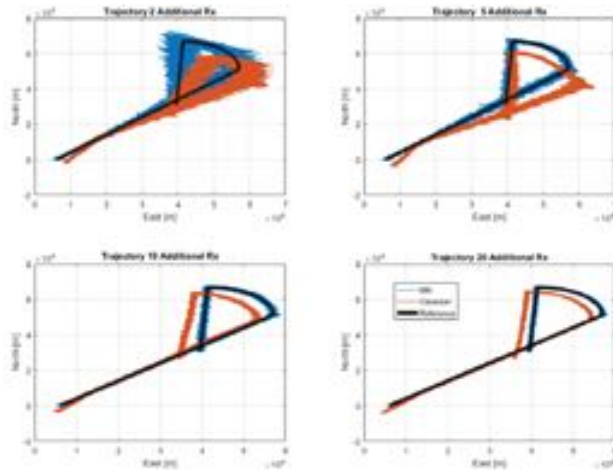


Fig. 7. Comparison between the actual trajectory (black) and that one estimated with the traditional (red) and with the MN algorithm (blue). Four configurations of the receivers network are considered by adding to the 3 base line Rx respectively: 2 (top-left), 5 (top-right), 10 (bottom-left) and 50 (bottom-right) additional Rx.

cases of the MN configurations, whereas a bias can be noted for the classic case. Specifically, the dashed lines are flat in the first part of the graph showing a bias between 1 and 3 km.

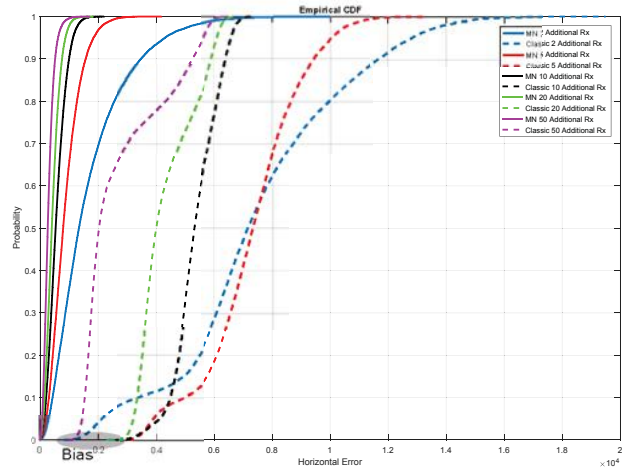


Fig. 8. CDFs of the horizontal position errors for the traditional (sketched line) and the MN TDOA algorithms. Five configurations of the receiving network are considered: BL+2Rx (blue); BL+5Rx (red); BL+10Rx (black); BL+20Rx (green); BL+50Rx (purple).

V. CONCLUSIONS

In the paper the extension of the traditional TDOA radiolocation algorithm, namely MN TDOA, has been implemented and tested. The tests proposed in this paper consider a simulated target with a non-uniform trajectory. The objective is to compare the tracking of the target carried out through the employment of the novel method with that produced by the traditional method. The comparison is proposed for different configurations of the receiving network, which besides the three high-end coastal receivers of the baseline configuration, includes a variable number of additional low-cost receivers randomly positioned at sea.

Again, the benefits of the MN TDOA applied to a network of non-homogeneous receivers are evident when compared to the traditional approach. The unknown bias between asynchronous receivers is automatically computed and accounted for, in order to achieve a more accurate estimate of the position of the transmitting target through triangulation. Given the hypothesis on the TOA error for the considered receivers and assuming the trajectory of the target described in experimental setup section, the following considerations can be done:

- With the MN TDOA, one achieves an HDOP equal to: 0.4 including 5 additional low-cost receivers; 0.2 with 10 additional low-cost receivers; and less than 0.1 with 20 additional low-cost receivers.
- For a small number of additional receivers most of the trajectories estimated with the traditional method present an evident offset, while the trajectories estimated with the MN algorithm are consistent with the actual trajectory.

In conclusion it appears evident that, thanks to the introduced enhancement of the actually employed radiolocation technique (which resolve synchronization issues between different receivers), it is possible to enlarge an existing network of ground-based coastal receivers (or shipborne receivers) with additional deployable low-cost receivers, extending

considerably the system coverage. It is worth to recall that, without any loss of generality, hereby the authors referred to AIS radiolocation, having already underlined that the same technique can be applied also to GSM or to any other kind of RF source.

REFERENCES

- [1] Lloyd's Register and International Maritime Organization, "Convention-for-the-Safety-of-Life-at-Sea-(SOLAS)," tech. rep., International Maritime Organization, 2016.
- [2] J. Behrens, B. Suhr, and L. C. Hauer, 2014.
- [3] S. Oh, D. Seo, and B. Lee, "S3 (Secure Ship-to-Ship) Information Sharing Scheme using Ship Authentication in the e-Navigation," *International Journal of Security and Its Applications*, 2015.
- [4] C. Gioia, F. Sermi, D. Tarchi, M. Vespe, and V. Kyovtorov, "Multi-Network TDOA: an opportunity for vessels radiolocation," *In proceeding of ENC 2017*, 2017.
- [5] P. F. Sammartino, M. Vespe, F. Oliveri, and D. Tarchi, "A new method to verify vessel positions (AIS message). Pre-operational validation and future perspectives," tech. rep., JRC Joint Research Centre, 2015.
- [6] I. Guvenc and C. Chong, "A survey on TOA based wireless localization and NLOS mitigation techniques," *IEEE Communications Surveys & Tutorials*, 2009.
- [7] A. Panwar, A. Kumar, and S. A. Kumar, "Least Squares Algorithms for Time of Arrival Based Mobile Source Localization and Time Synchronization in Wireless Sensor Networks," *Proceedings published by International Journal of Computer Applications (IJCA) International Conference on Computer Communication and Networks CSI-COMNET-2011*, 2011.
- [8] B. Friedlander, "A passive localization algorithm and its accuracy analysis," *IEEE Journal of Oceanic Engineering*, 1987.
- [9] R. Kaune, "Accuracy Studies for TDOA and TOA Localization," in *Fusion 2012*, 2012.
- [10] C. Gioia, F. Sermi, D. Tarchi, M. Vespe, and V. Kyovtorov, "Multi-Network TDOA: an opportunity for vessels radiolocation," in *European Navigation Conference (ENC)*, pp. 1–8, 2017.

Distribution of Nautical Information, Positions etc. Digitally Directly in to the Navigation System of a Sea Traffic Management Equipped Ship or Rescue Unit

Fredrik Kokacka

Swedish Maritime Administration, Gothenburg, Sweden, fredrik.kokacka@sjofartsverket.se

Summary

Currently all SAR information is transferred over voice communication, mostly VHF-radio.

By using the Sea Traffic Management (STM) Search and Rescue (SAR) tools the expected effect will be that misunderstanding and the administrative burden onboard the Rescue Units or Vessel of opportunity will significant be reduced. And the alert response will be quicker and more accurate which in the end will save lives. Due to that Audio communication via VHF or mobile phones expect to be lower, while information will be exchange digitally instead, there will be more space available for exchange of relevant information with audio equipment between the participating parties. The Swedish Maritime Administration (See Fig. 1) has implemented the solution in the Maritime Rescue and Coordinating Center (MRCC), and the Swedish Society for Rescue at Sea has installed the SAR tools on two rescue vessels.

Motivation

Sea Traffic Management STM is an information sharing framework that primarily deals with the benefits that different parties can get if they share information digitally with each other in real time. By using the infrastructure Maritime Connectivity Platform MCP there will be possible to digitally connect Shore Centre like VTS, MRCC, to connect ports and ships e.g. Rescue Units and other units, ships that can be engage in a rescue operation, called vessels of opportunity VoO

Today, when the Maritime Rescue and Coordinating Center is starting a search operation. The alarm information (type of distress situation) Search Area, positions of the distress object or other search related information (search patterns, routes, waypoints) are distributed to a Search and Rescue Unit (SRU) a Vessel of Opportunity (VoO) or to other resources participating in the SAR operation by voice information. To do this MRCC uses audio equipment, mostly maritime radio communication VHF but also ordinary phones.

By using a digital solution such as STM offer, this information can be distributed directly to the navigation equipment onboard the SRU or VoO. This requires that both the MRCC and the receiving units are STM equipped. At MRCC the management support system (Information and Control tool for Search and Rescue) have to be STM compatible and onboard the rescue units the navigation system have to be updated with STM functionalities and connected to internet via mobile internet or satellite.

Results

At the Maritime Rescue and Coordinating Center

In the STM compatible, Information and Control tool for Search and Rescue, the most important information that should be sent out from MRCC to the participating Rescue Units will be created:

- **Text message** with the essential information written in text e.g. number of persons in water PIW, identifying data of missing object etc.
- **Search Area**/distress position were the unit's should be heading. This will be decided when the SAR coordinator have collected all facts, calculated the drift with help of metrological projections.
- **Search patterns** or routes that the SAR coordinator wants the participants to follow during the search, all to have the optimal covering of the area that should be examined.

The SAR coordinator will create the distress message (text) Search Area and Search Pattern. The SAR coordinator then select which unit that will be use in the operation and just send the information digitally via MCP infra structure. This information will now be possible to display on the ECDIS onboard the selected STM ship.

Onboard the Rescue units/ship

On the STM equipped navigation system (Electronic chart display and information system ECDIS) the crew onboard will first of all have the possibility to read the test message with first alert information of the SAR operation that have been sent out from MRCC. The crew will also have the actual Search Area displayed and also the suggested search pattern that the SAR coordinator has decided. (See Fig. 2) Here the crew can read and discuss the immediate action and obtain a common understanding of the rescue operation. If the crew would like they can retrieve the voyage plan for STM vessels in vicinity all to have better situation of awareness. The rescue unit will also broadcast their own voyage plan so other STM vessels or rescue units will see their voyage plan.

Figures



Fig. 1: The SMA SAR symbol

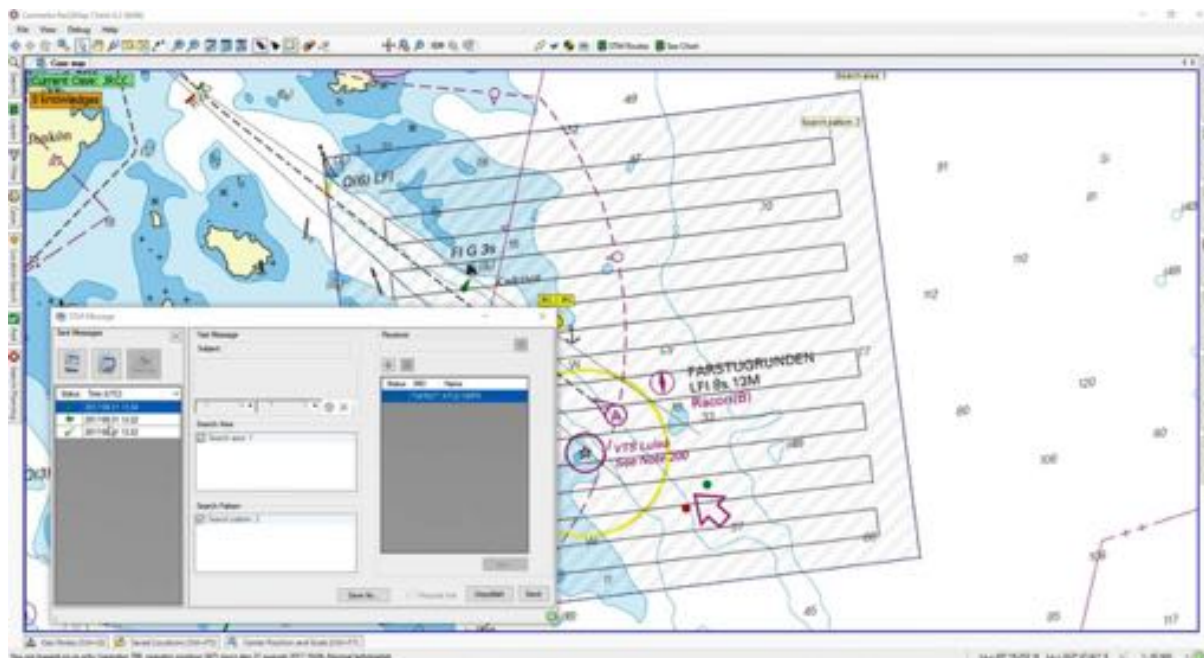


Fig. 2: Search area, search pattern and text message displayed on the electronic navigation system of a rescue vessel.

Workload and navigational control

The control levels of COCOM as framework for ship bridge HMI design

Thomas Porathe
Dep. of Design
NTNU, Norwegian University of Science and Technology
Trondheim, Norway
thomas.porathe@ntnu.no

Abstract—A future sustainable world will also rely of safe, efficient and environmentally friendly maritime transportation. This paper suggests a new way of looking at ship bridge design based on some theoretical constructs of information processing and cognitive engineering. It briefly references two maritime accidents where a mismatch between the availability of information and human performance can be detected. It then shortly discuss the impact of stress on human performance and present how Hollnagel's Contextual Control Model (COCOM) theory can be used to structure design work and bridge layout based on operator workload. The intention is to advance HMI design and integration of bridge equipment based on the different theoretical control levels. The *Scrambled* control level is presently not supported by modern bridge equipment and new research into this type of user interfaces is proposed.

Keywords—*control room design; navigation; ship bridge; COCOM*

Full paper in IEEE Xplore

Maritime Integrity Concept

Mr. Chris Hargreaves, Dr. Paul Williams
Research & Radio Navigation Directorate
General Lighthouse Authorities (GLA)
Trinity House
Harwich
UNITED KINGDOM

Abstract—Navigation integrity is a well-described and mature concept within the aviation community, the same cannot be said for the maritime domain. The aviation required navigation parameters (RNP) for instrument approach procedures demand certain levels of performance from the aircraft’s on-board navigation system. Inherent in these requirements is the concept of user-level integrity: the user’s navigation equipment is tasked with providing an integrity warning to the pilot if ever the error on the derived position-fix is likely to exceed the given threshold.

The performance requirements of electronic position-fixing at sea are currently derived from IMO Resolution A.1046 on the Worldwide Radio-Navigation System (WWRNS). This is a set of requirements, which must be met by global radio-navigation systems used to electronically plot a vessel’s position on a nautical chart. The WWRNS is required to be able to issue integrity alerts to the user in case of “system malfunction, non-availability or discontinuity” within a specified time-to-alarm (TTA). The determination of whether the system is in a state of “malfunction” is left up to the IALA marine-beacon DGPS infrastructure.

Various issues may affect the user’s position-solution of which the marine-beacon reference-stations would have no visibility or control. These include: local noise and multi-path on the vessel; obscuration of satellites to the user; un-corrected satellite orbit / clock errors; de-correlation of differential-corrections over distance. Since the user’s receiver is not required to assess the accuracy, or integrity of its own solution, the derived position-fix may be considerably degraded compared to the performance achievable at the reference-station. Thus DGPS-issued integrity warnings may not be relevant to the user’s position-solution.

Increased dependence on GNSS at sea, combined with the evolving e-Navigation concept, and technology that allows greater automation of shipping means electronic position-fixing systems must be guaranteed to be reliable. Implementation of a set of user-level performance-requirements akin to aviation RNP, coupled with user-level integrity assessment is a way to achieve better control of local effects which act to degrade GNSS position-fixing. Other augmentation systems such as SBAS provide the user’s receiver with integrity information and the parameters of error-models which conservatively estimate achievable accuracy. Receiver-Autonomous-Integrity-Monitoring (RAIM) may use such information in addition to redundant pseudo-range measurements to autonomously determine whether the risk of an erroneous position fix exists. Some maritime receivers claim to make use of SBAS and / or RAIM, however since neither are currently mandated for use, their implementation is not regulated and so is un-controlled. These

issues are discussed in this paper, and a maritime concept of user-level Integrity is described.

Keywords—maritime, GNSS, integrity, RAIM, e-Navigation

I. GNSS USE AT SEA

Currently GNSS, and GPS in particular, is used as a sole-means of electronically deriving a vessel’s position. Manual comparisons to GPS fixes can be made using other means, such as star-sights; visual bearings; or using the ship’s radar. In practice these techniques take time and experience to do accurately. The shipping industry has sought to cut operating costs by steadily reducing man-power on vessels and replacing experienced crew with cheaper inexperienced navigators. Pressures on navigator’s time and watch-keeper fatigue contribute to human-error being the largest single source of all marine accidents.

The IMO’s e-Navigation initiative [1] aims to improve safety and efficiency at sea. The efforts to bring about greater standardisation and harmonisation of electronic data through common data-formats and a shared data-communication network will enable smoother, automated transmission of data between ship systems, between different vessels, and to the shore. Processes such as communicating with Vessel Traffic Services (VTS) and Ports; exchanging route information and cargo manifests; providing an ETA; communicating intent; and ultimately many of the routine navigation functions on the ship may all be seamlessly automated by evolving e-Navigation services.

Indeed this process has already begun and many devices on a ship’s integrated bridge (radar, gyro, ECDIS, GMDSS radio, AIS etc.) take position information directly from the DGPS receiver.

To underpin the e-Navigation services of the future, vessels are likely to need a high degree of reliability and resilience in position-fixing and navigation data. Many e-Navigation services are likely to make use of the vessel’s position and velocity automatically and without navigator intervention. The security of these services will depend on the integrity and reliability of the position-solution derived on-board the vessel.

By relying on a single sole-means of deriving a position-fix, a great deal of reliance is placed on the one system. Electronic position-fixing at sea must be reliable, robust and trustworthy as stated by the IMO [1].

II. PERFORMANCE REQUIREMENTS

The performance of radio-navigation position-fixing services (for which DGPS is the de-facto standard) is governed by IMO Resolution A.1046 on the World-Wide Radio-Navigation Service (WWRNS) [5]. The performance requirements are set out in **Error! Reference source not found.**

Voyage Phase	Accuracy	Continuity	Integrity (TTA)	Availability
Ocean Water	100m (95%)	N/A	As soon as possible	99.8% (signal)
Coastal Water	10m (95%)	99.97% (15 mins)	10s	99.8% (signal)
Harbour Approach	10m (95%)	99.97% (15 mins)	10s	99.8% (signal)

TABLE I. IMO WWRNS PERFORMANCE REQUIREMENTS

The IMO Resolution describes only the capabilities of the radio-navigation service, and so stipulates system-level requirements: the user's receiver is not included (see Figure 1). Effectively A.1046 is a stipulation regarding the navigation signal-in-space – this is the aspect over which the GNSS system-provider has control, and so it makes sense for the IMO to specify performance at this level. GPS alone does not meet these requirements, since it cannot meet the rapid time-to-alarm needed to preserve Integrity. GPS augmented by IALA marine-beacon DGPS is a valid combination certified as a WWRNS, which can meet all of the requirements.

A major problem with stipulating only system-level requirements is that the user's experience of navigation can be significantly degraded compared to the theoretical capability of the system. For example, it is known that the DGPS user experiences reduced accuracy at distance from the reference-station. This is due to a reduced number of common-view satellites and also de-correlation in the broadcast differential-corrections over distance.

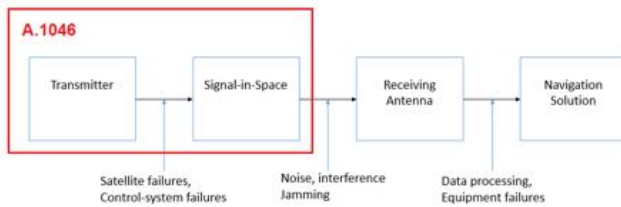


Figure 1 – Existing IMO requirements specify only the signal-in-space performance. Effects local to the user's receiver are not in scope.

The integrity consideration is particularly an issue, since the only demands A.1046 places is that the user can be warned of “system malfunction, non-availability or discontinuity”. The only integrity-threats considered are those arising from a failure in the GNSS component. The receiver is not required to estimate its own accuracy performance, or determine the integrity risk from threats local to the vessel.

Apart from a reduced subset of common-view satellites and de-correlation of corrections over distance, several important local effects contribute to user-error which are not present at the DGPS reference-station:

- Local L-band interference which may raise the background noise level, reduce signal-to-noise-ratio (SNR) and contribute to elevated measurement-errors or potential loss of signal tracking.
- Multi-path interference is highly dependent on the environment and will be an unpredictable error-source for a vessel, particularly one navigating near to the built environment such as within port or an inland waterway.
- Signal-obscuration may also be a problem since the line-of-sight propagation path may become blocked by port infrastructure such as cargo-cranes, or the vessel's own structure if the GPS antenna is mounted anywhere other than at the very top of the ship's mast.
- Multi-path reception of signals for which the direct path is blocked causes errors which are particularly severe. Such Non-Line-Of-Sight (NLOS) reception is a particular hazard of the marine environment.

A. User-Level Requirements

It is proposed that a set of requirements akin to the aviation Required Navigation Parameters (RNP) is established to govern maritime GNSS receiver-operation. We note the inherent conceptual leap from specifying a set of system requirements, to a user-level view of navigation performance. The user's receiver; its local environment; its data processing; and any integrity algorithms it runs will all be within the scope of the specification. Part of these requirements will be a set of performance tests to be applied before type-approval of new equipment. These tests are likely to be substantial, as every aspect of the receiver's operation will have to be tested to ensure compliance with a Minimum Performance Standard (MPS).

To provide user-level integrity will require a particular set of algorithms – these will have to be run by the user's receiver equipment. It will be necessary to mandate that future vessels' equipment implements this functionality while allowing equipment manufacturers some room to innovate and allow them to retain intellectual property over their own receiver processing. In this way, bespoke algorithms may be implemented as long as they can be shown, through testing, to meet the specifications laid down in the MPS.

Two parameters are key to the user-level performance requirements; Integrity and Continuity. As we shall see, far from being independent of one another, these two parameters are intimately entwined.

III. INTEGRITY CONCEPT

The concept of user-level integrity is that responsibility for determining the validity of a position-solution lies with the user's navigation receiver. The level of error considered intolerable in solution is given by the Horizontal Alert Limit

(HAL) for the intended operation. The receiver is tasked with issuing an alert to the user should it determine that there is the possibility of a position fix demonstrating a position error that exceeds the HAL. This determination is achieved through modelling the accuracy of the position-solution, and monitoring for various potential failings that could affect the output fix, according to some *threat model*. Additional data from the GNSS itself and/or any augmentation system may aid this determination, but the final decision is made by the user's equipment. The receiver thus presents to the mariner a **yes** or **no** decision as to whether the navigation system can be trusted at any positioning epoch.

If ever the algorithm determines that a fix should not be used, an alert should be issued to the navigator. Any fix for which the actual error exceeds the HAL, but is still declared usable, is termed Hazardously Misleading Information (HMI). This is a significant threat. The integrity risk requirement specifies a maximum probability of HMI over a nominal time-frame to limit the occurrence of the equipment misleading the user.

Part of the integrity monitoring process will be to determine the validity of the yes / no decision by estimating the probability of HMI (or integrity risk) for each position-fix. In practice it can be a much tougher task to estimate integrity-risk than to provide the yes / no decision in the first place. Good algorithm design is essential to this process.

If the system determines that the probability of HMI on a position-fix is larger than the requirement then the decision to use the fix cannot be trusted. In this case the receiver may output an 'Integrity un-monitored' alarm, or may err on the side of caution and provide the 'do-not-use' decision for that particular position-fix. We use a 'traffic light' system as an intuitive way to describe the output:

- **Red-Light** = a fault has been detected, do not use the fix.
- **Green-Light** = the fix is acceptable, and the integrity risk is within the requirement.
- **Yellow-Light** = the fix seems acceptable, but since integrity risk is not below the required level, this decision cannot be trusted. Use at own risk.

To avoid confusion the yellow-light condition may be replaced with a red-light 'do-not-use' warning.

The algorithm's "snapshot" risk per-epoch is related to the total risk over the given time-frame – an estimate of the correlation time of GNSS errors is used to relate individual epochs to the cumulative risk over a longer time-frame. We use 150 seconds as the correlation time as this is the figure adopted in aviation SBAS standards [4].

A. Continuity

The navigation-solution is considered usable only if accompanied by the green-light integrity guarantee. The mariner wishes to see the green-light preserved for a long enough time to allow them to do their job safely. A stipulation is made that the probability of losing the green-light each

epoch is kept to a very low figure to maximise the usability of the system. The probability of a switch to the red-light condition each epoch has to be quite precisely controlled by the receiver to preserve user-level continuity.

Part of the integrity-monitoring process to detect possible HMI is to set detection thresholds which cannot be breached without raising an alarm. Various parameters can be used to detect faults, such as the range-residuals after solution, or the separation between fixes found using different sub-sets of pseudo-range measurements. If the fault-detection threshold is set low then even small errors trigger detection and HMI is very unlikely, however alarms will be frequent and perhaps raised un-necessarily. Continuity should be preserved as a priority by raising detection thresholds such that false-alarm probability is tightly controlled. Setting thresholds too high guarantees good continuity, but at the cost of faults not being detected.

Integrity and continuity are like either end of a see-saw, the trick is to establish the right balance through careful budgeting of both continuity and integrity risk probabilities. These budgets need to be agreed as part of the performance specification.

B. Integrity Threats and Mitigations

Integrity will be assessed against a particular model of potential threats which may impact the solution. For the marine user we have a particular set of environmental hazards which we must consider:

- Multi-path
- Signal-obscuration
- NLOS reception (obscuration + multi-path)
- Local noise and interference
- Atmospheric delays and scintillation

Particular techniques will help us, for example we know that line-of-sight multi-path will induce time-varying pseudorange errors which will be limited in their maximum extent. It may be possible to design an error-model based on a Normal distribution which describes the magnitude and likelihood of multi-path errors. The use of SBAS in the aviation sector adopts just such a model [4] – this is possible because antenna-installation on an aircraft is highly regulated and reflecting surfaces are kept below the antenna ground-plane. We may not be able to make such an assumption for a marine antenna installation.

NLOS is a more problematic issue since the magnitude of the error depends on the path-length difference of the reflected signal, and this can be very large. Receiver autonomous integrity monitoring or fault-detection (RAIM, FD) algorithms can help here, using redundant information in the position-solution to detect large measurement errors. The need for RAIM depends largely on the severity of the NLOS problem at sea.

RAIM is good at spotting errors on individual measurements but will be no use against an elevated background noise, or jamming attack which can impact all

satellites in solution. A separate method of determining a clean radio-background may be needed. Interference-detection can be achieved by a variety of methods, such as using the reported satellites' SNR; C/No; the front-end gain-control; or a multi-antenna setup. Again the aviation world is able to very tightly control the local radio environment of an aircraft in flight; we are not so lucky in the maritime domain. The need for additional noise-monitoring is dependent on the likelihood of interference and jamming.

For both RAIM and interference-detection alarm thresholds must be set. A probability of false-alarm will exist. At the same time a small residual integrity-risk, due to missed-detection, will remain. An effective integrity monitor should strike a fine balance between the *probability of false alarm* (P_{FA}) and the *probability of missed detection* (P_{MD}). If an additional mitigation measure is needed, some of the continuity budget will have to be spent to accommodate it. Additional safety-checks cannot be included *ad-infinitem* without incurring cost to the continuity budget.

Today, atmospheric delays are usually calibrated out using an augmentation-system (DGPS or SBAS) to measure the state of the atmosphere and issue correction-data. In the time-frame that we are considering, the beginning of the era of e-Navigation [1] and the Multi-System Receiver (MSR) [3], from about the year 2025 onwards, most GNSS constellations will offer civilian-access signals on multiple frequencies. This evolution to multi-frequency operation allows the receiver to cancel ionospheric effects by itself without relying on an external augmentation system. Augmentation is therefore optional, so for this paper we shall assume it to be absent. In the Following analysis we shall assume that electronic position-fixing at sea is provided by:

- Dual-frequency multi-constellation GNSS receiver
- Integrity-provision is by RAIM algorithms running within the receiver.
- Integrity decision indicated to the navigator by red / green integrity light.

IV. PROPOSED PERFORMANCE REQUIREMENTS

It is sensible to put some numbers to the concepts. IMO resolution A.915 was written 17 years ago with the aim of setting out the future demands of maritime electronic position-fixing. Its intention was as a positioning document to ensure that marine requirements would not be overlooked as each of the GNSS constellations underwent a period of development and re-engineering.

The document sets out several requirements, the important ones for our consideration are:

- 10 m accuracy (95%) for most applications
- 10^{-5} integrity risk per 3-hours
- 99.97% continuity per 3-hours
- 99.8% overall availability (considered over 2 years)

A.915 has been criticised [2] for not adequately considering the relationship between snapshot risk and performance over a

longer time-period. The choice of a 3-hour operation interval was perhaps ill considered and overly long. Indeed when A.1046 adopted the 99.97% continuity requirement the time-interval was amended to a more sensible 15-minutes [5]. We propose the same reduction of time-interval for the integrity requirement. These figures are of course open for informed debate.

With our assumed error-correlation time of 150 seconds we derive that the 15-minute interval contains exactly six statistically-independent epochs, this gives per-epoch integrity and continuity risk probabilities:

- 99.97% continuity over 15-minutes equates to continuity risk per epoch of 5×10^{-5}
- 10^{-5} integrity over 15-minutes equates to integrity risk per epoch of 1.667×10^{-6}

A. Risk Budgeting

We consider each aspect of the system in turn and budget how much risk is posed by each component. Some aspects we can control, and others are fixed depending on the quality of the navigation-system and the particular threats which the user's receiver is subjected to.

Navigation risks can be pictorially represented by constructing a fault-tree. A top-level risk budget is assigned, and individual hazards are broken down into their substituent components with risk apportioned following every sub-division, an example developed for aviation is shown in Figure 2.

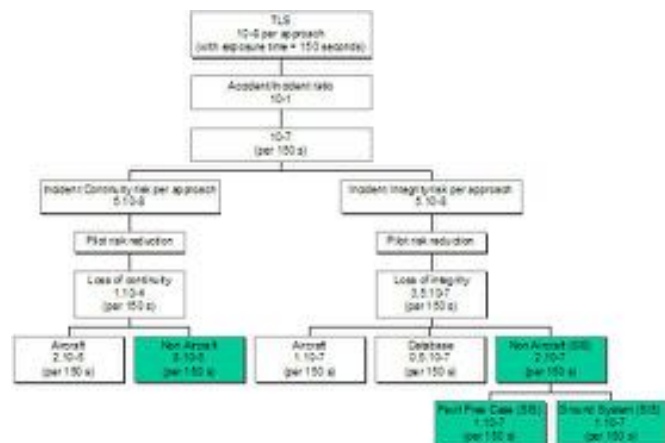


Figure 2 – ICAO Fault-tree used to certify SBAS use for aviation APV / CAT-I approach procedures.

It is unfortunate that the maritime world does not have an equivalent top-down fault-tree analysis of navigation risks stemming from an allowed Target Level of Safety (TLS). We will have to construct our own continuity and integrity 'branches' from the risk requirements that we do know.

The following apportionment is proposed for the continuity budget of 5×10^{-5} per epoch:

- 10^{-5} risk due to false-alarms from RAIM

- Small (negligible) probability due to hardware / software issues
- The remainder (4×10^{-5}) due to true-alarms in the GNSS component further divided into:
 - 4.17×10^{-7} probability of failure in the GNSS segment. Defined in the GPS SPS document as 'major satellite failures' these occur at a frequency of 3 per year, or 10^{-5} per service hour, equal to 4.17×10^{-7} per epoch.
 - The majority remainder (3.96×10^{-5}) apportioned to local integrity threats.

This is quite a conservative risk-allocation, since the component we can control (false-alarm rate) is given a relatively small fraction of the total continuity budget. It is assumed that most of the red-light events (80% of them) will be due to correct detection of navigation faults.

The green boxes in Figure 3 indicate how each allocation will be met by the system. Some uncertainty remains about the frequency with which local faults will occur in the GNSS component when used in a maritime context. If this component exceeds the budgeted allocation, additional continuity-preserving techniques will be required such as fault-detection with exclusion (FDE) or resilient backup systems.

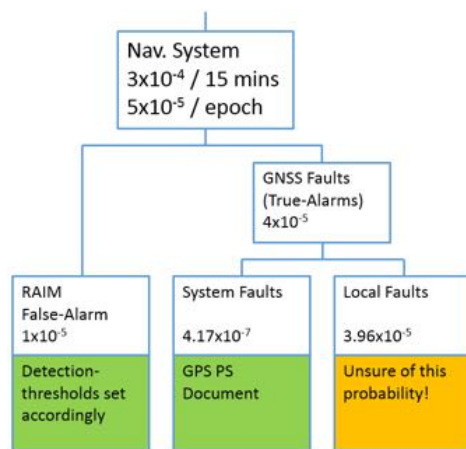


Figure 3 - Maritime continuity fault-tree 'branch' allocating per-epoch risk.

Having set the continuity risk-budget, we determine the detection-thresholds which yield the required false-alarm rates. It is then up to the receiver to determine whether these thresholds yield adequate detection-probabilities from RAIM and interference-detection.

The following apportionment is proposed for the integrity budget of 1.667×10^{-6} per epoch:

- Small (negligible) component due to hardware / software failure in the equipment.
- 8.33×10^{-7} risk allocated to the HPL for fault-free operation

- 8.33×10^{-7} risk allocated due to all faulted-state hazards not detected by RAIM.

This allocation is indicated in Figure 4.

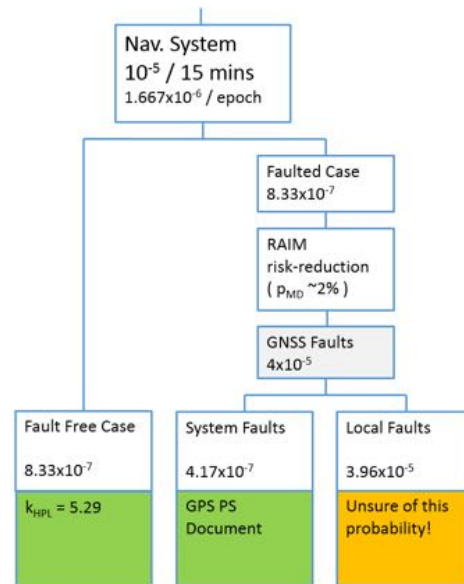


Figure 4 - Integrity fault-tree 'branch' allocating per-epoch integrity risk

We assume the same rate of failures in the GNSS space-segment and due to local faults that we did for the continuity budget. The ratio between the rate of failures (4×10^{-5}) and the required integrity risk (8.17×10^{-7}) determines the missed-detection probability which the RAIM algorithm must achieve ($\sim 2\%$). This informs the algorithm design and indicates how sophisticated the processing needs to be.

Again the colored boxes show how each component is met, the only unknown is whether the rate of local faults exceeds the amount budgeted.

V. ISSUES

We do not know whether the proposed setup will provide adequate integrity and continuity performance. The main issue is that the severity of the multi-path / NLOS threat in the marine environment is poorly classified. In particular we do not know if it causes the rate of alarms to exceed the assumed allocation of about 4×10^{-5} .

The design of the RAIM algorithm will also be dependent on this probability – in particular the ratio between rate of faults ($\sim 4 \times 10^{-5}$) and subsequent integrity risk ($\sim 8 \times 10^{-7}$) gives the missed-detection probability which the algorithm must achieve ($\sim 2\%$).

Fault-detection with exclusion can in some cases mitigate the effect of an integrity-alarm by attempting to determine which measurement data is faulty, and re-computing the position solution with the erroneous data deliberately excluded. If the new solution then passes the integrity tests a green-light can be shown. Even though a fault has occurred it

has been excluded from solution and does not harm the continuity of the resulting fix. Figure 5 shows increased allocation to local-faults can be made if we can guarantee a given percentage of the red-light alarms can be mitigated by FDE. Specifying a minimum performance for FDE is not a simple task, however.

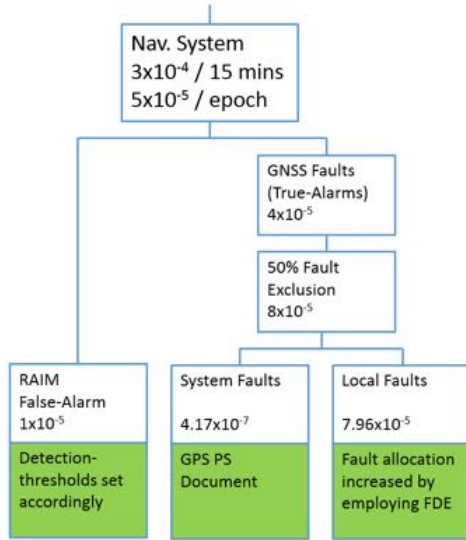


Figure 5 – Increased allocation to local-faults if FDE can be relied upon to preserve continuity

These local faults are expected to be dominated by the occurrence of large multi-path errors, in particular NLOS-reception of signals. Some study will be required to determine the true nature of signal-obscurtion and multi-path for typical GNSS antenna-installations on vessels. To this end a number of projects have been proposed (Nav-ISP element 1, SEASOLAS) which will conduct data collection and analysis of multi-path.

A very benign multi-path environment might actually reveal that the requirements can be met without FDE or RAIM. If local-faults are about as common as system-level faults ($\sim 4 \times 10^{-7}$) then we derive that a missed-detection probability of 100% would be acceptable, and hence the receiver has no need of a RAIM algorithm. This is unlikely to be true, however, and we believe receiver integrity-monitoring is a necessity.

Augmentations such as SBAS can help by detecting GNSS system-level faults and mitigating this component of risk, but the augmentation itself may incur a rate of false-alarm and so may harm the continuity performance of the solution. System-level faults may not be the biggest integrity threat to the receiver, however, and so the usefulness of augmentation may be limited. The decision of how best to employ GNSS augmentation in conjunction with DFMC receiver requires careful thought and budgeting of both continuity and integrity risks.

Another possibility might also be true – if the rate of multi-path and NLOS events are extremely common, even a sophisticated FDE algorithm may not be sufficient. If GNSS

alone cannot guarantee the required continuity then a backup system, which is dissimilar to GNSS, will be needed to take-over when the primary system is unavailable. The need for Resilient-PNT should be derived from the continuity performance-gap between what a GNSS receiver can reasonably deliver, and the user-level requirements.

A. Resilient-PNT

The IMO Multi-System Receiver (MSR) concept allows for an integrated GNSS receiver which also takes data from terrestrial navigation systems (eLoran, R-Mode) and other on-board navigation sensors such as the speed-log and gyro. By integrating GNSS with other dissimilar navigation systems it is possible to improve the resiliency of satellite navigation to short periods of disruption by allowing the position-fixing functionality to fall back to the alternate system(s).

Depending on which alternate systems are used, different levels of performance and hold-over times are available. Whichever backup system is employed this will create a Resilient-PNT system that will allow the mariner to continue his intended operation through primary system (GNSS) outage. We can derive backup-system integrity and continuity requirement by considering the continuity “credit” which is gained when the system is in use; we do this next.

The GNSS continuity requirement stands at 5×10^{-5} risk per epoch such that the rate of GNSS alarms must be less than the requirement, thus:

$$C_{req} \geq P_{alarm\ GNSS}$$

If we implement a backup system which itself gives some probability, or rate, of throwing an alarm ($P_{alarm\ RPNT}$) then the continuity requirement is related to this rate by the proportion of time for which the backup is in use. We call this the **R-factor** such that:

$$C_{req} \geq R P_{alarm\ RPNT}$$

The R-factor provides the new requirement for alarm-rates from the GNSS component:

$$R = \frac{C_{req}}{P_{alarm\ GNSS\ new}}$$

We derive a GNSS continuity “credit” due to the backup system:

$$C_{credit} = P_{alarm\ GNSS\ new} - P_{alarm\ GNSS}$$

$$C_{credit} = R - C_{req} = \frac{C_{req}}{P_{alarm\ RPNT}} - C_{req} = C_{req} \left(\frac{1 - P_{alarm\ RPNT}}{P_{alarm\ RPNT}} \right)$$

Depending on the amount of credit required, a backup system with the necessary R-factor can be specified:

$$R = \frac{C_{req}}{P_{alarm\ RPNT}}$$

The amount of credit added to the GNSS budget depends on the reliability of the chosen backup system. For example, if we see that local GNSS faults occur at a rate an order of magnitude above the requirement (about 5×10^{-4}) we need a

credit of $+4.5 \times 10^{-4}$ to make the system work. This leads to the requirement for a backup with R-factor 0.05%, which is equivalent to a rate of failure of the backup ($p_{\text{alarm RPNT}}$) of 10%.

The continuity-risk fault-tree analysis for this setup is shown in Figure 6.

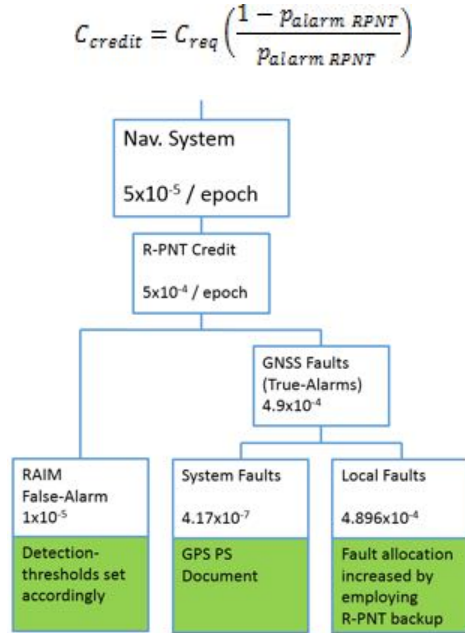


Figure 6 - Example Continuity fault-tree including a R-PNT backup system with R-factor 0.05%

The contribution to integrity from the backup system can then be calculated as a weighted-sum depending on the R-factor:

$$I_{\text{total}} = (1 - R) I_{\text{GNSS}} + R I_{\text{RPNT}}$$

The amount of integrity-risk contributed by the backup system is weighted according to its duty-cycle, or up-time. If we apportion a small amount (5×10^{-8}) of the total integrity-budget then with an R-factor of 0.05% we derive the requirement:

$$R I_{\text{RPNT}} < 5 \times 10^{-8} \\ I_{\text{RPNT}} < 10^{-4}$$

Ring-fencing some of the integrity risk and apportioning it to the backup system inevitably reduces the amount available for the primary (see Figure 7). A price is paid out of the integrity budget so that a backup can be used to provide a continuity-credit. There is a knock-on effect that a much greater probability of local faults means that the RAIM algorithm must achieve better fault-detection rates to preserve performance. Also the HPL k-factor is adjusted due to the apportioning of integrity risk to the backup system.

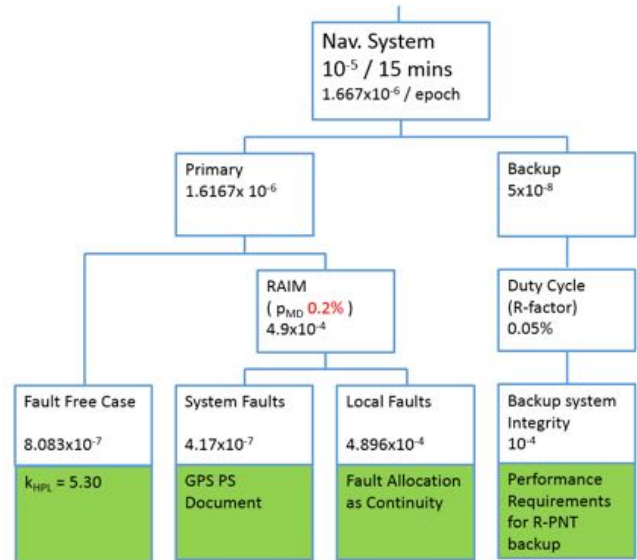


Figure 7 – Example Integrity Fault-Tree with R-PNT backup, R-factor 0.05%

A simple method for determining R-PNT backup-system requirements is shown:

- Apportion the continuity-budget allowing for known risks and also allocating false-alarm budgets.
- Determine the amount of continuity-credit needed to meet the requirements.
- Find the R-factor which delivers this credit.
- Backup continuity-risk is given by $5 \times 10^{-5} / R$
- Backup Integrity is given by $5 \times 10^{-8} / R$

R is effectively the fraction of GNSS-performance that the backup delivers. For a small R-factor, the requirements are easier to meet, and a simpler backup system is needed. For a large R-factor a much more sophisticated backup is needed, when R approaches 100% the backup must equal or exceed GNSS performance.

GNSS Continuity Credit Needed	R-Factor	Backup's Continuity risk / epoch	Backup's Integrity risk / epoch
$+4.995 \times 10^{-2}$	5%	0.1%	10^{-7}
$+9.95 \times 10^{-3}$	1%	0.5%	5×10^{-6}
$+4.95 \times 10^{-3}$	0.5%	1%	10^{-5}
$+9.5 \times 10^{-4}$	0.1%	5%	5×10^{-4}
$+4.5 \times 10^{-4}$	0.05%	10%	10^{-4}
$+5 \times 10^{-5}$	0.01%	50%	5×10^{-3}

TABLE II. CONTINUITY CREDIT, REQUIRED R-FACTORS AND BACKUP SYSTEM PERFORMANCE REQUIREMENTS

Integrity-risk is still defined according to the same HAL, so effectively the same accuracy requirements are demanded

(~10m, 95%) although for systems demanding a very small R-factor the integrity-risk at the HAL is greatly reduced.

VI. CONCLUSIONS AND FUTURE WORK

Maritime is critically dependent on GNSS, not only for providing the navigator with electronic position-fixing but the technology also supports many of the ship's sensors and also aids to navigation. The IMO e-Navigation initiative to improve electronic connectivity on-board ships, and between vessels and the shore, will add additional services which will also make use of vessel's reported position, increasing the dependency on GNSS. The drive toward increased automation in the industry will only place further burdens on the reliability of satellite-derived position fixing at sea.

The current set of regulations to specify the performance of electronic position-fixing may be considered inadequate since they do not cover the user's receiver and the local environment around the vessel. Positioning performance may be worse than the system-level regulations indicate, and the navigator would not be notified.

It is proposed that a user-level performance requirement be stipulated to govern the electronic position-fix derived from the vessel's on-board navigation receiver. This specification determines performance in two key areas:

1. Integrity: The navigator must be warned if the error on the fix is likely to exceed the HAL (25m). The probability of HMI shall be less than 10^{-5} per 15-minute operation.
2. Continuity: If the solution is currently available to the user, it shall remain so for the next 15-minutes with probability not less than 99.97%.

Some work will be needed to convince the international community of the need for new regulations, and to get the proposed figures adopted.

Breaking down the requirements into per-epoch "snapshot" risk probabilities we can begin to address how both continuity and integrity are to be provided to the navigator in light of potential local threats to GNSS signal-reception.

The particular hazards of the marine environment are mainly background radio-noise, interference, and the possibility of multi-path errors on the pseudo-range measurements. The rate of occurrence of these hazards is currently an unknown, which is a problem as designing suitable mitigation measures (RAIM algorithms, multi-system integration etc.) depends on knowing precisely the nature of the threats.

- It is likely that the maritime receiver will need to implement a RAIM algorithm to detect local pseudorange measurement faults. Missed-detection performance will depend on how common the faults are.
- Monitoring of the levels of background radio-noise and interference (jamming) may also be necessary as

threats which affect all satellites in solution are not reliably detectable using RAIM.

- If the frequency of GNSS integrity alarms is expected to be high then fault-detection with exclusion (FDE) may be required to preserve continuity.
- If threats to continuity are particularly severe, beyond the capability of FDE, then integration of GNSS with dissimilar backup navigation systems and sensors can mitigate the risk. Depending on how much continuity "credit" is needed, the quality of the backup system can be derived.
- A single parameter (the R-factor) is proposed that equates the duty-cycle of the backup R-PNT system to the required performance-parameters of the system. eLoran is capable of supporting an R-factor of about 0.5%-1%.
- Augmentation such as DGPS or SBAS may prove useful in improving accuracy and assisting receiver integrity algorithms, but future dual-frequency multi-constellation (DFMC) receivers may be able to meet the requirements stand-alone.

It is required to obtain certain figures before sensible decisions can be made. In particular these are:

- The severity of multi-path for a typical GNSS antenna installed on a marine vessel. This includes the derivation of a conservative bounding-distribution akin to the SBAS air-frame models used in aviation.
- Derivation of realistic probability of this bounding distribution being exceeded. Events such as NLOS reception of a reflected GNSS signal are expected to contribute significant un-bounded multi-path error.
- The risk due to elevated noise levels; jamming; or spoofing to a marine vessel engaged in typical duties in a variety of environments.

These risks may be location-specific, demanding that different backup systems are needed to augment GNSS in different phases of a voyage.

A large-scale study of threats to GNSS signal-reception in the marine environment is recommended in order to establish the required R-factor for the backup PNT systems, and the design of suitable RAIM algorithms.

REFERENCES

- [1] 'IMO Draft e-Navigation Strategy Implementation Plan', Report to Maritime Safety Committee, NCSR 1/28, Annex 7, July 2014.
- [2] Klepsvik, J. Baldauf, M. 'A critical look at the IMO requirements for GNSS', ION GNSS September 2007.
- [3] IMO Resolution MSC.401(95) – 'Performance Standards for Multi-System Shipborne Radionavigation Receivers', Adopted 8 June 2015.
- [4] RTCA DO-229/D – 'MOPS for GPS / SBAS airborne equipment', RTCA SC 159, 2006.
- [5] IMO Resolution A.1046 (27) – 'World-Wide Radio-Navigation System'. IMO 30th November 2011.

Performance Evaluation of a Tightly Coupled GNSS/IMU Integration Algorithm with Multi-Constellation/Multi-Frequency GNSS

Björn Reuper, Matthias Becker, Stefan Leinen

Chair of Physical and Satellite Geodesy

Technische Universität Darmstadt

Darmstadt, Germany

Email: reuper@psg.tu-darmstadt.de

Abstract—Localization algorithms based on global navigation satellite systems (GNSS) play an important role in automotive positioning. Due to the advent of autonomously driving cars, their importance will grow even further in the next years. Simultaneously, the performance requirements for these localization algorithms will increase because they are no longer used exclusively for navigation but also for control of the vehicle's movement. These requirements cannot be met with GNSS alone. Instead, algorithms for sensor data fusion are needed. While the combination of GNSS receivers with inertial measurements units (IMUs) is a common approach, it is traditionally executed in a single-frequency/single-constellation architecture, usually with the Global Positioning System's (GPS) L1 C/A signal. With the advent of new GNSS constellations and civil signals on multiple frequencies, GNSS/IMU integration algorithm performance can be improved by utilizing these new data sources. To achieve this, we upgraded our tightly coupled GNSS/IMU integration algorithm to process measurements from GPS (L1 C/A, L2C, L5) and Galileo (E1, E5a, E5b). After investigating various combination strategies, we chose to work with ionospheric-free combinations of L5 - L1 C/A and E5a - E1 pseudo-ranges preferably. Single-frequency pseudo-ranges on L1 C/A and E1 serve as backup when no L5/E5a measurements are available. Time-differenced carrier-phase measurements on L1 C/A and E1 provide the algorithm with pseudo-range-rate observations. The performance improvement of our upgraded localization algorithm is evaluated by comparing its results with the ones from the original algorithm. The estimation errors of both algorithm versions are obtained from differences to a higher-grade reference system, consisting of a geodetic GNSS receiver for real-time kinematic positioning (RTK) and a navigation grade IMU.

I. INTRODUCTION

Localization algorithms for automotive applications are predominantly based on *global navigation satellite systems* (GNSS). Since road vehicles frequently travel in surroundings with poor satellite visibility (urban canyons, tunnels, etc.), additional sensors providing information about the vehicle's position and/or movement are commonly used. The integration of GNSS and *inertial measurement units* (IMUs) in a fusion filter is the most prominent approach, often in combination with even more sensors (e. g. odometry, cameras, etc.). In tightly coupled GNSS/IMU integration algorithms, the sensor data fusion is performed in the range domain. The fusion filter inputs pseudo-range and pseudo-range-rate

measurements from the GNSS receiver and utilizes them to correct position, velocity and attitude estimates derived from IMU measurements. Additional outputs of the fusion filter are IMU errors together with the GNSS receiver clock bias and drift [1]. Traditionally, the only GNSS signal available to civil users was the *Global Positioning System's* (GPS) L1 C/A signal. With the advent of new GNSS constellations and civil signals on multiple frequencies, GNSS/IMU integration algorithm performance can be improved by utilizing these new data sources. This introduces new effects into the localization algorithm that need to be addressed. Some of these effects are the time offset between the different GNSS times [2], the difference between the receiver hardware delays affecting the signals from different GNSS (*inter-system bias*, ISB [3]) and *differential code biases* (DCBs [4]).

In this paper, we present an approach on how to deal with these challenges in a tightly coupled GNSS/IMU integration algorithm. In the beginning, our original integration algorithm that works with GPS L1 C/A measurements as the only GNSS data is presented (section II). The first upgrade step is the inclusion of civil GPS signals on additional frequencies (L2C and L5) in section III. Afterwards, Galileo signals on E1, E5a and E5b are added to the localization algorithm in section IV. To evaluate the performance of the upgraded algorithm in comparison to the original one, the estimation errors of the three algorithm versions are presented in section V. These estimation errors are obtained from differences to a higher-grade reference system, consisting of a geodetic GNSS receiver for *real-time kinematic positioning* (RTK) and a navigation grade IMU. Finally, we discuss our conclusions in section VI.

II. ORIGINAL GPS L1 C/A ALGORITHM

The original algorithm is a tightly coupled GPS/IMU fusion filter. The central component is a closed-loop error-state *Extended Kalman Filter* (EKF) with 17 states (see Table I). Errors in attitude, velocity and position are resolved in the local navigation coordinate frame (indicated by the superscript n) with the order *east-north-up* (ENU). Errors in gyroscope and accelerometer offset are resolved in the body coordinate frame (indicated by the superscript b) with the order

TABLE I
STATE VECTOR OF THE ORIGINAL ALGORITHM

States	Description	Symbol
1-3	Attitude error	$\Delta\psi_{nb}^n$
4-6	Velocity error	Δv_{en}^n
7-9	Position error	Δp_{en}^n
10-12	Gyroscope offset error	Δb_{ω}^b
13-15	Accelerometer offset error	Δb_a^b
16	Error of GPS receiver clock bias	$\Delta c\delta t$
17	Error of GPS receiver clock drift	$\Delta c\delta \dot{t}$

front-left-up (FLU). The subscripts of the first nine states refer to the two coordinate frames being referenced to each other. For example, v_{en}^n is the velocity of the navigation frame n with respect to the earth-fixed frame e , expressed in navigation frame coordinates. Errors in receiver clock bias δt and drift $\delta \dot{t}$ are multiplied by the speed of light c to get units of meters and meters per second, respectively.

The localization algorithm inputs 3-D angular velocities and accelerations from a *microelectromechanical systems* (MEMS) IMU as well as pseudo-ranges ρ and carrier-phase measurements ϕ from the GPS receiver. The carrier-phase measurements are time-differenced to remove the wavelength ambiguity. This results in pseudo-range-rate observations $\dot{\rho}$ which are input into the EKF for velocity determination. The localization algorithm operates in two different modes: initialization and normal mode.

For initialization of the EKF's states, different sources of information are used. In addition to the state estimates, *standard deviations* (std.) to model the initialization values' accuracy are provided as well:

- Roll and pitch angle are estimated from IMU-measured accelerations. Based on offset and noise characteristics of the IMU in use, the standard deviation is set to $3\sigma = 5^\circ$.
- The yaw angle is estimated from the GPS-derived velocity under the assumption that the vehicle is traveling in a straight line without side slip. Based on velocity estimation quality of the GPS-receiver used here, a standard deviation of $3\sigma = 10^\circ$ is employed.
- Velocity and receiver clock drift are estimated based on pseudo-range-rate observations $\dot{\rho}$. The pseudo-range-rates' variance is assumed as $\sigma_{\dot{\rho}}^2 = 0.1 \text{ m}^2/\text{s}^2$.
- Position and receiver clock bias are estimated from pseudo-ranges via a single-epoch navigation solution. The pseudo-ranges' variance σ_{ρ}^2 is modeled as the sum of two parts: $\sigma_{\rho,\theta}^2$, depending on the satellite's elevation θ , and $\sigma_{\rho,C/N_0}^2$, depending on the signal's carrier to noise ratio C/N_0 .
- Gyroscope and accelerometer offset are initialized as 0. Their initial variance is based on the nominal values for the bias repeatability given by the IMU's manufacturer.

Once initialization is completed, the algorithm enters normal operation mode. Whenever a new set of IMU measurements is received, the estimated values of attitude, velocity and position

are updated in a strapdown algorithm. Simultaneously, the state vector's covariance matrix is propagated forward in time in the EKF. When new measurements from the GPS receiver are available, they get processed in two steps:

- 1) Preprocessing: Based on the a-posteriori values of receiver clock bias and drift from the last time step, the a-priori values of these quantities are propagated. Corrections for satellite and receiver clock error as well as ionospheric and tropospheric refraction are applied to pseudo-ranges and pseudo-range-rates. The measurement noise covariance for pseudo-range and pseudo-range-rate measurements is calculated. All measurements are assumed to be uncorrelated with each other, the variances for pseudo-ranges and pseudo-range-rates are the same as in initialization mode. Lastly, positions and velocities of the received satellites are computed.
- 2) Measurement update: The innovation δz is formed as difference between the corrected pseudo-range and pseudo-range-rate measurements and their predicted counterparts. These predictions are based on the a-priori estimates of attitude, velocity and position. Plausibility checks for pseudo-ranges and pseudo-range-rates are employed to detect outliers. Finally, δz and the associated measurement noise covariance are used to determine corrections for the state vector's a-priori estimates. Simultaneously, the state vector's covariance matrix is updated to reflect the newly incorporated information.

III. MULTI-FREQUENCY GPS ALGORITHM

The overall pseudo-range error, often called *user equivalent range error* (UERE), is usually decomposed into two error types which are considered statistically independent: The *signal in space ranging error* (SISRE) and the *user equipment error* (UEE) [5].

$$\text{UERE} = \sqrt{\text{SISRE}^2 + \text{UEE}^2} \quad (1)$$

Modern dual-frequency receivers provide a typical *root mean square* (RMS) ionosphere error of 0.7 m, resulting in a UEE of 0.8 m and a UERE of 2.0 m (assuming no significant multipath error). In comparison, the UEE of modern single-frequency receivers is 7.0 m, resulting in a UERE of 7.2 m [5]. Hence, multi-frequency signals accessible to civil users provide the opportunity to drastically increase measurement accuracy. Today, the GPS L2C signal is available from a total of 19 active GPS satellites (7 block IIR-M and 12 block IIF), while the GPS L5 signal is available from the 12 block IIF satellites [6]. With the upcoming launches of block IIIA GPS satellites, both numbers will increase. For Galileo (see section IV), availability of civil multi-frequency signals is not an issue as all satellites provide civil signals on E1, E5a and E5b.

To input pseudo-range measurements on additional frequencies into the localization algorithm, we considered the following alternatives:

- 1) Treat the new measurements exactly as the old ones, i.e. retain the assumption that all measurements are

uncorrelated and assign similar variances to the new pseudo-range measurements as to the old ones.

- 2) Treat measurements stemming from the same satellite as a block, i.e. assign similar variances to the new pseudo-range measurements as to the old ones but assume that pseudo-range measurements on different frequencies, but from the same satellite, are highly correlated. Pseudo-ranges from different satellites are still considered uncorrelated.
- 3) Introduce additional variables into the EKF's state vector to estimate the ionospheric refraction. The simplest version of this alternative adds a single additional state representing the zenith ionospheric delay on a reference carrier frequency. The ionospheric refraction's dependency on carrier frequency and elevation is represented in the pseudo-range measurement model. More complex versions add one state for each satellite in view, resulting in a variable-length state vector.
- 4) Work with ionospheric-free linear combinations of pseudo-ranges.

Option 1) does not model the ionospheric refraction's dependency on the carrier frequency and is therefore clearly suboptimal. Option 2) does take this dependency into account. However, this is only done implicitly via the off-diagonal entries in the measurement noise covariance matrix. The result is an increased computational load as some of the measurements are now correlated to each other. Also, parameterizing the measurement noise covariance matrix becomes more difficult. While option 3) provides a high degree of flexibility, it also increases the algorithm's complexity significantly due to the additional variables in the state vector. Ionospheric-free linear combinations (option 4) offer the advantage of being able to keep many of the existing algorithm's features: Measurements from different satellites can still be considered uncorrelated and the EKF's state vector does not need to be changed. Also, the properties of ionospheric-free combinations are well known because they have been investigated since the launch of GPS, they are the preferred mode for ionospheric corrections according to the GPS interface specifications and the navigation data messages on L2C and L5 (CNAV) provide terms to correct for the effects of satellite-specific DCBs in the respective combinations [7], [8]. On the other hand, ionospheric-free linear combinations only support dual-frequency measurements and not three or even more measurement frequencies. They also suffer from increased code tracking noise [1]:

$$\sigma_{\rho, IF} = \frac{\sqrt{f_{\alpha}^4 \sigma_{\rho, \alpha}^2 + f_{\beta}^4 \sigma_{\rho, \beta}^2}}{|f_{\alpha}^2 + f_{\beta}^2|} \quad (2)$$

where $\sigma_{\rho, IF}$, $\sigma_{\rho, \alpha}$ and $\sigma_{\rho, \beta}$ are the code tracking error standard deviations for the ionospheric-free combination (IF), the first signal (α) and the second signal (β), and f_{α} and f_{β} are the first and second signal's carrier frequency. When taking into account the slightly different code tracking error standard deviations due to different transmission powers for each signal, this results in an amplification of the standard deviation by

a factor of ca. 3.36 (for L2C - L1 C/A combinations) or ca. 2.59 (for L5 - L1 C/A combinations) in comparison to single-frequency L1 C/A measurements [1].

We decided to implement option 4) because it offers the main advantage of multi-frequency measurements (eliminating the ionospheric error almost completely) while only requiring changes to the algorithm's GPS preprocessing and not to the EKF and its state vector. The lack of support for three or more carrier frequencies is not a significant issue, as the inclusion of more than two frequencies offers diminishing performance improvements when compared to the improvement achieved by integrating a second frequency. As the Kalman Filter possesses an inherent smoothing ability, it attenuates the increased measurement noise's effect, hence mitigating the second disadvantage of ionospheric-free linear combinations. While carrier-phase measurements are available for the signals on all frequencies, we continue to use only the ones on L1 C/A for calculation of pseudo-range-rates. That's because there are no significant frequency-dependent effects in time-differenced carrier-phase measurements.

According to the GPS interface specifications [7], [8], the ionospheric-free linear combinations based on the CNAV message for L1 C/A, L2C, L5I and L5Q are:

$$\rho_{IF} = \frac{(\rho_{\alpha} - \gamma_{\beta\alpha}\rho_{\beta}) + c(\text{ISC}_{\alpha} - \gamma_{\beta\alpha}\text{ISC}_{\beta})}{1 - \gamma_{\beta\alpha}} - cT_{GD} \quad (3)$$

where α and β stand for either L1 C/A, L2C, L5I or L5Q. $\gamma_{\beta\alpha}$ is the squared ratio between the respective carrier frequencies, c is the speed of light, ISC_i is the inter-signal correction term for the channel indicated by the subscript i (equivalent to the term "satellite-specific DCB" [4]) and T_{GD} is the timing group delay from the GPS *legacy navigation message* (LNAV). Accessing the ISCs is problematic as the *Receiver Independent Exchange Format* (RINEX) in its current version 3.03 only supports GPS LNAV data [9]. To avoid these restrictions, we make use of a CNAV-compatible RINEX-style format developed for the CNAV test campaign in 2013 [10] and the corresponding navigation files provided by the *Crustal Dynamics Data Information System* (CDDIS) [11]. For the calculation of satellite positions, we continue to use the ephemeris provided by the LNAV message in order to preserve compatibility with block IIR and earlier GPS satellites as well as Galileo, whose ephemeris representation is identical to GPS LNAV.

We initially implemented an algorithm capable of working with L2C - L1 C/A combinations, L5I - L1 C/A combinations, L5Q - L1 C/A combinations and single-frequency L1 C/A measurements simultaneously. Based on the available pseudo-range measurements at each epoch, the GPS preprocessing decides what data it forwards to the EKF and computes a matching variance. From most favorable to least favorable, the hierarchy is L5Q - L1 C/A > L5I - L1 C/A > L2C - L1 C/A > L1 C/A. The variance is given by:

$$\sigma_{\rho}^2 = \sigma_{\rho, \theta}^2 + \sigma_{\rho, C/N_0}^2 - \sigma_{iono}^2 \quad (4)$$

TABLE II
DIFFERENCES IN ESTIMATED RECEIVER CLOCK BIAS (COMPARED TO
SINGLE-FREQUENCY L1 C/A PROCESSING) AND POSITIONING
PERFORMANCE FOR THREE SETS OF MEASUREMENT DATA

Processed Code Observations	Mean and Std. of Difference (in m)	Positioning Performance (ranked)
L1 C/A	0 / 0 / 0 0 / 0 / 0	2 / 2 / 4
L2C(M+L) - L1 C/A	-6.5 / -7.5 / -6.9 1.5 / 1.8 / 2.4	3 / 3 / 2
L2C(M+L) - L1 C/A > L1 C/A	-1.5 / 0.7 / -4.3 1.7 / 1.7 / 2.1	4 / 5 / 1
L5(I+Q) - L1 C/A	1.6 / N/A / N/A 11.9 / N/A / N/A	7 / N/A / N/A
L5(I+Q) - L1 C/A > L1 C/A	-0.7 / -0.5 / -0.6 0.7 / 0.5 / 0.6	1 / 1 / 2
L5(I+Q) - L1 C/A > L2C(M+L) - L1 C/A	3.0 / -8.4 / -7.4 8.1 / 7.2 / 2.8	6 / 6 / 6
L5(I+Q) - L1 C/A > L2C(M+L) - L1 C/A > L1 C/A	0.3 / -0.6 / -5.3 2.0 / 1.5 / 2.1	5 / 4 / 5

where the first two terms $\sigma_{\rho,\theta}^2$ and $\sigma_{\rho,C/N_0}^2$ are the same as they were for the original GPS L1 C/A algorithm. The last term σ_{iono}^2 describes the magnitude of the accuracy improvement due to the elimination of ionospheric errors. It is 0 for single-frequency measurements and is assigned according to (5) for ionospheric-free combinations.

$$\sigma_{iono}^2 = \begin{cases} 25 \text{ m}^2, & \text{for } \theta \geq 20^\circ \\ \frac{\sin 20^\circ}{\sin \theta} \cdot 25 \text{ m}^2, & \text{for } \theta < 20^\circ \end{cases} \quad (5)$$

This way, the ionospheric-free linear combinations get assigned a lower measurement noise variance than single-frequency pseudo-ranges. This contradicts (2), which specifies an increased standard deviation of ionospheric-free linear combinations compared to single-frequency pseudo-ranges. The contradiction is resolved by looking at the Kalman Filter's assumptions for measurement noise: zero-mean, Gaussian and uncorrelated in time. Noise of this type is fully specified by its covariance matrix. Unfortunately, none of these assumptions is true for pseudo-range measurements. Consequently, the measurement noise's variance is increased, especially to account for the nonzero mean of pseudo-range errors. The mean error's absolute value for ionospheric-free combinations is substantially smaller than for single-frequency measurements, because the ionospheric error is the largest contributor to the overall error. That's why the ionospheric-free combinations are modeled with smaller measurement noise variance as far as the Kalman Filter is concerned. However, σ_{iono} is set somewhat smaller than the typical ionospheric error for single-frequency measurements (7.0 m according to [5]) to reflect the increased code tracking noise for ionospheric-free combinations.

While the measurement noise variance model turned out to be feasible, the idea to work with all possible ionospheric-free

linear combinations as well as single-frequency pseudo-ranges did not. Firstly, our GNSS receiver (a JAVAD TRIUMPH-LS) does not track the in-phase and quadra-phase component on L5 independently, but uses a combined I+Q tracking. The resulting pseudo-ranges receive the observation code C5X in RINEX 3.03 [9]. No ISCs are provided in the CNAV message for this type of code tracking, so the satellite-specific DCBs cannot be eliminated in the way they could for independent I and Q tracking. In the following results, GPS C5X pseudo-ranges are processed with the ISCs for GPS L5I. Secondly, the receiver-specific DCBs proved to be too large to facilitate an easy composition of different ionospheric-free combinations and single-frequency pseudo-ranges. While we did not estimate receiver-specific DCBs for this particular receiver, we found that the estimated receiver clock bias differs significantly depending on what types of code observations are processed.

These results are summarized in Table II. $\text{c}\delta t_{L1 \text{ C/A}}$, the receiver clock bias obtained from the EKF outputs when only processing L1 C/A pseudo-ranges, is treated as reference. The entries in the second column are gained by computing the mean and standard deviation of the differences $\text{c}\delta t_{L1 \text{ C/A}} - \text{c}\delta t_i$, where the subscript i indicates the type of processed code observations and is specified in the first column. The first line in each cell specifies the mean, the second line specifies the standard deviation. The three entries in each line stem from three different sets of measurement data, collected between December 2016 and November 2017. As the code biases in their nondifferential form cannot be separated from the receiver clock bias, the difference in receiver clock bias is an indication for the DCBs. The last column ranks the positioning performance in each data set from best (1) to worst (7), based on the RMS position error. For two of the three data sets, it was not possible to compute a solution with L5 - L1 C/A combinations only, because there were not enough block IIF satellites in view. The first data set contains just barely enough block IIF satellites, but the low number of pseudo-range measurements results in the highest standard deviation for the receiver clock bias difference as well as the worst positioning performance. The L2C - L1 C/A combinations exhibit large differences in receiver clock bias when compared to the single-frequency L1 C/A measurements (up to -7.5 m). Consequently, combining these two types of observations results in degraded positioning performance. The third data set is an exception and offers very good positioning performance when processing both L2C - L1 C/A combinations and single-frequency L1 C/A measurements together. This happens because while recording this data set, only very few older GPS satellites (block IIR and earlier) were received. Most of the visible satellites provided L2C signals, causing the solution to be close to the one where only L2C - L1 C/A combinations were processed. While the difference in estimated receiver clock bias could not be computed reliably when only processing L5 - L1 C/A combinations, the low values of mean and standard deviation as well as the good positioning performance when processing both L5 - L1 C/A

TABLE III
STATE VECTOR OF THE MULTI-GNSS ALGORITHM

States	Description	Symbol
1-3	Attitude error	$\Delta\psi_{nb}^n$
4-6	Velocity error	Δv_{en}^n
7-9	Position error	Δp_{en}^n
10-12	Gyroscope offset error	Δb_{ω}^b
13-15	Accelerometer offset error	Δb_a^b
16	Error of GPS receiver clock bias	$\Delta c\delta t_{GPS}$
17	Error of GPS receiver clock drift	$\Delta c\delta \dot{t}_{GPS}$
18	Error of Gal. receiver clock bias	$\Delta c\delta t_{Gal}$
19	Error of Gal. receiver clock drift	$\Delta c\delta \dot{t}_{Gal}$

combinations and single-frequency L1 C/A measurements together indicates that there are no significant DCBs for these two types of observations. The poor positioning performance whenever both L2C - L1 C/A and L5 - L1 C/A combinations are processed together suggests that substantial DCBs between these two types of observations exist. Due to these results, we decided not to work with all types of possible combinations simultaneously. Instead, we use L5 - L1 C/A combinations whenever they are available and single-frequency L1 C/A measurements as backup. L2C measurements and the resulting ionospheric-free combinations are discarded.

IV. MULTI-GNSS ALGORITHM (GPS AND GALILEO)

Road vehicles frequently travel in surroundings with partially obstructed sky view. These obstructions include buildings, trees, bridges and other vehicles. Consequently, the number of received satellites is smaller than it would be under an unobstructed sky. Received signals may suffer from reduced C/N_0 and increased multipath due to signal reflections on surrounding surfaces. During periods of limited satellite visibility, enabling the localization algorithm to process signals from additional GNSS constellations mitigates these negative effects by increasing the number of available satellites. Galileo implements the same ephemeris representation as the GPS LNAV message. It's also a *code division multiple access* (CDMA) system and shares two common carrier frequencies with GPS: L1/E1 at 1575.42 MHz and L5/E5a at 1176.45 MHz. All Galileo satellites broadcast civil signals on multiple frequencies. These characteristics make Galileo an ideal choice for a second GNSS to work together with GPS in automotive positioning.

To enable Galileo processing, we changed both the pre-processing routine and the EKF slightly. Two states were added to the EKF's state vector: Galileo receiver clock bias and drift (see Table III). Although the same receiver is used for both GNSS, the additional states are necessary to account for the offset between the different GNSS times as well as receiver-specific ISBs. Alternatively, 17 states could be maintained and the timing differences between GPS and Galileo could be compensated via the *GPS to Galileo Time Offset* (GGTO) extracted from one of the navigation messages or the *GPS to Galileo time system correction* (GPGA) in the

respective RINEX files. In our case, this approach did not succeed as the receiver-specific timing biases are too large to be ignored and the parameters in the navigation messages only address the satellite-specific timing biases. During the measurement update, pseudo-ranges and pseudo-range-rates to GPS satellites affect states 16 and 17, while pseudo-ranges and pseudo-range-rates to Galileo satellites affect states 18 and 19. All parameters concerning the EKF's stochastic model (e.g. σ_{ρ}^2 , $\sigma_{\dot{\rho}}^2$, system and initial state covariance matrices) are set to the same values for Galileo as they are for GPS. Since the additional states need to be initialized, the single-epoch navigation solutions entrusted with this task now output five quantities instead of four: 3-D position and two receiver clock biases estimated from pseudo-ranges on the one hand and 3-D velocity and two receiver clock drifts estimated from pseudo-range-rates on the other hand. Consequently, at least five observations are necessary to initialize all states, with at least one stemming from each GNSS.

For compatibility with GPS L5 - L1 C/A combinations, we chose to work with E5a - E1 combinations for Galileo preferably. The clock correction parameters for this type of combinations are distributed via Galileo's *Freely Accessible Navigation Message* (F/NAV). The parameters are also valid for single-frequency E5a processing, but not for E5b - E1 combinations and single-frequency pseudo-ranges on E1 or E5b. In order to process the latter three types of observations correctly, clock correction parameters from Galileo's *Integrity Navigation Message* (I/NAV) have to be used [12].

To find the best possible subset of Galileo pseudo-ranges to process, we conducted a similar analysis for Galileo observations as we did for GPS in section III, with single-frequency E1 processing as reference. The differences in the estimated receiver clock biases were much smaller. In all three data sets, the best positioning performance was achieved when processing GPS L5 - L1 C/A and Galileo E5a - E1 combinations primarily while using GPS L1 C/A and Galileo E1 single-frequency pseudo-ranges as backup whenever L5/E5a measurements were unavailable. Because all Galileo satellites broadcast civil signals on multiple frequencies, only 5 % of the processed code observations are single-frequency pseudo-ranges, compared to 67 % for GPS. Overall, 51 % of all processed code observations are single-frequency. Since the percentage of processed single-frequency Galileo pseudo-ranges is so small, they do not affect the positioning performance substantially. Consequently, we chose not to include the data from the I/NAV message and Galileo's ionospheric correction algorithm for single-frequency users in order to prevent unnecessary complexity. Clock correction parameters and the *Broadcast Group Delay* (BGD) from the F/NAV message as well as the GPS Klobuchar model are used instead. As it does for GPS L5, the JAVAD TRIUMPH-LS does not track the data and pilot components on Galileo E1 and E5a separately. Instead, a combined tracking of E1-B + E1-C is used on E1 and a combined tracking of E5a-I + E5a-Q is used on E5a. The resulting pseudo-ranges receive the observation codes C1X and C5X in RINEX 3.03, respectively.

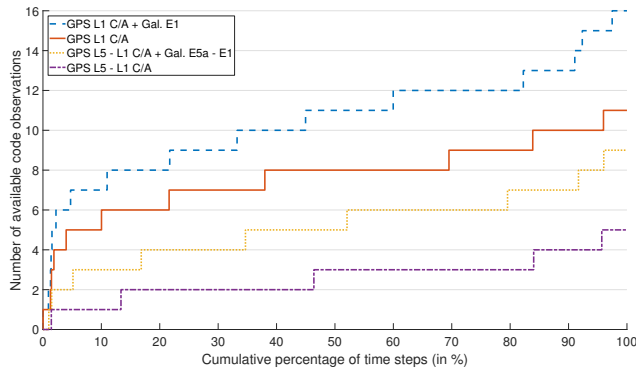


Fig. 1. Percentage of GNSS measurement time steps on which no more than the indicated number of code observations was received.

V. PERFORMANCE COMPARISON

In order to assess the performance of the upgraded localization algorithm, three sets of measurement data were collected and evaluated. GNSS input data for the integration algorithm were recorded with a JAVAD TRIUMPH-LS, operating at either 10 Hz (for the first two data sets) or 5 Hz (for the last data set). The measurement frequency was reduced because the receiver frequently crashed when recording data with more than 5 Hz over periods longer than 15 min. IMU input data for the integration algorithm were recorded with an Xsens MTi-G-700 operating at 100 Hz.

A reference solution was computed with Novatel's Waypoint - Inertial Explorer software, using multi-frequency GNSS data from two JAVAD TRIUMPH-LS (base with 1 Hz and rover with 10 Hz/5 Hz) and inertial data from a navigation grade IMU (iMAR iNAV-RQH-1003 operating at 300 Hz). Using RTK, inertial data and the ability to process and smooth the results both forwards and backwards in time, the resulting reference trajectory achieves 3-D position standard deviations of less than 10 cm in 95 % of the time.

The three sets of measurement data are:

- 1) Roughly two hour long drive over a distance of approx. 100 km on December 2nd, 2016, including towns with multi-story buildings on both sides of the road, villages with smaller houses, country roads (with and without forest) and freeways.
- 2) Roughly one hour long drive over a distance of approx. 13 km on December 2nd, 2016, through the inner city of Darmstadt, including two passages through tunnels, each lasting roughly 30 s.
- 3) Roughly 30 min long drive over a distance of approx. 8 km on November 30th, 2017, through the inner city of Darmstadt, including two passages through tunnels, each lasting roughly 30 s.

In Fig. 1 and Fig. 2, information from all three data sets is displayed jointly. In both figures, satellites with an elevation smaller than 5° are neglected. As Fig. 1 shows, single-frequency GPS L1 C/A pseudo-ranges from at least four satellites are available more than 95 % of the time, while at

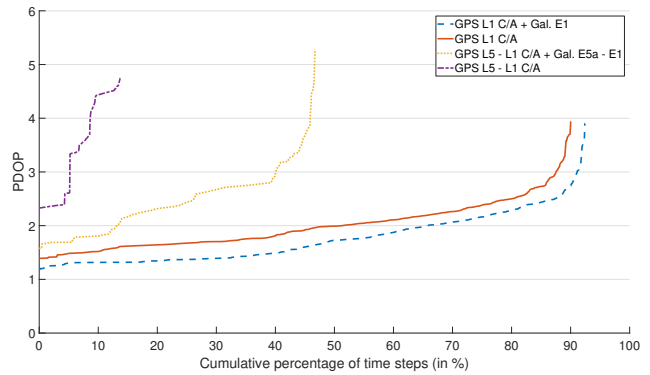


Fig. 2. Percentage of GNSS measurement time steps on which PDOP was no worse than indicated.

least eight satellites are available more than 60 % of the time. A maximum eleven satellites are received simultaneously. For L5 - L1 C/A combinations, the situation is considerably different: pseudo-ranges from at least four satellites are only available 15 % of the time, making initialization with only this type of observation impossible most of the time. This corresponds to the information in Table II, where only the first data set delivered a solution. When taking Galileo E5a - E1 combinations into account as well, the situation becomes a lot better. While now at least five satellites are needed to initialize all the states, this is true in ca. 65 % of the time. GNSS measurement time steps with eight or more visible satellites are still rare and account for less than 10 % of the total amount of GNSS measurement time steps. The best results occur for joint processing of single-frequency pseudo-ranges on GPS L1 C/A and Galileo E1: at least five satellites are visible more than 95 % of the time, at least eight more than 85 % of the time and at least twelve more than 35 % of the time. This demonstrates the advantages of our approach to work with ionospheric-free combinations preferably, but use L1 C/A and E1 single-frequency pseudo-ranges as backup whenever observations on L5/E5a are unavailable. The advantage is more pronounced on GPS than on Galileo since all Galileo satellites broadcast E5a signals while currently only 12 out of 31 GPS satellites broadcast L5 signals [6].

Fig. 2 displays how the varying number of simultaneously available pseudo-ranges affects the *position dilution of precision* (PDOP). PDOP is only calculated if a single-epoch navigation solution was computed successfully. Both variants of single-frequency processing provide a PDOP smaller than 3 more than 85 % of the time, while this percentage drops to roughly 40 % for dual-constellation ionospheric-free combinations and less than 10 % for GPS L5 - L1 C/A observations. The inclusion of Galileo E1 pseudo-ranges improves the signal geometry for all GNSS measurement time steps. In addition, the percentage of GNSS measurement time steps on which a valid single-epoch navigation solution was computed increases from ca. 90 % (for GPS L1 C/A) to more than 92 %. For ionospheric-free combinations, this percentage rises

TABLE IV
POSITIONING PERFORMANCE OF THE DIFFERENT ALGORITHM VERSIONS. MEAN, EMPIRICAL STANDARD DEVIATION AND RMS ARE GIVEN IN THE EAST-NORTH-UP COORDINATE FRAME.

Algorithm Version	Data Set	Mean of Error (in m)	Empirical Std. of Error (in m)	RMS of Error (in m)	Hor. 50 % / 95 % Error Quantiles (in m)	Vert. 50 % / 95 % Error Quantiles (in m)
GPS L1 C/A	1	[0.1; -0.9; -3.5]	[0.5; 1.2; 1.6]	[0.5; 1.5; 3.8]	1.1 / 2.6	3.6 / 5.7
	2	[-1.9; 0.7; -0.4]	[2.5; 2.5; 2.0]	[3.2; 2.6; 2.0]	2.3 / 4.6	1.6 / 4.1
	3	[0.2; 1.2; -0.7]	[2.0; 3.3; 3.9]	[2.0; 3.5; 4.0]	1.7 / 6.3	1.9 / 9.1
Multi-Frequency GPS	1	[-0.1; -0.9; -2.6]	[0.6; 1.1; 1.7]	[0.6; 1.5; 3.1]	1.2 / 2.7	2.7 / 5.2
	2	[-1.9; 0.5; 0.3]	[2.6; 2.4; 1.9]	[3.2; 2.5; 2.0]	2.3 / 4.6	1.1 / 4.6
	3	[0.4; 1.1; 0.1]	[2.0; 3.2; 3.4]	[2.0; 3.4; 3.4]	1.7 / 4.8	1.1 / 8.6
Multi-Frequency/ Multi-Constellation GNSS	1	[-0.0; -1.1; -2.9]	[0.5; 0.8; 1.4]	[0.5; 1.4; 3.2]	1.2 / 2.6	2.8 / 5.2
	2	[-1.8; -0.4; -0.2]	[2.4; 2.1; 2.0]	[3.0; 2.2; 2.0]	2.2 / 4.1	1.4 / 4.2
	3	[0.2; 0.7; 0.8]	[2.0; 3.2; 2.3]	[2.0; 3.3; 2.5]	1.2 / 4.0	0.7 / 6.5

from less than 14 % for GPS L5 - L1 C/A to more than 46 % when Galileo E5a - E1 combinations are included. It's also apparent that the availability of the minimal amount of satellites necessary to compute a solution does not necessarily mean that a solution can be computed in practice. E.g. while dual-frequency observations from at least five satellites are received ca. 65 % of the time with dual-constellation processing, a valid solution is only found ca. 50 % of the time. For the remaining 15 % of GNSS measurement time steps, no valid solution was computed because outliers were detected, the norm of the residuals was too large or the iteration process did not converge. The same holds for the other three processing types, although the effect occurs less often. Once again, the advantage of using single-frequency pseudo-ranges as backup to ionospheric-free combinations is demonstrated because the good signal geometry of single-frequency processing is combined with the superior accuracy of dual-frequency observations.

Table IV quantifies the positioning performance of the three different algorithm versions. Accuracy is quantified by the estimation error \tilde{x} and its statistical distribution. \tilde{x} is defined as the difference between the value \hat{x} , estimated by the navigation algorithm being evaluated, and the reference value x_{ref} .

$$\tilde{x}(k) = \hat{x}(k) - x_{ref}(k) \quad (6)$$

k is an arbitrary point in time and takes on values between 1 and $N_j \in \mathbb{N}$ during one data set j . The reference value is provided by the reference trajectory. Depending on the type of quantity being evaluated, \tilde{x} can be a scalar or a vector. In both cases, the error is a random variable and fully characterized by its cumulative distribution function (CDF) [13]. In this paper, we focus on the 3-D position error \tilde{p} , resolved in the local navigation coordinate frame with the order east-north-up. The reason for this focusing is the fact that the different variants of pseudo-range processing directly influence the position accuracy, while attitude and velocity estimation are mainly based on pseudo-range-rate observations. When comparing the three data sets in Table IV to each other, set 1 possesses the lowest empirical standard deviation while set 3 has the highest. Since set 1 is both the longest one and

features the least amount of signal path obstructions while the opposite is true for set 3, this outcome is plausible. Similar statements can be made for the RMS error, although data set 1 possesses a comparatively large vertical RMS. While this might stem from a high residual ionospheric error in case of single-frequency processing, the effect should be significantly smaller for multi-frequency processing. Since this is not the case, it's unclear what causes the large vertical RMS error. The comparison of the different algorithm versions shows that multi-frequency observations decrease the RMS error. For GPS L1 C/A vs. multi-frequency GPS, the respective column of Table IV displays a reduced RMS for four out of nine entries, while four entries stay the same and one increases slightly. Multi-frequency/multi-constellation GNSS offers the best or tied best RMS for all of the nine entries. With the exception of the marginally higher vertical component in data set 2, the same holds for the empirical standard deviation. This proves that the EKF's smoothing ability attenuates the effect of increased noise for the ionospheric-free linear combinations successfully. As far as error quantiles are concerned, the multi-frequency/multi-constellation algorithm version delivers the best results as well. With the exception of one of the six horizontal quantiles and two of the six vertical quantiles, the multi-frequency/multi-constellation version of the algorithm delivers the best or tied best error quantiles. The biggest improvement occurs for data set 3: Compared to single-frequency GPS L1 C/A processing, the 50 % / 95 % error quantiles improve from 1.7 m / 6.3 m to 1.2 m / 4.0 m (horizontally) and from 1.9 m / 9.1 m to 0.7 m / 6.5 m (vertically). Since data set 3 features the highest percentage of signal path obstructions, this outcome verifies that additional satellites are most beneficial in situations with poor - but existing - satellite visibility.

Although this paper's focus is the position error, Table V also presents some accuracy metrics for attitude (order roll-pitch-yaw) and velocity. As velocity estimation happens in the navigation coordinate frame, but velocity accuracy in the body coordinate frame is more important in the automotive domain, the accuracy metrics for velocity are evaluated in both frames. Only the results for the

TABLE V
ACCURACY METRICS FOR ATTITUDE (ROLL; PITCH; YAW), VELOCITY
AND POSITION ERROR. MULTI-FREQUENCY/MULTI-CONSTELLATION
ALGORITHM, ALL THREE DATA SETS.

Quantity	Unit	Mean	Empirical Std.	RMS
$\hat{\psi}_{nb}^n$	°	[-0.0; -0.0; -0.1]	[0.2; 0.2; 0.9]	[0.2; 0.2; 0.9]
\hat{v}_{en}^b	m/s	[-0.0; 0.0; -0.0]	[0.3; 0.2; 0.1]	[0.3; 0.2; 0.1]
\hat{v}_{en}^n	m/s	[-0.0; -0.0; 0.0]	[0.1; 0.1; 0.1]	[0.1; 0.1; 0.1]
\hat{p}_{en}^n	m	[-0.5; -0.6; -1.6]	[1.7; 1.9; 2.3]	[1.8; 2.0; 2.8]

multi-frequency/multi-constellation algorithm are shown and all three data sets were evaluated jointly. Compared to the other two algorithm versions, the only significant differences occur for the position error. The accuracy of attitude and velocity estimation is very high in all algorithm versions. The yaw angle's RMS error is substantially higher than the RMS error for roll and pitch. This is plausible because a road vehicle's yaw angle changes both faster and within a larger range than its roll and pitch angles. Additionally, yaw angle estimation within a GNSS/IMU integration algorithm is more difficult than the estimation of roll and pitch angles. That's because earth's gravity vector can be used for estimation of roll and pitch angles, but not for the yaw angle. The errors in yaw angle estimation also influence the quality of velocity estimation in the body coordinate frame: Standard deviation and RMS error in longitudinal and lateral direction are increased in comparison to the navigation frame, while the vertical velocity is estimated with the same quality in both coordinate frames.

VI. CONCLUSIONS

This paper describes a way to incorporate observations from multiple GNSS constellations and on multiple carrier frequencies into a tightly coupled GNSS/IMU integration algorithm. An existing algorithm working with GPS L1 C/A measurements only is upgraded to include code measurements on GPS L2C and GPS L5 in a first step. The pseudo-ranges on different carrier frequencies are used to form ionospheric-free linear combinations. These combinations directly cancel out most of the ionospheric error and can be processed without having to change the EKF's state vector. The increased code tracking noise of ionospheric-free combinations is filtered out due to the EKF's inherent smoothing capability and does not influence positioning performance negatively. Due to large DCBs on GPS L2C, these pseudo-ranges are discarded. Instead, GPS L5 - L1 C/A combinations are used whenever available and single-frequency L1 C/A pseudo-ranges serve as backup. This approach works well as long as there are no significant DCBs between these two types of observations. In order to verify this, the DCBs need to be calibrated and their long-term stability has to be investigated. We plan to do so in the future. When this process is expanded to all available signals, it may be possible to reintroduce L2C pseudo-ranges

and even additional signals (e.g. L1C) if the DCBs can be calibrated well enough and have sufficient long-term stability.

The inclusion of Galileo observations introduces two additional biases: the GGTO and an ISB. While the former could be compensated via information from one of the navigation messages, the latter proved to be too large to be ignored. As the two biases influence the observations in the same way, they can be subsumed into one bias term. To absorb the effects of this bias term and its possible drift over time, two states for Galileo receiver clock bias and drift were added to the EKF's state vector. Since an ISB influences pseudo-ranges in the same way as DCBs, it can be calibrated in the same way. If this is possible sufficiently well and the ISB has high long-term stability, the EKF's two additional states can be removed. While currently Galileo E5a - E1 combinations are used whenever available and single-frequency E1 pseudo-ranges serve as backup, a precise calibration of Galileo DCBs would enable the utilization of further Galileo signals (e.g. E5b, E5AltBOC) in case the E5a - E1 combination is unavailable. The results obtained so far indicate that the receiver clock drift is identical for both GPS and Galileo processing. This means that even without ISB calibration, one common drift state for GPS and Galileo is sufficient, resulting in a state vector with 18 entries.

The evaluation of three data sets proves the advantages of multi-frequency/multi-constellation observations. Inclusion of Galileo satellites increases the number of simultaneously available measurements and reduces the PDOP. This is especially true for ionospheric-free linear combinations because all Galileo satellites transmit E5a signals, while only 12 out of 31 GPS satellites transmitted L5 signals when the data sets were recorded. Consequently, only 5 % of the processed Galileo code observations are single-frequency pseudo-ranges while this number is 67 % for GPS and 51 % for both constellations combined. In terms of positioning performance, the utilization of ionospheric-free combinations reduces the RMS error, especially its vertical component. Due to the increased number of satellites and the usage of single-frequency code observations as backup, the error's empirical standard deviation decreases slightly as well. The largest improvements occur in situations with only a few visible satellites, e.g. densely populated areas with multi-story buildings close to the road.

The future launch and commissioning of block IIIA GPS satellites as well as further Galileo satellites will allow our algorithm to work with a large number of ionospheric-free combinations most of the time. As the percentage of single-frequency observations that have to be used as backup decreases, the positioning performance will improve further.

REFERENCES

- [1] P. D. Groves, *Principles of GNSS, Inertial, and Multisensor Integrated Navigation Systems*. Boston and London: Artech House, 2013.
- [2] A. D. Torre and A. Caporali, "An analysis of intersystem biases for multi-GNSS positioning," *GPS Solutions*, vol. 19, no. 2, pp. 297–307, 2015.
- [3] J. Paziewski and P. Wielgosz, "Accounting for Galileo–GPS inter-system biases in precise satellite positioning," *Journal of Geodesy*, vol. 89, no. 1, pp. 81–93, 2015.

- [4] O. Montenbruck, A. Hauschild, and P. Steigenberger, "Differential Code Bias Estimation using Multi-GNSS Observations and Global Ionosphere Maps," *Navigation*, vol. 61, no. 3, pp. 191–201, 2014.
- [5] J. W. Betz, *Engineering Satellite-Based Navigation and Timing: Global Navigation Satellite Systems, Signals, and Receivers*. Hoboken, New Jersey: Wiley, 2016.
- [6] Navigation Center. (2018) GPS Constellation Status. [Online]. Available: <https://www.navcen.uscg.gov/?Do=constellationStatus>
- [7] IS-GPS-200, *Interface Specification IS-GPS-200: NAVSTAR GPS Space Segment/Navigation User Segment Interfaces: Revision H, including IRNs 001 through 005*. Global Positioning Systems Directorate, 2017.
- [8] IS-GPS-705, *Interface Specification IS-GPS-705: NAVSTAR GPS Space Segment/Navigation User Segment L5 Interfaces: Revision D, including IRNs 001 through 004*. Global Positioning Systems Directorate, 2017.
- [9] IGS, *RINEX: The Receiver Independent Exchange Format: Version 3.03, Update 1*. International GNSS Service (IGS), RINEX Working Group and Radio Technical Commission for Maritime Services Special Committee 104 (RTCM-SC104), 2017.
- [10] O. Montenbruck and R. Langley. (2013) CNAV Test Data Set. [Online]. Available: <ftp://ftp.cddis.eosdis.nasa.gov/gnss/data/campaign/cnav/2013/06/aaaReadme.txt>
- [11] Crustal Dynamics Data Information System. (2018) Daily RINEX-Style Files for CNAV Data. [Online]. Available: <ftp://cddis.gsfc.nasa.gov/gnss/data/campaign/mgex/daily/rinex3/2018/cnav/>
- [12] Galileo OS-SIS-ICD, *Galileo Open Service Signal-in-Space Interface Control Document: Issue 1, Revision 3*. European Global Navigation Satellite Systems Agency, 2016.
- [13] F. Peyret, "Standardization of performances of GNSS-based positioning terminals for ITS applications at CEN/CENELEC/TC5," in *Proceedings of the Intelligent Transportation Systems World Congress 2013*, 2013.

Simulation and Verification for New Generation BDS Satellite Signals

Ying Wang, Tao Yan

China Academy of Space Technology (CAST)(Xi'an)
Xi'an, China
eaglesoars@126.com

Abstract—Satellite Launch Center successfully launched two BDS-3 satellites with a Long March-3B rocket on Sunday, November 5, 2017. After the satellites' downlink payload is opened, we use the 6m dish antenna system of China Academy of Space Technology (Xi'an) to receive, collect and analyze satellite navigation signals. Since the bad electromagnetic environment of B2, the signal is disturbed seriously. B1 frequency is relatively pure, so only some preliminary results of B1 signal analysis are given here. In this paper, the structure of the acquisition system, the simulation of B1 new signal and some preliminary analysis results of the software receiver are given. The processing results of the signal show that the two satellites' B1 signal is normally being transmitted in China.

Keywords—BDS-3; B1; In-Orbit Validation; QMBOC.

I. INTRODUCTION

China Satellite Navigation Office formally issued BDS Signal In Space Interface Control Document (SIS ICD) Open Service Signal B1C (Version 1.0) and B2a (Version 1.0) on 27 December 2017 [1]-[2]. So, including B1I, BDS has three Open Service (OS) signals which details are published [3]. It is beneficial to the research and application all over the world. Around 2020, a network of BDS-3 30 satellites will be completed to provide services to the world. The two satellites launched on 5 November 2017 are the first starters of the new generation of BDS system. From the spectrum analysis in this paper, the above three civil signals have been broadcasting to the user, including the B1C QMBOC signal [4].

At present, the two satellites actually contain 4 signal components, including B1I, B1C data (B1Cd), B1C_pilot (B1Cp) and an authorization signal which can be seen from 1575.42+14.322MHz. More signal components and the asymmetric spectrum design make B1 signal more different from Galileo E1 and GPS L1, even these signals can be compatible with each other [5]-[6].

In this paper, the signal acquisition and processing system including 6m dish antenna system is introduced in Section II. The main features of BDS-3 B1 signal are described in Section III. Then the signal data is collected in January 2018.

II. SIGNAL ACQUISITION AND PROCESSING SYSTEM

The GNSS monitoring laboratory built in 2015 is located in the Xi'an branch of the Chinese Academy of space technology (CAST). The main equipment is a 6m aperture dish antenna on

the top of the building. The aim is to receive the GNSS satellite signals and to carry out the signal quality analysis. Another task is to monitor the changes of the payload on the BDS satellites.

Around the 6m dish antenna, the system is mainly made up of several parts (See Fig.1):

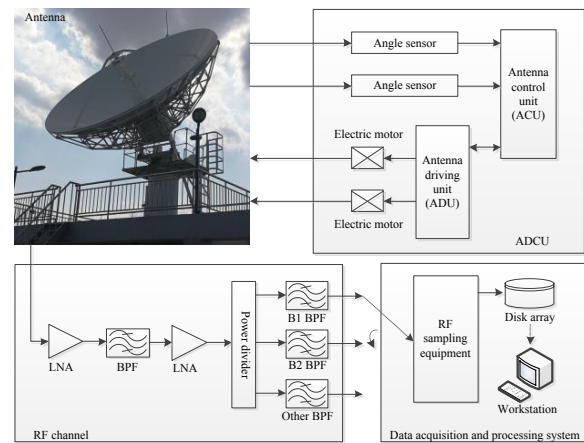


Fig.1 Block diagram of GNSS monitoring laboratory signal acquisition and processing system.

A. Antenna Driving and Control Unit(ADCU)

The ADCU includes two antenna angle sensors, two drive motors, ACU and ADU. The section of ACU has an interface to input the elevation angle and azimuth angle, and the antenna can be rotated to the specified position according to the setting. The ADCU is not yet able to track satellites automatically according to the ephemeris.

B. RF Channel

The RF channel includes two LNA and a wide band band-pass filter covering 1.1GHz~1.6GHz. The total gain of the RF channel is greater than 80dB. The power suppression for the mobile communication frequency is greater than 60dB.

C. Data Acquisition and Processing System

The high speed acquisition equipment can carry out 750Msps direct sampling and storage for radio frequency signals by 8bits. At this time, the center frequency of B1 signal is located at $1575.42 \times 750 = 75.42\text{MHz}$.

We don't have any hard receiver which can receive the new satellites' signal, so we don't know the orbit parameter. Fortunately, Celestrak have shown the NORAD Two-Line Element (TLE) on its website [7]. Since the position of the antenna and the satellites is known, we can calculate the azimuth angle and elevation angle. So the antenna can be adjusted at a fixed time and we just wait for the satellite to enter the visual field.

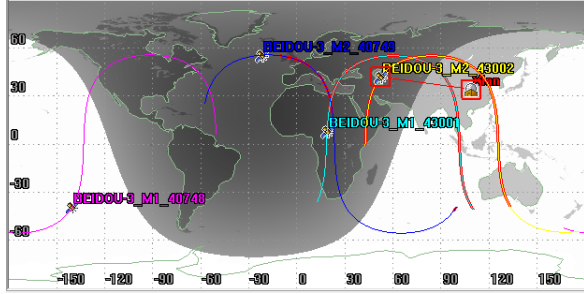


Fig.2 BDS-3 satellite orbit.

It is worth noting that there are four MEO BDSIII satellites in orbit actually now. The two experimental satellites (BEIDOU-3_M1_40748 and BEIDOU-3_M2_40749) launched in 2015 were not involved in the study. Two new satellites (BEIDOU-3_M1_43001 and BEIDOU-3_M2_43002) are the real BDSIII satellites for the global networking. As a simplification, M1 represents BEIDOU-3_M1_43001 satellite and M2 represents BEIDOU-3_M2_43002 satellite. It can be seen that the two satellites are on one MEO orbit.

III. BDS-3 B1 SIGNAL MODEL AND SIMULATION

From the SIS ICD [1]-[2], the structure of the B1 OS signal is shown in Table.1, and the minimum received power is shown in Table.2.

Table.1 BDS-3 B1 OS signal structure

Signal	Signal component	Carrier frequency (MHz)	Modulation
B1I		1561.098	BPSK(2)
B1C	B1Cd	1575.42	BOCs(1,1)
	B1Cp		QMBOC(6,1,4/33) BOCs(1,1) BOCs(6,1)

Table.2 BDS-3 B1 OS signal minimum received power

Signal	Satellite type	Minimum received power (dBW)
B1I		-163
B1C	MEO	-159
	IGSO	-161

From the signal structure and the power value, the power spectrum of the simulation signal is drawn (See Fig.3).

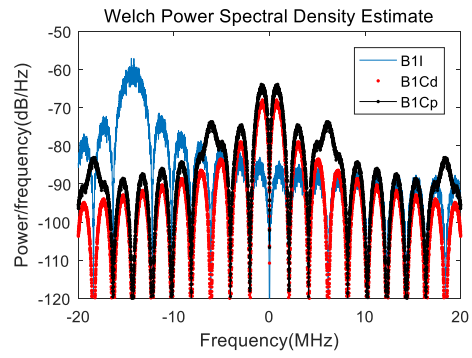


Fig.3 B1 power spectral density estimate of the simulation signal

Compared to other signal components, B1Cp is the most unique signal component, and there is the biggest difference from GPS and Galileo. Therefore, the simulation and verification takes B1Cp as an example. According to the SIS ICD, B1Cp can be expressed as

$$s_{B1Cp}(t) = \frac{\sqrt{3}}{2} C_{B1Cp}(t) \cdot sc_{B1Cp}(t) \quad (1)$$

where, $C_{B1Cp}(t)$ is the ranging code. The B1C pilot component subcarrier $sc_{B1Cp}(t)$ is expressed as

$$sc_{B1Cp}(t) = \sqrt{\frac{29}{33}} sc_{B1C-a}(t) - j \sqrt{\frac{4}{33}} sc_{B1C-b}(t) \quad (2)$$

and

$$\begin{aligned} sc_{B1C-a}(t) &= \text{sign}(\sin(2\pi f_{sc_B1C-a} t)) \\ sc_{B1C-b}(t) &= \text{sign}(\sin(2\pi f_{sc_B1C-b} t)) \end{aligned} \quad (3)$$

where, f_{sc_B1C-a} is 1.023MHz, f_{sc_B1C-b} is 6.138MHz.

Because $s_{B1Cp}(t)$ is a complex waveform, when receiving, the local signal must be its complex conjugate form. In the ideal case, the correlation function is

$$R_{B1Cp}(\tau) = \frac{29}{33} R_{B1C-a}(\tau) + \frac{4}{33} R_{B1C-b}(\tau) \quad (4)$$

This is the same as TMBOC for BDS L1C signal. But for Galileo CBOC, there is another component $\pm \frac{4\sqrt{29}}{33} R_c(\tau)$. $R_c(\tau)$ is the cross correlation of $sc_{B1C-a}(t)$ and $sc_{B1C-b}(t)$.

The correlation function is shown in Fig.4(a). The first shoulder is more flat, and the details are shown in Fig.4(b). The actual launching and receiving system will have some band limited devices, so Fig.5 is closer to the reality.

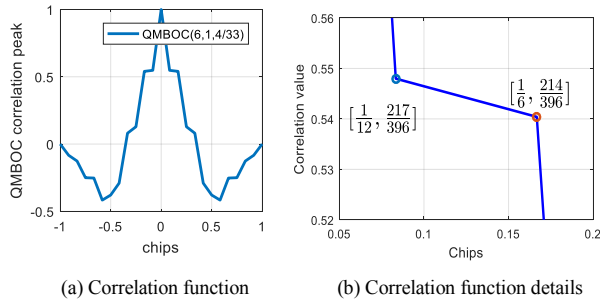


Fig.4 B1Cp ideal correlation function

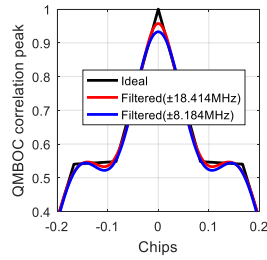


Fig.5 Filtered B1Cp ideal correlation function

IV. IN-ORBIT PERFORMANCE ANALYSIS

From the orbit simulation, the elevation angle and azimuth angle of CAST (Xi'an) to the two latest satellites are better in the morning of January 22, 2018. So the signal data at this time was collected. And all of the following analysis is based on these data.

A. Signal Waveform and Characteristic

In fact, even with 750Mps sampling rate, the spectrum of the GNSS signal is difficult to distinguish because of the communication signal interference. Therefore, it is necessary to add another band pass filter before ADC. In this condition, the signal waveform, PSD, statistical histogram and constellation diagram are shown in Fig. 6-10.

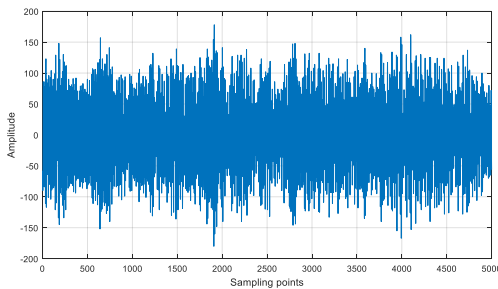


Fig.6 Digital signal sampling waveform

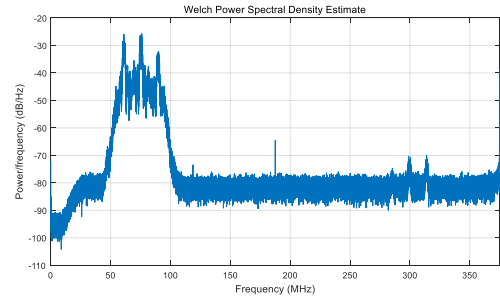


Fig.7 Filtered signal PSD

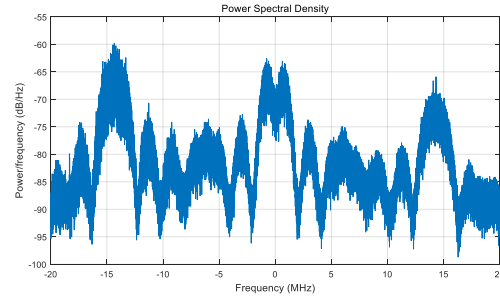


Fig.8 B1 signal PSD

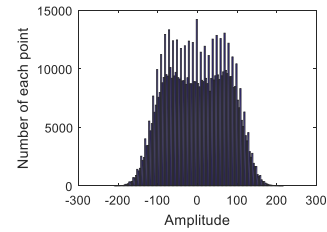
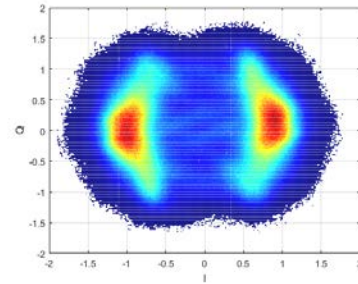
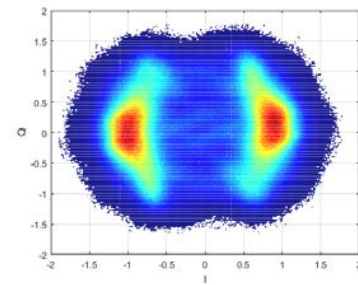


Fig.9 B1 signal waveform histogram



(a) M1 B1 signal



(b) M2 B1 signal

Fig.10 B1 signal constellation diagram

It can be confirmed from Fig.10 that M1 and M2 satellites are broadcasting same signals, including B1I, B1Cd, B1Cp. Due to the intermodulation component, there is a great difference between the actual PSD and the PSD of the linear additive signal of the previous simulation. Also, slightly different was shown from the two satellites baseband signal constellation.

B. Signal Acquisition and Tracking Results

Taking M1 B1Cp as an example, the process of acquisition and tracking is introduced. In order to exploit the QMBOC correlation properties, a narrow Early-Late spacing (0.7/12 chip) and a $\pm 8.184\text{MHz}$ filter have been adopted. With three order phase locked loop, the 10Hz code loop bandwidth and the 20Hz carrier loop bandwidth are used.

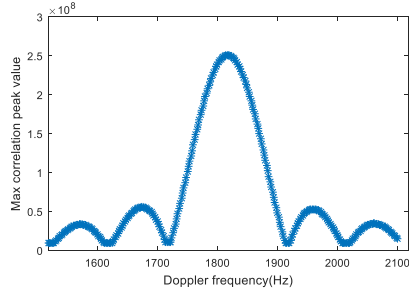
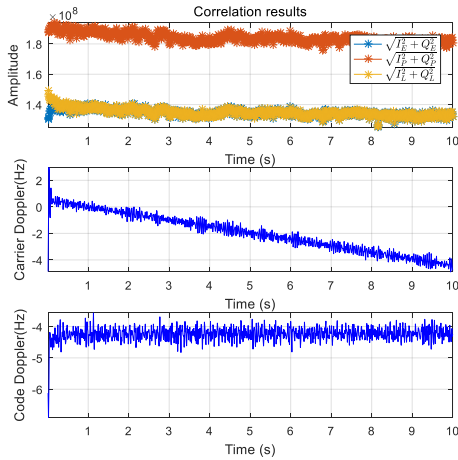
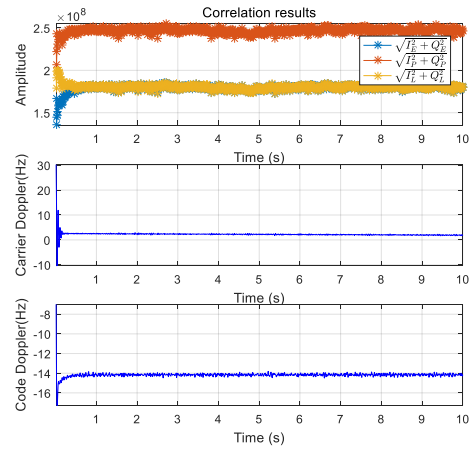


Fig.11 Acquisition results of the doppler frequency

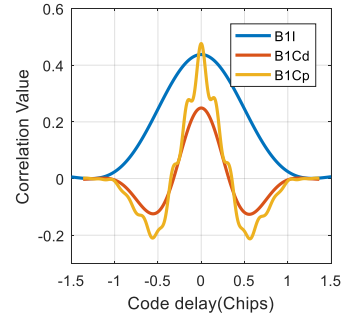


(a) M1 B1Cp signal



(b) M2 B1Cp signal

Fig.12 Tracking results

Fig.13 B1 signal correlation performance (B1I: $\pm 4.096\text{MHz}$, B1Cd: $\pm 4.096\text{MHz}$, B1Cp: $\pm 7.161\text{MHz}$)

Where the cross-correlation function value computed at the estimated center frequency shows the presence of the BOC modulation (shown in Fig.13). The B1Cd channel is BOC(1,1), and the B1Cp channel is MBOC(6,1). And the QMBOC correlation peak shows steeper slopes with respect to the B1Cp correlation peak.

C. Pseudorange

Since pseudorange is the most important measurement for navigation. The results of code pseudorange and carrier pseudorange have also been obtained processing. Then the code carrier divergence is evaluated.

First, after stable tracking, the 5s pseudorange data is extracted. Then in order to simplify and compare, the carrier pseudo range is calculated according to the center frequency of the carrier, and it is unified to the ns unit.

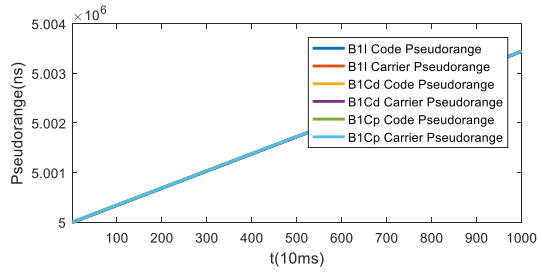
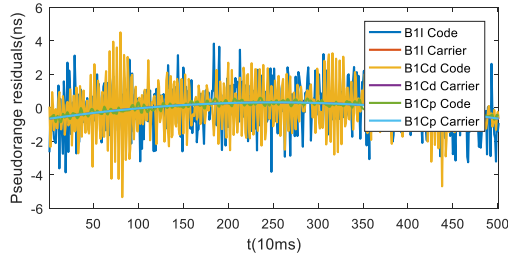
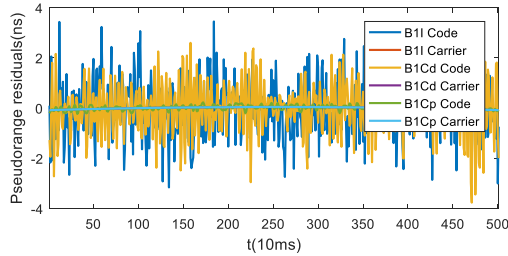


Fig.14 M1 signal pseudorange

The Original pseudorange results are shown in Figure 7. Due to the real distance and clock difference, the pseudorange is presented as a cluster of slashes. The first order fitting is carried out according to the B1Cp carrier pseudo range, and the residual results are obtained as Fig.15.



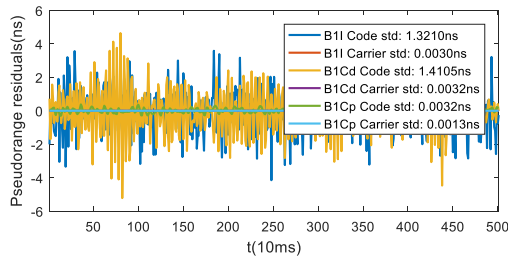
(a) M1 B1 signal



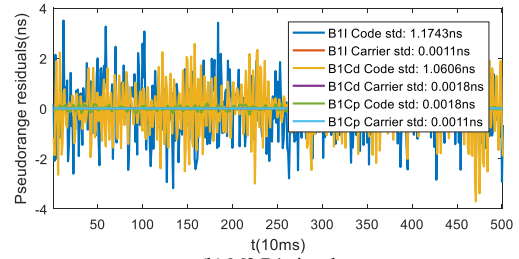
(b) M2 B1 signal

Fig.15 B1 signal pseudorange one order fitting residual

From Fig.15, the first order fitting residual reflects the real distance and the clock difference. In order to get the tracking pseudorange performance, the two order fitting is carried out. The residuals and the standard deviation are shown in Fig.16.



(a) M1 B1 signal

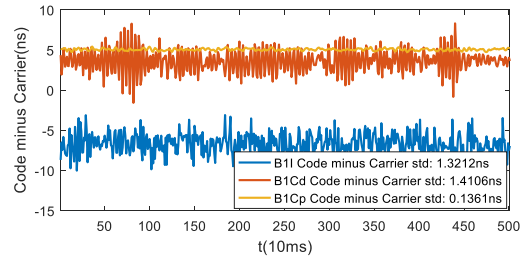


(b) M2 B1 signal

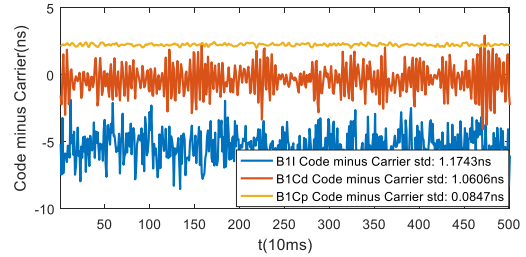
Fig.16 B1 signal pseudorange two order fitting residual

It's not surprising that BCp has better performance. The BOCs(1,1) code rate is equivalent to BPSK(2), so B1Cd has a similar performance to B1I.

Code-carrier divergence (CCD) can reflect the degree of separation between code and carrier, and affect the performance of carrier assisted pseudo code, so it is an important signal performance indicator. The results are shown in Fig.17.



(a) M1 B1 signal



(b) M2 B1 signal

Fig.17 Code minus Carrier pseudorange and its standard deviation

The code minus carrier pseudorange is stable. But for CCD, the 5s data is too short to fully reflect performance.

V. CONCLUSIONS

China is developing BDS-3 system to provide GNSS service to the world. This service will be a highly accurate and guaranteed global positioning service. In Xi'an, we collected and processed the signals of the first two BDS-3 satellites. For this purpose, we developed a software receiver. The post processing results have showed the base performance. The correlation functions were shown as a shape of the BOC and QMBOC. Also, B1Cp QMBOC signal has better tracking results than B1I BPSK(2) signal.

Due to the awful electromagnetic environment, B2a was not evaluated and B1 must have been affected by adjacent frequency communication signals. On the other hand, on the day of collecting data, Xi'an has stronger wind and it may have an impact on the data.

On 12 January 2018, the third and the fourth BDS-3 satellites were successfully launched again. Now, we are trying to collect and process the data. In the future, we will further try to do the first determination of a ground location using the signals of four BDS-3 satellites in Xi'an.

REFERENCES

- [1] China Satellite Navigation Office, "BeiDou Navigation Satellite System Signal In Space Interface Control Document Open Service Signal B1C (Version 1.0)," December, 2017.
- [2] China Satellite Navigation Office, "BeiDou Navigation Satellite System Signal In Space Interface Control Document Open Service Signal B2a (Version 1.0)," December, 2017.
- [3] China Satellite Navigation Office, "BeiDou Navigation Satellite System Signal In Space Interface Control Document Open Service Signal B2a (Version 2.1)," November, 2016.
- [4] Zheng Yao and Mingquan Lu, "Signal Multiplexing Techniques for GNSSs," IEEE Signal Processing Magazine, September, 2017.
- [5] Hein G, Avila-Rodriguez J et al, "MBOC: The new optimized spreading modulation recommended for Galileo L1 OS and GPS L1C." Proc. Of IEEE/ION PLANS, San Diego, CA.2006:883-892.
- [6] "European GNSS(Galileo) Open Service Signal In Space Interface Control Document (OS SIS ICD, Issue 1.2)," November 2015.
- [7] CeresTrack website, "NORAD two-line element sets, current datam," <http://www.celestrak.com/NORAD/elements/beidou.txt>, URL accessed on January 29, 2018.

Precise positioning with Android

Håkansson M.

KTH/Lantmäteriet, Gävle, Sweden, martin.hakansson@lm.se

Summary

Global Navigation Satellite System (GNSS) raw data was made available in the Application Programming Interface (API) of Android version 7.0 and forward¹. This means that raw observations, such as pseudoranges, Doppler shifts, signal strengths, and carrier phases, that was hidden from the App-developer in the earlier versions of the Operating System (OS) is now accessible on Android devices with GNSS chips manufactured 2016 and onwards. The availability of these raw data in the API opens up new possibilities for precise GNSS positioning in smartphones and tablets, as it is now possible to include external corrections in a convenient way in the positioning solution. Positioning techniques that was earlier possible only with the more expensive geodetic receivers are now also possible on cheaper devices available for the mass-market consumers.

However, even though these positioning techniques can now be employed on new Android devices, this does not necessarily mean that the same level of accuracy is obtained as for the geodetic receivers. One of the main weaknesses of these devices in comparison with the geodetic receivers are the inferior GNSS antennas of the former². The cheaper devices use small linearly polarized patch antennas for the reception of the GNSS signals, which results in poor handling of multipath from the surrounding environment.

This study investigates how multipath influences the positioning accuracy in both code and carrier phase based precise positioning techniques. An ideal environment with almost no multipath is created by the use of Eccosorb microwave absorbers and a clear sky condition. Results from this environment are compared with the corresponding results without Eccosorbs, which allows multipath reflections from below. The results are also compared with those of geodetic GNSS receivers and antennas.

Motivation and methodology

It was shown (before the release of Android 7.0) that the poor multipath handling of the GNSS antennas used in smartphones is a major limitation for achieving precise positions for these devices². Since the release of version 7.0 of Android a number of studies has been performed assessing the precise positioning performance of devices with this OS^{3,4,5}. Also, some of these studies have shown that dm to cm-level positioning is possible^{3,5}. However, these studies have only assessed the position qualities in terms of their repeatability, as the “true” positions of the devices were unknown during the tests. In addition, neither of these studies evaluated the position qualities under various multipath conditions even though it can be expected that multipath will have a significant impact on the final results.

In this study, precise positioning with GNSS observations from devices running Android 7.0 is assessed. The measurements were collected from locations with known coordinates which meant that the accuracy, and not only the precision, of the calculated positions could be determined. Testing was furthermore performed in two different setups, with different multipath impact.

¹ S. Malkos, “Google to provide raw GNSS measurements”, GPS World, vol. 27, nr. 7, p. 36, 2016

² K. Pesyna Jr. “Accuracy in the Palm of Your Hand: Centimeter Positioning with a Smartphone-Quality GNSS antenna”, GPS World, vol. 26, nr. 2, p. 16-31, 2015

³ S. Banville, F. Van Diggelen, “Precision GNSS for everyone: Precise Positioning Using Raw GPS Measurements from Android Smartphones”, GPS World, vol. 27, nr. 11, p. 43-48, 2016

⁴ S. Riley, W. Lentz, A. Clare, “On the Path to Precision – Observations with Android GNSS Observables”, In proceedings of ION GNSS 2017, p. 116-129, 2017

⁵ E. Realini, S. Caldera, L. Pertusini, D. Sampietro, “Precise GNSS Positioning Using Smart Devices”, Sensors, vol. 17, nr. 10, 2017

Results

Sample results from this study are presented in Figures 1-4. Figures 1 and 2 show the east and north components for estimated differential GPS (DGPS) positions in relation to the mean position (asterisk) and the true position (plus sign). These diagrams furthermore show the one standard deviation error ellipses of the estimated positions. Figure 1 shows estimated positions from measurements where Eccosorbs were not used (moderate multipath), while Figure 2 shows estimated positions with Eccosorbs (low multipath). Figures 3 and 4 show the corresponding diagrams for relative static float solutions based on carrier wave measurements alone. Each of these positions were estimated from 5 minutes of measurements collected every second.

This study shows that precise positioning based on carrier wave observations is possible even though the expected quality of the positions will be highly sensitive to the amount of multipath. In an environment with a moderate level of multipath and a clear sky, 5-minute solutions showed position uncertainties of less than one meter. In environments with almost no multipath and a clear sky the position uncertainties improved to less than 2 decimeters. DGPS did not show any great improvement in comparison with absolute code based positioning in either of the multipath environments.

Figures

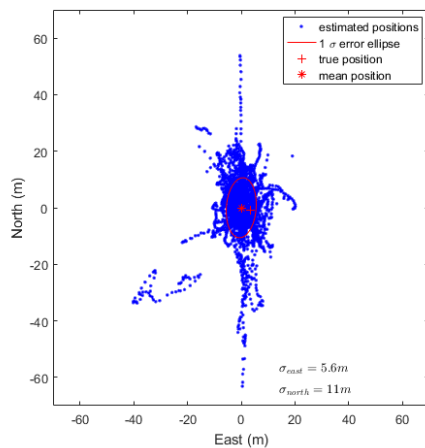


Figure 1. Estimated DGPS positions from Nexus 9 without Eccosorb

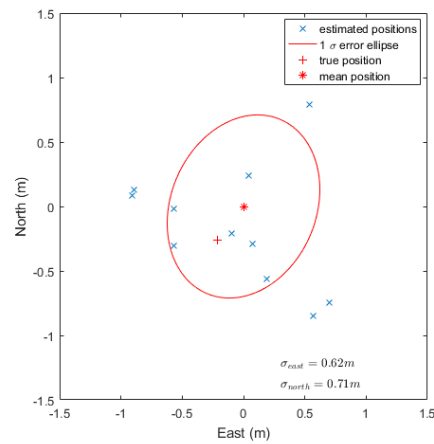


Figure 3. Estimated positions from Nexus 9 carrier measurements without Eccosorb

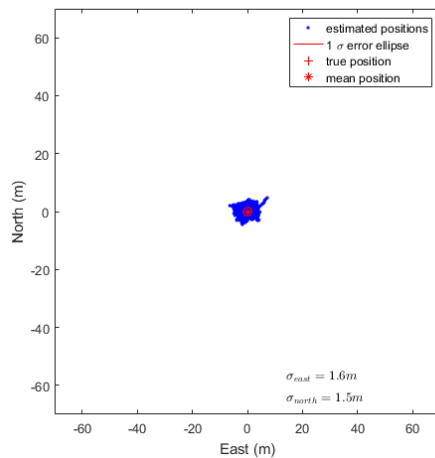


Figure 2. Estimated DGPS positions from Nexus 9 with Eccosorb

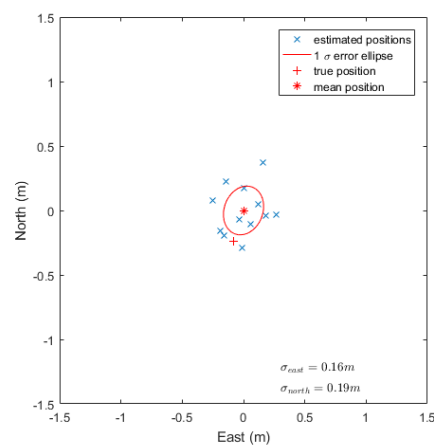


Figure 4. Estimated positions from Nexus 9 carrier measurements with Eccosorb

Modulation and Signal-Processing Tradeoffs for Reverse-GPS Wildlife Localization Systems

Andrey Leshchenko and Sivan Toledo
Blavatnik School of Computer Science, Tel-Aviv University

Abstract—Reverse-GPS wildlife localization systems are emerging as a key technology for regional high-throughput wildlife tracking. Two such systems have been designed, implemented, and deployed (in six sites on three continents). Both of the existing systems suffer from limitations due to the modulation that is used by transmitters, which are attached to wild animals, and due to the detection and estimation algorithms that they use to detect transmissions and estimate their arrival times. This paper investigates key tradeoffs associated with three different modulation schemes that wildlife tags can plausibly use. The factors that we investigate include the ability to detect weak signals from distant tags, the ability to accurately estimate the time-of-arrival at a given SNR, and the computational cost of these detection and estimation algorithms. Our key contributions are (1) evidence that BPSK modulation is superior in essentially all relevant metrics, except perhaps chip availability, to FSK and OOK; (2) evidence that OOK is a second-best choice and its main drawback is poor performance under interference from other tags; (3) algorithms to inexpensively search the frequency-delay space at moderate and high SNRs. We also report on implementation efforts designed to integrate robust processing of BPSK tags into a wildlife tracking system.

Full paper in IEEE Xplore

SWEPOS – A NATIONAL INFRASTRUCTURE FOR 3-DIMENSIONAL POSITIONING IN SWEDEN

SWEPOS, the national geodetic infrastructure for GNSS in Sweden was established by Lantmäteriet in cooperation with Onsala Space observatory and Chalmers University of Technology in the beginning of the 1990. SWEPOS started as a nationwide network of 20 CORS stations with 200 km interstation distance and between 2002 and 2010 a densification to 70 km interstation distance was done to support the establishment of a nationwide network-RTK service. From 2011 until now the network has been densified to 35 km and even down to 10 km in some very active areas and for large infrastructure projects. Today SWEPOS consists of almost 400 CORS stations and provides GNSS data for scientific studies, data to international organizations and postprocessing and RTK corrections to the users in Sweden. SWEPOS is also providing data to some private companies to support private nationwide RTK services in Sweden. The presentation will give a status for the national geodetic infrastructure for GNSS in Sweden, an infrastructure that is growing in importance for high precision positioning applications and scientific use of GNSS data. Expectations from the users on improved accuracy and increased availability puts new demands on the geodetic infrastructure for GNSS in Sweden. The presentation will describe the efforts that have been done the last years to meet the demands, both by densifying the CORS network but also by implementing support for the Galileo satellites. The presentation will also describe what will be done to continue to improve the national infrastructure for GNSS in Sweden.

Presenter; Peter Wiklund, Lantmäteriet, The National Mapping, Cadastral and Land Registration Authority

Results of DEMETRA Time Integrity service tested on Galileo

G. Signorelli¹, I. Sesia¹, P. Tavella^{1,2}

¹ INRIM, Italy

² BIPM, France –since November 2017

F. Fiasca

AIZOON, Italy

P. Defraigne

ORB, Belgium

L. Galleani

Politecnico di Torino, Italy

In the frame of the Horizon 2020 project DEMETRA (DEMonstrator of EGNSS services based on Time Reference Architecture) funded by the European Union, 9 different time dissemination services based on or alternative to the European GNSS have been designed and experimented. One of them was aimed to test a time integrity service to the GNSS users, to improve user timing accuracy as well as positioning.

The DEMETRA Time Integrity Service has been built as a first step of a Galileo time integrity system. The developed service monitors the status of Galileo satellite clocks, detecting in real time possible anomalies and generating automatic alerts in case the satellite is considered unusable. This kind of service will be very useful for users like industrial and scientists interested in timekeeping, but also space qualified clocks manufactures, the European Space Agency (ESA), the European GNSS Agency (GSA), and the European Geostationary Navigation Overlay Service (EGNOS). The Service has been tested in using Galileo public clock data retrieved from the Multi GNSS Experiment of the International GNSS Service (IGS). The service is currently still online and the integrity products available on the DEMETRA web page, accessible to the registered users. The first results will be presented in this paper as well as a comparison against the Galileo NAGU to assess possible improvements at user level, in addition to the information provided by the system itself. Moreover our results have been used to build a statistics on the anomalies that occurred on the Galileo satellite clocks.

The DEMETRA project has received funding from the European GNSS Agency under the European Union's Horizon 2020 research and innovation programme under grant agreement No 640658.

GNSS Time Interoperability based on Broadcast Corrections

Bogdanov P, Druzhin A, Primakina T

Russian Institute of Radionavigation and Time, Saint-Petersburg, Russia, bogdanov_pp@irt.ru

Summary

For calculating GNSS-GNSS Time offsets the following broadcast data can be used:

- corrections to convert from GNSS Time to Reference Time UTC(k);
- GNSS-GNSS Time Offset corrections (GGTO corrections).

Hence, users can calculate GNSS-GNSS Time offsets using the following approaches: based on broadcast GNSS - Reference Time Offset corrections, based on direct broadcasting GGTO corrections and based on broadcasting corrections by all GNSS relative to one GNSS.

These three approaches have been analyzed. For each of the approaches the analytical expressions for estimating the accuracy of calculated time offsets have been deduced. The approaches have been compared and the results of the comparison are presented.

Motivation

To implement positioning by signals from space vehicles (SV) of multiple GNSS constellations users' receivers have to be provided with the values of offsets between different GNSS time scales.

Users' receivers can get the values autonomously by processing navigation signals from SVs of multiple GNSS constellations. However, it is possible only when no less than four SVs of one GNSS constellation and some SVs of other GNSS are in view. As a result, this method can't be used in challenging environment.

The calculation of GNSS-GNSS time offsets can also be provided based on broadcast data. The corrections broadcast (or specified to be broadcast) by operational GNSS that can be used by the user to calculate GNSS-GNSS Time offsets are presented in Fig. 1.

Results

Comparison of the three approaches provided the following results.

Broadcasting GNSS Time offset corrections relative to Reference Time UTC(k) is implemented in all GNSS. However, the accuracy of calculating GNSS-GNSS Time offset based on these corrections depends to a large extent on the value of the offsets between UTC(k) scales. The accuracy can be increased by increasing the accuracy of steering UTC(k) to UTC and by providing additional information on UTC(k)-UTC offset to the users.

Broadcasting direct GNSS-GNSS Time Offset corrections provides higher accuracy than the previous approach but its implementation requires additional efforts, for some systems changing the navigation message is required.

Calculating GNSS-GNSS Time offsets based on broadcast GGTO corrections relative to one GNSS (GPS) is easier implemented than broadcasting direct corrections relative to all systems but provides lower accuracy.

The selection of the approach for GNSS Time Interoperability based on broadcast corrections is a kind of compromise between the accuracy of GNSS Time referencing and the efforts on its implementation and depends on the priorities of each system.

Figures

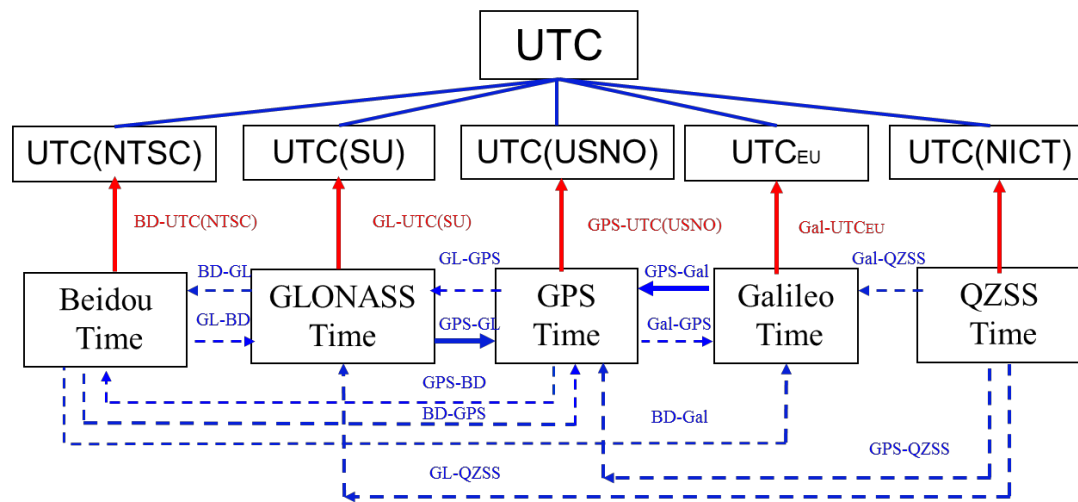


Fig. 1: Corrections broadcast (solid arrows) or specified but not broadcast (dashed arrows) by operational GNSS.

Study on Method of Laser Time and Frequency Transfer Between Satellite and Ground Station

Guoyong Wang
China Academy of Space Technology(Xi'an)
Xi'an, China
wangguoyong321@163.com

Yansong Meng, Lang Bian, Yuanbo Yao, Tao Yan,
Wenying Lei
China Academy of Space Technology(Xi'an)
Xi'an, China

Abstract—Time and frequency transfer is of great value in satellite navigation, communication and others fields. The existing link of time and frequency transfer based on laser pulse is mainly used for time transfer, it is unable to achieve the optical frequency transfer. In this paper, a method of satellite-ground time and frequency transfer based on ultra narrow linewidth laser and optical frequency comb is proposed. This method not only can implement the time transfer but also can implement the frequency transfer, which has the very high application value.

Keywords—Time transfer; Frequency transfer; Laser time and frequency Transfer; Ultra narrow linewidth laser; Optical frequency comb

Full paper in IEEE Xplore

UTC(k) Time Distribution Using Network RTK

Carsten Rieck*, Per Jarlemark*, Kenneth Jaldehag*, Gunnar Hedling+, Anders Frisk+

*RISE, Measurement Science and Technology, Box 857, S-50115 Borås, carsten.rieck@ri.se

+Geodesy, Lantmäteriet, S-80182 Gävle

Summary

This paper describes a novel method on how to utilize the reference infrastructure used for Network Real Time Kinematic (RTK) for the real-time dissemination of UTC¹.

Traceable time and frequency comparisons are essential to an increasing number of applications. GNSS is often cost-effectively used to disseminate a constellation's system time, but questionable traceability and the dependence on a third- and possibly non-metrological party for time keeping requires careful design for any serious application. GNSS time transfer using differential or PPP methods are today standard for metrological time keeping; the same proven methods are recommended in order to increase an industrial application's timing robustness and traceability to UTC.

Network RTK is today the main tool for land surveying and is based on double differencing of GNSS observations between a user/rover and a virtual reference station (VRS). The latter is a real-time combination of observations made by several stations of a reference network and helps to mitigate atmospheric error sources and binds a user's measurements to a local reference frame. With double differencing all clocks, i.e. satellite clocks and station clocks are eliminated, RTK is with its original intention not useable for comparisons of time and frequency. Single difference analysis² preserves the station clock differences and can be used to transfer the clock of the virtual reference. However, clocks in the reference network, even though they may be of metrological origin/quality, are most often already eliminated during stream generation at the reference receivers³. In order to disseminate a clock using a typical network RTK implementation the outgoing VRS stream must carry or supply clock information. This information has to be provided by a separate real-time analysis such as for example described in this paper. Results of a code based, and potentially phase aided, estimation of the clock difference between a UTC(k) and the VRS are imposed on the VRS data stream and thus provides direct access to a real-time realization of UTC. For formal UTC traceability, repeated calibration of the end-user equipment and a reviewed time transfer method has to be provided.



Fig. 1: SWEPOS reference station distribution.

¹ via a real-time realization of a UTC(k) such UTC(SP)

² Yanming Feng, Bofeng Li, "Four Dimensional Real Time Kinematic State Estimation and Analysis of Relative Clock Solutions", 23rd International Technical Meeting of the Satellite Division of The Institute of Navigation, Portland, OR, September 21-24, 2010, <http://gnss.curtin.edu.au/wp-content/uploads/sites/21/2016/04/Feng2010Four.pdf>

³ RTMC 3.x "demands" the clock reduction <http://www.rtcn.org/differential-global-navigation-satellite--dgns--standards.html>

Motivation

Among the set of SI quantities it is the unit of time that is currently the most accurate to realize. However, due to its highly dynamic nature and the stringent requirements set by industry standards and applications, the instability of commonly available frequency standards requires continuous phase comparisons in order to ensure synchrony of remote appliances over any practical time periods. Therefore many cost sensitive applications rely on the accuracy and stability of GNSS navigation solutions as their common clock and therefore try to minimize the hold over capacity of the local clock. Often, this results in an apparent lack of robustness and may jeopardize the resiliency of dependent systems. Further, recent and future directives and regulations, such as MiFID II/MiFIR for the European financial market, require traceability of event timing to UTC, which is not automatically provided by GNSS⁴. Thus, typical “to be compliant” applications demand a cost effective synchronization solution proving calibration and traceability. As the use of GNSS still is and will continue to dominate synchronization, the use of Network RTK for a regional UTC(k) distribution is an appropriate option.

Results

For a possible distribution of the Swedish national time scale UTC(SP) we have studied the behavior of SWEPOS⁵ as a typical Network RTK implementation. A VRS, for any given position, provides its virtual observations as the combination of a number of physical reference stations in its vicinity. One of those stations is chosen to provide the principle observations that are “improved” by the other stations of the VRS. The VRS inherits, among other properties, the clock information from the main contributor, a fact which is essential to a generic “out of band” estimation of the distributed clock relative UTC(SP). Figure 2 shows the typical GPSP3 code clock behavior of a set of arbitrarily chosen SWEPOS reference stations, as depicted in figure 1, versus UTC(SP). It is evident that groups of receivers are biased and feature similar behavior on top of the typical code noise. Clock estimation is done by using IGS ultra rapid orbit predictions and the resulting clock differences are used to alter the RTCM data stream inline between the SWEPOS service provider and the timing user. We analyze the performance of the different GNSS and suggest a real-time time transfer method for a stationary user.

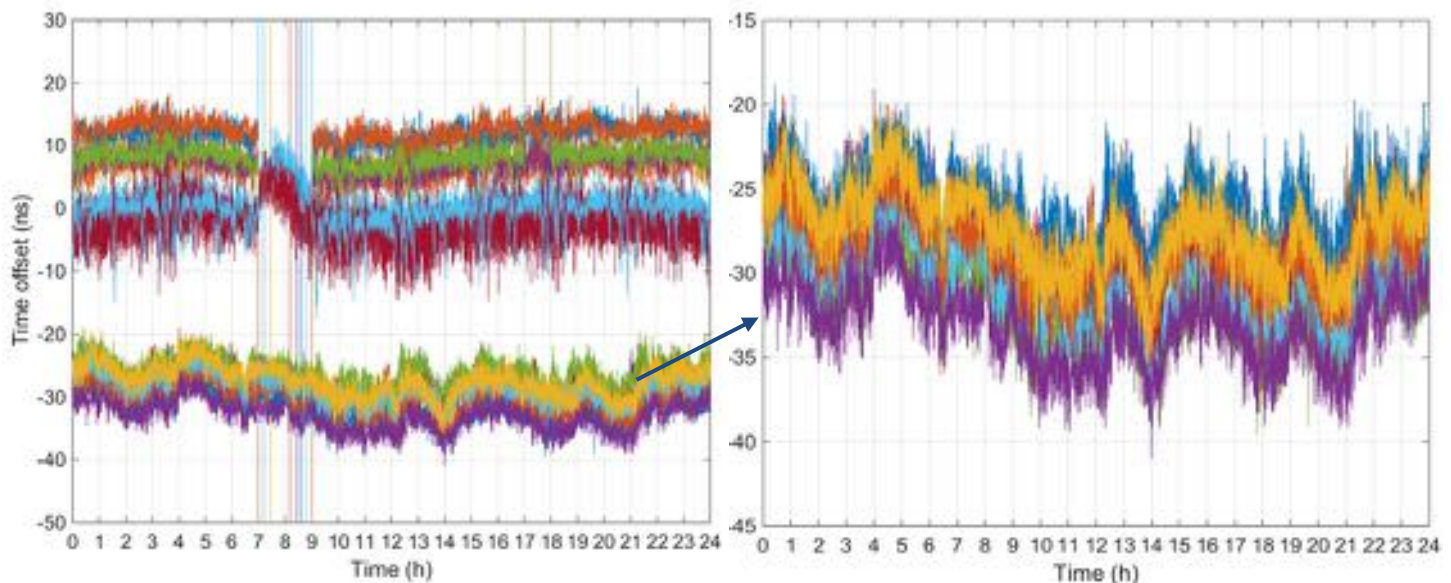


Fig. 2: Example of the behavior of a number of arbitrarily chosen station clocks. The traces depict differences of the station clocks versus UTC(SP) using GPS P3 code analysis. As the real station clocks are eliminated from the observations on the receiver level, biases and features seen are unlikely clock related.

⁴ It is still debated to what extent and under what circumstances GNSS provide traceability to UTC

⁵ <https://swepos.lantmateriet.se/> using Trimble TPP providing NTRIP streams for GPS, GLONASS and GALILEO

A Robust Timing Service for future EGNSS

H. Zelle, H. Veerman
Netherlands Aerospace Centre
Marknesse, the Netherlands
hein.zelle@nlr.nl

K. A. Aarmo, J.P. Boyero
European Commission
Brussels, Belgium

M. Kirkko-Jaakkola, S. Honkala, S. Söderholm,
S. Thombre
Finnish Geospatial Research Institute
Kirkkonummi, Finland

Abstract— This paper describes the definition of the proposed specific timing service for future versions of the European GNSS systems. A timing service concept is specified for Galileo and for EGNOS. Additional features to increase robustness of the services are developed, to increase the reliability of time determination in challenging circumstances. The concepts are tested and validated against specific threats related to timing. The robust timing service and its features are presented, together with the test results and recommendations for robust GNSS timing receivers.

Keywords—GNSS, timing, robustness, Galileo, EGNOS

I. INTRODUCTION

All global navigation satellite systems (GNSS) can be used to obtain time. As an intrinsic characteristic to all GNSS Systems, Galileo and EGNOS each provide time determination capabilities which are embedded within the current portfolio of services that they offer.

GNSS time is intensively used in critical infrastructure in sectors that are of strategic importance in modern society, such as Telecom, Power Grids and Finance. Failure of such critical infrastructures would have significant impact on vital societal functions, health, safety, security, economic or social well-being of people.

Given the need for ensuring the provision of the GNSS based timing services, the European Commission started a specific project in 2016, with the main objective "Definition of a Robust Timing Service for Galileo and for EGNOS". The project was launched under the EU Horizon 2020 Framework Programme and has been performed by a consortium of European partners with complementary competences with respect to timing.

This paper presents the project and its results. The focus is on the definition of a timing service based on Galileo and one based on EGNOS. Technical features are developed to mitigate threats and increase the robustness of EGNSS timing. Tests are designed and executed to validate if the robustness features mitigate the threats to GNSS timing. Only those proven successful are then considered to become part of the Robust Timing Services.

II. DEFINITION OF A ROBUST TIMING SERVICE

Two timing services are defined: one based on Galileo and one based on EGNOS. The service definition provides requirements and expected performance levels so that a user making use of the robust timing service will know what to expect regarding accuracy, reliability and availability of the service.

The first service is based on a Galileo receiver (dual-frequency preferred), providing Galileo System Time (GST) and offsets to compute UTC as well as GPS system time. The second service is based on EGNOS, providing EGNOS Network Time (ENT) as well as offsets to compute UTC and GPST. EGNOS currently only augments GPS signals, however in the future it will augment the Galileo signals as well.

For each service, the expected requirements for user hardware, receiver configuration and receiver calibration are specified. It is prescribed how time is to be obtained by the user receiver, including the required processing steps and algorithms. The service performance is specified in terms of service area, availability, accuracy, integrity, time to first fix, and timing stability. Specifying these values rigorously for timing services brings added value over the current treatment of GNSS timing as a capability of positioning services.

III. THREAT ANALYSIS

The most relevant threats to GNSS timing were identified and analyzed. The fact that most timing users make use of a GNSS-receiver together with a disciplined oscillator is taken into account: this setup provides significant resilience to short-lasting threats by itself. The primary threats selected for mitigation with technical solutions are interference, spoofing, multipath and faults in the navigation messages.

IV. ROBUSTNESS FEATURES

A number of technical features were studied in order to increase timing robustness, from GNSS system level (signal in space) to specific algorithms at the user receiver level.

1. Take advantage of the dual frequency Galileo receiver (EGNOS not yet supported) to eliminate ionospheric delays and mitigate narrow-band interference.
2. Use a multi-constellation (Galileo, GPS+EGNOS) receiver to provide resilience against system-level failures such as the January 2016 GPS glitch [2].
3. The use of Receiver Autonomous Integrity Monitoring techniques applied to timing (T-RAIM) was specifically requested for this project [1], to provide resilience against faults and outliers in the computation of the GNSS system time.

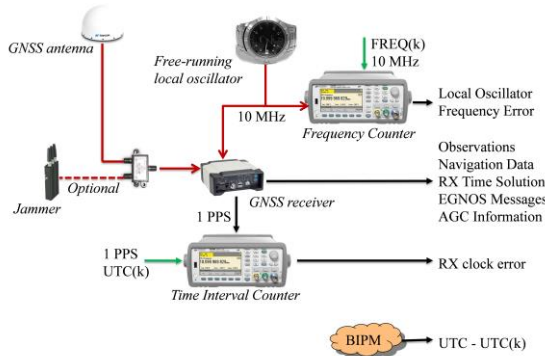


Fig. 1. Experimental test setup to collect GNSS data for post-processing in a software receiver. All observations are time-stamped with a local oscillator and a reference atomic time scale.

V. TESTING AND VALIDATION

To test if the robustness features indeed mitigate the identified threats, a number of tests were designed. These tests require a carefully designed setup which allows the implementation of the technical concept in a receiver, to introduce an artificial threat, and to measure the timing performance with and without the threat and mitigation measures.

The test setup is implemented based on a free-running local oscillator (imperfect by design) that drives a timing GNSS receiver which raw measurements are logged for post-processing. The post-processing is performed by a software receiver which implements the robustness feature. Threats are introduced on the signal input side (interference), or inside the software receiver (navigation message faults). The post-processed results can thus be compared to the original observations, time-stamped with the local oscillator. All observations are also time-stamped by a reference atomic clock synchronized with BIPM, to analyze the impact of the technical features on timing stability. Tests are evaluated by comparing the resulting Maximum Time Interval Error (MTIE) values against the ITU recommendation of MTIE for primary reference time clocks [3]. Fig. 1 shows the experimental test setup, up to the point where observations are fed into the software receiver.

VI. RESULTS

The paper will focus on the project results and the resulting recommendations for robust timing receiver implementation. A single test result is shown here as an example, demonstrating T-RAIM robustness. A faulty EGNOS clock correction is simulated by altering the navigation message of one EGNOS satellite, introducing a GPS satellite clock error. In the presence of the clock fault, the measured MTIE exceeds the expected MTIE, as shown in Fig. 2. Fig. 3 shows the same test, this time with T-RAIM enabled. The T-RAIM algorithm has detected the fault, and discarded the satellite, bringing the MTIE well below the expected value.

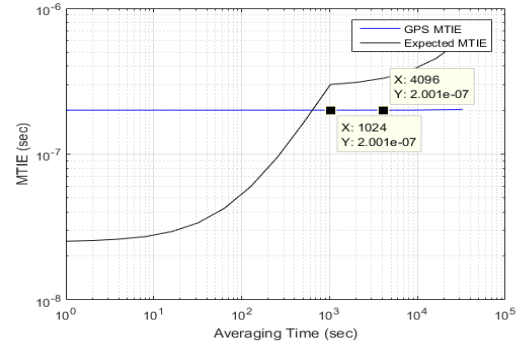


Fig. 2. Failed satellite clock, no mitigation

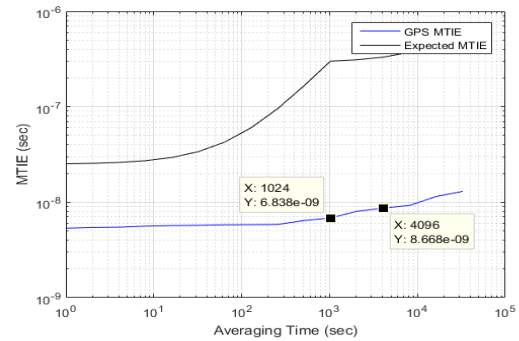


Fig. 3. Failed satellite clock, with T-RAIM mitigation

VII. SUMMARY AND CONCLUSIONS

The project was completed in October 2017. The results include the robust EGNSS timing service definition, processing specifications for receivers, and a number of tests that can be applied for receiver testing. Recommendations are provided for the EGNSS timing service provider as well as for future EGNSS timing receiver implementations.

REFERENCES

- [1] G. J. Geier, et al, "Prediction of the time accuracy and integrity of GPS timing." In Proc. 49th Frequency Control Symposium, San Francisco, CA, USA, May 1995, pp. 266–274.
- [2] Mujunen, J. Aatrokoski, M. Tornikoski, and J. Tammi, "GPS Time Disruptions on 26-Jan-2016," Aalto University publication series Science + Technology 2/2016, Helsinki, Finland, February 2016.
- [3] ITU-T G.8272/Y.1367, Amendment 1 (04, 2016), "Timing characteristics of primary reference time clocks"

GNSS Spoofing of Unmanned Aerial Vehicle with GNSS/INS Integrated Navigation System

Leyuan Sun, Wende Huang, Yifan Zhou

National University of Defense Technology, Changsha, China, sly_nudt@163.com

Summary

A UAV spoofing system was set up based on GNSS generated spoofing. The hardware composing included a receiving antenna, a ground-based radar (GBR), a simulated signal source¹, a transmitting antenna and a host computer. The receiving antenna received real GNSS signal and the GBR detected real-time locations of victim UAVs. In a spoofing process, spoofing navigation signal from the simulated signal source suppressed real GNSS signal and made victim receivers obtain spoofing position solutions. For UAVs guided with GNSS/INS integrated navigation system, abnormal GNSS data would be detected and ignored. Thus, spoofing signal must match real GNSS signal and spoofing tracks were required to diverge from real locations gradually. Two spoofing tracks were generated for a non-cooperative UAV whose dynamic performance was usually unknown through track generation algorithms. The first track was used as an excitation of system identification, and the relationship between spoofing distances and traction distances was established using a neural network. The spoofing distance is from the spoofing track to UAV's planning track which can be reckoned according to its real-time locations, while the traction distance is from the real track after spoofing to the planning track. Based on the spoofing law, a parametric feedback algorithm was used to plan the second spoofing track that could control the UAV to evade no-fly zones.

Motivation

For insuring the crowd safety, it is necessary to enforce a no-fly zone for non-cooperative Unmanned Aerial Vehicles (UAVs) in some special instances. GNSS spoofing is a feasible measure to force a UAV to bypass non-fly zones.

Results

A spoofing experiment was carried out on a GNSS/INS guided UAV to evaluate validity of the spoofing system. The flight course consisted of two voyages, separately for spoofing law identification and evading task. On the voyage of evading task, a no-fly cylinder zone whose radius was 500 meters was enforced on the planning track. Experiment results demonstrated spoofing GNSS signal had suppressed and displaced real navigation signal. The UAV had been guided to bypass the non-fly zone successfully.

¹ F. M. Schubert, R. Prieto-Cerdeira, P. Robertson, et al. "SNACS-the satellite navigation radio channel signal simulator", The 22nd International Technical Meeting of the Satellite Division of the Institute of Navigation, 2009.

Autonomous and Autonomy of GNSS Constellations on the Age of Intelligent

Wende Huang, Yifan Zhou, Leyuan Sun

National University of Defense Technology, Changsha, China, 15574944081@163.com

Summary

This paper proposed a framework of GNSS autonomous navigation in terms intelligent. The architecture was designed, and the whole constellation was viewed as a dynamic network, which consists of a number of intelligent Agencies (e.g. GNSS satellites). The Agency was classified into different roles according to its own functions. To maintain a robust network when the GNSS constellation was operated in an autonomous and autonomy mode, action rules of an Agency and efficient algorithms were employed. Then key technologies, such as task planning, autonomous orbit determination and time synchronization, fault detection and restoration, etc. were concluded to highlight important parts of the framework.

Motivation

GNSS autonomous navigation, which known as autonav for GPS, had been well studied in terms of autonomous and autonomy since 1990s. As for the implementing aspect, GPS satellites had been launched with the capacity of autonav since Block IIR, which gave the GPS constellation a partial if not a whole autonomous and autonomy ability. As the Age of Intelligent coming, at the same time, the GNSS satellite can provide more flexible and powerful computational capacity, it is time to review the whole thing to reconstruct the architecture and rearranged the technologies used in autonav, with the purposes of that the performances of navigation were improved and the intelligent level of the constellation as a whole was promoted.

Results

Numerical example for autonomous and autonomy of BeiDou constellation was given to validated the approach proposal.

GNSS ISL Based Navigation of Satellites in Geotransfer Orbits

Yifan Zhou, Wende Huang, Leyuan Sun

*College of Mechatronics Engineering and Automation, National University of Defense Technology
No.109, Deya Road, Changsha, 410073, China*

GNSS space receivers are widely used for onboard autonomous navigation of spacecraft platforms in low Earth orbit. However, at a higher orbit, the situation changes dramatically as most of the directional GPS transmit antennas no longer point toward the user. Besides, the very low power levels seen at the receiver's antenna can worsen the already poor relative geometry of the GNSS receiver to the GNSS satellites. Because inter-satellite links (ISLs) are designed for inter-satellite ranging and communication between the navigation satellites, the space coverage of ISLs is better than the normal GNSS signal, which means we can obtain more strong enough signals for navigation. To evaluate the performance of navigation based ISLs, the GNSS satellite visibility and signal model for an ISL receiver are proposed, considering the user aperture angle, the antenna pattern, the Earth tangent horizon mask, the GNSS satellite antenna pattern and the signal power threshold of the receiver. Then, we design an EKF based algorithm to estimate the orbit parameter of user spacecraft and different measurement strategies are analyzed. Simulation results show ISLs have the capabilities to estimate the orbit parameter of user spacecraft in most of the case and two antennas oriented in the nadir direction and zenith direction respectively is recommended to ensure the high estimation precision of three phases of the geotransfer orbit. Besides, the number of available GNSS satellite and different measurement strategies has great influence on the performance of the estimation.

DEVELOPMENT OF A REAL TIME KINEMATIC ALGORITHM FOR LOW-COST GNSS RECEIVER USE IN SUBURBAN AREAS

Shiou-Gwo Lin¹, Feng-Chi Yu²

¹*Department of Communications, Navigation and Control Engineering, National Taiwan Ocean University,
Keelung, Taiwan*

²*Institute of Service Industries and Management, Minghsin University of Science and Technology, Hsinchu,
Taiwan*

Abstract

Following the global spread of the global navigation satellite system (GNSS), data from an increasing number of satellites is available for use in positioning. Therefore, recent studies have indicated that using low-cost GNSS receiver's single-epoch data in open areas for ambiguity resolution has an extremely high success rate. The attainment of such high-precision and high-efficiency positioning has enabled the GNSS to be used for unmanned aerial vehicles and driverless cars. However, in practical applications, implementation of the GNSS RTK often fails because of obstacles and interference. To increase the success rate, this paper develop a method combined the concept of partial ambiguity resolution and outlier detection. The proposed method is mainly advantageous for eliminating the measurement of interference satellite. There are tens of field tests in Keelung, Taiwan. These experimental results show that the GPS/BDS/Galileo partial ambiguity resolution technology is applicable for suburban area RTK.

A NLOS Reduction Architecture Embedded Navigation Algorithm Based on LiDAR SLAM-Aided INS/GNSS Integration System

Guang-Je Tsai, Kai-Wei Chiang, Naser El-Sheimy

Dept. of Geomatics Engineering, National Cheng-Kung University, No. 1, Daxue Road, East District, Tainan City, tpp1114@gmail.com

Dept. of Geomatics Engineering, National Cheng-Kung University, No. 1, Daxue Road, East District, Tainan City, kwchiang@mail.ncku.edu.tw

Dept. of Geomatics Engineering, The University of Calgary, 2500 University Dr NW, Calgary, AB T2N 1N4, Canada, naser@geomatics.ucalgary.ca

Summary

In this paper, an integration system is proposed to overcome the non-line of sight (NLOS) signal and satellite signal outage for inertial navigation system/global navigation satellite system (INS/GNSS). The proposed integration system combines INS/GNSS and simultaneously localization and mapping (SLAM) and takes challenge in urban area with land vehicle. By using the LiDAR grid-based SLAM, this paper presents the SLAM-aided velocity measurement and error model to control the drift in INS-only situation and prevent the NLOS GNSS signal, especially in urban environment. Besides, the proposed integration system allows the grid-based SLAM to perform in outdoor environment and applies on speedy vehicle by using the initial information from INS/GNSS. It is worth mentioning that the multilayer map is used by selecting the point cloud set in different channels (height) to compose different maps, avoiding the various obstacles in outdoor. The results show that our real-time integration solution can reduce the large amount of error and achieve over 90% improvement by using the low-cost sensors, compared to the high-grade navigation system processed by post-processing via commercial software.

Motivation

In recent years, the issue of autonomous vehicle goes viral and more and more corresponding researches are also published. To meet the requirement of autonomous level from National Highway Traffic Safety Administration (NHTSA), it is important to improve the position accuracy no matter in open sky area or urban area. The required navigation performance should have the ability to identify which lane (1.5 meters) or where in lane (within 1.0 meter) as well as good integrity navigation system¹. INS/GNSS is one of the navigation system to provide the stable and robustness navigation information. However, it heavily relies on GNSS quality and even tightly couple (TC) integration scheme is also strongly influenced by NLOS GNSS signal. The proposed navigation algorithm integrates the INS/GNSS with SLAM together to improve the navigation performance, as shown in Fig.1. The goal of this research is to show the great potential of integration algorithm in autonomous vehicle applications even using the low-cost sensors.

Results

Fig. 2 shows the configuration of our positioning payload, consisting of low-cost IMU, GNSS receiver (C-MIGITS and ublox M8T), VLP LiDAR and reference navigation system (SPAN-LCI). It is clear that the original INS/GNSS (C-MIGITS with ublox GPS, in blue) result shifts from the reference (post-processing by commercial software, in red) due to the NLOS GNSS measurements (in orange) shown in Fig. 3. The real-time solution (in green) by using the proposed navigation algorithm can improve the positioning accuracy and avoid the NLOS measurements based on the velocity information from SLAM. By comparing the reference solution, the overall improvement is larger than 90%.

¹ S. Stephenson, et al., "Accuracy requirements and benchmarking position solutions for intelligent transportation location based services", In Proceedings of the 8th International Symposium on Location-Based Services, 2011.

Figures

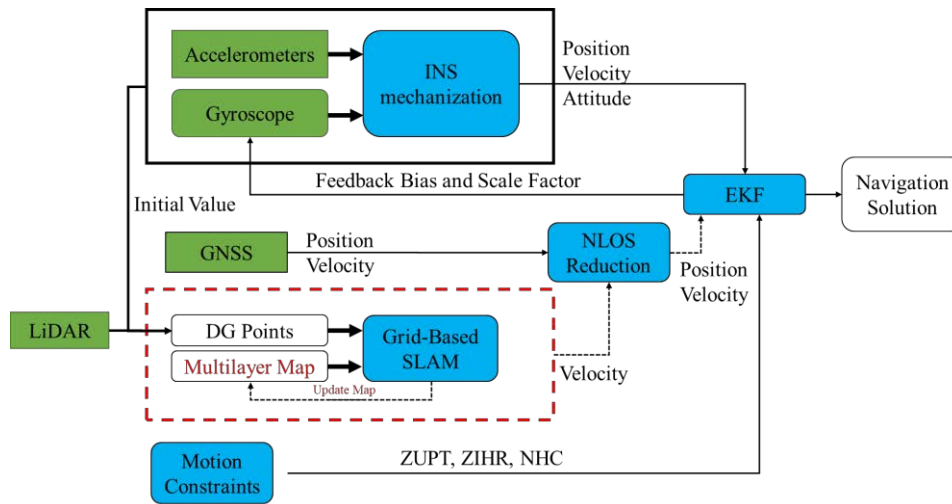


Fig. 1: Flowchart of integration navigation algorithm.



Fig. 2: Land vehicle positioning payload.



Fig. 3: Trajectories of three different results; SPAN-LCI (red line), C-MIGITS with ublox GPS (blue line), real-time SLAM-aided solution (green line), GNSS points (orange); SLAM-aided part (right) and enlarged SLAM-aided area.

Novel GPS Interference PDOA-Localization method

Max Nyström, Ryan Blay, Dennis Akos
Luleå University of Technology
University of Colorado Boulder
maxnystrom@gmail.com

Summary

This paper demonstrates a novel method of GNSS-interference localization utilizing nothing but 4 unsynchronized standard cellphones and a laptop. Experiments were done with true jamming events through cooperation with the Swedish Defence Research Agency, FOI (all use of interference was done accordingly to their regulations). Two methods of localization were tested and compared in terms of accuracy of localization. It is shown that localization through unsynchronized standard cellphones is comparable to more involved methods of localization.

Motivation

Interference of different sorts is a much discussed subject within the GNSS-community¹. As GPS signals are of low power, receivers are highly susceptible to interference, both unintentional and deliberate. As such, there is a need to develop practical ways of detecting and localizing interference sources.

Results

In the experiments featuring true jamming events, the cellphones were placed in a formation approximately 500 meters apart (see figure 1), and interference within the L1 band was then transmitted from different positions within the formation. The carrier-to-noise-density ratio values were processed with a laptop using a non-linear least square algorithm to estimate where the interference transmitter was positioned (see figure 2). Additionally GPS-front end modules were placed in the same formation in order to log IF-data. This data was used for localization through a TDOA approach which also involves a non-linear least square algorithm.

It is shown that the localization through the use of carrier-to-noise-density ratio values and PDOA methodology achieves an average error of 63 meters, which is comparable in accuracy to the TDOA approach (average of 48 meters), as well as more involved methods of PDOA localization².

¹ Amin, M. G., P. Closas, A. Broumandan, J. Volakis, "Guest Editorial: Vulnerabilities, threats, and authentication in satellite-based navigation systems," *Proceedings of the IEEE*, 104(6), pp. 1169-1173, 2016.

² Isoz, Oscar, Balaci, Asghar T., Akos, Dennis, "Interference Detection and Localization in the GPS L1 Band," *Proceedings of the 2010 International Technical Meeting of The Institute of Navigation*, San Diego, CA, January 2010, pp. 925-929

Figures



Fig. 1: Overview of testing area and the 4 receiving stations locations in the field.

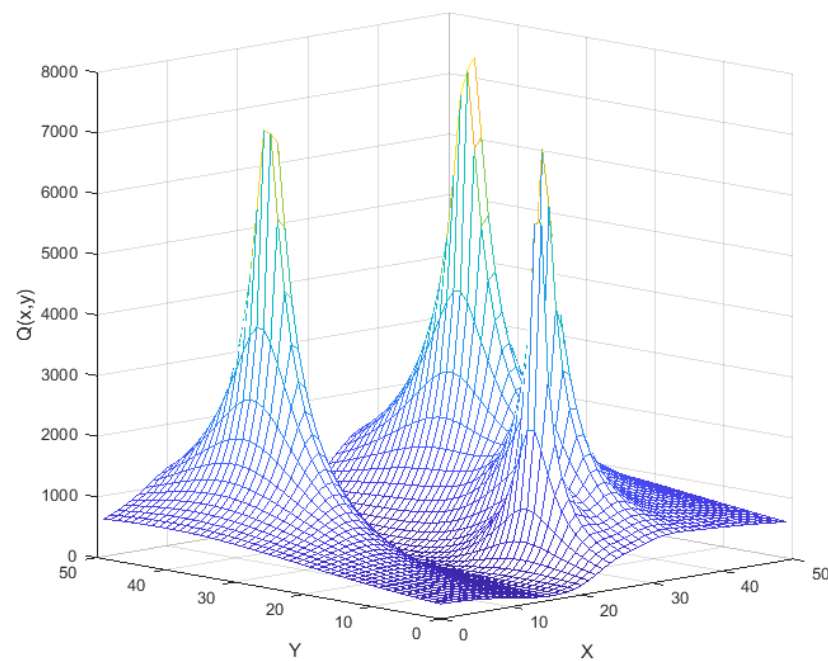


Fig. 2: Output of NLLS algorithm for PDOA localization, in which the lowest value of Q is the estimated position of interference.

BDS adjusted box-wing physical solar radiation pressure model considering the yaw attitude

Xiaoya Wang^{1,2}, Kewei Xi^{1,2}, Qunhe Zhao^{1,2}

¹Shanghai Astronomical Observatory, Chinese Academy of Sciences, 80 NanDan Road, Shanghai 200030, China.

Email: wxy@shao.ac.cn

²University of Chinese Academy of Sciences, Beijing 100049, China

Summary

The solar radiation perturbation is an important factor affecting the accuracy of satellite orbit, it related to the satellite attitude and satellite radiation characteristics. The special constellation of Beidou navigation system lead to a difference attitude control from GPS/GLONASS. Therefore, the traditional solar radiation pressure model can't meet the pressure of IGSO/MEO high precision orbit determination during the satellite attitude switching. It is necessary to establish a suitable high precision pressure model for Beidou navigation system. This paper establishes a new SRPM model which based on the BOX-WING model and also considering about radiation model parameters change during satellite attitude switch, the applicability and accuracy of the model was verified by measured data of Beidou tracking network (from MEGEX). The results show that compared to the BERN model, IGSO and MEO orbit residuals improve the accuracy of 10% to 30% during the attitude-switching period. Compared with the GBM final orbit, the residual values of POD and the residual error of long arc prediction based on are significantly decreased.

Motivation

The solar radiation perturbation is one of the most important factors affecting the accuracy of satellite orbit determination. The maximum level of acceleration can reach to $1e-8$ according to the orbit height and the intrinsic characteristics of different radiation pressure. The effect of pressure perturbation influence on navigation satellite orbit including photon, satellite attitude control error, parameter changes in optical properties of the surface of the planet, solar radiation constant and the mass change of satellite[1,2]. Because there is a strong correlation between the influence factors and the parameters, it's difficult to use a simple model to accurately describe the characteristics of pressure, so the study of solar radiation model has become an important work in the way of high precision orbit determination.

The traditional solar radiation model is mainly experience model based on a long time observed data in large GNSS observation network. The establishment of the BERN series model has tremendous improve the accuracy of GPS satellite precision orbit determination. In order to meet the demands of satellite navigation tasks, it must be ensure that the solar panel is perpendicular to the sun and the downlink antenna is as close as possible perpendicular to the ground. The way to solve the problem is to adjust the yaw angle according to the satellite sensor and satellite orbit attitude named yaw-steering mode. When the sun angle is less than a certain angle, the satellite will change control strategy. It gives priority to ensuring the alignment of downlink antenna and the yaw angle is fixed to zero named orbit-normal mode. For the BDS constellation, Geosynchronous Earth Orbit (GEO) satellite always keep in the orbit-normal mode. Inclined Geosynchronous Satellite Orbit (IGSO) and Medium Earth Orbit (MEO) use combination of yaw steering and orbit-normal. The Satellite attitude mode can be switched within a year at least two times. If the influence of attitude switching is not considered properly, it will lead to a decline in the accuracy of satellite orbit [3-5]. According to the research of Guo Jing et al, the approximate condition of BDS satellite attitude switching is that when the sun angle is less than 4 degree, the satellite attitude is converted to orbit-normal until the sun angle is greater than 4 degree, the orbit-normal will change to the yaw-steering[6,7].

The related research shows that it can meet the requirement of precision orbit determination when BERN model is used for BDS in yaw steering. However, due to the satellite's characteristics and constellation differences, the accuracy of orbit determination will decrease significantly. The solar radiation perturbation error mainly lies on inconsideration on the corresponding changes between the orbit-normal and yaw steering. Considering the construction of BDS constellation uncompleted and the limited site distribution, a physical solar radiation pressure model with the BDS attitude control strategy was established based on the Box-wing model. Compared with the BERN model, the new model SRPM takes into account

the structural characteristics and the yaw information. It can reflect changes of satellite area by using the subdivision body modelling area element. It can be better at reaction radiation characteristics and reflect the pressure force of the continuous variable.

Results

In order to analyze the orbit determination accuracy of BERN and SRPM models under yaw-steering/orbit-normal situation, the estimated orbit is compared with the precise orbit products of GFZ and the three-dimensional RMS is plotted in Figure 1.

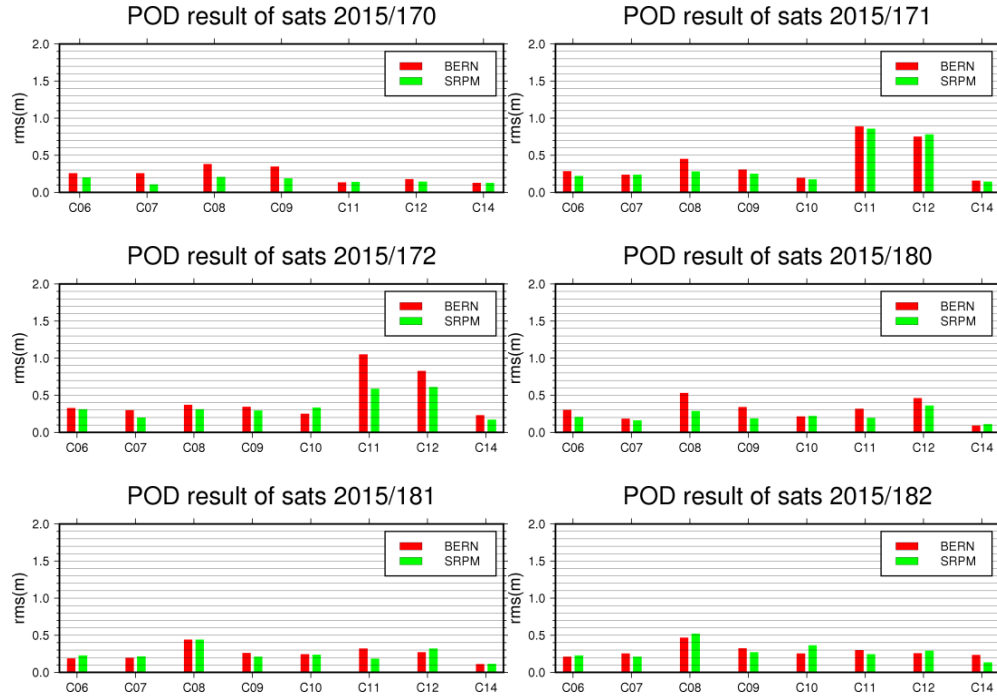


Fig. 1. Orbit determination precision during attitude conversion

It can be seen from Figure 1 that all the satellites are in yaw steering on DOY 170, the orbit determination accuracy of the SRPM model is better than the BERN model. The orbit determination result is better than 0.2m. The C11 and C12 are in the direction of yaw attitude transformation during DOY 171. The orbit determination accuracy for both of two satellites has decreased. However, the orbit determination results of other satellites remain stable. This shows that when the data of the tracking network is sufficient, the accuracy of the overall orbit determination can be stabilized during the attitude switching and the POD accuracy in the attitude switching will be reduced. The attitude conversion of satellite C11 and C12 on DOY 172 shows that the residual value of the SRPM model is smaller than the BERN model 0.4m and 0.2m respectively. On the DOY of 180/181, the satellite C08/C11/C12 is in orbit-normal, but the rest of the satellites are in yaw steering. From the orbit determination residuals, the orbit residuals of SRPM at yaw steering are smaller than that of BERN models. The overall performance is better than that of 0.5m. It is obvious that the orbit determination results for satellites are smaller during the yaw steering. However, the orbit determination residuals of some satellites are smaller by BERN models. The reasons should be further studied.

The overlap arcs can reflect the accuracy of GNSS orbit determination. It gives out the three dimensional RMS information of BERN and SRPM models overlapped for 2 days shown in Figure 2.

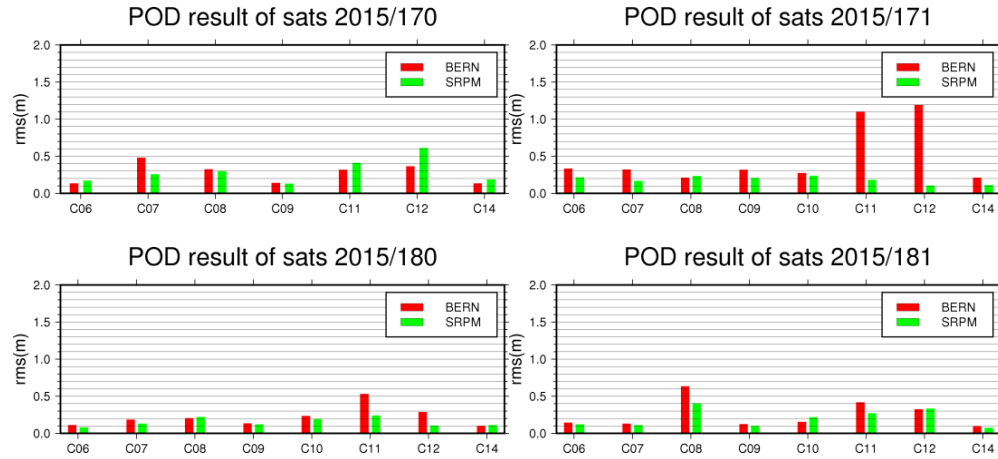


Fig. 2. Overlapping arcs during attitude conversion

From Figure 2, we can see that IGSO satellite overlapped arc residual error is smaller than that of BERN model during the yaw steering that can be reduced to 0.2m. However, the MEO satellite performs better under the BERN model. The C11 and C12 satellites have higher accuracy and maximum 1m is reduction in the SRPM model during the attitude switching. It can make sure the overlapped better than 0.5m and avoid the significantly descend of orbit accuracy during the attitude switch.

The most important way to check orbit accuracy is to predict the orbit by the same model as the orbit determination and then use statistical results to reflect the accuracy of the dynamic model. POD and orbit prediction based on these two models are respectively shown in Figure 3. The three-dimensional RMS statistical results was listed in Table 2 as below.

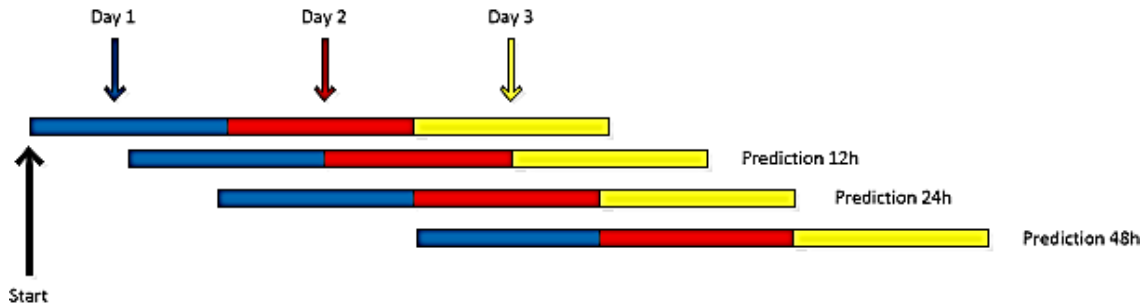


Fig. 3. Orbit Forecasting Method

Table 1 The predicted 12/24/48 hours orbit RMS for BERN and SRPM models

satellite\model	Pre 12h		Pre24h		Pre 48h	
	BERN	SRPM	BERN	SRPM	BERN	SRPM
C06	0.295	0.264	0.604	0.335	1.394	0.513
C07	0.288	0.258	0.761	0.298	1.571	0.458
C08	0.960	0.649	2.705	1.158	7.566	2.545
C09	0.286	0.248	0.560	0.299	1.434	0.526
C10	0.403	0.356	0.949	0.430	1.766	0.608
C11	0.834	0.527	2.020	0.804	5.381	1.488
C12	0.694	0.424	1.633	0.670	3.965	1.364
C14	0.344	0.244	0.674	0.325	1.228	0.578

Statistical results show that the accuracy is approximately the same when the two orbits are predicted to 12h. For the satellite with attitude switching, the prediction accuracy of SRPM can be increased by about 0.3m. The 24h orbit prediction accuracy of BERN model for satellite attitude switching decreases rapidly. It is mainly because there is a big error in attitude switching. The maximum predicting error for C08 reached 17.86m. However, at the same time the error of the SRPM model is only 3.8m. Statistical results show that the prediction accuracy of SRPM can be increased by about 0.4m for satellites in the yaw steering. The statistical accuracy of the orbit prediction of the BERN model is seriously reduced. For the 48h orbit prediction, it is similar to the 24h prediction. The SRPM model has maintained a better prediction effect. From the yaw-steering satellite statistics, the prediction results show that the maximum RMS can be reduced 0.7m compared with the BERN model.

Visual-Inertial SLAM by fusing Stereo and Inertial Measurement Units based on ORB-SLAM

Yi-Chieh Sun, Shau-Shiun Jan

National Cheng Kung University, Tainan 70101, Taiwan, jessica89103@gmail.com

National Cheng Kung University, Tainan 70101, Taiwan, ssjan@mail.ncku.edu.tw

Summary

Inspired by the work of monocular ORB-SLAM fusing with IMU¹, we follow the methods they adopted to achieve a visual-inertial SLAM, which are tightly-coupled and optimized-based method. In addition, we use stereo camera in order to acquire the information of scale. The IMU measurements between two keyframes are pre-integrated into a single compound measurement for the sampling rate of IMU is higher than the camera (see Figure 1). The initialization of a visual-inertial system is an important issue which we are focusing on. Several steps are included to initialize the mono visual-inertial ORB-SLAM. First step is to compute the bias of gyroscope. Next, scale and gravity vector are estimated without considering the accelerometer bias. As the direction of gravity is received, the magnitude of gravity is used to solve the accelerometer bias, and refine scale and gravity direction. Finally, the velocity of each keyframe can be computed from the position relation between two consecutive keyframes. When all the variables above are reliably estimated, the system starts fusing the IMU information. We expect that as the stereo camera provides the scale information, the equation solving the scale and gravity vector can be simplified and thus speed up the calculation. The estimation of gravity direction and the accelerometer bias can then be closer to the true value to improve the accuracy of the proposed method.

Since the stereo camera is able to provide the scale information, and research of fusing stereo and IMU based on the algorithm of ORB-SLAM has not yet been presented, this research proposes a visual-inertial SLAM by fusing stereo camera and IMU sensors based on ORB-SLAM.

Motivation

The simultaneous localization and mapping (SLAM) has been a popular research topic, and is widely used in robotic vision, virtual reality, and augmented reality. However, visual SLAM has some weakness while processing a pure rotation situation, moving object pass by, or non-textured area. These situations might affect the accuracy of pose estimation, and even result in tracking lost. In order to solve the problem, it is beneficial to fuse inertial measurement units (IMU) with SLAM. IMU observations are more appropriate for a quick movement during a short period of time, which is contrarily the weakness of a camera. On the other hand, the drift of the inertial sensor can be corrected by fusing data with camera since the image information does not drift if the camera is in a fixed location. Thus, camera and IMU measurements are able to complement each other to supply a more robust and accurate system.

In 2016, a research of fusing monocular camera and IMU sensors with ORB-SLAM has been presented¹. Following the approach of ORB-SLAM, the system is capable of closing loops and reusing its map to achieve zero-drift localization in the already mapped areas. The research overcomes the weakness of the IMU drift and the accurate state estimations from visual-inertial initialization can be received. However, monocular camera has a well-known problem of scale ambiguity. Hence, the system requires scale estimation and scale refinement. If the scale can be known at the start of the system, it is believed that the initialization procedure can be simplified and the calculation time can be reduced. Using a stereo instead of a monocular camera, the system can receive more information from images, which enhances the ability for tracking. Thus, more accurate pose estimations will be obtained and the robustness will be increased.

¹ Mur-Artal, Raúl, and Juan D. Tardós. "Visual-inertial monocular SLAM with map reuse." IEEE Robotics and Automation Letters 2.2 (2017): 796-803.

Results

To conclude, we present a tightly-coupled visual-inertial SLAM system. This ORB-SLAM-based system is fused with a stereo camera, providing complete localization and mapping in indoor areas with automatic initialization. We use the proposed method to process online dataset EuRoC and compare the performance with that of the mono visual-inertial ORB-SLAM system. First we compare the calculation time for the complete IMU initialization. Since the stereo camera provides the scale information, we believe that the calculation of the IMU initialization can be simplified and therefore reduce the time of receiving the accurate initialization. Second, the influence of the initialization performance on the accuracy in later optimization procedure is presented. In order to check whether a stereo camera provides more precise results than a monocular one, we then calculate the root mean square error (RMSE) of the trajectory, and compare the result with that of the mono visual-inertial ORB-SLAM. The robustness of our method is also checked. EuRoC dataset includes 11 sequences containing different flight dynamics and lighting conditions. While the mono visual-inertial ORB-SLAM lost track in one of the eleven sequence, we expect that our system will successfully process every sequences. Finally, the proposed method fusing stereo camera and IMU sensors based on ORB-SLAM is expected to have simpler initialization procedure, more accurate positioning result, and is more robust of processing in different conditions.

Figures

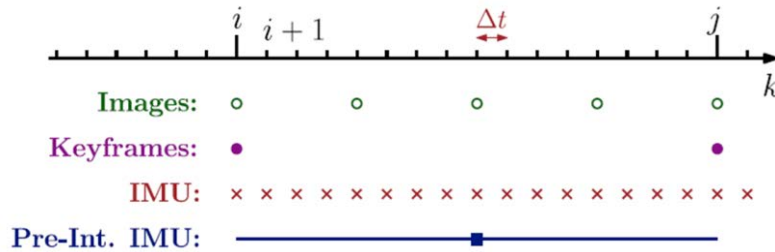


Figure 1: The concept of imu pre-integration

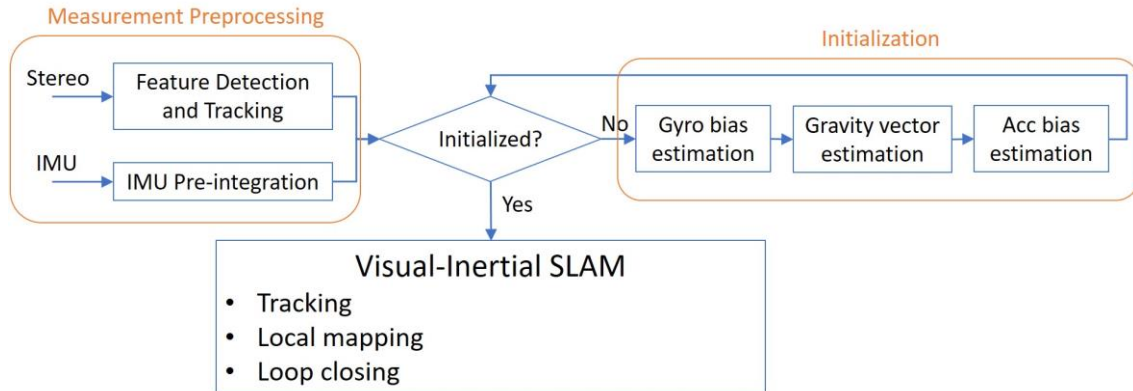


Figure 2: System flow chart

Vision Based Navigation for Asteroid Explorer

Yu-Tse Hsieh, Shau-Shiun Jan, Kai-Wei Chiang

National Cheng Kung University, Tainan 70101, Taiwan/ sam40168@gmail.com

National Cheng Kung University, Tainan 70101, Taiwan/ ssjan@mail.ncku.edu.tw

National Cheng Kung University, Tainan 70101, Taiwan/ kwchiang@mail.ncku.edu.tw

Summary

This research is to develop a method using low-cost mono-camera to provide vision-based navigation for asteroid explorer during descent phase. Terrain relative visual navigation (TRVN) (see Fig. 1) is integrated with terrain absolute visual navigation (TAVN) (see Fig. 2) to achieve precision landing on asteroid surface. We choose the nearest asteroid, Moon, as the simulation environment. Our research first applies a TRVN to obtain the explorer's relative position. Secondly, this research presents an algorithm of TAVN, where a large area lunar surface feature points database is created, which includes feature point's descriptor and the three-dimension position in the moon-fixed coordinate. When a lunar surface image is applied as an input, the algorithm detects all the feature points of the image and matches the descriptor with the database. The camera absolute position in the moon-fixed coordinate is then derived from the feature points matched with the database and the points' pixel position on the image. However, matching the descriptor with the database takes time to calculate the absolute position. Moreover, when the explorer descends below a certain height, matched feature points might be insufficient for the camera vision to calculate the absolute position. In these situations, TRVN is essential to provide the navigation for the explorer. The extended Kalman filter (EKF) is utilized in our study as the navigation engine to integrate TRVN and TAVN. EKF provides integrated navigation solutions by loose coupling, to correct the TRVN's accumulative error, and calculate the scale factor for TRVN by using the absolute position from TAVN. In addition, when the relative navigation tracking is lost, TAVN could provide positions for the explorer at the lower sampling rates. Therefore, when TAVN is in process or the camera vision is lack of matched feature points, TRVN could provide measurements for the navigation engine to output the navigation solution.

Motivation

Planetary and asteroid exploration is an essential way to unveil the mysteries of space. To discover whether there is any life or water in the outer space, we must take a closer look. Asteroid explorer autonomous precision landing is one of the crucial step for exploration and research. Traditionally, inertial navigation system (INS) and light detection and ranging (LiDAR) are mostly used. However, both of these sensors are expensive. Thus, the objective of this research is to develop a method using low-cost mono-camera to provide vision-based navigation for asteroid explorer during descent phase. Terrain relative visual navigation (TRVN) is integrated with terrain absolute visual navigation (TAVN) to achieve precision landing on asteroid surface. In recent years, visual odometry (VO) has been developed rapidly with low-cost sensor, camera, to provide the translation and rotation of vehicles. In general, VO has an accumulative error coming from scale-drift, rotation-drift, and translation-drift. In addition, the mono-camera cannot provide the scale factor relating to the real world. Hence, it is important to integrate monocular VO with absolute navigation algorithm to reduce the accumulative error and estimate the scale factor.

Results

This paper presents a mono-camera vision-based navigation for asteroid explorer. Integrating terrain absolute visual navigation (TAVN) and the terrain relative visual navigation (TRVN) to provide the scale factor for mono-camera visual odometry, and correct the accumulative error as well. To achieve the precision landing on asteroid surface. The experimental results including the positioning error statistics of TRVN, TAVN, and the integrated navigation engine are evaluated in the paper. As shown in the experimental results, the positioning performance of this proposed navigation algorithm is improved.

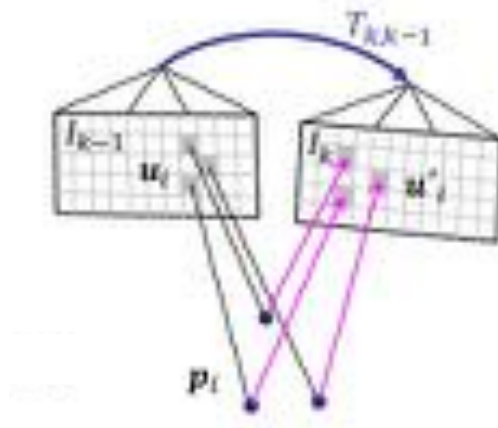


Fig. 1: The concept of TRVN algorithm

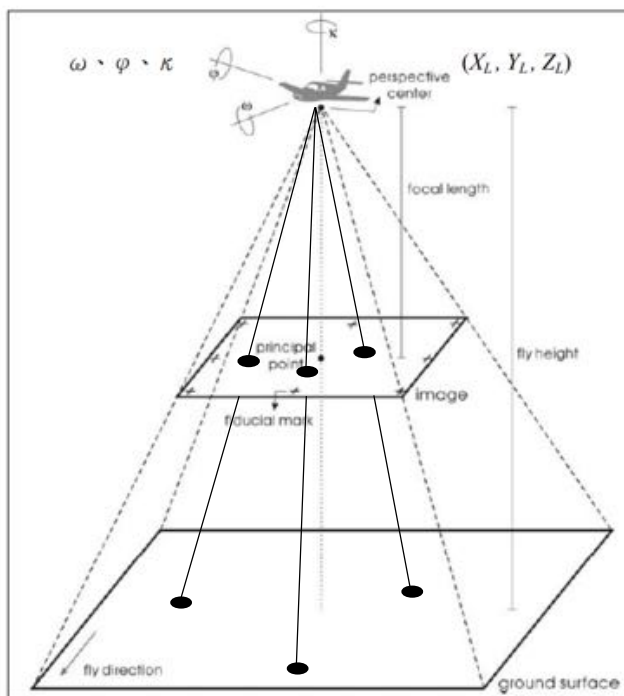


Fig. 2: The concept of TAVN algorithm

Estimation and analysis of GPS satellite DCB using regional GPS network

Deokhwa Han, Donguk Kim, Changdon Kee*

School of Mechanical and Aerospace Engineering and Institute of Advanced Aerospace Technology,
Seoul National University, Seoul, South Korea, gksejrgkh@snu.ac.kr

Summary

Differential Code Bias (DCB) is a major error source of GPS-based TEC (Total Electron Contents) measurement. To obtain precise ionospheric measurement, it is important to estimate DCB accurately.

The performance of DCB estimation is affected by size of GPS networks. When the satellite DCBs are estimated using only regional GPS networks, the estimation performance is degraded¹.

GPS-based TEC measurement is composed of TEC, satellite DCB and receiver DCB. From observed TEC measurement, the ionospheric modeling parameters and DCBs are estimated simultaneously. Therefore, ionosphere modeling accuracy affects the performance of DCB estimation². In general, ionosphere is more active in daytime and the ionosphere modeling performance can be degraded. This implies that the DCB estimation performance can also be degraded in daytime.

Regional GPS Networks have limited visibility for a certain satellite. Fig.1 shows the selected reference stations in South Korea and Fig.2 shows the elevation angle of several GPS satellites with respect to the given reference stations. Because the reference stations are distributed in small area, it was found that the all reference stations have very similar visibility for GPS satellites. Many studies assume that DCB is constant over entire day and estimate one set of satellite DCB per day^{1,3,4}. If the measurements are collected for one day, there are some satellites that most of measurements are collected in daytime like PRN 28. The estimated DCBs of those satellites have low accuracy, because the ionosphere modeling accuracy is degraded in daytime.

Recent study found that the satellite DCB have long-term stability and its variation is very small⁵. To overcome problem, we accumulate measurement for long period and estimated one set of satellite DCB from those measurement assuming that they are constant over several month. In this way, the problem of limited visibility in certain local time can be mitigated. Fig. 3 shows the elevation angle observed by SEJN station. From March 1 to September 1, the measurements were collected on the first day of each month. Because the period of GPS satellite is about 11 hour and 58 minutes, observed time changed about 4 minutes per day. In addition to this change, we apply the local time dependent weighting factor to give a small weight to measurements collected in daytime (see Fig.4).

The validation of results can be done by comparing the estimated DCBs with those published by International GNSS Service (IGS) community^{1,2,3}. However, it is difficult to evaluate the results precisely using the DCBs published by IGS, because DCBs can be different for each receiver type with the effect of Inter Receiver Satellite Bias (IRSB)⁶. We use alternative method to verify the result. After removing other error sources precisely, the dual-frequency positioning is carried out applying estimated satellite DCB. If

¹ Xue J-C, Song S-L, Zhu W-Y, Lu X-S, "A study on the reliability of the ionospheric VTEC and satellite DCB derived from a regional GPS network", *Chinese astronomy and astrophysics*, vol. 36, nr. 1, p. 73-85, 2012.

² Kao S, Tu Y, Chen W, Weng DJ, Ji SY, "Factors affecting the estimation of GPS receiver instrumental biases", *Surv Rev.*, vol. 45, nr. 328, p. 59-67, 2013.

³ Jin R, Jin S, Feng G, "M_DCB: Matlab code for estimating GNSS satellite and receiver differential code biases", *GPS Solut.*, vol. 16, nr. 4, p. 541-548, 2012.

⁴ Li LX, Zhang DH, Zhang SR, Coster AJ, Hao YQ, Xiao Z, "Influences of the day-night differences of ionospheric variability on the estimation of GPS differential code bias", *Radio Sci.*, vol. 50, nr. 4, p. 339-353, 2015.

⁵ Song S, Xue J, Zou, "The stability analysis of GNSS satellite DCB", IGS workshop 2016, February 8–12, Sydney, NSW, Australia, 2016.

⁶ Hauschild A, "Correlator- and Front-end-dependency of GNSS pseudorange biases for geodetic receivers", IGS workshop 2015, November 5–6, Bern, Switzerland.

the other error sources are removed correctly, residual errors are mainly dependent on the accuracy of DCB. Therefore, the results can be analyzed by pseudorange residual.

Motivation

The size of GPS networks is important factor for estimating satellite DCB. If GPS reference stations are distributed in small region, DCB estimation performance is degraded.

There are some cases that the DCBs are estimated with only regional GPS networks. For example, SBAS (Satellite-Based Augmentation System), which is the regional augmentation system, have to provide the corrections for ionospheric delay. Because of its limited distribution of reference station, the DCB estimation performance can be degraded. This results in degradation of correction.

We proposed the estimation method to mitigate these degradation.

Results

Test was carried out using five reference stations in South Korea (see Fig. 1). From March 1 to September 1 2014, data were collected on the first day of each month.

First, satellite DCBs were estimated using conventional method. In other words, only one-day data were used for DCB estimation. Next, satellite DCBs were estimated using proposed method. Using all collected data, satellite DCBs were estimated. There are 7 days, so there are 7 sets of satellite DCB which is estimated by conventional way, and 1 set of satellite DCB which is estimated by proposed method.

For each day, the residuals were calculated by applying the DCBs estimated by conventional method using the measurement of that day (see red line in Fig. 5). Also, the DCBs estimated by proposed method were applied to each day and the results were compared (see blue line in Fig. 5). In this process, the other error sources are removed precisely. The IGS ephemeris and clock product was used to prevent satellite related errors. Tropospheric error was removed by Saastamoinen model. Noise and multipath error was mitigated by using carrier leveling method.

Figure 5 shows the results. After dividing local time into several sections, RMS of pseudorange residuals are calculated. The red lines shows the results of conventional method and blue lines shows those of proposed method. When the conventional method is used, pseudorange residuals increased in daytime. This means that the DCB estimation error is relatively large during daytime. On the other hand, increase of residual in daytime is mitigated when using proposed method. These results confirmed that the proposed method can improve the accuracy of DCB estimation for regional GPS networks.

Acknowledgment

This research was supported by a grant (17CTAP-C129724-01) from Technology Advancement Research Program funded by the Ministry of Land, Infrastructure, and Transport of Korean government, contracted through SNU-IAMD at the Seoul National University.

Figures

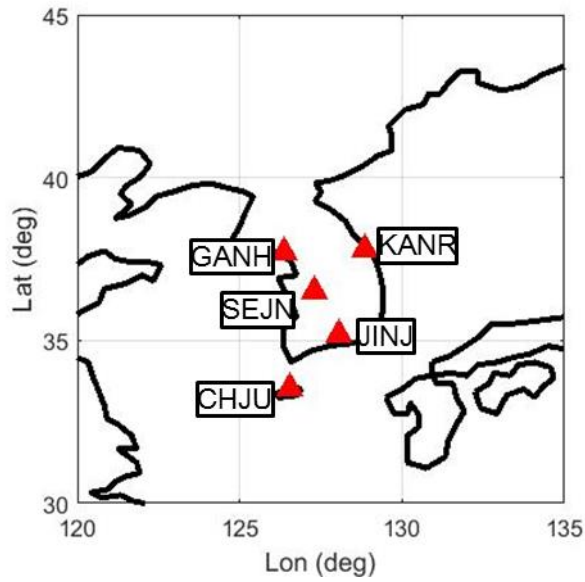


Fig. 1: Configuration of the reference stations in South Korea

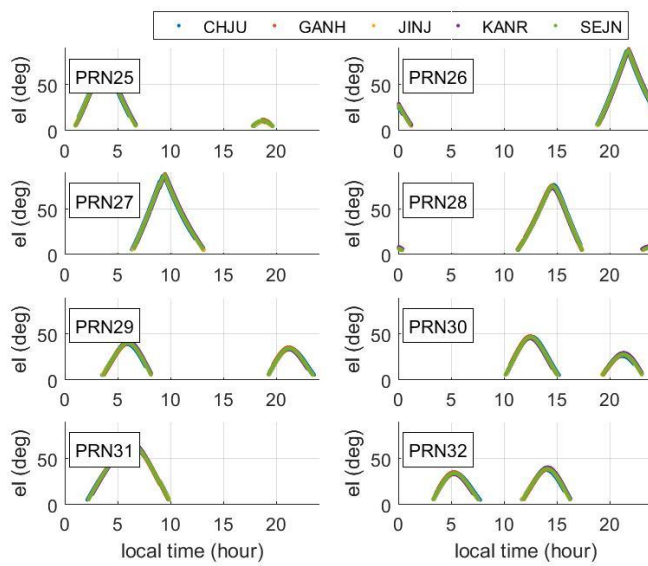


Fig. 2: Elevation angles on September 1, 2014 (PRN 25~32)

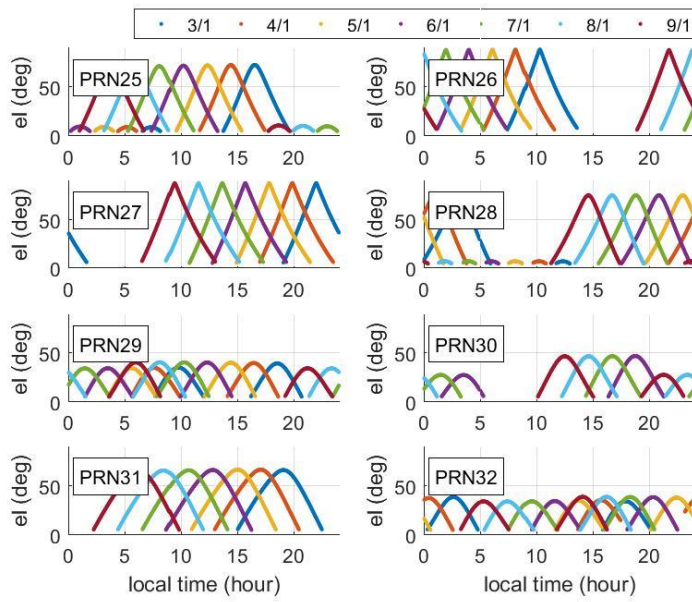


Fig. 3: Elevation angles from March 1 to September 1, 2014 (PRN 25~32)

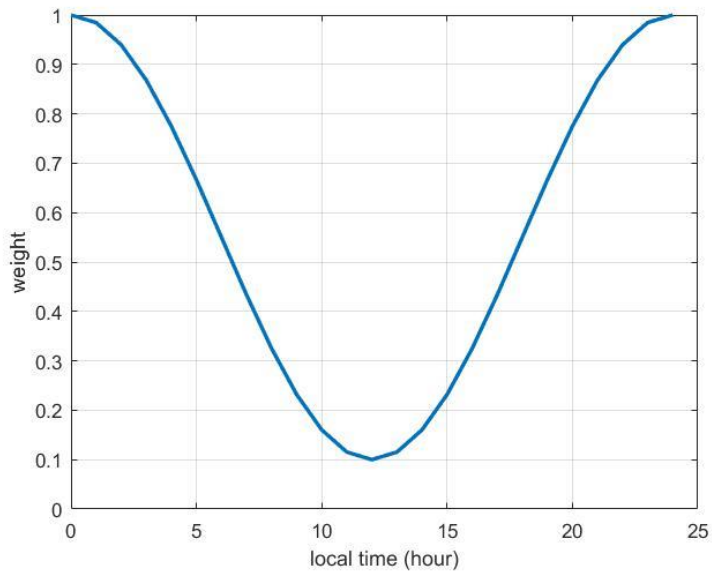


Fig. 4: local time dependent weighting factor

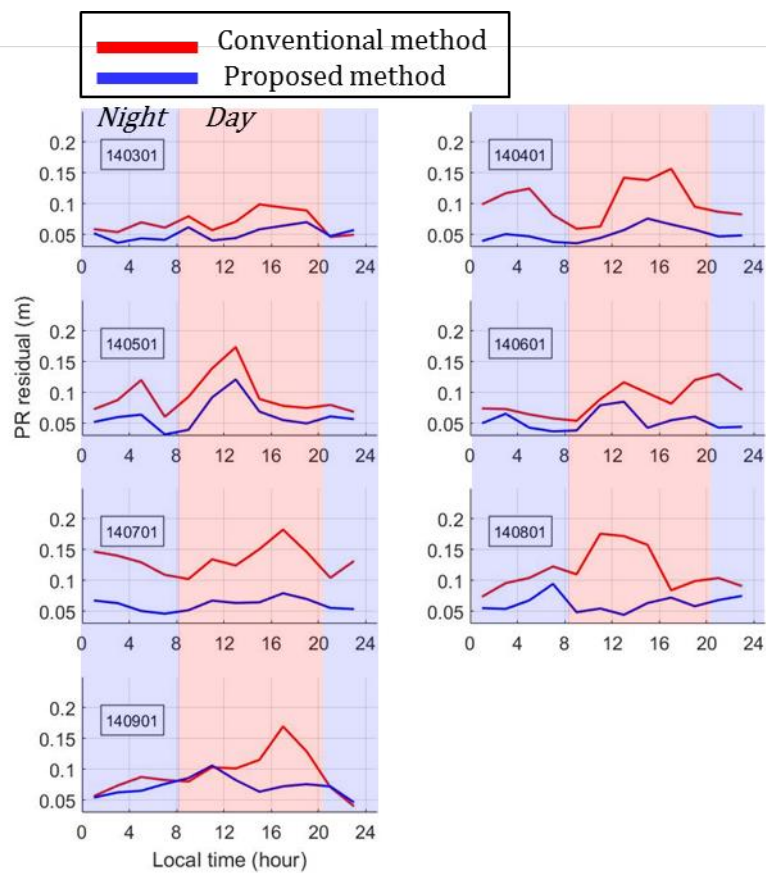


Fig. 5: pseudorange residual versus local time

Motion Conflict Detection in the Smart Tachograph

Daniele Borio, Eduardo Cano, Gianmarco Baldini

European Commission, Joint Research Centre (JRC), Ispra (VA), Italy
Email: {daniele.borio, eduardo.cano-pons, gianmarco.baldini}@ec.europa.eu

Abstract—The Smart Tachograph (ST), the new revision of the Digital Tachograph (DT), has to verify periodically the consistency of data from different sensors in order to mitigate the risks of frauds. In this respect, a test procedure is specified for the detection of motion conflicts originating from inconsistencies between Global Navigation Satellite System (GNSS) and odometry data. This paper provides an experimental evaluation of the motion conflict detection procedure specified by the ST regulation. Several hours of data were collected using two vehicles equipped with a multi-constellation GNSS receiver and an On-Board Diagnostics (OBD) data reader. The data collected were then used to implement the tests prescribed by the ST regulation and evaluate their effectiveness. The analysis shows that the new regulation significantly strengthens the DT against possible attacks, such as GNSS meaconing. In particular, an attacker is forced to falsify data simultaneously and coherently from both the vehicle sensor and the GNSS receiver. Moreover, it is shown that the metrics selected for the tests are resilient to data gaps and relative delays between GNSS and odometer data.

Full paper in IEEE Xplore

The Performance Analysis of applying Differential Distance Correction in BLE-based Indoor positioning System

Yun-Tzu Kuo, Jhen-Kai Liao*, Kai-Wei Chiang*

Department of Geomatics, National Cheng-Kung University, Tainan, Taiwan, yuki31210@gmail.com

* Department of Geomatics, National Cheng-Kung University, Tainan, Taiwan

Summary

Recently, indoor positioning has grasped much attention with the emergence of Internet of Things (IoT) which can provide various location-aware applications. Nowadays, many researchers are devoted to investigating a suitable wireless communication technology to build an indoor positioning system. However, there still doesn't exist an ideal solution to satisfy the varied indoor environments. Considering the cost, power consumption, and efficient deployment, Bluetooth Low Energy (BLE) is an appropriate alternative to provide indoor positioning application. Moreover, the ubiquitous smartphones make BLE-based indoor navigation system more convenient for users with no additional equipment. The Received Signal Strength Indicator (RSSI) broadcasted by BLE beacons is commonly used for positioning, but RSSI value fluctuates due to the effect of multipath and fading, which will lead to poor accuracy. Therefore, the novel method named differential distance correction is inspired by the concept of Differential Global Navigation Satellite System (DGNSS) and Real Time Kinematic (RTK) to reduce such phenomenon. This method utilizes the differential information from the reference station with known coordinate to correct the measurements from the rover station, which is also regarded as the user's device. It is considered that both reference and rover station are suffered from similar effect condition, hence the proposed method can reduce the correlative error. In this study, the power regression model is used for converting RSSI to distance, and the differential distance correction is adopted to obtain enhanced distance measurements. Furthermore, trilateration is selected as the primary positioning technique to locate the position of the rover. Finally, with better distance measurements, the proposed method can not only enhance the positioning accuracy of trilateration, but also reduce the number of beacons while maintaining similar accuracy.

Motivation

Trilateration is the principal method of GNSS and it can be implemented similarly in the indoor environment. However, the positioning accuracy is dependent on the accuracy of estimated distance converted from RSSI. RSSI values are variant because of the effect caused by the surrounding environment (i.e. multipath and fading effect) which will result in poor estimated distance and inaccurate positioning result. Therefore, the concept of differential distance correction motivated by DGNSS and RTK is developed in order to reduce such effect and improve the accuracy of trilateration. In the previous study, it is found that the proposed method is able to decrease the positioning error¹. Another evaluation is carried out for reducing the number of beacons while maintaining similar accuracy. Since the number of beacons is related to the positioning error², it might need a considerable number of beacons to achieve the desired accuracy. To overcome the limitation, the proposed method is developed not only to obtain better distance measurements to improve the accuracy of trilateration but also to reduce the cost of beacon infrastructure.

¹ Y. T. Kuo; J. K. Liao; K. W. Chiang, "BLE-based Indoor Positioning using Differential Distance Correction Technique", In Proceedings of the *International Symposium on GNSS (ISGNSS)*, Hong Kong, China, 10-13 December 2017.

² M. Ji; J. Kim; J. Jeon; Y. Cho, "Analysis of Positioning Accuracy corresponding to the number of BLE beacons in Indoor Positioning System", In Proceedings of the *17th International Conference on Advanced Communication Technology (ICACT)*, Seoul, South Korea, 1-3 July 2015, p. 92-95, 2015.

Results

The experiment is conducted in the classroom with the size of $8 \times 14 \text{ m}^2$. Six BLE beacons are arranged at known coordinates, so are the two reference stations. The rover station is placed at 7 different checkpoints respectively to evaluate the performance, as shown in Figure 1. The reference stations are used for estimating the error caused by the environment and building residual maps to correct the measurement of the rover station. Figure 2 illustrates the positioning result and the Cumulative Distribution Function (CDF) of positioning error at one of the checkpoints. Table 1 summarizes the overall performance of different cases with two indices including the 90% positioning error, and the Root-Mean-Square Error (RMSE). The case of 6 beacons indicates that all the beacons are used, while the case of 4 beacons means only B1, B2, B5, and B6 are adopted. Note that the “Correction” in Table 1 denotes that the differential distance correction is applied. The experimental result verifies that more beacons will improve the positioning accuracy, and the proposed method can further enhance the accuracy in both cases of 6 beacons and 4 beacons with which the RMSE reduced from 3.20 m to 1.98 m in 6 beacons, and from 3.33 m to 2.24 m in 4 beacons, respectively. Moreover, the accuracy of applying the proposed method still maintains even when fewer beacons are adopted with the positioning error of less than 3 m, which meets the accuracy of BLE and is sufficient for indoor navigation. To conclude, the proposed method has the ability to improve the positioning of trilateration and sustain similar accuracy while the number of beacons is reduced.

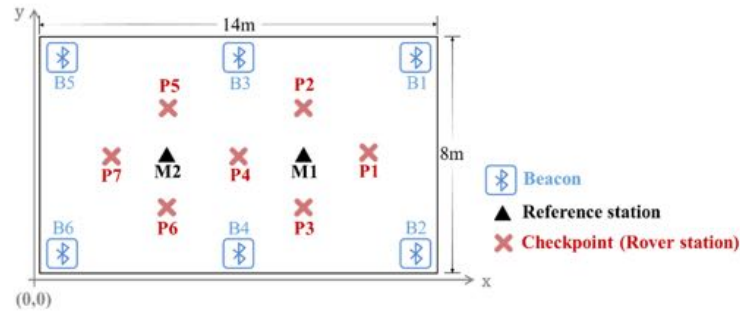


Fig. 1: The arrangement of the experimental field

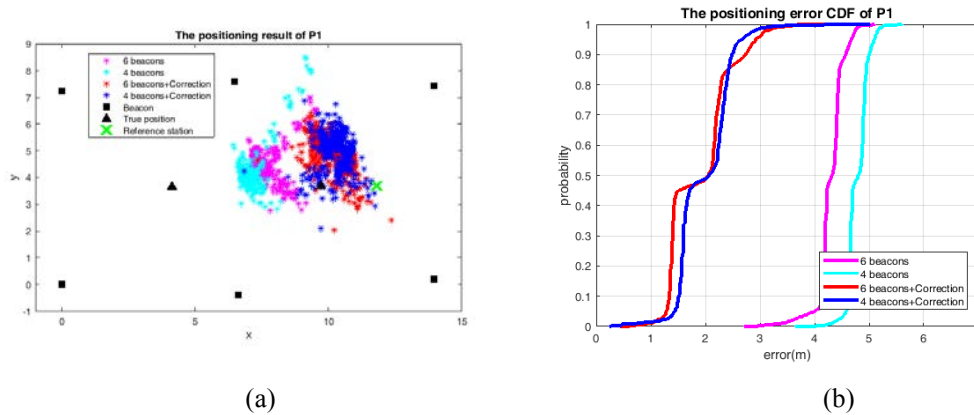


Fig. 2: (a) The visualization of the positioning result at P1 (b) The CDFs of the positioning error at P1

Table 1: The comparison of positioning errors in average

Unit: m	90% positioning error	RMSE
6 beacons	3.64	3.20
6 beacons+Correction	2.48	1.98
4 beacons	3.73	3.33
4 beacons+Correction	2.73	2.24

Title

Analysis on the performance degradations of maritime DGPS reference station by radio environment

Abstract

The maritime differential GPS (DGPS), which broadcasts GPS pseudorange corrections via medium frequency beacon signal to improve position accuracy and reliability, is a ground-based augmentation system as well as one of the most-used augmentation systems in maritime applications. Now maritime DGPS reference stations are established in South Korea for improvement of GPS navigation accuracy and needs of integrity. This paper investigates visibility and interference environment for performance degradation of some DGPS reference stations. We find that in case of some reference stations, visibility is satisfied with 7 degree elevation angle, but interference environment is not satisfied with reference standard of -50dBm. In order to analyze the effect of interference environment, this paper proposes a time differential measurement analysis method excluding error of signal noise. Finally, in this paper, it is shown that measurement analysis result of reference station under interference environment is three times the error than that of reference station on normal conditions.

Keywords

maritime DGPS, reference station, visibility analysis, interference analysis, multipath error

First Author

- Name: Sang Hyun PARK
- Organization: Korea Research Institute of Ships & Ocean Engineering
- Department: Public Technology Research Division
- Address: 32 1312beon-gil, Yuseong-daero, Yuseong-gu, Daejeon, 34103
- Country: Republic of Korea
- Phone: +82-42-866-3681
- E-mail: shpark@kriso.re.kr

Building high-resolution contact networks using WiFi localization

Ciro Gioia¹, Giovanni Strona², Pieter Beck², Dario Tarchi¹

1 European Commission, Joint Research Centre (JRC), Directorate for Space, Security and Migration, Demography, Migration & Governance Unit, Via E. Fermi 2749, I-21027 Ispra (VA), Italy

2 European Commission, Joint Research Centre (JRC), Directorate for Sustainable Resources, Bioeconomy Unit, Via E. Fermi 2749, I-21027 Ispra (VA), Italy

Email: {ciro.gioia, giovanni.strona, pieter.beck,dario.tarchi}@ec.europa.eu

Networks offer a synthetic way to model the connections between numerous real world entities, providing powerful analytical tools to tackle otherwise intractable and complex problems (Newman 2003). Among the many kinds of network, those mapping the contacts between people could support the future development of security strategies. Indeed, investigating how disease can spread through networks that map the contacts between people has proven very valuable to better understand epidemic processes, improve preparedness, and implement intervention actions (see, for example, Balcan et al. 2009). The huge recent theoretical developments in network science, coming from both physics and mathematics, are now highlighting how the most important gap keeping network science from becoming a game changer for human society is actually the lack of reliable, high-resolution contact networks.

Various attempts have been made to create such networks. For example, in an innovative experiment, scientists tracked the face to face contacts of visitors at a public exhibition for several days. For this, they used radio devices assigned to visitors at the entrance of the exhibition, recording each time two people came in close contact (Isella et al. 2011). Similar approaches were then applied at a primary school (Stehlé et al. 2011), and to explore the contacts between students at an American high school. In the latter case, researcher used sensor network motes distributed among all students, teachers, and staff (Salathé et al. 2010).

The global diffusion of cell phones with wi-fi technology is now offering the possibility to track individuals' movements without the need of dedicated technology. Their potential to create contact networks has been exploited, at a very large scale, to quantify the impact of human mobility on the epidemic dynamics of malaria in Kenia (Wesoloski et al. 2012). Here we apply a similar technique at a much smaller scale (and at a much higher spatial resolution); a unique dataset was collected during the JRC Open Day 2016 in Ispra (Italy), an event attracting about 8000 visitors. To monitor the flow of people during the event, 20 Wi-Fi access points were distributed on the JRC Ispra site. The devices continuously recorded a large variety of data including the identifier of the connected mobile phones, the Received Signal Strength Indicator and the time stamp. Such data were then used to estimate the user position using the technique described in (Alessandrini et al 2016). Before estimating the user's position, the data were cleaned to remediate three main problems: the presence of random generated MAC addresses, the inclusion of people that are not attending the event but are in the proximity of the access points, and the inclusion of static devices (printers, PCs etc.).

The results of the positioning process were assessed for their potential in building contact networks. In particular, we quantified events of spatio-temporal overlap for each pair of visitors, i.e. the number of times they were recorded in the same approximate position (± 0.0005 latitudinal/longitudinal degrees), at the same approximate time (± 3 minutes). It is clear how, in case of an epidemic outbreak, the number of

potential contacts between individuals would be a fundamental parameter to assess the likelihood of contagion. As an exploratory analysis, we investigated here how the structure of the underlying contact network between visitors changed assuming an increasing threshold in the number of potential contacts, χ . In particular, we recorded the percentage of visitors included in the network, the total number of connections between individuals (i.e. edges in the network), the percentage of visitors included in the largest (weakly) connected component of the network (where a weakly connected component represents a cluster of nodes where each node has at least one path to any other node in the cluster), and the number of weakly connected components in the network (Fig. 1).

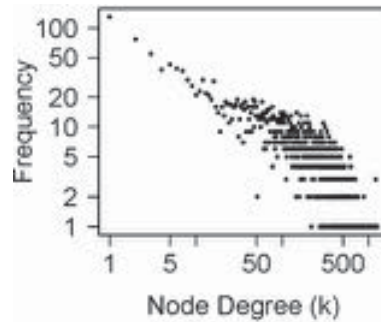


Figure 1 number of weakly connected components in the network

We then examined the degree distribution, i.e. the frequency distribution of the number of connections of each node, for a conservative value of $\chi = 5$ (i.e. a network where we connected only visitors that had been recorded at the same approximate location and time at least 5 times). This conforms to a power-law distribution (with $\gamma \approx 1.8$), where a few nodes have very high degree, while most of the nodes have a relatively low degree (Fig. 2). The average degree of such network is however very high (≈ 192), meaning that each visitor had a very high number of contacts with other visitors.

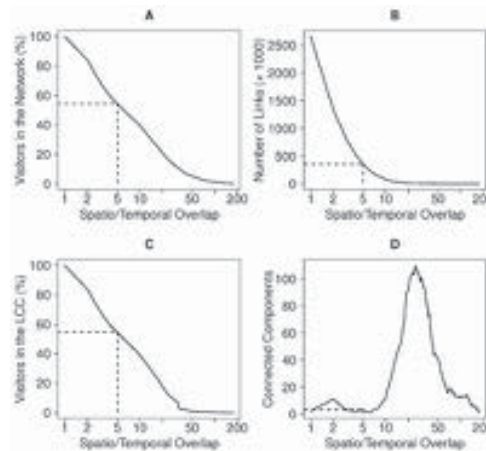


Figure 2

Using this network (or others generated according to different thresholds of spatio-temporal overlap) to simulate epidemic outbreaks could be a very useful approach to improve our understanding of contagion dynamics in real-world public settings involving relatively large

aggregations of people. In turn, this highlights how the use of Wi-Fi localization techniques to build high-resolution contact networks is highly relevant for various aspects of global security; for example, in the case of public event people flow monitoring can be analyzed and how a specific event can force group of people moving together. Our goal for the future is to build upon these preliminary findings to explore in depth the potential of the approach. In particular, our next steps will be directed towards the exploration of the trade-offs between setup complexity (e.g. spatial density of access points) and reliability of the obtained contact networks.

References

- Alessandrini, A., Gioia, C., Sermi, F., Sofos I., Tarchi, D., Vespe, M. (2016) WiFi positioning and Big Data to monitor flows of people on a wide scale. In proceeding of ENC 2016
- Balcan, D., Colizza, V., Gonçalves, B., Hu, H., Ramasco, J. J., & Vespignani, A. (2009). Multiscale mobility networks and the spatial spreading of infectious diseases. *Proceedings of the National Academy of Sciences*, 106(51), 21484-21489.
- Newman, M. E. (2003). The structure and function of complex networks. *SIAM review*, 45(2), 167-256.
- Wesolowski, A., Eagle, N., Tatem, A. J., Smith, D. L., Noor, A. M., Snow, R. W., & Buckee, C. O. (2012). Quantifying the impact of human mobility on malaria. *Science*, 338(6104), 267-270.
- Salathé, M., Kazandjieva, M., Lee, J. W., Levis, P., Feldman, M. W., & Jones, J. H. (2010). A high-resolution human contact network for infectious disease transmission. *Proceedings of the National Academy of Sciences*, 107(51), 22020-22025.
- Isella, L., Stehlé, J., Barrat, A., Cattuto, C., Pinton, J. F., & Van den Broeck, W. (2011). What's in a crowd? Analysis of face-to-face behavioral networks. *Journal of theoretical biology*, 271(1), 166-180.
- Stehlé, J., Voirin, N., Barrat, A., Cattuto, C., Isella, L., Pinton, J. F., ... & Vanhems, P. (2011). High-resolution measurements of face-to-face contact patterns in a primary school. *PloS one*, 6(8), e23176.
- Barrat, A., Cattuto, C., Colizza, V., Gesualdo, F., Isella, L., Pandolfi, E., ... & Stehlé, J. (2013). Empirical temporal networks of face-to-face human interactions. *European Journal of Physics Special Topics*, 222, 1295.

Theoretical performance analysis and comparison of VDFLL and traditional FLL tracking loops

Naveed Alam, JIN Tian

Faisal A. Khan

School of Electronic and Information Engineering
Beihang University,
100191, Beijing, China
Email: naveed.alam.na@gmail.com

Pakistan Space & Upper Atmosphere Research Commission
SUPARCO, GNSS Division,
Karachi, Pakistan

Abstract—GNSS signal tracking loops performance strongly affect by tracking parameters setting. If the tracking parameters are not set correctly then the tracking loop may not perform well which may compromise the accuracy of the receiver performance. Therefore, In this paper theoretical performance analysis and comparison of traditional frequency locked loop (FLL) and vector delay frequency locked loop (VDFLL) is presented. The performance analysis is conducted on the basis of tracking parameters setting such as noise bandwidth for the traditional FLL and process noise of dynamic for the VDFLL. Large numerical simulation is conducted to evaluate the tracking sensitivity and dynamic stress capacity over the specific range of noise bandwidth and process noise of dynamic for the traditional FLL and VDFLL respectively. The analysis results illustrate that the VDFLL can achieve 6-8 dB sensitivity and 6-40 g dynamic performance improvement over traditional FLL.

Full paper in IEEE Xplore

Inequality test and robust estimation for reliable navigation solution

Ciro Gioia

¹European Commission, Joint Research Centre (JRC),
Directorate for Space, Security and Migration,
Demography, Migration & Governance Unit, Via E. Fermi 2749, I-21027 Ispra (VA), Italy
Email: ciro.gioia@ec.europa.eu

Abstract—

Position information is a fundamental element of several applications carried out in very different environments. In some of these environments, classical navigation algorithms are not able to fulfil one or more of the requirements of the applications. Hence, alternative solutions have to be developed. In this paper a test based on one Gini index is used to trigger a robust estimation technique: three approaches, based on residuals, observation vector and standardized residuals have been developed. Specifically, Gini index is used to verify the consistency among the measurement set, if the Gini test fails a robust estimator is used. The proposed algorithm has been tested using a long static test performed in a challenging environment. From the analysis, it emerges that in the position domain the threshold value, for the Gini test, of 40 is a good compromise. The proposed approach is also compared with respect to a classical Fault Detection and Exclusion (FDE) technique. From the comparison it emerges that the proposed algorithm reduce mean horizontal and vertical errors of some two and eight meters respectively. Finally in the velocity domain, all the configurations perform similarly the only improvement using the proposed algorithms is in term of reliable availability which is improved of some 40% with respect to the a classical FDE technique.

Keywords—*Reliability, Robust Estimation, Gini, Integrity, FDE*

I. INTRODUCTION

In the recent years, there has been a growing of the number of applications and services relying on position related information. The most common position provider are Global Navigation Satellite Systems (GNSSs) [1], because GNSSs are able to provide Position Velocity Time (PVT) solution in all weather conditions and with global coverage [2]. Location Based Applications (LBAs) are carried out in different scenarios, characterized by different signal propagation conditions; in particular three environments can be identified:

- Favourable, where the signal broadcast by the satellites can reach directly the receiver. In these conditions, a single GNSS can provide position information with an accuracy of about 10 meters (in single point positioning) [3].
- Hostile, where the signals broadcast by the satellites are attenuated (fading) or distorted by obstacles (multipath). Moreover, these scenarios are usually characterized by a limited number of visible satellites,

which are usually in poor geometric conditions. All these aspects can sensibly degrade the navigation solution making GNSS-based navigation difficult and or unreliable.

- Very hostile, in this environments (indoor for example) GNSS signals are blocked by buildings, when the signals can pass through the walls they are very weak and can be tracked only with sophisticated techniques, as in the case of high sensitivity receivers. Moreover, also the quality of the measurements is very poor; these effects make GNSS-based positioning un-feasible in such scenarios.

The applications relying on GNSS-based position information are very different not only for the environment where the operations are performed but also for the performance requirements. Hence, PVT providers have to be able to provide a continuous accurate and reliable solution in all the above mentioned environments. In open sky, the performance requirements are easily fulfilled, while in signal degraded scenarios classical navigation algorithms are not able to fulfil one or more of the requirements mentioned before (accuracy, continuity, reliability); hence, alternative solutions have been developed. In the specialized literature, different solution have been proposed to face with one or more limitations of the classical algorithm. For example, to improve the number of available satellites multi-constellation solution has been investigated in several studies [4], [5], [6], [7], [8]. Although, the number of available satellite is a fundamental aspect, in signal degraded scenarios the quality of measurement is by far the foremost aspect; hence, a quality control, such as Fault Detection and Exclusion (FDE) techniques[9], [10], becomes a fundamental block of the navigation algorithm used in signal degraded scenarios. Moreover, when measurements from different GNSSs are used together some precautions have to be taken as shown for example in [11] where the group delay in Galileo and GLONASS case is evaluated, or in [12] and [13] where the inter system bias using GPS and Galileo together is assessed. In [14], the authors showed that in urban scenarios multi-constellation solution can even provide worse navigation solution with respect to the single system solution. Because, additional constellations provides more available satellites but could also introduce more outliers. Hence, quality control is a fundamental element of the navigation algorithm used for urban navigation, a complete literature review of the integrity approaches used in urban environments is available in [15].

The algorithm proposed exploits one of the most widely used econometric index to trigger a robust estimation technique. Specifically, Gini index is used to verify the consistency among the measurement set, this phase of the navigation algorithm is identified as inequality test. In the econometric field, Gini index is used to evaluate the inequality of the incomes, the inequality concept has been adapted to the GNSS navigation; this concept is used to design a test which provides an alarm when the inequality among the parameters under test overcomes a fixed threshold. Three different strategies exploiting the Gini index have been developed; the proposed approaches use residual, observation and standardized residuals, respectively. If the Gini test fails it means that at least one blunder is present in the measurement set, in order to mitigate the effect of the blunder a robust estimator is used instead of the classical Least Squares (LS) [16], [17] for the PVT estimate. LS estimators are widely used in GNSS-based navigation because their are mathematically convenient and have great statistical properties:

- Best Unbiased Estimator (BUE) under normally distributed errors,
- Best Linear Unbiased Estimator (BLUE) under non-normal error distributions.

However, LS estimator is very sensitive to outlier, in fact it has a breakdown point equals to zero; the breakdown point is the maximum number of outliers that an estimator can tolerate before it provides a poor estimate. In the case of the LS, even a single blunder strongly affects the estimate. In order to fill this gap different robust estimators have been developed [18]. In this paper, a Weighted Trimmed LS (WTLS) is adopted [19], which is the robust version of the Weighted LS (WLS) but it works on a subset of the initial set of measurements. This technique is similar to the LS estimators but has a breakdown point equals to 50%.

The proposed algorithm has been tested using a long-duration static test. During the test, a Javad Delta 3 receiver continuously collected observables which have been processed using the algorithm developed. The antenna of the receiver was placed in a parking lot between three high buildings which introduced some multipath effects, these create a very challenging environment where the proposed algorithm has been stressed.

The results are analysed in terms of solution availability, exclusion capabilities, horizontal and vertical position and velocity error statistics. The performance of the proposed algorithm is also compared with respect to the classical Forward-Backward (FB) algorithm. From the results, it emerges that the threshold value of 40 is good compromise for the inequality test. A low value of the threshold ($T < 10$) forces measurement exclusion degrading the navigation solution. While a threshold values higher than 50 is not effective preventing any exclusion hence no improvements in the position error can be noted. In the position domain, the proposed algorithm provides a reliable availability doubled with respect to a classical FDE technique. Statistical parameters of mean horizontal and vertical errors are reduced of some two and eight meters respectively. Finally, in the velocity domain, all the configurations perform similarly the only improvement using the proposed algorithms is in terms of the reliable availability which is improved of some 40% with respect to the FB technique.

II. RESULTS

In this section, the experimental results are described. At first, the values of the Gini index are analysed; then the results are analysed in terms of:

- reliable availability,
- multiple exclusions capabilities,
- horizontal and vertical position and velocity errors.

The performance of the proposed algorithm is also compared with respect to the classical FB algorithm.

A. Gini Index analysis

The Gini index values computed using the three strategies presented above are plotted as a function of the epoch index in Fig. 2 and Fig. 3. The estimated values of the indicator are plotted together with a scaled version of the horizontal and vertical position errors in Fig. 2 and Fig. 3 respectively. The scaling factor of the position error was applied only for visualization purposes to have the value of the index and the position errors in the same range.

From Fig. 2, it emerges that the strategies using residuals (upper box) and standardized residuals have a similar behaviour, the value of the indicator varies between 0.2 and 0.8; while when the observation vector is used (lower box) the values of the index are very small, in particular the values are in the interval 0.00001–0.0002. For all the three cases it can be noted that some of the largest position errors are associated with large variations of the Gini index, a more evident correlation between the horizontal position error and the Gini index values emerges when the observation vector is used. Similar conclusions can be drawn analysing the vertical position errors Fig. 3: also in this case the error time series is more correlated with the Gini values computed with the observation vector than in the case of the residuals and standardized residuals. Although the strategy using the observation vector seems to be the more promising the setting of the threshold is challenging due to the extreme low values of the index.

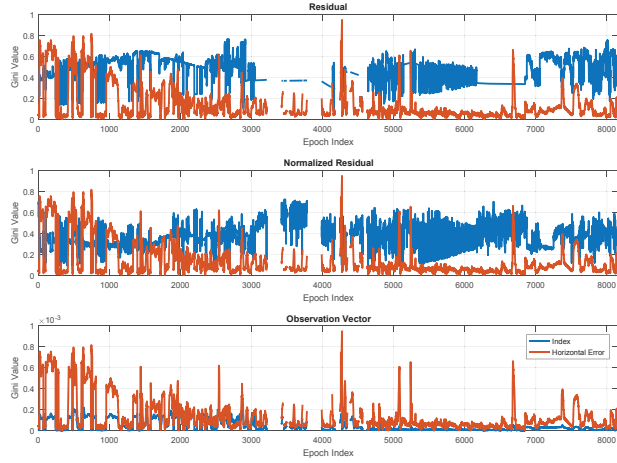


Fig. 1. Values of the Gini index and of the horizontal position error as a function of the epoch index.

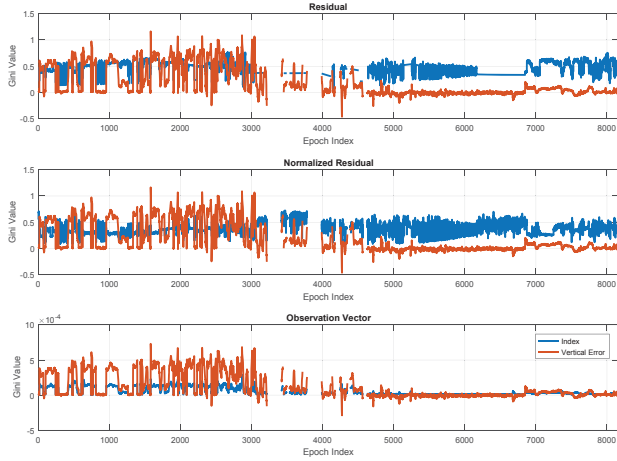


Fig. 2. Gini value and vertical position errors as a function of the epoch index.

B. Availability

In order to evaluate the impact of the threshold on the reliable availability (percentage of time when the solution is declared reliable) of the navigation solution, the position reliable availability obtained using the three developed strategies is shown in Fig. 4; the velocity reliable availability is plotted in Fig. 5.

From both figures, the difficulties of setting the threshold for the case of the observation vector (yellow lines) is evident: no solution is declared un-reliable and the reliable availability equals the availability of the solution. In the position case, Fig. 4 the curves related to the other two strategies are very similar: almost coincident till the threshold value equals some 35, then both lines tend to the value of the solution availability. But a small difference can be noted in the area between the threshold value of 35 and 70, in particular the blue line reaches the asymptotic value faster. In order to compare this results with respect to the classical FDE algorithm the same data have been processed with the FB algorithm and the solution

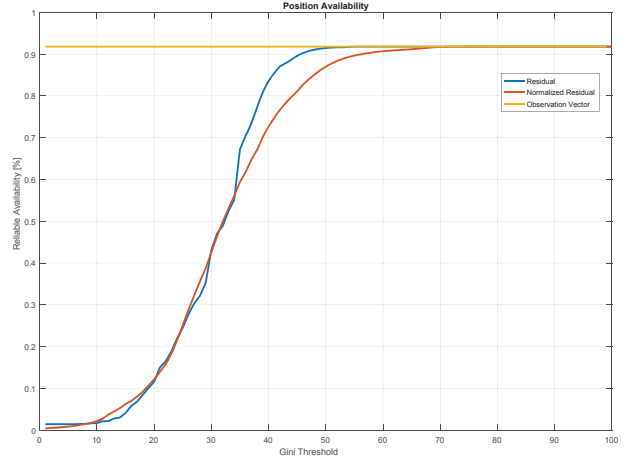


Fig. 3. Position reliable availability as a function of the inequality test threshold

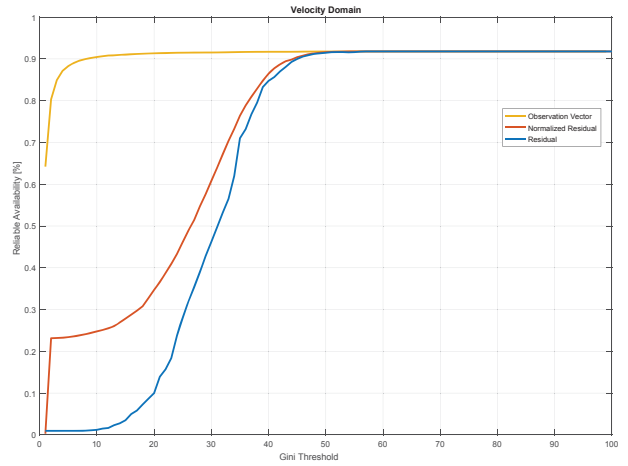


Fig. 4. Velocity reliable availability as a function of the inequality test threshold

availability obtained was 43.2% a similar value is obtained in the correspondence of the threshold value equals to 30. In the velocity domain the reliable availability values are higher than the position case, this is probably due to nature of the observables used to estimate the user velocity. Also in this case an asymptotic behaviour of the two lines can be appreciated, however the red line (standardized residuals case) is higher than the blue one (residual case). Finally, a jump in the solution availability can be noted for the case of the standardized residuals.

C. Measurement Exclusion

The mean number of simultaneous measurements exclusion as a function of the threshold value is shown in the upper part of Fig. 6; in the lower box, the maximum simultaneous number of rejected measurements is shown. From the graphs, it can be noted that the approaches using standardized residuals (dashed lines) reject less measurements than the approaches based on residuals for both case pseudorange and pseudorange-

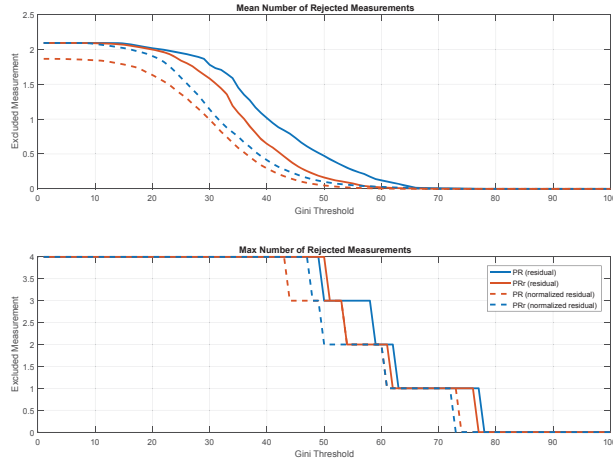


Fig. 5. Mean and maximum number of pseudorange and pseudorange-rate excluded as a function of the test threshold

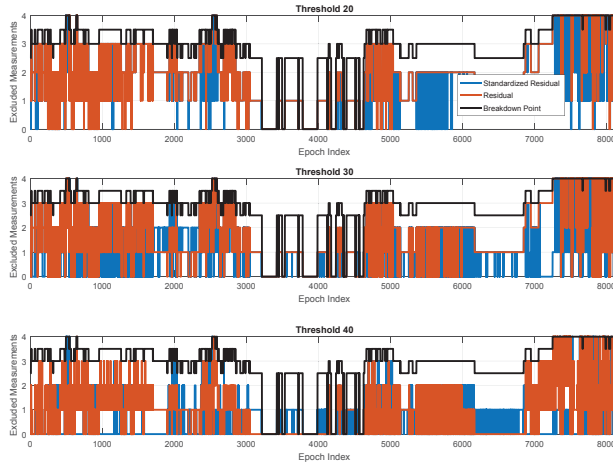


Fig. 6. Number of pseudorange excluded as function of the epoch index.

rate. Moreover in both approaches the number of pseudorange-rate (orange line) excluded is lower than the pseudorange (blue lines), this is probably due to the higher intrinsic robustness to multipath error of the Doppler shift observables.

The breakdown point of the estimator and the number of rejected pseudoranges are plotted as a function of the epoch index in Fig. 7. In the figure three values of the threshold are considered in the three different boxes. Moreover, the two approaches based on residuals and on standardized residuals are considered. From the figure, it can be noted that in all the considered cases the estimator works in the proximity of the breakdown point in the initial and final phase of the data collection.

The breakdown point of the estimator and the number of rejected pseudorange-rates are plotted as a function of the epoch index in Fig. 8. Also in this case the estimator works in the proximity of the breakdown point in the initial and final phase of the data collection.

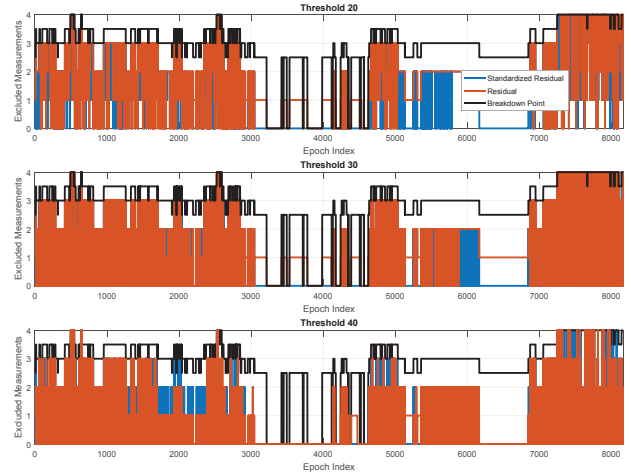


Fig. 7. Number of pseudorange-rate excluded as function of the epoch index.

D. Position and Velocity analysis

In order to assess the performance of the proposed algorithms, statistical parameters such as mean and standard deviation of the position and velocity errors are computed, for both horizontal and vertical channels.

In Fig. 9, the statistic parameters of the horizontal errors are plotted as a function of the test threshold. In the upper box, the configuration using residual is considered, while in the lower box the approach based on standardized residuals is shown. From the upper box, it emerges that in the initial part of the graph ($10 < T < 20$) the mean and the standard deviation are higher than in the central part of the plot ($20 < T < 40$); this is probably due to the too stringent conditions imposed by the threshold value which forces the exclusion of a high number of measurements. Then in the final part of the graph the parameters saturated because no exclusions are performed due to the too relaxed conditions. A similar behaviour can be noted in the case of the standardized residuals. Finally, if a comparison between the two strategy is performed, it can be noted that the lines relative to the standardized residuals case are higher.

In Fig. 10, mean and standard deviation of the horizontal errors are plotted as a function of the test threshold. In the upper box, the configuration using residual is considered, while in the lower box the approach based on standardized residuals is shown. From the upper box, it emerges that in the initial part of the graph ($10 < T < 20$) the mean and the standard deviation are higher than in the central part of the plot ($20 < T < 30$) a jump in the correspondence of the threshold value 30 can be noted; as in the horizontal case, a similar saturation is observed. Also for the vertical channel the lines relative to the standardized residuals case are higher.

In Fig. 11, horizontal position estimate associated with the reliability flag is shown three colours are used to indicate the reliability status of the solution. Red marker indicates un-reliable position, green marker indicates reliable position, orange marker indicates un-checked solution. In the upper boxes, the solution obtained using the strategy based on residuals are shown, different thresholds of the inequality test are considered: Fig. 11 a) threshold equals 20, Fig. 11 b)

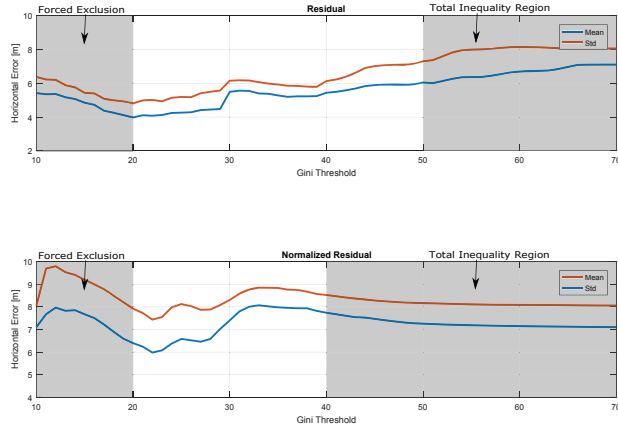


Fig. 8. Horizontal position error statistics as a function of the inequality test Threshold.

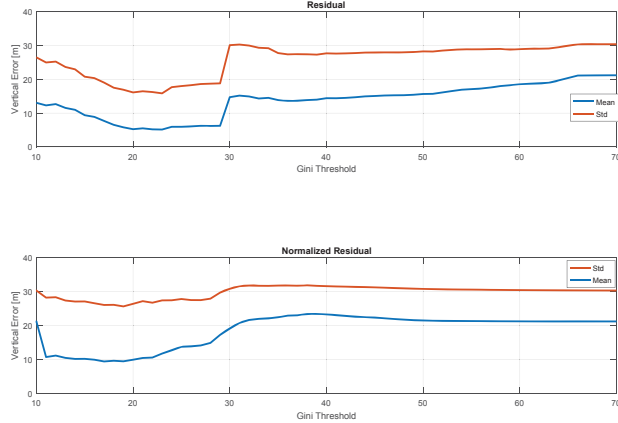


Fig. 9. Vertical position error statistics as a function of the inequality test Threshold.

threshold equals 30 and Fig. 11 c) threshold equals 40. In the lower boxes, the solutions obtained using the strategy based on standardized residuals using the same threshold values are shown.

The parameters of the horizontal and vertical errors are reported in Table I. From the table, it emerges that for the strategy based on residuals mean horizontal and vertical errors is reduced of some two and eight meters with respect to the classical FB scheme.

The parameters of the horizontal and vertical velocity

TABLE I. STATISTICAL PARAMETERS OF THE POSITION ERRORS CONSIDERING DIFFERENT CONFIGURATIONS AND THRESHOLDS.

Config	Mean Hor Err	Std Hor Err	Mean Ver Err	Std Ver Err	Reliable Avail
Gini R 20	4.08	6.38	14.53	16.25	16.43
Gini R 30	5.54	6.17	14.94	30.01	48.90
Gini R 40	5.58	5.02	5.20	27.70	87.10
Gini W 20	6.40	8.52	23.32	26.40	13.91
Gini W 30	7.40	8.30	19.09	30.82	46.43
Gini W 40	7.74	7.92	9.94	31.60	74.72
FB	7.26	8.95	13.10	25.63	43.20

TABLE II. STATISTICAL PARAMETERS OF THE VELOCITY ERRORS CONSIDERING DIFFERENT CONFIGURATIONS AND THRESHOLDS.

Config	Mean Hor Err	Std Hor Err	Mean Ver Err	Std Ver Err	Reliable Avail
Gini R 20	0.029	0.019	0.004	0.053	15.70
Gini R 30	0.028	0.020	0.004	0.056	53.21
Gini R 40	0.027	0.019	0.003	0.053	87.00
Gini W 20	0.030	0.020	0.003	0.057	36.57
Gini W 30	0.027	0.020	0.007	0.052	63.91
Gini W 40	0.027	0.019	0.007	0.051	87.75
FB	0.026	0.018	0.007	0.043	44.81

errors are reported in Table II. In the velocity domain, all the configurations perform similarly (only difference in the order of mm/sec can be noted) the only improvement using the proposed algorithms is in the reliable availability which is improved of some 40% with respect to the FB technique.

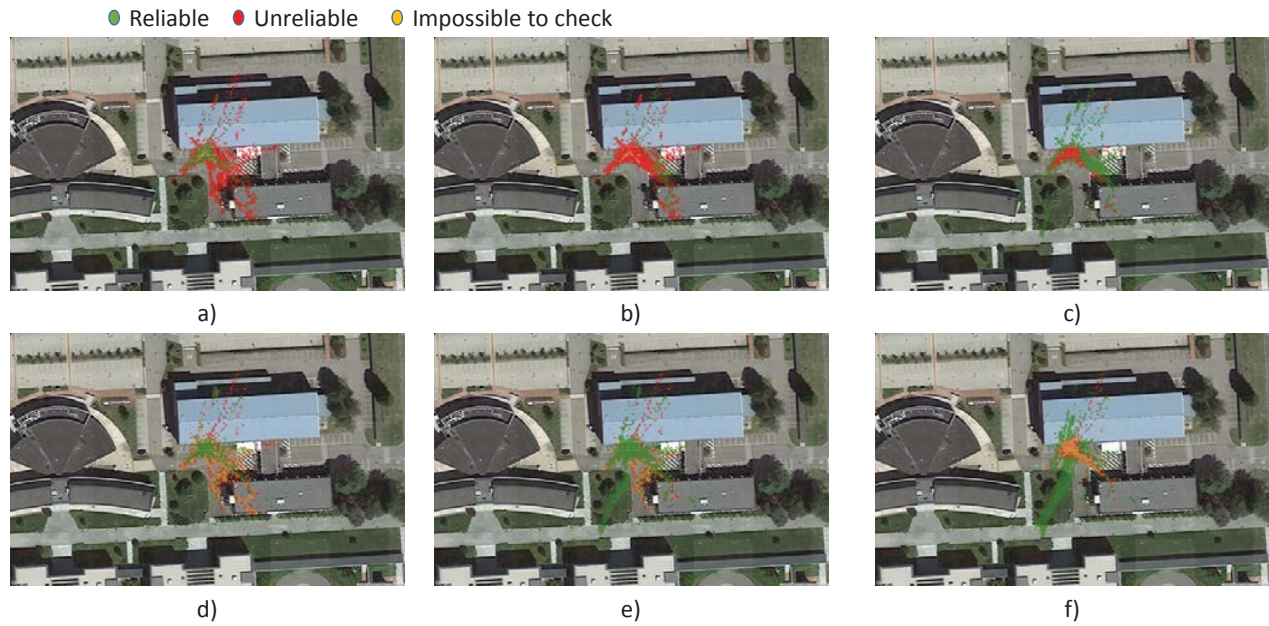


Fig. 10. Horizontal position estimate associated with the reliability flag. Red marker indicates un-reliable position, green marker indicates reliable position, orange marker indicates un-checked solution

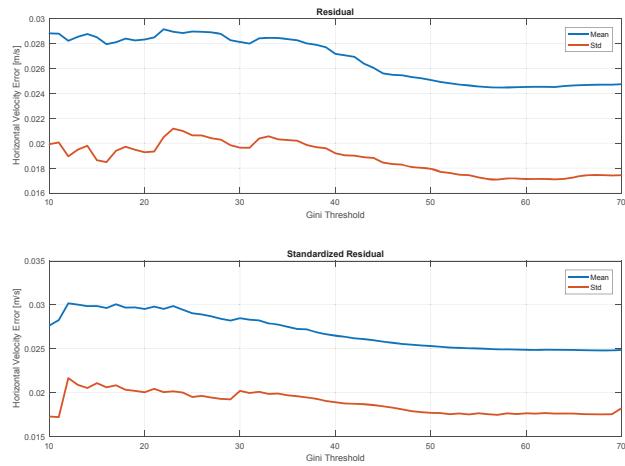


Fig. 11. Horizontal velocity error statistics as a function of the inequality test Threshold.

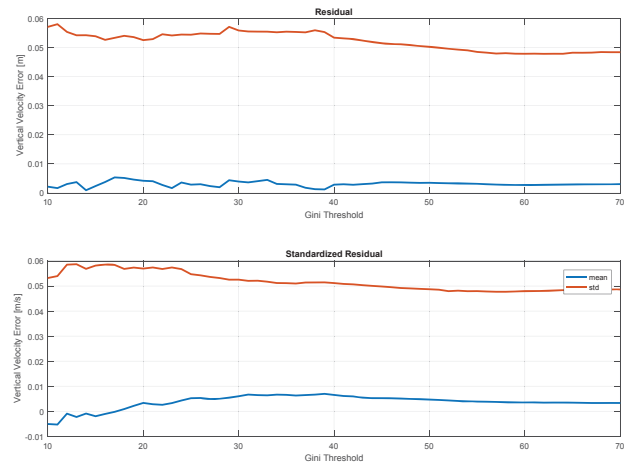


Fig. 12. Vertical velocity error statistics as a function of the inequality test Threshold.

III. CONCLUSIONS

This paper presented a navigation algorithm for signal degraded scenarios. The navigation algorithm exploits the synergy between a test based on the Gini index, namely inequality test, and a robust estimator.

A test to verify the consistency of the measurement set has been designed and implemented. The test uses the most widely econometric index, the Gini index. In the econometric field the indicator is used to evaluate the inequality in the incomes of a country. The inequality concept has been adapted to the GNSS positioning; If the test fails a robust estimator is triggered. The estimator used is WTLS which is a robust version of the WLS with a breakdown point equals to 50%.

Three different strategies have been implemented based on residuals, observation vector and standardized residuals respectively. From the analysis of the Gini index values, it emerges that the more promising strategy is the one exploiting the observation vector. But the threshold setting is an open challenge.

The proposed algorithms were tested using data collected in static condition in an environment with large multipath effect. From the result, it emerges that the threshold value equal to 40 is a good compromise for the inequality test. A low value of the threshold ($T < 10$) forces measurement exclusion degrading the navigation solution. While a threshold values higher than 50 is not effective preventing any exclusion hence no improvements in the position error can be noted.

The results in the position domain have been compared to a classical FDE technique; from the comparison, it emerges that the proposed algorithm (for both cases residuals and standardized residuals with the threshold set to 40) provides a reliable availability doubled with respect to the classical FB technique.

For the strategy based on residuals mean horizontal and vertical errors is reduced of some two and eight meters respectively. Finally in the velocity domain, all the configurations perform similarly the only improvement using the proposed algorithms is terms of reliable availability which is improved of some 40% with respect to the FB technique.

REFERENCES

- [1] European GNSS Agency, "Gnss market report," tech. rep., GSA, 2017.
- [2] B. Hoffmann-Wellenhof, H. Lichtenegger, and J. Collins, *Global Positioning System: Theory and Practice*. Springer, 1992.
- [3] E. D. Kaplan and C. Hegarty, *Understanding GPS: Principles and Applications*. Second Edition, Artech House, November 2005.
- [4] M. A. Sturza and A. K. Brown, "Integrated gps/glonass for reliable receiver autonomous integrity monitoring (raim)," in *Proceedings of the 46th Annual Meeting of The Institute of Navigation*, (Atlantic City, NJ), pp. 9–13, The Institute of Navigation, June 1990.
- [5] C. O'Driscoll, G. Lachapelle, and M. E. Tamazin, "Investigation of the Benefits of Combined GPS/GLONASS Receivers in Urban Environments," in *5th ESA Workshop on GNSS Signals and Signal Processing*, (NAVITEC), (London), Royal Institute of Navigation, 2010.
- [6] P. B. Ober and D. Harriman, "On the use of multiconstellation-raim for aircraft approaches," in *Proceedings of the 19th International Technical Meeting of the Satellite Division of The Institute of Navigation (ION GNSS 2006)*, (Fort Worth, TX), pp. 2587–2596, September 2006.
- [7] E. M. G. P. N. Misra, R. I. Abbot, "Integrated use of gps and glonass: transformation between wgs84 and pz-90," in *Proceedings of ION GPS-96*, 1996.
- [8] Z. Jiang, P. Groves, W. Y. Ochieng, and P. Mattos, "Multi-Constellation GNSS Multipath Mitigation Using Consistency Checking," *Proceeding of ION GNSS 2011*, 2011.
- [9] H. Kuusniemi, *User-Level Reliability and Quality Monitoring in Satellite-Based Personal Navigation*. PhD thesis, Tampere University of Technology, Finland, 2005. Publication 544.
- [10] C. Gioia, *GNSS Navigation in Difficult Environments: Hybridization and Reliability*. PhD thesis, University Parthenope of Naples, 2014.
- [11] F. Pisoni and P. Mattos, "Correction of pseudorange errors in galileo and glonass caused by biases in group delay," in *6th ESA Workshop on GNSS Signals and Signal Processing*, (NAVITEC), 2012.
- [12] J. Paziewski and P. Wielgosz, "Accounting for GalileoGPS inter-system biases in precise satellite positioning," *Journal of Geodesy*, vol. 89, p. 81, 2015.
- [13] C. Gioia and D. Borio, "A statistical characterization of the Galileo-to-GPS inter-system bias," *Journal Of Geodesy*, 2016.
- [14] D. Borio and C. Gioia, "Galileo: The added value for integrity in harsh environments," *Sensors*, 2016.
- [15] N. Zhu, J. Marais, D. Betaille, and M. Berbineau, "GNSS Position Integrity in Urban Environments: A Review of Literature," *IEEE Transactions on Intelligent Transportation Systems*, 2018.
- [16] E. M. Mikhail, *Observations and Least Squares*. IEP, 1976.
- [17] Y. Bar-Shalom, X. R. Li, and T. Kirubarajan, *Estimation with Applications to Tracking and Navigation*. New York: John Wiley and Sons, June 2001.
- [18] P. Huber, "Robust Estimation of Location Parameter," *The Annals of Mathematical Statistics*, 1964.
- [19] P. Rousseeuw and A. Leroy, *Robust Regression and Outlier Detection*. John Wiley & Sons, 1987.
- [20] B. Parkinson, J. Spilker, P. Axelrad, and P. Enge, *Global Positioning System: Theory And Applications*, vol. 1. Washington D.C., USA: American Institute of Aeronautics and Astronautics, 1996.
- [21] H. Kuusniemi, A. Wieser, G. Lachapelle, and J. Takala, "User-level reliability monitoring in urban personal satellite-navigation," *IEEE TRANSACTIONS ON AEROSPACE AND ELECTRONIC SYSTEMS*, vol. 43, pp. 1305–1318, October 2007.
- [22] R. Modarres and J. L. Gastwirth, "A Cautionary Note on Estimating the Standard Error of the Gini Index of Inequality," *OXFORD BULLETIN OF ECONOMICS AND STATISTICS*, 2006.

- [23] C. Gini, "The origins of the gini index," *Variabilit e Mutabilit*, 1912.
- [24] C. Gini, "Measurement of inequality and incomes," *The Economic Journal*, vol. 31, pp. 124–126, 1921.

A Direct Positioning Method for a Stand-Alone Global Navigation Satellite System (GNSS) Receiver

Mohamed Khalaf-Allah

Professorship of Communications Engineering
Chemnitz University of Technology
Chemnitz, Germany
mohamed.khalaf-allah@etit.tu-chemnitz.de

Abstract—The aim is to improve the state of the art of global navigation satellite system (GNSS) algorithms through the development of an algebraic direct positioning algorithm for a stand-alone GNSS receiver, i.e. point positioning. The developed direct method (DM) requires exactly five pseudorange measurements from five GNSS satellites in view to estimate the GNSS receiver's coordinates and clock offset without any matrix computations. It can be used stand-alone at discrete instants along the time axis or it can be used to provide initial estimates to iterative algorithms for quick convergence. The pseudorange measurements can be from a single or multiple GNSS constellations after performing coordinate conversion inside the receiver to relate the different geodetic reference frames of the different GNSS constellations. It is also assumed that proper mitigation of ionospheric, tropospheric, and satellite clock errors, has been performed.

Keywords—Position estimation; GNSS positioning; direct positioning method; non-iterative algorithm

I. INTRODUCTION

A global navigation satellite system (GNSS) is a space-based satellite radio navigation system that provides three-dimensional (3-D) receiver positioning by solving a set of nonlinear equations using pseudorange measurements. The current approach of solving the nonlinear equations is to linearize the pseudorange equations and calculate the receiver position iteratively, starting with an initial position guess. For near-earth navigation, the center of the earth is usually used as a good initial position guess to make iterative algorithms converge to the position solution. Non-iterative closed-form (CF) and direct solutions to the nonlinear pseudorange GNSS equations provide potential improvements. A direct solution that does not require an initial position guess is attractive for space navigation and for unusual planar array configurations using pseudo-satellites (pseudolites), where the iterative procedure is sensitive to the initial position guess [1, 2]. Moreover, solutions that require fewer iterations and floating-point operations (FLOPS) are attractive for high-speed vehicles, e.g. spacecrafts, where the computational and power resources may be limited. This results in reduced time to first fix (TTFF), which also helps to acquire more measurements quickly. CF solutions have been developed and presented in [3-10].

The developed algorithm has been filed in a patent application [11], and is described in the next section.

II. ALGORITHM DESCRIPTION

We focus on the estimation of the GNSS receiver coordinates x, y, z and its clock offset τ based on five pseudorange measurements (which are usually available in normal conditions) of a single GNSS receiver. Pseudorange measurements construct a system of quadratic (nonlinear) equations. Therefore, for a direct unambiguous analytical solution, five such equations are needed to estimate four unknowns (x, y, z, τ) and to eliminate the resulting ambiguity due to the quadratic nature of the equations. With extra pseudorange measurements, several sets of five measurements can be formed and utilized in, e.g. improving the estimation accuracy, integrity monitoring, fault detection and elimination.

The known positions of the five satellites in view are given as (a_i, b_i, c_i) , where $i = 1, \dots, 5$. t_i is the unknown actual time travelled by the signal from satellite i . T_i is the known travel time of the signal from satellite i as calculated by the GNSS receiver. τ , is the unknown constant clock offset between the synchronized clocks on the satellites and the GNSS receiver's clock. Thus, $t_i = T_i - \tau$. The unknown position of the GNSS receiver is given as (x, y, z) .

The i -th pseudorange measurement is expressed as $c(T_i - \tau) = \sqrt{(x - a_i)^2 + (y - b_i)^2 + (z - c_i)^2}$, where c is the speed of light in vacuum or the propagation speed of the GNSS signal in the medium between the GNSS satellites and receiver. Squaring both sides of the pseudorange measurement equation, the following five equations can be written

$$(x - a_1)^2 + (y - b_1)^2 + (z - c_1)^2 = c^2(T_1 - \tau) \quad (1)$$

$$(x - a_2)^2 + (y - b_2)^2 + (z - c_2)^2 = c^2(T_2 - \tau) \quad (2)$$

$$(x - a_3)^2 + (y - b_3)^2 + (z - c_3)^2 = c^2(T_3 - \tau) \quad (3)$$

$$(x - a_4)^2 + (y - b_4)^2 + (z - c_4)^2 = c^2(T_4 - \tau) \quad (4)$$

$$(x - a_5)^2 + (y - b_5)^2 + (z - c_5)^2 = c^2(T_5 - \tau) \quad (5)$$

Expanding equations (1) – (5) and then subtracting equations (2) – (4) from equation (1) successively and rearranging we get the following three expressions

$$(a_2 - a_1)x + (b_2 - b_1)y + (c_2 - c_1)z = c^2\tau \cdot I_1 + \frac{1}{2}A_1 \quad (6)$$

$$(a_3 - a_1)x + (b_3 - b_1)y + (c_3 - c_1)z = c^2\tau \cdot I_2 + \frac{1}{2}A_2 \quad (7)$$

$$(a_4 - a_1)x + (b_4 - b_1)y + (c_4 - c_1)z = c^2\tau \cdot I_3 + \frac{1}{2}A_3 \quad (8)$$

$$(a_5 - a_1)x + (b_5 - b_1)y + (c_5 - c_1)z = c^2\tau \cdot I_4 + \frac{1}{2}A_4 \quad (9)$$

Where

$$I_1 = T_2 - T_1$$

$$I_2 = T_3 - T_1$$

$$I_3 = T_4 - T_1$$

$$I_4 = T_5 - T_1$$

$$A_1 = c^2(T_1^2 - T_2^2) + (a_2^2 - a_1^2) + (b_2^2 - b_1^2) + (c_2^2 - c_1^2)$$

$$A_2 = c^2(T_1^2 - T_3^2) + (a_3^2 - a_1^2) + (b_3^2 - b_1^2) + (c_3^2 - c_1^2)$$

$$A_3 = c^2(T_1^2 - T_4^2) + (a_4^2 - a_1^2) + (b_4^2 - b_1^2) + (c_4^2 - c_1^2)$$

$$A_4 = c^2(T_1^2 - T_5^2) + (a_5^2 - a_1^2) + (b_5^2 - b_1^2) + (c_5^2 - c_1^2)$$

Multiplying equations (6) and (7) by I_2 and I_1 respectively, and then subtracting (7) from (6) and rearranging to cancel out τ we get

$$I_2[(a_2 - a_1)x + (b_2 - b_1)y + (c_2 - c_1)z] - I_1[(a_3 - a_1)x + (b_3 - b_1)y + (c_3 - c_1)z] = \frac{1}{2}(A_1I_2 - A_2I_1) \quad (10)$$

Similarly, equations (6) and (8) are multiplied by I_3 and I_1 respectively, and then subtracting (8) from (6) and rearranging to cancel out τ we get

$$I_3[(a_2 - a_1)x + (b_2 - b_1)y + (c_2 - c_1)z] - I_1[(a_4 - a_1)x + (b_4 - b_1)y + (c_4 - c_1)z] = \frac{1}{2}(A_1I_3 - A_3I_1) \quad (11)$$

Finally, equations (6) and (9) are multiplied by I_4 and I_1 respectively, and then subtracting (9) from (6) and rearranging to cancel out τ we get

$$I_4[(a_2 - a_1)x + (b_2 - b_1)y + (c_2 - c_1)z] - I_1[(a_5 - a_1)x + (b_5 - b_1)y + (c_5 - c_1)z] = \frac{1}{2}(A_1I_4 - A_4I_1) \quad (12)$$

To simplify equations (10) – (12), the following variables are defined

$$I_{11} = I_2(a_2 - a_1) - I_1(a_3 - a_1)$$

$$I_{12} = I_2(b_2 - b_1) - I_1(b_3 - b_1)$$

$$I_{13} = I_2(c_2 - c_1) - I_1(c_3 - c_1)$$

$$I_{14} = \frac{1}{2}(A_1I_2 - A_2I_1)$$

$$I_{21} = I_3(a_2 - a_1) - I_1(a_4 - a_1)$$

$$I_{22} = I_3(b_2 - b_1) - I_1(b_4 - b_1)$$

$$I_{23} = I_3(c_2 - c_1) - I_1(c_4 - c_1)$$

$$I_{24} = \frac{1}{2}(A_1I_3 - A_3I_1)$$

$$I_{31} = I_4(a_2 - a_1) - I_1(a_5 - a_1)$$

$$I_{32} = I_4(b_2 - b_1) - I_1(b_5 - b_1)$$

$$I_{33} = I_4(c_2 - c_1) - I_1(c_5 - c_1)$$

$$I_{34} = \frac{1}{2}(A_1I_4 - A_4I_1)$$

Thus, equations (10) – (12) can be rewritten as

$$I_{11}x + I_{12}y + I_{13}z = I_{14} \quad (13)$$

$$I_{21}x + I_{22}y + I_{23}z = I_{24} \quad (14)$$

$$I_{31}x + I_{32}y + I_{33}z = I_{34} \quad (15)$$

To further simplify the next equations, the following variables are introduced

$$I_1 = I_{23} \cdot I_{11} - I_{13} \cdot I_{21}$$

$$I_2 = I_{23} \cdot I_{12} - I_{13} \cdot I_{22}$$

$$I_3 = I_{23} \cdot I_{14} - I_{13} \cdot I_{24}$$

$$I_4 = I_{33} \cdot I_{11} - I_{13} \cdot I_{31}$$

$$I_5 = I_{33} \cdot I_{12} - I_{13} \cdot I_{32}$$

$$I_6 = I_{33} \cdot I_{14} - I_{13} \cdot I_{34}$$

Multiplying equations (13) and (14) by I_{23} and I_{13} respectively, and then subtracting (14) from (13) and rearranging to cancel out z yields

$$I_1 x + J_2 y = J_3 \quad (16)$$

Similarly, equations (13) and (15) are multiplied by I_{33} and I_{13} respectively, and then subtracting (15) from (13) and rearranging to cancel out z yields

$$I_4 x + J_5 y = J_6 \quad (17)$$

From (16) and (17) we can get a solution for x independent of the other unknown, y , z and τ , as

$$x = (J_3 \cdot J_5 - J_2 \cdot J_6) / (J_1 \cdot J_5 - J_2 \cdot J_4) \quad (18)$$

Similarly, we can get solutions for y , z and τ independent of the rest unknowns as

$$y = (J_1 \cdot J_6 - J_3 \cdot J_4) / (J_1 \cdot J_5 - J_2 \cdot J_4) \quad (19)$$

$$z = (K_1 \cdot K_6 - K_3 \cdot K_4) / (K_1 \cdot K_5 - K_2 \cdot K_4) \quad (20)$$

Where

$$K_1 = I_{22} \cdot I_{11} - I_{12} \cdot I_{21}$$

$$K_2 = I_{22} \cdot I_{13} - I_{12} \cdot I_{23}$$

$$K_3 = I_{22} \cdot I_{14} - I_{12} \cdot I_{24}$$

$$K_4 = I_{32} \cdot I_{11} - I_{12} \cdot I_{31}$$

$$K_5 = I_{32} \cdot I_{13} - I_{12} \cdot I_{33}$$

$$K_6 = I_{32} \cdot I_{14} - I_{12} \cdot I_{34}$$

And finally

$$\tau = (N_3 \cdot N_4 - N_1 \cdot N_6) / (c^2(N_1 \cdot N_5 - N_2 \cdot N_4)) \quad (21)$$

Where

$$M_1 = a_2 - a_1$$

$$M_2 = a_3 - a_1$$

$$M_3 = a_4 - a_1$$

$$M_4 = a_5 - a_1$$

$$M_{11} = M_2(b_2 - b_1) - M_1(b_3 - b_1)$$

$$M_{12} = M_2(c_2 - c_1) - M_1(c_3 - c_1)$$

$$M_{13} = M_2(T_2 - T_1) - M_1(T_3 - T_1)$$

$$M_{14} = \frac{1}{2}(M_2 A_1 - M_1 A_2)$$

$$M_{21} = M_3(b_2 - b_1) - M_1(b_4 - b_1)$$

$$M_{22} = M_3(c_2 - c_1) - M_1(c_4 - c_1)$$

$$M_{23} = M_3(T_2 - T_1) - M_1(T_4 - T_1)$$

$$M_{24} = \frac{1}{2}(M_3 A_1 - M_1 A_3)$$

$$M_{31} = M_4(b_2 - b_1) - M_1(b_5 - b_1)$$

$$M_{32} = M_4(c_2 - c_1) - M_1(c_5 - c_1)$$

$$M_{33} = M_4(T_2 - T_1) - M_1(T_5 - T_1)$$

$$M_{34} = \frac{1}{2}(M_4 A_1 - M_1 A_4)$$

$$N_1 = M_{21} \cdot M_{12} - M_{11} \cdot M_{22}$$

$$N_2 = M_{21} \cdot M_{13} - M_{11} \cdot M_{23}$$

$$N_3 = M_{21} \cdot M_{14} - M_{11} \cdot M_{24}$$

$$N_4 = M_{31} \cdot M_{12} - M_{11} \cdot M_{32}$$

$$N_5 = M_{31} \cdot M_{13} - M_{11} \cdot M_{33}$$

$$N_6 = M_{31} \cdot M_{14} - M_{11} \cdot M_{34}$$

REFERENCES

- [1] J. McKay, Optimization of a GPS-Based Navigation Reference System, MS Thesis, School of Engineering, Air Force Institute of Technology, Wright-Patterson AFB, OH, Dec. 1996.
- [2] M. Pachter, J. McKay, "Geometry Optimization of a GPS-Based Navigation System", Navigation: Journal of the Institute of Navigation, Vol. 44, No. 4, pp. 457-470, Winter 1997-1998.
- [3] S. Bancroft, "An Algebraic Solution of the GPS equations", IEEE Transactions on Aerospace and Electronic Systems, Vol. 21, No. 1, pp. 56-59, Nov. 1985.
- [4] J. Leva, "An Alternative Closed-Form Solution to the GPS Pseudo-Range Equations", IEEE Transaction on Aerospace and Electronic Systems, Vol. 32, No. 4, pp. 1430-1439, Oct. 1996.
- [5] L. Krause, "A Direct Solution to GPS Type Navigation Equations", IEEE Transactions on Aerospace and Electronic Systems, Vol. 23, No. 2, pp. 223-232, Mar. 1987.

- [6] J. Abel, J. Chaffee, "Existence and Uniqueness of GPS Solutions", IEEE Transactions on Aerospace and Electronic Systems, Vol. 27, No. 6, pp. 952-956, Nov. 1991.
- [7] J. Chaffee, J. Abel, "On the Exact Solutions of Pseudorange Equations", IEEE Transactions on Aerospace and Electronic Systems, Vol. 30, No. 4, pp. 1021-1030, Oct. 1994.
- [8] J. Hoshen, "The GPS Equations and the Problem of Apollonius", IEEE Transactions on Aerospace and Electronic Systems, Vol. 32, No. 3, pp. 1116-1124, Jul. 1996.
- [9] S. Nardi, M. Pachter, "GPS Estimation Algorithm Using Stochastic Modeling", Proceedings of the Conference on Decision and Control, Tampa, Florida, USA, Dec. 1998.
- [10] M. Pachter, S. Nardi "Stochastic Modeling in GPS Estimation", Advances in Intelligent System: Concepts, Tools and Applications, Kluwer Academic, Vol. 35, pp. 389-400, 1999.
- [11] M. Khalaf-Allah, "Method And System for 3D Position Estimation Of A GNSS Receiver Using Travel Time Measurements," US Patent US20160116600, Apr. 28, 2016.

Galileo Second Generation Improvements for the Everyday User

Patrik Sandin

RUAG Space AB, Gothenburg, Sweden, patrik.sandin@ruag.com

Abstract

Galileo second generation will include improvements for the everyday user that presents engineering challenges on many levels. A global navigation satellite system like the European Galileo system is a big piece of infrastructure that may seem permanent, fixed and immutable. This is not the case however, the Galileo system is evolving.

Galileo began Initial Services on 15 December 2016 and with 22 satellites now in orbit and 4 more to be launched in the third quarter this year it is heading towards full operational capability^{1,2}.

Although the Galileo satellites are designed for long lifetime, replenishment is eventually needed and planning is already in progress for when it is needed and how it should be done. At the same time experience with the current system and other navigation systems as well as the user community are gathered in order to define system improvements to be implemented on the new satellites, called the Galileo Second Generation (G2G).

Improvements in many areas of the Galileo system is looked at and for the satellites the improvements are related to³:

- new and improved services
- operational and system robustness improvements
- technology improvements

Although all of them are interesting from an engineering perspective, it is the first bullet that will have the most impact on the everyday user.

The changes for the everyday user will not be dramatic but she will experience better navigation performance through improved position accuracy and a new high accuracy certified timing service as well as much faster acquisition times allowing quick access to the navigation services.

In order to improve the situation for end users with security constraints and the emerging spoofing and jamming threats different levels of authentication are examined.

The current system was with the terrestrial users in mind but also space borne applications have been defined successfully. To improve for the space users the next generation will also provide space services by guaranteeing signal power in excess of the earth limb allowing space services all the way up to geostationary orbit around 36,000 km.

¹ ESA, "Another Eight Galileo Satellites for Europe", http://www.esa.int/Our_Activities/Navigation/Another_eight_Galileo_satellites_for_Europe.

² GSA, "Notice Advisory to Galileo Users (NAGU) 2017047", <https://www.gsc-europa.eu/notice-advisory-to-galileo-users-nagu-2017047>

³ ESA GNSS/Galileo Evolution Programme & Strategy Division, "GNSS Evolutions Phase A Activities and System Preliminary Requirements Review Process", ESA European GNSS Evolutions Programme (EGEP) Galileo Evolution Industry Days, 24/05/2016

From a user perspective it is also important that the different navigation systems are interoperable such that the user can benefit from the vast amounts of satellites provided by the different constellations, especially the American GPS, Russian GLONASS and the Chinese COMPASS/BeiDou. Therefore the G2G satellites must take into account the evolution of these systems as well.

We should also not forget how fast we as users are changing the way we are using available technology nowadays and how fast we are adapting our behavior. This makes it nearly impossible to foresee future uses and needs of a system like Galileo. The Galileo system therefore needs to be designed to be very adaptable and flexible, especially considering the long deployment times associated with these kinds of systems.

From an engineering perspective the improved Galileo system provides a lot of challenges. Especially it is a challenge to improve the system services and performance while still providing backwards compatibility and uninterrupted service for the end users. The engineering challenges include, but are not limited to:

- Service definitions and navigation data content and transmission schemes
- Signal generation chain improvements
- Inter-satellite links for data transfer and ranging of the satellites within the Galileo constellation
- Flexibility to adapt the system also when deployed
- Electric propulsion to reduce total system cost

We at RUAG Space are actively working with these issues and are currently doing studies regarding the signal generation chain and how this can be improved in different ways in order to increase the performance and in the end deliver a better and more accurate navigation solution to the end user, regardless if the user is out hiking in the woods, being out on the ocean in a boat or is being driven by her autonomous car to work.

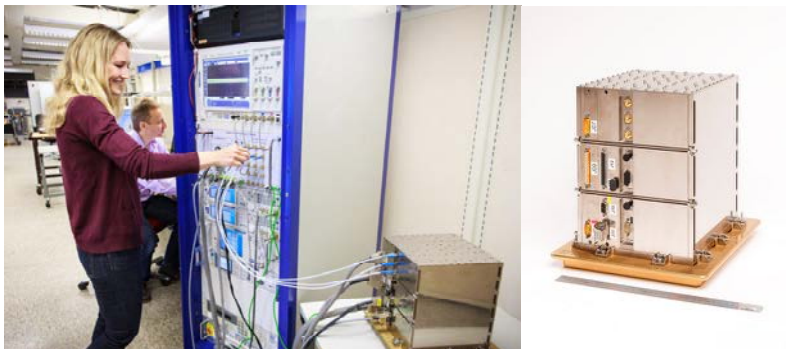


Figure 1: Studies being performed on Galileo Self-Compensating Device (SCD) engineering model that will improve the quality of the transmitted navigation signals by allowing compensation of on-board signal chain imperfections.

Collaborative Error Estimation and Integrity Monitoring Algorithms for Critical Applications

Leslie Montloin, Airbus Defence and Space
Philippe Brocard, Airbus Defence and Space

ABSTRACT

Critical navigation applications are extensively based on GNSS for positioning, guidance or timing. Most of the critical applications are intended to fulfil accuracy and integrity requirements. This paper proposes new algorithms based on a collaborative approach in which GNSS receivers of a network share their GNSS measurements to improve their accuracy, integrity and availability performances. The proposed algorithms aim at enhancing the accuracy, integrity and availability of the GNSS collaborators with respect to the infrastructure-free single-receiver algorithms (ABAS), while presenting low infrastructure costs.

The principle of the proposed approach that relies on GNSS measurement sharing is firstly presented. Next, two algorithms based on this data sharing principle are proposed. The first algorithm is a Kalman filter based technique aiming at estimating the ionospheric delay, the GNSS carrier phase ambiguities, and the Inter-Frequency Biases (IFBs) affecting GNSS measurements. The second algorithm is a detection algorithm aiming at detecting satellite IFB faults. The performances of both algorithms are assessed and the correlation between the algorithm performances and the number of GNSS receivers in the network is further discussed.

The results show that the proposed GNSS error algorithm provides ionospheric delay estimation with decimeter accuracy level, which is significantly better than the accuracy obtained with standard ionospheric error models [1]. The satellite fault detection is also significantly aided by the GNSS measurement sharing process. The system architecture (optimal number of GNSS receivers) can be adjusted knowing the accuracy and integrity requirements of the targeted application.

INTRODUCTION

Several fields of application require vehicles to be equipped with devices that provide, real time, precise and trustable positioning using GNSS. Historically, civil aviation has been the first safety critical application to use GNSS receivers for guidance, but maritime, rail and road (with autonomous car) applications are showing a

growing interest in this technology. Standalone GNSS cannot fulfill such requirements, in particular the integrity and accuracy ones. Accuracy characterizes the degree of conformance between the estimated position at a given time and its true position [7]. Integrity relates to the level of trust that can be placed in the information provided by the positioning system. It includes the ability of the system to provide timely and valid warnings to users when the position error exceeds a tolerable alert limit for the intended operation. GNSS augmentation systems have been developed to tackle this issue.

Existing augmentation systems are classified into Ground Based Augmentation System (GBAS), Satellite Based Augmentation System (SBAS) and Aircraft Based Augmentation System (ABAS). ABAS augmentation is a flexible and infrastructure free approach, but it has limited availability performances because the fault detection process has to be performed autonomously. On the other hand, GBAS and SBAS present improved accuracy availability performances because they include a pseudo-range error correction process and a fault detection process performed by a dedicated ground segment.

The challenge is to propose an innovative GNSS-based navigation system that provides accuracy aiding and integrity monitoring for GNSS ranging sources, while combining:

- Low infrastructure cost,
- Improved accuracy and availability performance compared to existing infrastructure-free approaches (ABAS),
- Flexibility/adaptability of the system design regarding the requirement level demanded by the targeted application.

The proposed solution presented in this paper is a collaborative approach based on GNSS measurement sharing. The GNSS receivers that are part of a network of collaborative users share GNSS single or dual frequency code and carrier phase measurements in order to estimate pseudo-range error corrections and to detect satellite-based feared events. More precisely, ionospheric delay corrections, carrier phase ambiguities and Inter-Frequency Biases (IFBs) corrections are estimated through the data

sharing approach in this paper. Thus it improves the accuracy, as well as the integrity and availability of the position solution of each user. In addition, the system architecture can be adapted to the accuracy and integrity requirement demanded by the targeted application. Any collaborative system presented in this paper is assumed to consist of:

- the user segment which represent the collaborative GNSS receivers, and a guaranteed data link to exchange data with the central processing facility,
- the central processing facility which collects the data transmitted by the GNSS receivers, processes them and broadcasts data to the receivers with a guaranteed data link.

Several techniques based on the GNSS collaborative approach have been proposed in the literature [8] [9] [10] [11] [12]. Among the developed techniques, some approaches propose to mitigate GNSS measurement errors using a GNSS receiver network. As an illustration, [10] estimates and mitigates satellite ephemeris errors, satellite clock errors, ionospheric errors and tropospheric errors by fusing camera-based lane boundary sensor measurements and GNSS code pseudo-range measurements from a network of GNSS receivers.

This paper aims at mitigating GNSS measurement errors by using a GNSS measurement collaborative approach without external sensor. More specifically, the **first goal** of this paper is to propose a new technique that aims at improving the accuracy of the user solutions by estimating the ionospheric errors, the L1/L2 IFBs errors, and the GNSS carrier phase ambiguities of the receivers that are part of the network. The classical approaches to mitigate the ionospheric delay are to use a fixed-location receiver with a known position through a GNSS differential technique, or to use SBAS corrections, or to use precise ionospheric delay models. This is not required in the proposed approach. The GNSS receivers of the network can be dynamic and the receiver position estimate is not needed.

The **second goal** of this publication is to propose a GNSS satellite fault detector based on the sharing of dual frequency phase measurements from the networked GNSS receivers. Existing publications on the integrity enhancement through collaborative approaches extend the concept of Receiver Autonomous Integrity Monitoring (RAIM) to a network of GNSS receivers [13][14][15]. The proposed approach aims at developing GNSS satellite fault detectors prior to the RAIM algorithms. This enables relaxing the missed detection requirement on the RAIM algorithms and decreasing the protection levels computed by each user.

The outline of the paper is as follows:

- Section I describes the principle and the performances of GNSS error (ionospheric delay, ambiguity and IFBs) estimation algorithm.
- Section II proposes a detector based on measurement sharing that aims to detect satellite IFB failures. This section also assesses the performance of this algorithm.
- Section III presents the conclusions of this paper.

I. GNSS data sharing approach for ionospheric delay and carrier phase ambiguity estimation

I.1. GNSS measurement models

This section describes the GNSS pseudo-range measurements of each receiver of the collaborative network. Let $\rho_{L1,r}^s(t_k)$ and $\phi_{L1,r}^s(t_k)$ be the GNSS L1 code and phase measurements of GNSS receiver r from satellite s at time epoch t_k . These measurements can be modelled as follows:

$$\begin{aligned}\rho_{L1,r}^s(t_k) &= \rho_{0,r}^s(t_k) + c[\delta t_r(t_k) - \delta t^s(t_k)] + I_{L1,r}^s(t_k) \\ &\quad + T_r^s(t_k) + Sat_r^s(t_k) + b_{L1,r} + b_{L1}^s \\ &\quad + \eta_{L1,\rho,r}^s(t_k) \\ \phi_{L1,r}^s(t_k) &= \rho_{0,r}^s(t_k) + c[\delta t_r(t_k) - \delta t^s(t_k)] - I_{L1,r}^s(t_k) \\ &\quad + T_r^s(t_k) + Sat_r^s(t_k) + b_{L1,r} + b_{L1}^s \\ &\quad + \lambda_{L1} A_{L1,r}^s(t_k) + \eta_{L1,\phi,r}^s(t_k)\end{aligned}\quad (1)$$

where:

- $\rho_{0,r}^s$ is the true range from satellite s to receiver r [m],
- δt_r is the clock error of receiver r [s],
- δt^s is the clock error of satellite s [s],
- $I_{L1,r}^s$ is the ionospheric delay on L1 [m],
- T_r^s and Sat_r^s are the tropospheric error and the satellite ephemeris induced error [m], respectively,
- $\eta_{L1,\rho,r}^s$ and $\eta_{L1,\phi,r}^s$ are the multipath and thermal noise on the L1 code measurement and L1 phase measurement, respectively [m],
- $b_{L1,r}$ and b_{L1}^s are the hardware (GNSS antenna + front-end stage) receiver bias and hardware (GNSS antenna + front-end stage) satellite bias on L1, respectively [m],
- $A_{L1,r}^s(t_k)$ is the phase ambiguity on L1 [cycle],
- λ_{L1} is the wavelength on L1 [m],
- c is the speed of light [m/s].

Similarly, the L2 code and phase measurements of GNSS receiver r from satellite s at time epoch t_k can be written by substituting L1 by L2 in Equation (1).

Note also that the ionospheric delay on L2 can be related to the ionospheric delay on L1 [2]:

$$I_{L2,r}^s(t_k) = \frac{\lambda_{L2}^2}{\lambda_{L1}^2} I_{L1,r}^s(t_k) \quad (2)$$

An important assumption made in the rest of this paper is that the GNSS receivers of the network are in the same area (the spatial disparity of the GNSS network is around 50km maximum), and the ionosphere layer is in nominal condition. This implies that the ionospheric spatial gradient is a few mm/km [4], leading to a variation of the ionospheric delay from a particular satellite up to a few centimeters over a region of several kilometers in radius. This can be neglected compared to the magnitude of the ionospheric delay that is a few meters in nominal conditions. Hence, the ionospheric delay $I_{L1,r}^s$ related to a given satellite s is considered to be roughly the same for all receivers r of the network. This delay is denoted as I_{L1}^s in the following.

Since the ionosphere delay from a particular satellite is nearly equal for all users of the network, it is proposed to fuse the GNSS measurements from that particular satellite collected over the GNSS receivers of the network to retrieve the ionosphere delay from the considered satellite. This fusion algorithm is further detailed in the next section.

1.2. GNSS data sharing algorithm

Each receiver r_i of the GNSS receiver network is able to transmit to the server:

- The GNSS code and phase measurements from a satellite s on L1 ($\rho_{L1,ri}^s$ and $\phi_{L1,ri}^s$) (for single and dual-frequency receivers)
- The GNSS code and phase measurements from a satellite s on L2 ($\rho_{L2,ri}^s$ and $\phi_{L2,ri}^s$) (for dual frequency receiver only).

The central facility collects the GNSS measurements and estimates the ionospheric delay that is common to all GNSS receivers of the network, as well as other terms that are receiver-specific (L1 ambiguities for single-frequency receivers, L1 and L2 ambiguities as well as L1/L2 Inter-Frequency Biases (IFBs) for dual-frequency receivers). These estimates are then broadcasted to the GNSS receivers via a guaranteed data link. This enables each user to estimate its navigation solution using the ionosphere delay estimate, as well as the L1/L2 IFBs and the ambiguity estimates, leading to improve the accuracy of the navigation solution. This process is represented in Figure 1.

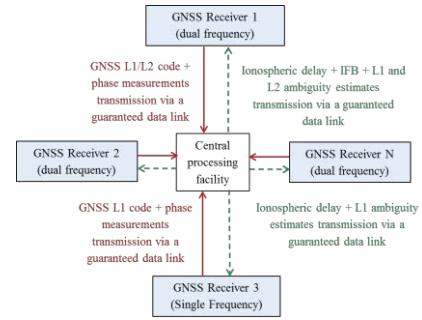


Figure 1 Principle of GNSS data sharing approach

Several data link can be envisaged for this architecture. If the receivers of the network are in proximity, the Dedicated Short-Range Communications (DSRC) is a candidate. It is a wireless communication channel designed specifically to support vehicle to vehicle (V2V) and vehicle to infrastructure (V2I) communications. Further details about the frequency band and bandwidth allocated to DSRC are available here [3].

Let us assume that a satellite s is visible by a set of N_{user} dual-frequency users at time t_k . Each user r_i transmits to the central facility measurements $\rho_{L1,ri}^s$, $\phi_{L1,ri}^s$, as well as $\rho_{L2,ri}^s$ and $\phi_{L2,ri}^s$ if the receiver r_i is a dual-frequency receiver. These measurements are firstly combined in order to remove the true ranges, the tropospheric delays, the ephemeris induced errors, as well as receiver and satellite clock errors. The combined and concatenated measurement vector that will be used in the sharing algorithm is as follows:

$$\mathbf{y}(t_k) = \begin{bmatrix} \mathbf{y}_{r_1}^s(t_k) \\ \vdots \\ \mathbf{y}_{r_i}^s(t_k) \\ \vdots \\ [\mathbf{y}_{r_{N_{user}}}^s(t_k)] \end{bmatrix} \quad (3)$$

where:

- $\mathbf{y}_{r_i}^s(t_k)$ is the combined measurement vector between satellite s and receiver r_i :

$$\mathbf{y}_{r_i}^s(t_k) = \begin{cases} \begin{bmatrix} \rho_{L1,ri}^s(t_k) - \phi_{L1,ri}^s(t_k) \\ \rho_{L2,ri}^s(t_k) - \phi_{L2,ri}^s(t_k) \end{bmatrix} & \text{if } r_i \text{ is dual-frequency} \\ [\rho_{L1,ri}^s(t_k) - \phi_{L1,ri}^s(t_k)] & \text{if } r_i \text{ is single-frequency} \end{cases} \quad (4)$$

Using Equations (1) and (2), terms of Equation (4) equal to:

$$\begin{aligned}
 \rho_{L1,ri}^s(t_k) - \phi_{L1,ri}^s(t_k) &= \begin{cases} 2I_{L1}^s(t_k) - \lambda_{L1}A_{L1,ri}^s(t_k) \\ +\eta_{L1,\rho,ri}^s(t_k) - \eta_{L1,\phi,ri}^s(t_k) \end{cases} \\
 \rho_{L2,ri}^s(t_k) - \phi_{L2,ri}^s(t_k) &= \begin{cases} \frac{2\lambda_{L2}^2}{\lambda_{L1}^2}I_{L1}^s(t_k) - \lambda_{L2}A_{L2,ri}^s(t_k) \\ +\eta_{L2,\rho,ri}^s(t_k) - \eta_{L2,\phi,ri}^s(t_k) \end{cases} \\
 \phi_{L1,ri}^s(t_k) - \phi_{L2,ri}^s(t_k) &= \left(\frac{\lambda_{L2}^2}{\lambda_{L1}^2} - 1 \right) I_{L1}^s(t_k) + b_{L1,ri} - b_{L2,ri} + b_{L1}^s - b_{L2}^s \\
 &\quad + \lambda_{L1}A_{L1,ri}^s(t_k) - \lambda_{L2}A_{L2,ri}^s(t_k) \\
 &\quad + \eta_{L1,\phi,ri}^s(t_k) - \eta_{L2,\phi,ri}^s(t_k)
 \end{aligned} \quad (5)$$

Let us denote Δb_{ri}^s the L1/L2 IFBs difference:

$$\Delta b_{ri}^s = b_{L1,ri} + b_{L1}^s - b_{L2,ri} + b_{L2}^s \quad (6)$$

The vector of unknowns consists of the carrier phase ambiguities for each receiver, the L1/L2 IFBs, and the ionosphere delay on L1 at time t_k :

$$\mathbf{x}(t_k) = \begin{bmatrix} \mathbf{x}_A \\ \mathbf{x}_b \\ I_{L1}^s(t_k) \end{bmatrix} \quad (7)$$

where:

- \mathbf{x}_A concatenates the unknown ambiguity on L1 and L2 for dual-frequency users and ambiguity on L1 for single-frequency users. In this publication, the ambiguities are considered as constant in the time domain. This means that a cycle slip detector is supposed to be implemented prior to the data sharing algorithm, and that the measurements affected by cycle slips are removed or corrected. \mathbf{x}_A is given as:

$$\mathbf{x}_A = \begin{bmatrix} A_{L1,r1}^s \\ \vdots \\ A_{L1,ri}^s \\ \vdots \\ A_{L1,rN_{user}}^s \end{bmatrix} \quad (8)$$

where:

$$\mathbf{A}_{ri}^s = \begin{cases} \begin{bmatrix} A_{L1,ri}^s \\ A_{L2,ri}^s \end{bmatrix} & \text{if } r_i \text{ is dual-frequency} \\ A_{L1,ri}^s & \text{if } r_i \text{ is single-frequency} \end{cases} \quad (9)$$

- \mathbf{x}_b concatenates the unknown L1/L2 IFB for each dual-frequency users. Since IFBs can be considered as constant in the time domain, \mathbf{x}_b is independent of the time index t_k . Let us note N_{DF} the number of dual-frequency receivers that monitor satellite s at t_k :

$$\mathbf{x}_b = \begin{bmatrix} \Delta b_{r1}^s \\ \vdots \\ \Delta b_{ri}^s \\ \vdots \\ \Delta b_{rN_{DF}}^s \end{bmatrix} \quad (10)$$

The linear measurement model that relates the state vector to the observation vector is as follows:

$$\mathbf{y}(t_k) = \mathbf{H}(t_k)\mathbf{x}(t_k) + \boldsymbol{\eta}(t_k) \quad (11)$$

where:

- $\mathbf{H}(t_k)$ is the observation matrix equal to:

$$\mathbf{H}(t_k) = \begin{bmatrix} \mathbf{H}_{r1}(t_k) \\ \vdots \\ \mathbf{H}_{ri}(t_k) \\ \vdots \\ \mathbf{H}_{rN_{user}}(t_k) \end{bmatrix} \quad (12)$$

$\mathbf{H}_{ri}(t_k)$ is computed such as $\mathbf{y}_{ri}^s(t_k) = \mathbf{H}_{ri}\mathbf{x}(t_k)$. From Equation (5), and using the notation $\alpha = \frac{\lambda_{L2}^2}{\lambda_{L1}^2}$, the observation matrix $\mathbf{H}_{ri}(t_k)$ can be written as follows for dual-frequency receivers r_i :

$$\begin{aligned}
 &\mathbf{H}_{ri}(t_k) \\
 &= \begin{bmatrix} 0 & \cdots & -\lambda_{L1} & 0 & \cdots & 0 & 0 & \cdots & 0 & \cdots & 0 \\ 0 & \cdots & 0 & -\lambda_{L2} & \cdots & 0 & 0 & \cdots & 0 & \cdots & 0 \\ 0 & \cdots & \lambda_{L1} & -\lambda_{L2} & \cdots & 0 & 0 & \cdots & 1 & \cdots & 0 \end{bmatrix} \begin{bmatrix} 2 \\ 2\alpha \\ \alpha - 1 \end{bmatrix} \begin{matrix} \mathbf{x}_A \\ \mathbf{x}_b \\ I_{L1}^s \end{matrix}
 \end{aligned} \quad (13)$$

The observation matrix $\mathbf{H}_{ri}(t_k)$ can be written as follows for single-frequency receivers r_i :

$$\begin{aligned}
 &\mathbf{H}_{ri}(t_k) \\
 &= \begin{bmatrix} 0 & \cdots & -\lambda_{L1} & 0 & \cdots & 0 & 0 & \cdots & 0 & \cdots & 0 \\ 0 & \cdots & 0 & -\lambda_{L2} & \cdots & 0 & 0 & \cdots & 0 & \cdots & 0 \end{bmatrix} \begin{bmatrix} 2 \\ 2\alpha \end{bmatrix} \begin{matrix} \mathbf{x}_A \\ \mathbf{x}_b \\ I_{L1}^s \end{matrix}
 \end{aligned} \quad (14)$$

- $\boldsymbol{\eta}(t_k)$ is the observation noise vector:

$$\boldsymbol{\eta}(t_k) = \begin{bmatrix} \boldsymbol{\eta}_{r1}(t_k) \\ \vdots \\ \boldsymbol{\eta}_{ri}(t_k) \\ \vdots \\ \boldsymbol{\eta}_{rN_{DF}}(t_k) \end{bmatrix} \quad (15)$$

From Equation (5), $\boldsymbol{\eta}_{ri}(t_k)$ is as follows for dual-frequency receivers:

$$\boldsymbol{\eta}_{ri}(t_k) = \begin{bmatrix} \eta_{L1,\rho,ri}^s(t_k) - \eta_{L1,\phi,ri}^s(t_k) \\ \eta_{L2,\rho,ri}^s(t_k) - \eta_{L2,\phi,ri}^s(t_k) \\ \eta_{L1,\phi,ri}^s(t_k) - \eta_{L2,\phi,ri}^s(t_k) \end{bmatrix} \quad (16)$$

$\boldsymbol{\eta}_{ri}(t_k)$ is as follows for single-frequency receivers:

$$\boldsymbol{\eta}_{ri}(t_k) = [\eta_{L1,\rho,ri}^s(t_k) - \eta_{L1,\phi,ri}^s(t_k)] \quad (17)$$

Let $\mathbf{C}(t_k)$ be the covariance matrix of $\boldsymbol{\eta}(t_k)$. Assuming that the code and phase measurement noises are independent over the GNSS receiver network:

$$\mathbf{C}(t_k) = \begin{bmatrix} \mathbf{C}_{r_1} & 0 & 0 & 0 & 0 \\ 0 & \ddots & 0 & 0 & 0 \\ 0 & 0 & \mathbf{C}_{r_i} & 0 & 0 \\ 0 & 0 & 0 & \ddots & 0 \\ 0 & 0 & 0 & 0 & \mathbf{C}_{r_{N_{user}}} \end{bmatrix} \quad (18)$$

The covariance matrix \mathbf{C}_{r_i} can be written as follows for dual-frequency receivers r_i :

$$\mathbf{C}_{r_i} = \begin{bmatrix} \sigma_{L1,\rho,r_i}^2 + \sigma_{\phi,L1,r_i}^2 & 0 & \sigma_{crossCov,\phi,L1,r_i}^2 \\ 0 & \sigma_{L2,\rho,r_i}^2 + \sigma_{\phi,L2,r_i}^2 & \sigma_{crossCov,\phi,L2,r_i}^2 \\ \sigma_{crossCov,\phi,L1,r_i}^2 & \sigma_{crossCov,\phi,L2,r_i}^2 & \sigma_{\phi,L1,r_i}^2 + \sigma_{\phi,L2,r_i}^2 \end{bmatrix} \quad (19)$$

where:

- σ_{L1,ρ,r_i}^s and $\sigma_{\phi,L1,r_i}^s$ are the standard deviations of the code and phase measurements from satellite s to receiver r_i on L1,
- σ_{L2,ρ,r_i}^s and $\sigma_{\phi,L2,r_i}^s$ are the standard deviations of the code and phase measurements from satellite s to receiver r_i on L2,
- $\sigma_{crossCov,\phi,L1,r_i}^s$ is the cross covariance term induced by the correlation between observations $\rho_{L1,ri}^s - \phi_{L1,ri}^s$ and $\phi_{L1,ri}^s - \phi_{L2,ri}^s$,
- $\sigma_{crossCov,\phi,L2,r_i}^s$ is the cross covariance term induced by the correlation between observations $\rho_{L2,ri}^s - \phi_{L2,ri}^s$ and $\phi_{L1,ri}^s - \phi_{L2,ri}^s$,

Note that, since the carrier phase measurement noise level is very low (millimeter level), the cross correlation terms are supposed to be negligible and are omitted in the rest of this publication.

The covariance matrix \mathbf{C}_{r_i} can be written as follows for single-frequency receivers r_i :

$$\mathbf{C}_{r_i} = \begin{bmatrix} \sigma_{L1,\rho,r_i}^2 + \sigma_{\phi,L1,r_i}^2 \end{bmatrix} \quad (20)$$

The data sharing algorithm is implemented in two successive steps:

- During the first step, a batch weighted linear least square is run on a limited batch size N_{Batch} in order to get a first estimate of the ambiguities, L1/L2 IFBs, and ionosphere delays,
- During the second step, a Kalman filter is launched using the outputs of the first step for the filter initialization.

1st step : Initialization

- Estimate $\hat{\mathbf{x}}(t_0)$ and the covariance matrix of $\hat{\mathbf{x}}(t_0)$ ($\hat{\mathbf{P}}(t_0)$) using a batch of N_{Batch} time epochs and a batch weighted linear least square algorithm.

2nd step: Kalman filter algorithm

- For time $t_k \geq t_1$:

$$\hat{\mathbf{x}}(t_k)^- = \mathbf{F}(t_k)\hat{\mathbf{x}}(t_{k-1})$$

$$\hat{\mathbf{P}}(t_k)^- = \mathbf{F}(t_k)\hat{\mathbf{P}}(t_{k-1})\mathbf{F}(t_k)^T + \mathbf{Q}(t_k)$$

$$\mathbf{K}(t_k) = \hat{\mathbf{P}}(t_k)^- \mathbf{H}(t_k)^T (\mathbf{C}(t_k) + \mathbf{H}(t_k)\hat{\mathbf{P}}(t_k)^- \mathbf{H}(t_k)^T)^{-1} \quad (21)$$

$$\hat{\mathbf{x}}(t_k) = \hat{\mathbf{x}}(t_k)^- + \mathbf{K}(t_k)(\mathbf{y}(t_k) - \mathbf{H}(t_k)\hat{\mathbf{x}}(t_k)^-)$$

$$\hat{\mathbf{P}}(t_k) = (\mathbf{I} - \mathbf{K}(t_k)\mathbf{H}(t_k))\hat{\mathbf{P}}(t_k)^-$$

where:

- $\hat{\mathbf{x}}(t_k)^-$ is the a-priory estimate of state vector \mathbf{x} at t_k ,
- $\hat{\mathbf{P}}(t_k)^-$ is the a-priory estimate of state vector covariance matrix at t_k ,
- $\mathbf{H}(t_k)$ is the observation matrix at t_k defined in Equation (12),
- $\mathbf{C}(t_k)$ is the observation covariance matrix at t_k defined in Equation (18),
- $\mathbf{y}(t_k)$ is the observation vector at t_k defined in Equation (3),
- $\hat{\mathbf{P}}(t_k)$ is the estimate of state vector covariance matrix at t_k ,
- $\hat{\mathbf{x}}(t_k)$ is the estimate of state vector \mathbf{x} at t_k ,
- $\mathbf{F}(t_k)$ is the state transition matrix at t_k . Considering that the L1/L2 IFBs are constant in the time domain and assuming no cycle slip over the estimation period, $\mathbf{F}(t_k)$ is defined as:

$$\mathbf{F}(t_k) = \begin{bmatrix} 1 & 0 & 0 & 0 \\ 0 & \ddots & 0 & 0 \\ 0 & 0 & 1 & 0 \\ 0 & 0 & 0 & e^{-\Delta t/\tau_I} \end{bmatrix} \quad (22)$$

- Δt is the sampling rate of the observation data [s],
- τ_I is the correlation time of the ionospheric delay [s],
- $\mathbf{Q}(t_k)$ is the predicted covariance matrix of the state noise vector at t_k defined as:

$$\mathbf{Q} = \begin{bmatrix} 0 & 0 & 0 & 0 \\ 0 & \ddots & 0 & 0 \\ 0 & 0 & 0 & 0 \\ 0 & 0 & 0 & (1 - e^{-2\Delta t/\tau_I})\sigma_I^2 \end{bmatrix} \quad (23)$$

- σ_I^2 is the variance of the ionospheric delay [s].

Note that, in order to aid the IFB estimation, the sum of the IFB on all GNSS receivers is supposed to be null. The following closure constraint is thus set in the Kalman filter:

$$\sum_{i=1}^{N_{DF}} \Delta b_{ri}^s = 0m \quad (24)$$

In order to account for this constraint, the estimation algorithm proposed in Equation (21) can be implemented by substituting matrices $\mathbf{y}(t_k)$, $\mathbf{H}(t_k)$ and $\mathbf{C}(t_k)$ by matrices $\mathbf{y}_{cl}(t_k)$, $\mathbf{H}_{cl}(t_k)$ and $\mathbf{C}_{cl}(t_k)$ respectively:

$$\mathbf{y}_{cl}(t_k) = \begin{bmatrix} \mathbf{y}(t_k) \\ 0 \end{bmatrix} \quad (25)$$

$$\mathbf{H}_{cl}(t_k) = \begin{bmatrix} \mathbf{H}(t_k) \\ \mathbf{H}_{IFB} \end{bmatrix} \quad (26)$$

$$\mathbf{H}_{IFB} = \left[\underbrace{0 \ \cdots \ 0}_{x_A} \middle| \underbrace{1 \ \cdots \ 1}_{x_b} \ \cdots \ 1 \right] \begin{matrix} 0 \\ \vdots \\ 0 \end{matrix} \quad (27)$$

$$\mathbf{C}_{cl}(t_k) = \begin{bmatrix} \mathbf{C}(t_k) & 0 \\ 0 & \sigma_{cl}^2 \end{bmatrix} \quad (28)$$

where:

- σ_{cl} is the closure constraint standard deviation. Note that the closure constraint is false when only one dual-frequency GNSS receiver is involved in the filter ($N_{DF} = 1$). Hence, the value of σ_{cl} is artificially inflated not to consider the closure constraint in the case $N_{DF} = 1$.

The estimations of the ionospheric delay, L1/L2 IFBs and ambiguities are then broadcasted to each user via the guaranteed data link.

1.3. Simulation results

1.3.1 Simulation setup

This section aims to analyze the shape of the error on the estimation of the ionospheric delay, carrier phase ambiguities and L1/L2 IFBs made by the estimation algorithm proposed in Section 1.2. The simulation parameters used for this analysis are indicated in Table 1.

Parameter	Notation	Statistical model	Model parameter values
Ionosphere delay	I_{L1}^s	Time-correlated noise following a zero-mean 1 st -order Gauss-Markov process $\mathcal{M}(\tau_I, \sigma_I^2)$	$\sigma_I = 4.5m$ $\tau_I = 1800s$
Ambiguity on L1 and L2 phase measurements	$A_{L1,ri}^s$ $A_{L2,ri}^s$	Time-constant ambiguity with a magnitude following a discrete uniform distribution on the interval $[A_{min}; A_{max}]$	$A_{min} = 0 \text{ cycle}$ $A_{max} = 20 \text{ cycles}$
Receiver/satellite IFB on L1 and L2	Δb_{ri}^s	Time-constant bias with a magnitude following an uniform distribution in $[-1; 1]$, and such that the closure constraint is met when $N_{DF} > 1$	$\sigma_{\Delta b} = 1m$
Closure constraint standard deviation	σ_{cl}		$\sigma_{cl} = 1m$ for $N_{DF} > 1$ $\sigma_{cl} = 10m$ for $N_{DF} = 1$
Multipath+thermal noise on L1 and L2 code measurements	$\eta_{L1,\rho,ri}^s$ $\eta_{L2,\rho,ri}^s$	Zero-mean white Gaussian noise $\mathcal{N}(0, \sigma_\rho^2)$	$\sigma_\rho = 1.0m$
Multipath+thermal noise on L1 and L2 phase measurements	$\eta_{L1,\phi,ri}^s$ $\eta_{L2,\phi,ri}^s$	Zero-mean white Gaussian noise $\mathcal{N}(0, \sigma_\phi^2)$	$\sigma_\phi = 2mm$
GNSS measurement sampling rate	$ t_{k+1} - t_k $		$\Delta t = 1s$

Table 1 Simulation parameters used for ionospheric delay estimation

The models for the code and phase multipath and thermal noise errors are assumed to be the same over all GNSS receivers of the network, and are assumed to be the same on L1 and L2 measurements. In addition, it is assumed in this simulation that all GNSS receivers of the network are dual-frequency receivers, so $N_{DF} = N_{user}$ in this section.

1.3.2 Simulation results

Figure 2 shows the evolution of the Kalman filter estimated L1/L2 IFB of one of the GNSS dual-frequency receiver involved in the estimation filter. Figure 3 shows the evolution of the Kalman filter estimated L1 and L2 ambiguities for the same receiver. Finally, Figure 4 shows the evolution of the Kalman filter estimated ionospheric delay common to all GNSS receivers. In this simulation,

the total number of users is set to $N_{user} = N_{DF} = 5$. The size of the batch weighted least square used to initialize the Kalman filter is $N_{Batch} = 10s$.

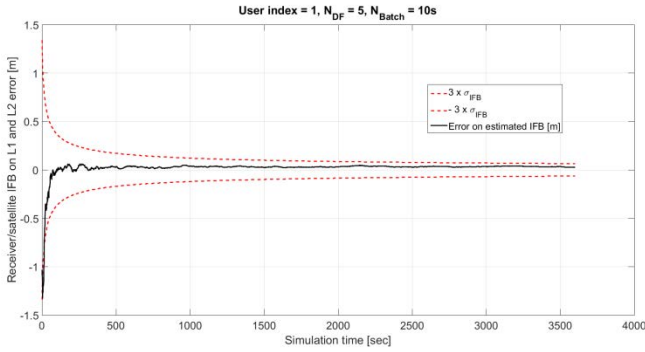


Figure 2 L1/L2 IFB error

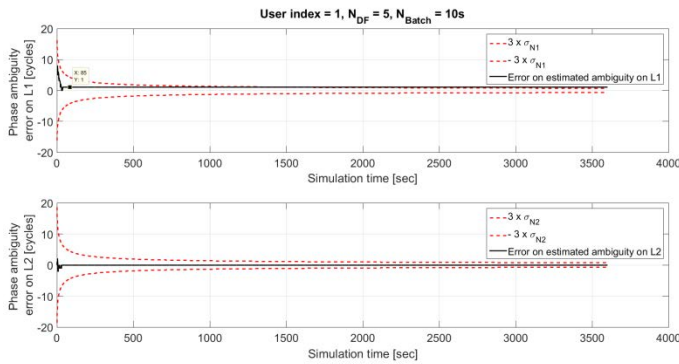


Figure 3 Carrier phase ambiguities on L1 and L2 error

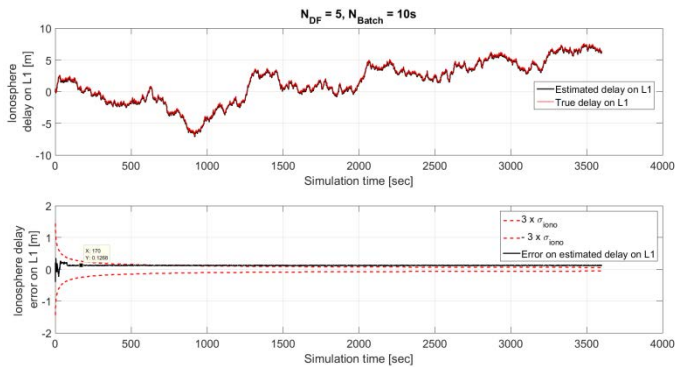


Figure 4 Ionospheric delay on L1 error

I.4. Estimation of error models

Section I.2 proposed an algorithm aiming at estimating the ionospheric delay, the carrier phase ambiguities and the IFBs using an approach based on the GNSS measurements sharing between multiple GNSS receivers. Section I.3 showed the evolution of the estimation errors on the ionospheric delay, on the ambiguities and on the IFBs in the time domain. In this section, these errors are further analyzed and error models are proposed.

I.4.1. Error analysis

From Figures 2, 3 and 4, it can be concluded that, after a transient period that lasts roughly 90s:

- the IFB error is a time correlated noise error, $\eta_{\Delta b_{ri}^s}$
The estimated IFB can be modelled as follows:

$$\widehat{\Delta b}_{ri}^s(t_k) = \Delta b_{ri}^s + \eta_{\Delta b_{ri}^s}(t_k) \quad (29)$$

- the L1 and L2 ambiguities is a time constant bias ($b_{A_{L1,ri}^s}$ and $b_{A_{L2,ri}^s}$) and the bias error has a magnitude of a few cycles. The estimated carrier phase ambiguities can be modelled as:

$$\hat{A}_{L1,ri}^s = A_{L1,ri}^s + b_{A_{L1,ri}^s} \quad (30)$$

$$\hat{A}_{L2,ri}^s = A_{L2,ri}^s + b_{A_{L2,ri}^s}$$

- the ionospheric delay estimation error is the sum of:
 - an estimation noise, mainly induced by the multipath and thermal noise on GNSS measurements, and denoted as $\eta_{I_{L1}^s}$,
 - a decimeter level constant bias ($b_{I_{L1}^s}$), that is induced by the fact that the ambiguities are not perfectly tracked by the filter, so a remaining bias component is absorbed by the ionospheric delay.

The estimated ionospheric delay on L1 can be modelled as:

$$\hat{I}_{L1}^s(t_k) = I_{L1}^s(t_k) + b_{I_{L1}^s} + \eta_{I_{L1}^s}(t_k) \quad (31)$$

I.4.2. Carrier phase ambiguity error model

Simulations have shown that the ambiguity biases can be modelled as time-constant bias which magnitude follows a zero-mean normal distribution characterized by a standard deviation $\sigma_{A_{L1}^s}$ on L1 and $\sigma_{A_{L2}^s}$ and L2:

$$b_{A_{L1,ri}^s} \sim \mathcal{N}(0, \sigma_{A_{L1}^s}^2) \text{ and } b_{A_{L2,ri}^s} \sim \mathcal{N}(0, \sigma_{A_{L2}^s}^2) \quad (32)$$

From Figure 5, increasing N_{user} from 2 to 10 GNSS receivers enables dividing the ambiguity bias standard deviation by a factor 1.5.

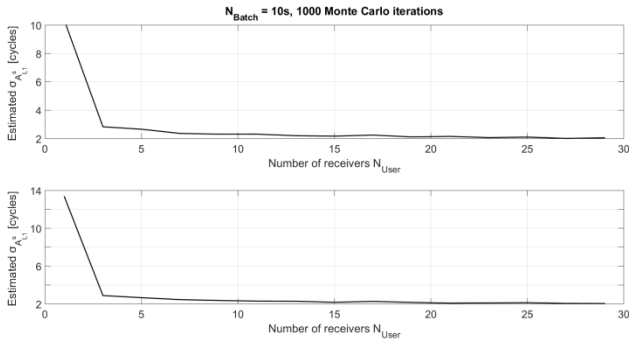


Figure 5 Standard deviation of the carrier phase ambiguity biases $\sigma_{A_{L1}^s}$ and $\sigma_{A_{L2}^s}$ as a function of number of receivers N_{DF}

As shown in Figure 5, the carrier phase ambiguity estimation for $N_{user} = 1$ is not accurate. This is because no closure condition can aid the IFBs tracking when only one GNSS receiver is involved in the estimation filter. Since the IFBs cannot be precisely estimated in this case, other variables, such as phase ambiguities cannot be precisely estimated as well.

I.4.3. Ionospheric delay error model

Simulations have shown that the ionospheric error bias can be modelled as a time-constant bias which magnitude follows a zero-mean normal distribution characterized by a standard deviation $\sigma_{b_{I_{L1}^s}}$:

$$b_{I_{L1}^s} \sim \mathcal{N}(0, \sigma_{b_{I_{L1}^s}}^2) \quad (33)$$

Similarly, the distribution of the ionospheric delay noise $\eta_{I_{L1}^s}(t_k)$ is roughly centered and follows a zero-mean Gaussian law characterized by a standard deviation $\sigma_{\eta_{I_{L1}^s}}$:

$$\eta_{I_{L1}^s}(t_k) \sim \mathcal{N}(0, \sigma_{\eta_{I_{L1}^s}}^2) \quad (34)$$

The evolutions of the standard deviations of the ionospheric bias $\sigma_{b_{I_{L1}^s}}$ (black curve) and of the ionospheric noise $\sigma_{\eta_{I_{L1}^s}}$ (red curve) as a function of the number of collaborators are represented in Figure 6.

As shown in Figure 6, the ionospheric delay estimation for $N_{user} = 1$ is not accurate. This is because no closure condition can aid the IFBs tracking in this case.

The ionospheric delay error is dominated by its time-constant bias component. The standard deviation of the bias component reaches several decimeters while the standard deviation of the noise component is a few centimeters.

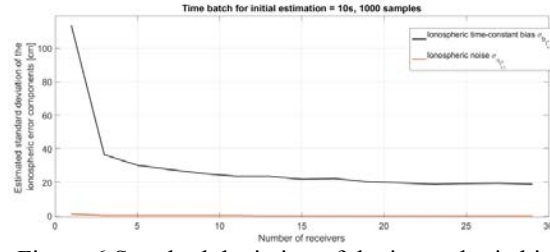


Figure 6 Standard deviation of the ionospheric bias $\sigma_{b_{I_{L1}^s}}$ and noise $\sigma_{\eta_{I_{L1}^s}}$ as a function of number of receivers N_{DF}

The noise component standard deviation is not significantly reduced when the number of GNSS receivers N_{user} increases. However, the standard deviation of the ionosphere bias component is correlated to the network size. Increasing N_{user} from 2 to 30 GNSS receivers enables dividing the ionospheric bias standard deviation by a factor 2.

Even with a small network size, the ionospheric delay is estimated with a decimeter accuracy level. This is significantly better than the accuracy obtained with standard ionospheric error models, such as the Klobuchar model [1].

I.4.4. Receiver/satellite IFB on L1 and L2 error model

Simulations have shown that the distribution of the IFB noise is roughly centered and follows a zero-mean Gaussian law characterized by a standard deviation $\sigma_{\eta_{\Delta b^s}}$:

$$\eta_{\Delta b_{ri}^s}(t_k) \sim \mathcal{N}(0, \sigma_{\eta_{\Delta b^s}}^2) \quad (35)$$

Figure 7 shows the evolution of $\sigma_{\eta_{\Delta b^s}}$ as a function of the number of GNSS receivers N_{user} .

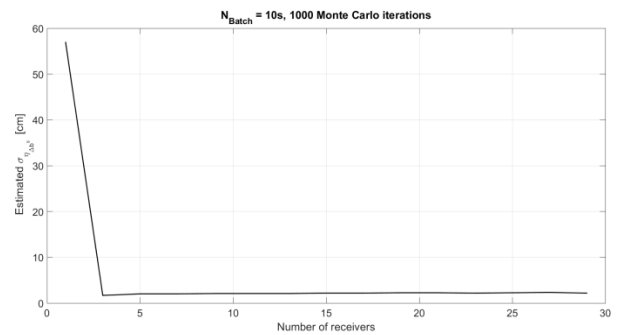


Figure 7 Standard deviation of the IFB noise $\sigma_{\eta_{\Delta b^s}}$ as a function of number of receivers N_{DF}

As shown in Figure 7, the IFB estimation for $N_{user} = 1$ is not accurate. This is because no closure condition can aid the IFBs tracking in this case.

In addition, the IFB estimation is not significantly aided by an increase in the number of GNSS receivers when $N_{user} > 1$. Indeed, the IFB estimation is mainly driven by the closure constraint applied in the estimation filter and is thus not strongly influenced by the collaborator network size.

I.4.5. Summary

To sum up, the statistical models that can be used to model the ionospheric delay error, the ambiguity errors, and the IFB error in steady state are indicated in Table 2.

Error source	Error model
Ionospheric delay error	Sum of : <ul style="list-style-type: none"> Time-constant bias $b_{I_{L1}^s}$ with a magnitude following a zero-mean Gaussian distribution $\mathcal{N}(0, \sigma_{b_{I_{L1}^s}}^2)$ Zero-mean noise $\eta_{I_{L1}^s}(t_k)$ following a zero-mean Gaussian distribution $\mathcal{N}(0, \sigma_{\eta_{I_{L1}^s}}^2)$
Ambiguity on L1 and L2 phase measurement errors	Time-constant bias $b_{A_{L1,ri}^s}$ and $b_{A_{L2,ri}^s}$ with a magnitude following a zero-mean Gaussian distribution $\mathcal{N}(0, \sigma_{A_{L1}^s}^2)$ for L1 and $\mathcal{N}(0, \sigma_{A_{L2}^s}^2)$ for L2
Receiver/satellite IFB on L1 and L2 error	Zero-mean noise $\eta_{\Delta b_{ri}^s}(t_k)$ following a zero-mean Gaussian distribution $\mathcal{N}(0, \sigma_{\eta_{\Delta b_{ri}^s}}^2)$

Table 2 Ionospheric delay, ambiguity and IFB error models

The magnitude of the IFB estimation error is not significantly reduced by the collaborative approach. However, both ambiguity and ionospheric delays are estimated with an accuracy that is similar or significantly better (for ionospheric delay) than the estimations performed by the classical approaches (Klobuchar). Hence, it is expected that this technique will enable improving the accuracy of the receiver position estimations. In addition, the estimation of the ambiguity is quasi-instantaneous, while the ambiguity estimation using classical approaches requires a non-negligible convergence time.

II. GNSS data sharing approach for satellite failure integrity monitoring

Section I proposes a GNSS data sharing algorithm aiming to estimate the IFBs, carrier phase ambiguities and ionospheric delay. This section shows how this algorithm can be used for the detection of GNSS faults. GNSS faults are defined as any error due to an anomaly of the satellite itself or to environmental effects on the GNSS ranging signal and

that affects punctually GNSS measurements.

II.1. Detectable GNSS fault modes

The sharing algorithm detailed in Section I enables estimating the carrier phase ambiguities, the ionospheric delays and the IFBs. Hence, this sharing algorithm aids the detection of any fault which associated detection test depends only on these quantities. For example, the following GNSS measurement combinations are frequently used in the fault detection algorithms since they are not affected by satellite and ephemeris errors, tropospheric errors and receiver clock errors:

- geometry-free measurements,
- code minus carrier measurements.

Code minus carrier measurements are used to detect some specific faults (i.e. faults uncorrelated across receivers), such as multipath faults. The geometry-free measurements are used to detect some common-mode faults (i.e. faults correlated among multiple receivers located in proximity), such as satellite IFB faults. The following paragraphs deal with the detection of satellite IFBs faults using the data sharing approach.

II.3. Satellite IFB fault detection algorithm

In this section, a satellite IFB fault detection algorithm based on GNSS measurement sharing between multiple GNSS receivers of a collaborative network is proposed.

Figure 8 depicts the general architecture of the proposed detection algorithm.

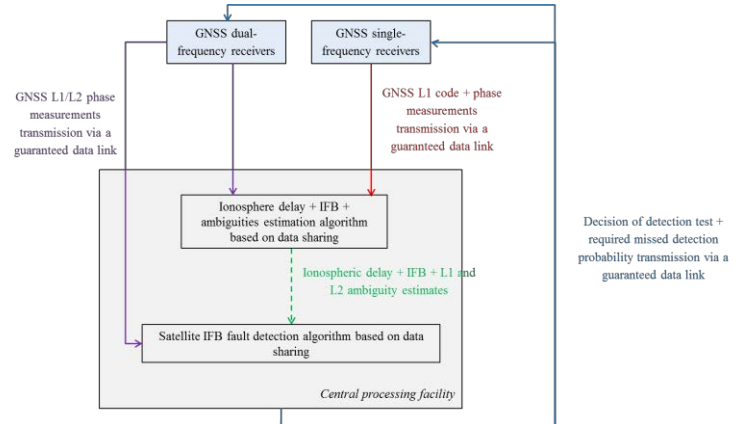


Figure 8 Satellite IFB fault detection algorithm architecture

The central facility firstly estimates the ionospheric delay from a particular satellite s , as well as carrier phase ambiguities and receiver/satellite IFBs for that satellite. This algorithm is further detailed in Section I. Next, the satellite IFB fault detection algorithm uses these estimates, as well as L1 and L2 phase measurements from

dual frequency receivers to decide if satellite s is affected by a satellite IFB fault.

II.3.1. Decision test definition

The decision of the detection test d is a binary variable defined as follows:

$$\begin{aligned} d &= 1 \text{ if } |\Delta\phi| > T \text{ (a satellite fault is detected)} \\ d &= 0 \text{ if } |\Delta\phi| \leq T \text{ (no satellite fault is detected)} \end{aligned} \quad (36)$$

where:

- T is the detection threshold,
- $|\Delta\phi|$ is the decision test defined at a time t_k as:

$$|\Delta\phi(t_k)| = \left| \frac{1}{N_{DF}} \sum_{i=1}^{N_{DF}} \left([\phi_{L1,ri}^s(t_k) - \phi_{L2,ri}^s(t_k)]_{meas} - [\phi_{L1,ri}^s(t_k) - \phi_{L2,ri}^s(t_k)]_{pred} \right) \right| \quad (37)$$

where:

- $[\phi_{L1,ri}^s(t_k) - \phi_{L2,ri}^s(t_k)]_{meas}$ is the difference between L1 phase measurement and L2 phase measurement from satellite s to receiver r_i ,
- $[\phi_{L1,ri}^s(t_k) - \phi_{L2,ri}^s(t_k)]_{pred}$ is the predicted L1/L2 phase difference from satellite s to receiver r_i .

Using the third line of Equations (5) and (6), the decision test $|\Delta\phi(t_k)|$ in nominal conditions can be written as:

$$\begin{aligned} |\Delta\phi(t_k)| &= \left(\frac{\lambda_{L2}^2}{\lambda_{L1}^2} - 1 \right) (I_{L1}^s(t_k) - \hat{I}_{L1}^s(t_k)) \\ &\quad + \frac{1}{N_{DF}} \sum_{i=1}^{N_{DF}} (\Delta b_{ri}^s - \widehat{\Delta b}_{ri}^s) \\ &= \left\{ \begin{aligned} &+ \frac{1}{N_{DF}} \sum_{i=1}^{N_{DF}} \lambda_{L1} (A_{L1,ri}^s(t_k) - \hat{A}_{L1,ri}^s(t_k)) \\ &- \frac{1}{N_{DF}} \sum_{i=1}^{N_{DF}} \lambda_{L2} (A_{L2,ri}^s(t_k) - \hat{A}_{L2,ri}^s(t_k)) \\ &+ \frac{1}{N_{DF}} \sum_{i=1}^{N_{DF}} (\eta_{L1,\phi,ri}^s(t_k) - \eta_{L2,\phi,ri}^s(t_k)) \end{aligned} \right. \quad (38) \end{aligned}$$

where each quantity is further detailed in Section I.

II.3.2. Detection threshold computation

The allowed probability of false alarm of the satellite IFB fault detector $P_{FA,SV\ IFB}$ is the probability that the difference between the predicted and measured L1/L2

phase is above a given threshold T , knowing that there is no IFB fault:

$$P_{FA,SV\ IFB} = P(|\Delta\phi(t_k)| > T \mid \text{no SV IFB fault}) \quad (39)$$

Assuming that the noises on the IFB estimates, ambiguity estimates, and carrier phase measurements are the same for all dual-frequency GNSS receivers r_i involved in the detection algorithm, the decision test $\Delta\phi(t_k)$ follows a zero-mean Gaussian distribution characterized by a standard deviation σ_{H0} in nominal condition:

$$\Delta\phi(t_k) \sim \mathcal{N}(0, \sigma_{H0}^2) \quad (40)$$

where:

$$\sigma_{H0} = \sqrt{\left(\frac{\lambda_{L2}^2}{\lambda_{L1}^2} - 1 \right)^2 (\sigma_{b_{L1}}^2 + \sigma_{\eta_{L1}}^2) + \frac{1}{N_{DF}} \left(\sigma_{\eta_{\Delta b}^s}^2 + \lambda_{L1}^2 \sigma_{A_{L1}^s}^2 + \lambda_{L2}^2 \sigma_{A_{L2}^s}^2 + \sigma_{L1,\phi}^2 + \sigma_{L2,\phi}^2 \right)} \quad (41)$$

For a given $P_{FA,SV\ IFB}$, the threshold T can be computed by solving Equation (39).

II.3.3. Missed detection probability computation

The performance of the detection algorithm can be quantified by estimating $P_{MD,SV\ IFB}$, that is the probability of miss detection of the satellite IFB fault. $P_{MD,SV\ IFB}$ is estimated as follows:

$$P_{MD,SV\ IFB} = P(|\Delta\phi(t_k)| \leq T \mid \text{SV IFB fault}) \quad (42)$$

In faulty condition, the carrier phase measurements $\phi_{L1,ri}^s(t_k) - \phi_{L2,ri}^s(t_k)$ from satellite s and processed by the GNSS receivers r_i of the network are affected by an error of magnitude $b_{IFB,SV}$ induced by the satellite IFB fault. Note that, since it is assumed in this paper that the users are located in a region of several kilometers in radius, the magnitude of error $b_{IFB,SV}$ is nearly equal for all users of the network. Hence, in faulty conditions, the decision test $\Delta\phi(t_k)$ follows a Gaussian distribution characterized by a bias $b_{IFB,SV}$ and by a standard deviation σ_{H1} :

$$\Delta\phi(t_k) \sim \mathcal{N}(b_{IFB,SV}, \sigma_{H1}^2) \quad (43)$$

where:

- $\sigma_{H1} = \sigma_{H0}$ is defined in Equation 41.

For a given $b_{IFB,SV}$, the missed detection probability $P_{MD,SV\ IFB}$ can be computed by solving Equation 42.

II.3.4. RAIM missed detection probability

In order to meet the integrity requirement, the system must check:

$$\frac{P_{OCC,SV\ IFB} P_{MD,RAIM} P_{MD,SV\ IFB} P_{MI|MD,SV\ IFB}}{P_{IR,req,SV\ IFB}} \leq \quad (44)$$

where:

- $P_{IR,req,SV\ IFB}$ is the integrity risk allocated to IFB fault,
- $P_{OCC,SV\ IFB}$ is the probability of occurrence of IFB fault,
- $P_{MD,RAIM}$ is the probability of RAIM miss detection of IFB fault,
- $P_{MI|MD,SV\ IFB}$ is the impact probability, that is the probability that the positioning error exceeds the alert limit assuming that the IFB fault occurs.

If $P_{MD,SV\ IFB}$ is dimensioning, the satellite IFB fault detector will lead to reduce considerably the required $P_{MD,RAIM}$, which leads to reduce the protection levels related to satellite IFB faults and to have a better availability of the solution.

II.4. Simulation results

The performance of the IFB fault detector in terms of missed detection probability $P_{MD,SV\ IFB}$ is quantified in this section. The simulation parameters used for this analysis are indicated in Table 3.

Parameter	Notation	Parameter values
Standard deviation of estimation error on ionospheric delay, ambiguity, receiver/satellite IFBs	$\sigma_{b_{I_{L1}}}$ $\sigma_{\eta_{I_{L1}}}$ $\sigma_{A_{L1}^s}$ $\sigma_{A_{L2}^s}$ $\sigma_{\eta_{Ab^s}}$	See Section I
Standard deviation of multipath+thermal noise on L1 and L2 phase measurements	$\sigma_{L1,\phi}$ $\sigma_{L2,\phi}$	2mm
False alert probability allocated to SV IFB fault detector	$P_{FA,SV\ IFB}$	$10^{-5}/150s$
Integrity risk allocated to SV IFB faults	$P_{IR,req,SV\ IFB}$	$10^{-7}/150s$
Occurrence probability of SV IFB faults	$P_{OCC,SV\ IFB}$	$10^{-5}/hr/SV$ for error magnitude $\geq 1.5m$
Impact probability of SV IFB faults	$P_{MI MD,SV\ IFB}$	1 for error magnitude $\geq 1.5m$

Table 3 Simulation parameters used SV IFB fault detection

Figure 9 shows the evolution of the missed detection probability of the satellite IFB fault detector as a function of the magnitude of the satellite IFB fault $b_{IFB,SV}$.

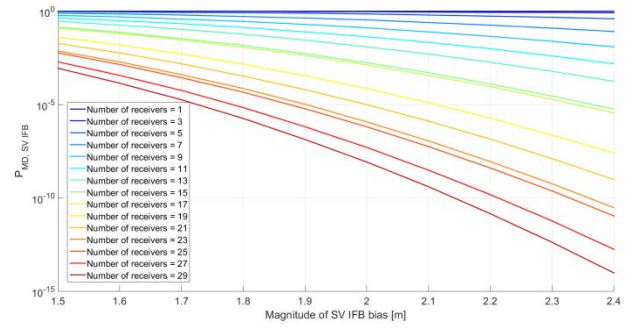


Figure 9 Missed detection probability of the satellite IFB fault detector

From Figure 9, the collaborative data sharing approach enables significantly enhancing the detection performance of the satellite IFB fault detector. Small biases ($b_{IFB,SV} = 1.5m$) are not detected when only one dual-frequency receiver is used, while this bias is detected with a probability of 10^{-3} when data from 29 receivers are shared.

Simulations have shown that the probability $P_{OCC,SV\ IFB} P_{MD,SV\ IFB} P_{MI|MD,SV\ IFB}$ induced by the smallest IFB fault $b_{IFB,SV} = 1.5m$ is below the required integrity risk when the number of receivers is equal or above 22 users. This means that, if N_{DF} is equal or larger than 22 receivers, the network receivers do not have to implement an autonomous integrity monitoring algorithm to monitor satellite IFB faults, and they do not have to account for satellite IFB faults in the protection level computation. However, if N_{DF} is lower than 22 receivers, the network receivers have to implement an autonomous integrity monitoring algorithm to monitor satellite IFB faults.

The next figure shows the evolution of the reduction ratio $\left(1 - \frac{PL_{SV\ IFB}(N_{DF})}{PL_{SV\ IFB}(N_{DF}=1)}\right)$ of the protection levels as a function of N_{DF} . This reduction ratio has been computed using a classical LSR RAIM algorithm [6] with 8 satellites in view. The allocated probability of false alert is set to $10^{-5}/150s$.

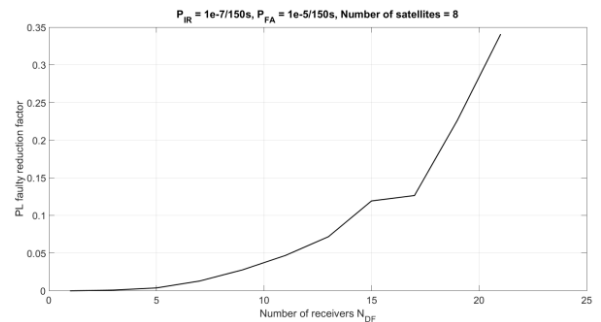


Figure 10 Reduction ratio of LSR RAIM satellite IFB fault protection levels as a function of the number of receivers N_{DF}

From Figure 10, using $N_{DF} = 20$ receivers allows reducing the LSR RAIM satellite IFB fault protection levels of 30%.

III. CONCLUSIONS

The goal of this paper is to propose innovative algorithms based on GNSS measurement sharing between multiple GNSS receivers that are part of a collaborative network. Two algorithms are proposed in this paper.

The first algorithm fuse GNSS L1 and L2 measurements (for dual-frequency receivers) from all GNSS receivers of the network through a linear Kalman filter in order to estimate the ionospheric delay, the L1/L2 IFBs and the carrier phase ambiguities. The shape of the ionospheric delay, IFB, and ambiguity estimation errors at the Kalman filter output and these estimation errors have been modelled using Gaussian laws. More specifically, it has been underlined that:

- The IFB estimation quality is not highly correlated to the network size and is mainly driven by the closure constraint set to aid the IFB estimation,
- The ambiguity and ionospheric delay estimation quality is driven by the number of GNSS receivers sharing their measurements in the central facility. The carrier phase ambiguity accuracy is roughly 2 cycles, and the ionospheric delay accuracy is roughly 10 cm for a network size of 30 receivers, which is significantly better than the accuracy obtained with standard ionospheric models, such as Klobuchar model.

The network size can thus be adapted to the accuracy requirement level demanded by the targeted application. Note also that future works related to this algorithm are listed below:

- Analysis of the performance of the algorithm if the GNSS network consists of both single and dual frequency receivers (simulations presented in this paper assumes that all receivers are dual-frequency receivers),
- Test of the algorithm on real GNSS measurements.

The second algorithm fuses GNSS L1 and L2 phase measurements from all GNSS dual-frequency receivers and outputs of the first algorithm in order to detect some satellite faults, more specifically the satellite IFB faults. It has been underlined that:

- The performances of this detector are highly correlated to the network size.
- The minimal network size, i.e. the minimal number of dual-frequency receivers for which the satellite IFB threat does not have to be considered in the protection level computation, can be determined.

This number depends on the integrity requirement level demanded by the targeted application. The network size can thus be adapted to the integrity requirements.

REFERENCES

- [1]: "Ionospheric time-delay algorithm for single-frequency GPS users", J.A. Klobuchar, IEEE transactions on aerospace and electronic systems, Vol AES-23, No. 3, May 1987
- [2]: "GPS Satellite Surveying", Wiley-Interscience, A. Leick, 2nd edition, 1995
- [3]: "Collaborative Positioning – Concepts and Approaches for more Robust Positioning", A. Kealy, G. Retscher, C. Toth, D. Brzezinska, FIG Congress 2014 Engaging the Challenges, 2014
- [4]: "Assessment of Nominal Ionosphere Spatial Decorrelation for LAAS", J. Lee, S. Pullen, S. Datta-Barua, P. Enge, PLANS 2006
- [5]: "Recursive Least Squares with Forgetting for Online Estimation of Vehicle Mass and Road Grade: Theory and Experiments", A. Vahidi, A. Stefanopoulou, H. Peng, January 2005
- [6]: "Receiver Autonomous Integrity Monitoring of GNSS Signals for Electronic Toll Collection", D. Salos, A. Martineau, C. Macabiau, B. Bonhoure, D. Kubrak, IEEE Transactions on Intelligent Transportation Systems, 2014
- [7]: "Minimum Operational Performance Standards for airborne supplemental navigation equipment using Global Positioning System (GPS), DO-208", RTCA, SC159, July 1991
- [8]: "Collaborative signal processing", A. Soloviev, J. Dickman, GPS world, 2014
- [9]: "Peer-to-Peer Cooperative Positioning: Part I, GNSS-aided acquisition", R. Garello, L. Lo Presti, G. E. Corazza, J. Samson, Inside GNSS, March/April 2012
- [10]: "Estimation of Spatially Correlated Errors in Vehicular Collaborative Navigation with Shared GNSS and Road-Boundary Measurements", J. Rife, X. Xiao
- [11]: "Peer-to-Peer Cooperative Positioning Part II: Hybrid Devices with GNSS & Terrestrial Ranging Capability", R. Garello, J. Samson, M. A. Spirito, H. Wymeersch, Inside GNSS, July/August 2012
- [12]: "Angle-of-Arrival Assisted GNSS Collaborative Positioning", B. Huang, Z. Yao, X. Cui, M. Lu, Sensors MDPI, 2016
- [13]: "Collaboration-Enhanced Receiver Integrity Monitoring (CERIM)", J. Rife, IEEE, 2011
- [14]: "Collaboration-Enhanced Receiver Integrity Monitoring with Common Residual Estimation", J. Rife, PLAN, 2012
- [15]: "A closed loop EKF and multi-failure diagnosis approach for cooperative GNSS positioning", Liu, Haiying, Meng, Xiaolin, Chen, Zhiming, Stephenson, Scott, Peltola, Pekka, GPS Solutions, 2016

High Precision Separation Method of Baseband Waveform for GNSS Signals

Tao Yan, Ying Wang, Xiao Liu
China Academy of Space Technology (Xi'an)
Xi'an, China
iamyantao@126.com

Abstract—For the modernized GNSS signals, multiple signal components are needed to be transmitted at a frequency simultaneously. Separation of time-domain waveform for single signal component is valuable, which is helpful to analyze the signal distortion and signal quality. The precision of traditional separation method suffers from degradation due to the influence of other signal components. This paper proposes two methods to eliminate the interference between different signal components. The analysis results show the proposed method can achieve high precision separation of baseband waveform for GNSS signals and has no special constraints on the randomness of navigation message symbols.

Keywords—signal distortion; waveform separation; navigation message; GNSS

I. INTRODUCTION

With the modernization of GPS and GLONASS, and the development of emerging Galileo and BeiDou system (BDS), the structure of GNSS signals is becoming more and more complex. On one hand, each service signal includes a data component and a pilot component. Therefore, there are usually 3~4 signal components needing to be transmitted at a frequency. For example, three signal components, E1B, E1C and E1A, are transmitted at Galileo E1 frequency^[1]. On the other hand, in order to maximize the high power amplifier, new constant envelope multiplexing methods, like interplex^[2], CASM^[3] and POCET^[4], are applied for GNSS signals, which make the time-domain waveform more complex. Interplex is suggested for multiplexing the Galileo E1 signal^[5].

More service signal means higher spectrum utilization efficiency and better service performance. Nevertheless, it is also more difficult to analyze the time-domain of single signal components. The time-domain waveform of signal component can characterize the signal quality, waveform anomaly, and signal distortion^{[6]-[7]}. In addition, unknown modulation type of GNSS signal can be analyzed through the time-domain baseband waveform^[8]. More importantly, the time-domain waveform can be used to evaluate the channel characteristic of satellite payload. The amplitude-frequency characteristic and group delay characteristic can be analyzed based on time-domain waveform^{[9]-[10]}. The key of these applications mentioned above is to separate the baseband waveform from the constant envelope composite signal.

The basic of waveform separation is the periodic of PRN code and the randomness of navigation message or secondary

code. The civil open signal usually uses the short PRN code length. The period of primary code is usually 1ms, 4ms and 10ms. When the navigation message (data component) or secondary code (pilot component) is completely random, the baseband waveform can be separated by accumulation of multiple primary periods. In order to obtain acceptable results, signal is usually received by high gain antenna^[11]. In the actual situation, the complete randomness cannot be satisfied. Thus, the separated waveform has residual error due to other signal component, which would lead to the degradation of precision.

In this paper, we propose two methods to improve the precision of waveform separation. In the first way, the baseband waveforms of different short code signal components are obtained following traditional method. Then the influence of other signal components is reduced according to the correlation of their navigation message. In the second way, different periods of primary code are grouping accumulated according to the values of navigation message. The resulting baseband waveform is the weighted sum of those accumulation results. The remaining parts are organized as follow: Section II presents the signal model, and discusses the problem of traditional method. Section III introduces these two waveform separation methods. Section IV analyzes the performance of the above methods. Conclusions are summarized in section V.

II. SIGNAL MODEL AND PROBLEM FORMULATION

A. Signal Model

The modernized GNSS signals are usually combined into a constant envelope composite signal. The single frequency constant envelope composite signal can be expressed as^{[12]-[13]}:

$$s(t) = \sum_{n=1}^N A_n e^{j\theta_n} s_n(t) + IM(t) \quad (1)$$

where N is the total number of signal components. $s_n(t)$ denotes the n th signal component. A_n and θ_n represent the amplitude and phase of $s_n(t)$. $IM(t)$ denotes all the inter-modulation signal terms, which are used to keep the envelope constant. Generally speaking, the total power of inter-modulation terms is much less than that of useful signal components. Therefore, we can neglect the impact of $IM(t)$ in the latter analysis.

For civil signal, $s_n(t)$ has the following unified expression, i.e.

This work is supported by the National Natural Science Foundation of China (NSFC), Grant 61627817.

$$\begin{aligned}
 s_n(t) &= d(t)c(t)sc(t) \\
 &= \sum_{m=0}^{M-1} d_{n,m} \sum_{i=0}^{L_n-1} c_{n,i} p_n(t-iT_{n,c}-mL_nT_{n,c}) \\
 &= \sum_{m=0}^{M-1} d_{n,m} s_{base,n}(t-mL_nT_{n,c})
 \end{aligned} \quad (2)$$

where $d(t)$ is the navigation message or secondary code, $c(t)$ is the PRN code waveform, $sc(t)$ is the subcarrier. $d_{n,m} \in \{1, -1\}$ is the message symbol of the n th signal component during the m th primary code period. $\{c_{n,i}\} \in \{1, -1\}$ is the PRN code sequence of the n th signal component with length L_n . $T_{n,c}$ is the chip duration of the n th signal component. Note that the duration of one message is assumed to one primary code period. $p_n(t)$ denotes the modulated symbol, which is the rectangle function for BPSK modulated signal. $s_{base,n}(t)$ is the baseband waveform of the n th signal component during one code period, which is expressed as

$$s_{base,n}(t) = \sum_{i=0}^{L_n-1} c_{n,i} p_n(t-iT_{n,c}) \quad (3)$$

The purpose of waveform separation is to recover $s_{base,n}(t)$ from $s(t)$.

B. Problem Formulation

To recover $s_{base,n}(t)$, θ_n and $\{d_{n,m}\}$ are firstly obtained by correlation operation. The m th code period of $s(t)$ is given by

$$s^m(t) = \begin{cases} s(t) \approx \sum_{n=1}^N A_n e^{j\theta_n} s_n(t), & mT_n \leq t < (m+1)T_n \\ 0, & \text{otherwise} \end{cases} \quad (4)$$

where $m=0, 1, 2, \dots, M-1$. Based on traditional method, the estimation of $s_{base,n}(t)$ is calculated by

$$\begin{aligned}
 \tilde{s}_{base,n}(t) &= \frac{1}{M} e^{-j\theta_n} \sum_{m=0}^{M-1} d_{n,m} s^m(t) \\
 &= A_n s_{base,n}(t) + \sum_{p=1, p \neq n}^N \frac{1}{M} \sum_{m=0}^{M-1} d_{n,m} d_{p,m} \cdot A_p e^{j(\theta_p - \theta_n)} s_{base,p}(t)
 \end{aligned} \quad (5)$$

where $R_{n,p} = \frac{1}{M} \sum_{m=0}^{M-1} d_{n,m} d_{p,m}$ is the correlation value of navigation messages between the n th and p th signal component.

When these messages are completely random, we have $R_{n,p} = 0$. Then we can derive out that $\tilde{s}_{base,n}(t) = A_n s_{base,n}(t)$. Thus, $\tilde{s}_{base,n}(t)$ can be seen as the recovery baseband waveform of the n th signal components. However, these messages are not random. Equation (5) should be rewritten as

$$\begin{aligned}
 \tilde{s}_{base,n}(t) &= \text{Re} \left\{ \frac{1}{M} e^{-j\theta_n} \sum_{m=0}^{M-1} d_{n,m} s^m(t) \right\} \\
 &= A_n s_{base,n}(t) + \text{Re} \left\{ \sum_{p=1, p \neq n}^N R_{n,p} \cdot A_p e^{j(\theta_p - \theta_n)} s_{base,p}(t) \right\}
 \end{aligned} \quad (6)$$

Obviously, other signal components have an impact on the waveform of the n th signal component. Especially, when $\theta_p = \theta_n$, the impact is critical.

III. WAVEFORM SEPARATION METHODS

In order to improve the precision of waveform separation, we have to eliminate the impact of other signal components. In this section, we introduce two high precision separation methods.

A. Method One

The first method removes directly the influence of other signal components from $\tilde{s}_{base,n}(t)$. To explain the principle, we consider the case of two signal components. The two signal components are in-phase. The m th code period of $s(t)$ is given by

$$s^m(t) = A_1 d_{1,m} s_1(t) + A_2 d_{2,m} s_2(t), mT_n \leq t < (m+1)T_n \quad (7)$$

According to the traditional separation method, we can obtain

$$\begin{cases} \tilde{s}_{base,1}(t) = A_1 s_{base,1}(t) + A_2 R_{1,2} s_{base,2}(t) \\ \tilde{s}_{base,2}(t) = A_1 R_{2,1} s_{base,1}(t) + A_2 s_{base,2}(t) \end{cases} \quad (8)$$

where $R_{2,1} = R_{1,2}$. Solving the equations (8), we have

$$\begin{aligned}
 A_1 s_{base,1}(t) &= \frac{\tilde{s}_{base,1}(t) - \tilde{s}_{base,2}(t) R_{1,2}}{1 - R_{2,1} R_{1,2}} \\
 A_2 s_{base,2}(t) &= \frac{\tilde{s}_{base,2}(t) - R_{1,2} \tilde{s}_{base,1}(t)}{1 - R_{1,2} R_{2,1}}
 \end{aligned} \quad (9)$$

$s_{base,1}(t)$ and $s_{base,2}(t)$ are the baseband waveforms of the 1th and 2th signal components, respectively.

When there are N short code signal components, we can obtain similar equations as follow:

$$\begin{cases} \tilde{s}_{base,1}(t) = A_1 s_{base,1}(t) + \sum_{p=2}^N R_{1,p} A_p e^{j(\theta_p - \theta_1)} s_{base,p}(t) \\ \tilde{s}_{base,2}(t) = A_2 s_{base,2}(t) + \sum_{p=1, p \neq 2}^N R_{2,p} A_p e^{j(\theta_p - \theta_2)} s_{base,p}(t) \\ \vdots \\ \tilde{s}_{base,N}(t) = A_N s_{base,N}(t) + \sum_{p=1}^{N-1} R_{N,p} A_p e^{j(\theta_p - \theta_N)} s_{base,p}(t) \end{cases} \quad (10)$$

The baseband waveforms of N signal components can be obtained by solving the equations (10).

B. Method Two

The second method is to accumulate multiple code periods according the combination of message symbols. The resulting baseband waveform is the weighted sum of multiple groups of accumulations.

We still consider two signal components. Without loss of generality, we try to separate the baseband waveform of the 1th signal component. Both of $d_{1,m}$ and $d_{2,m}$ have two possible values. Thus, the combination of $[d_{1,m} \ d_{2,m}]$ have four possible values. Define binary number $\mathbf{v} = (1 - [d_{1,m} \ d_{2,m}]) / 2$. $\mathbf{v} \in \{0, 1, 2, 3\}$.

Assume that there are M_0 period to satisfy $\mathbf{v} = 0$, i.e. $d_{1,m} = 1$ and $d_{2,m} = 1$. The accumulation result of the M_0 period is expressed as

$$s_{\Sigma, \mathbf{v}=0}(t) = 1 \cdot \sum_{m=1}^{M_0} s^m(t) = M_0 (A_1 s_{base,1}(t) + A_2 s_{base,2}(t)) \quad (11)$$

There are M_1 period to satisfy $\mathbf{v} = 1$, i.e. $d_{1,m} = 1$ and $d_{2,m} = -1$. The accumulation result of the M_1 period is expressed as

$$s_{\Sigma, \mathbf{v}=1}(t) = 1 \cdot \sum_{m=1}^{M_1} s^m(t) = M_0 (A_1 s_{base,1}(t) - A_2 s_{base,2}(t)) \quad (12)$$

There are M_2 period to satisfy $\mathbf{v} = 2$, i.e. $d_{1,m} = -1$ and $d_{2,m} = 1$. The accumulation result of the M_2 period is expressed as

$$s_{\Sigma, \mathbf{v}=2}(t) = -1 \cdot \sum_{m=1}^{M_1} s^m(t) = M_0 (A_1 s_{base,1}(t) - A_2 s_{base,2}(t)) \quad (13)$$

There are M_3 period to satisfy $\mathbf{v} = 3$, i.e. $d_{1,m} = -1$ and $d_{2,m} = -1$. The accumulation result of the M_3 period is expressed as

$$s_{\Sigma, \mathbf{v}=3}(t) = -1 \cdot \sum_{m=1}^{M_1} s^m(t) = M_0 (A_1 s_{base,1}(t) + A_2 s_{base,2}(t)) \quad (14)$$

Obviously, $\sum_{i=0}^3 M_i = M$. The resulting baseband waveform of the 1th signal components is

$$\bar{s}_{base,1}(t) = \sum_{i=0}^3 \frac{1}{2^N} s_{\Sigma, \mathbf{v}=i}(t) = A_1 s_{base,1}(t) \quad (15)$$

For N signal components, there are 2^N possible combinations of message. According to the value of $\mathbf{v} = (1 - [d_{1,m} \ d_{2,m} \ \dots \ d_{N,m}]) / 2$, we can obtain 2^N accumulation results, i.e.

$$s_{\Sigma, \mathbf{v}=i}(t) = M_i \left(A_1 s_{base,1}(t) + \sum_{p=2}^N d_{1,i} d_{p,i} A_p e^{j(\theta_p - \theta_1)} s_{base,p}(t) \right) \quad (16)$$

where $i=0 \sim 2^N-1$. $d_{1,i}$ and $d_{p,i}$ are the message symbols of the 1th and p th when $\mathbf{v} = i$. The resulting baseband waveform of the 1th signal components is

$$\bar{s}_{base,1}(t) = \sum_{i=0}^{2^N-1} \frac{1}{2^N} s_{\Sigma, \mathbf{v}=i}(t) = A_1 s_{base,1}(t) \quad (17)$$

For practical application, only the real part is needed, i.e.

$$\bar{s}_{base,1}(t) = \text{Re} \left(\sum_{i=0}^{2^N-1} \frac{1}{2^N} s_{\Sigma, \mathbf{v}=i}(t) \right).$$

IV. PERFORMANCE ANALYSIS

In this section, we analyze the performance of traditional method and the proposed methods. Considering that there are two in-phase signal components. Both of them are BOC(1,1) modulated signals. The example is a simplified model of GPS L1C signal and Galileo E1OS signal, which neglects the BOC(6,1) components. The signal bandwidth is $\pm 8.184\text{MHz}$. The sampling rate is 600MHz . In the thermal noise environment, the carrier-to-noise-density ratio (C/N_0) is used. The message symbols of two signal components are random, and satisfy the designed correlation value $R_{1,2}$.

Fig. 1 shows the time-domain characterization of ideal BOC(1,1) signal. Fig. 1(a) is the time-domain waveform. Fig. 1(b) is the eye diagram. Fig. 1(c) is the modulation constellation. In order to evaluate the performance of waveform separation method, we use the jitter of chip drop edge (1σ). For ideal BOC(1,1) signal, the jitter is $\sigma_{ideal} = 2.588\text{ns}$, which is introduced by the finite sampling rate and band-limitation.

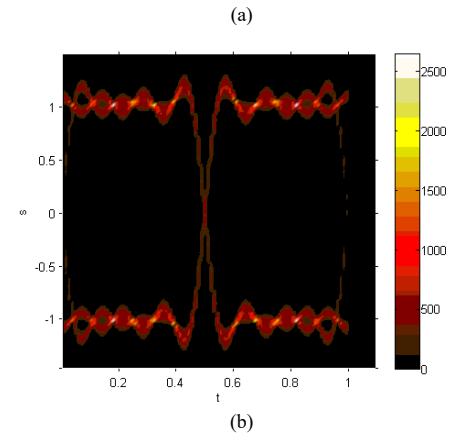
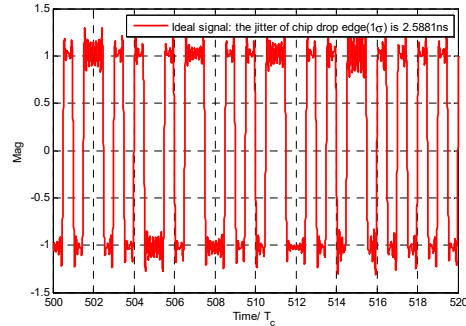
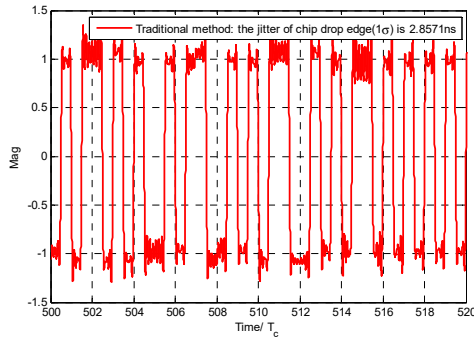
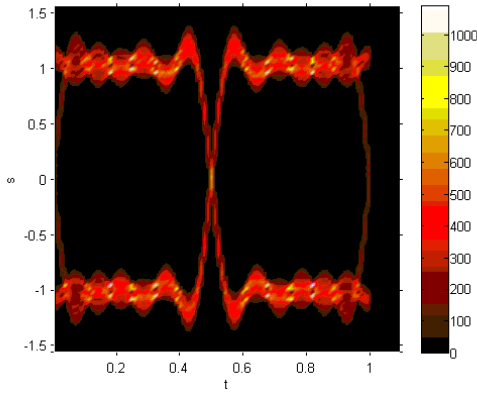


Fig. 1. The time-domain characterization of ideal BOC signal. (a) Baseband waveform. (b) Eye diagram.

Fig. 2, Fig 3, and Fig 4 show the time-domain characterizations of baseband waveforms using traditional method, the proposed methods one and proposed method two, respectively. Their jitters are $\sigma_{Tra} = 2.8571\text{ns}$, $\sigma_{one} = 2.6670\text{ns}$ and $\sigma_{two} = 2.6679\text{ns}$. The code period number is $M=1000$. The correlation value of message symbols is $R_{1,2}=0.05$. $C/N_0=80\text{dB-Hz}$. The analysis error of traditional method is $error_{Tra} = \sqrt{\sigma_{Tra}^2 - \sigma_{ideal}^2} = 1.2103\text{ns}$. The analysis error of the proposed method one is $error_{one} = \sqrt{\sigma_{one}^2 - \sigma_{ideal}^2} = 0.6439\text{ns}$. The analysis error of the proposed method two is $error_{two} = \sqrt{\sigma_{two}^2 - \sigma_{ideal}^2} = 0.6476\text{ns}$. Obviously, the precision of the proposed method is higher than that of traditional method. Moreover, the eye diagram of baseband waveform obtained by traditional method is blurring.

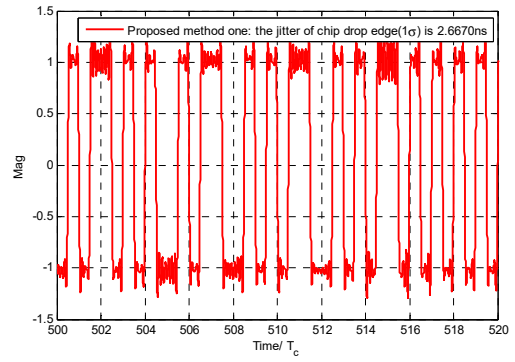


(a)

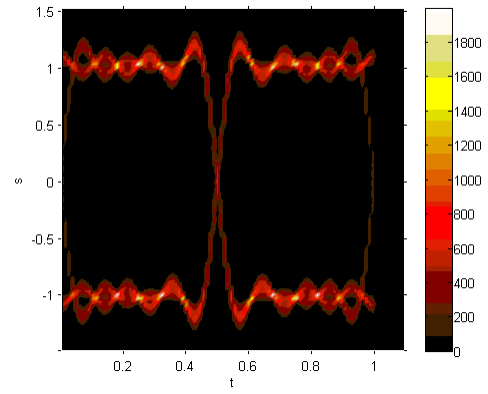


(b)

Fig. 2. The time-domain characterization of baseband waveform separated by traditional method. (a) Baseband waveform. (b) Eye diagram.

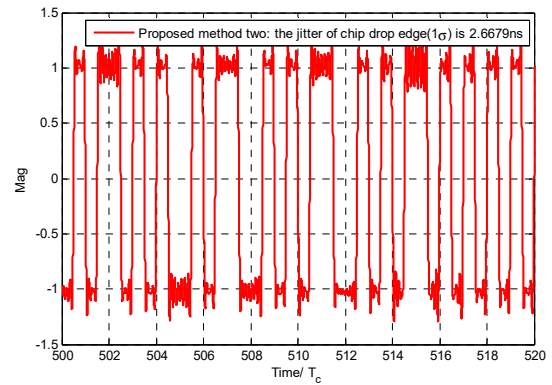


(a)



(b)

Fig. 3. The time-domain characterization of baseband waveform separated by proposed method one. (a) Baseband waveform. (b) Eye diagram.



(a)

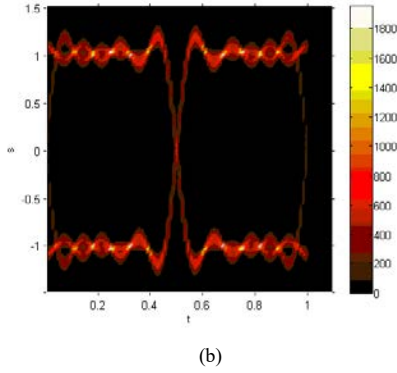


Fig. 4. The time-domain characterization of baseband waveform separated by proposed method two. (a) Baseband waveform. (b) Eye diagram.

To further assess the performance of waveform separation methods, let $M=1000$, $C/N_0=80\text{dB-Hz}$, we can obtain the jitter in different values of $R_{1,2}$, as shown in Fig. 5. It can be observed that the analysis error become larger with the increase of correlation values $R_{1,2}$. On the contrary, the analysis precision of the proposed methods is almost unchanged with correlation values $R_{1,2}$.

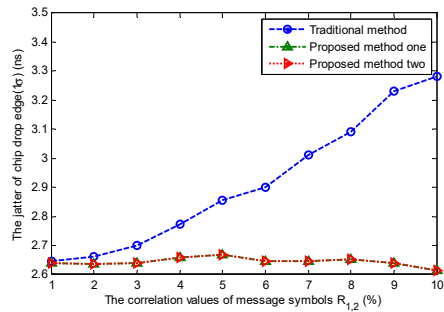


Fig. 5. The jitter of chip drop edge versus $R_{1,2}$

Fig. 6 shows that jitter of chip drop edge in different code period number. $C/N_0=80\text{dB-Hz}$. The correlation value of message $R_{1,2}=0.1$. We can see that the precision of the proposed methods is obviously higher than that of traditional method.

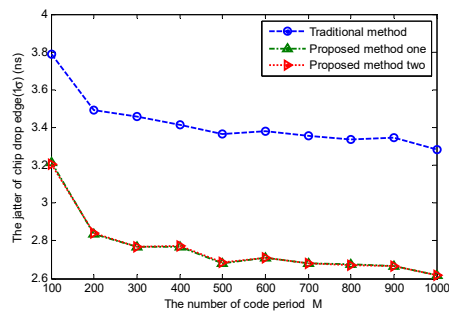


Fig. 6. The jitter of chip drop edge versus M

V. CONCLUSIONS

The separation of baseband waveform is helpful for analyzing the signal quality and waveform anomaly for GNSS signals. The analysis precision of tradition waveform separation is limited due to the interfere from other signal components. In this paper, we propose two separation methods of baseband waveform for GNSS signals. The proposed methods can remove the influence of other signal components. Thus, our methods can provide high analysis precision. The simulation results verify the correctness and effectiveness of the proposed methods. Compared with the traditional method, the proposed methods have no special requirements on the randomness of navigation message.

REFERENCES

- [1] Galileo Open Service Signal In Space Interface Control Document (2016), OS SIS ICD, Issue 1.3.
- [2] S. Butman, U. Timor. Interplex-An Efficient Multichannel PSK/PM Telemetry System. IEEE Transaction on Communications, 1972, 20(3), 415-419.
- [3] P.A. Dafesh, T.M. Nguyen, S. Lazar. Coherent Adaptive Subcarrier Modulation (CASM) for GPS Modernization. ION NTM 1999, 649-660.
- [4] P.A. Dafesh, C.R. Cahn. Phase-Optimized Constant-Envelope Transmission (POCET) Modulation Method for GNSS Signals. ION GNSS 2009, 2860 - 2866.
- [5] G.W. Hein, J.A. Avila-Rodriguez, L. Ries, L. Lestarquit, J.L. Issler, J. Godet, T. Pratt. A candidate for the Galileo L1 OS optimized signal. Proceedings of the 18th International Technical Meeting of the Satellite Division (ION GNSS 2005), Long Beach, CA, September, 2005, 833-845.
- [6] S. Thoelet, M. Vergara, M. Sgammini, C. Enneking, F. Antreich. Characterization of Nominal Signal Distortions and Impact on Receiver Performance for GPS (IIF) L5 and Galileo (IOV) E1 /E5a Signals. Proceeding of 27th International Technical Meeting of the ION Satellite Division, ION GNSS+ 2014, Tampa, Florida, September, 2014, 3113-3128.
- [7] J.B. Pagot, P. Thevenon, O. Julien. Threat Model Design for new GNSS signals. Proceeding of the 2016 International Technical Meeting, ION ITM 2016, Monterey, California, January, 2016, 970-982.
- [8] Bavaro M, Curran J, Fortuny J. First Signals of BeiDou Phase 3 Acquired at Ispra, Italy . GPS World, 2015, <http://gpsworld.com/first-signals-of-beidou-phase-3-acquired-at-ispra-italy/>.
- [9] G. Sebastian, G. Christoph. Analysis of GIOVE-A L1-Signals. ION GNSS 19th International Technical Meeting of the Satellite Division, 26-29 Sept.2006, Fort Worth, TX.
- [10] S. Thoelet, M. Vergara, M. Sgammini, C. Enneking, F. Antreich. Characterization of Nominal Signal Distortions and Impact on Receiver Performance for GPS (IIF) L5 and Galileo (IOV) E1 /E5a Signals. ION GNSS+ 2014, 3113-3128.
- [11] J.R.I. Christie, P.B. Bentley. GPS signal quality monitoring system. ION GNSS 17th International Technical Meeting of the Satellite Division 2004. USA: Sun Diego, 2004. 9: 21-24.
- [12] T. Yan, Z. Tang, J. Wei, B. Qu, Z. Zhou. A Quasi-constant Envelope Multiplexing Technique for GNSS Signals [J]. Journal of Navigation, 2015, 68(4): 791-808.
- [13] K. Zhang, Y. Li, H. Zhou, F.Wang. Analytical Transmission Model of POCET Technique for Compass B1 and B3 Signals. Proceedings of the 25th International Technical Meeting of the Satellite Division of The Institute of Navigation , Nashville, 2012, TN 277-285.

GNSS signals simulation to assess the immunity of navigation equipment with spatial interference cancellation

A.Kaverin, V.Logutov, S.Chernov

FSUE VNIIFTRI, Russian Federation, a_kaverin@vniifttri.ru

Summary

The abstract presents the results of GNSS signals simulation system development. The system allows to form a spatial field of GNSS and interference signals.

Motivation

One of the effective ways to improve the interference immunity of GNSS-receivers is a spatial signal processing, realized by antenna interference canceller.

Therefore, you must fulfill the following conditions for assessing the characteristics of the interference immunity of such systems:

- distribute in space signals of navigation spacecraft and interference signals;
- ensure the availability required amount of interference at the antenna interference canceller;
- parameters of navigation and interfering signals must be known with sufficient accuracy.

Field tests with such conditions are very difficult. Therefore, appropriate to apply the GNSS signals simulation in anechoic environment (fig. 1), that allows:

- to minimize reflections of radiowaves;
- to form a spatial navigation field of GNSS signals and interference signals;
- to simulate the movement of the vehicle, including changes of orientation.

Results

This approach has several features. Firstly, the work area in the anechoic chamber is determined by the size and characteristics of the chamber. Second, duration of navigation signals reproduction depends on the dynamics of the modeled object. Thirdly, it is necessary to calibrate the time delay of navigation signals and their power levels with regard to their radiation in the anechoic chamber. It is possible to achieve accuracy of coordinates simulation at a level of 0.5-1.5 meters after calibration (fig. 2).

As a result, it is possible to do GNSS signals simulation to assess the noise-immunity of a GNSS-receivers with high accuracy.

Figures

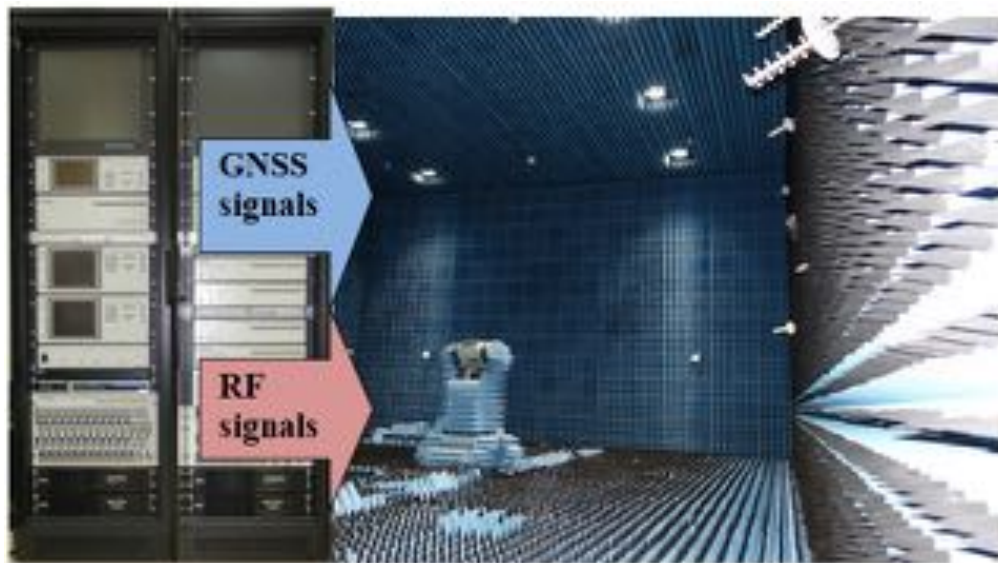


Fig. 1: Composition of equipment used for simulation.



Fig. 2: Results of measurements of coordinates after equipment calibration.

GNSS performance monitoring platform

Pierre Casenove, Jean Maréchal, Norbert Suard

DSO/NT/SPG, CNES, Toulouse, France, pierre.casenove@cnes.fr

DSO/NT/SPG, CNES, Toulouse, France, jean.marechal@cnes.fr

DSO/NT/SN, CNES, Toulouse, France, norber.suard@cnes.fr

Summary

The Navigation and Time Monitoring Facility (NTMF) is a platform designed to monitor the performance of SBAS and GNSS systems in order to support CNES and French government decisions as well as the ESA and GSA in EU programs management. It is currently monitoring all operational SBAS and GPS, GLONASS and GALILEO constellations. All high level standard Key Performance Indicators (KPIs) and specific detailed KPIs are monitored a posteriori, on a daily automated basis, using tools independent from the system operators. Thanks to NTMF platform CNES is able to publish on a daily basis consolidated RINEX files for each SBAS and for GPS and Galileo constellation, daily results for each monitored system and monthly synthesis for the main KPIs.

NTMF platform could also contribute to the UNOOSA-ICG IGMA project.

The paper will present the detailed architecture of the platform, the monitored KPIs for both SBAS and GNSS constellations, some of the results obtained and finally the data dissemination of our products. The planned evolutions of the platform will also be presented, in views of future GNSS services.

Motivation

NTMF platform has been developed in order to ensure independent performance assessment of all SBAS and GNSS systems in operation. The results are analyzed by CNES GNSS experts and performance reports are produced on a quarterly basis for French needs, in particular for the civil aviation and the follow up of European GNSS programs.

Platform results are also used to support two contracts established with the GSA, one to monitor EGNOS performance (SPMS) and the second to monitor Galileo (GRC-MS).

Results

SBAS services performance is monitored through the 4 main criteria (accuracy, integrity, availability and continuity) by the platform. Time service information provided by these systems is also assessed. Accuracy and availability of GNSS constellations are also monitored for open services. Finally, ICD compliance is assessed for GPS, SBAS and Galileo.

The platform is in charge of data acquisition and consolidation, performance tool automation and results publication through public and private FTP and web servers. It is composed of 22 servers receiving work orders and 3 workstations. Six different tools are used to assess the different KPI, along with CNES dedicated scripts to extract key values and sum up them in monthly synthesis. A total of one thousand treatments are executed each night by the platform to provide all results.

Based on the daily results obtained, it is possible to launch longer-term treatments and assess performance over long periods. As an example, the EGNOS LPV200 service availability and continuity throughout a 9-month period will be presented and compared to EGNOS operator SDD declaration (see Fig. 1 and Fig. 2).

The daily processing allows also analyzing specific events, like the ionosphere perturbation from the 6th to 8th September 2017 (Fig.3).

Figures

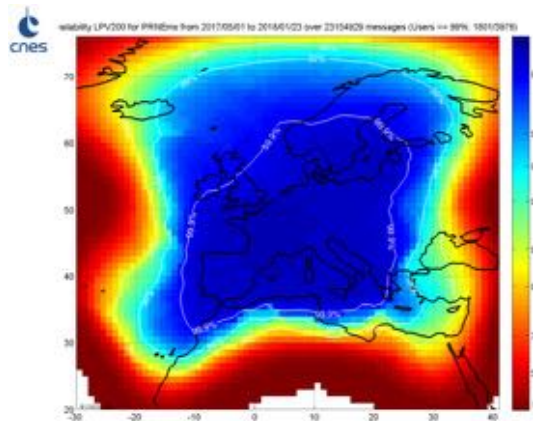


Fig. 1: EGNOS LPV200 continuity from 05/01/17 to 01/23/18 compared to SDD commitment.

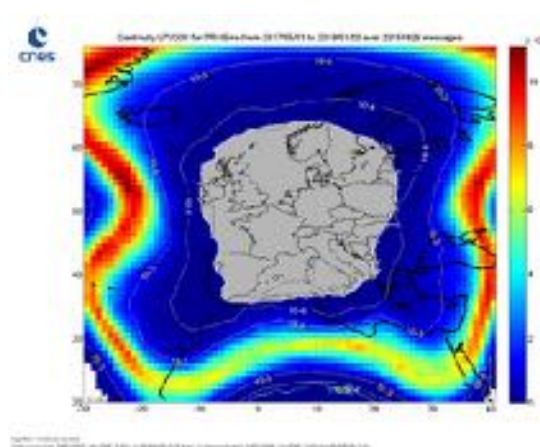


Fig. 2: EGNOS LPV200 continuity from 05/01/17 to 01/23/18 compared to SDD commitment.

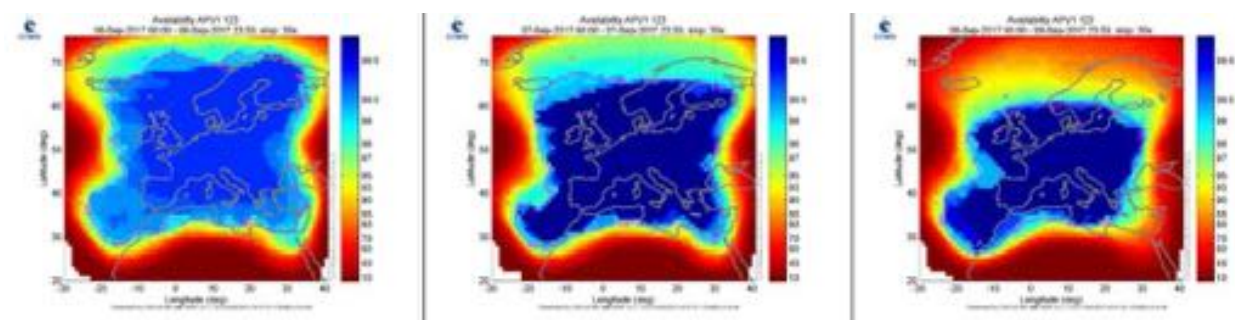


Fig. 3: September 2017 ionospheric event of Egnos APV1 service availability.

GNSS-based Earth's Center of Mass motion observation

Delong N., Couhert A.⁺, Mercier F.⁺

Orbit Determination Department, CNES, Toulouse, France, nicolas.delong@cnes.fr

⁺Orbit Determination Department, CNES, Toulouse, France

Summary

This paper shows a new approach to determine the network Center of Figure (CF) motion relative to the Earth Center of Mass (CM) (usually known as geocenter motion) using the IGS GNSS satellite constellation solutions and a LEO satellite. First, a theoretical analysis exhibits the effect of a CF variation on the constellation clocks solution, without changing the ephemeris. A GNSS satellite clock correction model is thus proposed. This model is validated using real GNSS data (GPS and Galileo). Second, the derived model is used to adjust the corresponding CM-CF correction in the Jason2 LEO GPS Precise Orbit Determination (POD for altimetry). Finally, the identified geocenter motion is compared against independent (DORIS and SLR) estimates.

Motivation

Geocenter correction models are usually derived from SLR measurements, and can be used to define DORIS and SLR station positions. This is not the case for GNSS satellite IGS solutions¹. Seasonal differences, especially along the Z (North-South) axis are observed between GPS-based and DORIS+SLR-based orbits². These 4-mm Z annual variations affect Mean Sea level observations³.

The aim of this study is to appraise the phenomenon and propose a solution to take it into account in LEO GPS orbits.

Results

The theoretical analysis describes the influence of a Centre of Figure (CF) variation on the GNSS constellation clock estimates. The constellation orbits are defined in the Centre of Mass (CM). The geocenter motion is usually defined by the vector CF-CM. The impact is assessed for the ideal case of a perfectly homogenous distribution of the ground network stations. A clock correction model, which can be used for any GNSS constellation, is proposed. This model is validated for two different constellations, GPS and Galileo. Preliminary results can be seen on Figure 1.

This formulation is then applied to solve for the geocenter motion using Jason2 POD, (10-day arcs of GPS measurements), from 2008 to 2017. A seasonal model of geocenter variations is then derived, and compared to independent models, with a good consistency as seen from Figure 2.

Finally, the effect on Jason 2 precise orbits is gauged, showing that the annual Z differences between GPS-based and DORIS-only orbits is reduced from ~4 mm to the 1 mm level.

As a conclusion, this study shows a way to get consistent orbits regardless of the tracking system used.

¹ Rebischung, "Can GNSS contribute to improving the ITRF definition ?", PhD thesis, Observatoire de Paris, June 2014

² Couhert et al, "Long-term Analysis of Possible Remaining Sources of Orbit Error", OSTST Meeting 2014, Lake Constance, Germany

³ Morel and Willis "Terrestrial reference frame effects on global sea level rise determination from TOPEX/Poseidon altimetric data", Advances in Space Research, Volume 36, Issue 3, 2005, Pages 358-368

Figures

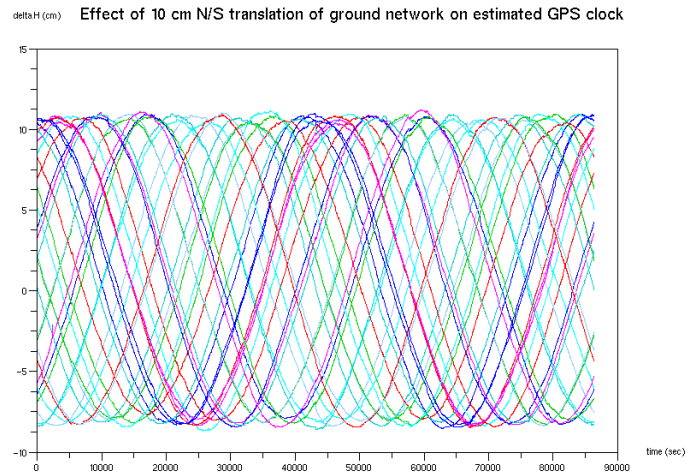


Fig. 1: Effect of 10 cm North/South translation of ground network on estimated GPS satellite clocks

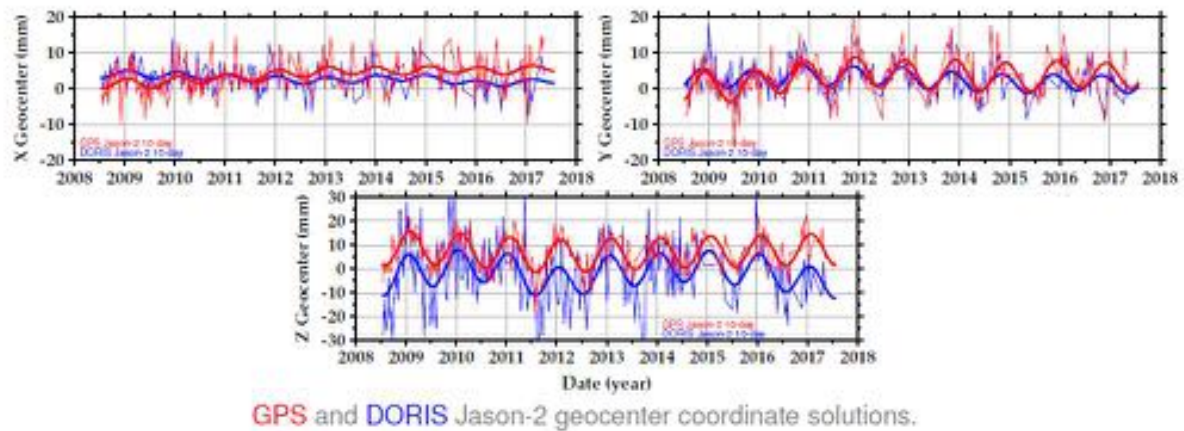


Fig. 2: CM correction estimation and the derived model from GPS (red) and from DORIS (blue)

Small UAV's Attitude Estimation with Tightly Coupled Low-cost GNSS/INS Integration using Multiple GNSS Receivers

Marton Farkas⁺, Szabolcs Rozsa^{*}, Balint Vanek[°]

⁺Hungarian Academy of Sciences Institute for Computer Science
and Control, Budapest, 1111, Hungary, farkas.marton@sztaki.mta.hu

^{*}Department of Geodesy and Surveying, Faculty of Civil Engineering,
Budapest University of Technology and Economics, Budapest, 1111, Hungary

[°]Hungarian Academy of Sciences Institute for Computer Science
and Control, Budapest, 1111, Hungary

Summary

The attitude estimation at UAV field is based commonly on MEMS IMU sensors. The inertial measurement units (IMU) provide data necessary to all navigation tasks, but the drift error of the gyroscope and the accelerometer sensors decrease the reliability of these measurements, particularly when low-cost devices are used in the flight control systems. Thus it would be advantageous to enhance the attitude determination with an independent technique, such as the global navigation satellite systems. Real Time Kinematic (RTK) technique is well known in surveying and commercial positioning, too. The presented attitude determination method uses not only GPS but Glonass and Galileo measurements. Due to the high flight dynamics of UAVs, the multi-constellation solution is more advantageous than the single constellation solution. From the technical point of view, it is interesting to examine how these several satellite constellation's data can be integrated with inertial sensor measurements to estimate the attitude angles, sensor biases and integer ambiguities. The other focus of this research is the study how the tightly coupled inputs affect the performance of the constrained integer ambiguity resolution method. The applicability of this fusion technique is studied and tested in the low-cost UAV environment to ensure the broadest application field possible.

Motivation

There are several IMU based solutions using Euler angle¹ estimation or Quaternion², and the GNSS based attitude estimation is getting more widespread³. A paper was submitted by us about the attitude estimation of UAVs using only GNSS measurements⁴. The presented Tightly Coupled Extended Kalman Filter based attitude estimation method determinates the Euler angles of the UAV using accelerometer, gyroscope, magnetometer and single baseline, single frequency GNSS code and phase measurements. The used UAV and the mounted sensors are shown at Fig. 1.

Results

The first results show, that the multi-GNSS attitude determination algorithm provided the attitude angles with the accuracy of 1-5 degrees compared to the independent IMU solution, that means that the accuracy of the GNSS attitude angles are comparable to the accuracy of the attitude angles obtained from the IMU. Moreover it was also confirmed, that the availability of GNSS attitude estimation strongly depends on the

¹ LI, Wei; WANG, Jinling. Effective adaptive Kalman filter for MEMS-IMU/magnetometers integrated attitude and heading reference systems. *The Journal of Navigation*, 2013, 66.1: 99-113.

² SABATINI, Angelo M. Quaternion-based extended Kalman filter for determining orientation by inertial and magnetic sensing. *IEEE Transactions on Biomedical Engineering*, 2006, 53.7: 1346-1356.

³ GIORGI, Gabriele; TEUNISSEN, Peter JG. Carrier phase GNSS attitude determination with the multivariate constrained LAMBDA method. In: *Aerospace Conference, 2010 IEEE*. IEEE, 2010. p. 1-12.

⁴ FARKAS, Marton; ROZSA, Szabolcs; VANEK Balint. Multi-GNSS attitude estimation of UAVs during landing. *International Association of Geodesy Symposia*, submitted on 29 October 2017. With Editor.

flight dynamics, which is usually much higher in case of UAVs compared to commercial aircrafts (see Fig. 2 and Fig. 3).

Figures



Fig. 1: UAV with the mounted GNSS sensors.

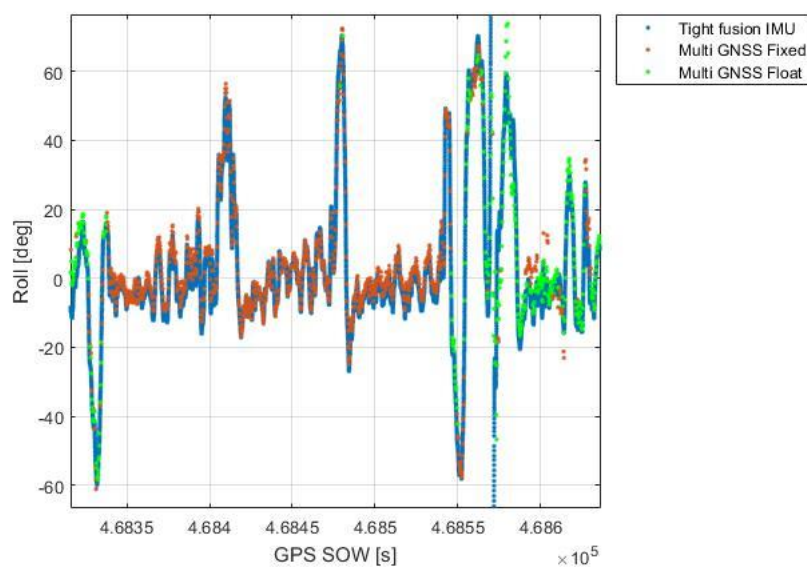


Fig. 2: UAV test roll angle results in degree.

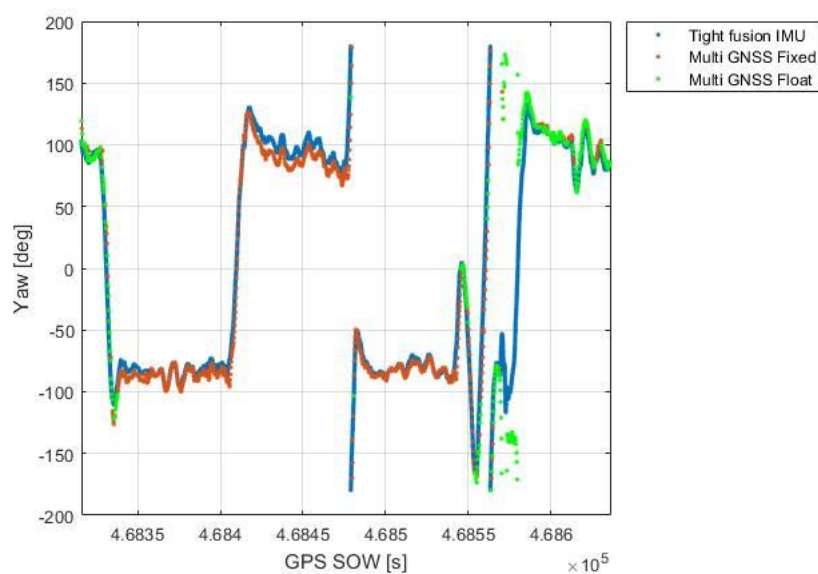


Fig. 3: UAV test yaw angle results in degree.

Enhancing Robot Navigation using Sensor Fusion and Fuzzy Kalman Filter for Obstacle Avoidance

Amin Bassiri, Azad University
Qazvin, Tehran, Iran
amin.bassiri@gmail.com

Mohammadreza Asghari Oskoei
Allameh Tabataba'i University, Tehran,
Iran, oskoei@atu.ac.ir,

Research Fellow, University of Essex,
(UK) masgha@essex.ac.uk

Anahid Basiri, Centre for
Advanced Spatial Analysis,
University College London,
London, UK, a.basiri@ucl.ac.uk

Abstract—With the developments and popularity of autonomous systems such as mobile robots, obstacle avoidance has become more and more important as it is one of the most important safety features of autonomous navigation. The moving objects, e.g. Autonomous Mobile Robots, are assumed safe and controllable, particularly in dense urban areas, as long as they do not hit anything. This paper proposes and implements a multisensory system based on an enhanced Fuzzy Kalman Filtering for robot navigation, for the purpose of accurate and smooth obstacle avoidance. Several sensors, including Ultrasound (US) and laser sensors are embedded in an autonomous robot agent and the results of the proposed system show a significant improvement in the smoothness of the manoeuvres and also the accuracy of the obstacle avoidance.

Keywords—robot navigation; ultraSonic; landmarks; obstacle avoidance.

I. INTRODUCTION

Autonomous cars, autonomous mobile robots, drones and several other systems, which have the authority and autonomy to move, are now about to release or already commercialized and in the market. Despite the popularity and the wide range of applications that they can be applied for, the main concern of both users and the system developers, i.e. safety, has not yet been fully addressed (Aras et al., 2016). This is perhaps the main reason that the autonomous cars and autonomous mobile robots have faced several safety, liability, and even legal challenges to be commercialised and used.

One of the key safety features of such autonomous systems is the obstacle avoidance (Zaki et al. 2014), (Cherubini and Chaumette, 2013). It is commonly agreed that autonomous mobile robots and drones are controllable and safe as long as they don't hit anything. For the time being, in order to meet the safety targets in the urban areas, autonomous robots are navigated through the maximum controllable height to minimise any risk of hitting urban features and objects on the way (Montiel et al., 2014). However, this may come at other costs, such as higher power cost and also compromising the performance, and full-functionality age of the device. Therefore the system should ideally recognise, plan and avoid the obstacles at a high accuracy level and in a very smooth

manoeuvre. This paper focuses on the detection and avoidance of obstacles.

This paper proposes and implements a multi-sensor navigation system enhanced by Fuzzy Kalman Filtering (FKF). The proposed system uses ultrasonic and laser sensors and is implemented and tested on a robot in a test lab with an unstructured interior obstacles distributed. The results of the test show a significant improvement in the smoothness and the accuracy of the both manoeuvre and the obstacle avoidance.

This paper is structured as follow; in the second section the Fuzzy Kalman Filtering, used by the proposed system, is explained. Then in the third section, the implemented multi-sensor robot navigation and the experiment results are examined. Finally section three the conclusion and future work are discussed.

II. FUZZY KALMAN FILTERING

A. Kalman Filtering

Kalman filter (KF) is a predictor corrector method (Julier and Uhlmann, 1997). Kalman Filtering process is basically has got five main stages, as shown in Figure 1 (Karambakhsh et al. 2011). In the first step the Kalman gain is calculated based on priori or an initial condition as the input. This gain is then used in conjunction with the error to predict the output, and to correct the estimation of the state vector (Step 2). At the third stage the error covariance matrix is computed, which will be used at stage four when the posteriori state vector is updated and the (Step 3 and 4). An a priori estimate of the state vector is predicted for the next iterative cycle using the model of the system (Step 5).

B. Kinematic Model of the Mobile Robot

The mobile robot model, which has been used in this paper, is a unicycle robot type with two differential motors and two degrees of freedom to move. QuickBot, the robot that has been used here, is equipped with four ultrasonic sensors on the front-left and four ultrasonic sensors on the front-right. It has a two-wheel differential drive system moved by two differential motors equipped with an optical encoder for each, figure 2 shows the QuickBot robot and its sensors.

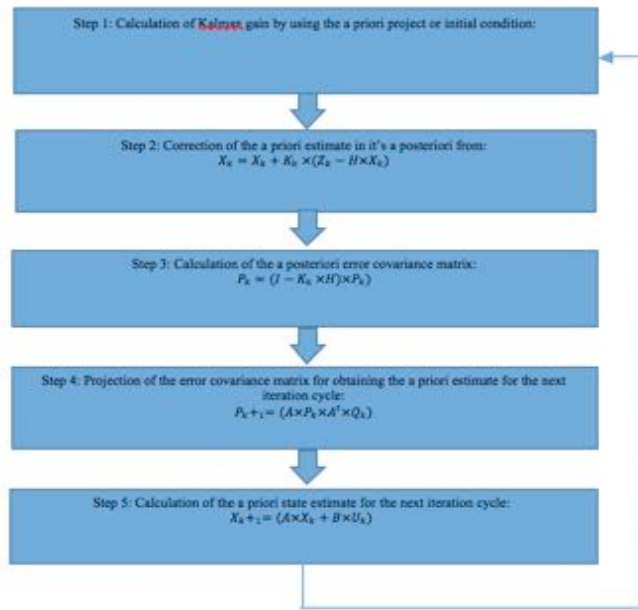


Fig. 1. The Kalman Filter Process

The configuration of the mobile robot is characterized by the position (X, Y) and the orientation in a Cartesian coordinate. Figure 3 shows the variables used in the kinematic model, where VR and VL are the linear velocity of the right and left wheels, respectively. W is the angular velocity of the mobile robot, X,Y are the actual position coordinates. θ represents the orientation of the robot and L is the distance between the driving wheels.

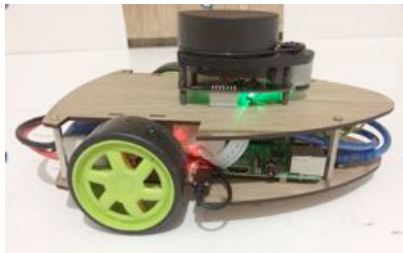


Fig. 2. Mobile robot with laser sensor

The kinematic model (Omrane et al., 2016) is given by the following equations:

$$\begin{aligned} \frac{dx}{dt} &= \frac{VL + VR}{2} \cos\theta \\ \frac{dy}{dt} &= \frac{VL + VR}{2} \sin\theta \\ \frac{d\theta}{dt} &= \frac{VL - VR}{L} \end{aligned}$$

In simulation, we use the discrete form to build a model of the robot. Then, the discrete form of the kinematic model is given by the following equations:

$$X(k+1) = X_k + T \frac{Vrk + Vlk}{2} \cos\theta_k$$

$$\begin{aligned} Y(k+1) &= Y_k + T \frac{Vrk + Vlk}{2} \sin\theta_k \\ \theta(k+1) &= \theta_k + T \frac{Vrk - Vlk}{L} \end{aligned}$$

Where X (k+1) and Y(k+1) represent the position of the centre axis of the mobile robot and T is the sampling time. These equations are used to simulate the robot in MATLAB software. This paper improves the performance of this model, using Fuzzy Logic Controller (FLC), which is briefly explained, in the next subsection.

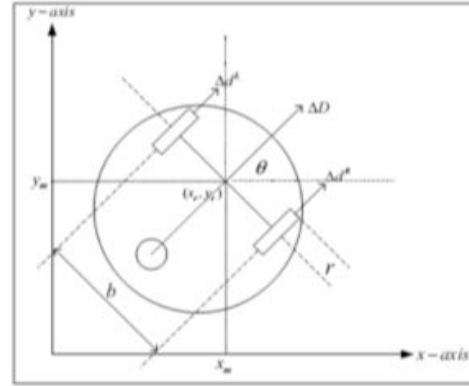


Fig. 3. Kinematic model of the mobile robot.

C. Obstacle Avoidance using Fuzzy Logic Controller

The first step to realize a fuzzy controller is fuzzification which transforms each real value's inputs and outputs into grades of membership for fuzzy control terms. The second part is fuzzy inference which combines the facts acquired from the fuzzification of the rule base and conducts the fuzzy reasoning process. There are some methods of fuzzy inference depending on the uses and the form of the membership function. When the input and the output variables and membership function are defined, the fuzzy rule is presented as the following form if-then rules (Ishibuchi et al., 1995). The subsets of the outputs, which are calculated by the inference engine, are transformed into classes in the third part of fuzzy logic, i.e. defuzzification block.

The developed fuzzy controller manages at the same time navigation and obstacle avoidance tasks. Many academic studies proposed and used the fuzzy logic theory as a solution to control mobile robots Driankov and Saffiotti, 2013), (Martínez-Soto et al., 2014), (Lee, 1990), (Han, 2004), (Norouzi, 2009), (Yelane et al., 2016). The basic structure of the fuzzy controller is composed of three blocks: the fuzzification, inference, and defuzzification. The proposed and developed fuzzy logic controller (FLC) for navigation task used two inputs: the distance d and the angle orientation ϕ . The outputs of the controller are the speed of the right (VR) and the left wheels (VL). The values of the two inputs are given by the following equations:

$$d = \sqrt{(X_t - X)^2 + (Y_t - Y)^2}$$

$$\Phi = \theta_t - \theta, \text{ Where}$$

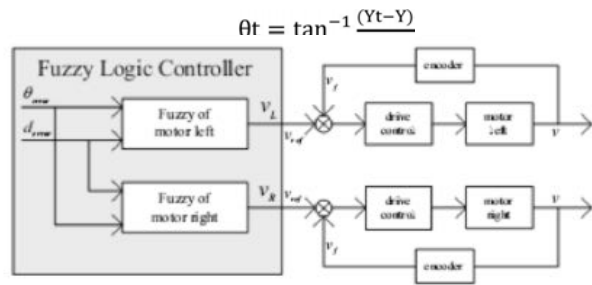


Fig. 4. Methods of the conventional tracking fuzzy control system.

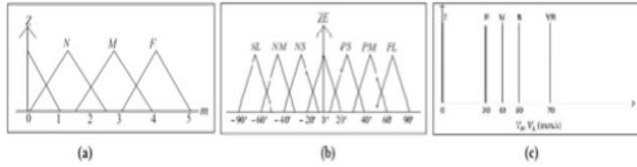


Fig. 5. (a) Input membership function for distance, (b) Input membership function for angle, (c) Output membership function for velocity.

Triangular and trapezoidal membership functions (Paksoy et al., 2012) are used in the fuzzification block. The variable d is partitioned in the universe of discourse $[0, 500 \text{ mm}]$, which is defined by five triangular membership functions: very small (VS), small (S), medium (M), big (B), and very big (VB).

The orientation angle can take values between -180 degree and 180 degree. So the interval of $[-180^\circ 180^\circ]$, is defined by seven membership functions: negative big (NB), negative medium (NM), negative small (NS), zero (Z), positive small (PS), positive medium (PM), and positive big (PB).

For velocity, five singleton membership functions are considered; Z (zero), F (far), M (medium), B (big), and VB (very big).

Having defined the membership function, the expert system is designed and developed using 35 if-then rules, defined by experts. Table 1. The fuzzy rule bases are presented in Table 1. Now the Fuzzy Inference System is ready to be deployed for the robot navigation and be tested in real-world environment.

TABLE I. THE FUZZY RULE BASES FOR THE CONTROLLER.

III. IMPLEMENTATION AND EXPERIMENTS

A full obstacle avoidance capability allows the robot to move independently in almost any un/semi-structured environment without any collisions. This paper implements this using the proposed fuzzy inference system in section 2. The input data from UltraSonic (US) sensors on the front-left and four Ultrasonic sensors on the front-right are integrated by two symmetric sonar sensors data, one located on the left and one on the right side of the robot. Thus, four fuzzy controllers are used to implement the obstacle avoidance behaviour. This process is shown again in Figure 10. The fuzzy controller is to make the manoeuvre smoother and more efficient. This has two components; (a) controlling the (linear) velocity using a

membership function according to the distance from the obstacle; (b) make the turning decisions more context-aware, i.e. according to the available capacity (spatial and power) the angular velocity is changing gradually to make the robot rotation and turnings smoother to make a manoeuvre around the obstacle. The fuzzy controller has full access to all sensor readings and processes input data, including its location, distance from the obstacle, available space for making manoeuvre, to control the robot. The outputs of each command are the linear velocity and angular velocity of the mobile robot.

The test environment, shown in figures 11,12,13 and 14 is intentionally designed and built to be unstructured to test the performance of the robot in similar environment. Also the test environment has changed several times with different sets of obstacles. The number and location of the obstacle are different at each test scenario. However, at each scenario the very robot starts from the very same point of origin. The scenarios, and achieved results are presented here.

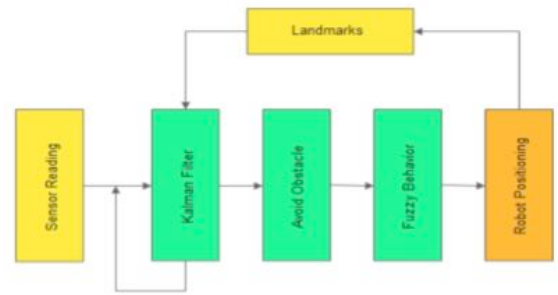


Fig. 6. Intelligence Embodiment Architecture.

A. First Scenario

The simulations were performed at the different environments, with different settings of obstacles. The first scenario, shown in figure 7, the obstacles are located in a way that the direct line between the origin and the destination could be blocked by only one of the obstacles.

Distance (D)		NB		NM		NS		Z		PS		PM		PB	
		V _R	V _L	V _R	V _L	V _R	V _L	V _R	V _L	V _R	V _L	V _R	V _L	V _R	V _L
	VS	B	Z	M	Z	F	Z	S	F	Z	F	Z	F	Z	M
S	VB	Z	B	Z	M	Z	S	F	Z	M	Z	B	Z	VB	
M	VB	Z	VB	Z	B	Z	M	M	Z	B	Z	VB	Z	VB	
B	VB	Z	VB	Z	VB	Z	B	B	Z	VB	Z	VB	Z	VB	
VB	VB	Z	VB	Z	VB	Z	VB	VB	Z	VB	Z	VB	Z	VB	

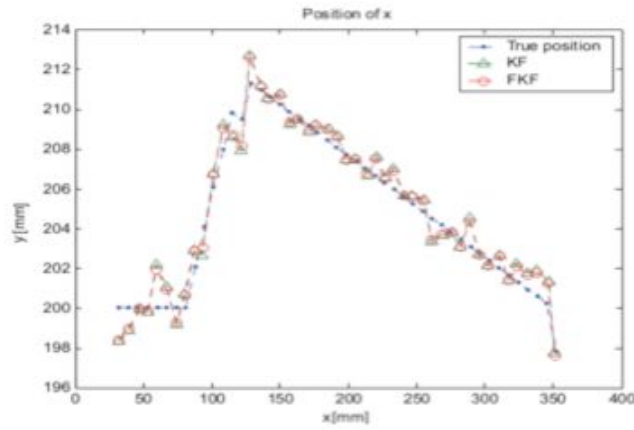


Fig. 7. The comparison of robot motion in x-axis using only KF and FKF

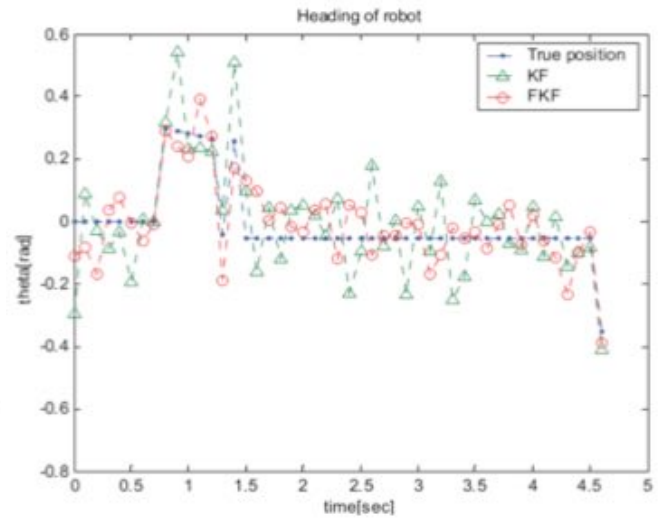


Fig. 9. The comparison of robot motion in y-axis using KF and FKF

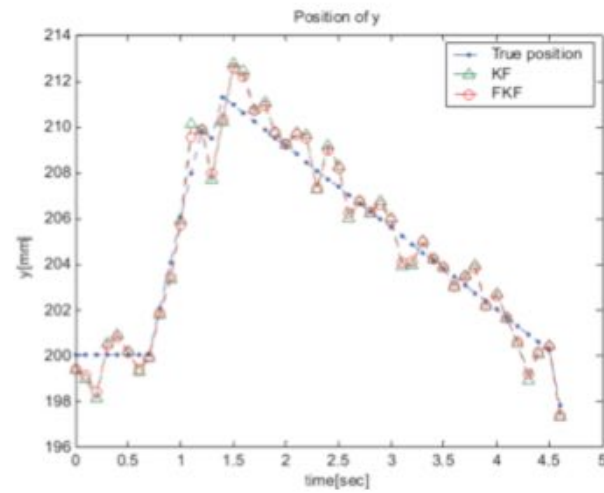


Fig. 8. The comparison of robot motion in y-axis using only KF and FKF

Fig. 7 shows the trajectory of movement of the robot while the obstacle is located on the left hand side of the robot heading to the planned destination from the origin. The simulation results are shown in Fig. 8 and Fig. 9 respectively. The three captured paths represent footprints of the robot using its actual location, Kalman Filter calculated. Fig. 11 and Fig. 12 show similar experiments using other maps. Second simulation experiment (Fig. 10) has three obstacles in the workspace. The robot moves from start position (30,200) to destination position (350,220). The results changes of xy-position, y-position and heading of robot are show in Fig. 11, Fig. 12 and Fig. 13 respectively.

B. Second Scenario

Unlike scenario one, at the second scenario, the other two obstacles block the direct line between the origin and the destination points, see figure 10. However the obstacle one may turn into an obstacle itself if the deviation from the straight path, to avoid obstacle two, is too much.

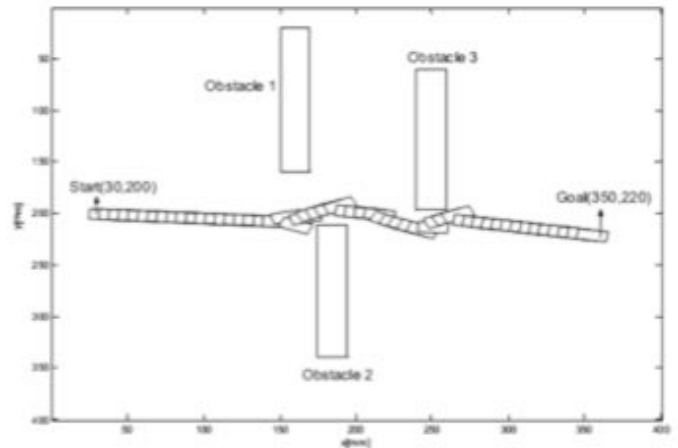


Fig. 10. The trajectory of the robot movement

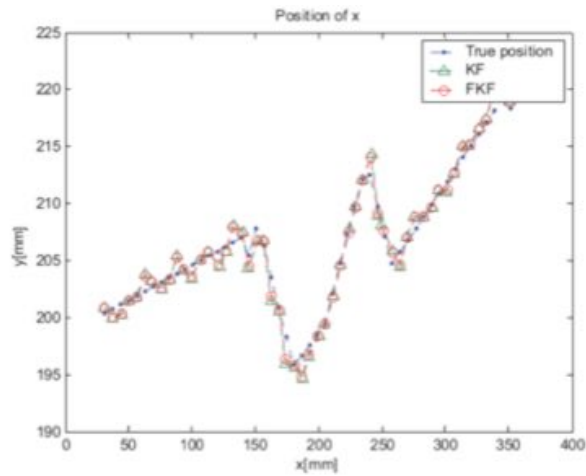


Fig. 11. The comparison of robot motion in xy-axis using only KF and FKF

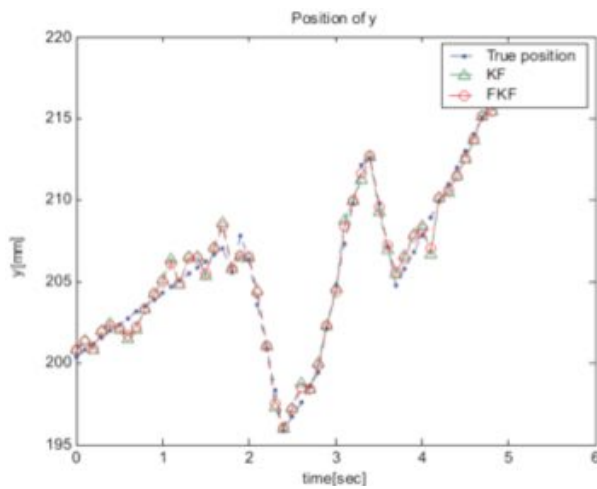


Fig. 12. The comparison of robot motion in y-axis using KF and FKF

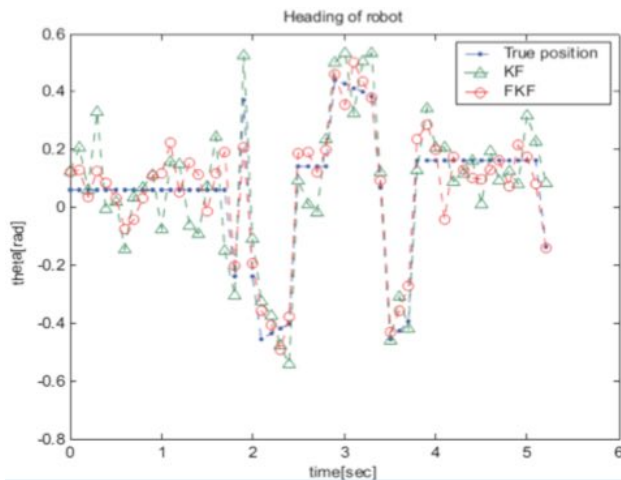


Fig. 13. The comparison of robot heading using KF and FKF

C. Third Scenario

Third simulation experiment, the robot moves from the start position (30,200) to destination position (350,260) by the workspace has seven obstacles (Fig. 14). Fig. 15 and Fig. 17 show the results of xy-position, y-position and heading changes of robot respectively.

In the third experiment, the number of obstacles are increased to seven, three on the left and four on the right hand side of the robot heading from the designed origin to the destination, see figure 14. As it has shown in table 2, the best accuracy improvement, i.e. comparing Kalman Filter and Fuzzy Kalman Filter, is achieved in this scenario. This may indicate that Fuzzy Kalman Filtering can potentially improve the accuracy and performance of the robot in more complex environments. This may also justify the computational complexity that is loaded to the system due to Fuzzy Inference System as in simpler environment improved accuracy might seem statistically significant.

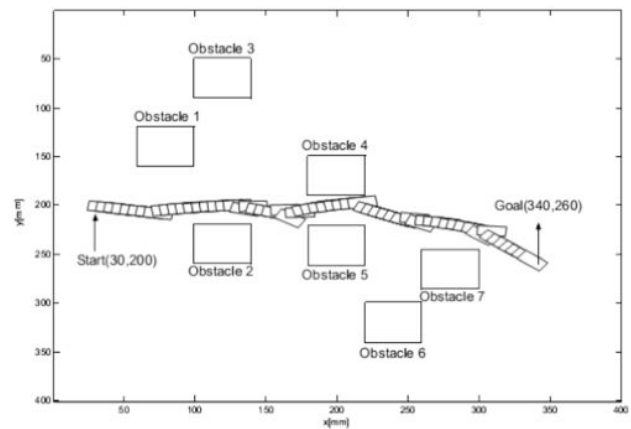


Fig. 14. The trajectory of the robot movement

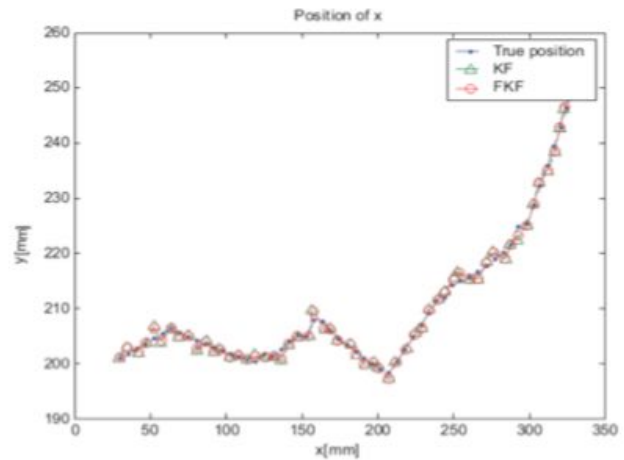


Fig. 15. The comparison of robot motion in xy-axis using only KF and FKF

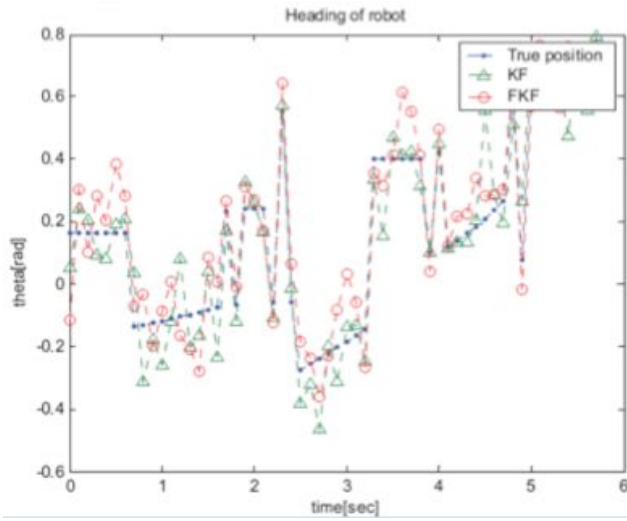


Fig. 16. The comparison of robot heading using KF and FKF

The quantitative results of the simulation experiments are shown in the above Table 2. From the table we can conclude that, the robot can move from start position to goal position with higher accuracy when FKF is used together improving the performance of robot motion.

TABLE II. THE SAMPLE RESULTS FROM THE SIMULATION EXPERIMENTS

1	Simulation		Action		KF (true position)		KF (estimated position)		FKF (estimated position)		Percentage Error			
	Sampling time interval (sec)										KF		FKF	
					X (mm)	Y (mm)	X (mm)	Y (mm)	X (mm)	Y (mm)	X (%)	Y (%)	X (%)	Y (%)
1	0.5	straight			67.06	200.00	68.93	200.17	68.05	200.13	2.79	0.08	1.48	0.06
					81.08	200.00	81.28	199.90	81.19	199.91	0.24	0.04	0.13	0.04
					87.78	202.07	87.34	201.79	87.56	201.87	0.50	0.13	0.25	0.09
					114.73	209.81	114.27	209.84	114.47	209.87	0.40	0.01	0.22	0.03
	0.7	ccw			81.08	200.00	81.28	199.90	81.19	199.91	0.24	0.04	0.13	0.04
					87.78	202.07	87.34	201.79	87.56	201.87	0.50	0.13	0.25	0.09
					114.73	209.81	114.27	209.84	114.47	209.87	0.40	0.01	0.22	0.03
					142.20	203.99	142.00	203.99	142.00	203.99	0.13	0.08	0.08	0.03
	0.8	cw			81.08	200.00	81.28	199.90	81.19	199.91	0.24	0.04	0.13	0.04
					87.78	202.07	87.34	201.79	87.56	201.87	0.50	0.13	0.25	0.09
					114.73	209.81	114.27	209.84	114.47	209.87	0.40	0.01	0.22	0.03
					142.20	203.99	142.00	203.99	142.00	203.99	0.13	0.08	0.08	0.03
	1.2	cw			81.08	200.00	81.28	199.90	81.19	199.91	0.24	0.04	0.13	0.04
					87.78	202.07	87.34	201.79	87.56	201.87	0.50	0.13	0.25	0.09
					114.73	209.81	114.27	209.84	114.47	209.87	0.40	0.01	0.22	0.03
					142.20	203.99	142.00	203.99	142.00	203.99	0.13	0.08	0.08	0.03

2	0.5	straight	170.52	209.16	171.54	209.21	171.07	209.23	0.59	0.02	0.31	0.03
			62.94	202.34	63.68	201.97	63.34	201.99	1.17	0.18	0.63	0.17
		straight	75.59	203.12	76.60	204.72	76.09	204.47	1.33	0.78	0.67	0.66
			81.91	203.51	83.30	204.63	82.63	204.44	1.70	0.55	0.87	0.45
		ccw	107.20	205.07	106.73	204.02	106.97	204.19	0.44	0.51	0.21	0.42
			157.0	206.3	157.0	207.8	157.1	207.5	0.00	0.71	0.04	0.61
	2.0	cw	157.0	206.3	157.0	207.8	157.1	207.5	0.00	0.71	0.04	0.61
			107.20	205.07	106.73	204.02	106.97	204.19	0.44	0.51	0.21	0.42
		ccw	81.91	203.51	83.30	204.63	82.63	204.44	1.70	0.55	0.87	0.45
			75.59	203.12	76.60	204.72	76.09	204.47	1.33	0.78	0.67	0.66
		straight	62.94	202.34	63.68	201.97	63.34	201.99	1.17	0.18	0.63	0.17
			170.52	209.16	171.54	209.21	171.07	209.23	0.59	0.02	0.31	0.03
3	0.5	straight	58.42	205.49	58.06	207.66	58.12	207.32	0.61	1.05	0.51	0.88
			69.58	205.63	70.06	206.05	69.85	206.01	0.68	0.20	0.38	0.18
		ccw	75.18	204.9	73.84	206.3	74.51	206.0	1.78	0.68	0.88	0.53
			97.61	202.32	97.19	201.54	97.36	201.67	0.42	0.38	0.25	0.32
		cw	142.20	203.99	142.00	204.21	142.08	204.19	0.13	0.10	0.08	0.09
			142.20	203.99	142.00	204.21	142.08	204.19	0.13	0.10	0.08	0.09
	0.6	ccw	75.18	204.9	73.84	206.3	74.51	206.0	1.78	0.68	0.88	0.53
			97.61	202.32	97.19	201.54	97.36	201.67	0.42	0.38	0.25	0.32
		cw	142.20	203.99	142.00	204.21	142.08	204.19	0.13	0.10	0.08	0.09
			142.20	203.99	142.00	204.21	142.08	204.19	0.13	0.10	0.08	0.09
		straight	58.42	205.49	58.06	207.66	58.12	207.32	0.61	1.05	0.51	0.88
			69.58	205.63	70.06	206.05	69.85	206.01	0.68	0.20	0.38	0.18

The data from sensors, i.e. Laser, Ultrasonic, and other prior data including landmarks are simulated in V-rep environment, and MATLAB Fuzzy Kalman Filter. The results are compared against Classic Kalman Filter and the comparison shows a significant improvement the performance of estimating the robot location.

In this simulation, which is implemented in V-Rep software, a simulated robot called K-Junior is used. By adding the Ultrasonic sensor on the robot and three landmarks in the simulation environment, we released the robot once with KF and then with FKF, see figure 17. With FKF an increase in routing accuracy is observed. This is particularly significant in rotational speed and rotary speed situations, as shown in figures 18.



Fig. 17. Simulating obstacle avoidance behaviour robot with Ultrasonic sensor and K.F algorithm in V-rep software

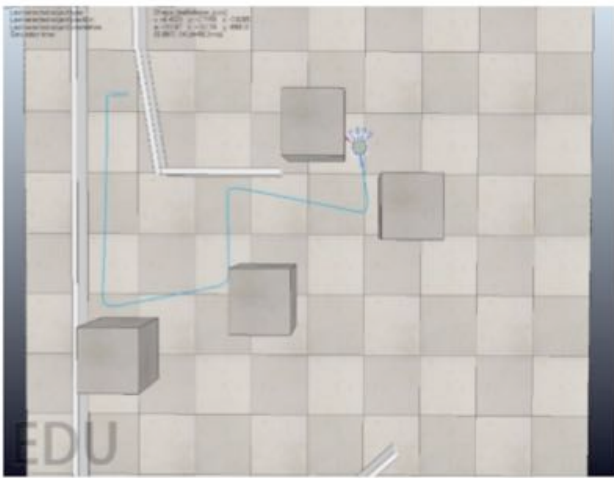


Fig. 18. Simulating obstacle avoidance behaviour robot with Ultrasonic sensor and K.F algorithm in V-rep software

In another experiment, instead of using Ultrasonic sensor, a laser sensor is used. Since the laser sensor has a greater vision range than the Ultrasonic sensors and measures more depth, it has a better performance in the environments with low barriers. However, the existence of multiple barriers may compromise the speed of manoeuvre near each obstacle as the robot passes slowly and passes through the barriers step-wise (compare figure 19 and figure 20). Although the fuzzy controller can improve this problem, there are still problems remaining, e.g. if more than one obstacle is located relatively close to each other, then the trajectory of movement could become zigzag shape. This, though, can be resolved by adding more sensors and also using Ramer–Douglas–Peucker algorithm (Saalfeld, 1999).

In order to improve rotational and rotary movement accuracy, this paper uses Laser, Ultrasonic, and landmarks data are used simultaneously. The output trajectory for the robot, which uses all the multi-sensor data of the maneuvers, is shown in figure 20.

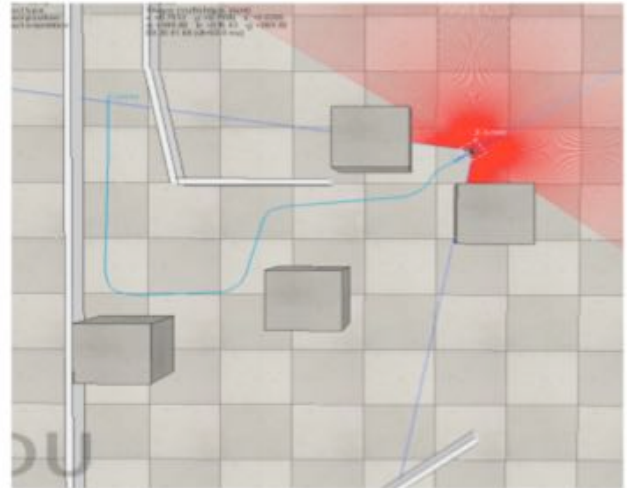


Fig. 19. Simulating obstacle avoidance behaviour robot with Laser-Landmarks sensors and K.F algorithm in V-rep software



Fig. 20. Simulating obstacle avoidance behaviour robot with Laser-Landmarks sensors and FKF algorithm in V-rep software

Since we manually entered the systematic error to the system in the simulator environment of V-rep software, there is no non-systematic error. After testing in the simulator environment, we again conducted tests in real conditions using differential two-wheeled mobile robot with two degrees of freedom and Arduino Board Uno for processing the robot and eight ultrasonic sensors and a laser sensor with range of 270 degrees and three landmarks via Wi-Fi signals which this test was performed within Mechatronics Research Laboratory (MRL) - Qazvin Islamic Azad University (QIAU).

With regards to the systematic and non-systematic errors, sensor measurements and the robot's behaviour the

improvement in the accuracy has obtained but not as much as the simulator had predicted. When the robot uses the Fuzzy Kalman Filter, it clearly performs better in the manoeuvres in comparison with the case where it uses the Classic Kalman Filter method alone and the result was acceptable. The video of this manoeuvre is available on <https://youtu.be/7mLpTpAgDAU>.

IV. CONCLUSION

This paper proposed and implemented an enhanced multi-sensor robot positioning and navigation using fuzzy controller. The Fuzzy Inference System provides the robot with capabilities of making decision regarding routing and path finding. The use of fuzzy logic allows the robot to have smoother manoeuvres, with much fewer dramatic transitions between states, and also with improved accuracy. It also tends to be much more resistant to input deviations as the enhanced Kalman Filtering can merge sensors data for location estimation, while the output of Kalman Filter is used to adjust different speeds to wheels, and/or different direction, and generating smoother path instead of zigzagged path. Experimental results demonstrate that generated path in new fuzzy controller is smoother consequently the map quality is improved as well experimental results demonstrate that generated path in new fuzzy controller is smoother consequently the map quality is improved as well. Future work shall include adding more sensors to improve the accuracy of the positioning solution, development of wider range of fuzzy behaviours, testing the system in different environments and scenarios, and implementation of adaptation mechanism into the fuzzy behaviours using Genetic Algorithms.

REFERENCES

- [1] Aras, M. S. M., Mazlan, K., Ahmad, A., Ali, N. M., Karis, M. S., Khamis, A. & Azmi, M. W. N. (2016, December). Analysis performances of Laser Range Finder and blue LED for Autonomous Underwater Vehicle (AUV). In *Underwater System Technology: Theory and Applications (USYS)*, IEEE International Conference on (pp. 171-176). IEEE.
- [2] Cherubini, A., & Chaumette, F. (2013). Visual navigation of a mobile robot with laser-based collision avoidance. *The International Journal of Robotics Research*, 32(2), 189-205.
- [3] Driankov, D., & Saffiotti, A. (Eds.). (2013). *Fuzzy logic techniques for autonomous vehicle navigation* (Vol. 61). Physica.
- [4] Han, L. R. (2004). *A Fuzzy-Kalman filtering strategy for state estimation* (Doctoral dissertation).
- [5] Ishibuchi, H., Nozaki, K., Yamamoto, N., & Tanaka, H. (1995). Selecting fuzzy if-then rules for classification problems using genetic algorithms. *IEEE Transactions on fuzzy systems*, 3(3), 260-270.
- [6] Julier, S. J., & Uhlmann, J. K. (1997). A new extension of the Kalman filter to nonlinear systems. In *Int. symp. aerospace/defense sensing, simul. and controls* (Vol. 3, No. 26, pp. 182-193).
- [7] Karambakhsh, A., Khanian, M. Y. A., Meybodi, M. R., & Fakharian, A. (2011). Robot navigation algorithm to wall following using fuzzy Kalman filter. In *Control and Automation (ICCA)*, 2011 9th IEEE International Conference on (pp. 440-443). IEEE.
- [8] Lee, C. C. (1990). Fuzzy logic in control systems: fuzzy logic controller. I. *IEEE Transactions on systems, man, and cybernetics*, 20(2), 404-418.
- [9] Montiel, O., Sepúlveda, R., Murcio, I., & Orozco-Rosas, U. (2014). Geo-navigation for a mobile robot and obstacle avoidance using fuzzy controllers. In *Recent advances on hybrid approaches for designing intelligent systems* (pp. 647-669). Springer International Publishing.
- [10] Martínez-Soto, R., Castillo, O., & Castro, J. R. (2014). Genetic algorithm optimization for type-2 non-singleton fuzzy logic controllers. In *Recent Advances on Hybrid Approaches for Designing Intelligent Systems* (pp. 3-18). Springer International Publishing.
- [11] Norouzi, M., Karambakhsh, A., Namazifar, M., & Savkovic, B. (2009). Object based navigation of mobile robot with obstacle avoidance using fuzzy controller. In *Control and Automation, 2009. ICCA 2009. IEEE International Conference on* (pp. 169-174). IEEE.
- [12] Paksoy, T., & Pehlivan, N. Y. (2012). A fuzzy linear programming model for the optimization of multi-stage supply chain networks with triangular and trapezoidal membership functions. *Journal of the Franklin Institute*, 349(1), 93-109.
- [13] Omrane, H., Masmoudi, M. S., & Masmoudi, M. (2016). Fuzzy logic based control for autonomous mobile robot navigation. *Computational intelligence and neuroscience*, 2016.
- [14] Saalfeld, A. (1999). Topologically consistent line simplification with the Douglas-Peucker algorithm. *Cartography and Geographic Information Science*, 26(1), 7-18.
- [15] Yelane, M. A. A., Pawar, M. S. B., & Vaidya, S. R. (2016). Design Approach of a Shortest Path for Robot Navigation Using Fuzzy Logic & PSO.
- [16] Zadeh, L. A. (1965). Fuzzy sets. *Information and control*, 8(3), 338-353.
- [17] Zaki, A. M., Arafa, O., & Amer, S. I. (2014). Microcontroller-based mobile robot positioning and obstacle avoidance. *Journal of Electrical Systems and Information Technology*, 1(1), 58-71.
- [18] Zein-Sabatto, S., Sekmen, A., & Koseyaporn, P. (2003). Fuzzy behaviors for control of mobile robots. *J Syst Cybern Inform*, 1, 68-74.

Design Analysis of a Hyperbolic Landing Navigation System for Aircraft

Thanh Bang Le, Petr Makula, Josef Bajer

Dept. of Aerospace Electrical Systems

University of Defence

Brno, Czech Republic

{thanhbang.le; petr.makula; josef.bajer}@unob.cz

Marie Richterova

Dept. of Communication and Information Systems

University of Defence

Brno, Czech Republic

marie.richterova@unob.cz

Abstract— Radio navigation is widely used nowadays, especially to precisely estimate aircraft position during the approach and landing phase of flight. However, it is challenging to ensure the accuracy of aircraft navigation using a transmission channel that changes rapidly due to noise and interference. To increase the safety and reliability of aircraft in the approach and landing phase, a hyperbolic landing system is proposed as a non-autonomous system. The main goal of this paper is to analyze the mechanism of radio signal propagation between the transmitters and receiver of a novel hyperbolic navigation system that uses the TDOA method. The paper evaluates the effects of the radio channel environment on the proposed system in the landing phase of flight. The theoretical analysis is verified by MATLAB simulations.

Keywords—*aircraft navigation; TDOA; Doppler effect; radiowave propagation; Rician channel; multipath channel*

Full paper in IEEE Xplore

Adaptive Carrier Tracking for Vehicular Communication under High Dynamic Environment

J. Yin*, R. Tiwari and M. Johnston

School of Engineering

Newcastle University

Newcastle upon Tyne

United Kingdom

Email: *j.yin3@ncl.ac.uk

Abstract—In vehicular communication, consistent and continuous vehicular positioning under any circumstance is very important in order to avoid collision or latency. The Global Positioning System (GPS) is a fully operated satellite based system which can provide position, navigation and timing services anytime and anywhere. Within GPS receiver signal processing, the carrier tracking loop has been concerned as one of the most important aspects. Under a highly dynamic urban environment, low C/No and Doppler frequency shift have been highlighted as two of the most significant effects that can cause loss of lock. Conventional ways to overcome this are methods such as increasing the integration time and tracking bandwidth or implementing aided tracking methods such as Kalman filter aided phase lock loop, however, longer integration time has higher computational cost, higher tracking bandwidth reduces the tracking bandwidth and Kalman filter methods depend on prior information, therefore performance will be degraded if the prior information mismatches the reality. Therefore, with the aim to solve these challenges, in this paper we propose to deploy an adaptive Kalman filter aided third order phase lock loop (AKF aided 3rd order PLL) for tracking low CNR GPS signal under challenging environments. The improvements of this new approach are demonstrated by field experiments and compared with the conventional algorithm.

Index terms – *Dynamic environment, Third order Phase Lock Loop, Adaptive Kalman Filter, Software-based GPS Receiver*

I. INTRODUCTION

Precise positioning with the help of a global positioning system (GPS) receiver is in demand for vehicle to vehicle communication (V2V), particularly under very challenging environments and all-time availability for autonomous or semiautonomous vehicles. The carrier tracking loop has been considered as one of the most important aspects but also the weakest link in GPS signal processing. High dynamics and low C/No are typical characteristics in a vehicular environment where the carrier tracking loop often suffers a loss of lock because of these effects. The common carrier tracking loop in a stationary GPS receiver is a second order phase lock loop (2nd order PLL), however third order phase lock loop (3rd order PLL) offers superior noise rejection and lower steady-state error than second order phase lock loop, meanwhile instead of being sensitive to acceleration, third order PLL is more sensitive to jerk. Due to these benefits, third order PLL is more adaptive to vehicular communication under dynamic

urban environments. 3rd order PLL, however, limits the trade off between tracking bandwidth and tracking accuracy, since tracking bandwidth needs to be relatively high in order to track the high Doppler frequency shift range whilst tracking bandwidth has to be relatively low in order to retain the tracking accuracy due to the low C/No. A study of aided weak signal tracking proposes to implement Kalman filter and extended Kalman filter on carrier tracking loop [1] which have been proven to have more robust and accurate results, however the performance of the Kalman filter is highly dependent on prior knowledge, a reality mismatch of prior knowledge could lead to high computation cost and a degradation of the tracking loop's performance.

In this paper we propose to implement an adaptive Kalman filter aided third order phase lock loop (AKF aided 3rd PLL) carrier tracking loop to track highly dynamic and low C/No GPS L1 band signal. This method is proposed because a 3rd order PLL is sensitive to acceleration jerk and the adaptive Kalman filter can significantly reduce the noise level entering the loop filter, estimate Doppler frequency shift and self-adjust its measurement noise covariance based on innovation sequence updates. For evaluating this tracking approach, field experiments were conducted in a multipath environment which is common scenario of the vehicle to vehicle communication in the urban environment. The experimental site for our study is dense covered building area with a narrow sky view. A software based GPS receiver was used in data collection. The results have superior performance compared to third order PLL stand along.

The remainder of this paper is organized as follows: in section II, transfer functions of the third order phase lock loop and adaptive Kalman filter have been derived. Section III introduces the system implementation and experimental setup and its results. Finally, a conclusion is made in section IV.

II. CARRIER TRACKING WITH 3RD ORDER PLL AND ADAPTIVE KALMAN FILTER

After successfully acquiring the GPS signal [2], in order to maintain the replica signals phase synchronization with the incoming GPS signal, the phase lock loop has been considered a crucial component. The 3rd order PLL is chosen in this paper due to its sensitivity to jerk and weak signals.

A. 3rd order PLL system processing

The incoming GPS signal $U_i(t)$ can be expressed as Eq.(1) in time domain [3],

$$U_i(t) = A \times N_{(t)} \times C/A_{(t-\tau)} \cos(2\pi[f_c + f_d]t + \phi_i) + n(t) \quad (1)$$

where A is the signals amplitude, $N_{(t)}$ is the navigation data bit, τ is the code delay of the received signal, C/A represents the spreading code, f_c is the incoming carrier frequency in Hz and f_d is the Doppler frequency shift, ϕ is the carrier phase in radians, $n(t)$ is the total noise. Assuming the code delay has been mitigated, Eq.(1) can be represented as Eq.(2)

$$U_i(t) = A \times N_t \times \cos(2\pi f_c t + \phi_i) \quad (2)$$

At receiver side, local signal oscillator generates carrier signal $U_o(t)$, with coarse acquired frequency \hat{f}_c . After mix with the income GPS signal $U_i(t)$ the I and Q components can be presented as Eq.(3) [4].

$$\begin{aligned} I &= \frac{A \times D_t}{2} [\cos(2\pi(f_c + \hat{f}_c)t + \phi_i + \phi_0) + \cos(\phi_{err})] \\ Q &= \frac{A \times D_t}{2} [\sin(2\pi(f_c + \hat{f}_c)t + \phi_i + \phi_0) + \sin(\phi_{err})] \end{aligned} \quad (3)$$

After processing a long enough coherent integration, the high frequency component will be eliminated and Eq.(3) can be represented as Eq.(4)

$$\begin{aligned} I &= \frac{A \times D_t}{2} \cos(\phi_{err}) \\ Q &= \frac{A \times D_t}{2} \sin(\phi_{err}) \end{aligned} \quad (4)$$

if ϕ_{err} is 0, the I component has the navigation message and the Q component has only noise. The output of phase discriminator U_d can be calculated by $ATAN(Q/I)$ as Eq.(5) which has a linear detecting range from $-\pi/2$ to $\pi/2$

$$U_d = \phi_{err} = ATAN\left(\frac{Q}{I}\right) \quad (5)$$

The output of the phase discriminator U_d will enter the loop filter, the output of the loop filter U_f is equal to $K_o U_d$ where K_o is the filtering gain. The output of loop filter is considered as a control signal to the voltage control oscillator (VCO). The angular frequency ω_o of the VCO is proportional to the control signal U_f , and as we know phase is equal to the integration of angular frequency, these relationships can be expressed as Eq.(6) and Eq.(7),

$$\frac{d\omega_o(t)}{dt} = K_o U_f(t) \quad (6)$$

$$\phi_o(t) = \int_0^t \frac{d\omega_o(t)}{dt} dt = K_o \int_0^t U_f(t) dt \quad (7)$$

Therefore, if the phase difference ϕ_{err} between the incoming signal and the replica signal is not 0, the nonzero signal U_f will control the VCO to keep generating the signal U_o with phase value ϕ_o until ϕ_{err} is 0 and the PLL is stable.

So far we have derived the phase lock loop in time domain, in order to analyse the performance of the PLL, the transfer function in frequency domain can be obtained through the Laplace transform. The Laplace transform of VCO is given as as Eq.(8) in S domain.

$$\mathcal{L}\{\phi_o t\} = \mathcal{L}\{K_o \int_0^t U_f(\tau) d\tau\} = \frac{K_o}{s} \quad (8)$$

The transfer function $H(s)$ can be expressed as Eq.(9).

$$H(s) = \mathcal{L}\{f(t)\} = \frac{\theta_i(s)}{\theta_o(s)} = \frac{KF(s)}{s + KF(s)} \quad (9)$$

where K is the total gain which equals $K_d K_o$, where K_d is the gain of phase discriminator and $F(s)$ is the loop filter transfer function in the S domain.

Through Eq.(9) we can see that the performance of PLL is highly dependent on the loop filter $F(s)$. In 3rd order PLL, $F(s)$ can be represented as Eq.(10)

$$F(s) = \left(\frac{\tau_2 s + 1}{\tau_1 s}\right)^2 \quad (10)$$

where τ_1 and τ_2 are the time of delay. Substituting Eq.(10) into Eq.(9), the transfer function can be expressed as Eq.(11),

$$H(s) = \frac{\frac{K\tau_2^2}{\tau_1^2} s^2 + \frac{2K\tau_2}{\tau_1^2} s + \frac{K}{\tau_1^2}}{s^3 + \frac{K\tau_2^2}{\tau_1^2} s^2 + \frac{2K\tau_2}{\tau_1^2} s + \frac{K}{\tau_1^2}} \quad (11)$$

Assume $b_3 \omega_n = \frac{K\tau_2^2}{\tau_1^2}$, $a_3 \omega_n^2 = \frac{2K\tau_2}{\tau_1^2}$, $\omega_n^3 = \frac{K}{\tau_1^2}$ where ω_n is the natural frequency, a_3 and b_3 are proportional to the damping factor, then the transfer function (11) can be represented as Eq.(12)

$$H(s) = \frac{b_3 \omega_n s^2 + a_3 \omega_n^2 s + \omega_n^3}{s^3 + b_3 \omega_n s^2 + a_3 \omega_n^2 s + \omega_n^3} \quad (12)$$

In modern GPS signal processing, GPS signal is a discrete digital signal therefore the transfer function 12 needs to transfer to Z domain through the bilinear transform as Eq.(13).

$$s = \frac{2}{t_s} \frac{1 - Z^{-1}}{1 + Z^{-1}} \quad (13)$$

substitute Eq.(13) to Eq.(12), the filter transfer function is given as Eq.(14)

$$\begin{aligned} F(Z) &= C_1 + \frac{C_2}{1 - Z^{-1}} + \frac{C_3}{(1 - Z^{-1})^2} \\ C_1 &= \frac{1}{K} \frac{8b_3 \omega_n t_s + 2\omega_n^3 t_s^3}{8 + 4b_3 \omega_n t_s + 2a_3 \omega_n^2 t_s^2 + \omega_n^3 t_s^3} \\ C_2 &= \frac{1}{K} \frac{-4\omega_n^3 t_s^3 + 8a_3 \omega_n^2 t_s^2}{8 + 4b_3 \omega_n t_s + 2a_3 \omega_n^2 t_s^2 + \omega_n^3 t_s^3} \\ C_3 &= \frac{1}{K} \frac{8\omega_n^3 t_s^3}{8 + 4b_3 \omega_n t_s + 2a_3 \omega_n^2 t_s^2 + \omega_n^3 t_s^3} \end{aligned} \quad (14)$$

In this format, 3rd order phase lock loop is very easily to implement through a software defined GPS receiver.

B. Adaptive Kalman Filtering

Even though conventional PLL has been widely used in carrier tracking loops, the trade off of its tracking accuracy and tracking bandwidth is a significant drawback, and under highly dynamic environments, the tracking bandwidth needs to be increased in order to track Doppler frequency shift caused by movement. This larger tracking bandwidth causes higher noise levels and leads to the carrier tracking loop being less sensitive to low C/No signal. Therefore, aided tracking algorithms, especially Kalman filter based PLL is worth evaluation. Kalman filter based carrier tracking loops have been proposed to track weak signal [5]. An optimal Kalman filter aims to minimize the mean square error between the real and estimated signals through prior information and model equations. The covariance matrix of processing noise Q and measurement noise R are predefined, however in practice, precise noise covariance is hard to obtain. This could lead to performance degradation if the predefined information is mismatched from the reality. Therefore, in order to mitigate these challenges, in this research we implement an adaptive Kalman filter which self adjusts the measurement noise covariance R to aid 3rd Order PLL.

A linear state model will be presented in this section in order to implement Kalman filter directly instead of taking a linearized algorithm like the Jacobian matrix. The algorithm of a linearized model can be highly reduced. According to mineralization and time-invariant system model, the state equation and measurement equation can be expressed as

$$x_t = Ax_{t-1} + Bu_{t-1} + w_{t-1} \quad (15a)$$

$$z_t = Hx_t + v_{t-1} \quad (15b)$$

Where x is the state matrix, A and B are state transition and control input matrix, u is the control variable, z is the measurement matrix respectively, H is the transfer matrix, w and v are processing and measurement noise. Due to the relative movement between GPS satellite and receiver, the frequency of incoming signal can be expressed as Eq.(16),

$$f_d(t) = f_v + f_a(t) \quad (16)$$

f_d is the overall incoming signal Doppler frequency shift, f_v is the frequency shift caused by relative velocity and f_a is the rate of frequency shift. From Eq.(16) the period of frequency shift in Δt can be expressed as Eq.(17)

$$f_d(t + \Delta t) = f_d(t) + f_a(\Delta t) \quad (17)$$

The phase shift Θ_t over period Δt is

$$\begin{aligned} \Theta_t &= \int_0^{\Delta t} f_d(t + \tau) d\tau \\ &= \int_0^{\Delta t} (f_d(t) + f_a(\tau)) d\tau \\ &= f_d(\Delta t) + \frac{1}{2} \Delta t^2 \end{aligned} \quad (18)$$

Therefore, the state vector x contains $[\theta_e f_d f_a]^T$, and the processing model of the equation can be presented as Eq.(19) in matrix format:

$$\begin{aligned} \begin{bmatrix} \theta_e \\ f_d \\ f_a \end{bmatrix}_k &= \begin{bmatrix} 1 & 2\pi\Delta(t) & \frac{2\pi\Delta(t)^2}{2} \\ 0 & 1 & 2\pi\Delta(t) \\ 0 & 0 & 1 \end{bmatrix} \begin{bmatrix} \theta_e \\ f_d \\ f_a \end{bmatrix}_{k-1} - \begin{bmatrix} 1 \\ 0 \\ 0 \end{bmatrix} f_{nco_d} \\ &+ \begin{bmatrix} 1 & 0 & 0 \\ 0 & 1 & 0 \\ 0 & 0 & 1 \end{bmatrix} W_n \end{aligned} \quad (19)$$

where θ_e is the phase difference between the incoming signal and the output of the NCO, f_{nco_d} is the replica Doppler frequency at time $k-1$, the processing noise $(W_n) \sim (\mathcal{N}\{0, Q\})$ is a noise vector $[W_{\theta_e} \ W_{f_d} \ W_{f_a}]^T$, the spectrum intensity matrix Q_c in continuous time is given as Eq.(20),

$$Q_c = \begin{bmatrix} Q_{\theta_e} & 0 & 0 \\ 0 & Q_{f_d} & 0 \\ 0 & 0 & Q_{f_a} \end{bmatrix} \quad (20)$$

The covariance matrix is Q in discrete time can be calculated as Eq.(21) [6].

$$Q = \int_0^{\Delta t} A_{k,k-1} Q_c A_{k,k-1}^T \quad (21)$$

From equation 22 $A_{k,k-1}$ can be obtained as follow

$$A_{k,k-1} = \begin{bmatrix} 1 & 2\pi\Delta(t) & \frac{2\pi}{2}\Delta(t)^2 \\ 0 & 1 & 2\pi\Delta(t) \\ 0 & 0 & 1 \end{bmatrix} \quad (22)$$

Substitute Eq.(20) and Eq.(22) into Eq.(21) we have covariance matrix Q as Eq.(23),

$$\begin{aligned} Q &= Q_{\theta} \begin{bmatrix} \Delta t & 0 & 0 \\ 0 & 0 & 0 \\ 0 & 0 & 0 \end{bmatrix} + Q_d \begin{bmatrix} \frac{\Delta t^3}{2} & \frac{\Delta t^2}{2} & 0 \\ \frac{\Delta t^2}{2} & 0 & 0 \\ 0 & 0 & 0 \end{bmatrix} \\ &+ Q_a \begin{bmatrix} \frac{\Delta t^5}{20} & \frac{\Delta t^4}{8} & \frac{\Delta t^3}{6} \\ \frac{\Delta t^4}{8} & \frac{\Delta t^3}{3} & \frac{\Delta t^2}{2} \\ \frac{\Delta t^3}{6} & \frac{\Delta t^2}{2} & \Delta t \end{bmatrix} \end{aligned} \quad (23)$$

where Q_{θ} is caused by receiver oscillator phase bias, and Q_d is caused by receiver oscillator frequency bias, the value of Q_a can be obtained by LOS jerk [7]. With known Allan variance parameters of the clocks noise, the covariance Q_d and Q_{θ} in Eq.(23) can be obtained as Eq(24).

$$\begin{aligned} Q_{\theta} &= S_f = 2h_0 \\ Q_d &= S_g = 8\pi h_{-2} \end{aligned} \quad (24)$$

In our experiment, we chose a crystal clock as our reference clock, this value have been determined as table I [8].

The output of the phase discriminator $\Theta_{e,k-1}^{mea}$ is considered as a measurement result, the measurement can be modelled as Eq.(25) [9].

TABLE I
 ALLAN VARIANCE PARAMETERS FOR VARIOUS CLOCKS

Oscillator type	$h_0(Hz)$	$h_1(Hz)$	$h_2(Hz)$
Crystal	2×10^{-19}	7×10^{-21}	2×10^{-20}
Ovenized Crustal	8×10^{-20}	2×10^{-21}	4×10^{-23}
Rubidium	2×10^{-20}	7×10^{-24}	4×10^{-29}

$$\begin{aligned}
 \Theta_e &= \frac{1}{\Delta t} \int_0^{\Delta t} [\Theta_e(k-1) + f_d(k-1)\tau + \frac{\tau^2}{2} f_a(k-1)] d\tau \\
 &\quad - \frac{1}{\Delta t} \int_0^{\Delta t} f_{ncod}(k-1)\tau d\tau \\
 &= \Theta_e(k-1) + \frac{1}{2} f_d(k-1)\Delta t + \frac{1}{6} f_a(k-1)\Delta t^3 \\
 &\quad - \frac{1}{2} f_{ncod}(k-1)\Delta t
 \end{aligned} \tag{25}$$

Therefore in matrix format it can be expressed as Eq.(26)

$$\Theta_e = \begin{bmatrix} 1 & \frac{2\pi\Delta t}{2} & \frac{2\pi\Delta t^2}{6} \end{bmatrix} \begin{bmatrix} \Theta_e(k-1) \\ f_d(k-1) \\ f_a(k-1) \end{bmatrix} - \frac{2\pi\Delta t}{2} f_{ncod} + V_{k-1} \tag{26}$$

where $(V_n) \sim (\mathcal{N}\{0, R\})$ is a Gaussian white noise sequence. In the Kalman filter algorithm, the covariance matrix P_t and Kalman gain K_t can be obtained as

$$\begin{aligned}
 P_t &= A_t P_{t-1} A_t^T + Q \\
 K_t &= P_{t-1} H^T (H_t P_{t-1} H_t^T + R)^{-1}
 \end{aligned} \tag{27}$$

where state transition matrix A and transfer matrix H can be expressed as Eq.(28),

$$A = \begin{bmatrix} 1 & 2\pi\Delta(t) & \frac{2\pi\Delta(t)^2}{2} \\ 0 & 1 & 2\pi\Delta(t) \\ 0 & 0 & 1 \end{bmatrix} \tag{28}$$

$$H = \begin{bmatrix} 1 & \frac{2\pi\Delta t}{2} & \frac{2\pi\Delta t^2}{6} \end{bmatrix}$$

In this paper, the measurement covariance is unknown, therefore, in order to obtain the measurement covariance R , we need to analyse the measurement update Eq.(29),

$$\hat{x}_{t|t} = \hat{x}_{t|t-1} + K(z - H_t \hat{x}_{t|t-1}) \tag{29}$$

where $\hat{x}_{t|t}$ is the posterior estimation and $\hat{x}_{t|t-1}$ is the prior estimation at time $t-1$, K is Kalman gain, and z measurement value, the innovation sequence ξ can be express as

$$\begin{aligned}
 \xi &= z - H_t \hat{x}_{t|t-1} \\
 &= H_t x_t + V_t - H_t \hat{x}_{t|t-1} \\
 &= H_t (x_t - \hat{x}_{t|t-1}) + V_t
 \end{aligned} \tag{30}$$

A study [10] has proved that the covariance of the innovation sequence ξ is independent from time and approximate to its sample covariance as Eq.(31)

$$\begin{aligned}
 C_t &\equiv E \{ \xi_t \xi_{t-k}^T \} \\
 C_t &= \frac{1}{N} \sum_{t=k}^N \xi_t \xi_{t-k}^T
 \end{aligned} \tag{31}$$

where k represents k time back from t , N represent the number of sample points.

Estimated covariance \hat{C}_t can be obtained as Eq.(32)

$$\hat{C}_t = (z_t - H_t \hat{x}_{t|t-1})(z_t - H_t \hat{x}_{t|t-1})^T \tag{32}$$

Substitute Eq.(18b) into the innovation sequence, ξ can be expressed as

$$\xi = Hx_t + v_t - H\hat{x}_{t|t-1} \tag{33}$$

Substitute Eq.(33) into Eq.(31) Then estimated covariance \hat{C} can be expressed as Eq.(34)

$$\begin{aligned}
 \hat{C}_t &= E \{ (H(x_t - \hat{x}_{t|t-1}) + v_t)(H(x_t - \hat{x}_{t|t-1}) + v_t)^T \} \\
 &= HE \{ (x_t - \hat{x}_{t|t-1})(x_t - \hat{x}_{t|t-1})^T \} H^T + E \{ v_t v_t^T \}
 \end{aligned} \tag{34}$$

where $\hat{x}_{t|t-1}$ is the prediction value of x_t . The variance of prediction $\hat{x}_{t|t-1}$ and x_t is given as Eq.(35)

$$P_{t|t-1} = [E(x_t - \hat{x}_{t|t-1})(x_t - \hat{x}_{t|t-1})^T] \tag{35}$$

Substitute Eq.(35),Eq.(34) can be rewritten as

$$\hat{C}_t = H P_{t|t-1} H^T + R \tag{36}$$

Finally, measurement noise covariance R is estimated as Eq.(37) recursively.

$$\hat{R} = \frac{1}{N} \sum_{i=k}^N \xi_i \xi_{i-k}^T - H_t P_{t|t-1} H_t^T \tag{37}$$

In a time-invariant system, the covariance of the innovation sequence \hat{C}_t can be obtained through measurement value updates. The matrix $P_{t|t-1}$ can be defined by Kalman filter and the processing covariance Q .

III. IMPLEMENTATION AND EXPERIMENT RESULTS

In this section we demonstrate the algorithm implementation of the adaptive Kalman filter

A. System Implementation

The integrated system diagram of Adaptive Kalman filter aided 3rd order PLL is illustrated as Fig 1 below:

The output of the phase discriminator U_d is considered as the measurement value of the Adaptive Kalman filter, the measurement noise covariance matrix R can be updated as time increases. An optimal phase offset will become an input of the loop filter, since we implement 3rd order PLL, therefore, the order of loop filter is 2nd order. Finally, the output of loop filter become a control value of the voltage control oscillator in order to generate a replica carrier signal with same phase as the incoming signal. The integration algorithm is given

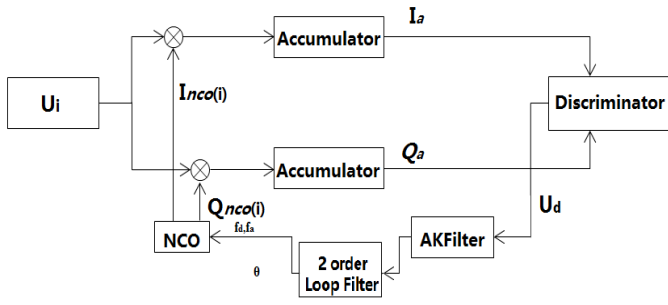


Fig. 1. Processing diagram of Loop filter

below, processing and measurement is as Eq.(23) and Eq.(29) Covariance matrix P is initialed as Q , since Q has been derived before, therefore P can be obtained as Eq.(38)

$$P_{t|t-1} = \begin{bmatrix} 1 & \Delta(t) & \frac{\Delta(t)^2}{2} \\ 0 & 1 & \Delta(t) \\ 0 & 0 & 1 \end{bmatrix} P_{t-1} \begin{bmatrix} 1 & \Delta(t) & \frac{\Delta(t)^2}{2} \\ 0 & 1 & \Delta(t) \\ 0 & 0 & 1 \end{bmatrix}^T + Q \quad (38)$$

Measurement covariance matrix R is equal to

$$R = \lim_{n \rightarrow \infty} \frac{1}{n} \sum_{i=1}^n \xi_i \xi_i^T - \begin{bmatrix} 1 & \frac{\Delta t}{2} & \frac{\Delta t^2}{6} \end{bmatrix}_t P_{t|t-1} \begin{bmatrix} 1 & \frac{\Delta t}{2} & \frac{\Delta t^2}{6} \end{bmatrix}_t^T \quad (39)$$

Kalman Gain and measurement update is the same as a standard Kalman filter, then the updated states \hat{x} at time t will use for phase offset ϕ_e update as Eq.(40)

$$\phi_e = K \left[C_1 \hat{x}_{t|t} + \frac{C_2 \hat{x}_{t|t}}{1-Z^{-1}} + \frac{C_3 \hat{x}_{t|t}}{(1-Z^{-1})^2} \right] \quad (40)$$

Where K is the total gain, therefore as time increases the phase offset will keep adjusting until the phase difference is zero.

B. Experiment setup and Results

A field experiment was conducted at the Dovenshire car park Newcastle university, England as Fig 2 demonstrated, experiment was undertaken for 3 days repeatedly. A USRP based software receiver works as a front-end device, furthermore, in order to obtain a precise time synchronization, an atomic clock has been deployed as a reference time source. Carrier tracking algorithms will be implemented after data collection as a post process.

The effective carrier to noise ratio C/N_o is an important parameter to describe GPS receiver performance, the higher C/N_o indicates a better phase estimation and location determination. Typical range of C/N_o for GPS receiver in open sky is 37dB to 45dB. Considering the weak signal, the C/N_o estimation of this experiment is using Narrowband-Wideband power ratio method [11]. In order to obtain a better tracking capability, tracking bandwidth for 3rd Order PLL is set to be 13 Hz. The C/N_o comparison as Fig.3 illustrate, C/N_o is approximate 14dB which is relatively low, however with the help of the adaptive Kalman filter, the C/N_o has been

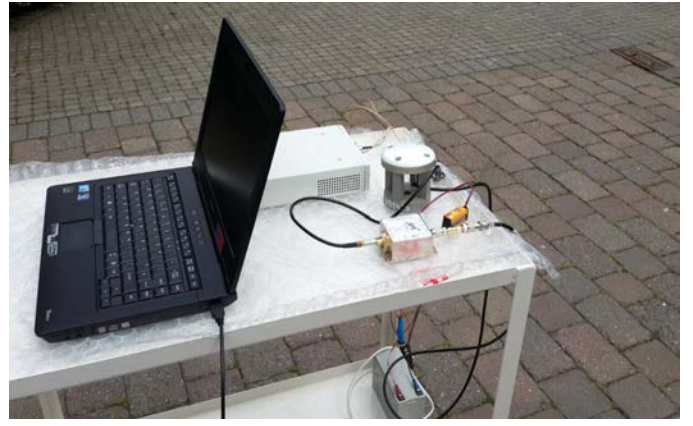


Fig. 2. Experiment setup

improved 2dB in average compare to conventional 3rd Order PLL because of the noise level being reduced by the adaptive Kalman filter.

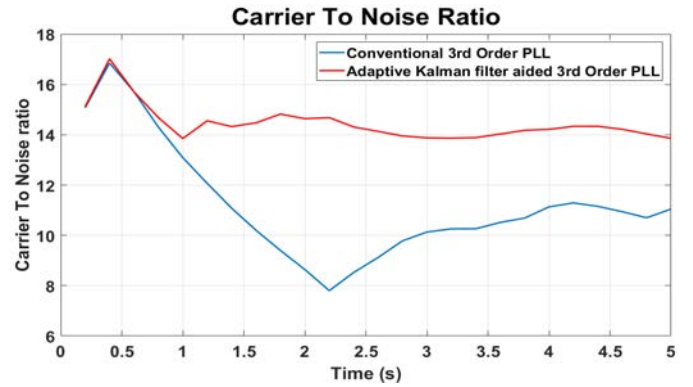


Fig. 3. Carrier to Noise ratio at 13Hz

These can also be seen from phase error and phase variance comparison which are presented in Fig 4 and Fig 5, with the help of the adaptive Kalman filter, the phase error and phase variance have all been reduced.

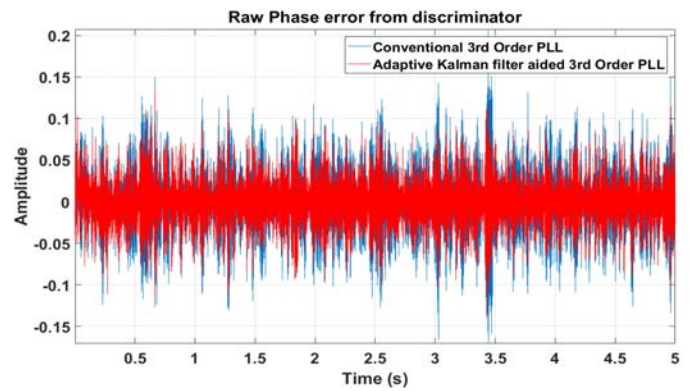


Fig. 4. Phase error from Discriminator at bandwidth 13Hz

As Fig 5 present, AKF aided 3rd Order PLL has less phase variance which offers more robustness and is more adaptive to

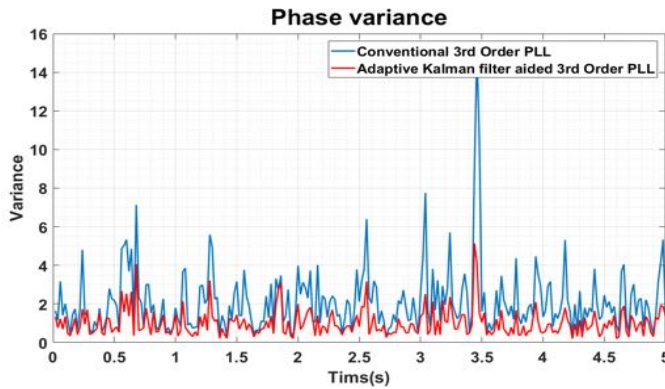


Fig. 5. Phase variance comparison

dynamic environments. Fig 6 indicates the phase lock status, AKF aided 3rd Order PLL is more stable compare to the conventional 3rd Order PLL.

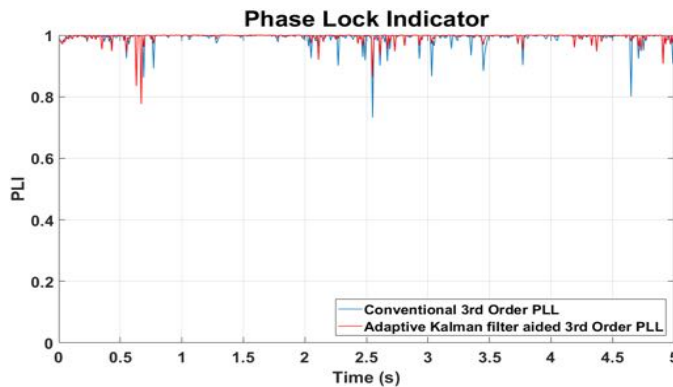


Fig. 6. Phase Lock Indicator at 13Hz

ACKNOWLEDGMENT

The authors would like to thank Nottingham Scientific Ltd (NSL), for providing a precise atomic clock so that the field experiment can be completed successfully.

IV. CONCLUSIONS

This paper has presented a novel AKF aided 3rd Order PLL tracking loop in order to track highly dynamic and low C/N_o GPS signal.

The transfer function of conventional 3rd Order PLL and its loop filter have been derived and analyzed in both time and frequency domain. Due to the drawbacks of conventional 3rd Order PLL, an adaptive Kalman filter aided 3rd Order PLL is proposed and implemented in order to estimate the Doppler frequency shift and minimize the noise level. Within the adaptive Kalman filter, the measurement noise matrix is completely unknown and estimated by innovation sequence updates.

The new tracking approach has been tested using real GPS data which is collected from a software based GPS receiver. The tracking results indicate that C/N_o can be improved

2dB using this new approach. This new approach can make the carrier tracking loop more stable and robust compared to the conventional 3rd Order PLL. Advantages of these new approach make it more suitable to vehicular communication under urban environments.

REFERENCES

- [1] M. L. Psiaki, "Attitude sensing using a global-positioning-system antenna on a turntable," *Journal of Guidance, Control, and Dynamics*, vol. 24, no. 3, pp. 474–481, 2001.
- [2] J. Yin, R. Tiwari, and M. Johnston, "Low-cost dual polarized gps antenna for effective signal acquisition in multipath environment," in *Navigation Conference (ENC), 2017 European*. IEEE, 2017, pp. 359–365.
- [3] X. Niu, B. Li, N. I. Ziedan, W. Guo, and J. Liu, "Analytical and simulation-based comparison between traditional and kalman filter-based phase-locked loops," *GPS solutions*, vol. 1, no. 21, pp. 123–135, 2016.
- [4] R. Tiwari, H. Strangeways, and S. Skone, "Modeling the effects of ionospheric scintillation on gps carrier phase tracking using high rate tec data," in *26th International Technical Meeting of The Satellite Division of the Institute of Navigation (ION GNSS+ 2013)*, Nashville, Tenn, 2013, pp. 2480–2488.
- [5] M. L. Psiaki and H. Jung, "Extended kalman filter methods for tracking weak gps signals," in *ION GPS 2002: 15 th International Technical Meeting of the Satellite Division of The Institute of Navigation*, 2002.
- [6] N. Ziedan and J. Garrison, "Bit synchronization and doppler frequency removal at very low carrier to noise ratio using a combination of the viterbi algorithm with an extended kalman filter," in *Proceedings of the 16th International Technical Meeting of the Satellite Division of The Institute of Navigation (ION GPS/GNSS 2003)*, 2001, pp. 616–627.
- [7] D. R. Salem, C. ODriscoll, and G. Lachapelle, "Methodology for comparing two carrier phase tracking techniques," *GPS solutions*, vol. 16, no. 2, pp. 197–207, 2012.
- [8] R. Grover and P. Y. Hwang, "Introduction to random signals and applied kalman filtering," *Wiley, New York*, p. 431, 1992.
- [9] M. L. Psiaki, "Smoother-based gps signal tracking in a software receiver," in *Proceedings of ION GPS*, vol. 2001, 2001, pp. 2900–2913.
- [10] R. Mehra, "On the identification of variances and adaptive kalman filtering," *IEEE Transactions on automatic control*, vol. 15, no. 2, pp. 175–184, 1970.
- [11] B. Parkinson and S. J. Gelb, *Global Positioning System, Volume 1 - Theory and Applications*. American Institute of Aeronautics and Astronautics, 1996.

Ju Hyun Lee
Department of Radio Navigation
Navcours
Daejeon, Republic of Korea
jhlee@navcours.com

Abstract— China has been developing BDSBAS which is a BDS-based SBAS. BDS sends test signals using the B1I signal in order to develop, test and validate the BDSBAS. The SBAS correction information classified into three categories of fast correction, long term correction, ionosphere correction. In contrast, BDSBAS provides pseudorange correction information from ionosphere correction information and equivalent clock correction parameters. BDSBAS also provides integrity information through RURAI and UDREI. BDSBAS doesn't always provide reliable correction information in countries without the monitoring station. It is necessary to confirm the reliability of correction information with GIVEI, describing reliability of ionosphere correction, and UDREI, describing reliability of equivalent clock correction. In this paper, we analyze the BDS performance by designing a software-based BDS receiver that processes BDSBAS correction information. For this study, USRP-based RF Front End is used and software-based BDS receiver is designed.

Keywords—*BDS, BDSBAS, Augmentation service information*

I. INTRODUCTION

BDS is under development in order to provide global service by 2020 (Phase III). BDS is being developed to provide SBAS (Satellite Based Augmentation System) as well as satellite navigation service. China carried out the design, test and construction of the BDSBAS (Beidou Satellite-based Augmentation System) based on the ICAO (International Civil Aviation Organization) standards. Currently, BDSBAS is under development in order to DF (Dual Frequency) service based on the SBAS DFMC (Dual Frequency Multiple Constellation) standards. BDSBAS will be providing open service offered by 3 GEO satellites and B1C, B2a signals. In 2018, 1 GEO satellite will be launched. From 2020, Another 2 GEO satellite will be launched. The test signal of BDSBAS is transmitted on the B1I signal. The ionospheric vertical delay, the BDS differential correction and the integrity information for correcting pseudorange measurements over China are included in the test signal. In the BDS-ICD (Interface Control Documents, version 2.1), such BDSBAS correction

information is described as the augmentation service information.

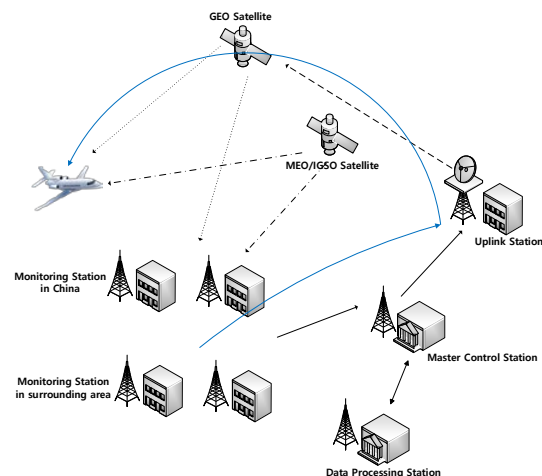


Fig. 1. System Architecture of BDSBAS

In this paper, we analyzed the BDS performance by designing a software-based BDS receiver that processes BDSBAS correction information. We also analyzed the ionospheric delay computed by grid ionospheric delay algorithm. For this study, USRP-based RF Front End is used and software-based BDS receiver is designed. And, we compute the ionospheric delay with dual frequency algorithm and Klobuchar model for verifying the ionospheric grid information of BDSBAS.

II. BDSBAS

A. Content of BDSBAS Data

The navigation message of BDS B1I signal consists of D1 and D2. The navigation message broadcasted by GEO satellites is D2. The D2 navigation message contains the basic navigation information and the augmentation service

information. Fig. 2 shows the frame structure and the information contents of the navigation message in format D2.

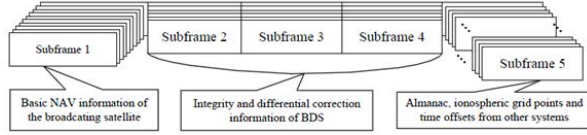


Fig. 2. Frame structure and information contents of NAV message in format D2

The ionospheric grid information is included in Subframe 5. The integrity and the differential correction information of BDS are included in Subframe 2 through Subframe 4.

B. BDS Differential Correction Information

The BDS differential correction information is expressed in equivalent clock correction (Δt). Δt is used to correct the residual error of the satellite clock offset and ephemeris. Δt is not available if the value is -4096. UDRE (User Differential Range Error) is used to describe the error of equivalent clock correction in meters. UDRE is provided as an index in the D2 navigation message. The effective range of UDREI is 0 to 15. If UDREI is 14, the differential correction for satellite is not monitored. So, it can't be used. If UDREI is 15, the differential correction for satellite is not available. TABLE I shows the corresponding relationship between UDRE and UDREI.

TABLE I. UDREI definitions

UDREI	UDREI (meters, 99%)
0	1.0
1	1.5
2	2.0
3	3.0
4	4.0
5	5.0
6	6.0
7	8.0
8	10.0
9	15.0
10	20.0
11	50.0
12	100.0
13	150.0
14	Not monitored
15	Not available

C. BDSBAS Ionospheric Grid Information

The BDSBAS ionospheric reference altitude is 375 km. The ionospheric grid covers 70 to 145 degrees east longitude and 7.5 to 55 degrees north latitude. The IGP consists of the vertical delay at grid point (τ) and its error index (GIVEI). Fig. 3 shows the coverage of BDSBAS. The effective range of the vertical ionospheric delay is between 0 to 63.625 m.

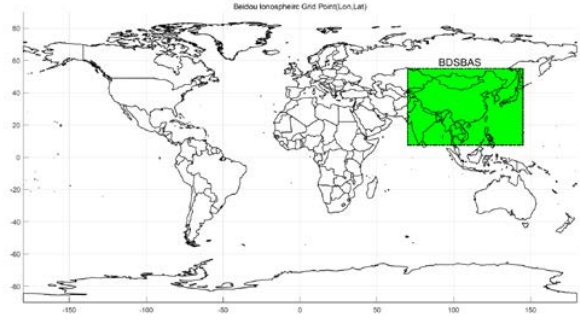


Fig. 3. Coverage of BDSBAS

The IGP isn't monitored when the vertical ionosphere delay is 63.750 m. It isn't available when the vertical ionospheric delay is 63.875 m. The grid ionospheric vertical error (GIVE) describes the delay correction accuracy at ionospheric grid points and its index is GIVEI. The effective range of GIVEI is 0 to 15. If GIVEI is 14 or more, the delay correction information is not used.

D. User Grid Ionospheric Correction Algorithm

The ionospheric pierce point (IPP) is calculated using the elevation angle and the azimuth angle according to the user receiver position and the position of each satellite. There have to be at least effective three grid points surrounding the user IPP. The IPP's ionospheric delay can be calculated from the vertical ionospheric delay through the bilinear interpolation algorithm. The IPP is represented with the latitude (ϕ_{pp}) and the longitude (λ_{pp}). If there are four IGPs surrounding the IPP, the principle of the four points interpolation method is given by

$$\tau_{vpp}(\phi_{pp}, \lambda_{pp}) = \sum_{i=1}^4 W_i(x_{pp}, y_{pp}) \tau_{vi} \quad (1)$$

τ_{vi} is the vertical ionospheric delay of four grid points. Fig. 4 shows the user's IPP and its surrounding grid points.

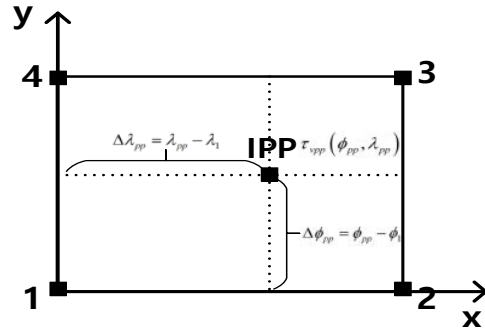


Fig. 4. User IPP and Grid points

The weight to obtain the vertical ionospheric delay value of the IPP depends on the distance between the IPP and the IGP. This weight is estimated by the vertical ionospheric delay of each IGP as shown in (1). From (2) to (5) are used to obtain the weight of each point.

$$W_1 = (1 - x_{pp})(1 - y_{pp}) \quad (2)$$

$$W_2 = (x_{pp})(1 - y_{pp}) \quad (3)$$

$$W_3 = (x_{pp})(y_{pp}) \quad (4)$$

$$W_4 = (1 - x_{pp})(y_{pp}) \quad (5)$$

III. TEST SETUP AND RESULTS

A. Test Setup

This paper uses BDS receiver consisting of RF front end and BDS SDR (Software-Defined Radio). BDS SDR includes the signal processing part, the tracking loop filter part, the data processing part and the navigation processing part. Test setup is summarized in TABLE II.

TABLE II. Test Setup

Common Set	Setting
Antenna	NovAtel GPS-703-GGG
RF-Front End	USRP N210
Sampling Frequency	25MHz
Intermediate Frequency	4.661MHz
Integration Time	1ms
Satellite Singal	BDS B1I
Receiver Position (longitude, latitude)	36.4°, 127.3°

We have to check the accuracy of the correction information in order to use equivalent clock correction and the delay correction at ionospheric grid points. To use equivalent clock correction, we need to check UDREI. BDSBAS provides UDREI for satellites PRN 18 or less. If the error of UDRE is less than 10m, the value of equivalent clock correction is added to the observed pseudorange. Fig. 5 shows checking results of UDREI from collected the signal at 11 (UTC+09:00) on Sep. 11, 2017.

To compute the ionospheric delay with grid ionospheric delay algorithm, we need to check GIVEI. BDSBAS provides the vertical delay at grid point ($d\tau$) only for GEO satellites PRN 1 to PRN 5. In order to compute the ionospheric delay, it is necessary to confirm that 3 or more IGPs are available. Fig. 6 shows the plotting of GIVEI at different times on the same day. In case of figure (a), we can compute the ionospheric delay because 4 IGPs are valid. However, since 2 IGPs are valid in case of figure (b), the ionospheric delay can't be computed. Fig. 7 shows the change of GIVEI at grid points around Korea for 14 hours.

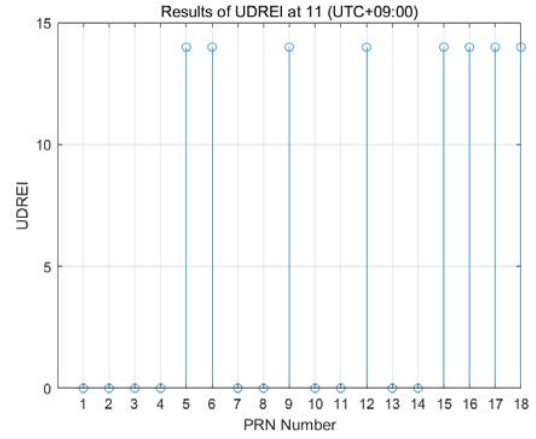
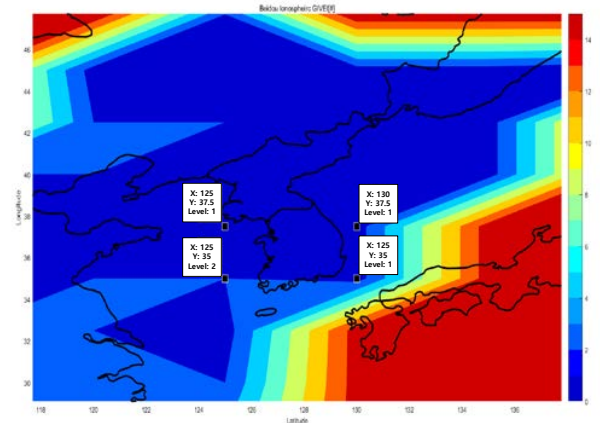
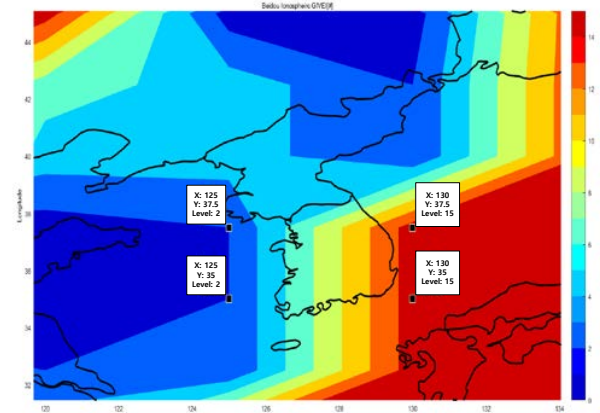


Fig. 5. Results of UDREI



(a) GIVEI at 11(UTC+09:00)



(b) GIVEI at 14(UTC+09:00)

Fig. 6. Results of GIVEI at different time

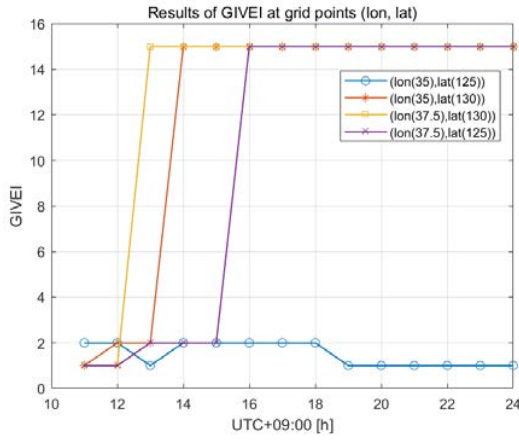


Fig. 7. GIVEI at grid point around Korea

B. Test Results

Prior to analyzing the BDS navigation performance, we analyzed the ionospheric delay values computed from the ionospheric vertical delay at grid point. For this purpose, we respectively calculate the ionospheric delay with dual frequency algorithm, Klobuchar model algorithm and the algorithm of grid ionospheric. We collected the B11 signal from 11(UTC+09:00) to 24(UTC+09:00) on September 11, 2017. And, we confirmed that there are three or more valid IGP's available between 11(UTC+09:00) and 13(UTC+09:00) o'clock. TABLE III summarizes the ionospheric delay error for each algorithm. Diff 1 is the difference of ionospheric delay value between Dual Frequency algorithm and Klobuchar algorithm. Diff 2 is the difference of ionospheric delay value between Dual Frequency algorithm and BDSBAS.

TABLE III. Ionospheric delay error for each algorithm

Time	Mean of ionospheric delay [m]				
	Dual Frequency algorithm	Klobuchar model	BDSBAS	Diff 1 (Dual Freq. - Klo)	Diff 2 (Dual Freq. - BDSBAS)
11	11.2828	2.0135	2.1004	9.2693	9.1824
12	12.9030	2.0094	2.9177	10.8936	9.9852
13	12.0996	2.0163	2.5987	10.0833	9.5009

The mean of the ionospheric delay with dual frequency algorithm is about 12.095m. The mean of the ionospheric delay with Klobuchar model algorithm and the algorithm of grid ionospheric is respectively about 2.013m, 2.539m. On average, the difference of ionospheric delay value between Dual Frequency algorithm and Klobuchar algorithm is 10.082m, and the difference of ionospheric delay value between Dual Frequency algorithm and BDSBAS is 9.556m.

Fig. 8 - Fig. 11 show the scatter plots for horizontal and vertical RMS errors for each time. The horizontal RMS error reduced or increased when using the augmentation service information of BDS. The vertical RMS error almost increased when using the augmentation service information of BDS.

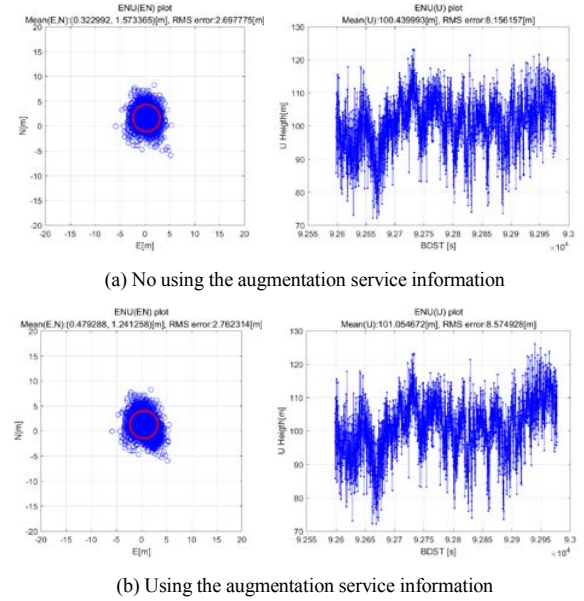


Fig. 8. Scatter plot of BDS at 11(UTC+09:00)

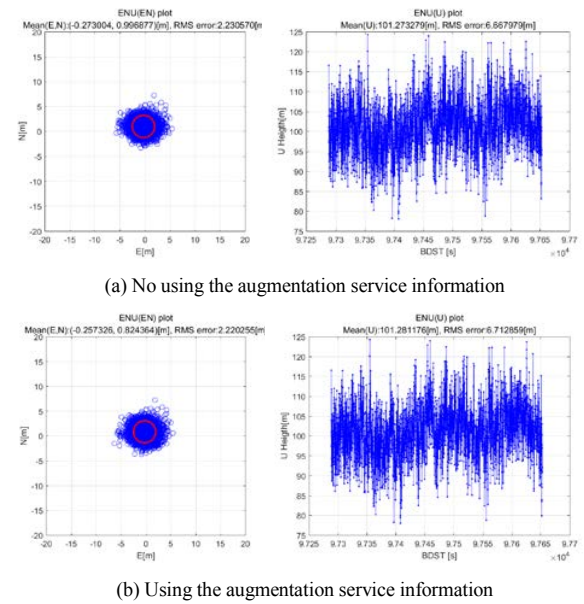
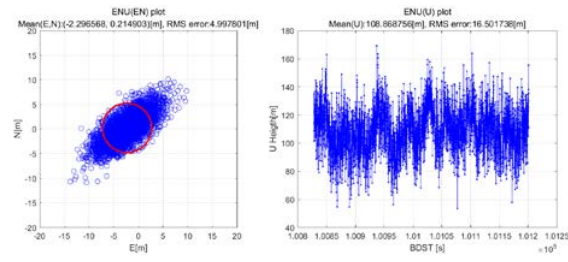
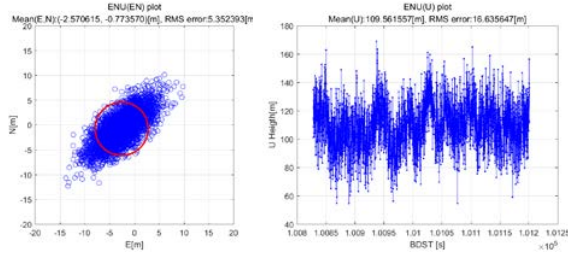


Fig. 9 Scatter plot of BDS at 12(UTC+09:00)

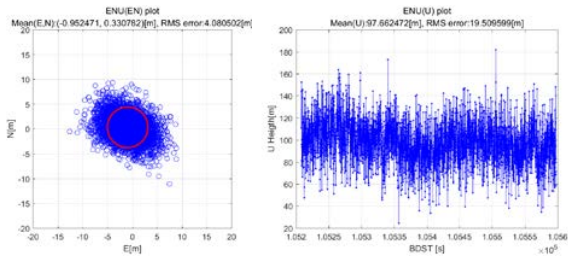


(a) No using the augmentation service information

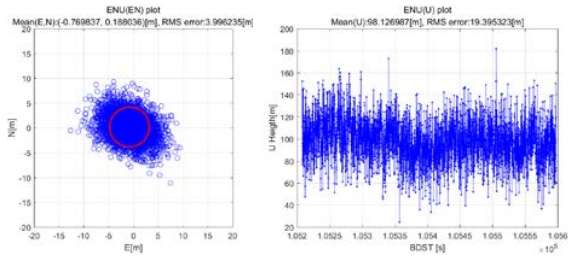


(b) Using the augmentation service information

Fig. 10. Scatter plot of BDS at 13(UTC+09:00)



(a) No using the augmentation service information



(b) Using the augmentation service information

Fig. 11. Scatter plot of BDS at 14(UTC+09:00)

Fig. 12 and Fig. 13 are graphs summarizing the horizontal RMS error and the vertical RMS error by time zone. From the graph, we can know that the augmentation service information of BDS has no significant effect on the performance of BDS.

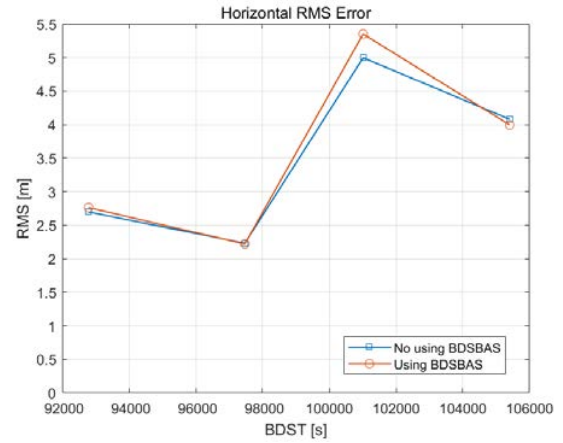


Fig. 12. The horizontal RMS error

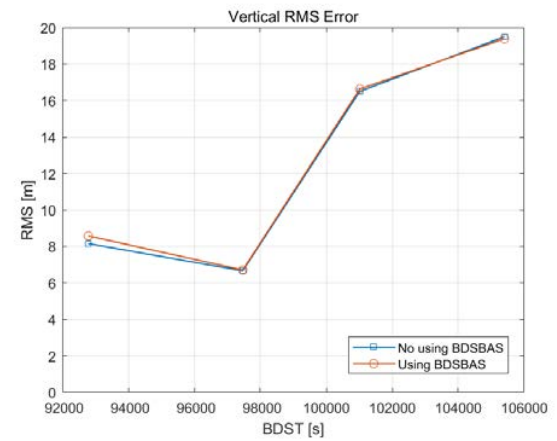


Fig. 13. The vertical RMS error

IV. CONCLUSIONS

In this paper, we analyzed the BDS performance by designing a software-based BDS receiver that processes BDSBAS correction information. We checked GIVEI from 11(UTC+09:00) to 24(UTC+09:00) o'clock in order to calculate the ionospheric delay error. As a result, the time available for the ionospheric grid information in Korea was approximately three hours. BDSBAS provides an unavailable the ionosphere vertical delay value for the eastern grid centered on Korean for most of the time. And, we analyzed BDS performance using the test signal of BDSBAS. When using the augmentation service information of BDS, the horizontal RMS error has improved in some cases, but, the horizontal RMS error value has increased in most cases. The vertical RMS error has mostly increased in error. BDSBAS correction information has little effect on BDS performance. China has not yet provided BDSBAS as a open service. BDSBAS correction information is provided as the augmentation service information through the BII signal for testing. So, surrounding

area of China such as Korea are not always provided with reliable BDSBAS information. In conclusion, it is difficult to use BDSBAS at present in Korea.

ACKNOWLEDGMENT

This work has been supported by the National GNSS Research Center program of Defense Acquisition Program Administration and Agency for Defense Development.

REFERENCES

- [1] Jun Shen, Development of BeiDou Navigation Satellite System (BDS) – A System Update Report (2016-2017), The 57th Meeting of the Civil GPS Service Interface Committee Portland, Oregon, Sep. 25-26, 2017
- [2] BDS-SIS-ICD-2.1[S].BDS Management Office of China, 2016
- [3] Geng Yu, Mo Peng, The research on grid ionospheric delay algorithm of BDSBAS, *Advances in Computer Science Research*, 2016, Vol. 63, 128-134
- [4] DO-229D (SC-159). Minimum operational performance standards for global positioning system/wide area augmentation system airborne equipment (WAAS) [S]. Washington, DC: RTCA Inc., 2006
- [5] J. Lee, K. Park and W. Jeong, Analysis of Positioning Accuracy for DGNSS-based Land Navigation Using GPS/BDS Navigation Satellite System, *Transactions of KSAE*, 2017, Vol. 25, No. 4, 422-429
- [6] J. H. Noh, J. H. Lee and S. J. Lee, Performacne Anaysis of BDS using the Test Signal of BDSBAS, *International Symposium on GSN* 2017, Dec. 10-13, 2017

R-Mode - Safe Navigation in the Baltic Sea

Stefan Gewies¹, Carsten Rieck², Jesper Bäckstedt³, Per Gustafson⁴

¹ Institute of Communications and Navigation, German Aerospace Center (DLR),
Kalkhorstweg 53, 17235 Neustrelitz, Germany, email: Stefan.Gewies@dlr.de

² RISE Measurement Science and Technology, RISE Research Institutes of Sweden AB,
Box 857, 50115 Borås, Sweden, email: carsten.rieck@ri.se

³ Business area Construction and Engineering, Swedish Maritime Administration,
Östra Promenaden 7, 601 78 Norrköping, Sweden, email: Jesper.backstedt@sjofartsverket.se

⁴ Gutech AB,
Industrigatan 21c, 234 35 Lomma, Sweden, email: per@gutech.se

Although a lot of the vessels are nowadays equipped with sensors and supporting systems for position and navigation purposes, accidents caused by collisions and groundings still happens every year. The forecasted expansion of the world trade and cruise market foresees the construction of ever larger vessels, and will therefore cause a substantial increase of the traffic situation complexity. Thus the demand for reliable systems for position, navigation and time (PNT) will remain as one of the key issues in the maritime user community. Within this scope, international bodies, as for example the International Maritime Organization (IMO) and the International Association of Marine Aids to Navigation and Lighthouse Authorities (IALA), currently strengthen their efforts for more reliable systems.

Global Navigation Satellite Systems (GNSS), today the primary mean for PNT information on-board of a vessel, are highly vulnerable to unintentional and intentional interference, e.g. jamming and spoofing. A possible backup system to it, the Long-Range Navigation (LORAN) system, was in substantial parts shutdown in the years 2010 to 2015. Only in certain regions it is still usable. Today, in case of a temporal loss of GNSS no system can provide absolute positioning on a global scale. One candidate for a terrestrial backup system is R(anging)-Mode which utilizes existing maritime communication infrastructure for the broadcast of modified signals, which allow distance estimation to the transmitter. First

feasibility studies were done in the North Sea [1, 2], in China [3] and in South Korea [4].

The Baltic Sea is due to the high number of vessels along the shipping routes and its sensitive marine ecosystem a suitable region for the implementation and testing of a terrestrial backup system to GNSS. It will supplement navigation information in order to reduce the risk of collisions and groundings. New marine applications that require a continuous provision of position information will be made possible at sea, in coastal areas and in harbours.

The R-Mode Baltic project (2017 to 2020) will consider the results of previous R-Mode studies and build and demonstrate a first R-Mode testbed in the southern part of the Baltic. The testbed will implement both of the in [1] and [2] discussed approaches. This comprises the following six research, development and implementation activities:

R-Mode implementation on IALA beacons: IALA beacons provide code differential corrections for GNSS transmitted in the Medium Frequency (MF) radio band. The beacons are distributed ashore along the shipping routes with high vessel density. The service area has typically a radius of 200 to 500 km. Ground wave dominates the radio wave propagation. There are already different proposals for the implementation of R-Mode on

this communication channel. During the project those will be analysed and the best one will be selected for later implementation. Furthermore, concepts for the mitigation of one of the dominating error sources, the refraction of MF radio wave at the E layer of the ionosphere during the night, will be developed and the best will be selected for further implementation.

R-Mode implementation on Automatic Identification System (AIS) base stations: AIS base stations provide information from ashore to the maritime user using AIS messages, which are transmitted in the Very High Frequency (VHF) radio band. Like IALA beacons, AIS base stations can be found ashore along important shipping routes and in specific areas like harbours. Due to the line-of-sight propagation of the VHF radio wave the service area is typically restricted to below 100 km radius. Within the R-Mode Baltic project the implementation on AIS and VHF Data Exchange System (VDES) frequencies will be proven. An optimal signal design will be selected and algorithms for range estimation will be developed. AIS base station equipment will be adjusted for the transmission of R-Mode signals.

Time synchronization: A necessary requirement for the transnational network of R-Mode transmitter is the sufficient time synchronization at the IALA beacon and AIS base station. R-Mode timing shall be completely independent of GNSS. Currently available alternative time comparison methods and corresponding required station clock performance will be analysed with respect to their metrological and economical properties and will give input to the project internal R-Mode requirements. Further, self-synchronization of R-Mode will be studied as an alternative to conventional transfer methods. For the demonstration the most suitable method will serve as proof-of-concept.

Building a testbed in the Baltic Sea: The southern part of the Baltic Sea is characterized by dense traffic consisting of tankers, container ships, bulk carriers, ferries and special ships passing through the region. AIS base stations and IALA beacons of Poland, Sweden and Germany will be upgraded in order to be able to transmit R-Mode signals beside the unmodified legacy signals. R-Mode

receivers will enable maritime users to estimate their position without GNSS support. The testbed will remain installed beyond the end of the project and will offer its service to maritime user.

R-Mode receiver for MF and VHF: Based on already existing GNSS receiver platforms, hardware for two prototype receivers and processors with different grade of integration will be developed. The included software will meet the R-Mode requirements and will include the research results on R-Mode implementation on VHF and MF, e.g. skywave mitigation. The prototypes will show their capabilities at the end of the R-Mode Baltic project in the Baltic Sea testbed.

PNT data processing (DP) and Pilot Plug Unit (PPU): As a first application of the R-Mode system an implementation of PNT DP as outlined by IMO in [5] will be expanded by new R-Mode processing channels for MF and VHF. This enables rapid switching to R-Mode based positioning when GNSS signal reception is disturbed or lost. Furthermore, as a second application an existing PPU will be adjusted to accommodate for R-Mode solutions.

The project is funded by European Union through European Regional Development Fund within the Interreg Baltic Sea Region Programme.

- [1] G. Johnson, P. Swaszek, ACCSEAS Project Report - Feasibility Study of R-Mode using AIS Transmissions, (2014).
- [2] G. Johnson, P. Swaszek, ACCSEAS Project Report - Feasibility Study of R-Mode using MF DGPS Transmissions, (2014).
- [3] Q. Hu, Y. Jiang, J.B. Zhang, X.W. Sun, S.F. Zhang, Development of an Automatic Identification System Autonomous Positioning System, *Sensors-Basel*, 15 (2015) 28574-28591.
- [4] S. Woo-Seong, L. Sang-Jeong, Evaluation of AIS-TWR for Maritime Asynchronous R-mode, *J. Navig. Port Res.*, 41 (2017) 87-92.
- [5] IMO, MSC.1/Circ.1575 GUIDELINES FOR SHIPBORNE POSITION, NAVIGATION AND TIMING (PNT) DATA PROCESSING, (2017).

GPS multipath mitigation technique with low hardware complexity

Jin Hyuk Lee, Jae Hee Noh, Gwang Hee Jo, Sang Jeong Lee

Department of Electronics Engineering
Chungnam National University
Daejeon, Korea

jh_lee@cnu.ac.kr, jhnoh3555@cnu.ac.kr, j_ghee@cnu.ac.kr,
eesjl@cnu.ac.kr

Chansik Park

Department of Electronics Engineering
Chungbuk National University
Cheongju
chansp@cbnu.ac.kr

Abstract—In this paper, we propose an technique to mitigate multipath error. To evaluate the performance of the proposed technique, we designed a multipath mitigation performance analysis software platform and compared with narrow correlator and multipath elimination technique.

Keywords—multipath; narrow correlator; MET;

I. INTRODUCTION

When receiving a signal from a GPS receiver, not only a direct signal but also a multipath signal is also incident due to the obstacle effects around the receiver. In this case, the multipath signal affects the code-tracking loop of the GPS receiver, causing an error in the pseudorange measurement and increasing the positioning error. Various studies have been conducted to mitigate the influence of multipath signals. Typical techniques are Narrow Correlator[1], Multipath Elimination Technique(MET)[2]. The Narrow Correlator is a simple structure that uses three correlators. It is a technique to reduce the range of multipath signals affecting the code tracking loop by narrowing the chip interval of Early and Late correlators. The MET uses five correlators and estimates and removes multipath errors from the correlation function model of the GPS signal. The MET is superior to the Narrow Correlator but it has a high hardware complexity. Therefore, in this paper, we propose a technique that can provide similar performance to the MET using three correlators like Narrow Correlator.

In this paper, we propose a GPS multipath mitigation technique with low hardware complexity. The technique uses early, prompt and late correlators like general GPS receiver and it can change the chip interval between early correlator and late correlator so that it can acquire the correlation value for the desired chip interval at any time. Therefore, it can reduce the hardware complexity by using three correlators and applying the techniques requiring more than five correlators such as MET and Multipath Estimating Delay Lock Loop(MEDLL)[3]. In addition, by implementing MET or MEDLL, it can provide better performance than Narrow Correlator with three

correlators. In order to evaluate the feasibility of the proposed technique, we designed a multipath mitigation performance evaluation platform and compared the performance of multipath error estimation by implementing the existing techniques such as the MET and the proposed technique. Simulation results show that the performance of the proposed technique is similar to that of the MET when the receiver is moving at low speed.

II. MULTIPATH OVERVIEW

A. Multipath Signal

Multipath signal is a signal that the GPS signal is reflected by the surrounding obstacle and incident into the receiver. In this case, the GPS signal's power is reduced. The multipath signal affects the code-tracking loop of the GPS receiver. So, the multipath signals cause the GPS receiver to measure incorrect measurements and increase navigation errors. Fig. 1 shows the direct and multipath signals incident on the receiver.

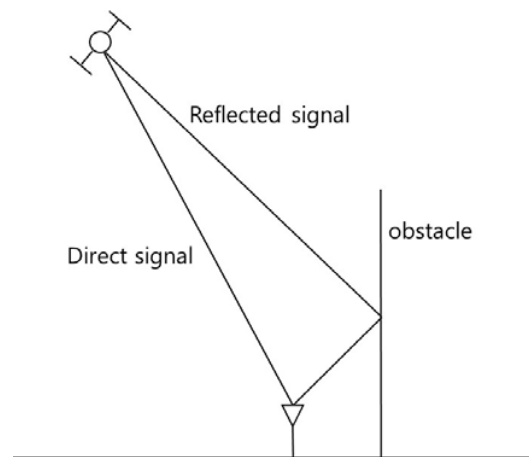


Fig. 1. Direct signal and multipath signal

B. Narrow Correlator

In general GPS receiver, chip interval between early correlator and late correlator is 1.0 chip. Narrow Correlator is a technique to reduce the chip interval between early correlator and late correlator from 1.0 chip to 0.2 chip or less unlike wide correlator. Fig. 2 shows code phase error for wide correlator and narrow correlator in a multipath signal environment[1].

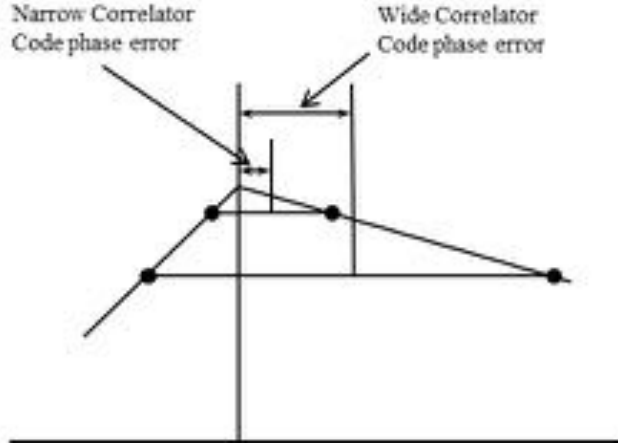


Fig. 2. Code phase error for wide correlator and narrow correlator

C. Multipath Elimination Technique

MET uses early, very early, very late, late correlators. The technique calculates each slope using two early correlators and late correlators, and calculates the compensation value of the code phase using the calculated slope. The code phase correction value is given by (1)[2].

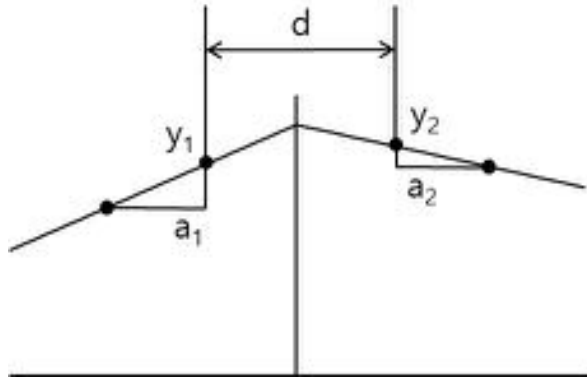


Fig. 3. Multipath Elimination Technique

$$T = \frac{y_1 - y_2 + d / 2(a_1 + a_2)}{a_1 - a_2} \quad (1)$$

T is the code tracking error, a_1 is the slope of the early correlators, and a_2 is the slope of the late correlators. d is the chip interval of early and late correlators. y_1 and y_2 are the correlation values of early and late correlators.

III. PROPOSED TECHNIQUE

The proposed technique uses early, prompt, late correlators. The technique performs correlations by adjusting the chip intervals between early correlator and late correlator per sample, and stores correlation values. In this way, the use of three correlators shows the effect that multiple correlators exist. Then, the technique applies the MET using stored multiple correlation values. Fig. 4 shows the correlator structure of the proposed technique.

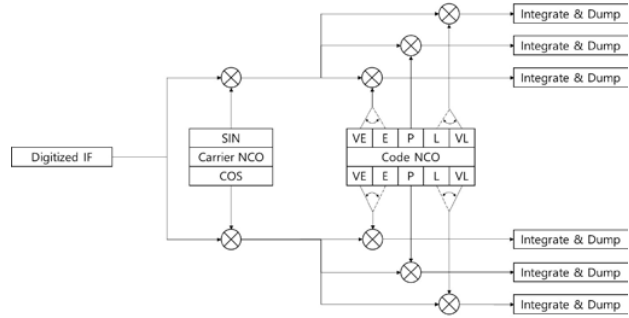


Fig. 4. Correlator structure of proposed technique

IV. SIMULATION

A. Simulation Platform

Multipath mitigation performance evaluation platform consists of a signal generator and a signal receiver. Fig. 2 shows the platform.

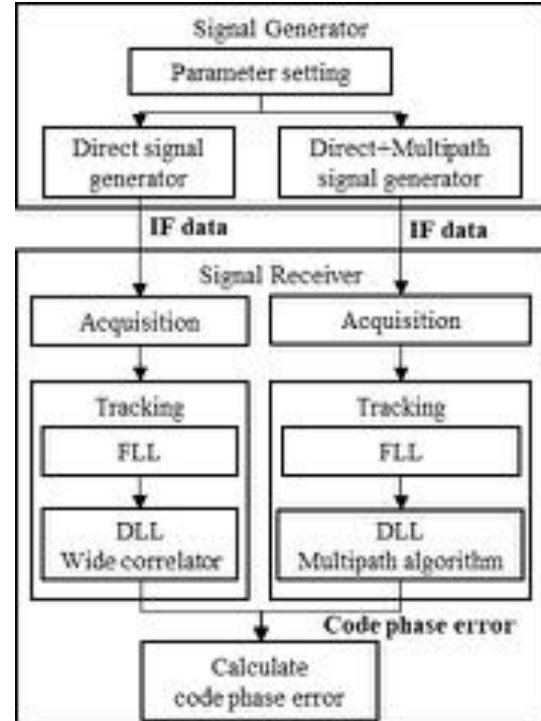


Fig. 5. Multipath mitigation performance evaluation platform

The signal generator sets parameters for direct signal and multipath signal generation, and generates a direct signal and a multipath signal. The signal receiver collects the signal and performs acquisition. After acquisition, the receiver performs tracking to track the signal. Frequency Lock Loop(FLL) and Delay Lock Loop(DLL) are performed in the tracking. The FLL estimates the Doppler frequency of the signal, and the DLL estimates the code phase error. In the DLL, multipath mitigation techniques are implemented. The wide correlator calculates code phase error of the direct signal, and multipath mitigation techniques calculate the combined signal of the direct signal and the multipath signal. Lastly, the receiver calculates code phase error to test the performance of techniques using calculated code phases. The platform implementation results for the direct signal are shown in Fig 6, Fig. 7 and Fig. 8.

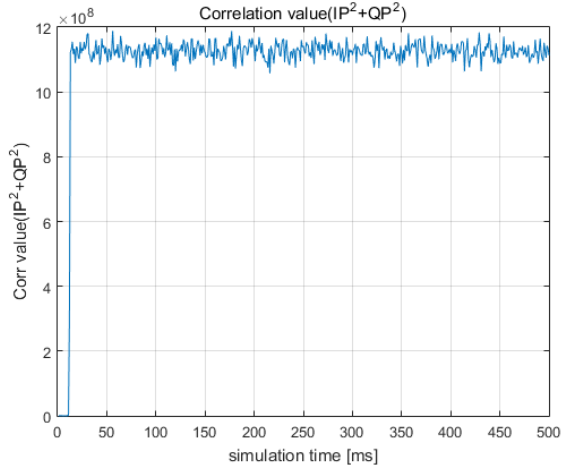


Fig. 6. Correlation value

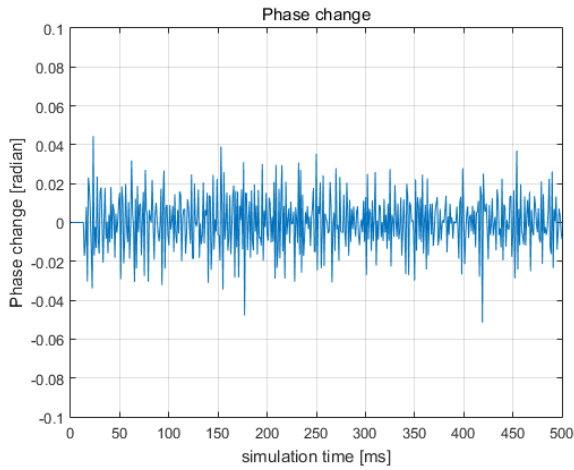


Fig. 7. Phase change(PLL output)

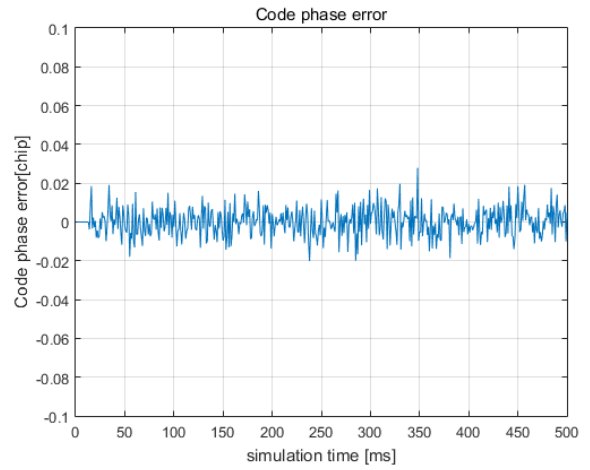


Fig. 8. Code phase error(DLL output)

B. Simulation Setup

Multipath signal generation parameters are set to verify the validity of the proposed technique. Also, the position of the receiver is fixed. The multipath mitigation techniques applied to the receiver are the narrow correlator, the MET and the proposed technique. Simulation setup is summarized in Table I.

TABLE I. SIMULATION SETUP

Parameter	Setting
Relative amplitude	0.5
Relative phase	0, 180 [degree]
Relative chip	0 – 1.1
Receiver movement	stop

C. Results

In this paper, to evaluate feasibility of the proposed technique, the simulation was performed on the proposed technique, narrow correlator and MET. As a performance index, we compared the accuracy of the estimated code phase as the multipath chip error. As the envelope result of the simulation, the proposed technique showed better performance than the narrow correlator using the same number of correlators, and showed similar performance to the MET. Fig. 9 shows the envelope according to the technique. As the computational cost result of the simulation, the proposed technique showed worst performance than the narrow correlator using the same number of correlators. But the proposed technique showed better performance to the MET. Table II shows the computational cost for multipath mitigation techniques.

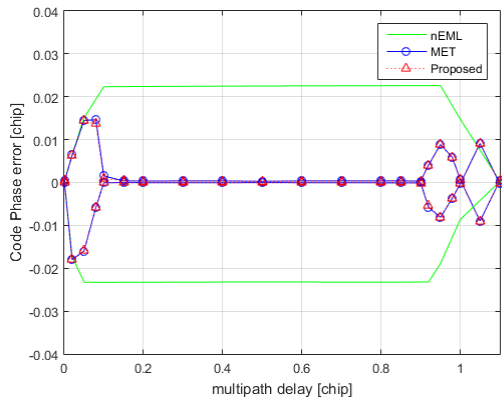


Fig. 9. Multipath error envelope

TABLE II. COMPUTATIONAL COST FOR MULTIPATH MITIGATION TECHNIQUE

Multipath mitigation technique	Computational cost
Wide correlator	1
Narrow Correlator	1.06
MET	1.33
Proposed technique	1.17

V. CONCLUSIONS

In this paper, we designed a performance evaluation platform for multipath mitigation. In this platform, the MET technique is implemented to compare the proposed technique and the proposed technique. In this paper, we simulated Narrow Correlator, MET and proposed techniques. As a result, we confirmed that the proposed technique is superior to Narrow Correlator and similar to MET.

REFERENCES

- [1] A. J. Van Dierendonck, P. Fenton and T. Ford, "Theory and Performance of Narrow Correlator Spacing in a GPS Receiver", *Journal of The Institute of Navigation.*, vol. 39, No. 3, pp. 265-283, Fall 1992.
- [2] B. townsend and P. Fenton, "A Practical Approach to the Reduction of Pseudorange Multipath Errors in a L1 GPS Receiver", *proceedings of ION GPS-94, Salt Lake City, September 1994.*
- [3] R. Van Nee, J. Siereveld, P. Fenton, and B. Townsend, "The Multipath Estimating Delay Lock Lopp : Approaching Theoretical Limits," *proceedings of IEEE PLANS 94, Las Vegas, April 1994.*

Using smartphones for positioning in a multipath environment

Saemundur E. Thorsteinsson*, Greipur G. Sigurdsson⁺

*University of Iceland, Electrical and Computer Engineering, Reykjavik, Iceland, saemi@hi.is

⁺Icelandic Road and Coastal Administration, Reykjavik, Iceland

Summary

In this paper, measurements are presented from a few generations of smartphones. The measurements are based on the existing core satellite constellations without any augmentation systems. Measurements have been taken using a few generations of smartphones. A comparison of the results is presented. Smartphone positioning can be prone to error in a shadow-rich, multipath environment common in cities.

Motivation

People have become very dependent upon their smartphones for positioning and navigation in cities. The positioning is usually based on GNSS but Wi-Fi and triangulation of mobile base stations are sometimes used for positioning and location-based services are increasingly important features for mobile terminals. The city environment can be disadvantageous for GNSS positioning due to „urban canyons“ where high buildings cast their shadow on to the environment and large parts of the sky cannot be seen from the smartphone. The environment is also reflective causing satellite signals' multipath which can be detrimental for the positioning accuracy. Furthermore, the GNSS antennas used in mobile phones are usually no more sensitive to right hand circular polarised signals than they are to left hand circular polarised signals, therefore offering no attenuation to multipath.

Results

The smartphones were located in a reflective shadow rich city environment. The measurements are compared to a known position in World Geodetic System – 1984 (WGS-84). A sample result is shown in Fig. 1 where the correct position is shown as a red square and individual measurements as blue dots. The Figure indicates a fixed error of about 25 m.

Figures

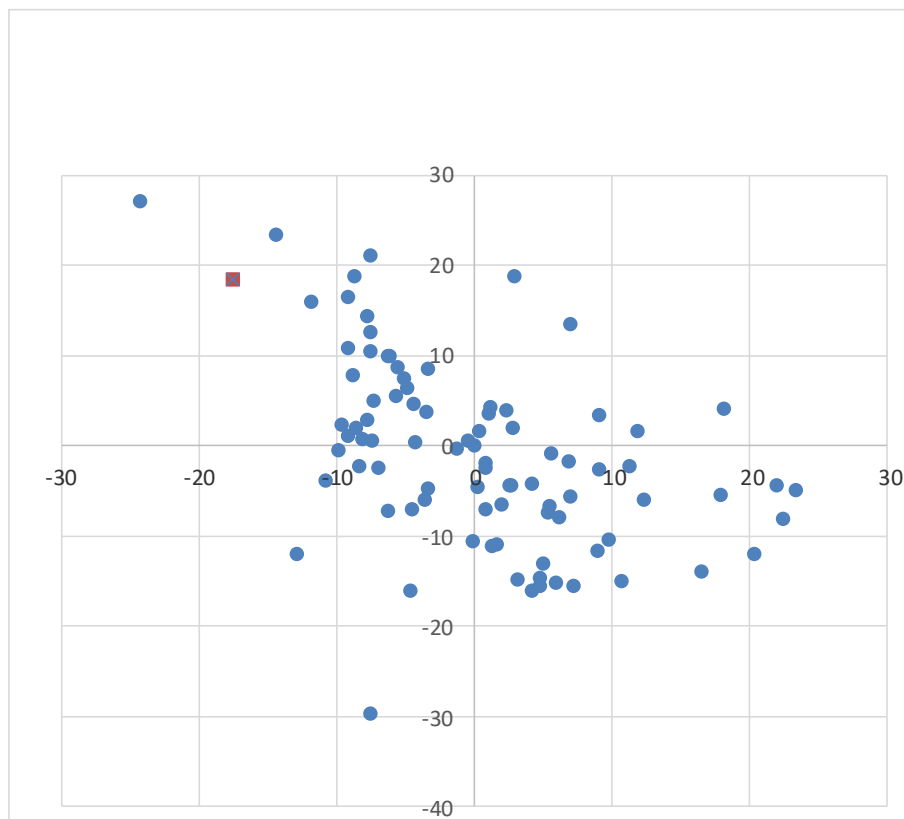


Figure 1. A scatter diagram from measurements in a shadow-rich multipath city environment using a smartphone, Samsung Galaxy S5. The average value is in the middle and the axes are in metres. The “correct position is marked as a red square.

A proposed fault detection and exclusion method applied to multi-GNSS single-frequency PPP

Anna Innac, Salvatore Gaglione, Salvatore Troisi

Department of Science and Technology
University of Naples Parthenope
Napoli, Italy
[anna.innac; salvatore.gaglione;
salvatore.troisi]@uniparthenope.it

Antonio Angrisano

G. Fortunato University
Benevento, Italy
antonio.angrisano@unifortunato.eu

Abstract— In the last few years, Precise Point Positioning (PPP) has become widespread as a standalone positioning technique. Unlike classical GNSS point positioning, which uses the pseudorange observables from four or more visible satellites and the broadcast ephemeris to obtain the user instantaneous position, PPP takes the advantage of the more precise carrier phase measurements, attempting to account for all the GNSS errors and biases. PPP is able to provide accuracy level comparable to differential positioning. In particular, the single-frequency (SF) PPP technique is attracting great interest, since SF GNSS devices are widely used for most positioning and navigation applications. For this aim, the paper proposes a SF-PPP approach based on the use of code and single-frequency ionosphere-free linear observables combination, collected from GPS and Galileo systems. In addition, an integrity monitoring algorithm is modified to be applied to SF-PPP for the detection, isolation and the removal of faulty measurement sources. The proposed strategy is tested using real and simulated data gathered in static mode. Results demonstrate the effectiveness of the proposed integrity monitoring algorithm, applied to SF-PPP.

Keywords—PPP, Single-frequency, GNSS, RAIM.

Full paper in IEEE Xplore



ISBN 978-91-88041-14-2